INFORMATION TO USERS

This manuscript has been reproduced from the microfilm master. UMI films the text directly from the original or copy submitted. Thus, some thesis and dissertation copies are in typewriter face, while others may be from any type of computer printer.

The quality of this reproduction is dependent upon the quality of the copy submitted. Broken or indistinct print, colored or poor quality illustrations and photographs, print bleedthrough, substandard margins, and improper alignment can adversely affect reproduction.

In the unlikely event that the author did not send UMI a complete manuscript and there are missing pages, these will be noted. Also, if unauthorized copyright material had to be removed, a note will indicate the deletion.

Oversize materials (e.g., maps, drawings, charts) are reproduced by sectioning the original, beginning at the upper left-hand corner and continuing from left to right in equal sections with small overlaps. Each original is also photographed in one exposure and is included in reduced form at the back of the book.

Photographs included in the original manuscript have been reproduced xerographically in this copy. Higher quality 6" x 9" black and white photographic prints are available for any photographs or illustrations appearing in this copy for an additional charge. Contact UMI directly to order.

UMI

A Bell & Howell Information Company
300 North Zeeb Road, Ann Arbor MI 48106-1346 USA
313/761-4700 800/521-0600

Experimental Studies of Deposition by Debris Flows: Process, Characteristics of Deposits, and Effects of Pore-Fluid Pressure

by

Jon J. Major

A dissertation submitted in partial fulfillment
of the requirements for the degree of

Doctor of Philosophy

University of Washington

1996

Approved by Thomas C. Dunne
Chairperson of Supervisory Committee

Program Authorized to Offer Degree Geological Sciences

Date February 5, 1996

In presenting this dissertation in partial fulfillment of the requirements for the Doctoral degree at the University of Washington, I agree that the Library shall make its copies freely available for inspection. I further agree that extensive copying of this dissertation is allowable only for scholarly purposes, consistent with "fair use" as prescribed in the U.S. Copyright Law. Requests for copying or reproduction of this dissertation may be referred to University Microfilms, 1490 Eisenhower Place, P.O. Box 975, Ann Arbor, MI 48106, to whom the author has granted the "right to reproduce and sell (a) copies of the manuscript in microform and/or (b) printed copies of the manuscript made from microform."

Signature Jon J. Myr

Date February 5, 1996

University of Washington

Abstract

Experimental Studies of Deposition by Debris Flows: Process, Characteristics of Deposits and Effects of Pore-Fluid Pressure

by Jon J. Major

Chairperson of the Supervisory Committee: Professor Thomas Dunne
Department of Geological Sciences

This study examines deposition by experimental debris flows (to 15 m^3) composed of mixtures of gravel (to 32 mm), sand, and loam using the 95-m-long, 2-m-wide, 31° U.S. Geological Survey debris-flow flume. It examines the depositional process, relations between flow kinematics and deposit character, and fluid pressure in debris at, and following, deposition. These data permit evaluation of competing hypotheses regarding debris-flow deposition.

Experimental debris flows invariably developed surges; deposits developed abruptly on a 3° runout slope as sediment transported by shallow (< 10 cm deep) surges accumulated. Finer source debris formed thinner deposits. Deposits developed by a combination of forward pushing, vertical accretion, and lateral shunting of previously deposited debris. Unsaturated debris flows deposit sediment dominantly through forward pushing and sourceward horizontal accretion; deposits are lobate, have large aspect ratios (≥0.5), and commonly exhibit arcuate surface ridges. Saturated debris flows progressively deposit sediment primarily through vertical accretion from successive surges; deposits are lobate, but elongate, have small aspect ratios (≤0.3), nearly flat surfaces, and lack prominent surface ridges. Observed progressive accretion is contrary to commonly assumed *en masse* sedimentation by debris flows.

The depositional process is recorded primarily by deposit morphology and surface texture and is not faithfully registered by interior sedimentary texture. Homogeneous internal textures can be interpreted as the result of deposition by a single surge. Individual debris

flows as well may leave little distinctive signature in the sedimentary record. Superposed deposits from similar yet separate flows could not be distinguished without the aid of an artificial marker horizon. These results show that methods of estimating flow properties from deposit thickness or from relations between particle size and bed thickness are in error. Relations between sediment composition and deposit thickness are incompatible with deposition by a simple viscoplastic material.

Experimental debris flows deposited sediment despite measured basal fluid pressures that were lithostatic to nearly lithostatic. These data refute hypotheses that propose uniform fluid-pressure dissipation as a control on deposition. Modeling and laboratory analyses of gravity-driven consolidation reveal that characteristic pressure-dissipation times in quasistatic debris exceed surge periods and durations typical of debris flows. Numerical simulations of transient changes in fluid-pressure and effective-stress fields in 2-dimensional quasistatic domains reveal that excess fluid pressures remain elevated, and effective stresses depressed, everywhere except adjacent to margins in wide thin bodies for time scales that exceed durations typical of debris flows. Observed deposition, measured fluid pressures, and modeling results suggest that debris-flow deposition is controlled by a balance between a diminishing driving stress and locally increasing resisting stresses along flow margins rather than by a uniform bodywide increase of effective stress.

TABLE OF CONTENTS

LIST OF FIGURES

LIST OF TABLES

Number *Page*

ACKNOWLEDGMENTS

There is a Chinese proverb that claims that before a person accomplishes great things he must look foolish to the crowd. I'm certain there were moments when that proverb was appropriate as I grappled with chaotic ideas in the formative stages of this dissertation. With sage advice and sometimes not so gentle prodding, Tom Dunne, Dick Iverson, Dave McTigue, Jody Bourgeois, and Lew Wedgewood prevented me from wandering down dark alleys in the pursuit of an important solvable problem, and provided constructive criticism when I finally put thoughts on paper and wrote this dissertation. Tom Dunne and Dick Iverson played especially important roles in the development and outcome of this dissertation, and I am grateful for their tutelage. I am indebted to Tom for our many discussions, for his probing questions which I could never answer at the time, and for his support during this endeavor. His penchant for asking challenging questions forced me to think about things a little more deeply than I might have otherwise. I am especially indebted to Dick for freely sharing his ideas and data on debris flows during our many discussions and debates. Dick is the person foremost responsible for my interest in, and pursuit of, fluid pressures and fluid flow in mass movements. Never one to shy away from challenging dogma, his criticisms of the presentation of ideas in an earlier draft have made this written product a much stronger document than it was.

Collecting the data required for this study, especially from the large-scale experiments at the U.S. Geological Survey debris-flow flume, was labor intensive, and I thank many individuals for their assistance in bringing this study to fruition. Rick LaHusen and Kevin Hadley provided invaluable assistance with the nuts and bolts of data acquisition. Dick Iverson, Carl Zimmerman, Brooke Fiedorowicz, Tony Bequette, Steve Brantley, Carolyn Driedger, Mark Reid, Tom Hale, Kurt Spicer, Dennis Saunders, Dallas Childers, Ted Melis, Ron Shreve, Colleen Riley, Gordon Stratford, and Ben Schonfeld assisted with surveys of the experimental deposits; Carl Zimmerman and Colleen Riley helped reduce those data. Brooke Fiedorowicz ably conducted the extensive suite of compaction-permeameter tests and helped map deposit morphology and sedimentology. Tom Pierson willingly spent a couple of days in the rain helping with the tedious task of measuring particle orientations. Dave McTigue and Steve Macias, University of Washington, and Bob Donaghe, U.S. Army Corps of Engineers, conducted soil tests in an effort to define physical properties of the debris-flow sediments discussed in this work. Tony Bequette fabricated several pieces of equipment and turned sketches and dreams into reality. Dr. Albert Kobayashi and Duc Tran, University of Washington

Department of Mechanical Engineering, graciously provided access to the finite-element code ABAQUS, as well as a set of user's manuals. My trip to Jiangjia Gully, China, was made possible through the efforts of Harvey Jobson and Anna Lenox of the U.S. Geological Survey. Dr. Zhang Shucheng and Wang Yuyi graciously hosted my visit to the Dongchuan Debris-Flow Observatory, and my traveling companion Ted Melis made it a trip to remember.

Discussions, and sometimes contentious debates, with members of my committee and various colleagues helped solidify my thinking during the course of this study. I thank Dave McTigue and Evelyn Roeloffs for patiently listening to and answering my many questions about the mechanics of porous media. Jim Vallance, Kelin Whipple, Tom Pierson, Kevin Scott, Juli Morgan, Ron Shreve, Hiroshi Suwa, Ted Melis, and Takashi Yamada contributed to discussions regarding the significance of the characteristics of the experimental, as well as natural, debris-flow deposits, and critiqued many of my ideas.

This dissertation would not exist if not for the support of John Costa of the U.S. Geological Survey Cascades Volcano Observatory. John encouraged my decision to apply for the USGS graduate training program, supported my decision to return to school, and granted me the necessary time, through a leave of absence, to fulfill course work and residency requirements for this degree. Most of all, upon my return to CVO, he agreed that a study on the mechanics of debris-flow deposition was relevant to the mission of CVO and worthy of support by the USGS; he expected in return only that some good science come from this endeavor. I am extremely grateful to John for risking this investment in me and granting me this opportunity.

Finally, I thank my wife, Michelle, for her support during pursuit of this degree. She soothed frayed nerves, lifted my spirits as necessary, endured a long-distance marriage, spent many hours alone as my working days became ever longer, and helped process necessary pages during the final push to complete the written document.

Dedicated to HJM, RJJ, and HXG

-- three who saw this labor begin, but never saw it end

CHAPTER 1

INTRODUCTION

"A wall of boulders, rocks of all sizes, and oozing mud suddenly appear around the bend in a canyon preceded by a thunderous roar. As the boulder-choked wall passes, the channel remains filled with a debris-laden torrent of mud and boulders clanking and grinding together. The debris flows across an alluvial fan, engulfing structures and cars in its path, covering roads, fields and pastures with a blanket of thick muck, and slowly coming to a stop as the debris spreads in a lobate form with a steep terminal snout and margins....while mobile it flows much like wet concrete..." (Johnson, 1984).

The process so vividly described by Johnson, known as debris flow, is one of the most significant geomorphic processes in steep, mountainous terrain worldwide. A debris flow is a gravity-driven flow of a water-saturated, highly concentrated mixture typically composed of poorly sorted rock, soil, organic matter, and sundry debris. It is part of a broader spectrum of geologic agents classified as sediment gravity flows -- flows in which fluid and sediment are intimately mixed and the whole mass driven by gravity rather than gravity acting only on the fluid, which then transports sediment, as is the case with typical streamflow (e.g., Middleton and Southard, 1977). This agent of mass movement, both awe inspiring and potentially lethal, has fascinated, yet perplexed, earth scientists and engineers for several decades. A single flow can transport a volume of sediment equivalent to that moved cumulatively during several centuries by other geomorphic agents operating at lesser rates of landscape denudation (e.g., Selby, 1982). Debris flows occur in a wide range of geologic and climatic settings (e.g., Innes, 1983; Costa, 1984); they have volumes that range from a few tens of cubic centimeters (Johnson, 1970) to more than 100 million cubic meters (e.g., Janda and others, 1981; Fairchild, 1985; Pierson, 1995); they have velocities that range from a few to a few tens of meters per second (e.g., Pierson, 1985a,b, 1986; 1995; Fairchild and Wigmosta, 1983; Major and Voight, 1986; Major and Newhall, 1989; Rodolfo and others, 1989; Waitt, 1989; Cruden and Lu, 1992; Harris and Gustafson, 1993; DeGraff, 1994; Major and others, 1996); and they can affect lowlands more than 100 km from their initial source, particularly in volcanic regions (e.g., Scott, 1988a; Pierson, 1995). Debris flows have become the subject of heightened scientific and engineering interest as population centers have expanded into mountainous regions and increased the potential for encounters between humans, their civil works, and natural geomorphic hazards.

The significance of debris flows as a geomorphic agent was recognized nearly seven decades ago (Blackwelder, 1928), but only in the past few decades has their significance as a socio-economic force been widely appreciated. This aspect of debris flows has been poignantly recognized in several recent catastrophes, many associated with volcanic eruptions. Landslides and debris flows, triggered by rainfall and rapid melting of heavy winter snowpack, were so extensive in Utah in 1983 that 22 of 28 counties were declared federal disaster areas (Bowles, 1985). During the 1985 eruption of Nevado del Ruiz volcano in Colombia, more than 20,000 people perished when a large debris flow, triggered by the rapid melting of snow and ice at the volcano's summit, swept through the town of Armero (Pierson and others, 1990). In 1991, the eruption of Pinatubo volcano in the Philippines dispersed more than 5 cubic kilometers of volcanic sediment into surrounding valleys (W.E. Scott and others, 1996). Much of that sediment subsequently has been mobilized as debris flows by typhoon rains and has laid to waste more than 300 square kilometers of primarily agricultural land (Rodolfo and others, 1996; Pierson and others, 1996). These recent catastrophes emphasize the intensifying need to identify catchments in which debris flows will occur, and to understand and ultimately predict their initiation, their physical behavior once they occur, and the factors that control their transport and deposition (Costa, 1984; Whipple, 1992; Davies, 1993).

Progress in understanding debris flows has been made on several fronts: (1) Several field studies have advanced knowledge of the initiation, movement, downstream transformation, and subsequent impact of debris flows (e.g., Janda and others, 1981; Pierson, 1985b; Gallino and Pierson, 1985; Pierson and Scott, 1985; Costa and Wieczorek, 1987; Webb and others, 1988, 1989; Scott, 1988a,b; Weirich, 1989; Pierson and others, 1990; Whipple and Dunne, 1992; DeGraff, 1994; Whipple, 1994; Major and others, 1996). (2) Conceptual advances have been made toward understanding debris-flow initiation -- particularly the occurrence of and transformation of landslides to debris flows (Iverson and Major, 1986; Ellen and Fleming, 1987; Iverson and LaHusen, 1989; Eckersely, 1990; Reid, 1994; Anderson and Sitar, 1995). (3) Recent laboratory studies have focused on measurements of the rheological behavior of natural-sediment slurries to define parameter sensitivity and to provide constraints for applications of mathematical models (e.g., O'Brien and Julien, 1988; Murray, 1990; Phillips and Davies, 1991; Major and Pierson, 1992; Dade, 1992; Major, 1993; Coussot and others, 1993; Coussot and Piau, 1995). (4) Large-scale experiments are testing and refining new hypotheses regarding the mechanical behavior of debris flows (Iverson and LaHusen, 1993a,b; Iverson and others, 1994; Iverson, 1995a).

Much of what we know about the flow behavior and the transport and deposition of sediment by debris flows has come from limited observations of the natural process, analysis of small-scale experiments, and *interpretation* of field deposits (e.g., Jahns, 1949; Sharp and Nobles, 1953; Johnson, 1965, 1984; Fisher, 1971; Hampton, 1975; Okuda and others, 1980; Pierson, 1980; Janda and others, 1981; Costa and Jarrett, 1981; Li and others, 1983; Costa, 1984; Costa and Williams, 1984; Koster and Steel, 1984; Pierson and Scott, 1985; Pierson, 1985a, 1986; Major and Voight, 1986; Hooke, 1987; Scott, 1988a; Rodolfo and others, 1989; Pierson and others, 1990; Blair and McPherson, 1994). Thus, despite the progress that has been made on various aspects of the debris-flow problem, relatively little actually is known of the relation between the behavior of debris flows, the depositional process, and the characteristics of their deposits. Nevertheless, geologists commonly infer kinematic behavior and rheological properties of debris flows from the sedimentologic, morphologic, and stratigraphic characteristics of debris-flow deposits and from mudlines along channels (e.g., Fink and others, 1981; Voight and others, 1983; Johnson, 1965, 1984; Nemec and Steel, 1984; Shultz, 1984; Pierson, 1985a; Major and Voight, 1986; Van Steijn and others, 1988; Scott, 1988a,b; Rodolfo and others, 1989; Harris and Gustafson, 1993; Masson and others, 1993; DeGraff, 1994; Kim and others, 1995). In contrast to the interpretations drawn in several studies, Enos (1977) and Postma (1986) argue that deposit character is set during the final stages of movement and perhaps bears little relation to the dominant flow behavior during the primary transport stage, a disturbing conclusion that indicates that little insight regarding flow behavior can gained from studies of deposits.

Competing rheological models have been proposed to explain the features observed in flowing debris, the mobility and transport capacity of flowing debris, and the characteristics of the resulting deposits. These models can be grouped broadly into three categories that describe the dominant process of momentum exchange and energy dissipation: (1) a single-phase viscoplastic material model; (2) a multiphase dilatant-grain-flow model; and (3) a multiphase effective-stress model. Johnson (1965, 1970, 1984) describes many features of debris flows and their deposits and assumes that debris flows can be adequately described as single-phase, viscoplastic materials, namely Bingham fluids. In this model, material remains rigidly elastic until applied shear stress exceeds a threshold value, the plastic yield strength. Once the yield strength of the debris has been exceeded, the mass flows as a linearly viscous fluid and energy dissipation occurs solely through fluid viscosity. Plastic yield strength and fluid viscosity, therefore, are the sole factors that control flow mobility and sediment deposition. As long as shear stress driving fluid motion exceeds the plastic yield strength the flow

remains mobile. When the basal shear stress driving fluid motion drops below the yield strength of the debris, the flow abruptly stops and deposits its sediment *en masse*, effectively "freezing" in place. This model neglects interactions among particles, such as collisions, rubbing, and grinding among at least the coarsest clasts, and interactions between particles and the channel boundary, which commonly are observed in debris flows (e.g., Costa and Williams, 1984).

The multiphase nature of debris flows and the importance of particle interactions have been pointed out by several investigators (e.g., Johnson, 1965, 1984; Takahashi, 1981, 1991; Iverson and Denlinger, 1987; Iverson and LaHusen, 1993a; Iverson, 1994). Takahashi and coworkers (Takahashi, 1981, 1991; Takahashi and others, 1992) attempt to account for the multiphase nature of debris flows and have proposed a model that describes the transport and accumulation of debris based on the concept that momentum transfer and energy dissipation occur exclusively by particle collision (Bagnold; 1954; Takahashi, 1981). In this model, rapid shearing causes an assemblage of uniformly sized grains to dilate. Particle collisions create a dispersive pressure that maintains the ability of the granular mass to shear. When particle collisions become insufficiently vigorous, as the driving shear stress diminishes, the dispersive pressure drops, the material ceases to maintain its dilated state, and the mass locks up, again effectively "freezing" *en masse*. Although this model clearly considers particle interactions, it has several shortcomings (Iverson and Denlinger, 1987; see Chapter 5). One severe shortcoming is that for typical values of grain friction angle, fluid density, and solid-particle density, the model constrains flow mobility (and therefore deposition) to slopes much steeper (~14°-18°) than the slopes across which many debris flows actually travel (see Table 2.1).

Models that conceptualize debris flows and landslides as bodies of cohesionless material in which effective stresses and excess pore-fluid pressures are important also have been proposed (e.g., Hooke, 1967; Shreve, 1968; Hutchinson, 1986; and Iverson and LaHusen, 1993a). In these models, pore-fluid pressures modify the dynamics and deposition of debris. Maintenance of fluid pressures that are in excess of hydrostatic has been proposed as a mechanism that may enhance the mobility of landslides and debris flows and may provide particle support (e.g., Shreve, 1968; Hampton, 1975; Pierson, 1981). Drainage of pore fluid from the granular debris, and consequent reduction of excess fluid pressures and enhancement of effective stresses, has been proposed as a mechanism that induces deposition (e.g., Hooke, 1967, 1987; Hutchinson, 1986). For example, Shreve (1968) proposed that a thin layer of compressed, highly pressurized air trapped at the base of the Blackhawk (CA) landslide

supported the overlying weight of the debris and accounted for that landslide's extraordinary mobility. He also proposed that gradual leakage of this pressurized fluid along the margins and through the mass increased frictional resistance at the base of the mass, which brought the landslide to a halt. Hutchinson (1986), too, proposed generation and dissipation of excess pore-fluid pressures as an explanation for the mobility and runout distance of cohesionless debris flows. In his model, undrained loading leads to a uniform distribution of excess fluid pressure and to the temporary loss of shear strength of the mass. A rigidly translating body of debris remains mobile until the basal excess pore-fluid pressure diminishes to the extent that the stress resisting sliding motion exceeds the driving shear stress. Hutchinson used a simple, one-dimensional consolidation model to predict the time necessary for the excess pore-fluid pressure at the base of the otherwise rigid mass to diminish by the necessary amount.

Previous investigations have attempted to test certain aspects of some hypotheses in small-scale laboratory experiments. However, results from small-scale experiments are not necessarily applicable to the natural process. Previous experimental studies commonly have employed small quantities (≤100 liters) of fine-grained debris, such as cohesive clay slurries. Physico-chemical effects related to cohesive debris, which are important at the small scale, are probably negligible at the field scale (e.g., Middleton, 1990), and inertial effects important at the field scale are not well-simulated at the small laboratory scale. More relevant insights regarding flow and deposition of debris would be gained from careful measurements and analyses of natural flows. However, the capricious nature of debris flows makes systematic observations and measurements of natural events both difficult and dangerous (e.g., Okuda and others, 1980; Li and others, 1983; Pierson, 1986). Even when natural events are observed, measurements typically include surface and flow-front velocities, flow depth, discharge, and composition--data that are important, but not necessarily the data that are critical to evaluate competing hypotheses regarding transport and deposition of debris.

The current state of knowledge regarding the linkage between debris-flow behavior, the depositional process, and deposit character is based primarily on *interpretation* of deposits; studies of natural flows are limited and data are sparse, and existing experimental studies are small scale and do not necessarily preserve proper similitude. Thus, there exists a critical need to study debris-flow behavior, deposition, and debris-flow deposits under conditions in which the size, timing, and nature of the flow can be reasonably controlled, in which environmental parameters such as composition,

volume, water content, and channel confinement can be varied, and at a scale that approaches the natural process. This dissertation therefore focuses on a study of large-scale experimental debris flows (to 15 m^3). I focus on the depositional process, characteristics of resulting deposits, and the effects of pore-fluid pressure in an effort to evaluate the link between process and form, and to evaluate two competing models of debris-flow deposition--the Bingham model and the fluid pressure/effective stress model.

Advances in computer technology and microelectronics over the past several years have made possible new forms of data acquisition. These technical advances combined with the construction of a large debris-flow flume by the U.S. Geological Survey provided an opportunity not only to study relations between debris-flow deposits and experimental flows having known physical properties and flow behavior, but also to measure, for the first time, fluid pressures in debris flows as they decelerate and deposit sediment. These kinds of measurements are necessary to evaluate proposals regarding the effects of fluid pressures on debris-flow deposition.

To understand the effects of pore-fluid pressures on debris-flow deposition and on the post-depositional behavior of debris-flow deposits, I have examined: (1) the nature of pore-fluid pressures in debris flows as they decelerate and deposit sediment; (2) the nature of fluid drainage and pressure-dissipation in large experimental debris-flow deposits; (3) the characteristic time scales over which excess pore-fluid pressures dissipate in debris-flow deposits composed of a range of sediments; (4) the influence of substrate permeability on the drainage of pore fluid and the dissipation of fluid pressure in debris-flow deposits; and (5) whether local dissipation of excess fluid pressure is more, or less, important to debris-flow deposition than bodywide dissipation of excess fluid pressure in the sediment mass.

The objectives of the work presented in this thesis are to test the following hypotheses: (1) Kinematic behavior of debris flows and the nature of the depositional process are faithfully recorded and uniquely preserved by sedimentologic, stratigraphic, and morphologic features of their deposits. (2) Uniform, bodywide dissipation of fluid pressures in excess of hydrostatic rather than plastic yield strength controls deposition by debris flows. (3) Dissipation of excess fluid pressures during late-stage movement of debris flows is significantly enhanced by substrates that are one or more orders of magnitude more permeable than the flowing debris.

The work presented in this thesis is drawn from a blend of field study; analysis of deposits from large-scale debris-flow experiments; measurement of fluid pressures in large-scale experimental debris flows and their deposits; small-scale laboratory experiments on one-dimensional, gravitationally driven consolidation of granular slurries; and analytical and numerical analysis of the transient behavior of excess-fluid-pressure and effective-stress fields during gravitationally driven deformation in both one- and two-dimensional domains. Although the work is a blend of these approaches, each chapter is written as a separate study. The chapters are drawn together through appropriate cross reference, and a synthesis of the whole study is provided at the end.

In chapter 2, I present the findings of my studies of deposits from several large-scale experimental debris flows (to 15 m^3) at the U.S. Geological Survey debris-flow flume in west-central Oregon, and I supplement those findings with study of recent debris-flow deposits in Jiangjia Ravine, southwest China, from flows that behaved in a fashion similar to those simulated by the large-scale experiments. Study of the experimental deposits is linked, for the first time, to detailed kinematic behavior of the parent flow. These analyses address the first objective of this work outlined above and provide, for the first time, experimentally founded constraints for the sedimentologic and geomorphic interpretation of debris-flow deposits.

Chapter 3 presents the measurements of fluid pressures made in the runout area at the debris-flow flume as experimental flows decelerated and deposited sediment. The measurements document that a significant proportion of the total bed normal stress in the debris flow during waning-stage movement and deposition is balanced by pore-fluid pressure, and that excess pore-fluid pressure dissipates rapidly to gradually depending upon the composition and depth of the sediment. These measurements suggest that the post-depositional behavior of the pore-fluid pressure may be described by a simple model of fluid-pressure diffusion and soil consolidation. In this chapter, I develop a conceptual framework for gravity-driven, one-dimensional consolidation of granular slurries having incompressible constituents in terms of a simple, linear formulation, which is cast in terms of the transient behavior of excess pore-fluid pressures. Following development of this simple theory, predictions from the model are compared to fluid-pressure and surface-displacement data collected from a series of simple laboratory experiments that used sediments representative of natural debris flows and that allowed substrate permeability to vary. The model is also compared to fluid-pressure data collected from deposits of the large-scale experimental debris flows.

Debris flows and their deposits are, however, three-dimensional bodies having width and length as well as depth. Thus, an obvious concern regarding evolution of the fluid-pressure and effective-stress fields in field-scale deposits is the effect of multidimensional drainage. Chapter 4 extends the treatment of gravity-driven consolidation to a two-dimensional domain. This chapter explores, through numerical experiments, the consequences of having lateral, as well as vertical, flow paths on the evolution of the fluid-pressure and effective-stress fields, the consequences of considering the evolution of those fields as coupled and uncoupled entities, and the consequences of having a domain in which sediment permeability varies in space.

Measurements of fluid pressures in decelerating debris flows and analysis of the evolution of the excess-fluid-pressure and effective-stress fields yields considerable insight into the mechanics of debris-flow deposition, into post-depositional behavior of debris-flow deposits, and into some of the sedimentologic features (or lack thereof) unveiled in Chapter 2. These data and analyses address the second two hypotheses outlined above. Ramifications of the physical and numerical experiments as they relate to debris-flow deposition and deposit stability are discussed in chapter 5.

CHAPTER 2

DEBRIS-FLOW DEPOSITION: ANALYSIS OF LARGE-SCALE EXPERIMENTS

INTRODUCTION

Geologists commonly infer the flow conditions and physical properties of debris flows from the morphologic, sedimentologic, and stratigraphic characteristics of their deposits, from mudlines along channels, and from their physical interactions (such as scour (e.g., Howard, 1995)) with channels. But how good are those inferences? For nearly three decades, deposition of sediment by debris flows and kindred high-sediment-concentration fluids has been envisaged as *en masse* emplacement, a consequence of the principal models that describe flow mobility and deposition, namely the viscoplastic, the dispersive-stress, and the sliding-consolidation conceptual models (e.g., Johnson, 1965, 1970; Sparks, 1976; Middleton and Southard, 1977; Hiscott and Middleton, 1979; Takahashi, 1981; Fink and others, 1981; Pierson, 1981; Costa and Jarrett, 1981; Lowe, 1982; Innes, 1983; Costa, 1984; Shultz, 1984; Hutchinson, 1986; Major and Voight, 1986; Carey; 1991; Battaglia, 1993; Masson and others, 1993; Blair and McPherson, 1994; Kohlbeck and others, 1994; Whipple, 1994; Kim and others, 1995). Within the context of a Bingham model, rheological properties of flow, such as material yield strength and viscosity, commonly have been estimated from the thickness of deposits, from the size of the largest particles supported within a deposit, and from estimates of flow velocity and channel geometry (e.g., Johnson, 1984). Some investigators have also used relations between maximum particle size and bed thickness to infer depositional processes, grain-support mechanisms, and strength properties of flows (e.g., Nemec and Steel, 1984; Walton and Palmer, 1988; Collinson and Thompson, 1989; Arguden and Rodolfo, 1990); others have used inferred rheological properties to reconstruct estimates of paleoslope gradients (e.g., Kim and others, 1995).

Properties of geologic processes inferred from deposits are used widely in interpretive studies. Depositional processes, grain-support mechanisms, and paleoslope gradients commonly are used as criteria for establishing depositional environments of sediments preserved in the geologic record. Incorrect assessments of these properties can lead to incorrect environmental interpretations (e.g., Blair and McPherson, 1994). When evaluations of geologic hazards hinge on proper interpretations, assessments of the properties of geologic processes assume greater significance. For example, estimates of debris-flow yield strength and viscosity are used in some numerical models that predict

areas of inundation by debris flows as part of flood-hazard assessments on alluvial fans and urban floodplains (e.g., O'Brien and others, 1993). Estimates of these properties commonly are drawn from laboratory experiments and from field analyses of debris-flow deposits. Table 2.1 summarizes observed and estimated properties of several debris flows.

Contrary to the common assumption that high-sediment-concentration fluids deposit sediment *en masse*, Fisher (1966) and Branney and Kokelaar (1992) have shown that massive pyroclastic-flow deposits can result from prolonged incremental sedimentation. Therefore, sedimentary textures in many otherwise massive pyroclastic-flow deposits can result from incremental, and not *en masse*, deposition. Pyroclastic flows are cohesionless grain flows that are similar to debris flows except that the fluid filling pore spaces is hot gas rather than liquid water. Because debris-flow deposits exhibit many sedimentary characteristics similar to those of pyroclastic-flow deposits (e.g., Sparks, 1976), it seems reasonable to ask whether or not it is possible that debris-flow deposits, too, can result principally from progressive incremental deposition rather than from *en masse* emplacement and, if so, under what conditions? Smith and Lowe (1991) summarized features of deposits from large volcanic debris flows and suggested that deposition from such high-discharge events need not always occur by *en masse* sedimentation. Lacking a sufficient physical basis for a strong conclusion, this suggestion remains speculative and its applicability to smaller nonvolcanogenic debris flows remains uncertain. Vallance (1994) presents experimental evidence that dry mixtures of small glass beads (less than 2 mm in diameter) flowing down a laboratory flume can form otherwise massive deposits in an incremental fashion, and he presents sedimentologic evidence that suggests the deposit of the Osceola Mudflow from Mount Rainier volcano, Washington, may have resulted from incremental deposition rather than *en masse* emplacement as has been previously supposed.

There are few field studies that link direct observation of flow behavior and depositional process to characteristics of deposits (e.g., Lawson, 1982). The capricious nature of many high-sediment-concentration flows makes systematic observations and measurements of natural events both difficult and dangerous. Thus, interpretive studies of deposits typically lack corroboration by direct observation. Furthermore, in contrast to numerous experimental studies of water flow and associated fluvial deposition, few studies of sediment deposition by debris flow under controlled conditions have been made. Existing experimental studies of debris-flow deposition discuss results from small-scale cohesive flows; channels typically have been less than 20 cm wide and a few meters or less long,

volumes of source material have been limited to about 100 liters, and debris commonly has consisted of clay, sand, or clay/sand slurries (e.g., Hampton, 1975; Hooke and Rohrer, 1979; Mizuyama and Uehara, 1983; Van Steijn and Coutard, 1989; Zimmerman, 1991; Liu, 1995). Experiments at these scales, however, can be influenced by physico-chemical effects, especially in cohesive debris, that may not be important at the field scale (Iverson and LaHusen, 1993a) and they typically do not simulate inertial effects which are significant at the field scale. In this chapter I present results from several experiments at a large debris-flow flume. These results represent one aspect of a cooperative study designed to enhance scientific understanding of debris flows from initiation to deposition by examining large-scale flows under controlled conditions (Iverson and others, 1992). Experiments in the cooperative study have been designed to develop, test, and refine mathematical models describing the transport mechanics of debris flows; to examine flow of debris against obstacles and through curved channels; and to study the depositional process of large experimental flows and the morphology, sedimentology, and stratigraphy of the resulting deposits. This chapter focuses on the latter two objectives. As part of this comprehensive research program experimental debris flows as large as 15 m^3 in volume were released and their kinematic behavior and depositional process documented. Deposits subsequently were mapped and dissected to examine both their surficial and internal characteristics and to relate those characteristics to initial conditions of the source debris and to specific flow behavior.

LARGE-SCALE DEBRIS-FLOW FLUME

The U.S. Geological Survey (USGS), in cooperation with the U.S. Forest Service, constructed a large flume to conduct controlled experiments (Iverson and others, 1992). Located in the H.J. Andrews Experimental Forest, Willamette National Forest, Oregon (Figure 2.1), the flume facilitates experimental study of the dynamics and deposits of rapid flows of up to 20 m^3 of debris.

The flume is a reinforced concrete channel 95 meters long, 2 meters wide, and 1.2 meters deep. The smoothly bedded structure slopes 31° along the upper 88 meters and gradually flattens to a 3° runout surface across the lower 7 meters (Iverson and LaHusen, 1993a; Figure 2.2). Ten meters below the head of the flume, a steel gate, which controls the release of debris, is attached to the flume walls. In 1993 and 1994, the concrete runout surface at the flume mouth extended about 14 meters. Following the 1994 experiment season, the concrete runout area was extended to 25 meters. Beyond

the concrete the runout area is covered with gravel. Windows in the sidewall of the flume allow flows to be observed and photographed as they pass. Ports built into the channel within the flume and into the runout surface beyond the flume house sensors used to measure forces exerted by flows on the bed and pore-fluid pressures at the base of, and within, the debris mass. Ultrasonic transponders and infrared lasers are suspended over the channel and the runout area and are used to measure depth as flows sweep past the instrumented sites (Iverson and others, 1992; Iverson and LaHusen, 1993a). Still and video cameras document the release, transport, and deposition of each experimental flow from several perspectives.

EXPERIMENTAL DEBRIS FLOWS

To create a debris flow, sediment was loaded behind a steel gate at the head of the flume, saturated with water, and then released. The sediment used in the experiments discussed in this chapter is derived chiefly from local fluvial sources. Several experiments consisted of a poorly sorted mixture of sand and gravel, having clasts as large as 32 mm in diameter, that contained about 1 percent mud (defined here as particles < 63 μm in diameter) (Figure 2.3, Tables 2.2, 2.3). A few experiments used a mixture composed of gravel, sand, and loam to provide a greater quantity of mud (about 2 to 4 percent by weight; Figure 2.3, Tables 2.2, 2.3). The loam was composed dominantly of sand and silt; therefore, even the finer grained mixtures used at the flume were cohesionless (Appendix A). Though rounded, the clasts in the sediment mixtures predominantly are bladed (Figure 2.4); mean axial ratios, a:b and a:c, are 1.33 and 2.10, respectively. The form of these clasts factors strongly in the development of particle fabric discussed below.

The sediment mixtures used in the experiments were chosen on the basis of composition, size, and availability. (1) A goal of the experiments was to simulate debris flows using realistic geologic debris (Iverson and LaHusen, 1993a). The sediments chosen represent poorly sorted mixtures of cohesionless debris. Although these mixtures avoid potential effects of cohesion owing to clay, observations over the past several years show that cohesion is not important in many debris flows (Middleton, 1990). Even in some clay-rich debris flows cohesion appears to be negligible (Franz and Voight, 1995; Appendix A) (2) Mixtures composed solely of sand and gravel simulate the simplest possible system of cohesionless debris representative of realistic debris flows. Loam was added to some experimental mixtures to study effects of additions of small amounts of mud. (3) Particle size

was restricted to ≤ 32 mm to avoid excessive wear on the flume; for safety reasons (see below); and because of sediment availability. (4) Large quantities of mixtures were readily available from a local commercial source and required little custom mixing.

Experimental flows (Figure 2.5) typically are thin, rapidly moving, unsteady, and nonuniform. Following gate release, the mass of source material rapidly elongates and thins as it flows (Iverson and LaHusen, 1993a). Observations through the windows in the flume wall indicate, however, that a significant component of the downslope motion occurs as basal slip. Mean shear rates of the flowing material are probably on the order of 20 s^{-1} or less (Iverson and LaHusen, 1993a), comparable to, but typically greater than, mean shear rates inferred (from depth and velocity) for many natural debris flows (Phillips and Davies, 1991; Table 2.1).

The leading edge of each flow commonly is marked by a diffuse "wave" of saltating, coarse particles that precedes the massive body of flow (Figure 2.6). These saltating particles are highly energetic, and many particles commonly bounce over the flume walls. Partly for this reason sediment having particles larger than about 32 mm has not been used.

Experimental flows invariably develop waves that surge down the channel (Figure 2.5). These waves develop spontaneously along the channel within the massive body of the flows, but they do not always develop at the same location, nor do the same number of waves always develop. Larger, faster moving surges commonly overtook, and cannibalized, slower moving surges. Surges typically sweep down the flume at velocities from 6 to 13 m/s. At a location 67 meters downslope from the release gate, surge waves in seven experiments had an average speed of 11 m/s and a period of 1 second (Iverson and others, 1994). Inter-wave surface-particle velocities typically were on the order of 4 to 7 m/s. Waves commonly were <10 to 20 cm deep (crest to bed); inter-wave flow generally was thinner (Iverson and others, 1992, 1994). Froude numbers of the experimental flows commonly were greater than 2 and approached values as large as 13.

The pulsing nature of the experimental flows is not uncommon in natural debris flows. Flow surges have been noted in a variety of physiographic settings, and commonly have periods that range from a few seconds to several minutes or longer (e.g., Jahns, 1949; Sharp and Nobles, 1953; Hooke, 1967; 1987; Morton and Campbell, 1974; Wasson, 1978; Costa and Williams, 1984; Pierson, 1986;

Davies, 1988; Davies and others, 1991; Cruden and Lu, 1992; Harris and Gustafson, 1993; Zhang, 1993). Previous explanations for the pulsing nature of debris flows include episodic input from multiple source areas (e.g., Sharp and Nobles, 1953); piecemeal landsliding from a single source area (e.g., Sharp and Nobles, 1953); episodic damming and release of debris within a channel (e.g., Gallino and Pierson, 1985); and intrinsic instability (Davies, 1986, 1988, 1990). The behavior of the experimental flows at the debris-flow flume shows clearly that surge waves can develop as a result of mechanical instability within a flow from a single source mass, and that they can form in the absence of any constrictions or blockages within a channel.

Data from the suspended depth meters and the load cells on the channel bed show that dynamic bulk densities of the flowing material are on the order of 2000 kg/m^3. These densities are nearly identical to the static bulk density of the unconsolidated source material (Iverson and others, 1992; Iverson and LaHusen, 1993a). From these data Iverson and LaHusen (1993a) infer that grain friction, the result of enduring grain contacts, plays an important role in the momentum transport and energy dissipation within debris flows.

LARGE-SCALE EXPERIMENTAL DEBRIS-FLOW DEPOSITS

Analysis of experimental deposits included: (1) surveying deposits using an electronic distance measuring device (EDM) and theodolite to measure their shape and thickness distribution; (2) mapping surface textures; (3) mapping the distribution of tracer particles; (4) measuring the three-dimensional orientation of surface clasts; (5) measuring the near-surface density of the sediment mass (R.M. Iverson, unpublished data); (6) dissecting deposits to examine interior textures and to collect sediment samples; and (7) reviewing video images and still photographs of the depositional process. Deposits typically were removed from the runout area before a subsequent flow was released. In one experiment, however, deposits from two flows were allowed to accumulate in order to examine the effect of *in situ* debris on deposition by a subsequent flow and to examine the stratigraphic development of a sequence of debris-flow deposits. The following discussion focuses on experiments conducted in 1992, 1993, and 1994.

INDIVIDUAL DEPOSITS

Experimental flows deposited sediment abruptly beyond the flume mouth on a smooth, concrete surface that slopes at 3°. Deposits developed by a combination of forward pushing, horizontal and vertical accretion, and lateral shunting of previously deposited debris. Attributes of the experimental deposits are given in Table 2.2. Flows not confined across the runout surface traveled as much as 17 meters beyond the flume; flows laterally confined across the concrete runout surface traveled as much as 30 meters beyond the flume. Deposits typically were less than 40 centimeters thick, were composed of a poorly sorted and unstratified mixture of particle sizes, and exhibited morphologic features that are common to many natural deposits, such as lobate planforms; steep, blunt margins; marginal levees; and arcuate surface ridges.

The depositional process of each experimental flow was strongly influenced by the water content of the source material, whereas deposit planforms were influenced both by initial water content and by substrate topography. The deposits from clearly unsaturated flows accumulated substantially differently than did those from flows that appeared to be saturated. Lawson (1982), too, observed variations in deposition from sediment flows at the toe of Matanuska Glacier in response to differences in water content. It must be emphasized here that the apparent saturation of source material listed in Table 2.2 is only an approximation, owing to leakage of water at the gate and to masses of air that remained trapped in the interstices of the sediment. In all of the experiments prior to August, 1994, the degree of saturation was estimated from piezometric measurements of the water table that developed in the source debris during application of water (R.M. Iverson, personal communication, 1995). Starting with the August 1994 experiment, piezometric measurements of water head were supplemented with measurements of water input (via flow meters) and water loss (into collection tanks). Analysis of the water-mass-balance data suggests that substantial pockets of air may remain trapped even in granular debris when water is applied relatively rapidly despite piezometric data that suggest that the material is essentially saturated (R.M. Iverson, personal communication, 1995).

In all experiments, sediment mixtures sustained a net volume decrease between flow initiation and deposition (R.M. Iverson, unpublished data). Deposits composed of mixtures of sand and gravel typically had dry bulk surface densities 3% to 45% greater than their source debris, whereas deposits composed of the loamy sediment apparently densified to a greater extent, having dry bulk surface

densities 10% to 75% greater than their source debris (Table 2.2). The propensity for significant densification of the loamy mixtures was readily apparent during the application of water to the source debris. Those mixtures visibly underwent several percent volume change as water was applied, indicative of the higher porosity and greater compressibility of that material in contrast to the sand and gravel mixtures.

Deposits From Unsaturated Flows

Deposit morphology

Deposits from unsaturated flows typically formed relatively thick lobes that had a high aspect ratio, defined as the ratio of mean deposit width to maximum unconfined deposit length. Three deposits (May 21, June 10, and July 16, 1992) exhibited relatively equant planforms, had aspect ratios greater than 0.5, and had margins that were steep and blunt (Figures 2.7, 2.8. 2.9, 2.10A; Table 2.2). Mean thicknesses were approximately 16 to 20 centimeters, and maximum thicknesses were approximately 35 centimeters (Figure 2.9; Table 2.2). Surface morphology was dominated by subtle to prominent arcuate ridges that had relief ranging from a few to several centimeters (Figures 2.7, 2.10A), similar to surface ridges observed on natural deposits (e.g., Jahns, 1949; Curry, 1966; Shaller, 1991). Surface sedimentology was dominated by gravel (8 to 32 mm diameter) (Figures 2.7, 2.11). A fourth deposit, composed of sand, gravel, and loam (August 31, 1994, Table 2.3, Figure 2.3), exhibited a morphology more characteristic of deposits resulting from saturated flows (discussed below) even though its source debris was only about 70 percent saturated (Figure 2.9). It is possible that following release, the source debris for this deposit underwent sufficient volume decrease to form a debris flow that was essentially saturated, yielding a deposit having a signature more characteristic of a saturated source. The dry bulk densities of the surface of the source debris and of the deposit from this experiment suggest that the sediment may have densified 25% to 50% during transport (Table 2.2; R.M. Iverson, unpublished data).

Depositional process

Sequential photographs reveal that deposits from unsaturated flows formed mainly by successive surges partly overriding and partly shoving forward debris deposited by previous surges at the mouth of the flume (Figure 2.11). In other words, new material was progressively added to the proximal end of the enlarging deposit. Sediment deposition generally migrated from the toe of

the deposit upslope as later surges pushed into and shouldered aside, but generally did not override, sediment deposited by earlier surges.

The general pattern of sourceward accretion of unsaturated-flow deposits is reflected by locations of colored tracer particles placed in the source material for the flow in May 1992. Costa (1992) found that granule-sized tracer particles placed near the front of the source material typically were found near the front and along the margins of the resulting deposit (Figure 2.12) whereas tracer particles placed near the rear of the source material generally were found near the rear of the deposit within the lower confines of the flume. Tracer particles at the rear of the source area were not found beyond the mouth of the flume. This dispersal pattern of tracer particles clearly indicates a mode of primarily horizontal, rather than vertical, accretion of sediment within this deposit.

Deposits From Saturated Flows

Deposit morphology

Deposits from saturated flows were longer and thinner than those from unsaturated flows. Maximum thicknesses of saturated-flow deposits typically were less than 30 centimeters and they commonly had low aspect ratios, usually less than about 0.3 (Figures 2.9, 2.13; Table 2.2). A few saturated flows, however, formed deposits having aspect ratios greater than 0.3, and as large as 0.84. In contrast to most experiments, the flows that formed those deposits encountered sediment deposited in a previous experiment rather than the smooth runout surface (e.g., April 8, 1993), were confined across the runout surface and deposited sediment onto a gravel substrate, or, during curved-channel experiments (Iverson and others, 1994), flowed onto substrate having an adverse (uphill) gradient (July and September, 1993). In all experiments where saturated sand-and-gravel flows traveled unconfined across the uniformly sloping runout zone, aspect ratios of deposits were less than or equal to 0.3. Unconfined flows that contained approximately 2 to 4 percent mud (notably May 1994) had aspect ratios slightly larger than 0.3.

Deposits from saturated flows typically had low-relief surface morphology and variable margins (Figures 2.10B, 2.13). Surfaces of these deposits were usually flat, punctuated in places by inconsistently developed marginal levees, and were marked by clusters and streaks of coarse clasts that distinguished the boundaries of surges (Figures 2.13, 2.14, 2.15). Analogous clusters of coarse clasts were identified on bedding planes of Cretaceous debris-flow deposits by Kim and others (1995).

They infer that such clusters reflect gravels deposited during flow surges. Saturated flows generally do not develop deposits that exhibit the prominent surface ridges prevalent on deposits from unsaturated flows, which suggests that ridges may be used as indicators of relative water content, and perhaps relative strength, of source flows. Margins of the saturated-flow deposits range from steep and blunt, especially in distal reaches, to tapered and nearly wedge-shaped.

Depositional process

Deposits from saturated flows developed dominantly through incremental vertical, rather horizontal, accretion of sediment transported by shallow (< 10 cm deep), successively overlapping surges (Figures 2.14, 2.15). Although later surges did push into and shoulder aside some of the earlier deposited debris, they more commonly overrode, and were sometimes deflected by, debris already emplaced (Figures 2.14, 2.15). This mode of deposition is in contrast to the depositional process of unsaturated flows. Nevertheless, the locus of deposition gradually migrated upslope when the mass and momentum of trailing flow diminished (Figures 2.14, 2.15). Perhaps most significantly, the largest surge, regardless of its position relative to the flow front, commonly swept across the entire deposit emphasizing the nature of incremental vertical accretion of these deposits (e.g., Figure 2.14 E-J).

Colored tracer particles tracked the depositional process by saturated flows. Groups of colored tracer particles (in these cases 16-32 mm gravel that had been sifted from the source debris and painted) were placed in the source sediments of the May and July 1994 experiments. In each experiment, red particles were placed at the front base of the source mass and yellow particles were placed near the centroid of mass. Additionally, black particles were placed on the rear surface of the source mass of the May 1994 experiment (Figure 2.16). Locations of colored particles were mapped on the surfaces of the respective deposits (Figure 2.17) and relative stratigraphic positions were noted when observed. For each deposit, colored particles exposed in trench spoils were mapped with respect to their location in plan view; however, their relative stratigraphic position could not be ascertained accurately.

The dispersal pattern of tracer particles (Figure 2.17) and the surface morphology and sedimentology associated with individual surges (Figure 2.15) demonstrate clearly that vertical accretion of sediment during a single event can play a significant role in debris-flow deposition.

Locations of tracer particles in the May 1994 deposit reflect a combination of vertical and horizontal sedimentation (Figure 2.17A). Red particles placed at the lower front of the source mass were smeared along the length of the base of the deposit, but were concentrated primarily in the distal half of the deposit and in the "spray" of particles that had saltated ahead of the flow and were deposited beyond the primary mass of the sediment. Yellow particles were located dominantly in the proximal half of the deposit and lay stratigraphically above red particles (Figure 2.18). Black particles were located primarily on the surface of the proximal one-third of the deposit. This dispersal pattern is somewhat similar to that observed by Costa (1992) in the deposit from an unsaturated flow (see Figure 2.12). Overall, particles in the sediment mass retained their general relative horizontal position with respect to initial location in the source debris, but elongation of the source mass during transport and vertical accretion by successively overlapping surges have left a clear imprint on the resulting deposit (compare Figures 2.15 and 2.17A). Locations of tracer particles in the July 1994 deposit reflect dominantly vertical accretion of sediment. Surface and subsurface locations of tracer particles show clearly that the center of mass of the source debris elongated and overrode the sediment located at the front of the source debris (Figure 2.17B). Red particles were found dominantly in the proximal part of the deposit whereas yellow particles, though concentrated in the distal half of the deposit, were found along the length of the surface. This dispersal pattern contrasts strongly with those observed in the May 1992 and May 1994 deposits and shows that sediment in the source debris can exchange relative horizontal positions as a result of progressively overlapping surges. Vallance (1994) observed similar relations in laboratory experiments with glass beads.

RELATIONS AMONG MORPHOLOGIC PARAMETERS

Previous experimental and field investigations have examined relations among various morphologic features of debris-flow deposits and fans and possible controlling parameters such as source volume, channel width, channel gradient, depositional surface gradient, and size of drainage basin (e.g., Mizuyama and Uehara, 1983; Zimmerman, 1991; Whipple, 1994; Liu, 1995). For example, Liu (1995) showed that the morphology of deposits from small (< 100 liter) cohesive debris flows is related primarily to source volume, original depositional slope, and bulk wet density of the debris. Deposit area and maximum deposit length were positively related to source volume and depositional slope whereas they were inversely related to bulk density.

For comparison with small-scale experiments, I have examined various morphometric parameters of deposits as a function of initial source volume. These morphometric parameters include: unconfined area, maximum length, mean width, aspect ratio, and maximum thickness of deposits. At the USGS debris-flow flume, channel width, channel gradient, and deposit slope are fixed. Variables that can be reasonably controlled included source volume, source composition, and channel confinement across the runout surface. Owing to leakage of water in the source area, saturation of the source debris can be controlled only approximately; thus, bulk wet density of the source debris is not easily controlled. Unconfined area, maximum length, and mean width of saturated-flow deposits exhibit a weak positive relation to source volume; aspect ratio and maximum thickness of those deposits appear to be independent of source volume (Figure 2.19). Data for unsaturated-flow deposits are too few to draw conclusions. Despite the limited data, unsaturated- and saturated-flow deposits are clearly separated on plots of unconfined area, maximum length, and mean width, which suggests that bulk wet density and rheologic character of flows may play an important role in controlling deposit morphology. Although the limited data from the large-scale experiments regarding morphometric relations are not conclusive, they are consistent with, and do not contradict, results obtained from small-scale experiments.

Channel confinement exerted a stronger influence on travel distance and deposition than did channel gradient. Similar observations have been made for natural debris flows (e.g., Fannin and Rollerson, 1993). In all experiments in which flows were allowed to spread laterally upon reaching the base of the flume, sediment remained on the concrete runout surface and traveled no farther than 17 meters beyond the end of the flume. In a few experiments (Table 2.2) the channel was confined across the length of the concrete runout slope. In those experiments, which employed volumes of source material and water contents comparable to other saturated-flow experiments, flows swept entirely across the 14-meter-long concrete runout surface and traveled as much as an additional 16 meters (Figures 2.9, 2.15). Deposition in these experiments proceeded in an incremental manner through sediment accumulation by shallow, overlapping surges, and the largest surge, responsible for the distal extent of each deposit, swept entirely across debris deposited by the earlier surges.

Photographic analyses, maps of surface morphology and sedimentology, and maps of tracer-particle locations in deposits show clearly that deposition by a single debris flow can involve horizontal sourceward accumulation of debris as well as progressive vertical accretion. These data also show

that deposit morphology and surface texture register the complex depositional history of debris-flow deposits and provide a link between deposit character and flow behavior. But do internal textures of debris flows faithfully register the depositional process? I now turn attention to an analysis of the internal sedimentology and stratigraphy of the experimental deposits.

INTERIOR TEXTURE AND SEDIMENTOLOGY

Deposits were examined within days to a few weeks after accumulation so that sedimentary features recorded within the deposits would be primary features that resulted from emplacement by mass flow rather than secondary features from fluvial alteration or reworking of the deposits. Areas disturbed by rainfall runoff or afterflow from the flume were, however, typically confined to narrow portions of the proximal few meters of the deposits. Each deposit that was examined was allowed to drain until trenching produced vertically standing exposures.

There were no discernible textures that were clearly related to the observed sourceward accretion of debris by unsaturated flows. Deposits from those flows commonly exhibited inverse sorting of particles larger than 8 mm ($<-3\phi$) (Figures 2.7, 2.11, 2.20A, 2.21; Table 2.3). Clasts at the surface were distinctly coarser and better sorted than were subsurface particles, and in general the basal 5 centimeters of these deposits was lacking in the coarsest particle sizes (Table 2.3; Figures 2.20A, 2.21). Otherwise, the internal textures of these deposits appeared to be massive and homogeneous. Well-sorted gravel commonly concentrated on the downslope sides of surface ridges. Except for the concentrated surface gravel there was no difference in interior sedimentary texture between ridges and intervening troughs. If the ridges are related to compressional deformation of the debris by impact of later surges, there is no internally preserved textural evidence of such compression, such as detectable displacement along shear planes. Systematic bulk sampling of debris throughout the deposit also failed to detect textures indicative of sourceward accretion. The deposit of the experiment in July 1992 as well as that examined by Costa (1992) had bulk particle-size distributions that were virtually identical to the source material (Table 2.3). No detectable longitudinal or lateral sorting of particle sizes occurred (Figure 2.21; Table 2.3).

Deposits from saturated flows typically lacked discernible internal texture related to the observed vertical accretion of debris. These deposits locally exhibited inverse grading of particles coarser than 8 mm (Figures 2.15, 2.20B-D). At these locations the subsurface was more poorly

sorted than the surface and the mean particle size was substantially finer than the mean particle size at the surface (Table 2.3; Figures 2.22-2.25). At locations that lacked distinct clusters of surface gravel, deposits typically were massive, homogenous, and unsorted, and there was little vertical variation in grain size characteristics (Figures 2.22-2.25; Table 2.3). Clusters of surface gravel are related to deposition by fronts of surge waves. In vertical section, these clusters are scanty sedimentologic evidence of construction of the deposit by multiple surges. Typically, there is little, if any, discernible subsurface texture to indicate deposition by vertical accretion. The only clear evidence, in vertical section, that deposits resulted from multiple surges is found near deposit margins where finer-grained, poorly sorted debris sometimes overlies well-sorted gravel deposited by the leading edge of the debris flow (Figure 2.20D). I detected no significant grain-size variation longitudinally and only scattered variation laterally, which typically reflected well-sorted gravel deposited by the leading wave of saltating particles (Figures 2.20D, 2.22-2.27; Table 2.3). This general lack of spatial variation of grain-size distribution results from the short runout distance and rapid deposition of sediment by the experimental flows.

MULTIPLE DEPOSITS

To gain further insight on interior textures and relations between debris deposited by separate flows, the deposits from two identical flows, released on consecutive days (April 7 and 8, 1993), were allowed to accumulate (Figure 2.28). The first deposit (April 7, 1993) accumulated in the manner typical of saturated flows: it was deposited incrementally by a series of shallow, closely spaced surges. The elongate deposit extended 12 meters beyond the end of the flume and spread to a maximum width of about 4 meters (Figures 2.9, 2.15). The deposit was widest where it exited the flume and gradually tapered to its distal end. The deposit was convex in cross-section, had rounded margins, and a flat surface. Along its central axis, the deposit was thickest at the mouth of the flume, thinned abruptly from 28 centimeters to 18 centimeters across a distance of less than 2 meters, maintained nearly constant thickness for the next 9 meters, and rapidly tapered to the distal end (Figure 2.9). Margins of the deposit were dominated by well-sorted gravel; clusters and streaks of well-sorted gravel, related to individual surges, dominated the surface texture of the proximal half of the deposit (Figure 2.15).

Prior to release of the second flow (April 8, 1993), an approximately 1-centimeter-thick marker layer of distinctive beach sand was spread across the surface of the first deposit (Figure 2.28). The sand covered all but an 8-square-meter patch near the proximal end of the deposit. The beach

sand was much different in color and grain size than the fluvial sand that composed the source material for the debris flows. This marker layer was introduced to provide an unambiguous and easily detectable contact between major depositional units. The area of the first deposit left uncovered by the marker layer provided a location to examine direct contact between the major depositional units.

Emplacement of the second deposit was affected significantly by the first deposit. When the leading edge of the second flow reached the proximal end of the existing deposit, it developed an "impact" jump, a result of supercritical flow encountering an obstacle on the channel bed. The flow then crashed onto the proximal end of the first deposit for a few seconds before smoothing out and overriding that deposit in a series of successive surges. Accumulated sediment from the first deposit against the inner left wall at the mouth of the flume as well as the topography of that deposit beyond the mouth of the flume (Figure 2.9) directed the second flow toward the right side of the runout zone (Figures 2.9, 2.15, 2.28). The first deposit enhanced the bed roughness felt by the second flow. As a result of enhanced bed roughness and redirection of flow toward the side of the runout area, the second flow did not travel as far beyond the flume mouth as the first flow, and it left a deposit much less elongated than the deposit of the April 7 flow (Table 2.2).

Sediment textures and clast orientations on the surface of the second deposit were mapped before the debris fan was trenched. Similar to the underlying deposit, the second deposit contained clusters of well-sorted gravel along its margin as well as on its surface (Figure 2.15). Again, clusters of well-sorted gravel marked boundaries of flow surges. Thickness of the second deposit was comparable to that of the underlying deposit (Figure 2.9). However, maximum thickness was skewed toward the right side of the runout zone, a reflection of the forced direction of flow.

Upon trenching I found it difficult to distinguish the two deposits without aid of the marker horizon (Figure 2.29). Each deposit appeared to be massive and homogeneous, and the compound deposit, in the area lacking the marker sand, could be interpreted easily as the product of a single surge. Figure 2.30, which shows deposit texture and stratigraphy immediately adjacent to the exposure shown in figure 2.29B, illustrates clearly that the lower deposit was not scoured by the second flow, negating erosion as the cause for my inability to detect the contact between units.

The individual deposits, as well as the compound deposit, were sampled in several locations to determine if spatial variation in size distribution is a useful method of distinguishing the two deposits. Sediment samples from each unit show no systematic variation of grain-size distribution in either lateral or longitudinal transects (Figures 2.23-2.25; Table 2.3). Minor differences in bulk samples of each deposit are probably attributable to minor differences in size distributions of source debris (Figure 2.3; Table 2.3). The compound deposit was sampled vertically at 6-cm intervals in 6 locations. At three of those locations the marker sand that separated the two deposits was clearly evident (2EW/4NS; 6EW/5NS; 6EW/6.5NS); at two locations the marker sand was absent (2EW/5NS; 4EW/4.5NS); and at one location a small lens of marker sand was uncovered during the course of sampling (4EW/6.5NS) (see Figures 2.23-2.25; Table 2.3). In locations where the sand was absent discrimination between deposits was based on mapped sediment thicknesses. At these six locations the coarsest particles (16-32 mm; -4ϕ) in the April 7 deposit were more concentrated in the upper part of the deposit than in the lower part of the deposit. Only three of the six locations exhibited a similar size grading in the April 8 deposit (see Figures 2.24, 2.25).

Vertical variations of grain-size in the compound deposit did not effectively distinguish the individual deposits. I could only distinguish the two deposits at three of the six sites using relative weight percentages of the coarsest particles in the upper part of the April 7 deposit and the lower part of the April 8 deposit as the criterion for distinction. Of those three sites the marker sand was present at two (2EW/4NS; 4EW/6.5NS) to provide verification of the inferred distinction. Without *a priori* knowledge of the presence of two distinctly separate deposits, it would be difficult, on the basis of grain-size analyses, to conclude confidently that the compound deposit resulted from deposition by other than a single flow unit.

My inability to distinguish deposits from separate, but closely spaced, debris flows is not unique to these experiments. In December 1984 Weirich (1989) observed two debris flows emanate, within minutes of each other, from different watersheds in the San Dimas Experimental Forest, California, and flow into San Dimas Reservoir. The reservoir was drained the following summer. The proximal deposits from these flows were unstratified, matrix-supported mixtures of organic and inorganic debris, readily distinguishable from the reservoir substrate, but not distinguishable from each other. Only after the flows had mixed sufficiently with reservoir water farther downslope, and had segregated their organic and inorganic debris, could their respective deposits be distinguished.

PARTICLE ORIENTATION

Several investigators have measured particle orientation in debris-flow deposits to determine whether or not such deposits exhibit particle fabric and, if so, to define the style of the fabric (e.g., Lindsay, 1968; Lawson, 1979; Johnson, 1984; Fritz and Ogren, 1984; Mills, 1984, 1991; Major and Voight, 1986; Kohlbeck and others, 1994; Vallance, 1994). Here, I present the results of analyses of particle orientation that developed on the surfaces of three experimental deposits (Table 2.4). Although the results are specific only to those deposits, similar particle orientation developed on deposits from all of the experimental flows. At each location where particle orientation was measured, a grid was placed on the surface, and particles larger than 8 mm (-3ϕ) were measured at up to 25 points on the grid. For each particle chosen, I measured the orientation of the longest dimension (a axis) and the orientation and dip of the shortest dimension (c axis) with respect to the orientation of the flume. The c axis represents the pole to the plane that contains the longest (a) and intermediate (b) axes. Directional orientation was measured using a protractor because steel rebar in the concrete flume and in the runout area interfered with a magnetic compass. For this same reason, I have not obtained data on particle orientation within the bodies of the deposits.

The orientation data (Table 2.4) were analyzed by the eigenvalue method for a sample size N (e.g., Mark, 1973; Mills, 1984). This method involves a three-dimensional analysis of eigenvalues (λ_i) and their mutually associated eigenvectors (V_i). Eigenvalues describe the axis lengths, or shape, of a three-dimensional ellipsoid that provides the statistically preferred fit to the spatial data. The eigenvectors describe the spatial orientation of those axes. In the following analysis eigenvector V_1 represents the direction of maximum clustering of the shortest dimension (c axis), which is the pole to the average a-b plane; eigenvector V_3 represents the direction of minimum clustering, and is orthogonal to the preferred plane that contains the shortest dimensions. Normalized eigenvalues represent the degree of clustering, or the fabric strength. Two values, S_1 and S_3, where $S_i = \lambda_i/N$, are used to test whether the preferred orientations of the c axis are significantly different from a random sampling of orientations drawn from a uniform population (Mark, 1973; Mills, 1984).

Particles larger than 8 mm (-3ϕ) exhibited well-defined preferred orientation (Figures 2.31-2.33; Table 2.4). The longest dimension of these clasts aligned roughly parallel to surge margins. The linear orientation of these particles thus changes with position along surge boundaries. At the toe

of a cluster of gravel deposited by a surge, the long axis is oriented roughly perpendicular to the direction of flow (e.g., Figure 2.32, sites 1 and 5); however, along lateral margins the long axis is oriented roughly parallel to the direction of flow (e.g., Figure 2.32, sites 2, 7, and 12). These relations hold not only along the perimeter of deposits, but also on more central parts of the deposit where individual surges stopped. Short-dimension orientations exhibited both cluster- and girdle-type distributions (Figures 2.31-2.34). The preferred plane that contains the longest and intermediate axes exhibited relatively high-angle upslope or inward-dipping imbrication (Table 2.4). Although such imbricate structure reflects the orientation of the statistically preferred a-b plane, several clasts also exhibited downflow or outward-dipping imbrication.

Particle orientation measured in the experimental deposit is similar to that measured in many natural debris-flow deposits, but it is also similar to orientation developed in coarse, fluvial deposits. Johnson (1984) describes linear orientations very similar to those measured on the experimental deposits, that is, long dimensions that align roughly parallel to deposit boundaries, but planes that dip steeply outward from margins. Owens (1973) notes that long axes of particles in debris-flow levees tended to orient in the direction of the slope and dip at an angle slightly less than the slope angle. Innes (1983) reports no preferred orientations of particle long-axes in debris-flow lobes, but a pronounced preferred orientation of long axes in debris-flow levees, with most clasts oriented roughly in the direction of the slope. Mills (1984) and Major and Voight (1986) found that volcanic debris-flow deposits from Mount St. Helens exhibited weak, but clear, linear fabric and a reasonably strong planar orientation of long axes. Those deposits contained particles having both flow-transverse and flow-parallel orientations of long axes that generally dipped gently upslope. Kohlbeck and others (1994) found that long axes of boulders were oriented primarily perpendicular to flow direction and that long axes of smaller particles (≥5 cm long) were oriented parallel to flow direction and dipped upstream in ungraded, unsorted lahar deposits from the 1985 eruption of Nevado del Ruiz volcano, Colombia. Vallance (1994) noted a generally weak, but clear, imbricate pattern to clast long-axes developed within the deposit of the Osceola Mudflow from Mount Rainier volcano, Washington. Along valley walls, clasts exhibited a relatively strong downslope fabric, whereas within the main body of the deposit long axes developed a generally weak girdle pattern approximately parallel to the bedding plane. Of particular significance in this case is that clast fabric was developed throughout the thickness of the deposit, which ranges from 2 to 25 meters. Gravelly fluvial deposits, on the other hand, typically exhibit flow-transverse long-axis orientation and intermediate axes that dip rather

steeply upslope (e.g., Collinson and Thompson, 1989), similar to the particle orientation observed in places in the experimental debris-flow deposits. The strength of both the linear and planar fabrics measured in the experimental deposits of this study is attributed to the generally bladed shape of the particles (see Figure 2.4), whereas typically weaker fabrics in many natural debris-flow deposits are attributed to more equant particle shapes not distinct enough to develop pronounced orientation (e.g., Major and Voight, 1986).

NATURAL DEBRIS-FLOW DEPOSITS

Study of debris-flow deposits in southwest China complemented analyses of the experimental deposits. The deposits studied are in Jiangjia Gully, a tributary to the Xiaojiang River in the Yunnan Province, approximately 200 km northeast of Kunming. This site was selected because (1) the valley is inundated annually by numerous rainfall-triggered debris flows (Li and others, 1983; Zhang, 1993); (2) each debris-flow "event" lasts for several hours and is characterized by numerous surges (Li and others, 1983; Zhang, 1993; Figure 2.35); (3) the gradient of the depositional area is comparable to that of the USGS flume (3°-5°); and (4) nearly all debris flows in the past 30 years have been observed and documented from an established observation post (Zhang, 1993). This site provided an opportunity to study recent, unreworked deposits from well-documented events. It also provided an opportunity to compare deposits from debris flows having kinematic behavior similar to that of the experimental flows (i.e. many surges), but whose source material was finer grained (as much as 7 to 10 weight percent clay; Zhang, 1993) than the source debris of the experimental flows.

Debris-flow deposits along Jiangjia Gully were examined in late July, 1994. Individual deposits from flows on June 16, June 25, and July 19, 1994, were well preserved along the channel; older deposits from flows in 1983 and 1992 are well preserved on and within a major terrace that occupies a large proportion of the valley. Similar to the experimental deposits at the USGS flume, the morphology and surface sedimentology of deposits in Jiangjia Gully record the intermittent nature of the source flows. Several deposits consist of lobate landforms that have undisturbed surface ridges, clusters of coarse clasts, and aligned particles (e.g., Figures 2.36, 2.37). The stratigraphy and sedimentology in vertical sections of these field deposits, however, do not faithfully record the intermittent nature of a single flow event, nor do they faithfully record features useful to distinguish distinctly separate events. Deposits from individual events typically exhibit a massive, homogeneous

texture (Figure 2.38), which may or may not show grading of the coarsest stones, despite the fact that each deposit represents sediment accumulated during several surges. Although not every surge spilled onto the floodplain, many did, and video recordings show clearly that depositional areas commonly were inundated by numerous surges. Likewise, deposits from different flow events can develop sequences of massive deposits that are not easily recognized as the product of multiple flows (Figure 2.39). Excavation of overlapping deposits from flows in June, 1994, revealed that deposits from flows composed of similar source debris clearly known to have occurred days apart are difficult to distinguish in vertical section, similar to observations from the experimental deposits. At least five flows during the 1983 monsoon season are claimed to have deposited the assemblage of sediment shown in Figure 2.39B (Dr. Wang Yuyi, Chinese Academy of Sciences, personal communication, 1994), yet it is difficult to distinguish individual units. Some stratigraphic breaks between major depositional units were obvious, such as fluvially reworked deposit surfaces and subtle to obvious textural changes (Figures 2.40, 2.41). In general, the terraces and floodplain of Jiangjia Gully are composed of a monotonous, massive assemblage of debris-flow sediment; deposits from water floods, or of sediment reworked by fluvial processes, are rare in this valley. Chinese researchers who study debris-flow deposits here and in several other river valleys in southwest China use fluvially reworked surfaces, obvious textural changes, clay accumulations thought to result from ponded surface water, and clean stones (thought to have been washed by surface flow) as criteria to delineate stratigraphic breaks. While some criteria are clearly reliable, others are subtle and subjective, and their effectiveness is debatable.

Mingling of sediments deposited by different surges from a single debris flow over relatively short periods of time mutes stratigraphic contacts. Figure 2.37 illustrates a debris-flow lobe that does not sharply overlie the substrate sediment but rather grades into the substrate sediment. This relation between the morphology and sedimentology of the debris-flow deposit represents the leading edge of a flow surge that clearly mixed with sediment deposited earlier in the flow history. This sort of mingling of sediments provides a plausible explanation for the apparent lack of stratigraphic contacts within sediments known to have resulted from multiple surges. It also suggests that debris deposited by various surges must maintain a state of low effective stress over time scales that are long compared to the typical period of surges or duration of a debris flow.

DISCUSSION

Despite the complex behavior of most debris flows, geologists commonly infer the kinematic behavior and physical properties of such flows from the characteristics of their deposits, from mudlines along channels, and from their physical interactions with channels. Results of recent large-scale flume experiments provide new insight on deposition by debris flows and on allowable interpretations that can be constructed from the characteristics of their deposits. Although these experimental results are valid strictly for rapid, near-source deposition of cohesionless sediments, they are the first well-constrained experimental observations of debris-flow deposition that approaches the field-scale process. Thus, even limited insight obtained from these experiments provides a more solid foundation than purely inferential conclusions drawn from only field analysis of debris-flow deposits. I believe these results have significant implications for many natural debris flows and their deposits because (1) many natural flows exhibit surging behavior (Davies, 1986, 1988); (2) cohesion is relatively unimportant in many debris flows (Middleton, 1990); (3) cohesive strength is negligible even in clay-rich debris flows, such as the Osceola Mudflow from Mount Rainier volcano, Washington (Franz and Voight, 1995; see Appendix A); and (4) deposits from clay-rich flows having kinematic characteristics similar to the experimental flows, such as in Jiangjia Gully, exhibit sedimentologic features similar to those observed in the experimental deposits.

Experimental results show clearly that debris-flow deposition can occur by incremental accretion and not just by simple *en masse* emplacement of sediment, especially when the source debris, or the attendant flow, is nearly saturated. Clear evidence that deposits were the result of incremental deposition by multiple surges typically was recorded in deposit morphology and surface sedimentology only. Despite the unequivocal incremental nature of sediment accumulation, the sedimentary and morphologic characteristics of several experimental debris-flow deposits can easily be misinterpreted as having resulted from a single surge; incremental accretion may not be interpreted easily from the nature of the deposits, especially from examination of interior sedimentary characteristics. Although surface clusters and streaks of well-sorted gravels clearly marked boundaries of individual surges, internal textures did not faithfully record the progressive nature of deposition. Indeed, not only were individual surges from a single flow not faithfully recorded, but in one experiment deposits from similar yet separate debris flows were not distinguishable without aid of an introduced marker horizon.

Widespread morphologic characteristics of debris-flow deposits, such as lobate planforms, steep blunt margins, and marginal levees, in conjunction with typically unsorted and unstratified sediments, result from flows having exceptional sediment concentration and indicate deposition by mass-movement rather than by fluvial processes. Such features commonly are used as field criteria for distinguishing debris-flow deposits from fluvial deposits (e.g., Costa and Jarrett, 1981; Johnson, 1984; Hooke, 1987; DeGraff, 1994). The experimental results do not contradict such an interpretation.

Inferences regarding hydraulic behavior and rheological properties of flow or the mechanics of deposition, drawn from deposit characteristics, are questionable. For example, massively textured deposits commonly are interpreted to be the result of *en masse* sedimentation by "frictional freezing" (e.g., Cas and Landis, 1987; Ghibaudo, 1992). While this interpretation is not entirely without justification, the experimental results clearly illustrate that the full thickness of a debris-flow deposit may not result in this manner. Because debris-flow deposits generally have been assumed to result from simple *en masse* sedimentation, it has been common practice to infer debris-flow yield strength from deposit thickness or from large clasts apparently suspended in deposits (e.g., Johnson, 1970, 1984; Pierson, 1980; Fink and others, 1981; Li and others, 1983; Voight and others, 1983; Costa, 1984; Pierson, 1985b; Major and Voight, 1986; Van Steijn and others, 1988; Rodolfo and others, 1989; Whipple and Dunne, 1992; Cruden and Lu, 1992; Kim and others, 1995; see Table 2.1). If deposition is dominated by vertical accretion, however, the resulting deposit thickness has little bearing on intrinsic yield strength (see Figure 2.29B). The utility of relations between maximum particle size and bed thickness (e.g., Nemec and Steel, 1984), and computations of flow strength from the size of the largest supported particle, are also subject to the same skepticism. Vertical accretion of sediment by surges can produce beds that appear to "support" oversized particles that were emplaced instead as tractive bedload. For some active sediment flows at the Matanuska Glacier, Lawson (1982) found it difficult to distinguish material transported by traction (observed through a plexiglass wall) from particles actually suspended in the flows, an observation that lends support to the idea that some particles that appear to be suspended within a deposit may in fact have been transported by traction. Computations of, and inferences regarding, strength of flow based on relations between clast sizes and bed thickness are, therefore, not necessarily justifiable.

The experimental results as well as analyses of field deposits in Jiangjia Gully show clearly that multiple deposits of similar sediment can accumulate without obvious stratigraphic contact, particularly if there is little time between events, if source materials are similar, or if travel distances are short. The experimental results, combined with analysis of field deposits, suggest that distinctive source materials, facies variations over long travel distances, or sufficient time for development of unconformities or marker horizons may be required to generate stratigraphic features distinct enough to permit differentiation of individual debris flows under natural conditions. Even if sedimentary features are present to delineate stratigraphic contacts between assemblages of massively textured sediment, those contacts may represent breaks between sequences of sediment deposited by multiple events rather than breaks between sediment deposited by individual events. Evaluations of debris-flow hazards and reconstructions of geomorphic histories commonly utilize estimates of debris-flow frequency and magnitude. Results presented here suggest that event frequency may be underestimated and that event magnitude, defined as the volume of debris transported by a single debris flow (Hungr and others, 1984), may be overestimated. Further study is needed to determine if individual deposits resulting from debris flows having an annual or longer recurrence interval can be readily distinguished in sedimentary sections.

Linear and planar orientations of particle axes in the experimental deposits demonstrate that strong clast fabric can develop in debris flows. The experimental deposits typically displayed a pronounced particle orientation: long axes oriented parallel to surge margins and particles dipped relatively steeply upslope or inward away from margins. The strength of the fabric in these deposits suggests that the largest particles were free to move independently of one another during flow despite the high sediment concentration and the mass-flow process. The strength of this fabric is, clearly, a function of the particle shape. In the experimental deposits, the largest particles were typically blade shaped, and rod-shaped and blade-shaped particles develop stronger fabrics than more equant-shaped particles (Drake, 1974). Many natural debris-flow deposits, in which clast shapes commonly are more equant, tend to exhibit girdle rather than cluster fabrics, and linear orientations, though clear, typically are weak (e.g., Mills, 1984, 1991; Rappol, 1985; Major and Voight, 1986; Vallance, 1994).

The experiments indicate that fabric style and strength may not necessarily distinguish debris-flow deposits from water-laid deposits. Kohlbeck and others (1994) infer that relatively strong orientations of clast long axes in ungraded, unstratified lahar deposits resulted from an initial debris-

flow surge followed by subsequent water-rich surges that reworked the sediments. They assume that strong particle fabric and imbricate structure form only through fluvial processes and that such particle orientations can be used to distinguish debris-flow processes from fluvial processes. The experimental results reported in this chapter suggest that fabric style and strength appear to be more a function of particle shape than depositional process; they also support previous investigations that demonstrate that primary clast fabrics can develop in debris-flow deposits.

Use of particle orientation in debris flows as indicators of paleocurrent direction is problematic. Fisher (1971), Owens (1973), and Innes (1983) assert that elongate particles generally align in the direction of flow, possibly modified by local topography. Mills (1984, 1991), Major and Voight (1986), Kohlbeck and others (1994), and Vallance (1994) have found both flow-parallel and flow-transverse orientations of elongate particles. The experimental results demonstrate that elongate particles generally orient parallel to surge margins and thus exhibit both flow-parallel and flow-transverse orientations, depending on position within the deposit. The experimental results do not contradict previous findings that suggest debris-flow deposits exhibit flow-parallel orientations having upslope imbrication, but they indicate that accurate interpretation of paleocurrent direction from debris-flow deposits is difficult unless one knows the spatial position of the clasts with respect to surge margins. Determination of paleocurrent directions from debris-flow deposits without appreciation for these nuances can produce results that may be in error by as much as 90 degrees.

CONCLUSIONS

Recent large-scale flume experiments indicate that caution is needed when attempting to infer flow dynamics, hydraulic conditions, rheological properties, or event frequencies of debris flows from the sedimentologic, stratigraphic, and morphologic characteristics of their deposits. Although the results are valid strictly for rapid, near-source deposition of cohesionless sediment, they are the first well-constrained experimental observations of debris-flow deposition that approaches the field-scale process. The experimental flows and the resulting deposits perhaps best simulate debris flows that occur in small, steep catchments rather than the large-magnitude debris flows that can occur as the result of volcanic eruptions (e.g., Table 2.1; Pierson, 1995). However, recognition that cohesive strength is not important in many debris flows and the similarity between deposits from clay-rich debris flows having kinematic characteristics similar to the experimental flows, such as in Jiangjia

Gully, China, and the experimental deposits bolsters confidence that these experimental results may be more widely applicable.

The experiments show clearly that a deposit from a single debris flow can accumulate through incremental accretion of sediment from numerous shallow surges. Deposits developed by a combination of forward shoving, horizontal and vertical accretion, and lateral shunting of previously deposited debris. Flows developed from strongly unsaturated source debris, and that do not enhance their water content along the channel, tend to deposit sediment through dominantly horizontal accretion of debris toward the source area with only modest overlap of subsequent surges. Deposits from unsaturated flows generally are lobate, have large aspect ratios, steep margins, and commonly exhibit prominent arcuate surface ridges that apparently result from compression of deposited sediment by subsequent surges. Saturated flows, on the other hand, deposit sediment as shallow surges progressively overlap. Deposition occurs primarily through vertical accretion; sourceward accretion typically occurs only after flow mass and discharge diminish. Deposits from saturated flows also are lobate, but typically are more elongate, have small aspect ratios (typically less than or equal to 0.3), nearly flat surfaces, blunt to tapered margins, and generally lack prominent arcuate surface ridges.

Aggradation by multiple surges during a single event was apparent only in deposit morphology and in surface sedimentary textures. Interior textures of deposits did not faithfully record incremental accretion. Clusters and streaks of surface gravel commonly delineate individual, or amalgamated, surges. In vertical section, basal lenses of coarse gravel, indicative of deposition by more than one surge, were preserved locally only near flow margins. Few of the dynamic aspects of the depositional process are thus recorded by interior textures.

Individual debris flows may not leave a distinctive signature in the sedimentary record. Deposits resulting from two similar yet separate experimental flows on consecutive days could not be identified without aid of an introduced marker horizon. Likewise, natural debris-flow deposits in southwest China that resulted from flows that occurred days to weeks apart also were difficult to distinguish from each other. Studies of floodplain and alluvial-fan deposits may thus underestimate debris-flow frequencies and overestimate debris-flow magnitudes, even in near-source regions where most events are likely to have inundated the landscape.

Owing to the ability of debris-flow sediments to accumulate incrementally without registering interior textures that record deposition by discrete surges, or even by individual flows, computation of the rheological properties of a flow based on the characteristics of a deposit is questionable. The experimental results suggest that techniques to estimate flow properties from deposit thickness or from relations between particle size and bed thickness may not be justified. Although sections of a deposit may result from *en masse* sedimentation locally by a single surge, this does not demand that the entire thickness of a deposit at all locations formed in that manner.

Interpretation of an assemblage of sediment as the product of a debris-flow based on an analysis of deposit features appears justified based on results of the large-scale experiments. Lobate planforms, steep margins, marginal levees, and particularly unsorted and unstratified textures are characteristic of the deposits that resulted from the experimental debris flows. However, interpretations regarding depositional mechanics, dynamic behavior, physical properties of flow, or event frequency cannot easily, or accurately, be inferred from deposit characteristics.

Table 2.1 Observed and inferred characteristics of debris flows.

[-- means no data reported]

Location	Gradient (m/m)	Flow depth (m)	Mean peak velocity (m/s)	Peak discharge (m^3/s)	Apparent Newtonian viscosity (Pa-s)	Bingham viscosity (Pa-s)	Yield strength (Pa)	Reference
Nonvolcanic								
Hanshui Gully, China	--	3-5	10-15	1000-2500	1.5-2	--	30-50	Li and Luo (1981)
Bullock Creek, N.Z.	0.105	1	0.8-5	10-20	210-810	19-71	1300-2400	Pierson (1980)
Wrightwood, CA	0.123	1	1.1	--	450	--	600	Johnson (1970)
	0.09-0.31	1	0.6-3.8	--	10-6000	40-100	--	Morton and Campbell (1974)
	0.105	1.2	1.2-4.4	--	210-600	--	--	Sharp and Nobles (1953)
Lesser Almatinka River, USSR	0.10-0.18	2-10.4	4.3-11.1	--	--	--	--	Niyazov and Degovets (1975)
Matanuska Glacier, AK	0.02-0.47	0.01-2	0.001-1.3	--	--	--	--	Lawson (1982)
Mayflower Gulch, CO	0.268	1.5	2.5	--	2900	--	--	Curry (1966)

Table 2.1 (continued)

Dragon Creek, AZ	0.059	5.8	7	--	2780	--	22	Cooley and others (1977)
Jiangjia Gully, China	0.069-0.077	--	--	2420	150	--	200-300	Li and others (1983)
Rudd Canyon, UT	--	2.2	3	24	--	--	120-1250	Pierson (1985b)
Baby Yar, USSR	0.006-0.010	7	5	2200	--	--	--	Mironova and Yablonskiy (1992)
Owens Valley, CA	--	--	4.5-7.8	8-435	--	22-1000	80-2150	Whipple (1994)
Monument Creek, Grand Canyon, AZ	0.063-0.068	1.2-2.9	3.4-4.0	100-120	--	--	--	Webb and others (1988, 1989)
Ophir Creek, NV	0.035-0.249	6-7	7-22	--	--	--	--	Watters (1983)
Mount Cayley, B.C.	~ 0.2	--	21-34	--	--	--	25,000	Cruden and Lu (1992)
British Columbia mountains	0.176-0.325	2-6	3-9.4	90-566	--	--	--	Hungr and others (1984)
St. Elias Range, Yukon Territory	0.14-0.25	--	5-6.3	21-36	340-8230	--	--	Harris and Gustafson (1993)
French Alps	0.34-0.54	0.25-7.2	1.8-4.2	5-89	--	--	1000-10,000	Van Steijn and others (1988)

Table 2.1 (continued)

Reshun Gol, Pakistan Hindu Kush	--	2-3	1.7-3	80	--	--	--	Wasson (1978)
Volcanic								
Rio Reventado, Costa Rica	0.046-0.174	1.8-12	2.9-10	54-407	--	--	--	Waldron (1967)
Nojiri River, Japan	0.058	2.3	13	--	--	--	--	Watanabe and Ikeya (1981)
Mount St. Helens, WA								
Pine Creek	0.03-0.09	6-15.2	12-17.7	7300-28,600	--	20-12300	400-1100	Pierson (1985a); Fink and others (1981)
Muddy River	0.02	4.7	14.4	--	130-1200	--	--	Pierson (1985a)
North Fork Toutle River	--	5-8	6-12	8000	--	130-475	0-250	Fairchild (1985); Wigmosta (1983)
southwest flank	0.07-0.23	2-4	5-30	--	430-5300	280-5000	900-1200	Major and Voight (1986)
Nevado del Ruiz, Colombia								

Table 2.1 (continued)

Rio Guali	0.009-0.111	4-10	5-12	1100-20,000	--	--	--	Pierson and others (1990)
Rio Molinos/Q. Nereidas	0.011-0.239	5-14	4.8-14.7	4200-19,900	--	--	--	Pierson and other (1990)
Rio Azufrado	0.024-0.143	13-25	12-17	10,500-48,000	--	--	--	Pierson and others (1990)
Redoubt volcano, AK								
Drift River	0.004-0.012	≤ 8	1-12	1000-60,000	--	--	--	Dorava and others (1993); Dorava and Meyer (1994)
Mount Pinatubo, Philippines								
east side channels	0.0002-0.02	<1-6	4-6	--	--	--	--	Major and others (1996)
Mayon volcano, Philippines[1]	0.079	--	3.8	--	6500	600	460-2320	Rodolfo and others (1989)

[1] Rainfall-triggered debris flow not associated with a volcanic eruption.

Table 2.2. Attributes of experimental debris-flow deposits

Date (mmddyy)	Source debris[e]	Approximate degree of saturation (percent)	Source volume (m^3)	Depositional area (unconfined) (m^2)	Length beyond flume mouth (m)
052192[a]	s,g	< 100	≈ 13	39.6	8.8
071692	s,g	< 100	7.4	23.4	6.3
092592	s,g	100	6.6	52.9	14.1
040793	s,g	100	6.2	38.8	11.9
040893	s,g	100	6.5	46.4	10.0
050693	s,g	90	12.1	60.2	14.7
072293[b]	s,g	100	9.4	31.8	---
091593[b]	s,g	90	11.5	46.7	---
091693[b]	s,g	100	10.8	48.9	---
101993[c]	s,g	100	10.0	64.1	30.3
102193[c]	s,g	100	8.9	20.0	21.3
041994	s,g	100	8.4	69.0	15.2
042194	s,g	100	9.2	65.8	16.7
052694	s,g,l	98	9.0	80.6	14.9
072194[c]	s,g,l	100	10.3	67.4	29.0
083194[d]	s,g,l	67	9.0	50.9	21.4

a From J.E. Costa (unpublished data).
b Curved-channel experiment.
c Channel confined across concrete runout pad; deposition primarily on gravel-covered runout surface.
d Channel confined 8.5 m across runout pad.
e s,g = sand and gravel mixture; s,g,l = sand, gravel, and loam mixture.

Table 2.2. (continued)

Length beyond confined channel (m)	Mean width (m)	Aspect ratio	Maximum thickness (m)	Source debris bulk dry density[f] (kg/m^3)	Deposit bulk dry density[f] (kg/m^3)
8.8	4.5	0.51	0.35	---	---
6.3	3.7	0.60	0.36	1630	1720
14.1	3.7	0.26	0.28	---	---
11.9	3.2	0.27	0.24	2000	---
10.0	4.6	0.46	0.20	---	---
14.7	4.0	0.27	0.23	1820-2000	2520-2620
6.2	5.2	0.84	0.28	1630	1130-1610
9.0	5.2	0.58	0.44	1590-2010	1830-1870
7.4	6.6	0.89	0.43	1580-1720	1830-2020
15.8	4.1	0.26	0.26	1540-2210	1700-1870
6.5	3.1	0.48	0.25	1490-1630	1780-1880
15.2	4.5	0.30	0.32	1630-1810	1870-1930
16.7	3.9	0.23	0.24	1630-1960	1830-1940
14.9	5.4	0.36	0.22	1400-1700	1630-2470
14.6	4.6	0.32	0.18	1480-1600	1630-1700
12.8	4.0	0.31	0.14	1340-1410	1680-2050

f Collected at source debris and deposit surfaces (R.M. Iverson, unpublished data).

Table 2.3. Sedimentological characteristics of experimental debris-flow deposits

[Location is given with respect to a 1-m^2 grid system on the concrete runout zone; EW coordinates are measured in reference to the end of the flume (mouth of flume is at 0EW) and NS coordinates are measured in reference to the right margin of the runout zone (5NS defines the centerline of the flume). M_z and σ_I are the mean grain diameter and sorting coefficient, respectively, defined by Folk (1984) D_{50} is the median grain diameter]

Experiment date	Sample location	Stratum depth	Sediment content (wt.%)			M_z		D_{50}		Sorting
			gravel	sand	mud	mm	phi units	mm	phi units	σ_I
071692	0.5EW/4NS	upper 4 cm	68	31	1	4.20	-2.07	8.94	-3.16	2.37
		8 cm abv base	59	40	1	2.93	-1.55	4.41	-2.14	2.37
		basal 5 cm	56	43	1	1.21	-1.27	2.91	-1.54	2.26
	0.5EW/5NS	upper 3 cm	74	25	1	4.89	-2.29	9.92	-3.31	2.27
		12 cm abv base	54	44	2	2.31	-1.21	2.83	-1.50	2.43
		basal 5 cm	50	48	2	1.87	-0.90	2.00	-1.00	2.27
	0.5EW/6.5NS	upper 3 cm	68	31	1	4.06	-2.02	8.69	-3.12	2.24
		8 cm abv.base	55	43	2	2.39	-1.26	2.83	-1.50	2.37
		basal 5 cm	54	44	2	2.27	-1.18	2.71	-1.44	2.43
	1EW/5NS	10-15 cm abv base	58	41	1	2.73	-1.45	4.00	-2.00	2.39
		basal 5 cm	51	48	1	1.96	-0.97	2.11	-1.08	2.23
	2EW/5NS	surface	97	2.9	0.1	14.12	-3.82	13.93	-3.80	0.92
		subsurface	67	32	1	4.00	-2.00	8.34	-3.06	2.33
	3EW/4NS	surface	84	15.5	0.5	5.62	-2.49	5.66	-2.50	1.70
		subsurface	64	35	1	3.76	-1.91	8.46	-3.08	2.39
		surface	94.6	5.2	0.2	10.41	-3.38	11.79	-3.56	1.19
		subsurface	64	35	1	3.73	-1.90	7.36	-2.88	2.37

Table 2.3 (continued)

	upper 3 cm	71	28	1	4.59	-2.20	9.38	-3.23	2.30
	9 cm abv base	65	34	1	3.89	-1.96	8.00	-3.00	2.39
	basal 5 cm	64	35	1	3.39	-1.76	6.36	-2.67	2.24
3EW/5.5NS	upper 3 cm	71	28	1	4.20	-2.07	9.25	-3.21	2.30
	12 cm abv base	53	45	2	2.23	-1.16	2.60	-1.38	2.43
	basal 5 cm	49	50	1	1.84	-0.88	1.88	-0.91	2.25
3EW/7NS	upper 3 cm	69	30	1	4.38	-2.13	8.82	-3.14	2.29
	middle	62	36	2	3.51	-1.81	7.11	-2.83	2.52
	basal 5 cm	57	41	2	2.73	-1.45	4.00	-2.00	2.51
3.5EW/7.5NS	surface	83	16.3	0.7	5.82	-2.54	8.28	-3.05	1.77
	10-15 cm abv base	54	44	2	2.31	-1.21	2.71	-1.44	2.43
	basal 5 cm	55	44	1	2.20	-1.14	2.68	-1.42	2.27
4.5EW/4NS	upper 3 cm	66	32	2	3.78	-1.92	8.46	-3.08	2.38
	basal 3 cm	55	43	2	2.31	-1.21	2.83	-1.50	2.33
4.5EW/5.5NS	upper 5 cm	64	34	2	3.81	-1.93	8.00	-3.00	2.45
	middle	60	39	1	3.05	-1.61	4.66	-2.22	2.40
	basal 5 cm	59	40	1	2.73	-1.45	4.00	-2.00	2.37
4.5EW/7NS	upper 5 cm	60	39	1	2.83	-1.50	4.38	-2.13	2.27
	middle	57	41	2	2.60	-1.38	3.68	-1.88	2.44
	basal 5 cm	59	40	1	2.75	-1.46	4.00	-2.00	2.38
6EW/4.5NS	surface	97	2.9	0.1	13.83	-3.79	13.55	-3.76	0.90
	subsurface	57	42	1	2.73	-1.45	3.68	-1.88	2.39
3.5EW/3.5NS	bulk	65	34	1	3.92	-1.97	8.28	-3.05	2.42
4.5EW/7.5NS	bulk	64	35	1	4.03	-2.01	8.17	-3.03	2.39
6EW/7NS	bulk	60	39	1	3.23	-1.69	4.89	-2.29	2.39

Table 2.3 (continued)

092592	2.5EW/5.5NS	surface	87.4	11.8	0.8	12.38	-3.63	12.82	-3.68	1.43
		upper 5 cm	58.1	40.1	1.8	3.03	-1.60	5.35	-2.42	2.46
		basal 5 cm	54.7	43.3	2.0	2.22	-1.15	2.68	-1.42	2.34
	5.5EW/5.5NS	upper 5 cm	68.2	31.0	0.8	3.97	-1.99	8.51	-3.09	2.19
		basal 5 cm	59.6	38.5	1.9	3.01	-1.59	5.21	-2.38	2.38
	7EW/5.5NS	upper 5 cm	55.4	43.1	1.5	2.55	-1.35	3.46	-1.79	2.44
		basal 5 cm	52.9	44.8	2.3	2.14	-1.10	2.73	-1.45	2.40
	10EW/5.5NS	upper 5 cm	54.4	43.7	1.9	2.43	-1.28	3.36	-1.75	2.42
		basal 5 cm	55.5	42.4	2.1	2.38	-1.25	3.10	-1.63	2.42
	14EW/5.5NS	upper 3 cm	62.3	36.4	1.3	3.12	-1.64	4.79	-2.26	2.32
		basal 3 cm	59.8	39.1	1.1	3.10	-1.63	5.24	-2.39	2.43
	2.5EW/5.5NS	bulk	57.3	40.7	2.0	2.81	-1.49	4.29	-2.10	2.41
	5.5EW/5.5NS	bulk	62.9	35.7	1.4	3.66	-1.87	8.00	-3.00	2.32
	7EW/5.5NS	bulk	54.7	43.6	1.7	2.35	-1.23	2.89	-1.53	2.44
	10EW/5.5NS	bulk	55.3	42.9	1.8	2.36	-1.24	2.95	-1.56	2.50
	12EW/4NS	bulk (total)	75.5	23.6	0.9	5.31	-2.41	10.70	-3.42	2.29
		bulk (surface)	96.8	3.0	0.2	15.35	-3.94	15.35	-3.94	0.70
		bulk (subsurface)	67.4	31.6	1.0	4.11	-2.04	9.13	-3.19	2.41
	13.5EW/7.5NS	bulk	63.5	34.8	1.7	3.76	-1.91	8.22	-3.04	2.44
	14EW/5.5NS	bulk	60.5	37.6	1.9	3.20	-1.68	5.98	-2.58	2.43
040793	source		60.6	38.0	1.4	2.93	-1.55	4.23	-2.08	2.34
	source		63.3	35.6	1.1	3.68	-1.88	7.36	-2.88	2.39
	0.5EW/7.5NS	upper 6 cm	63.2	35.9	0.9	3.81	-1.93	8.28	-3.05	2.39
		basal 6 cm	58.7	40.9	0.4	2.75	-1.46	3.76	-1.91	2.36

Table 2.3 (continued)

2EW/4NS	upper 6 cm	65.2	34.2	0.6	3.89	-1.96	8.06	-3.01	2.26
	basal 6 cm	67.1	32.6	0.3	4.00	-2.00	8.06	-3.01	2.12
2EW/5NS	upper 6 cm	54.5	44.4	1.1	2.39	-1.26	2.81	-1.49	2.44
	basal 6 cm	61.4	37.6	1.0	2.66	-1.41	3.41	-1.77	2.19
2EW/7NS	upper 6 cm	57.8	41.1	1.1	2.60	-1.38	3.48	-1.80	2.42
	middle 6 cm	61.2	38.1	0.7	3.53	-1.82	6.87	-2.78	2.34
	basal 6 cm	56.4	43.3	0.3	2.48	-1.31	2.79	-1.48	2.28
4EW/4.5NS	upper 6 cm	70.8	28.8	0.4	4.20	-2.07	8.88	-3.15	2.21
	basal 6 cm	73.7	26.1	0.2	4.66	-2.22	9.25	-3.21	2.05
4EW/6.5NS	upper 6 cm	63.5	35.9	0.6	3.86	-1.95	8.06	-3.01	2.33
	basal 6 cm	58.7	41.1	0.2	2.66	-1.41	3.12	-1.64	2.24
6EW/5NS	upper 6 cm	62.6	36.9	0.5	3.76	-1.91	8.06	-3.01	2.35
	basal 7 cm	59.9	39.8	0.3	2.71	-1.44	3.46	-1.79	2.21
6EW/6.5NS	upper 6 cm	59.3	40.3	0.4	3.12	-1.64	4.56	-2.19	2.35
	basal 6 cm	59.7	40.1	0.2	2.75	-1.46	3.58	-1.84	2.26
8EW/5NS	upper 6 cm	59.6	39.8	0.6	3.03	-1.60	4.08	-2.03	2.34
	basal 6 cm	55.7	43.6	0.7	2.50	-1.32	2.99	-1.58	2.33
10EW/5NS	upper 4 cm	62.7	36.6	0.7	3.34	-1.74	5.90	-2.56	2.27
	middle 4 cm	65.8	33.9	0.3	3.71	-1.89	6.32	-2.66	2.09
	basal 4 cm	62.2	37.6	0.2	2.81	-1.49	3.66	-1.87	2.07
2EW/5NS	bulk	53.1	45.7	1.2	2.31	-1.21	2.75	-1.46	2.45
4EW/5NS	bulk	66.8	32.4	0.8	3.81	-1.93	8.06	-3.01	2.27
6EW/5NS	bulk	63.0	36.3	0.7	2.97	-1.57	3.97	-1.99	2.22
8EW/5NS	bulk	57.4	41.9	0.7	2.62	-1.39	3.41	-1.77	2.38
10EW/5NS	bulk	64.3	35.2	0.5	3.41	-1.77	5.82	-2.54	2.23

Table 2.3 (continued)

040893	source		57.6	40.6	1.8	2.65	-1.41	3.86	-1.95	2.35
	source		64.6	33.8	1.6	3.23	-1.69	5.28	-2.40	2.31
	source		62.8	35.6	1.6	3.14	-1.65	5.21	-2.38	2.33
	2EW/4NS	upper 6 cm	66.3	32.8	0.9	3.61	-1.85	6.45	-2.69	2.27
		basal 6 cm	66.4	33.1	0.5	3.53	-1.82	6.73	-2.75	2.19
	2EW/5NS	surface	74.4	23.7	1.9	4.26	-2.09	9.19	-3.20	2.41
		upper 6 cm (below surface)	61.5	37.0	1.5	3.12	-1.64	5.10	-2.35	2.38
		6-12 cm	62.6	36.3	1.1	3.32	-1.73	5.90	-2.56	2.33
		12-18 cm	59.5	39.5	1.0	2.71	-1.44	4.20	-2.07	2.29
	4EW/4.5NS	upper 6 cm	62.7	36.2	1.1	3.23	-1.69	5.82	-2.54	2.32
		basal 6 cm	61.7	37.4	0.9	3.18	-1.67	5.50	-2.46	2.36
	6EW/3NS	upper 7 cm	62.2	36.5	1.3	3.25	-1.70	6.11	-2.61	2.38
		basal 7 cm	60.4	38.9	0.7	3.01	-1.59	5.28	-2.40	2.44
		basal 3 cm	54.4	44.4	1.2	2.11	-1.08	2.95	-1.56	2.60
	6EW/5NS	upper 3 cm	67.3	31.1	1.6	4.08	-2.03	8.46	-3.08	2.41
		basal 3 cm	68.8	30.3	0.9	4.29	-2.10	8.63	-3.11	2.29
	6EW/6.5NS	upper 7 cm	65.6	33.9	0.5	3.63	-1.86	5.82	-2.54	2.19
		basal 7 cm	69.7	29.3	1.0	4.23	-2.08	8.69	-3.12	2.38
	8EW/2.5NS	upper 3.5 cm	67.8	31.4	0.8	3.92	-1.97	8.40	-3.07	2.34
		basal 3.5 cm	60.0	38.6	1.4	2.87	-1.52	5.10	-2.35	2.52
	2EW/2NS	bulk	65.4	34.2	0.4	4.00	-2.00	8.22	-3.04	2.33
	2EW/5NS	bulk	62.7	36.3	1.0	3.16	-1.66	5.43	-2.44	2.34
	2EW/7NS	bulk (without surface clasts)	59.5	40.0	0.5	2.79	-1.48	4.26	-2.09	2.41
	4EW/2NS	bulk	70.1	29.3	0.6	4.29	-2.10	9.71	-3.28	2.47
	4EW/4.5NS	bulk	62.5	36.1	1.4	3.32	-1.73	5.78	-2.53	2.36
	4EW/6.5NS	bulk	66.2	33.2	0.6	3.86	-1.95	8.06	-3.01	2.28
	4EW/8NS	bulk	66.8	32.6	0.6	4.00	-2.00	8.57	-3.10	2.49

Table 2.3 (continued)

	6EW/1NS	bulk	73.0	25.3	1.7	4.59	-2.20	10.34	-3.37	2.50
	6EW/3NS	bulk	61.9	37.0	1.1	3.01	-1.59	5.46	-2.45	2.45
	8EW/1NS	bulk	69.3	29.2	1.5	4.35	-2.12	9.25	-3.21	2.43
	8EW/2.5NS	bulk	65.6	33.3	1.1	3.71	-1.89	8.06	-3.01	2.44
052694	source		13.5	84.4	2.1	0.50	0.99	0.41	1.27	1.67
	source		12.8	83.3	3.9	0.41	1.28	0.34	1.55	1.82
	source		19.6	76.1	4.3	0.56	0.83	0.42	1.25	2.11
	source		19.2	76.7	4.1	0.57	0.81	0.44	1.19	2.03
	1EW/2.5NS	bulk	49.4	46.0	4.6	1.69	-0.76	1.85	-0.89	2.79
	1EW/5NS	bulk	21.3	71.0	7.7	0.52	0.94	0.39	1.36	2.47
	1EW/7.5NS	bulk	49.2	46.2	4.6	1.65	-0.72	1.78	-0.83	2.79
	4EW/2.5NS	bulk	50.6	44.4	5.0	1.76	-0.82	2.14	-1.10	2.78
	4EW/5NS	bulk	49.8	45.5	4.7	1.73	-0.79	1.95	-0.96	2.81
	4EW/7.5NS	bulk	48.6	46.9	4.5	1.63	-0.70	1.63	-0.70	2.81
	7EW/2NS	bulk	55.3	40.5	4.2	2.25	-1.17	3.58	-1.84	2.79
	7EW/5NS	bulk	48.6	46.4	5.0	1.61	-0.69	1.67	-0.74	2.81
	7EW/7NS	bulk	50.9	44.9	4.2	1.80	-0.85	2.14	-1.10	2.70
	9EW/2NS	bulk	34.4	60.2	5.4	0.98	0.04	0.50	1.01	2.87
	9EW/5NS	bulk	22.1	70.8	7.1	0.57	0.81	0.39	1.36	2.52
	9EW/6.5NS	bulk	23.6	71.3	5.1	0.59	0.74	0.42	1.25	2.31
	11EW/5NS	bulk	54.3	41.9	3.8	2.30	-1.20	3.68	-1.88	2.69
	11EW/6.5NS	bulk	45.6	50.2	4.2	1.40	-0.49	2.91	-1.54	2.72
	13EW/5NS	bulk	65.5	31.4	3.1	3.43	-1.78	8.94	-3.16	2.66
	13EW/7NS	bulk	25.2	69.0	5.8	0.77	0.38	0.43	1.23	2.66
072194	source		37.0	60.9	2.1	1.20	-0.27	1.10	-0.14	1.91
	source		39.1	58.7	2.2	1.29	-0.37	1.20	-0.27	1.96
	3EW/5NS		39.7	57.0	3.3	1.21	-0.28	1.20	-0.26	2.09
	6EW/5NS		35.4	60.8	3.8	1.04	-0.05	1.05	-0.06	1.97
	10EW/5NS		34.7	62.7	2.6	1.06	-0.10	0.96	0.06	2.06
	14EW/5NS		38.8	59.4	1.8	1.25	-0.32	1.13	-0.18	1.99
	14.5/5NS		31.5	66.3	2.2	0.97	0.04	0.91	0.14	1.81
	17EW/5NS		38.8	59.1	2.1	1.27	-0.35	1.09	-0.12	1.97
	20EW/5NS		41.6	55.8	2.6	1.46	-0.55	1.31	-0.39	2.22
	24EW/5NS		41.3	56.4	2.3	1.41	-0.49	1.25	-0.32	2.11

Table 2.3 (continued)

	28EW/5NS	39.5	57.6	2.9	1.36	-0.44	1.13	-0.18	2.26
	17EW/3NS	41.3	56.5	2.2	1.41	-0.50	1.28	-0.36	2.10
	20EW/3NS	40.3	57.3	2.4	1.32	-0.40	1.27	-0.35	2.04
	24EW/3NS	37.0	60.3	2.7	1.16	-0.22	1.06	-0.08	1.97
	17EW/7.5NS	43.1	54.9	2.0	1.51	-0.60	1.40	-0.49	2.19
	20EW/8NS	42.7	55.1	2.2	1.49	-0.58	1.37	-0.45	2.16
	24EW/8.5NS	50.6	47.6	1.8	1.98	-0.99	2.06	-1.04	2.26
083194	source	51.8	46.6	1.6	2.51	-1.33	2.31	-1.21	2.61
	source	61.8	36.8	1.4	4.28	-2.10	8.13	-3.02	2.49
	source	54.2	43.8	2.0	2.72	-1.44	3.12	-1.65	2.69
	source	48.0	49.9	2.1	2.03	-1.02	1.63	-0.71	2.83

Table 2.4. Summary of eigenvalue-method analyses of clast fabrics

[Analyses are for clasts larger than 8mm (-3ϕ) in the 4-8-93, 5-6-93 and 5-26-94 deposits. Eigenvector V_1 represents the axis of maximum clustering of the c-axis, which is the pole to the average a-b plane. Eigenvector V_3 represents the axis of minimum clustering of the c axis. The values S_i are measures of fabric strength. Values of $S_1 > 0.473$ and $S_3 < 0.203$ are significant at the 0.05 level (Mark, 1973). Seventeen to 27 clasts were measured at each site. See Figures 2.31-2.33 for site locations. Azimuthal orientation (see Figure 2.31) is: east=0°; north=90°; west=180°; and south=270°]

Date (mmddyy)	Site	N	V_1 azimuth	V_1 dip	S_1	Preferred a-b plane azimuth	Preferred a-b plane dip	V_3 azimuth	V_3 dip	S_3
040893	1	27	303	20	0.545	033	70 NW	208	10	0.129
	2	25	253	68	0.628	163	22 NE	150	5	0.155
	3	25	144	25	0.507	054	65 SE	236	7	0.144
	4	25	114	2	0.471	024	88 SE	023	8	0.173
	5	25	154	1	0.543	064	89 SE	063	12	0.123
	6	25	228	46	0.533	138	44 NE	326	6	0.198
	7	25	254	60	0.681	164	30 NE	140	13	0.109
	8	25	299	63	0.517	209	27 NW	069	18	0.194
	9	25	294	33	0.546	204	57 NW	025	3	0.083
050693	1	25	264	56	0.605	174	34 NE	012	11	0.145
	2	24	197	51	0.597	107	39 E	098	8	0.166
	3	25	331	55	0.463	061	35 NW	202	24	0.233

Table 2.4 (continued)

	4	25	333	09	0.606	063	81 NW	242	6	0.096
	5	25	265	51	0.646	175	39 N	174	2	0.116
	6	25	288	72	0.601	018	18 N	162	11	0.085
	7	18	332	16	0.613	062	74 NW	070	29	0.144
	8	17	198	68	0.721	108	22 E	080	10	0.045
	9	19	294	81	0.776	024	9 NNW	174	5	0.089
	10	21	201	68	0.489	111	22 NE	307	6	0.136
	11	17	250	78	0.687	160	12 NE	122	7	0.123
	12	22	202	45	0.527	292	45 NE	297	4	0.057
052694	1	20	189	82	0.629	099	8 ENE	037	7	0.154
	2	25	128	84	0.695	038	6 SE	027	1	0.062
	3	24	343	77	0.735	073	13 NNW	094	5	0.123

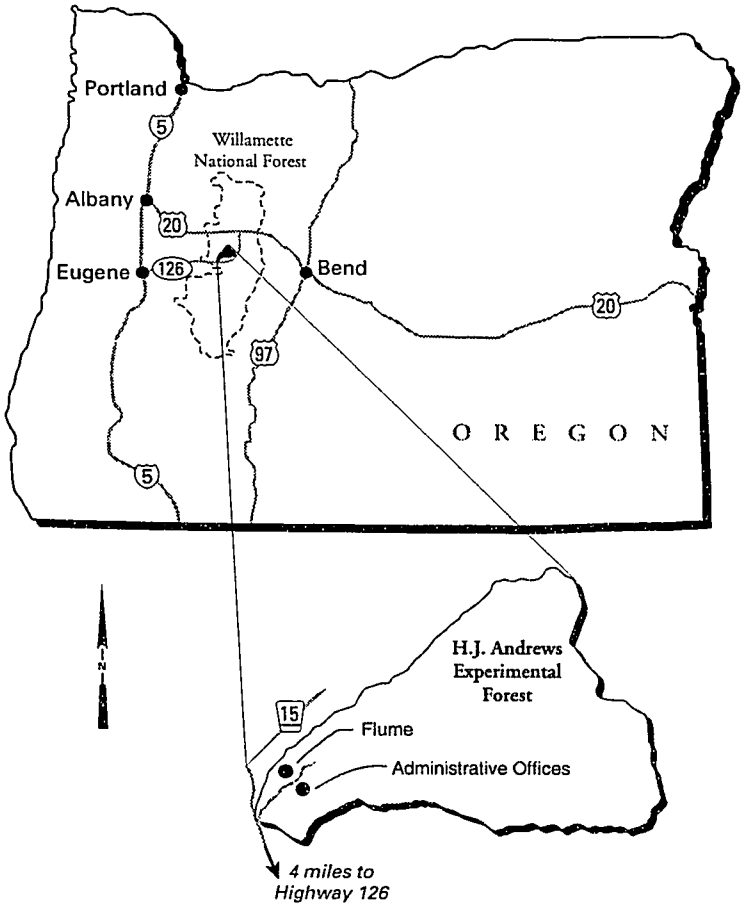

Figure 2.1. Location of U.S. Geological Survey debris-flow flume at H.J. Andrews Experimental Forest, Oregon (from Iverson and others, 1992).

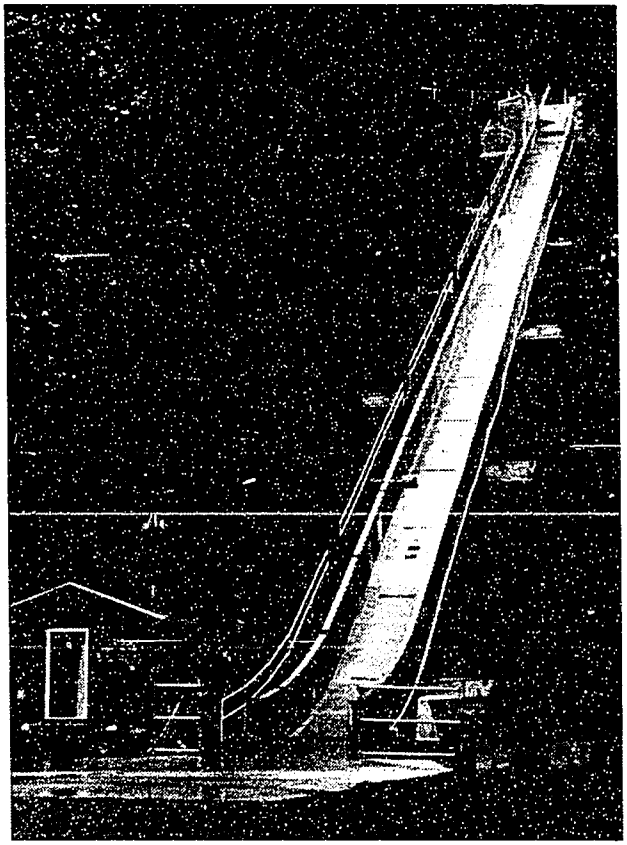

Figure 2.2. U.S. Geological Survey debris-flow flume.

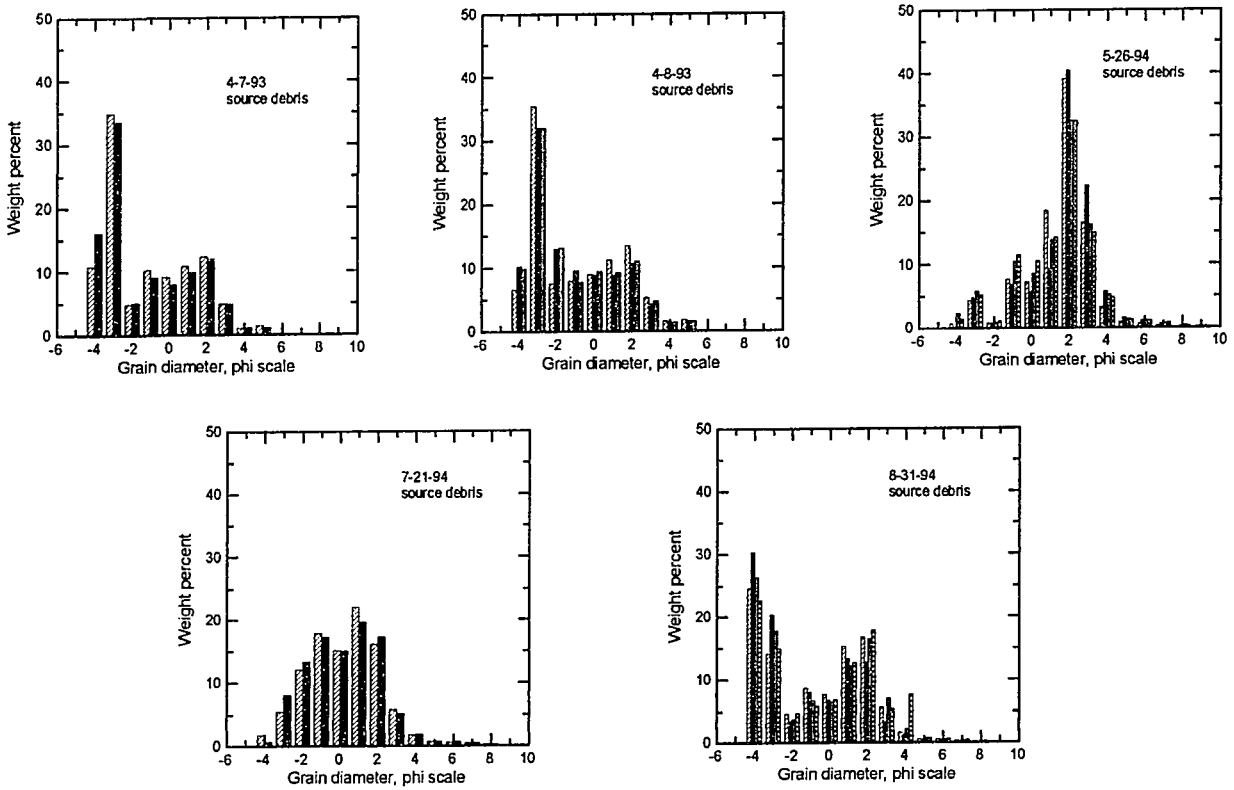

Figure 2.3. Grain-size distribution histograms of source debris used in experiments. Multiple charts on a single graph reflect multiple samples. The source material used for all other experiments shown in Table 2.2 is the same as that shown for the April 7 and April 8, 1993 experiments.

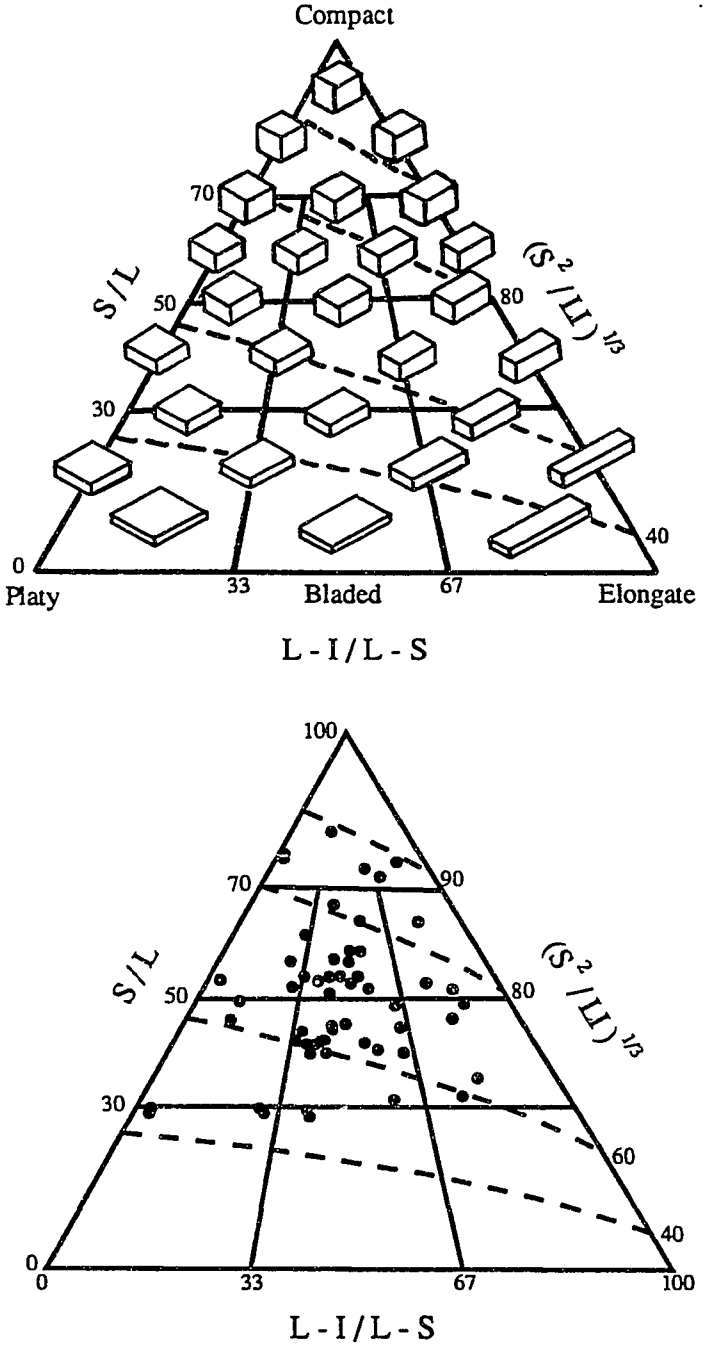

Figure 2.4. Form diagram for 8- to 32-mm-diameter particles in the experimental source material. Upper diagram (from Folk, 1984) illustrates particle shapes associated with various positions on the diagram. L = longest axis; I = intermediate axis; S = shortest axis.

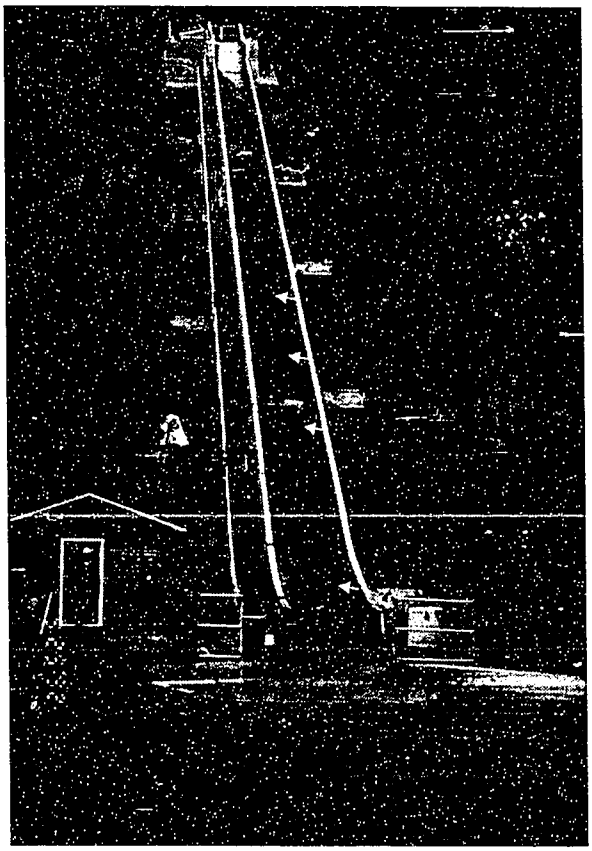

Figure 2.5. Experimental debris flow descending flume on September 25, 1992. Note the surge waves that have developed in the flow (arrows), and the runout surface beyond the flume.

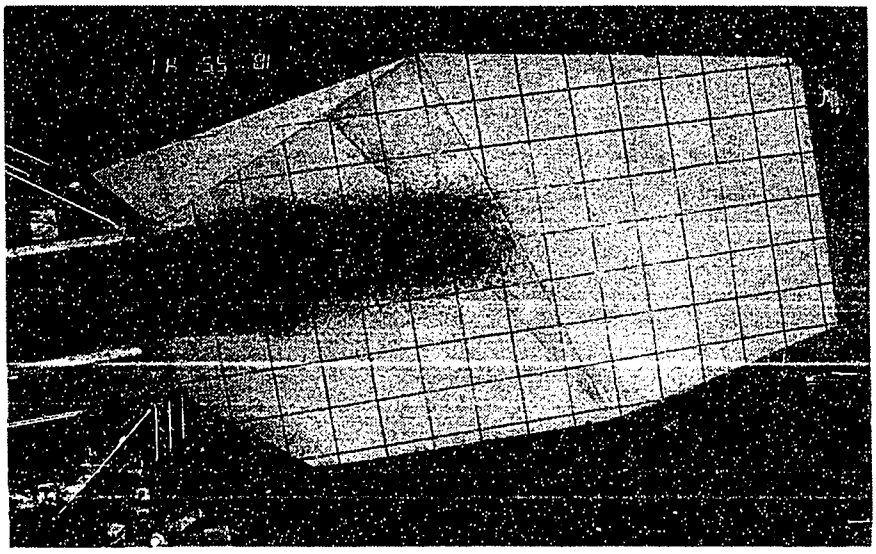

Figure 2.6. Overhead view of an experimental debris flow exiting flume. Note that the leading edge of the flow is characterized by a diffuse wave of saltating coarse particles. Lines on runout pad define a 1-meter-square grid.

Figure 2.7. Examples of experimental debris-flow deposits from unsaturated flows. Characteristic features similar to those in natural deposits include: lobate planforms, steep margins, and concentrated surface gravel. Note the prominent arcuate surface ridges on each deposit. A. Deposit of June 10, 1992. B. Deposit of July 16, 1992. Compare figure B with figure 2.11.

Figure 2.8. Example of steep, blunt margin developed in deposit from an unsaturated experimental debris flow.

Figure 2.9. Isopach maps of experimental deposits. Contour interval is 4 cm. May 21, 1992, data from J.E Costa (unpublished data).

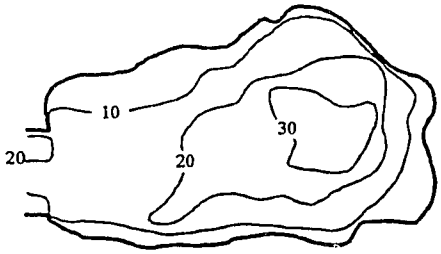

5-21-92

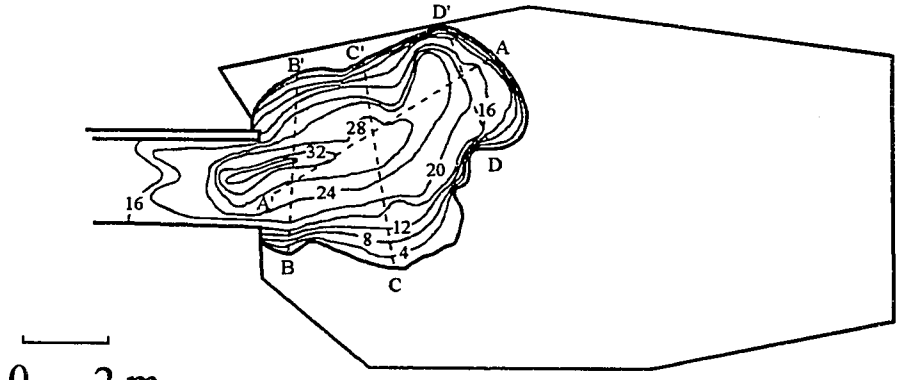

7-16-92

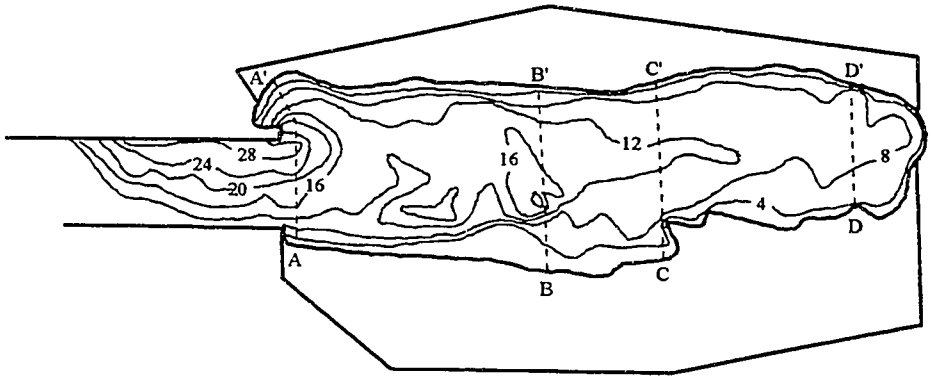

9-25-92

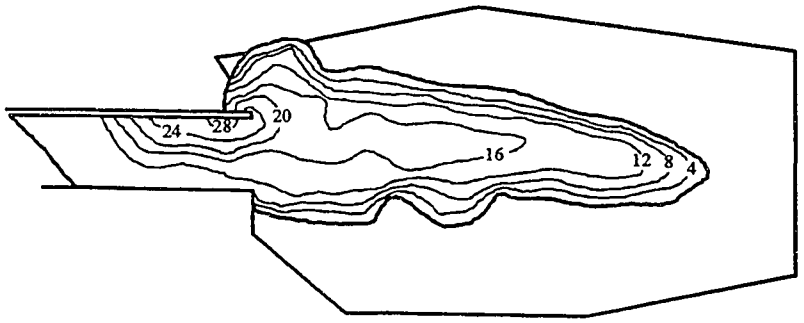

4-7-93

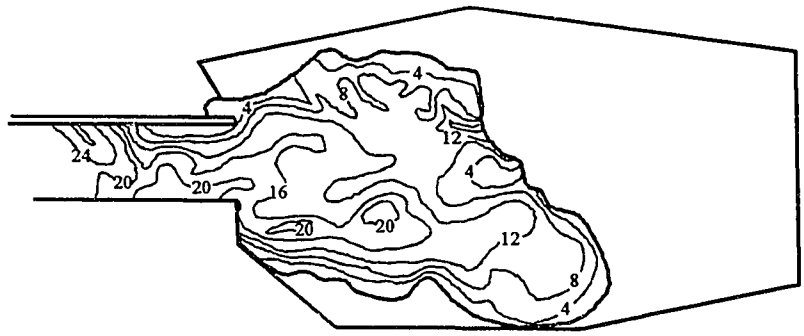

0 2 m

4-8-93

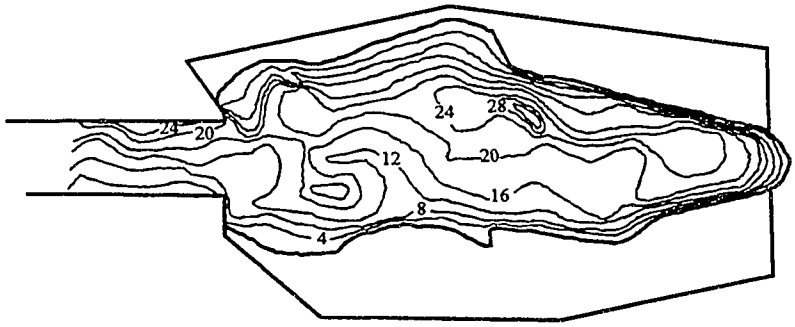

5-6-93

Figure 2.9 (continued)

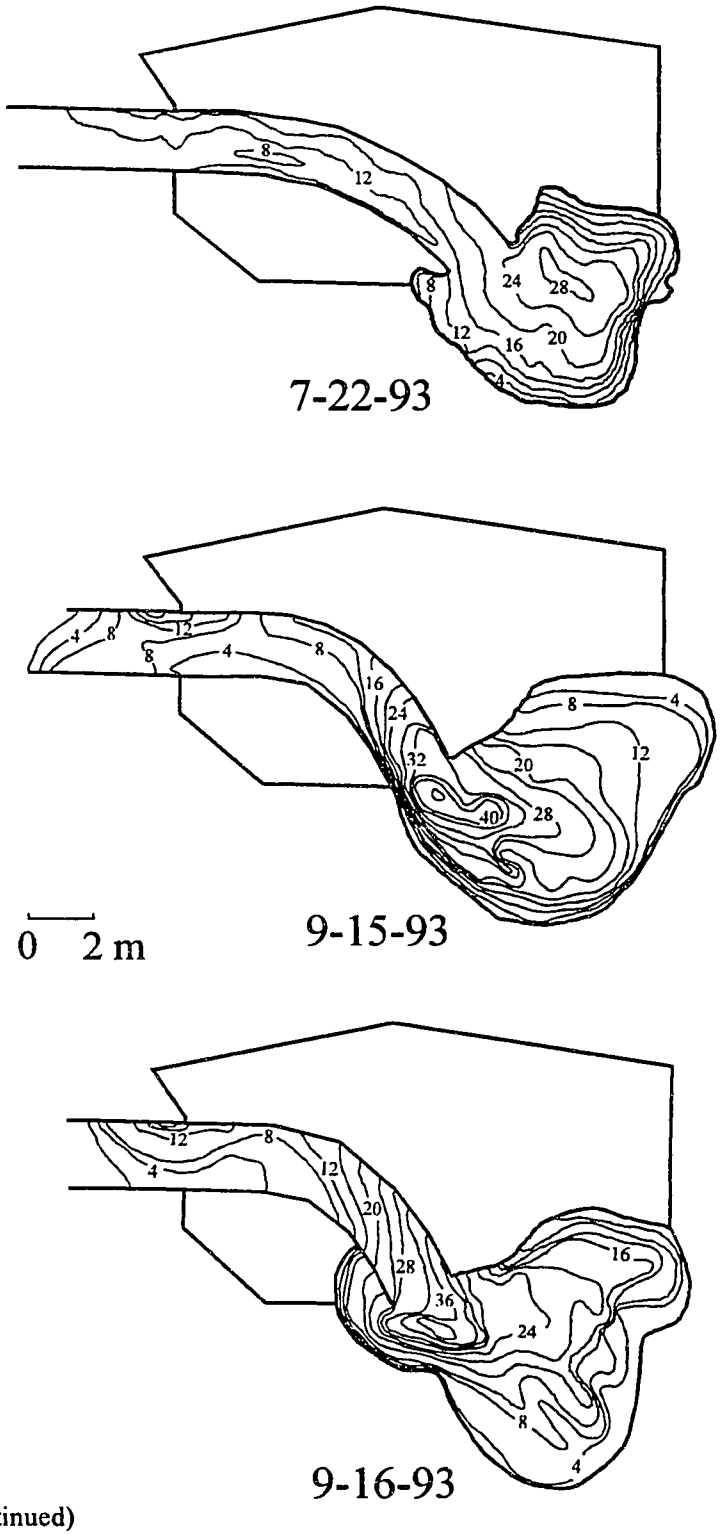

Figure 2.9 (continued)

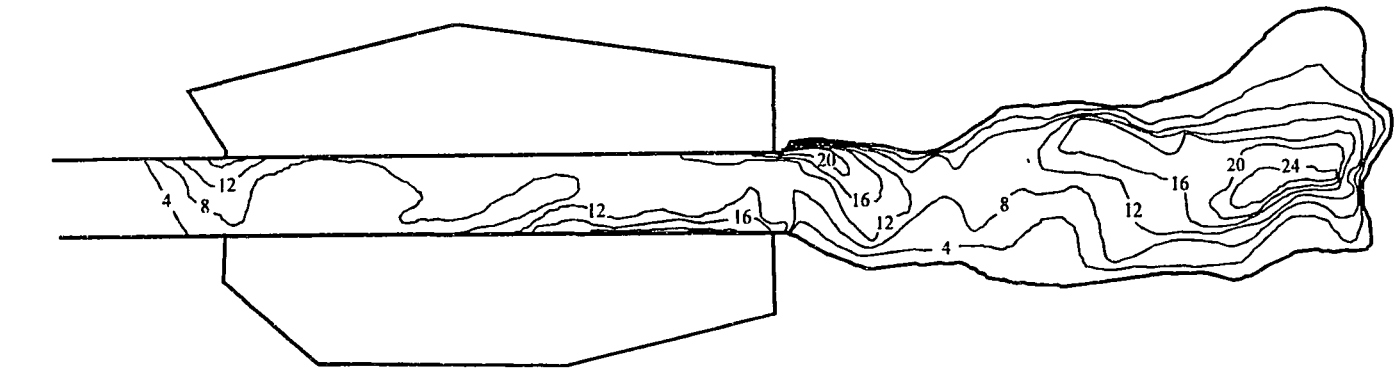

10-19-93

0 2 m

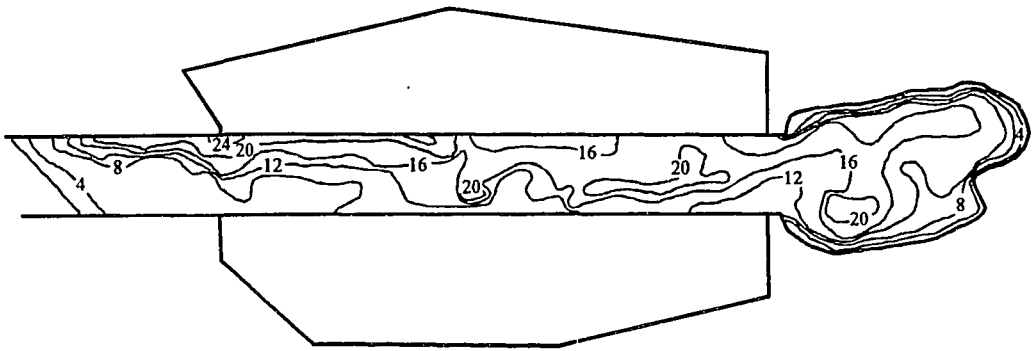

10-21-93

Figure 2.9 (continued)

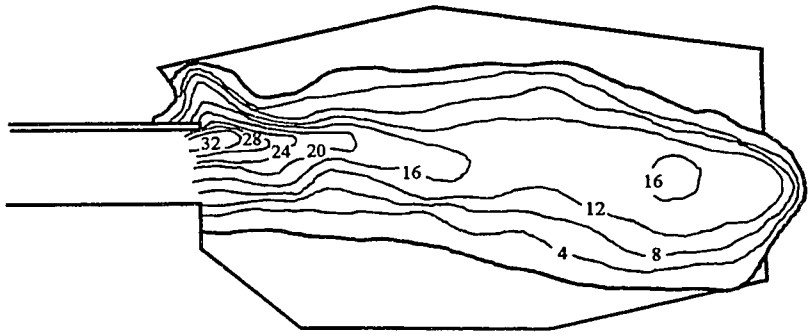

4-19-94

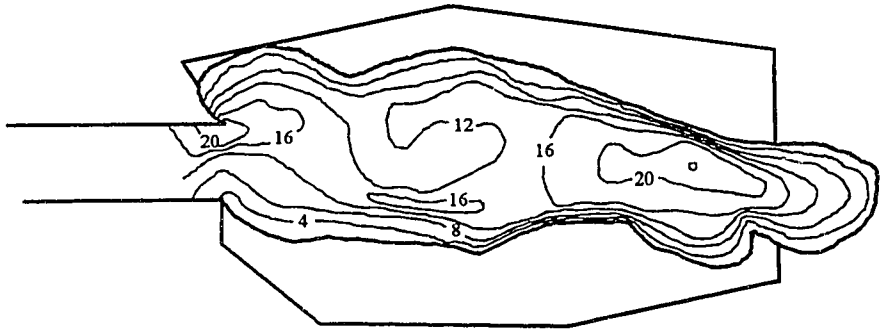

0 2 m

4-21-94

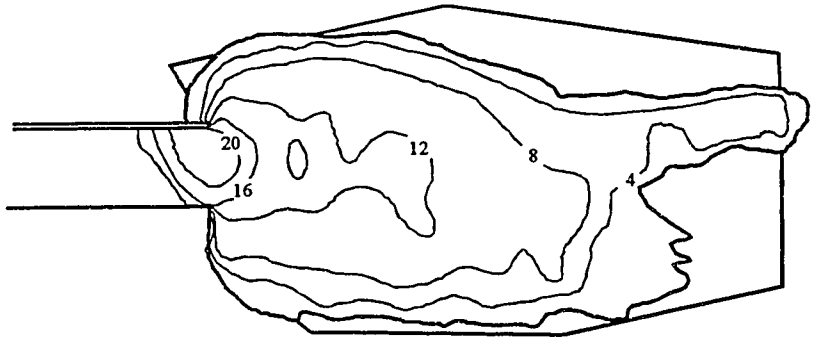

5-26-94

Figure 2.9 (continued)

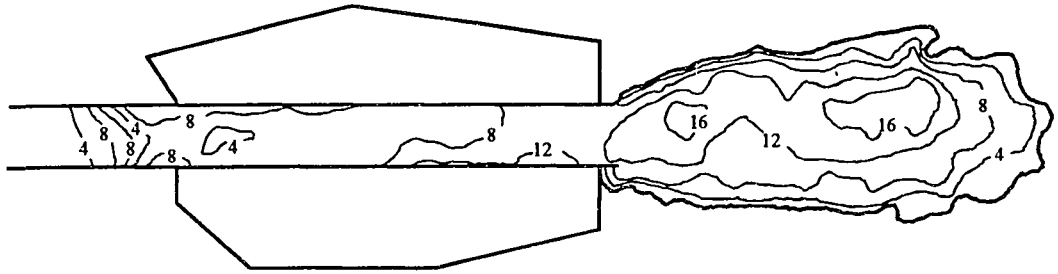

7-20-94

0 2 m

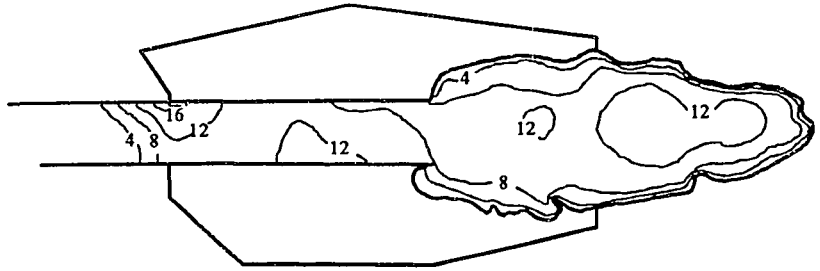

8-31-94

Figure 2.9 (continued)

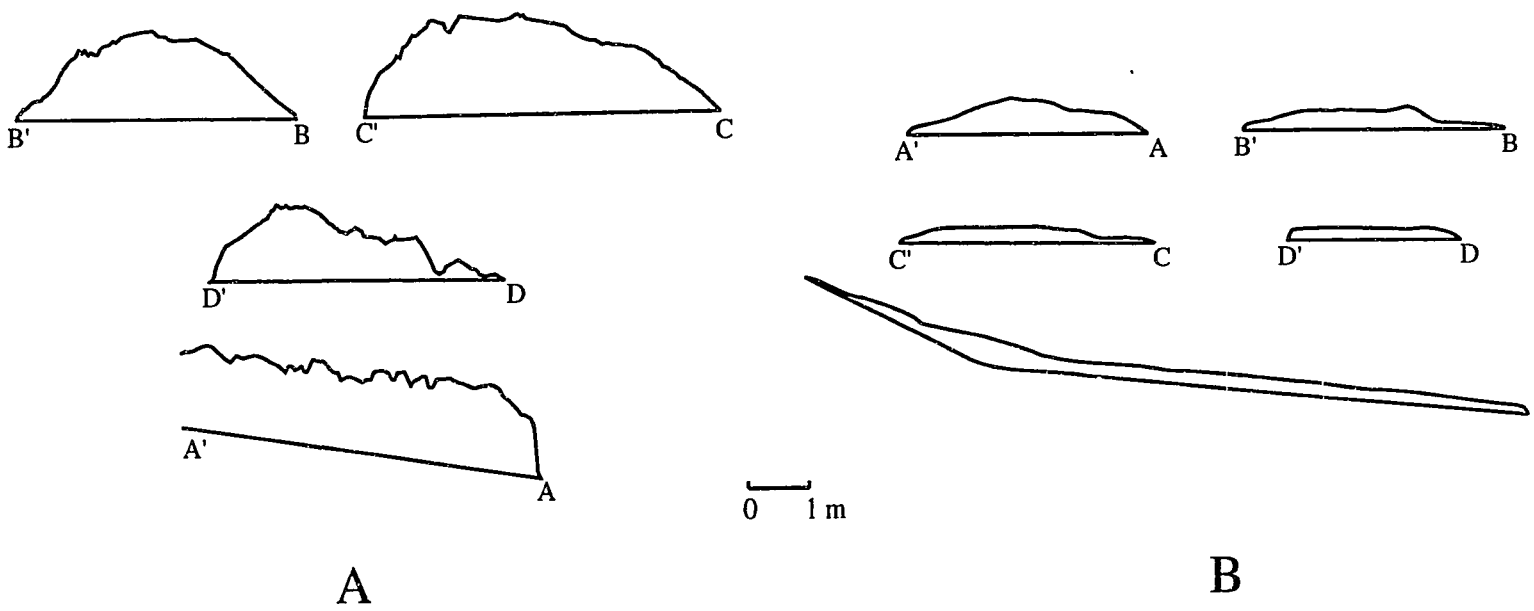

Figure 2.10. Profiles of two experimental debris-flow deposits. A. Deposit from unsaturated flow (July 16, 1992). Note surface ridges. Vertical exaggeration is 5x. B. Deposit from saturated flow (September 25, 1992). Vertical exaggeration is 2x. Section locations shown in Figure 2.9. Longitudinal profiles along central axis of deposit.

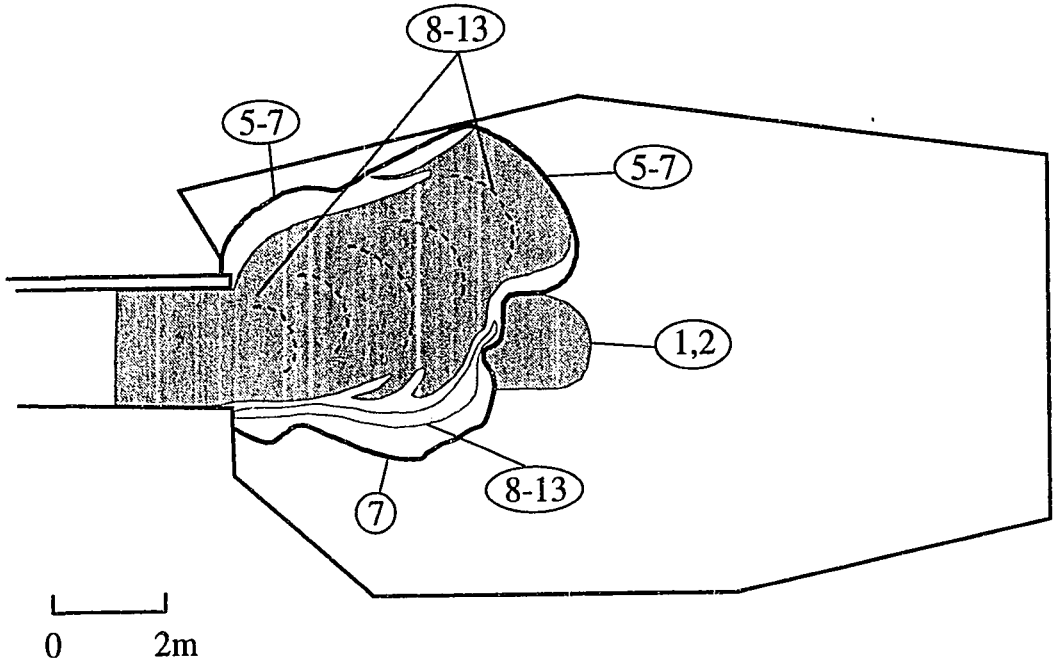

Figure 2.11. Surface texture developed on deposit from unsaturated flow on July 16, 1992. Dark stippled pattern represents dominantly gravel surface; light stippled pattern represents gravelly sand surface; white areas represent sandy surface. Dashed lines represent areas of positive surface relief. Numbers refer to surge or surges responsible for surface texture observed at location.

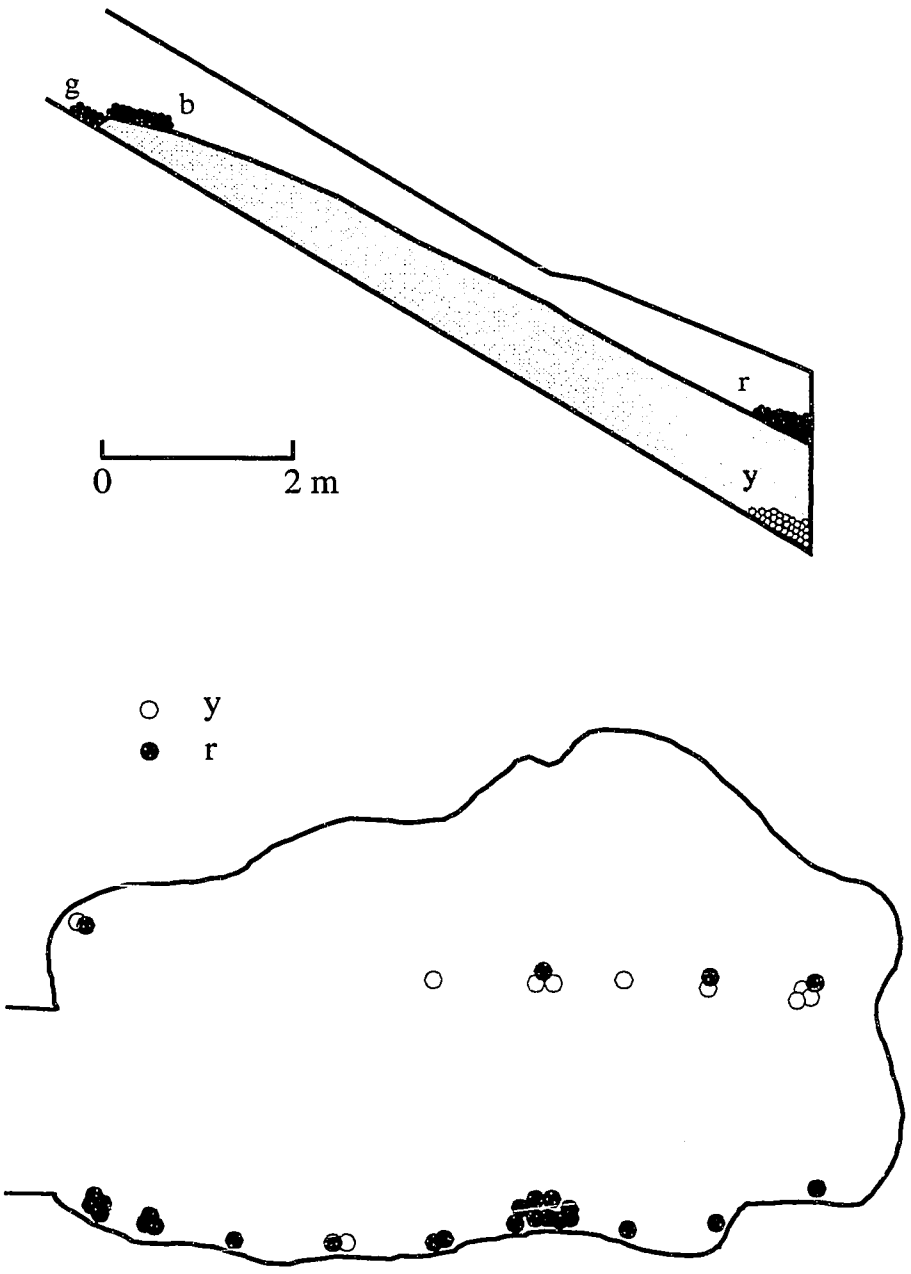

Figure 2.12. Locations of colored tracer particles in source debris and deposit of May 21, 1992, flow (from Costa, 1992; unpublished data). Clusters of symbols in deposit represent relative percentages of particles rather than individual clasts. Yellow particles were found exclusively at the base of the deposit. y = yellow particles; r = red particles; b = blue particles; g = green particles.

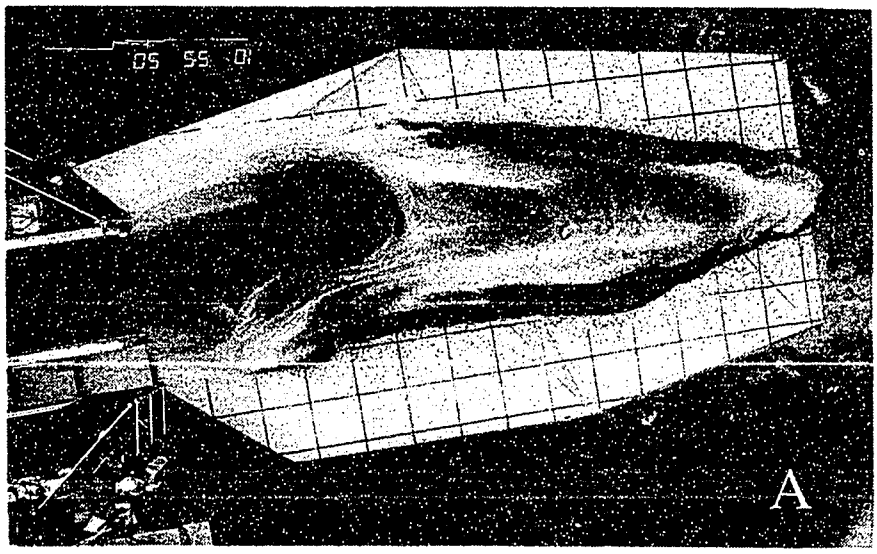

Figure 2.13. Example of experimental debris-flow deposit from a saturated flow (May 6, 1993). Note the elongate shape of the deposit. A. Overhead view. Note effects of deposition by multiple surges. Dark areas represent concentrated surface gravel; light areas represent a wet, sand-dominated surface. B. Ground-level view. Note areas of gravel accumulation, which are light colored. Compare areas of surface gravel (lighter color) with dark patches illustrated in Figure 2.13A.

Figure 2.13 (continued)

Figure 2.14. Sequence of photographs illustrating debris-flow deposit forming by progressive vertical accretion of sediment transported by successively overlapping surges. The sequence encompasses approximately 9 seconds. A region of saltating dry particles precedes the main body of flow (A). Note how one large surge sweeps completely over previously deposited material (E-J). Lobate morphology and concentrated patches of surface gravel (arrows in E, F) identify surge margins. Compare this sequence of photographs with figures 2.13B and 2.15. A one-meter grid provides scale.

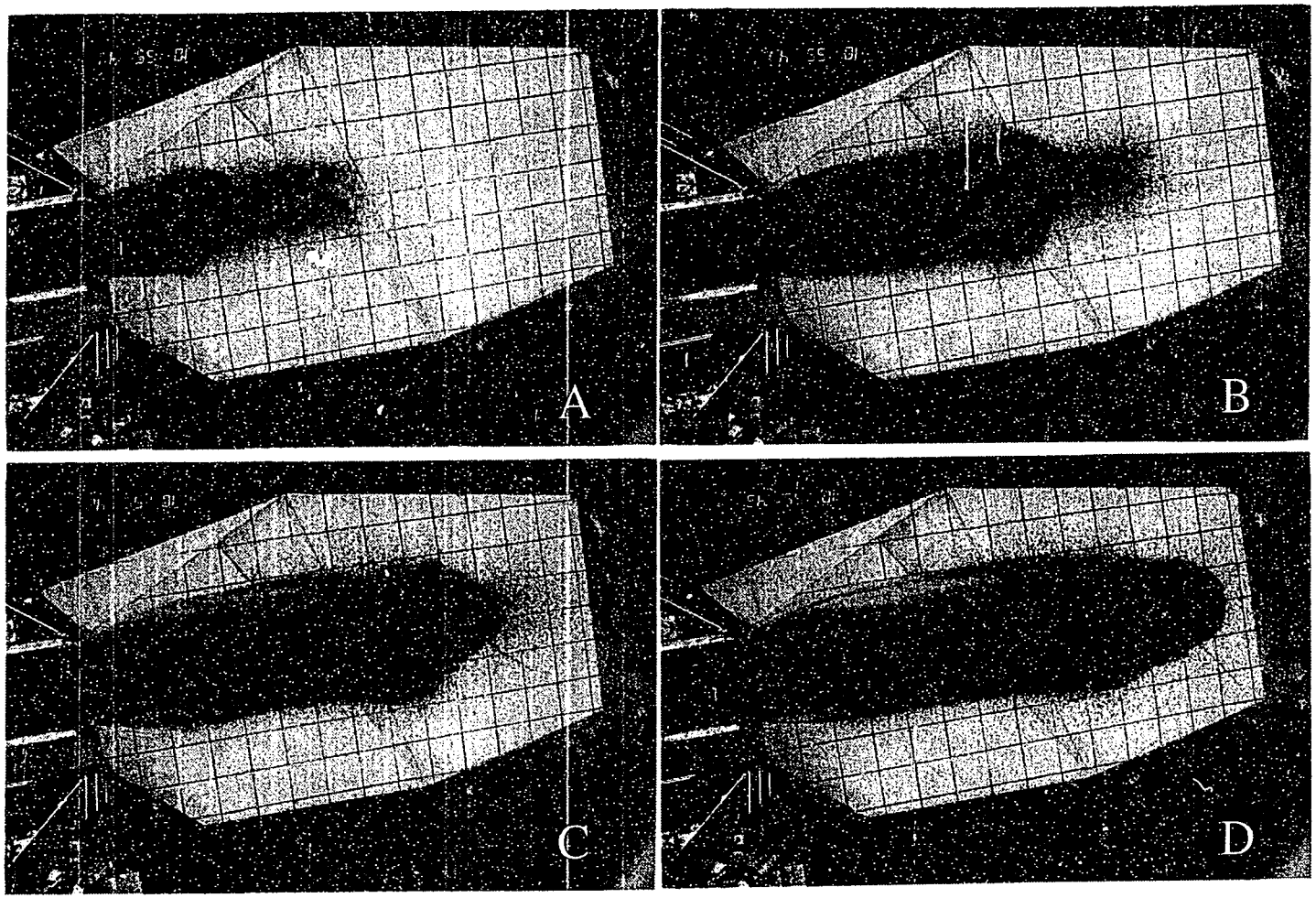
A
B
C
D

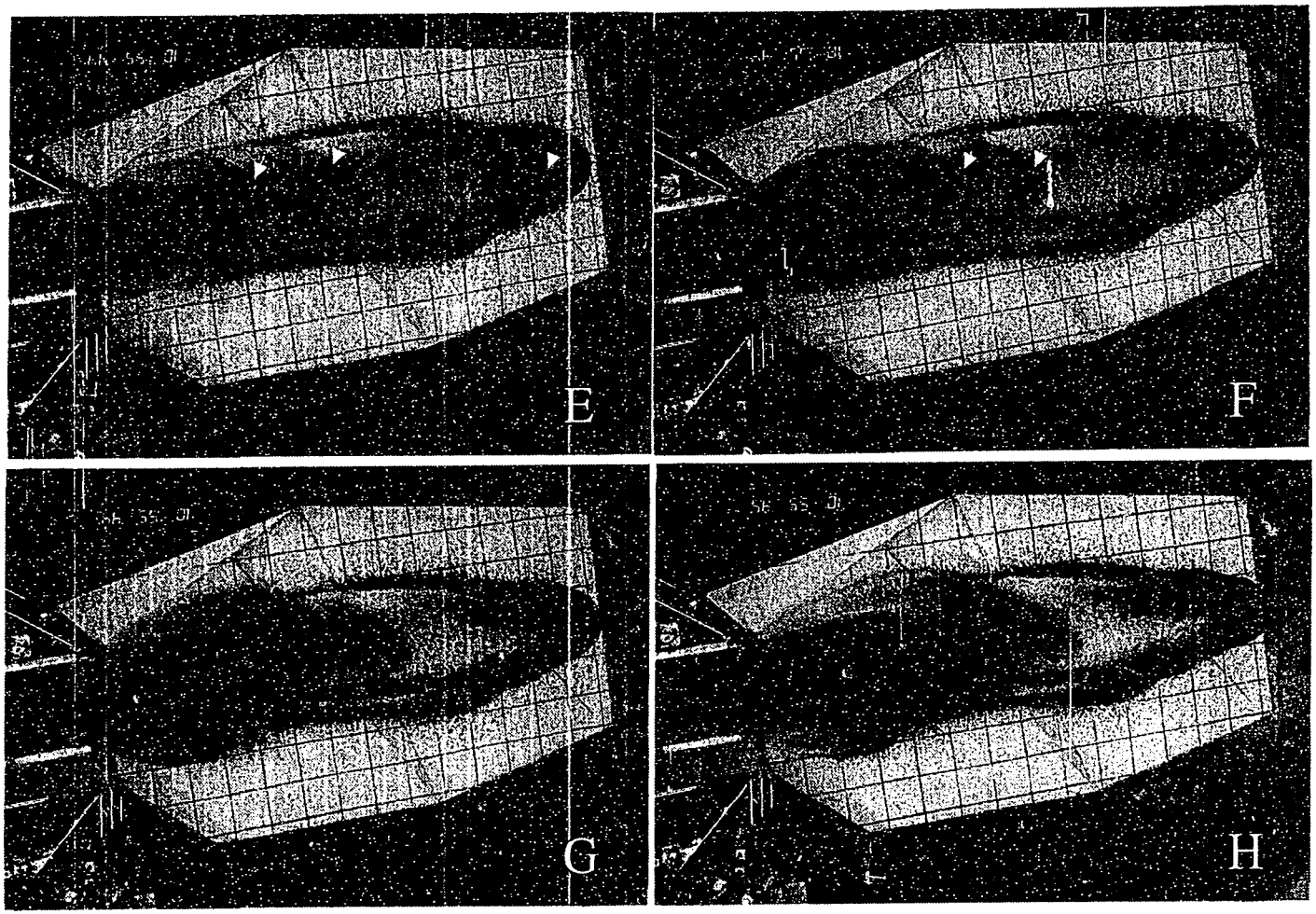

Figure 2.14 (continued)

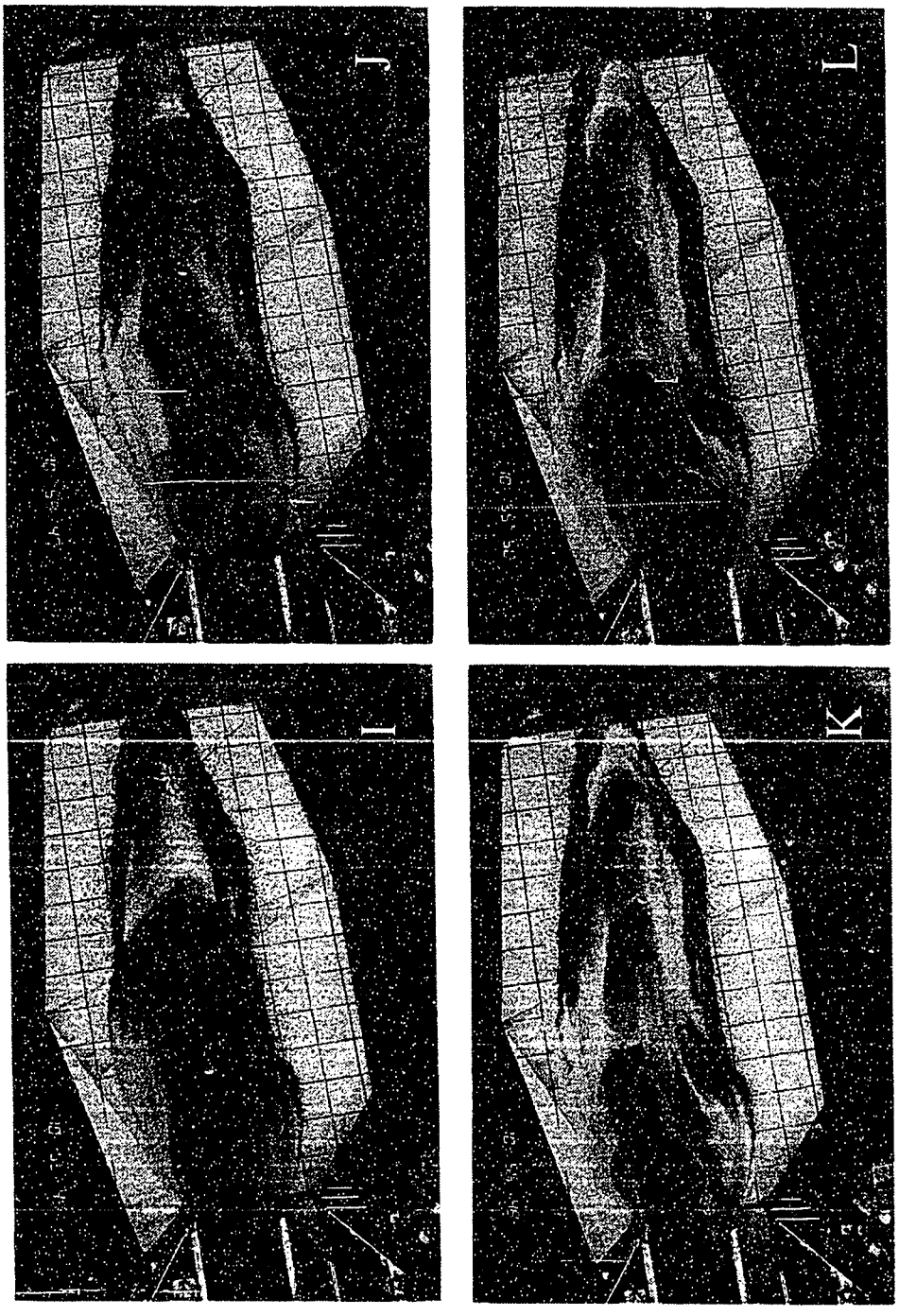

Figure 2.14 (continued)

Figure 2.15. Examples of surface textures developed on deposits from saturated flows. Dark stippled pattern represents dominantly gravel surface; light stippled pattern represents gravelly sand surface; white areas represent sandy surface. Dashed lines represent areas of minor positive surface relief. Numbers refer to surge or surges responsible for surface texture observed at that location. Deposits from October 1993 and July 1994 extended farther than photographic coverage thus precluding development of a "surge" map.

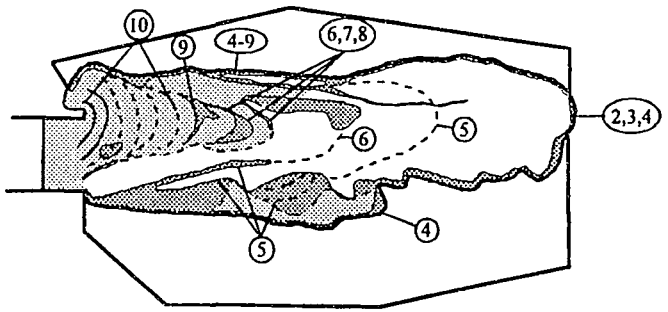

9-25-92

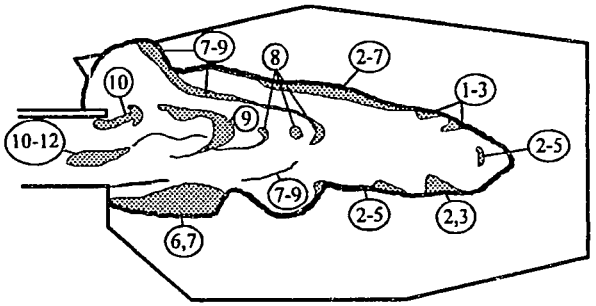

4-7-93

0 2 m

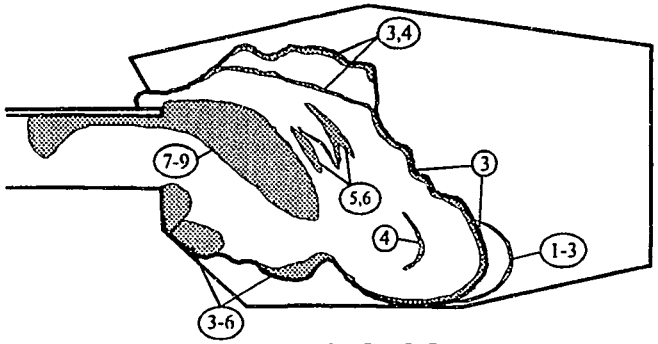

4-8-93

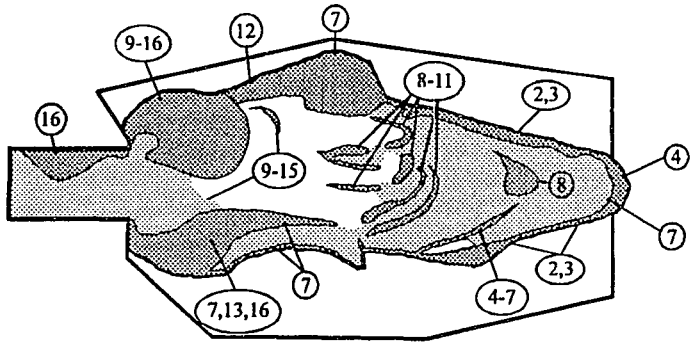

5-6-93

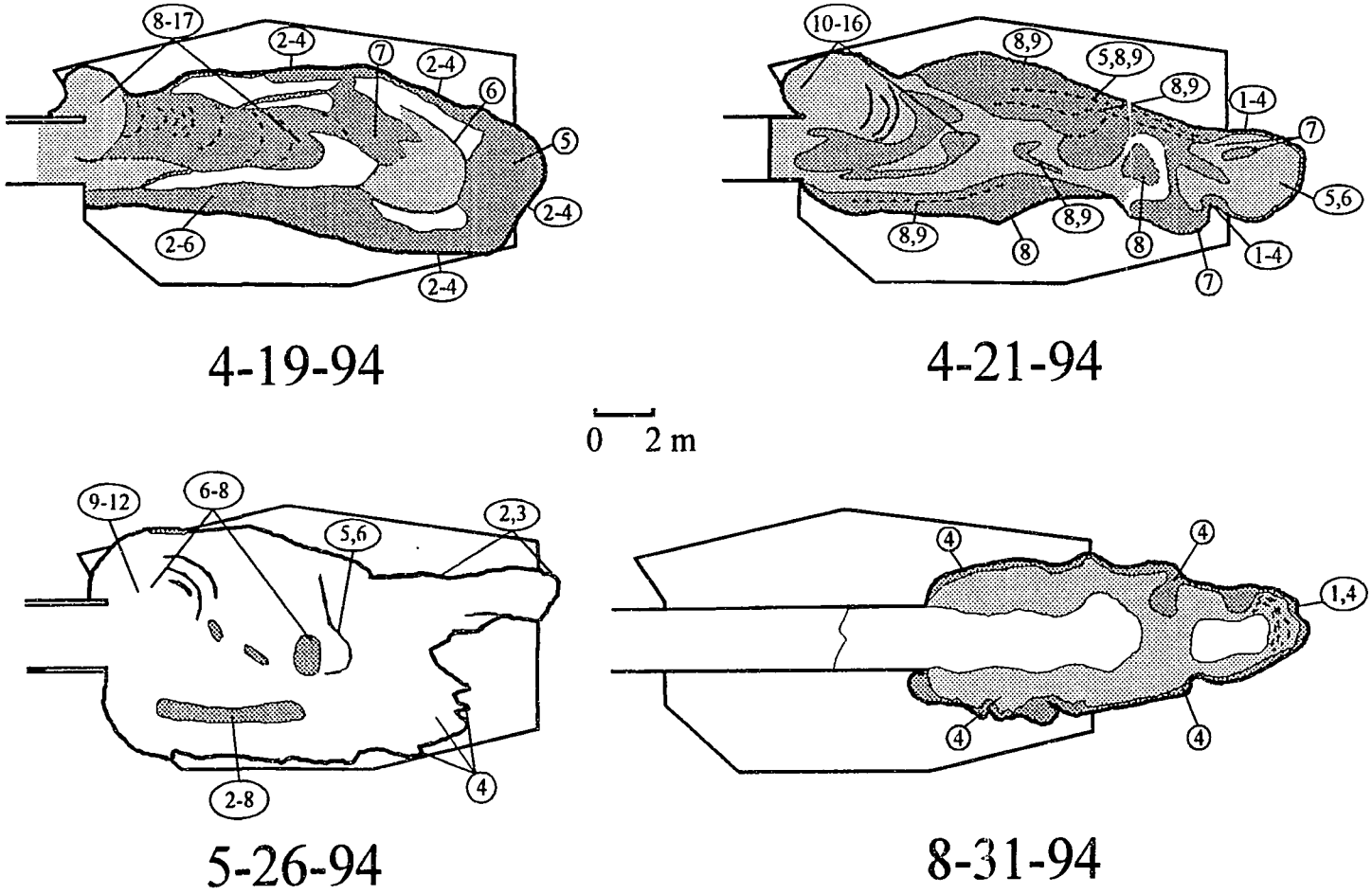

Figure 2.15 (continued)

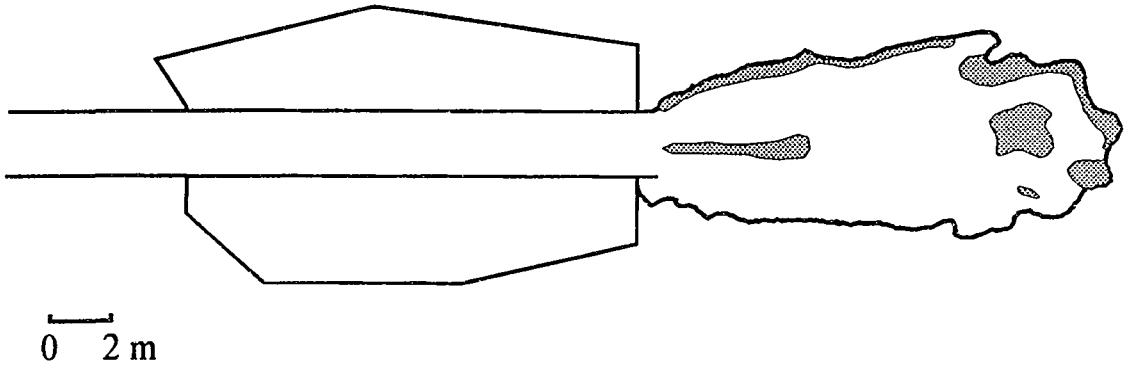

7-20-94

Figure 2.15 (continued)

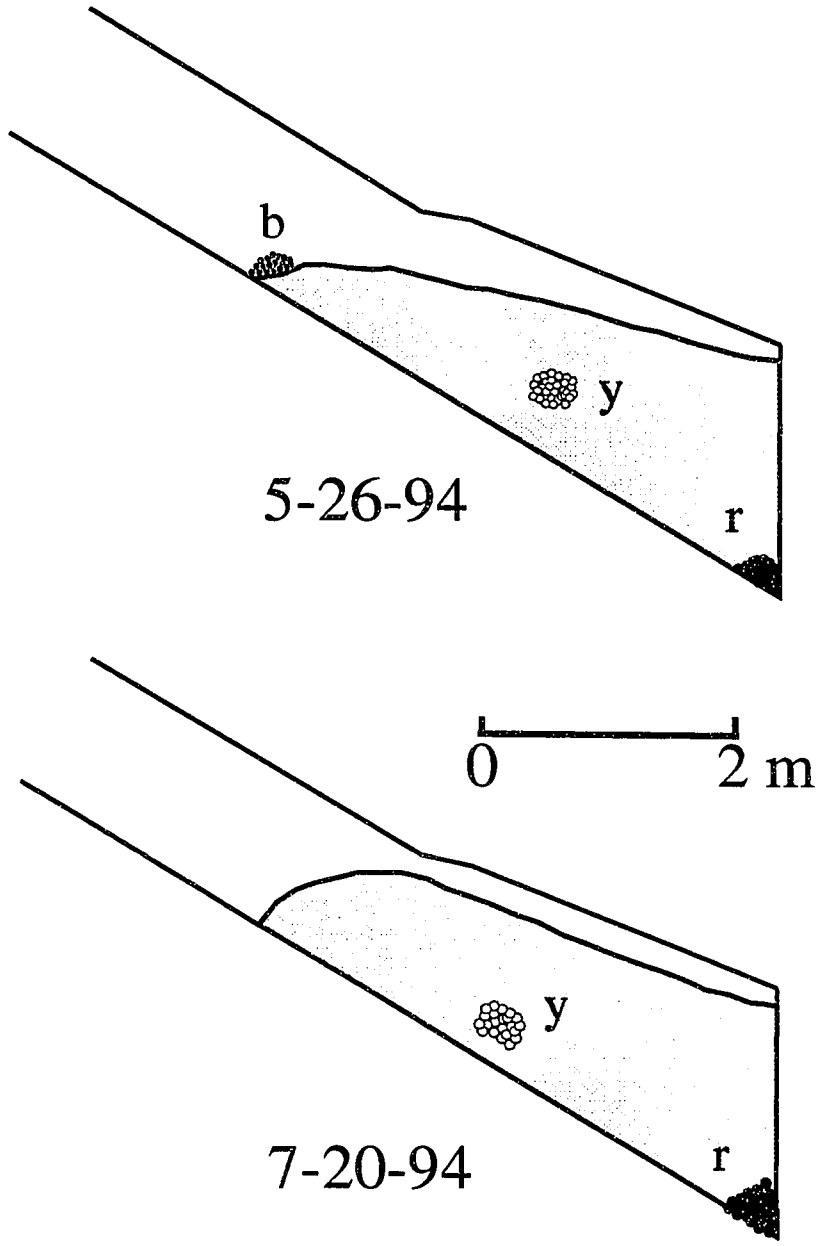

Figure 2.16. Starting locations of colored tracer particles in source debris of May 26 and July 20, 1994, flows. Red particles (r) were placed at the base of the front of the debris; yellow particles (y) near the centroids of mass; and, in the May 26 debris, black particles (b) were placed on the rear surface.

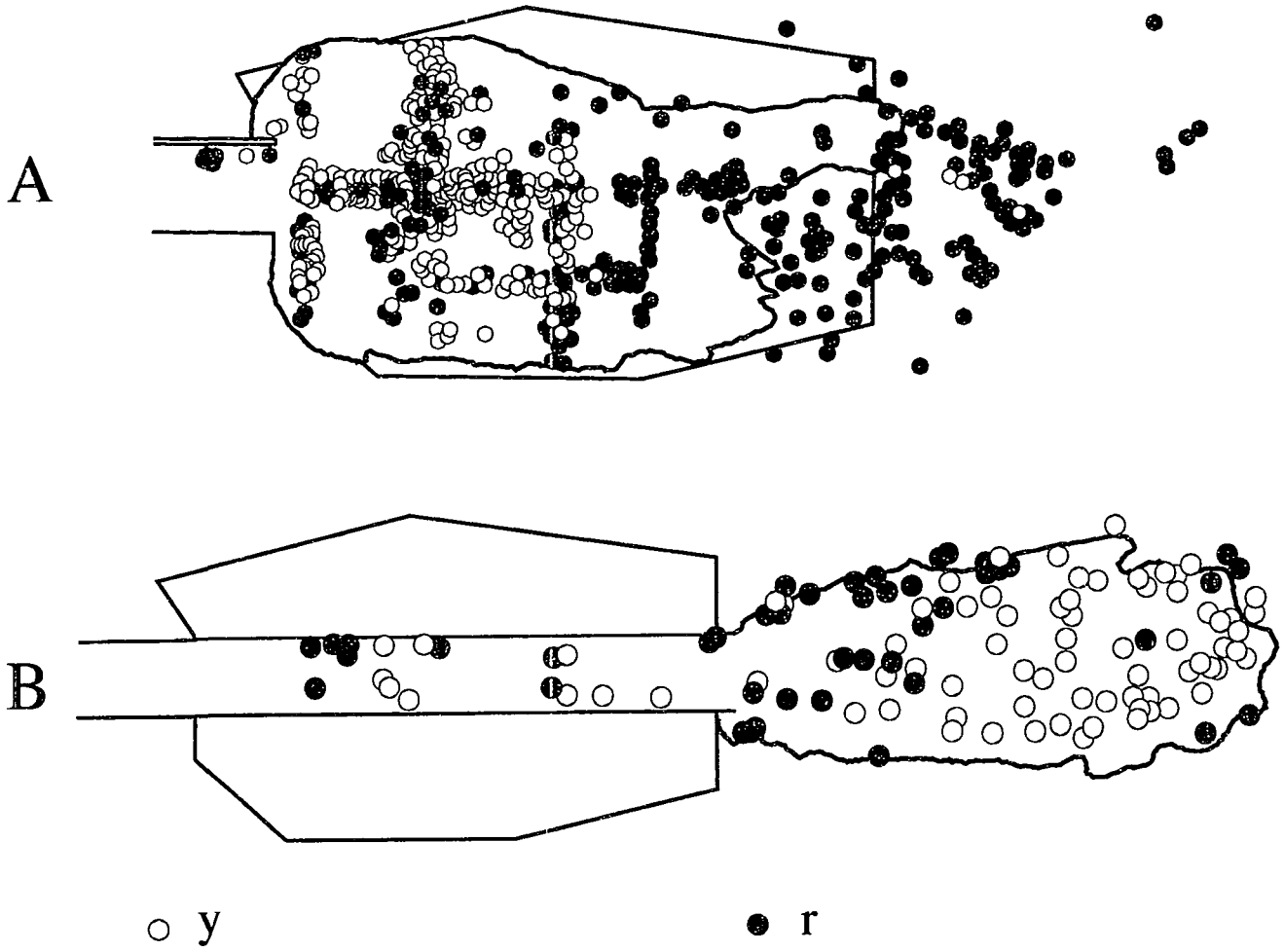

Figure 2.17. Locations of colored tracer particles in deposits. A. May 26, 1994, deposit. B. July 20, 1994, deposit. y = yellow particles; r = red particles.

Figure 2.18. Stratigraphic locations of tracer particles in deposit of May 26, 1994. Note that the yellow particles (y) stratigraphically overlie red particles (r). See Figure 2.16 for starting positions of particles in source debris, and Figure 2.17 for spatial distribution of particles within deposit. A. Location 4EW/5NS. B. Location 6EW/3NS. C. Location 5EW/3NS. D. Location 8EW/3NS.

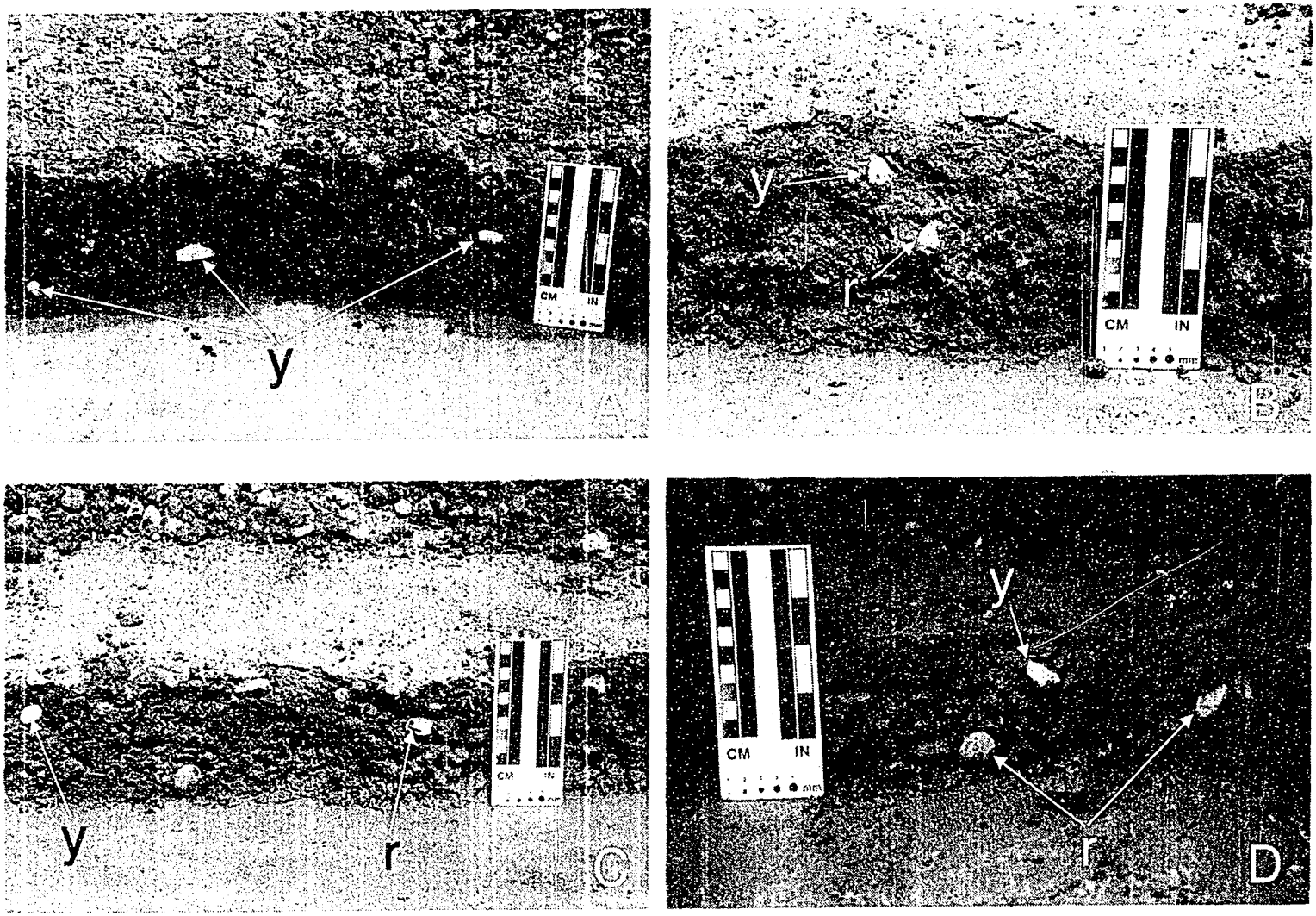
y
CM
IN
A
y
r
CM
IN
B
y
r
C
CM
IN
y
r
D

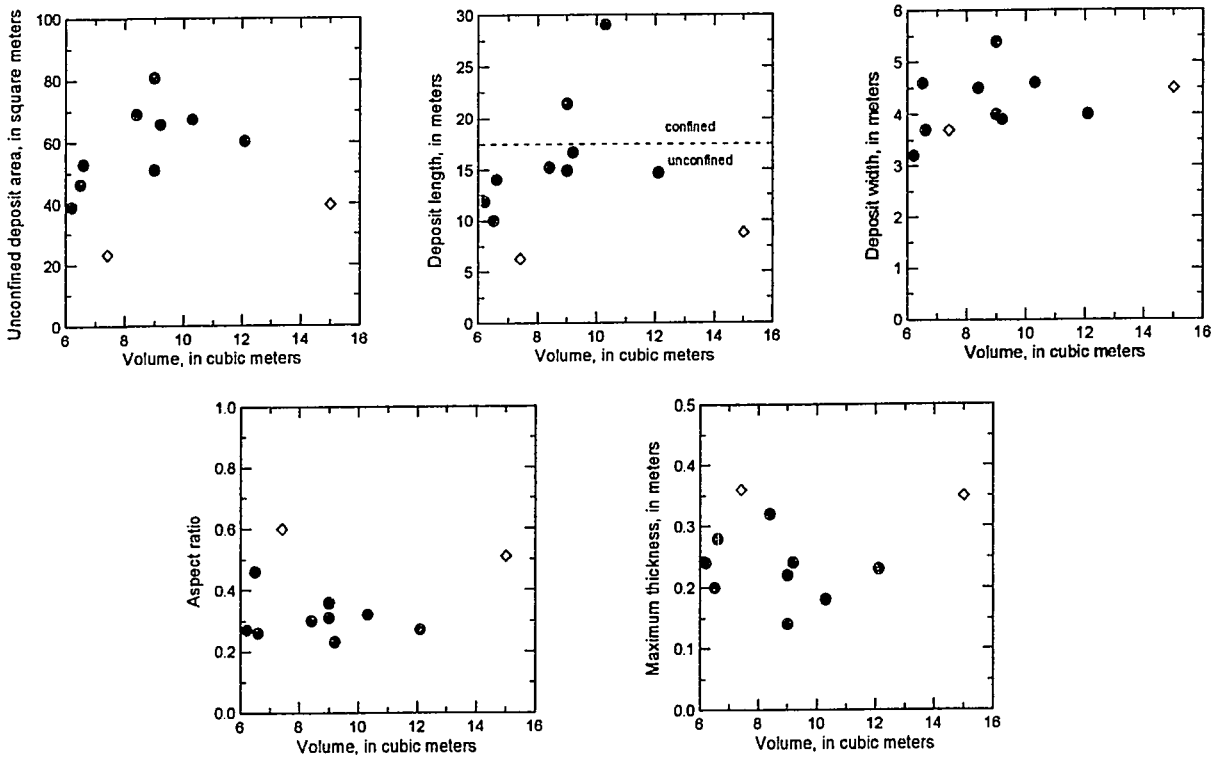

Figure 2.19. Morphometric relations between properties of experimental deposits and volume of source debris. Circles are saturated-flow deposits; diamonds are unsaturated-flow deposits. See Table 2.2.

Figure 2.20. Typical interior textures of experimental debris-flow deposits. A. Deposit from unsaturated flow (July 16, 1992). B, C, and D. Deposits from saturated flows (B. September 25, 1992; C. Composite deposit of April 7 and April 8, 1993; D. May 6, 1993.) Note trough-like structure in the September 25, 1992, deposit (B) related to subsequent surge emplacement. Note also the gravel lens near margin deposited by an early surge in May 6, 1993, deposit (D).

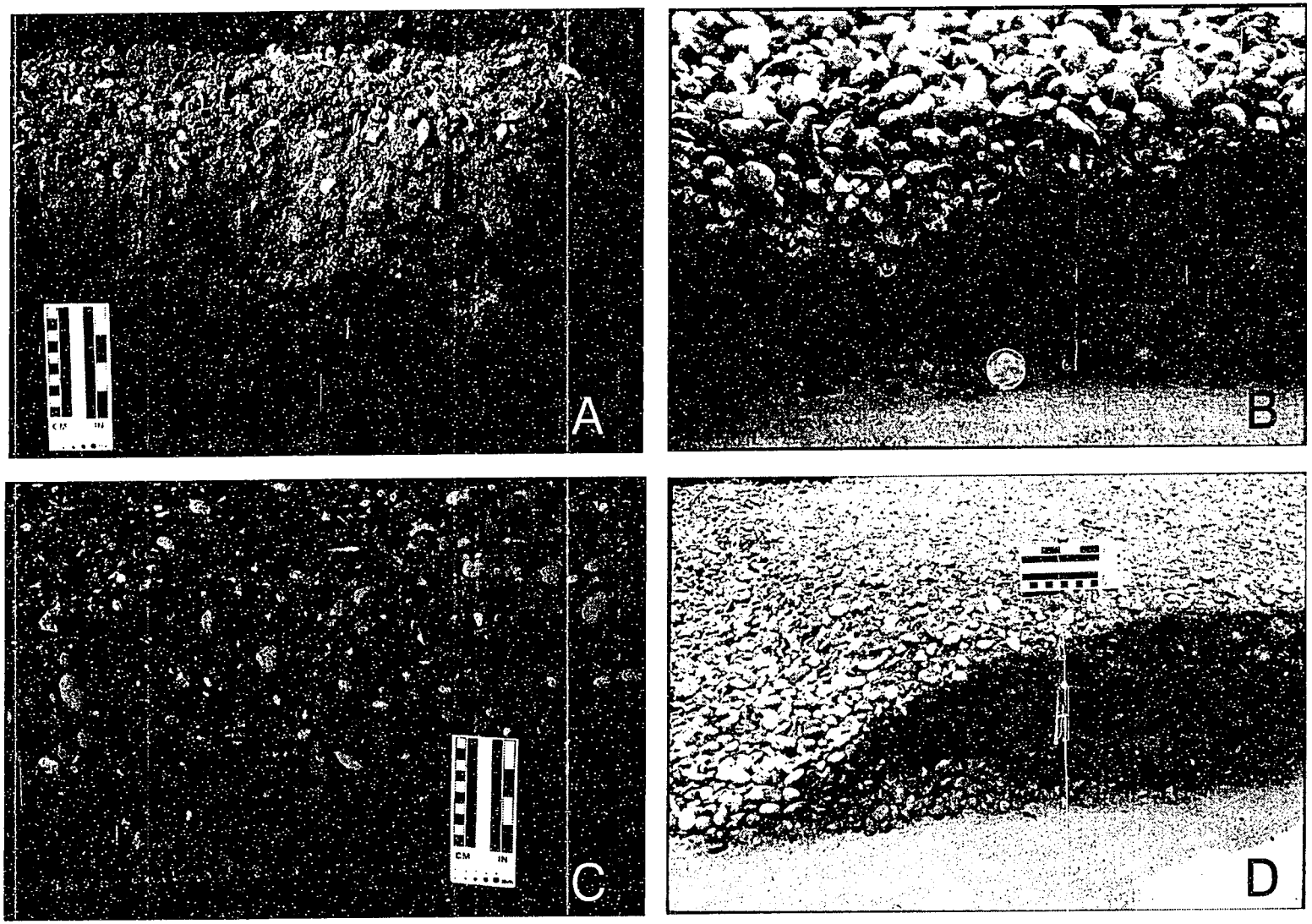
A
B
C
D

Figure 2.21. Grain-size-distribution histograms for July 16, 1992, deposit. Sample location given by EW/NS grid coordinates. See Table 2.3 for coordinate definitions. See Figure 2.11 for definition of stippled patterns.

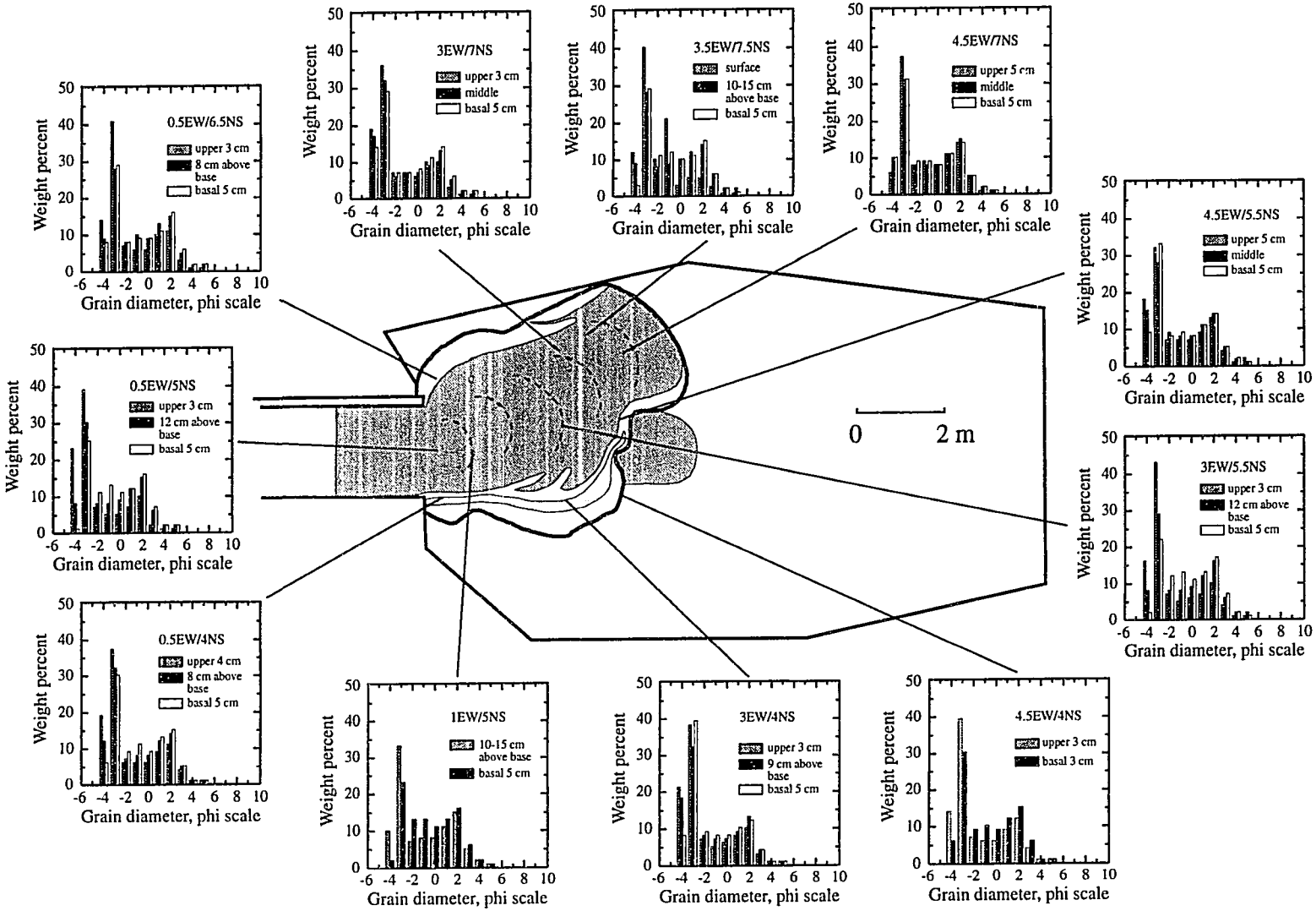
0.5EW/6.5NS
upper 3 cm
8 cm above base
basal 5 cm
3EW/7NS
upper 3 cm
middle
basal 5 cm
3.5EW/7.5NS
surface
10-15 cm above base
basal 5 cm
4.5EW/7NS
upper 5 cm
middle
basal 5 cm
4.5EW/5.5NS
upper 5 cm
middle
basal 5 cm
0.5EW/5NS
upper 3 cm
12 cm above base
basal 5 cm
3EW/5.5NS
upper 3 cm
12 cm above base
basal 5 cm
0.5EW/4NS
upper 4 cm
8 cm above base
basal 5 cm
1EW/5NS
10-15 cm above base
basal 5 cm
3EW/4NS
upper 3 cm
9 cm above base
basal 5 cm
4.5EW/4NS
upper 3 cm
basal 3 cm
Weight percent
Grain diameter, phi scale
0
2 m

Figure 2.22. Grain-size-distribution histograms for September 25, 1992, deposit. Sample location given by EW/NS grid coordinates. See Table 2.3 for coordinate definitions. See Figure 2.15 for definition of stippled patterns and dashed lines.

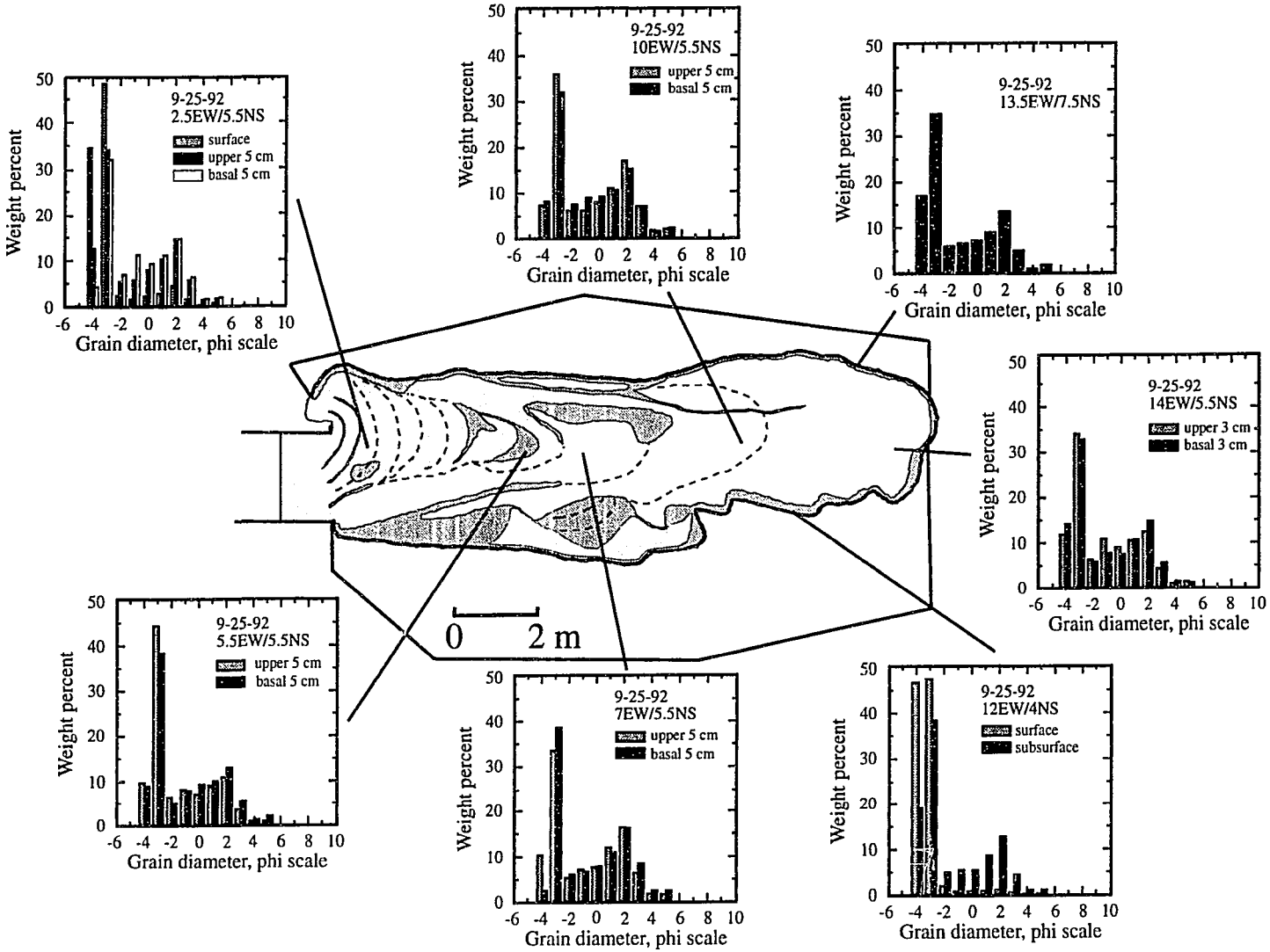
9-25-92
2.5EW/5.5NS
surface
upper 5 cm
basal 5 cm
Weight percent
Grain diameter, phi scale
9-25-92
10EW/5.5NS
upper 5 cm
basal 5 cm
9-25-92
13.5EW/7.5NS
9-25-92
14EW/5.5NS
upper 3 cm
basal 3 cm
9-25-92
5.5EW/5.5NS
9-25-92
7EW/5.5NS
9-25-92
12EW/4NS
subsurface
0 2 m

Figure 2.23. Grain-size-distribution histograms for April 7, 1993, deposit. Sample location given by EW/NS grid coordinates. See Table 2.3 for coordinate definitions. See Figure 2.15 for definition of stippled patterns and dashed lines.

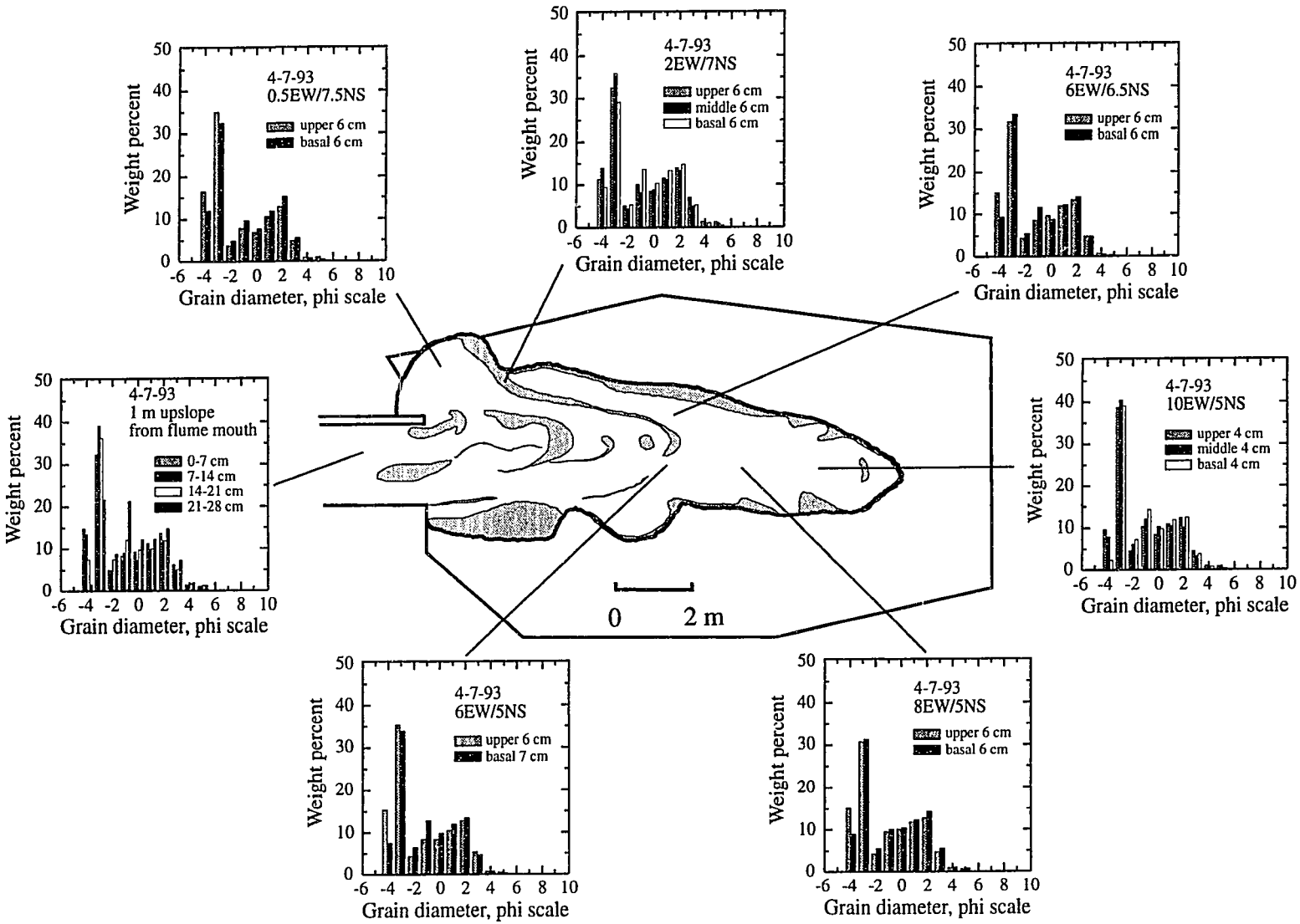
4-7-93
0.5EW/7.5NS
upper 6 cm
basal 6 cm
4-7-93
2EW/7NS
upper 6 cm
middle 6 cm
basal 6 cm
4-7-93
6EW/6.5NS
upper 6 cm
basal 6 cm
4-7-93
1 m upslope
from flume mouth
0-7 cm
7-14 cm
14-21 cm
21-28 cm
4-7-93
10EW/5NS
upper 4 cm
middle 4 cm
basal 4 cm
4-7-93
6EW/5NS
upper 6 cm
basal 7 cm
4-7-93
8EW/5NS
upper 6 cm
basal 6 cm
Weight percent
Grain diameter, phi scale
0
2 m

Figure 2.24. Grain-size-distribution histograms for April 8, 1993, deposit. Sample location given by EW/NS grid coordinates. See Table 2.3 for coordinate definitions. See Figure 2.15 for definition of stippled patterns and dashed lines.

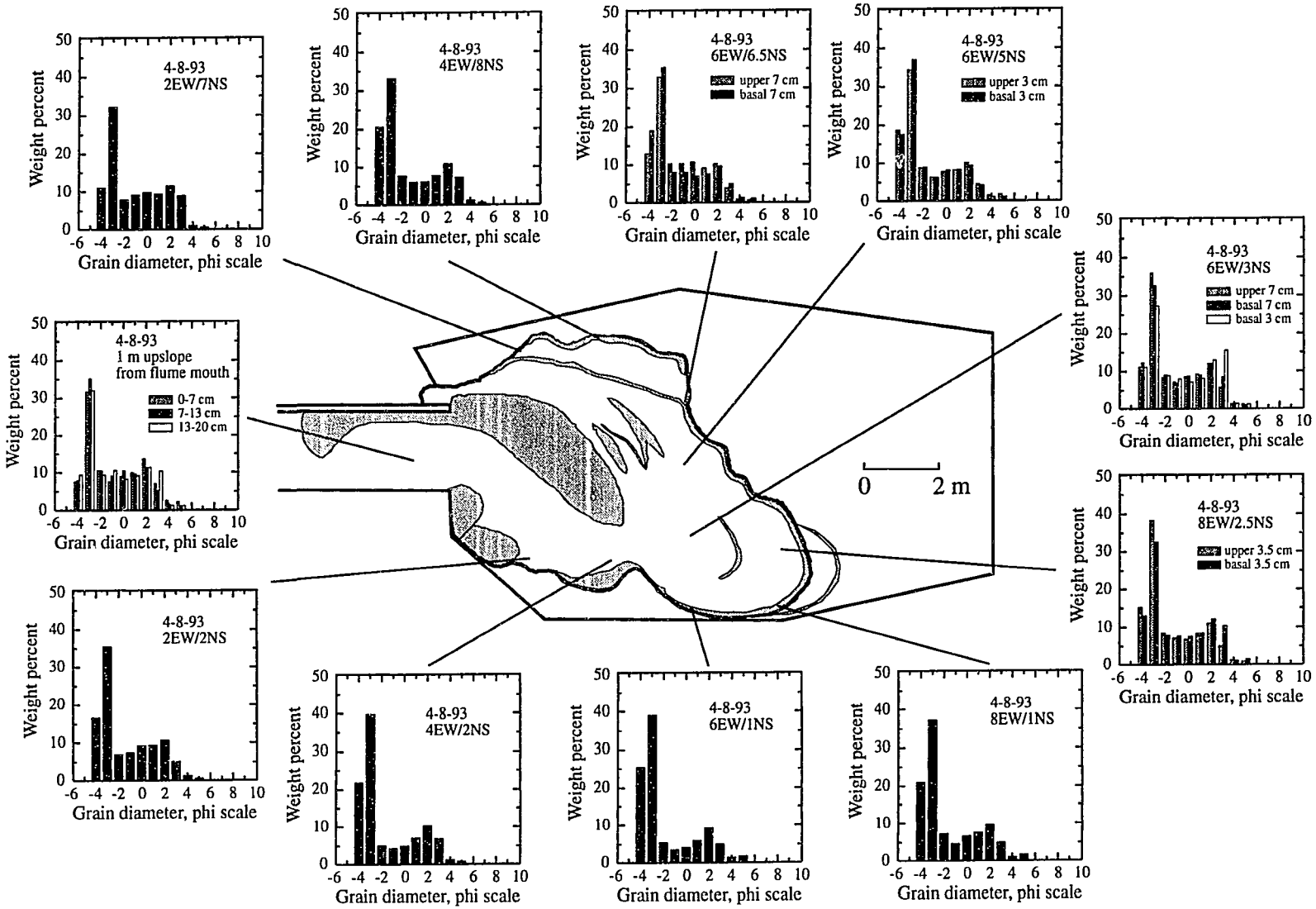
4-8-93
2EW/7NS
4-8-93
4EW/8NS
4-8-93
6EW/6.5NS
upper 7 cm
basal 7 cm
4-8-93
6EW/5NS
upper 3 cm
basal 3 cm
4-8-93
6EW/3NS
upper 7 cm
basal 7 cm
basal 3 cm
4-8-93
1 m upslope
from flume mouth
0-7 cm
7-13 cm
13-20 cm
4-8-93
8EW/2.5NS
upper 3.5 cm
basal 3.5 cm
4-8-93
2EW/2NS
4-8-93
4EW/2NS
4-8-93
6EW/1NS
4-8-93
8EW/1NS
Weight percent
Grain diameter, phi scale
0
2 m

Figure 2.25. Grain-size-distribution histograms for combined April 7 and April 8, 1993, deposit. Sample location given by EW/NS grid coordinates. See Table 2.3 for coordinate definitions. See Figure 2.15 for definition of stippled patterns and dashed lines.

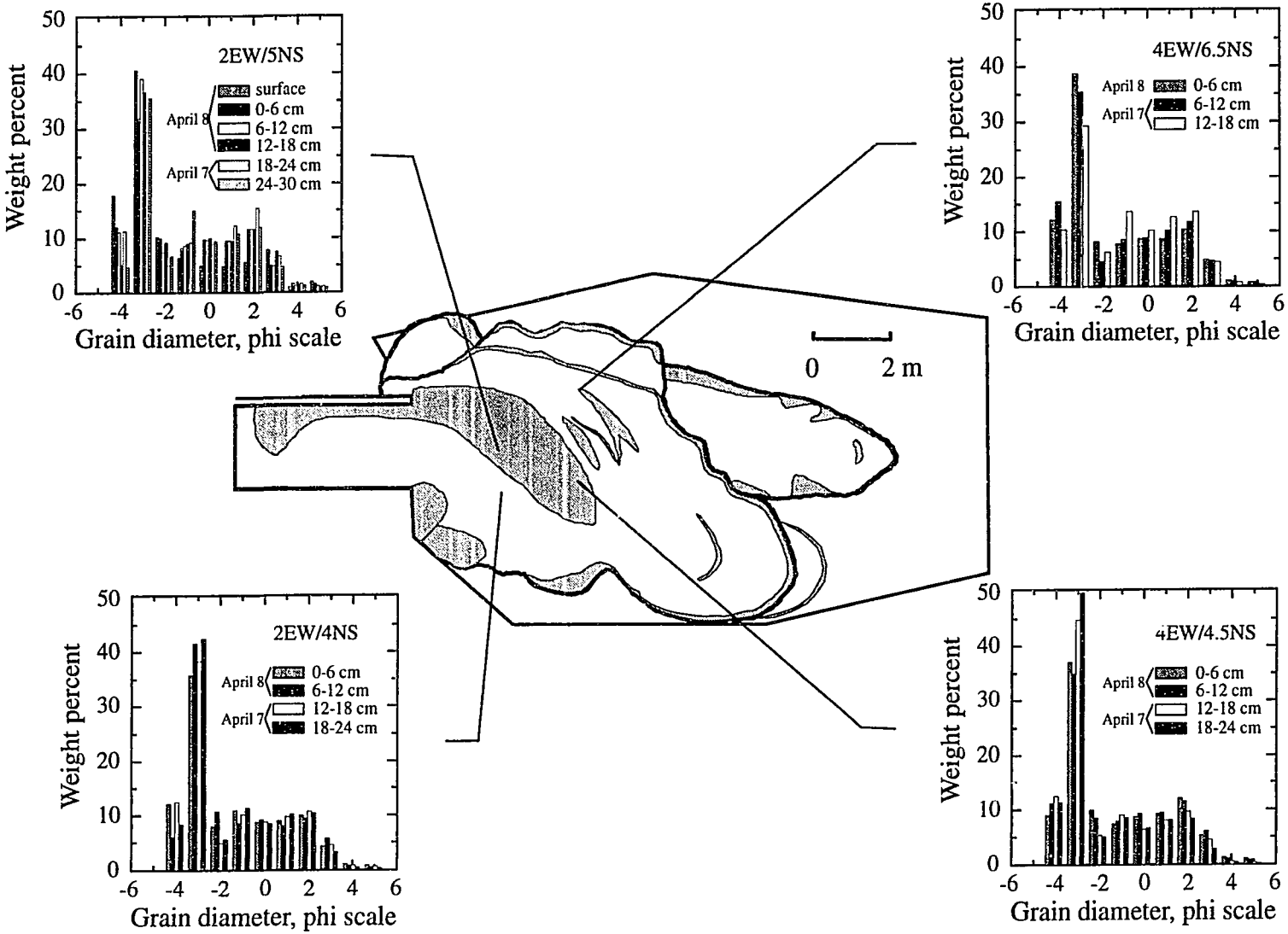
2EW/5NS
surface
April 8
0-6 cm
6-12 cm
12-18 cm
April 7
18-24 cm
24-30 cm
Weight percent
Grain diameter, phi scale
4EW/6.5NS
April 8
0-6 cm
6-12 cm
April 7
12-18 cm
0
2 m
2EW/4NS
0-6 cm
6-12 cm
12-18 cm
18-24 cm
4EW/4.5NS

Figure 2.26. Grain-size-distribution histograms for May 26, 1994, deposit. Sample location given by EW/NS grid coordinates. See Table 2.3 for coordinate definitions. See Figure 2.15 for definition of stippled patterns and dashed lines.

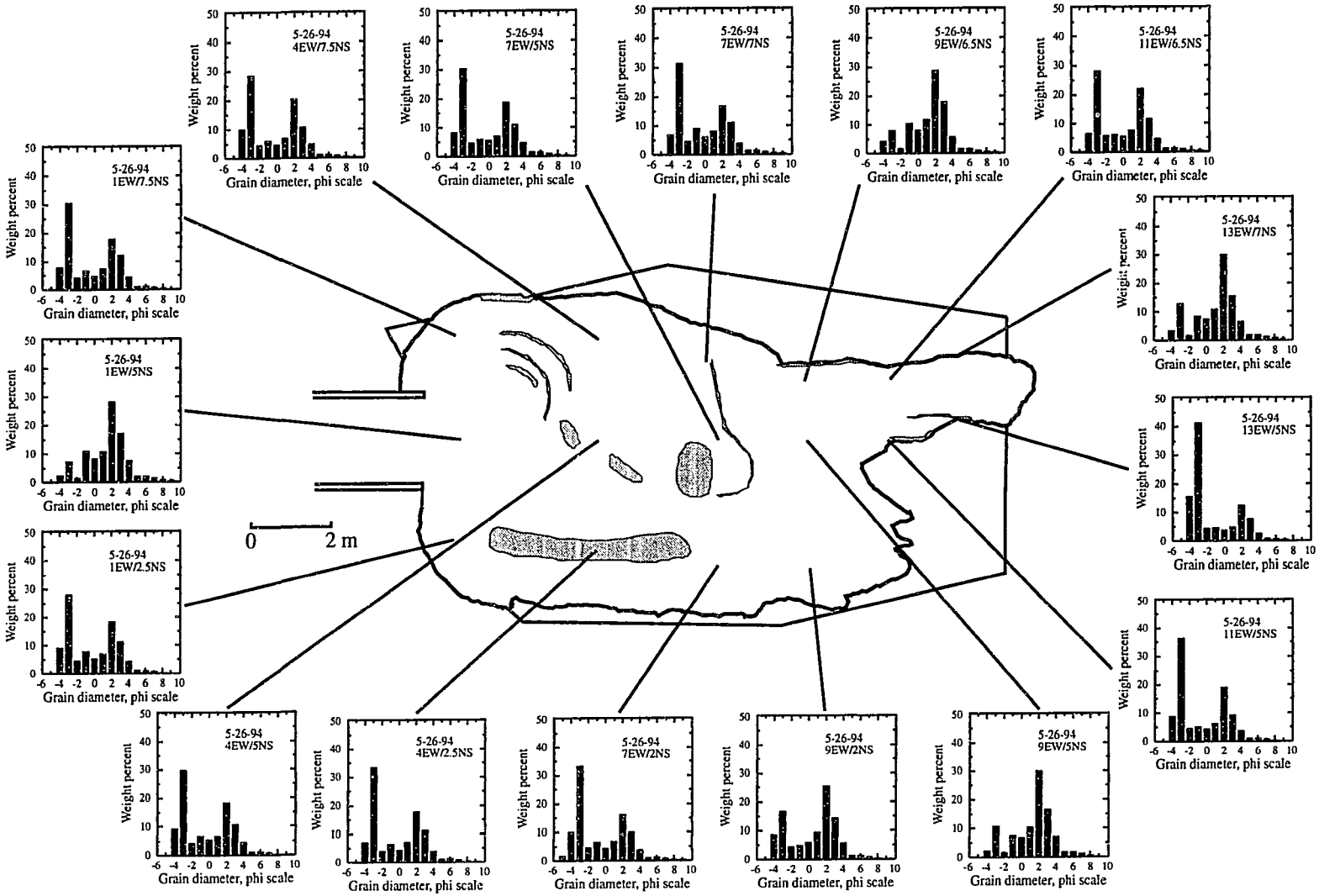
5-26-94
4EW/7.5NS
5-26-94
7EW/5NS
5-26-94
7EW/7NS
5-26-94
9EW/6.5NS
5-26-94
11EW/6.5NS
5-26-94
1EW/7.5NS
5-26-94
13EW/7NS
5-26-94
1EW/5NS
5-26-94
13EW/5NS
5-26-94
1EW/2.5NS
5-26-94
11EW/5NS
5-26-94
4EW/5NS
5-26-94
4EW/2.5NS
5-26-94
7EW/2NS
5-26-94
9EW/2NS
5-26-94
9EW/5NS
Weight percent
Grain diameter, phi scale
0
2 m

Figure 2.27. Grain-size-distribution histograms for July 20, 1994, deposit. Sample location given by EW/NS grid coordinates. See Table 2.3 for coordinate definitions. See Figure 2.15 for definition of stippled patterns and dashed lines.

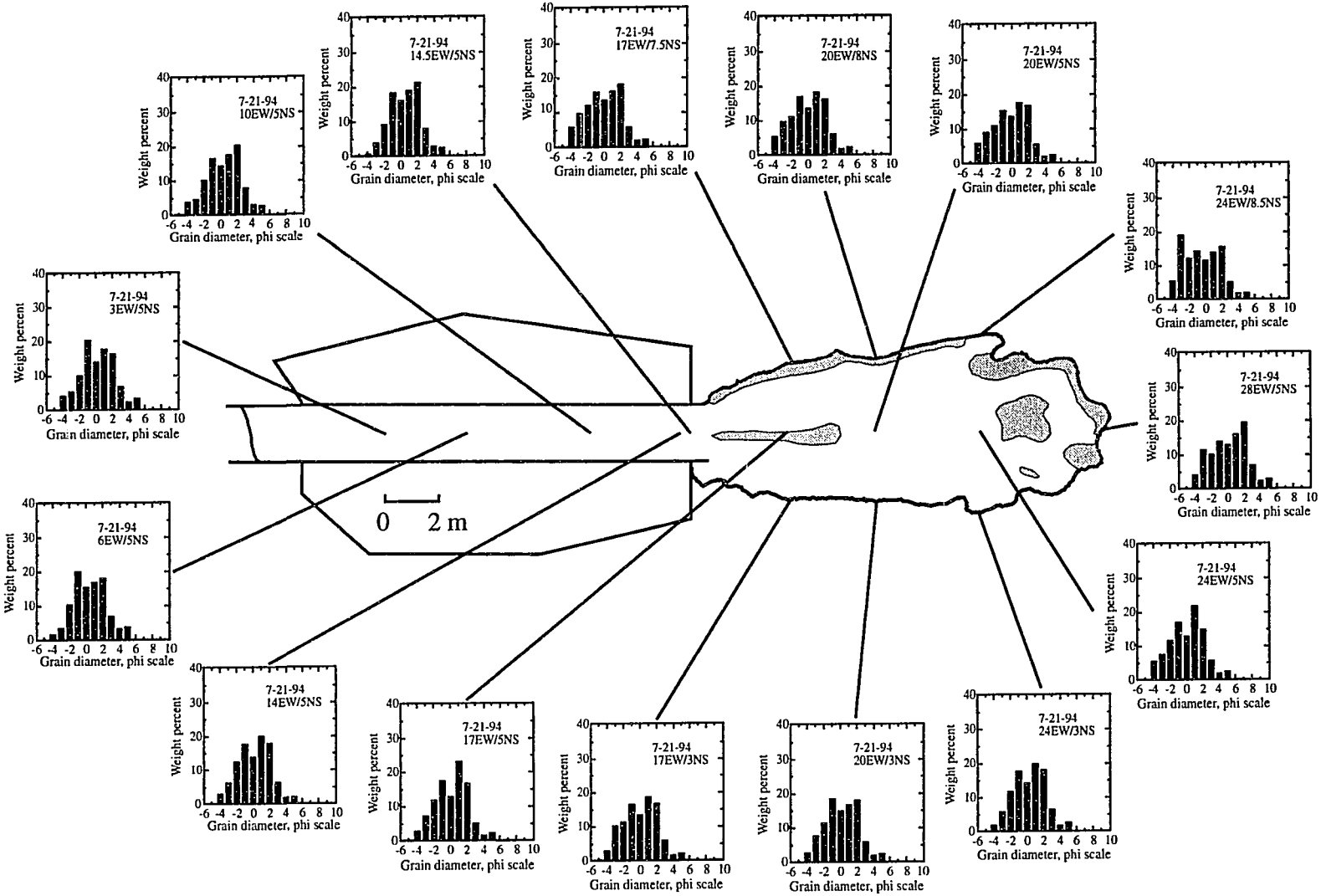
7-21-94
10EW/5NS
7-21-94
14.5EW/5NS
7-21-94
17EW/7.5NS
7-21-94
20EW/8NS
7-21-94
20EW/5NS
7-21-94
24EW/8.5NS
7-21-94
3EW/5NS
7-21-94
28EW/5NS
7-21-94
6EW/5NS
7-21-94
24EW/5NS
7-21-94
14EW/5NS
7-21-94
17EW/5NS
7-21-94
17EW/3NS
7-21-94
20EW/3NS
7-21-94
24EW/3NS
Weight percent
Grain diameter, phi scale
0 2 m

Figure 2.28. Deposits from two flows (April 7, 1993, and April 8, 1993) allowed to accumulate. Note the light-colored sand, which was used as a marker horizon, spread across the surface of the April 7, 1993, deposit.

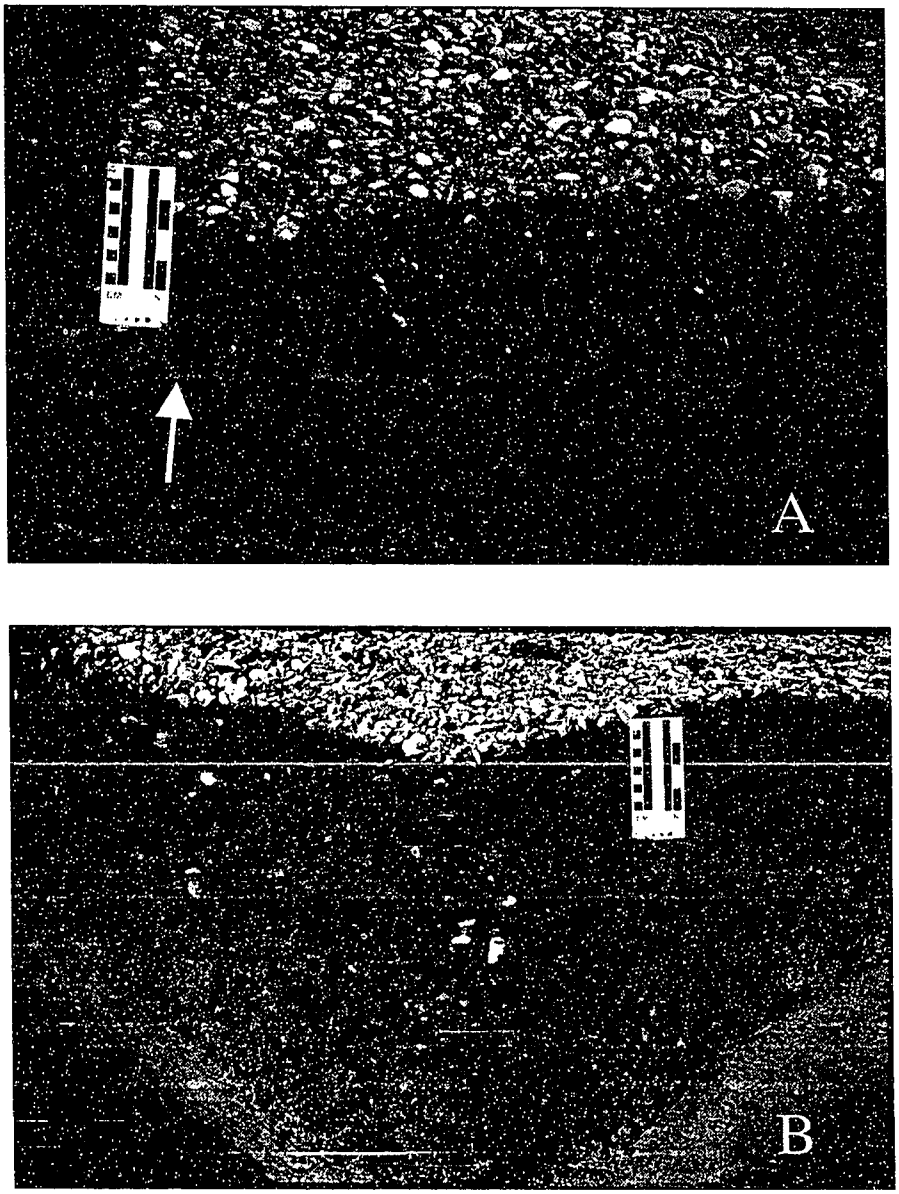

Figure 2.29. Interior texture of deposits shown in Figure 2.28. A. Texture at location where marker sand is present. The deposit above the marker sand is from flow on April 8, 1993; deposit below marker sand is from flow on April 7, 1993. B. Texture at location where marker horizon is absent. Note homogeneity of the compound deposit.

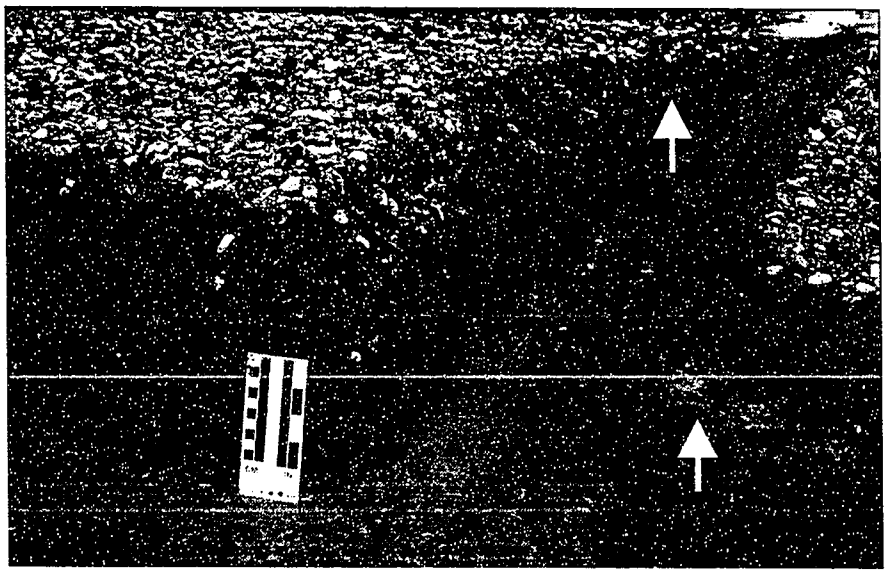

Figure 2.30. Interior texture of debris fan shown in Figure 2.28. View showing location in vicinity where marker sand was left off April 7 deposit. Note sand in right foreground and central background (arrows). The section behind the scale is the same section shown in figure 2.29B.

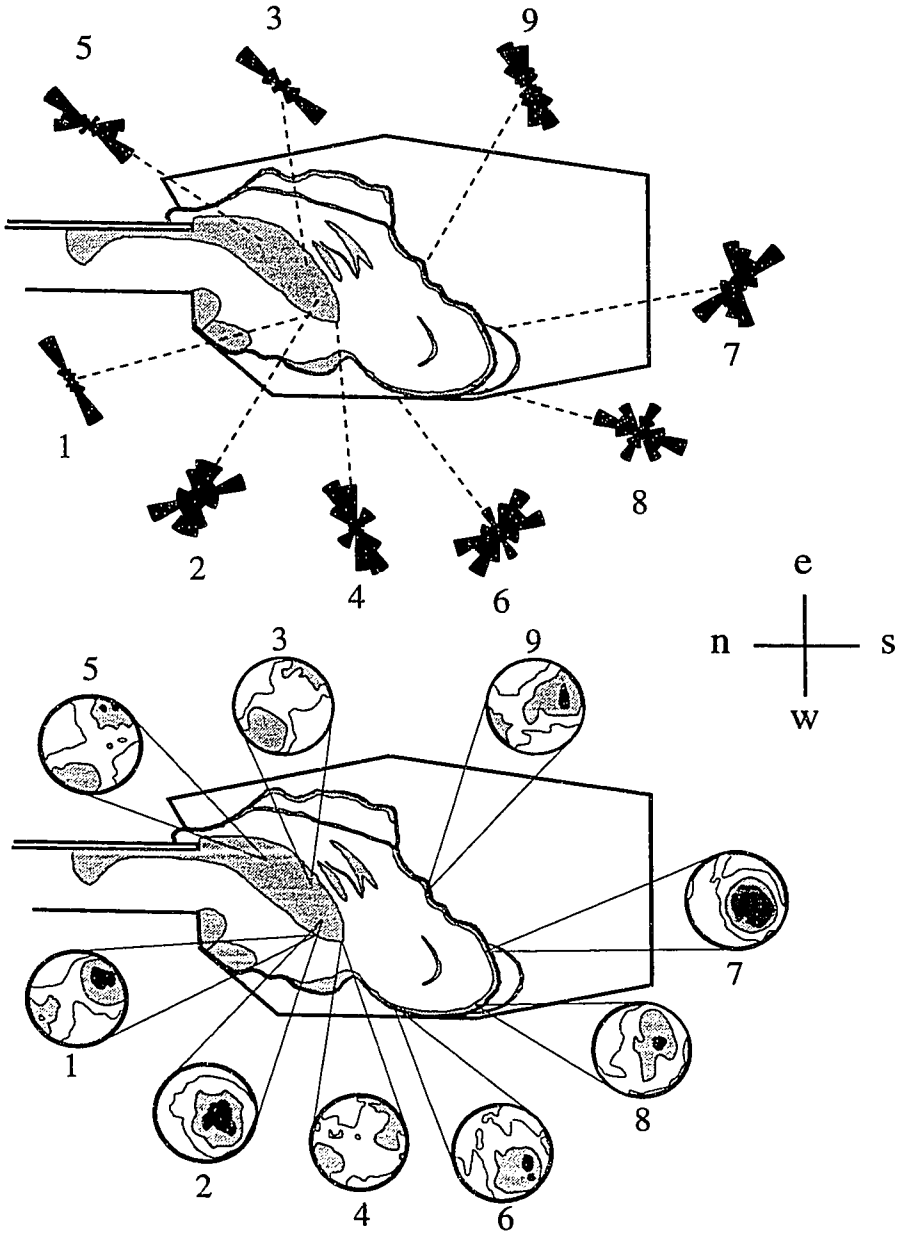

Figure 2.31. Diagram illustrating surface-particle orientation on April 8, 1993 deposit. The upper diagram illustrates orientation of the longest axis of particles ≥ 8mm in diameter. The lower diagram represents lower-hemisphere equal-area projections of the shortest axes of measured particles. Diagrams are contoured using the method of Kamb (1959) with contour intervals of two standard deviations. Solid shade indicates areas of highest concentration; lightest stipple pattern indicates areas of lowest concentration. Location numbers correlate with positions listed in Table 2.4.

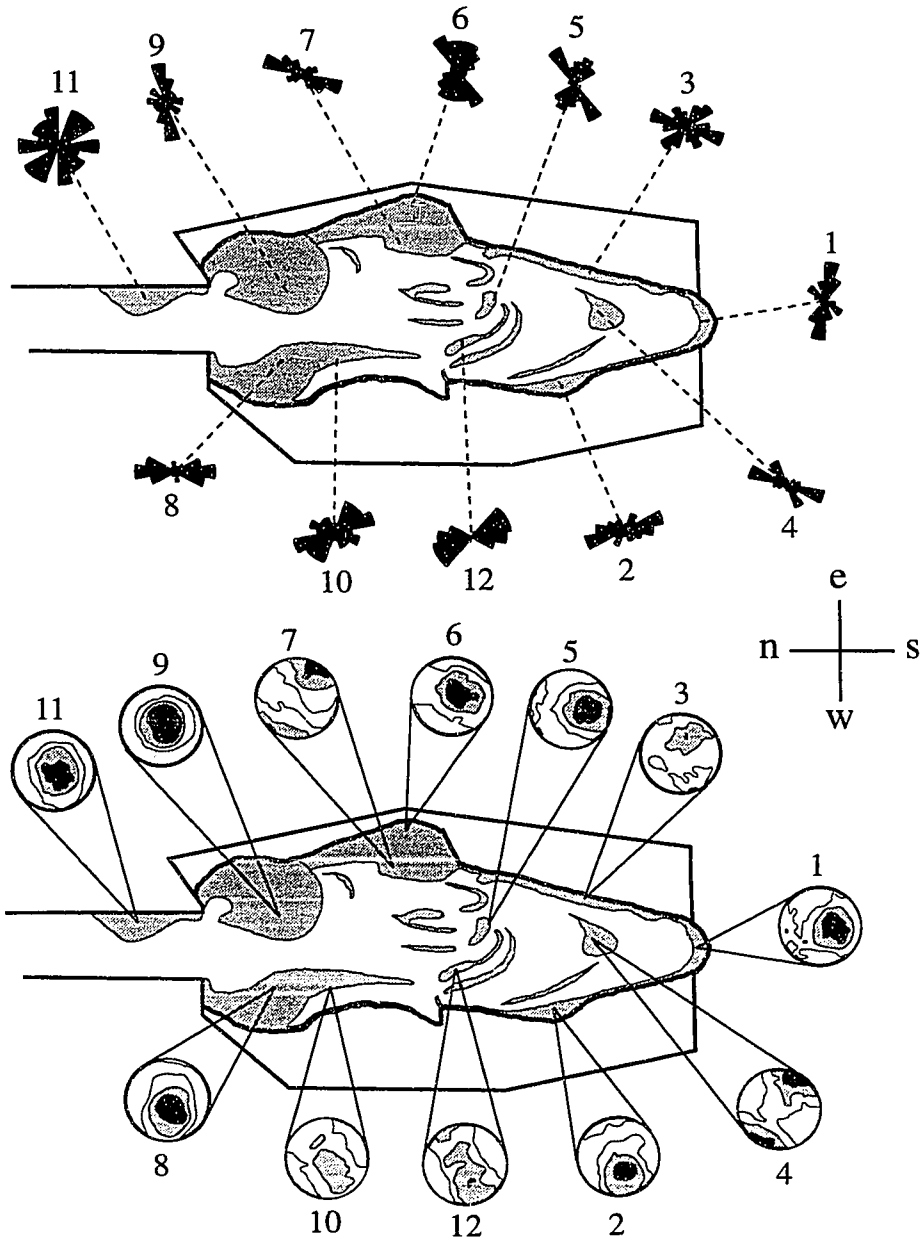

Figure 2.32. Diagram illustrating surface-particle orientation on May 6, 1993 deposit. The upper diagram illustrates orientation of the longest axis of particles ≥ 8mm in diameter. The lower diagram represents lower-hemisphere equal-area projections of the shortest axes of measured particles. Diagrams are contoured using the method of Kamb (1959) with contour intervals of two standard deviations. Solid shade indicates areas of highest concentration; lightest stipple pattern indicates areas of lowest concentration. Location numbers correlate with positions listed in Table 2.4.

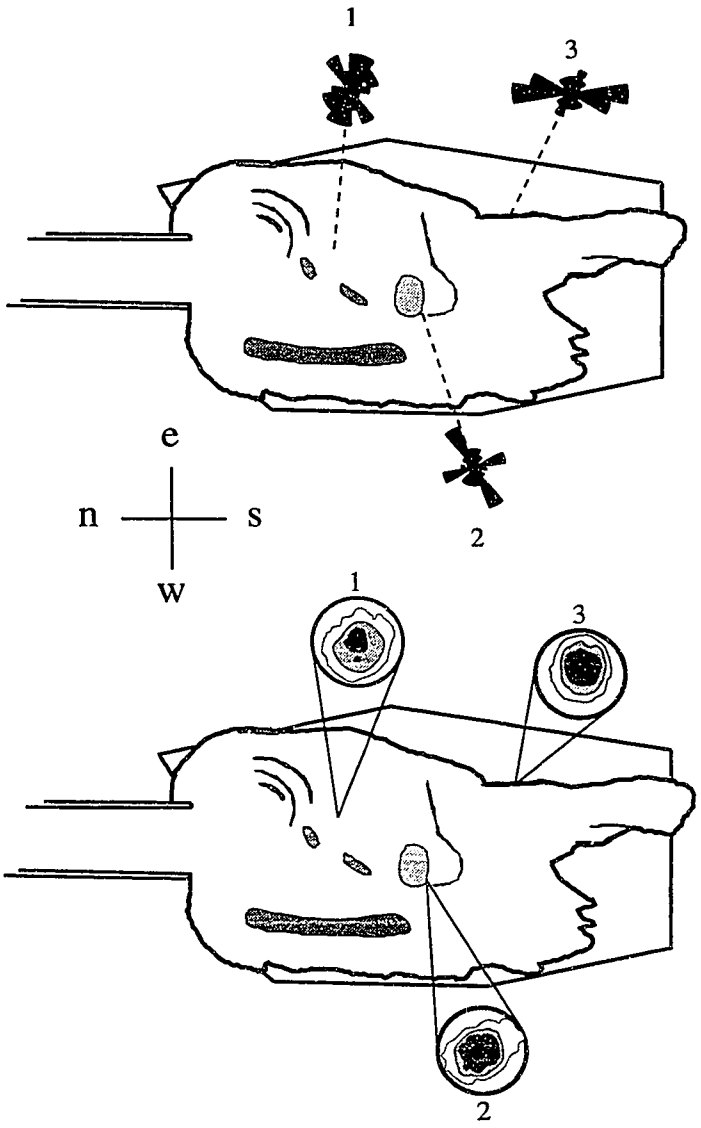

Figure 2.33. Diagram illustrating surface-particle orientation on May 26, 1994 deposit. The upper diagram illustrates orientation of the longest axis of particles ≥ 8mm in diameter. The lower diagram represents lower-hemisphere equal-area projections of the shortest axes of measured particles. Diagrams are contoured using the method of Kamb (1959) with contour intervals of two standard deviations. Solid shade indicates areas of highest concentration; lightest stipple pattern indicates areas of lowest concentration. Location numbers correlate with positions listed in Table 2.4.

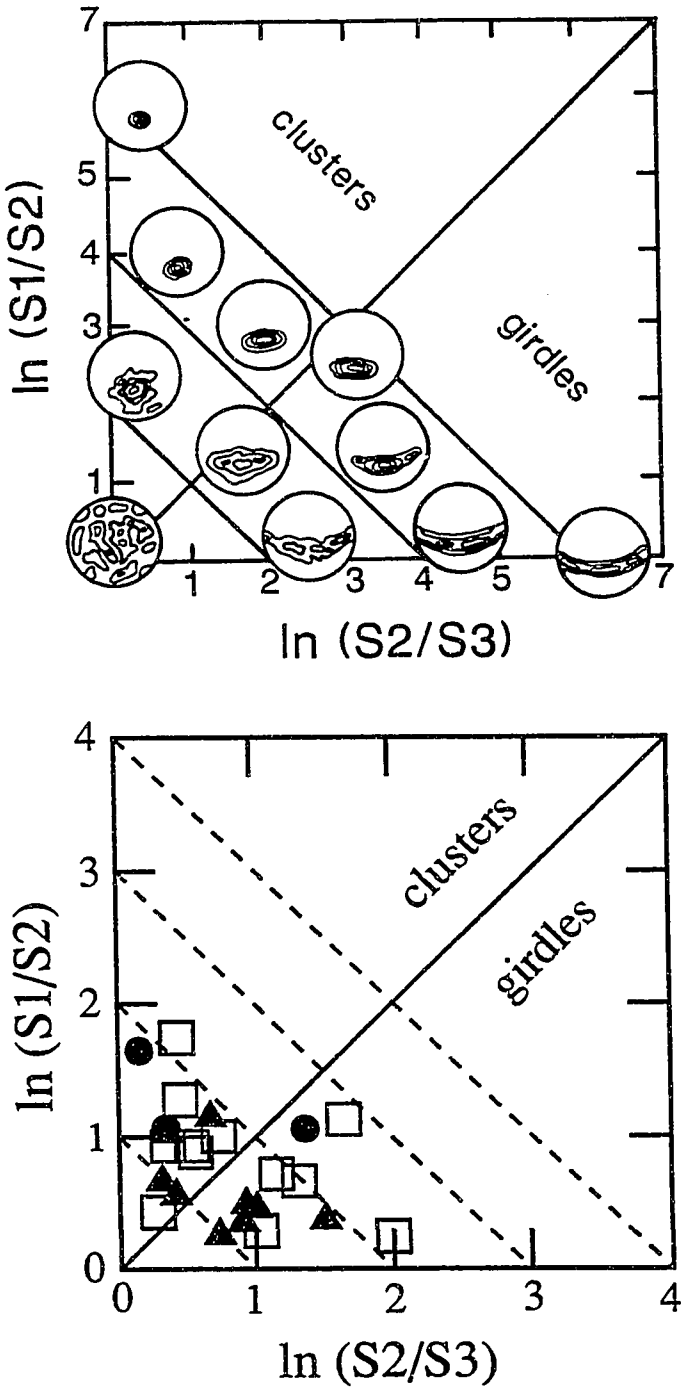

Figure 2.34. Logarithmic plot of ratios of normalized eigenvalues for orientations of particle short axes on April 8, 1993 (triangles); May 6, 1993 (squares); and May 26, 1994 (circles) deposits. Upper diagram illustrates relation of fabric shapes and strengths in different parts of the graph (from Woodcock, 1977); lower diagram illustrates results.

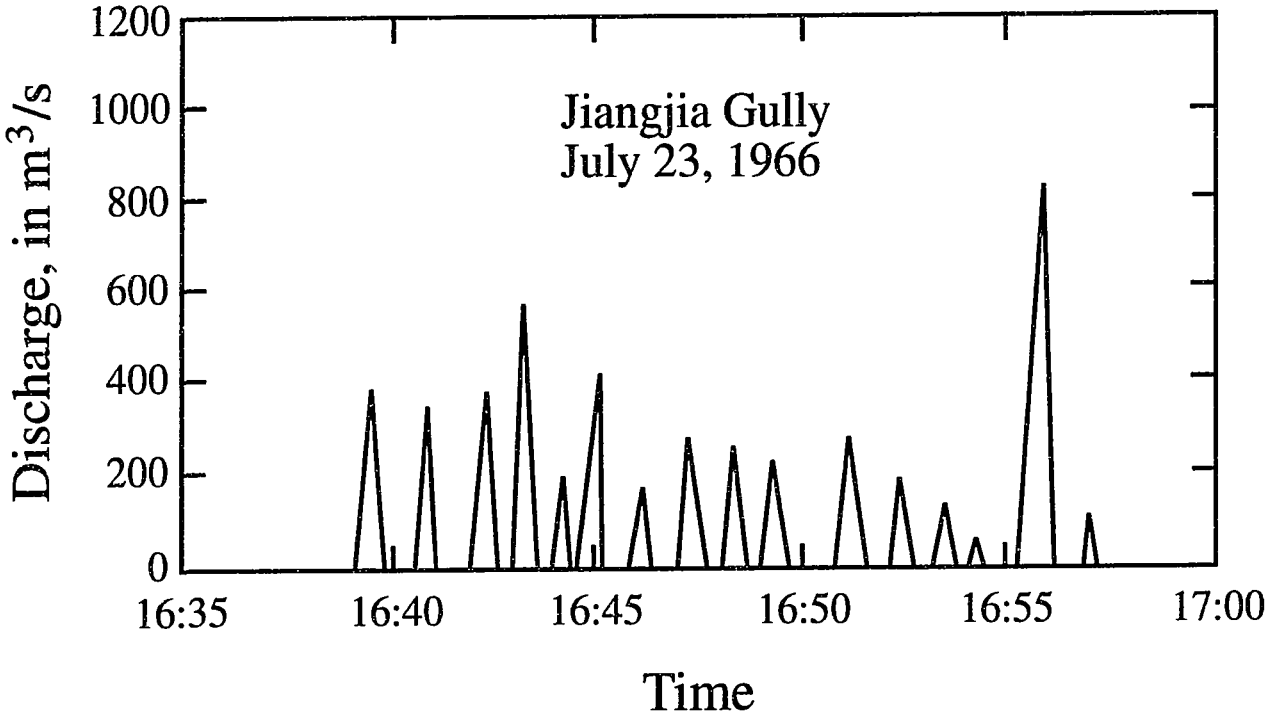

Figure 2.35. Hydrograph of debris flow in Jiangjia Gully, Yunnan Province, China (from Zhang, 1993). Note the numerous surges associated with this debris flow.

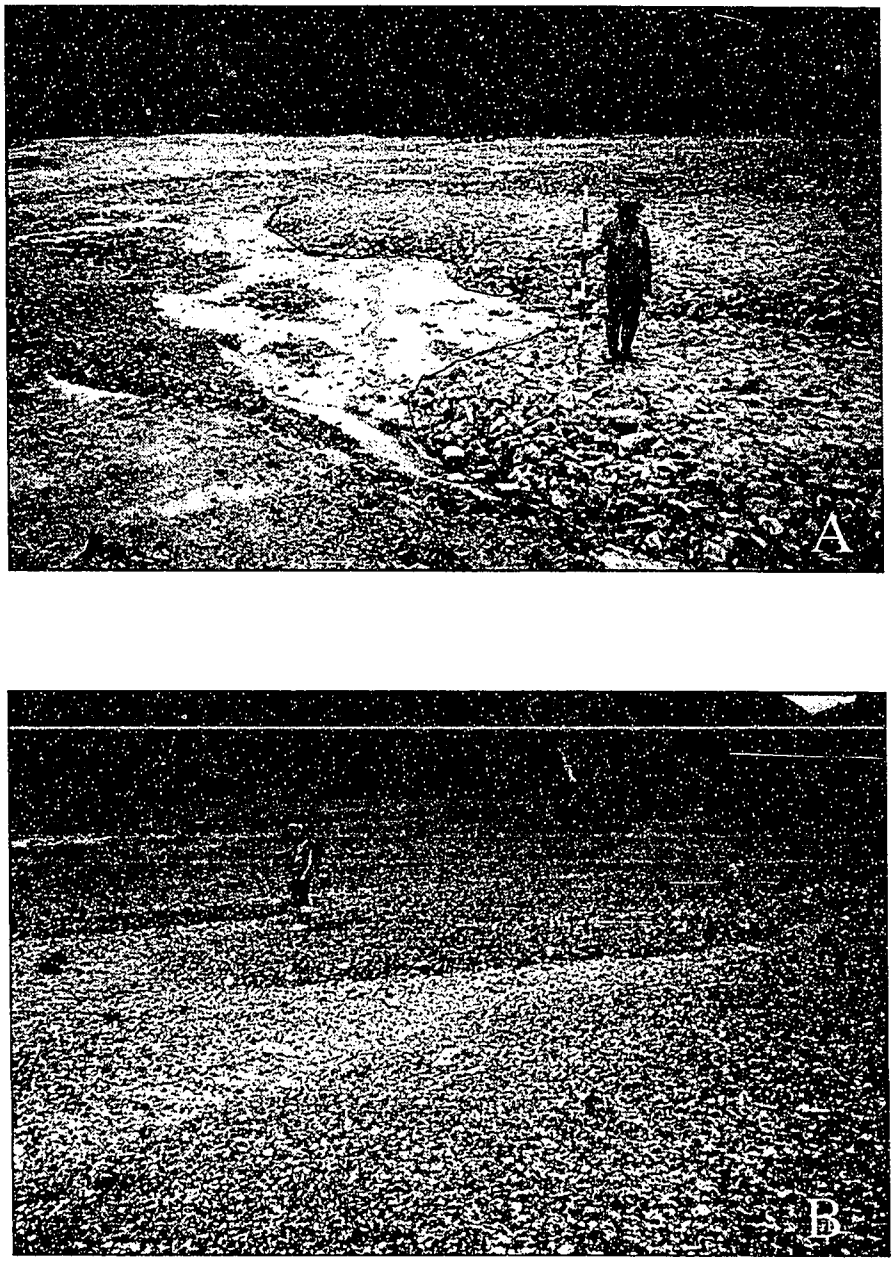

Figure 2.36. Lobate debris-flow deposits in Jiangjia Gully, China. Note multiplicity and overlapping of lobes.

Figure 2.37. Lobate debris-flow deposit in Jiangjia Gully, China. Note how the lobe grades into, and does not sharply overlie, the substrate. Flow direction from top to bottom.

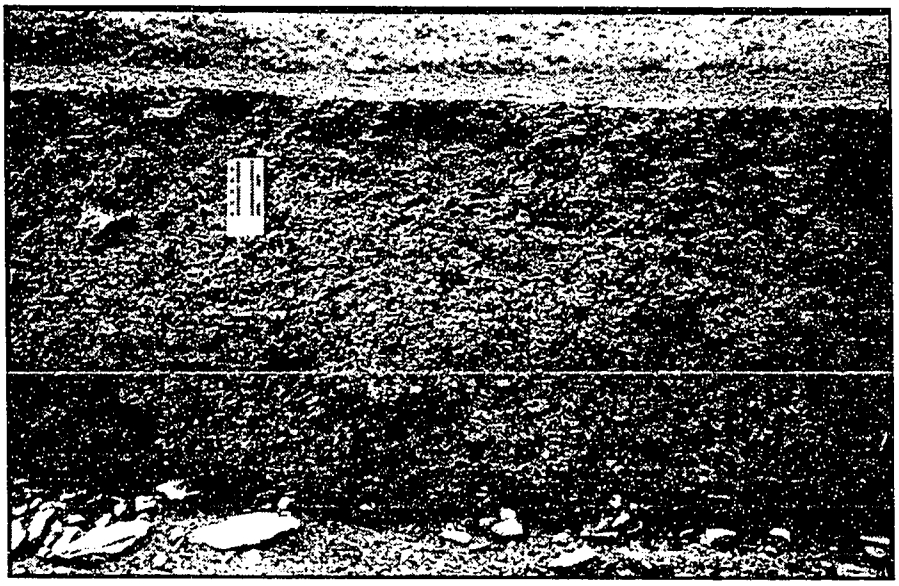

Figure 2.38. Debris-flow deposit of July 19, 1994, Jiangjia Gully, China. Deposit resulted from flow having numerous surge waves (e.g., see Figure 2.35), yet deposit texture is massive and homogeneous. Scale units in inches and centimeters.

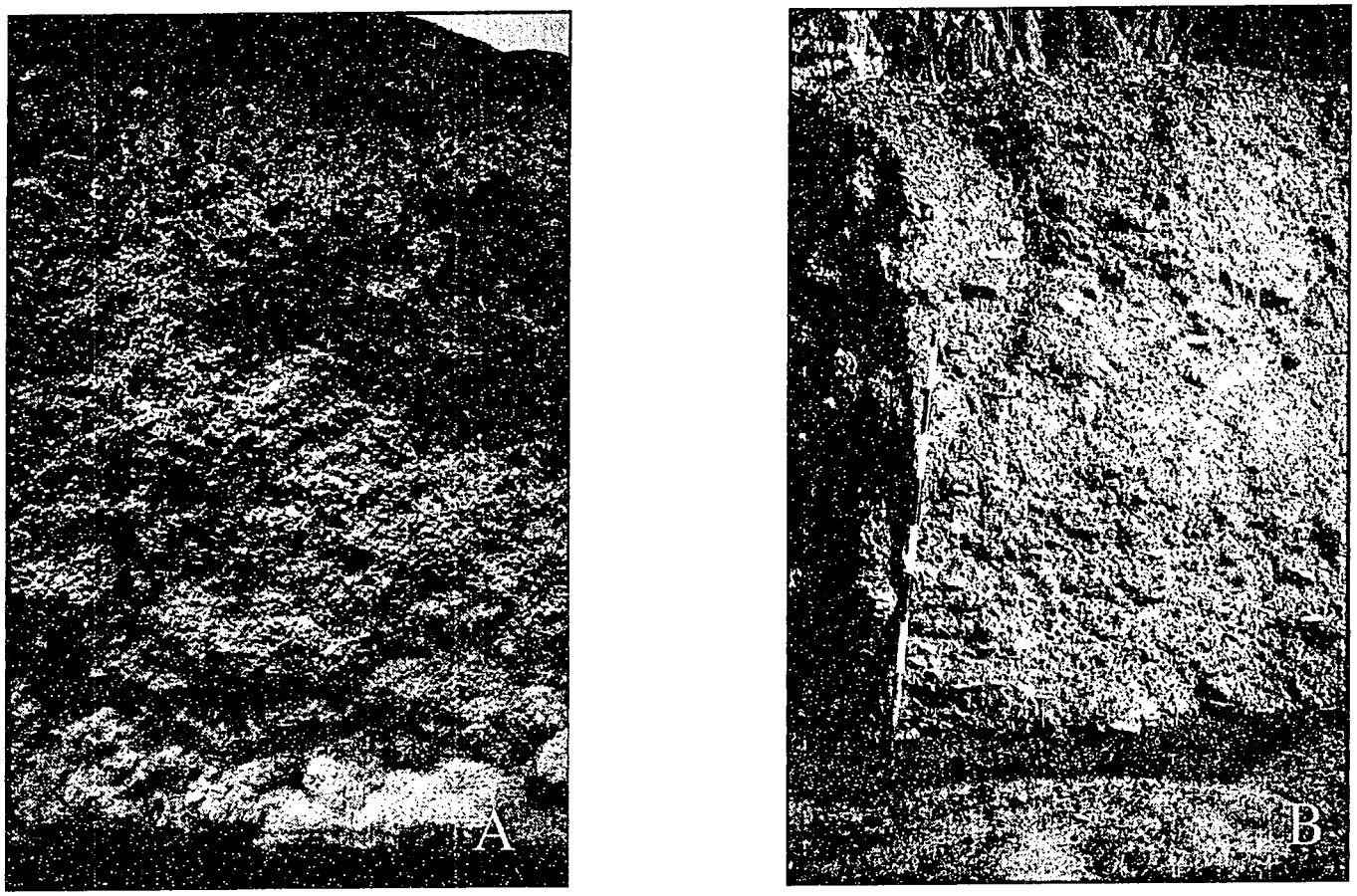

Figure 2.39. Debris-flow deposits exposed in terraces along Jiangjia Gully, China. Note the generally homogeneous, massive texture of the deposits. Surveyor's staff and shovel for scale.

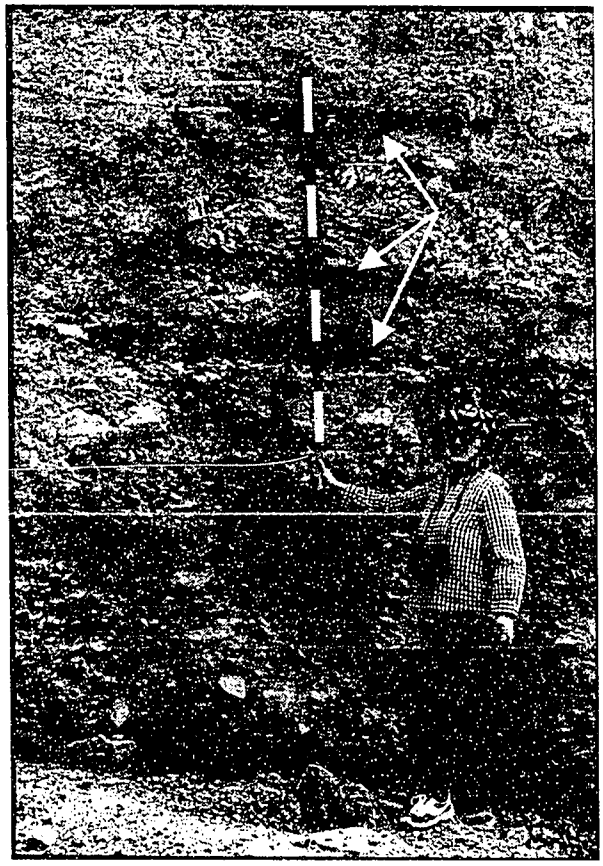

Figure 2.40. Debris-flow deposits separated by fluvially reworked sediment (arrows), Jiangjia Gully, China.

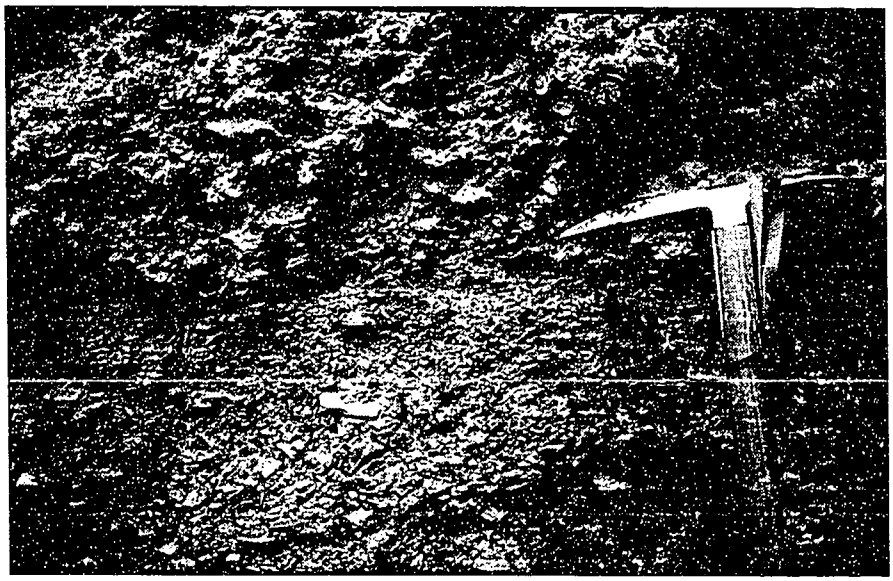

Figure 2.41. Textural changes delineating contact between debris-flow deposits. Note the abrupt coarsening of the upper unit (immediately below axe head).

CHAPTER 3

GRAVITY-DRIVEN ONE-DIMENSIONAL CONSOLIDATION OF DEBRIS-FLOW SLURRIES

INTRODUCTION

Experimental and natural debris-flow deposits remain weak for minutes to days after deposition. Deposits at the USGS debris-flow flume typically did not support the weight of a person, except locally along margins, for tens of minutes to several hours after emplacement. Additionally, translatory waves have been observed to remobilize surfaces of debris-flow deposits (Sharp and Nobles, 1953). Analysis of experimental deposits revealed that aggradation of sediment by closely spaced surges is apparent in deposit form and in surface sedimentary textures, but is not readily recorded in deposit stratigraphy. Such observations suggest that debris-flow deposits can be remobilized, at least locally, by subsequent surges. In order for deposits to remain weak, debris strength must remain low. Because debris flows are composed of mixtures of sediment and water, a likely hypothesis for the observed weakness of many deposits is that the interstitial pore fluid bears some, or perhaps all, of the weight of the debris so that pore-fluid pressure is elevated in excess of hydrostatic. If elevated pore-fluid pressure is responsible for the observed weakness of freshly deposited debris, then deposit stability is strongly influenced by the characteristic time needed for that excess fluid pressure to dissipate and the period between surges and separate debris flows. Deposit stability in turn influences the preservation of sedimentary structures and stratigraphic sequences in debris-flow deposits. If deposits are rigid and if there is sufficient time between surges and debris flows to allow for reworking or weathering of deposit surfaces, stratigraphic boundaries can be established. However, if deposits remain weak and if the time between surges and debris flows is sufficiently short then sediments transported by surges can shoulder into and apparently mix with previously deposited sediment, blurring any distinction of stratigraphic contact (for example, see Figure 2.37). But what constitutes sufficiently short time? Do deposits achieve, and then maintain, pore-fluid pressure in excess of hydrostatic? If so, how long do pressures remain in excess of hydrostatic?

Fluid pressures can also modify the dynamics and deposition of debris flows. Contrary to a single-phase viscoplastic material, in which a critical thickness of debris caused by plastic yield

strength of the material affects deposition, seepage of pore fluid from debris flows and kindred mass movements, and the attendant dissipation of pore-fluid pressure, has been proposed as a mechanism that induces deposition (e.g., Jahns, 1949; Hooke, 1967, 1987; Shreve, 1968; Pierson, 1981, 1984; Hutchinson, 1986). Hutchinson (1986) proposed a model in which a uniform bodywide dissipation of excess pore-fluid pressure in a consolidating sliding mass controlled mobility and deposition. In the experimental debris flows at the USGS flume, however, little water drained from the bodies of sediment until *after* they were deposited. Indeed, when the sediment mass contained about three or more percent mud little fluid drained from the mass for several hours following deposition. Despite proposals that fluid drainage and attendant dissipation of pore-fluid pressures induce deposition, no work has been done to investigate the nature of the pore-fluid-pressure field in a debris flow at the time of deposition to actually test these proposals. Furthermore, there has been little investigation of the characteristic time scales over which excess pore-fluid pressures dissipate in debris flows and their deposits; little investigation of the influence of substrate permeability on the drainage of pore fluid and dissipation of fluid pressure in debris flows and their deposits; and little examination of the characteristic nature of the fluid drainage and pressure-dissipation process in debris-flow deposits.

The purposes of this chapter are to examine, for the first time, the nature of the pore-fluid-pressure field in a field-scale debris flow at the time of deposition; to examine the consolidation behavior of debris-flow slurries representative of many debris flows in the western U.S.; and to determine the characteristic times over which excess fluid-pressures in debris-flow deposits, if they exist, dissipate. Consolidation of debris-flow slurries is examined with respect to slurry composition and with respect to substrate permeability.

FLUID PRESSURES IN FIELD-SCALE DEBRIS-FLOW DEPOSITS

MATERIALS AND METHODS

Fluid pressure and total bed normal stress were measured at the base of experimental debris flows and deposits at the USGS debris-flow flume during seven experiments in 1994. A 90-kg-capacity (200-lb-capacity) load cell, attached to a 500 cm^2 plate (Figure 3.1), and a screened fluid-pressure sensor were installed in a port on the concrete runout surface, located along the centerline of the flume 7.5 m beyond its mouth (Figure 3.2). The fluid-pressure sensor was covered with a 230-mesh screen and its port hole filled with water to provide rapid and direct hydraulic connection to pore

fluid at the base of the experimental debris. Fluid pressures and bed normal stresses measured at this site initially reflect variations of fluid pressure and flow depth behind the flow front as the debris flows decelerate. As sediment accumulated at the base of the flume, measurements at the site reflect changes in fluid pressure and bed stress in a rapidly thickening pile of sediment. Following sediment deposition, the measurements reflect fluid pressure and bed normal stress in a consolidating, quasistatic, debris-flow slurry. Although the relative location of the point of measurement within a deposit shifted among experiments owing to variations in deposit geometry, measurements generally occurred near the middle of deposits from flows that were unconfined across the runout surface, and within the extended channel for deposits of confined flows (see Figure 2.9). Because the runout surface onto which the experimental flows deposited sediment is composed of concrete, the basal boundary is impermeable. An automated data collection system was activated before the flows reached the runout surface in order to measure basal fluid pressure and total bed normal stress during deceleration and deposition. Data collection continued for several hours after each experiment.

The sediments used in the large-scale experiments were composed chiefly of local alluvium. Some of the mixtures were augmented with loam, which was added to increase the mud content ($\leq 63\mu$m in diameter). Primarily two types of source sediment were used: mixtures of sand and gravel that contained less than 1 to 2 percent mud; and mixtures of sand, gravel, and loam that commonly contained 2 to 4 percent mud (Table 3.1; Figure 2.3). The sediment mixtures were supplied by a local company, and were mixed at the company facility. However, it was apparent upon delivery that not all sediment loads were thoroughly mixed. Some of the heterogeneity exhibited in the sediment size analyses (Figure 2.3) reflects incomplete mixing. During the transport phase of the experimental debris flows, some particle segregation occurred; gravel-sized particles (2-32 mm in diameter) commonly accumulated at the front of, and on the surface of, surge waves (see Chapter 2). The sub-gravel fraction, however, appeared to be homogeneous in the deposits. Homogenization resulted from mixing during the loading of sediment at the head of the flume and during the flow of debris down the flume following release.

Pore fluid that drained from the experimental deposits was collected during several experiments. Fluid freely and rapidly drained from deposits of the sand-and-gravel dominated flows (e.g., the experiments of April 19, April 21, June 21, and July 20, 1994) and was collected in gallon-sized plastic jars that were then sealed with duct tape. Pore-fluid drained considerably less freely

from the deposits of finer-grained sediments (May 26 and August 31, 1994). Sediment transported by fluid that drained from the May 26 deposit was scraped, after it had dried, from the concrete runout surface; fluid that drained from the August 31 deposit was collected from the concrete surface by using suction devices. Considerably less drainage fluid (and associated sediment) was collected from the finer-grained deposits than from the coarser-grained deposits.

MEASUREMENTS

Both fluid pressure and total bed normal stress responded rapidly to passage of surges and deposition of sediment. Sudden increases in signal magnitude reflect surges passing across the sensing plate; the progressive increase in signal magnitude reflects accumulation of saturated sediment (Figures 3.3a-g). Decay of basal fluid pressure following deposition reflects longer-term diffusive behavior during consolidation of the debris-flow deposits. The pulsatile character of the basal fluid pressure and total normal stress at early time complements observations that the experimental deposits formed primarily by incremental accumulation of sediment deposited by overlapping surges (cf. Chapter 2). In Figure 3.3, fluid pressure is shown in units of water head rather than in standard units of pressure (Pa). This choice is one of convenience. Providing fluid pressure in units of centimeters of water head allows easy comparison between the magnitude of total fluid pressure and the magnitude of hydrostatic pressure at the measurement point; hydrostatic pressure at the base of a saturated deposit equals the thickness of the deposit. Bed normal stress, on the other hand, is shown in standard SI units. Although fluid pressure and bed normal stress are shown in different units, they are plotted to the same scale. Centimeters of water head can be converted to their approximate pressure value in Pa using a multiplication factor of 100. The precise conversion is: centimeters of water head x 98 = pressure in Pa.

Variations in the fluid pressure and total normal stress during flow deceleration and deposition are essentially in phase, within 1 to 8 Hz resolution, in the coarser-grained experimental flows (April, June, and July 1994). Crests and troughs in both signals track each other closely during that period. In contrast, measurements of basal fluid pressure and total bed normal stress in the main channel farther up slope, made at 2 kHz resolution, reveal that increases in bed normal stress precede changes in basal fluid pressure by as much as one-half of a second, which indicates that on steeper slopes the leading edge of a flow typically is drier than the trailing flow (R.M. Iverson, personal communication,

1995). These measurements are consistent with observations that coarse, dry fronts form in many natural debris flows (e.g., Pierson, 1980, 1985b; Costa and Williams, 1984). Differences between the measurements in the flume channel and on the runout surface may be related primarily to the lower time resolution with which data were collected in the runout area. However, it is possible that wetter material from farther back in the flow may have caught up with the flow front by the time flows reached the runout area.

Changes in fluid pressure during flow deceleration initially lagged behind changes in total bed normal stress by as much as two seconds in flows composed of finer grained material (May and August 1994), in contrast to the signal variations observed in the coarse-grained flows. After a few seconds the basal fluid pressure was in phase with, and of comparable magnitude to, the measured total bed normal stress (Figure 3.3e-g). The initial lag of the fluid pressure signal may be related to the relative impermeability of the source sediment rather than to the front of the flow being substantially drier than trailing flow. Visual observations and photographic records of deposition by the finer-grained flows do not suggest that flow fronts were significantly drier than immediately trailing parts of flow. The different rates with which fluid seeped from the coarser-grained and finer-grained deposits indicate that it is more difficult for pore fluid to migrate in the finer-grained sediments. Therefore, there may be a slight delay in the hydraulic connection between the sensor and the base of a fine-grained flow.

Fluid pressure is nonuniformly distributed behind the flow front in debris flows, yet it can balance a substantial proportion of the total weight of overburden. Behind the flow front, the ratio of fluid pressure to total bed normal stress rose rapidly to gradually. Fluid pressures measured at the base of the experimental deposits ranged from about 50 percent (hydrostatic) to approximately 100 percent (lithostatic) of the value of the measured total bed normal stress during the few seconds of flow passage and sediment deposition at the sensing plate (Figures 3.3a-g). Fluid pressure typically balanced about 80 percent or more of the total bed normal stress behind the flow front. Fluid pressures of comparable magnitude were measured in much of the flow mass farther up slope in the channel during several experiments (Iverson and LaHusen, 1993b). Measured fluid pressures of this magnitude in the runout area indicate that fluid pressures capable of balancing much of the weight of the overlying debris persist in debris flows during deceleration and sediment deposition. Such high fluid pressures were maintained until sediment was completely deposited.

In several experiments, fluid pressures appear to balance more than 100 percent of the total bed normal stress (e.g., June, July, and August 1994). Although the flows in these experiments probably had a substantial proportion of their total bed normal stress balanced by fluid pressure in the runout area, direct quantitative comparison between fluid pressure and total normal stress is subject to skepticism. Close examinations of those data show that the measured total normal stress following sediment deposition is anomalously low, yielding saturated bulk densities < 1800 kg/m^3. As a result, measured basal fluid pressures appear to exceed measured total bed normal stresses, in some instances substantially. It is unclear why the measured values of total bed normal stress in these experiments appear to be low. However, each of these experiments had unique aspects. The experiments of June 1994 were designed to measure impact force on a vertical wall (Iverson and others, 1994). In those experiments, flows slammed into a vertical wall placed about 1 meter down slope from the sensing plate. The flows and deposits in the vicinity of the plate were highly disturbed through interaction with the wall (Iverson and others, 1994). Possibly a substantial proportion of the weight of the sediment in the vicinity of the sensing plate was borne by friction forces at the sediment/wall interface. The July and August 1994 flows were confined across much of the runout surface, so that deposition over the sensing plate occurred within or immediately beyond confined channels. Again, perhaps part of the sediment weight was borne by channel walls. Although the data from these experiments are consistent with data obtained in other experiments and show that fluid pressures support the weight of overlying debris, their significance must be tempered by the possibility that they represent a more complicated stress field that cannot be interpreted in terms of a simple one-dimensional balance of stresses.

The time necessary to dissipate basal pore-fluid pressures in excess of hydrostatic ranged widely, over several orders of magnitude. Variation of this time depended mainly upon the composition of the experimental debris; deposit thicknesses were generally of the same magnitude. In the coarse sand-and-gravel deposits (April 19, April 21, June 21, June 23; see Table 3.1) excess pore-fluid pressure dissipated within tens of seconds to tens of minutes after sediment deposition (Figures 3.3a-d), consistent with the observed rapid drainage of pore fluid. Modest amounts of finer-grained debris added to the source sediment greatly affected fluid-pressure behavior. Sediment used in the May, July, and August 1994 experiments contained approximately 2 to 4 weight percent mud (Table 3.1). In those deposits, basal fluid pressures remained at or near their immediately post-depositional magnitudes for several to several tens of minutes before dissipating (Figures 3.3e-g).

Pore-fluid pressure remained in excess of hydrostatic in those deposits for a few to more than 10 hours.

Variations in the rates with which fluid drained from deposits affected sampling of pore fluids. Rapid drainage of turbid pore fluid from coarser-grained deposits permitted collection of liter-sized samples. The pore fluid that drained from these deposits was composed of water and sediment, although sediment volume concentrations were only about 2 percent (Table 3.2). Sediment within this pore fluid was dominantly silt and clay, although particles as large as 0.5 mm were incorporated. In contrast, pore fluid typically oozed slowly from the finer-grained deposits over periods of several hours. The slow release of pore fluid prevented large-quantity sampling of fluid. Pore fluid seeped sufficiently slowly from the May 1994 deposit that it was not possible to collect any fluid for analysis. Instead, sediment transported by the pore fluid was scraped from the runout surface after the fluid evaporated. Pore fluid that drained from the August deposit had to be collected with suction devices, such as syringes. Sediment concentrations of the pore fluid from the finer grained deposits appear to have ranged from about 6 to 16 percent by volume. Sediments in these pore fluids were also composed dominantly of silt and clay, but they also contained measurable amounts of sand, and included particles as large as 2 mm. The relatively high proportion of sand in the pore fluid from the August 1994 experiment may include accidental sand retrieved by the suction devices, although the pore-fluid sediment scraped from the concrete following the May 26 experiment also contains a measurable proportion of sand. These data show that pore fluid in the experimental debris flows was composed both of water and sediment. Fine sediment suspended in water affects fluid viscosity, which in turn affects dissipation of pore-fluid pressures. This topic is discussed later in this chapter.

Dissipation of fluid pressure is a diffusive process affected by physical properties of the porous medium and the viscosity of the pore fluid. The eventual dissipation of initially lithostatic fluid pressures in the experimental debris-flow deposits and the wide variations in the time needed for those fluid pressures to dissipate suggest that the post-depositional behavior of the debris-flow deposits may be described by a soil-consolidation model. In the remainder of this chapter I examine the nature of pore-fluid hydraulics and the consolidation behavior of debris-flow slurries.

SOIL CONSOLIDATION -- A GENERAL OVERVIEW

The treatment of consolidation of porous media and attendant pore-fluid hydraulics is concerned largely with the application of an external surface load (e.g., Lambe and Whitman, 1969). The classical view of soil consolidation, put forward by Karl Terzaghi some 70 years ago (e.g., Skempton, 1960), is that a load applied to the surface of a saturated soil is borne initially by local increases in fluid pressure beyond hydrostatic. Following application of a surface load, local excess pore-fluid pressure dissipates, and the soil mass deforms, when stresses are transferred gradually from the pore fluid to the solid skeleton as fluid escapes and pore spaces close. Volumetric deformation of the soil mass can occur only if fluid can drain from the medium, provided that the individual constituents are incompressible. The magnitude of deformation is governed by the stress-strain relations of the medium. The time scale of the response depends on the permeability of the medium, the compressibility of the medium, and the length scale over which fluid must migrate. In the early development of consolidation theory, soil deformation was coupled to soil stresses through a linearly elastic constitutive model. Thus, the theory is limited to a state of infinitesimal strain. Although soil displacements can be large in magnitude, they are assumed to be small in comparison to the dimensions of the medium. Body forces generally are ignored in conventional consolidation analysis because, for most geotechnical problems, soils are in equilibrium with the geostatic stress field.

Later studies have considered more sophisticated models of soil consolidation. These considerations include, for example, coupling of strain to both soil stress and fluid pressure; nonlinear stress-strain relations; elastoplastic constitutive models; and finite strains (e.g., Biot, 1941; Davis and Raymond, 1965; Gibson and others, 1967; Carter and others, 1979). A few studies have considered the problem of consolidation that proceeds under gravitational, so-called self-weight, loading (e.g., Gibson and others, 1967; Lee and Sills, 1981; Been and Sills, 1981; Audet and McConnell, 1992). This kind of consolidation occurs in soils not in equilibrium with the geostatic stress field; for example, in lakes or estuaries owing to slow, continuous input of sediment; in hydraulic fills not artificially compacted; in sediments rapidly deposited as slurries; and in large sedimentary basins. Although studies have addressed gravitational loading and have accounted for large strains, they have focused attention primarily on the behavior of highly compressible clays, and their treatments have been cast in terms of the transient behavior of void ratio, a measure of pore volume. The need for a large-strain, nonlinear theory is easily understood when dealing with effective stresses of tectonic magnitude (tens of MPa) or when considering the very high porosity and physical structure of clay

sediments; in clay soils it is common to have strains as large as several tens of percent (Lambe and Whitman, 1969, p. 298).

In this chapter I examine gravity-driven consolidation of granular sediment slurries at low effective stresses (a few kPa). This type of consolidation is likely to occur when a dilated, nearly liquefied, sediment slurry is suddenly deposited, such as occurs when sediment is deposited by a debris flow. A simple model for this style of consolidation is constructed by including a gravitational body force in a linear, one-dimensional model of consolidation that treats the soil medium as a linearly elastic body and uses a constitutive rule proposed by Biot (1941) to relate strains to total stress and fluid pressure. I begin with a very simple one-dimensional treatment of consolidation for several reasons: granular sediments typically are much less compressible than clays (e.g., Lambe and Whitman, 1969, p. 297); the effective stresses of concern are low (order 1-10 kPa); limited measurements of changes in thickness of large-scale experimental debris-flow deposits suggest that bulk volume strains may be on the order of 5 percent of less (about 1 cm change in a 20-cm-thick deposit); debris-flow deposits typically are much broader than they are thick, therefore vertical fluid flow likely is dominant; and a linear model is retained because it provides a convenient starting point that avoids complications owing to large changes in soil porosity. Unlike the consolidation theory of Gibson and others (1967) and Lee and Sills (1981), I cast the mathematical formulation in terms of the transient behavior of nonequilibrium, or excess, pore-fluid pressure and retain the classical linear-elastic, small-strain approach. Unlike the treatment by Lee and Sills (1981), which provided only solutions for a few self-weight consolidation problems, I compare predicted solutions against measured laboratory and field data. Following the mathematical development of a simple theory, I compare predictions of the theory to data collected from a series of laboratory experiments using sediments that bracket a broad range of the physical properties of many debris flows in the western U.S. and to data collected from deposits of several experimental debris flows. I then discuss the significance of these results with respect to debris-flow deposition, deposit stability, and stratigraphic distinction of deposits.

MATHEMATICAL FORMULATION

Expressions that describe the one-dimensional consolidation behavior of sediment slurries depend on conservation laws that describe the balance of linear momentum of the solid-fluid system; the balance of fluid mass within the porous body; a rule that relates solid strains to total stresses and fluid pressure; a relation that partitions total stress into stresses acting on the solid constituents and into fluid pressure; and a relation that describes fluid flow resulting from gradients in fluid pressure. The basic governing equation that describes one-dimensional consolidation of a porous body is an expression that describes the simple diffusion of a nonequilibrium fluid pressure. This expression is derived by combining the conservation law that balances the mass of fluid in a porous body with a rule that relates volume strain in the body to total stress and fluid pressure and with a rule that relates fluid flux to gradients in fluid pressure. An initial fluid pressure condition can be described through consideration of the conservation law that balances the linear momentum of the solid-fluid system and through assumptions regarding the volume strain of the porous body following the instantaneous application of the force that causes deformation. Solution of the problem posed by the governing diffusion equation leads to expressions that describe the transient behavior of fluid pressure, of stresses acting on the solid constituents, of volume strain of the body, and of surface displacement.

Consider an Eulerian system in which displacements and strains in the matrix of a saturated, porous body are small in comparison with the dimensions of the body. The balance law for linear momentum of a quasistatic solid-fluid system, in which inertial terms are neglected, is given by the well-known Cauchy equations for stress equilibrium

$$\frac{\partial \sigma_{ji}}{\partial x_j} + \rho_t g_i = 0 \tag{3.1}$$

where σ_{ji} are the components of the total stress, representing the sum of fluid and solid stresses, ρ_t is the total mass density of the solid-fluid mixture, and g_i is the gravitational acceleration in the coordinate direction. The total mass density is defined as $\rho_t=\rho_f \phi+\rho_s(1-\phi)$, where ρ_s and ρ_f are the solid-particle and fluid densities, respectively, and ϕ is the porosity. For the one-dimensional system with z defined positive upwards (Figure 3.4), (3.1) reduces to

$$\frac{\partial \sigma_{zz}}{\partial z} - \rho_t g = 0. \tag{3.2}$$

Integrating (3.2),applying the boundary condition that $\sigma_{zz} = 0$ at $z = H$ (Figure 3.4), and substituting in the definition of total mass density yields

$$\sigma_{zz} = -\rho_s g (H-z) + (\rho_s - \rho_f) g \int_z^H \phi \, dz. \tag{3.3}$$

When a body force, rather than an applied surface load, is responsible for the deformation of a one-dimensional porous body, the total stress acting at any point in the porous body is a function of depth and is not some uniformly constant value. Here, I assume that ρ_t initially is a constant value; thus, the total stress acting at any point in the system is a linear function of depth below the surface and (3.3) becomes

$$\sigma_{zz} = -[\rho_f + (\rho_s - \rho_f)(1 - \phi)] g (H - z). \tag{3.4}$$

A constitutive rule proposed by Biot (1941) that relates strain to total stresses and pore-fluid pressure was recast in terms of conventional elastic moduli by Rice and Cleary (1976). A minor regrouping of their expression yields

$$\varepsilon_{ij} = \frac{1}{2G}[\sigma_{ij} - \frac{\nu}{1+\nu}\sigma_{kk}\delta_{ij}] + \frac{1}{3K_b}(1 - \frac{K_b}{K_s}) p \delta_{ij} \tag{3.5}$$

in which G and ν are the shear modulus and drained Poisson's ratio, respectively, of the porous medium; K_b and K_s are elastic bulk moduli of the porous medium and solid particles, respectively; p is the total pore-fluid pressure; δ_{ij} is the Kronecker delta; i and j represent coordinate directions; and the usual convention of summation over repeated indices holds.

In fluid-filled porous media, total stresses are partitioned between stresses acting on the solid material and pressure in the pore fluid. This partitioning of total stress is conveniently expressed by the concept of effective stress (Terzaghi, 1923; Skempton, 1960). The most general form of effective stress can be written as

$$\sigma'_{ij} = \sigma_{ij} + \alpha p \delta_{ij} \tag{3.6}$$

where σ'_{ij} is the effective stress and p is the pointwise total fluid pressure. Equations based on the Biot-type constitutive rule are compatible with standard Hookean elastic equations only if $\alpha=(1-K_b/K_s)$ (Iverson and Reid, 1992). The definition of effective stress most useful for describing the partitioning of total stress acting in soils and other Coulomb materials is given by (Terzaghi, 1923; Jaeger and Cook, 1979)

$$\sigma'_{ij} = \sigma_{ij} + p \delta_{ij} . \tag{3.7}$$

Equations (3.6) and (3.7) are compatible only if the porous body is substantially more compressible than the individual solid constituents ($K_b \ll K_s$), a condition common for geologic materials subject to low effective stresses.

If we assume that the solid particles are incompressible ($K_s \to \infty$), then substitution of (3.7) into (3.5) and utilization of the identity (Timoshenko and Goodier, 1970, p. 10-11)

$$\frac{2G}{3K_b} = \frac{1-2\nu}{1+\nu} \tag{3.8}$$

gives, after some algebraic manipulation, elastic strain in terms of effective stress

$$\varepsilon_{ij} = \frac{1}{2G}[\sigma'_{ij} - \frac{\nu}{1+\nu}\sigma'_{kk}\delta_{ij}]. \tag{3.9}$$

In one dimension, the bulk volume strain of a porous body composed of incompressible solids is given, in terms of effective stress, by

$$\varepsilon_{zz} = \frac{(1-2\nu)}{2G(1-\nu)}\sigma'_{zz}. \tag{3.10}$$

For infinitesimal strain, the one-dimensional balance law for fluid mass in a porous body can be written in terms of the volume flux of fluid through the body and the volume strain of the porous body. This balance law, which assumes that the constituents are incompressible, is given by

$$\frac{\partial \varepsilon_{zz}}{\partial t} + \frac{\partial q}{\partial z} = 0 . \tag{3.11}$$

Substituting (3.7) and (3.10) into (3.11), and rewriting the total fluid pressure, p, in terms of a hydrostatic fluid pressure, p_h , and a nonequilibrium, or excess, fluid pressure, p_*, such that

$$p_* = p - p_h \tag{3.12}$$

where $p_h = \rho_f g(H-z)$ yields, after some manipulation,

$$\frac{\partial \sigma_{zz}}{\partial t} + \frac{\partial p_*}{\partial t} + \frac{2G(1-\nu)}{(1-2\nu)} \frac{\partial q}{\partial z} = 0 . \tag{3.13}$$

I assume in this formulation that sediment slurries are deposited essentially instantaneously. Thus, the gravitational body force that drives consolidation of the deposited slurry is effectively "applied" instantly. Although the body-force-dependent total stress can vary with depth, it is assumed not to change with time. Therefore, the first term in (3.13) is assumed to be zero. The measured total bed stress acting at the base of the experimental debris-flow deposits indicates that this is a reasonable assumption (see Figure 3.3).

The volume flux of fluid per unit area of porous medium is related to gradients in nonequilibrium fluid pressure through Darcy's Law. For a one-dimensional system, this is written as

$$q = -\frac{k}{\mu} \frac{\partial p_*}{\partial z} \tag{3.14}$$

in which k is the hydraulic permeability of the medium and μ is the dynamic viscosity of the pore fluid. Substituting this expression into (3.13) yields a diffusion equation in terms of nonequilibrium fluid pressure

$$\frac{\partial p_*}{\partial t} - D \frac{\partial^2 p_*}{\partial z^2} = 0 \tag{3.15}$$

in which the diffusion coefficient, D, is defined as

$$D = \frac{k}{\mu}\frac{2G(1-\nu)}{(1-2\nu)}. \tag{3.16}$$

Utilizing the identity given in (3.8), the diffusion coefficient can be recast in terms of the bulk modulus of the porous body, a measure of its compressibility, as

$$D=\frac{kK_b}{\mu}\frac{3(1-\nu)}{1+\nu}. \tag{3.17}$$

For values of Poisson's ratio typical of granular soils (e.g., Lambe and Whitman, 1969) equation (3.17) reduces approximately to

$$D = \frac{kK_b}{\mu}. \tag{3.18}$$

From this derivation, we see that the diffusion of excess pore-fluid pressure results from volume deformation of a porous body and from fluid flow that relaxes gradients in nonequilibrium fluid pressure. Furthermore, we see that diffusion of nonequilibrium pore-fluid pressure depends on properties of both the porous medium and the pore fluid, namely the permeability and compressibility of the porous body and the viscosity of the pore fluid.

The governing equation described by (3.15) holds regardless of the nature of the force causing consolidation. The significant difference between an applied surface load and gravitational, self-weight, loading is manifest in the nature of the total stress acting at any point in the system (equation 3.4) and in the initial fluid-pressure profile that develops following instantaneous loading.

An initial condition (a perturbation to a reference state) can be imposed on the fluid pressure in the porous body if we assume that both the fluid and solid constituents of the porous body are

incompressible and if we assume that the body-force loading is rapid relative to the time required for the pore fluid to begin to diffuse. Such conditions are appropriate for rapidly deposited slurries subject to low effective stresses. Under these conditions no volume change of the porous body is allowed during instantaneous loading at t=0. We can determine the initial (perturbation) fluid pressure in the instantaneously undrained state by substituting (3.7) into (3.10) and setting $\varepsilon_{zz}=0$, which yields

$$-\sigma_{zz} = p\,. \tag{3.19}$$

Equating (3.19) with (3.4) yields

$$[\rho_f+(\rho_s-\rho_f)(1-\phi)]g(H-z) = p\,. \tag{3.20}$$

In terms of hydrostatic and nonequilibrium fluid pressures, this initial condition is represented by

$$\begin{aligned} p_h &= \rho_f g(H-z) \\ p_*(z,0) &= (\rho_s-\rho_f)(1-\phi)g(H-z)\,. \end{aligned} \tag{3.21}$$

We therefore see that when a gravitational body force is responsible for causing deformation of a porous medium, and when gravitational loading is rapid relative to the time required for pore fluid to diffuse, then the porous body is initially liquefied and the initial total-fluid-pressure profile is a *linear* function of depth, fluid density, and submerged weight of the solid fraction, and is not a uniformly constant value as is the case when the gravitational body force is neglected (e.g., Lambe and Whitman, 1969). Measurements of basal fluid pressure in the experimental debris-flow deposits indicate that this is a realistic initial condition in rapidly deposited slurries (Figure 3.3).

Solution of (3.15), subject to a no-flux basal boundary condition, a freely draining surface, and the initial condition defined in (3.21) (see Figure 3.4), yields an expression for the transient nonequilibrium fluid-pressure field (Carslaw and Jaeger, 1959, p. 97)

$$p_* = 8p_{*o}\sum_{n=0}^{\infty}\frac{1}{(2n+1)^2\pi^2}\cos(\lambda_n z)\,e^{-\lambda_n^2 Dt} \tag{3.22}$$

in which p_{*o} is the initial nonequilibrium fluid pressure at $z = 0$ (see equation 3.21), and λ_n are eigenvalues defined as

$$\lambda_n = \frac{(2n+1)\pi}{2H}. \tag{3.23}$$

With a solution in hand for the transient fluid-pressure field, I can compute the transient behavior of other quantities of interest, such as effective stress, volume strain, and surface displacement. Combining (3.4), (3.7), (3.21) and (3.22) yields an expression for the transient behavior of effective stress

$$\sigma'_{zz} = -(\rho_s - \rho_f)(1-\phi)g\left[(H-z) - 8H\sum_{n=0}^{\infty}\frac{1}{(2n+1)^2\pi^2}\cos(\lambda_n z)e^{-\lambda_n^2 Dt}\right]. \tag{3.24}$$

The transient behavior of volume strain can be found by substituting (3.24) into (3.10) to yield

$$\varepsilon_{zz} = -\frac{(1-2\nu)}{2G(1-\nu)}(\rho_s - \rho_f)(1-\phi)g\left[(H-z) - 8H\sum_{n=0}^{\infty}\frac{1}{(2n+1)^2\pi^2}\cos(\lambda_n z)e^{-\lambda_n^2 Dt}\right]. \tag{3.25}$$

By definition, for small strain,

$$\varepsilon_{zz} = \frac{\partial u_z}{\partial z} . \tag{3.26}$$

Integrating (3.25) and imposing the condition that u(0,t) = 0 yields an expression for displacement of the form

$$u_z = -\frac{(1-2\nu)}{2G(1-\nu)}(\rho_s - \rho_f)(1-\phi)g\left[(Hz - \frac{z^2}{2}) - 8H\sum_{n=0}^{\infty}\frac{1}{(2n+1)^2\pi^2}\frac{\sin(\lambda_n z)}{\lambda_n}e^{-\lambda_n^2 Dt}\right]. \tag{3.27}$$

Setting z = H in (3.27) yields an expression for transient behavior of surface displacement

$$u_H = -\frac{(1-2\nu)}{2G(1-\nu)}(\rho_s - \rho_f)(1-\phi)g\left[\frac{H^2}{2} - 8H\sum_{n=0}^{\infty}\frac{1}{(2n+1)^2\pi^2}\frac{\sin(\lambda_n H)}{\lambda_n}e^{-\lambda_n^2 Dt}\right]. \tag{3.28}$$

LABORATORY EXPERIMENTAL STUDY

Equations (3.22), (3.24), (3.25) and (3.28) form the basis upon which this simple, linear, constant-coefficient model for gravity-driven, one-dimensional consolidation of granular sediment slurries can be tested. These equations provide predictions of the transient behavior of nonequilibrium fluid pressure, effective stress, volume strain, and surface displacement that can be compared to measurements made in laboratory slurries and in deposits from large-scale experimental debris flows. For consolidation in the presence of a freely draining bed rather than an impermeable bed, appropriate boundary conditions yield modified forms of these equations (Appendix D).

I conducted one-dimensional laboratory experiments of self-weight consolidation using granular sediments that consisted of poorly sorted mixtures of gravel (to several mm in diameter), sand, and finer particles (Table 3.3). These sediments came from three sources: the source debris used at the USGS debris-flow flume for the May 26, 1994 experiment; the clay-rich Osceola Mudflow deposit from Mount Rainier, Washington, collected from a quarry near Huckleberry Creek, some 40 km from the source area (Vallance, 1994); and the 1980 North Fork Toutle River debris-flow deposit from Mount St. Helens, Washington, collected at the Kid Valley bridge about 47 km from the mountain (Scott, 1988a). These particular materials were chosen for two reasons: they represent debris-flow sediments having a range of clay content and they represent sediment properties that probably bracket the physical characteristics of most debris flows in the western U.S., both volcanogenic and nonvolcanogenic.

The suite of experiments conducted in this study included both impermeable and freely draining beds. Two types of substrates were used in the permeable-bed experiments: pea gravel having particle diameters that ranged from 2 to 16 mm (-1ϕ to -3ϕ) and a mean permeability of 3 x 10^{-10} m^2; and compacted, 0.25 to 2 mm (2ϕ to 0ϕ) sand having a mean permeability of 7 x 10^{-11} m^2. Each impermeable bed experiment was repeated for each sediment used. For the experiments conducted with flume sediment, I repeated the experiments using each permeable substrate material. For the experiments using the Mount Rainier and Mount St. Helens sediments, I conducted only one experiment with each permeable substrate material. I attempted to use similar solids concentrations and slurry depths in each replicate experiment; however, there was some variation in these parameters among experiments (Table 3.4).

The laboratory apparatus consists of a simple, smooth-walled, cylindrical aluminum tank 25.4 cm in diameter and approximately 1 m tall (Figure 3.5). A water-filled, 36-cm-tall standpipe is used to maintain backpressure in substrate sediment during permeable-bed experiments. In permeable-bed experiments, substrate material is filled to the level of the standpipe and saturated with water. Hydrostatic pressure in the standpipe prevents gravitational drainage of the substrate sediment. Substrate material is removed from the tank and the standpipe outlet is capped during impermeable-bed experiments.

The experimental protocol consisted of mixing approximately 50 liters of sediment with tap water, introducing the saturated slurry into the tank, logging the pore-fluid pressure at various positions in the slurry, and tracking surface displacement. The sediment used for each experiment was combined with water in a small construction mixer until the mixture appeared to have the consistency of wet concrete. No effort was made to mix sediment with a predetermined volume of water. If too much water was added, the mixture separated into two phases: sediment in water. After mixing, the sediment slurry was divided immediately into several smaller buckets, each of which was poured rapidly into the cylindrical tank. A sample of each slurry was retained to measure its water content and to calculate the volume fraction of solids (Table 3.4). Local fluid pressure was measured in each experiment using screened pressure probes suspended at various levels in the central part of the tank (Figure 3.5). Data from these sensors were logged directly to a personal computer through an 8-channel A/D conversion board. The software that controlled data collection was programmed to sample each occupied channel at an initial rate of 8 Hz, and to step gradually to slower sampling rates as elapsed time increased. Changes in surface displacement of the slurry through time were measured manually in several experiments by tracking displacement along the sidewall of the tank.

The magnitude of the local nonequilibrium fluid pressure in each experimental slurry was determined by subtracting the local hydrostatic pressure from the measured total pressure. The value of the diffusion coefficient, D (equations 3.15-3.18), was determined by comparing predicted values of nonequilibrium fluid pressure (equation 3.22) to measured values using a variation of the standard χ^2 statistic (e.g., Iman and Conover, 1983). Differences between predicted values of nonequilibrium fluid pressure, based on a selected value of D, and measured values at several time steps were squared and summed. The square root of the summed-squares value was then minimized in order to obtain a best-fit value for the diffusion coefficient. Similar minimization methods have been used to determine parameter values in other applications of diffusion models (e.g., Rosenbloom and Anderson, 1994).

RESULTS

LABORATORY EXPERIMENTS

Initial Fluid Pressures

Locally measured initial total fluid pressures in the experimental slurries are linear with depth (Figure 3.6), and are of lithostatic magnitude (Figure 3.7). The initial fluid pressure was considered to be that value measured locally at each sensor following completion of the sediment loading. There is negligible difference in the form of total-fluid-pressure profile resulting from variations in the composition of source sediment or from variations in substrate material, indicating that the physical mechanism responsible for generating fluid pressure in quasistatic granular slurries is independent of sediment composition, grain size, grain shape, or substrate material.

Measured initial fluid pressures indicate that the experimental slurries were fully liquefied immediately after loading, consistent with the initial condition imposed in the one-dimensional, gravity-driven consolidation theory. Following loading of each sediment slurry, illustrated by the sharp pressure peaks at early time in Figures 3.7a-d, the initial total pressure was approximately double to more than double the magnitude of hydrostatic fluid pressure at all levels. Initial total fluid pressures of this magnitude are expected for liquefied porous media having porosities that range from about 20 to 40 percent (equations 3.20, 3.21). These values of total pressure indicate that the magnitude of nonequilibrium fluid pressure initially equaled or exceeded the magnitude of hydrostatic fluid pressure throughout the sediment column (equation 3.21; Table 3.4). These data show clearly that grain contacts initially bore little, if any, load, despite the fact that 60 percent or more of the volume of each slurry was composed of solid particles. The measured initial fluid pressures are thus consistent with the assumption that gravitational loading is rapid relative to the time needed for pore fluid to diffuse in poorly sorted sediment slurries and that there is little, if any, volume strain in the slurries during loading. As long as particle contacts remain nonexistent, or at most non-load-bearing, fluid supports the full particle weight and the nonequilibrium fluid pressure equals or exceeds the hydrostatic pressure. Because the initial fluid pressures were of lithostatic magnitude, initial porosities at different levels in each slurry could be determined from values of initial fluid pressure (equations 3.20, 3.21). Calculations of initial slurry porosity are summarized in Table 3.4.

Transient Total-Fluid-Pressure Response

Total fluid pressures remained at or near lithostatic magnitudes until pore fluid began to migrate and induce volume change. The time necessary for the migration of a sufficient quantity of pore fluid to greatly affect the initially lithostatic fluid pressures ranged from a few tens to several hundreds of seconds, illustrated by the pressure plateaus commonly measured in the experiments (Figures 3.7a-d). An initial drop in fluid pressure below lithostatic magnitude happens as soon as solid particles establish load-bearing contacts. When particle contacts become well established significant stresses are transferred from the fluid to the solid skeleton and fluid pressures drop, in some instances very rapidly. The fragile nature of particle contacts in metastable sediment slurries is illustrated in Figure 3.7a. In experiment C4, fluid pressures at all levels started dropping rapidly after approximately 30 minutes (1800 seconds). Shortly thereafter, the established network of particle contacts was apparently partly disrupted and stresses were transferred back to the fluid, illustrated by the sudden rise in fluid pressure at all levels. The network of particle contacts was not completely disrupted, otherwise the fluid pressure would have risen to a lithostatic value. Pierson (1981) observed similar spikes in fluid pressures when static sediment slurries were disturbed.

The nature of the basal boundary significantly affected the response of fluid pressure at the base of a slurry column, but had little effect on the characteristic response of fluid pressures in higher parts of the column. When fluid flow is permitted across the basal boundary, fluid pressure at the base of the column dissipates rapidly after sediment loading (Figures 3.7b-d). In experiments that used sediment from the USGS flume, lithostatic to nearly lithostatic fluid pressure near the base of the slurry was maintained for only a very short period of time, if at all (Figure 3.7b). In experiments that used clay-rich Osceola Mudflow sediment (Figure 3.7c), lithostatic to nearly lithostatic fluid pressure was maintained for several hundreds of seconds near the base of the slurry. Though this time scale is of a magnitude comparable to that observed in the impermeable-bed experiments that used the more granular flume sediment, it is one to two orders of magnitude shorter than the length of time that nearly lithostatic fluid pressure is maintained at shallower levels in the same experiment; it is also significantly shorter than the length of time that a comparable magnitude of fluid pressure is maintained in the same debris when the bed is impermeable. Rapid reduction of pore-fluid pressure at the base of the slurry column is the direct result of having a freely draining boundary in near proximity. The significance of the more moderate influence of a freely draining boundary on fluid pressure at higher levels in the slurry is discussed later in this chapter.

Diffusion of Nonequilibrium Fluid Pressure

The foremost feature of the predicted transient response of nonequilibrium fluid pressure (equation 3.22) is that pressure diffusion begins at the *base* of the slurry; the diffusion front migrates upward from the base (Figures 3.8a-d). This transient response is contrary to that predicted by analyses that neglect body forces, in which pressure diffusion begins at the surface and migrates downward (e.g., Lambe and Whitman, 1969). The response predicted in the formulation developed here, and measured in the experimental slurries, is a direct consequence of the initial-pressure condition imposed by inclusion of a gravitational body force: fluid flows, and pressure diffuses, in response to a gradient in nonequilibrium pressure, and rapid gravitational loading generates the highest nonequilibrium pressure at the base of the system. When the basal boundary is impermeable, the greatest nonequilibrium fluid pressure is located at, and remains at, the base of the sediment column (Figure 3.8a,d). In contrast, when the basal boundary is freely draining ($k_{substrate}/k_{slurry}$ ~10-100), the locus of peak nonequilibrium fluid pressure is displaced upward. Although nonequilibrium fluid pressure can diffuse both upward and downward, the transient response is not symmetric; the locus of peak nonequilibrium fluid pressure is initially at the base of the column and gradually migrates toward the center of the column (Figure 3.8b,c,d). Again, this is a direct consequence of the initial-pressure condition imposed by the gravitational body force.

Nonequilibrium fluid pressures shown in Figure 3.8 have been normalized by the initial values of the nonequilibrium fluid pressures at the base of the slurries (equation 3.21). Values at any level along the curves depicted in the figure represent the magnitude of nonequilibrium fluid pressure as some fraction of the basal fluid pressure. Each curve represents a different increment of time. Time in this figure, and in subsequent figures, is nondimensionalized to remove effects of length scale. Real time in the impermeable-bed experiments has been normalized by H^2/D, where H is the slurry thickness; times in permeable-bed experiments have been normalized by $(H/2)^2/D$. These length scales represent the maximum distances that parcels of fluid in each experiment must travel to reach an equilibrium-pressure surface.

Variations in substrate permeability of at least an order of magnitude appear to have little influence on the evolution of the fluid-pressure field in debris-flow slurries; the predicted and measured transient responses of nonequilibrium fluid pressure in the presence of a freely draining boundary are similar for both the gravel and sand substrates (Figure 3.8b,c,d). As long as the

substrate is about an order of magnitude more permeable than the debris-flow slurry the composition of the substrate has little effect on the evolution of the fluid-pressure field in the consolidating debris.

The value of the diffusion coefficient, D, shown in Figures 3.8a-d represents the value that provides the best overall correspondence between predicted and measured nonequilibrium fluid pressure at all levels in the sediment column. In general this coefficient is similar to a value computed, by a χ^2 statistic, for an intermediate-level probe. Table 3.5 lists the optimal values of the diffusion coefficient at each level and also compares the depthwise best-fit value of the diffusion coefficient with the consolidation coefficient, C_v, a kindred coefficient estimated from changes in surface displacement with time (ASTM, 1995). The optimal values of the diffusion coefficient determined in the laboratory experiments are several orders of magnitude smaller than values common for unlithified granular sediments or even many lithified rocks (e.g., Roeloffs, 1996). They appear to be more similar to values common for clays, shales, and unfractured igneous rocks. The cause for these exceptionally low values is related to the extremely compressible nature of these slurries, and is discussed below. An interesting pattern emerges from the optimal values of D computed at various levels. For nearly all experiments the value of the diffusion coefficient generally decreases downward in the sediment column, in some cases by a few orders of magnitude across the depth of the slurry (Table 3.5). This decrease in the value of coefficient appears to be most pronounced in the permeable-bed experiments, but that appearance may be biased by a lack of data sufficiently close to the base of slurries in the impermeable-bed experiments. Nonetheless, this trend in the data shows that in gravity-driven consolidation the physical structure of the porous body changes with depth in the sediment column, which suggests that the pressure-diffusion and soil compaction process is not simply linear, as assumed, even for shallow granular slurries.

Effective Stress, Volume Strain, and Surface Displacement

Effective Stress

Effective stress follows a transient response pattern analogous to that exhibited by nonequilibrium fluid pressure: effective stress increases initially at the base of the sediment column and the stress increase "diffuses" upward (Figures 3.9a-d). Computation of the evolution of effective stress illustrated in Figure 3.9 requires two parameters: an estimate of the diffusion coefficient, D, and an estimate of the porosity, ϕ, of the slurry (equation 3.24). The diffusion coefficient used in the

calculations represents the depthwise best-fit value computed for the evolution of the nonequilibrium fluid pressure (Figure 3.8; Table 3.5). The porosity used in the calculations is the mean of the initial porosity values computed at each level in a slurry from the magnitude of nonequilibrium fluid pressure following sediment loading (equation 3.21; Table 3.4). Effective stress shown in Figure 3.9 has been normalized by the magnitude of hydrostatic fluid pressure at the base of the slurry. Hence, the values along the curves depicted in Figure 3.9 at any level, at any time, represent the magnitude of the effective stress as some fraction of basal hydrostatic fluid pressure. The effective stress converges to a depth-dependent linear profile when the nonequilibrium fluid pressure has dissipated fully and the solid particles have settled fully (equation 3.24). The linear profile represents simply the difference between a lithostatic total stress and a hydrostatic fluid pressure. With sufficient time, fluid would drain completely from a slurry overlying a permeable bed and the effective stress profile would converge to a lithostatic profile for dry sediment. The theory of consolidation presented here does not account for unsaturated conditions in drained debris-flow deposits.

Effective stress profiles evolve slightly differently over permeable and impermeable beds. Although the stress increase "diffuses" upward in each case, effective stress instantly achieves its maximum value at the base of a slurry overlying a permeable bed that can drain freely because the nonequilibrium fluid pressure instantly dissipates at that boundary (see Figure 3.8). Hence, when a debris-flow slurry overlies a permeable bed, larger magnitude effective stresses exist in the basal part of the slurry sooner than they would if the slurry overlay an impermeable bed.

Volume Strain

Volume strain is likewise accommodated initially at the base of a slurry and the strain front, which results from closure of pore space, migrates upward (Figures 3.10a-d). Computation of the evolution of volume strain within a slurry requires, in addition to estimates of D and ϕ, an estimate of the elastic properties of the porous body, namely a measure of its deformability (see equations 3.8 and 3.25). The values of D and ϕ used in the calculations are the same as those used for the calculations of effective stress. Methods of estimating appropriate elastic moduli are discussed below. Volume strain at any position within a slurry has been normalized by the magnitude of volume strain at the base of the slurry (Figure 3.10). Thus, values along the curves of the evolving strain profile at any level and at any time represent some fraction of the total strain that has occurred at the base

of the sediment column. Similar to the effective stress profiles, volume strain profiles converge on depth-dependent linear profiles when nonequilibrium pressure dissipates fully. This results directly from equation 3.10, which shows that, in one dimension, volume strain of the porous body is directly proportional to effective stress, and that the proportionality constant simply reflects the ability of the porous body to deform elastically (equations 3.8 and 3.10). The fact that strain is accommodated initially, and primarily, in the deeper parts of the sediment column corresponds well with the determination that the diffusion coefficient decreased with depth in the sediment column. However, as pore spaces compress and volume strain increases the material becomes elastically stiffer (and harder to compress), and permeability decreases. From equation 3.18, we might expect that increased elastic stiffness and reduced permeability counteract each other and thereby maintain a constant value of diffusion coefficient. Apparent variation of the diffusion coefficient with depth suggests that magnitude changes in permeability outweigh magnitude changes in elastic stiffness of the debris that occur as a result of closure of pore space. Thus, because it becomes more difficult for fluid to flow through constricted pore spaces the value of the diffusion coefficient decreases. The predicted strain profile is corroborated by the observation that material excavated from the upper part of the sediment column remained soupy and easily liquefied following an experiment, whereas that excavated from the lower part of the column was much more compact and not easily liquefied.

Minimum estimates of the bulk volume strain averaged over the entire sediment column in these experiments range from about 3 to 10 percent; the average bulk volume strain for all experiments was about 5 percent (Table 3.6). These values were determined by measuring the total displacement of the slurry surface over the timespan of the experiment, computing the change in total slurry volume, and normalizing the volume change by the initial volume. These strain values are considered to be minimum estimates of the bulk volume strain owing to the possibility that undetected compaction may have occurred prior to initiation of data collection. However, initial pore-fluid pressures of lithostatic magnitude at all levels in all slurries indicate that little, if any, significant volume change occurred immediately after loading.

Surface Displacement

Estimates of elastic moduli are needed to predict evolution of volume strain and surface displacement in debris-flow slurries (equations 3.25 and 3.28). Because it is difficult to generalize

values of elastic moduli of soils with much accuracy, specific soils must be tested when accurate estimates are needed (Lambe and Whitman, 1969). Even then, values of elastic moduli are highly sensitive to the experimental conditions (such as specimen porosity), especially those of soils that are loose and highly compressible even at low effective stresses. Approximate physical properties of the experimental material discussed in this chapter are summarized in Table 3.7 (see Appendix A). Estimates of various elastic moduli (Young's modulus, E, bulk modulus, K_b, constrained modulus, D_c) for the materials used at the USGS flume were extracted from tests of large-scale soil samples conducted in 6-inch-diameter (15.2-cm-diameter) and 15-inch-diameter (38.1-cm-diameter) triaxial load cells (Appendix A). In each test, the soil specimen was compacted to a density that approximated the densities of the experimental deposits. The tests, by the U.S. Army Corps of Engineers Waterways Experiment Station Soil Division, were conducted under conditions that approximated confined compression, so-called K_0 consolidation (Lambe and Whitman, 1969). Confining stress applied to each cell was increased incrementally, and the axial load was increased to a value that maintained a constant specimen cross section. In principle such tests prevent lateral strains in the specimen. In the extraction of elastic moduli from these test data, I have assumed that there was no lateral displacement of the specimen. Isotropic compression and standard triaxial-load-cell compression tests were conducted on 4-inch-diameter (10.2-cm-diameter) specimens of the Mount St. Helens and Osceola Mudflow debris. In those tests, sediments larger than 10mm were removed from the specimen. Methodologies described in Lambe and Whitman (1969) were used to extract estimates of elastic moduli from the test data, and are discussed in Appendix A.

Consolidating granular slurries are significantly more compressible than estimated from the results of standard soil tests. Good agreement between predicted surface displacement and measured surface displacement of a consolidating debris-flow slurry is achieved only if the effective elastic bulk modulus is approximately 1 to 2 orders-of-magnitude lower than that estimated by standard soil tests (Figure 3.11; Table 3.7; Appendix A). Predicted surface displacements based on values of elastic moduli estimated from soil tests, on values of the depthwise best-fit values of D, and on estimates of the average initial value of ϕ (Table 3.4) substantially underestimate measured displacements (Figure 3.11a-c; Table 3.7). Matching predicted displacement profiles to measured profiles reveals that the effective bulk modulus (see equations 3.8, 3.16, and 3.18) for the loamy mix used at the flume and for the debris from Mount St. Helens is on the order of 10^5 Pa (Figures 3.11a,c). Estimates of the bulk modulus obtained from isotropic compression tests of the Mount St. Helens' debris suggest a

value of 10^6 to10^7 Pa (Table 3.7; Appendix A). The Osceola Mudflow debris also has an apparently low effective bulk modulus, which is about half that of the more granular material (5 x 10^4 Pa)(Figure 3.11b). Estimates of the bulk modulus for the Osceola sediment obtained from isotropic compression tests also are on the order of 10^6 to10^7 Pa. The lower values of the effective bulk modulus were used in calculations to predict the transient response of volume strain (equation 3.25).

EXPERIMENTAL DEBRIS-FLOW DEPOSITS

Diffusion of Nonequilibrium Fluid Pressure

Predicted transient responses of nonequilibrium fluid pressures within the experimental debris-flow deposits at the USGS flume are similar to those for the laboratory experiments (Figures 3.12a-d). However, there are two primary differences. (1) The experimental deposits were as much as an order of magnitude thinner than the quasistatic laboratory slurries and thus the timespans needed for complete dissipation of the nonequilibrium fluid pressure were shorter. As a result, more of the late-stage response of the nonequilibrium fluid pressures was captured in these deposits than in the impermeable-bed laboratory experiments (compare the magnitudes of the normalized nonequilibrium fluid pressures in Figure 3.3 with those in Figure 3.8). (2) The values of the diffusion coefficient for the debris-flow deposits represent the best-fit between predicted fluid pressure profiles and the measured basal nonequilibrium fluid pressure only. Measurements of fluid pressures at higher levels in deposits were not made. As discussed above, values of the diffusion coefficient at the base of a slurry typically are smaller than values estimated at higher levels in deposits, and values estimated at the base of a deposit may not provide the best depthwise fit between predicted and measured values of nonequilibrium fluid pressure in the context of the linear theory. The estimated values for the debris-flow deposits therefore represent minimum values of the best-fit value that characterizes each deposit.

Comparison of predicted fluid-pressure profiles with measured basal nonequilibrium fluid pressure in each experimental deposit illustrates the influence of fine sediment on fluid-pressure diffusion. Deposits composed of sand and gravel (April and June 1994) are characterized by diffusion coefficients that range from 10^{-2} to10^{-4} m^2/s. Those composed of mixtures that included loam (May, July, and August 1994) are characterized by diffusion coefficients on the order of 10^{-6} to10^{-7} m^2/s. The estimated values of basal diffusion coefficient of the loamy debris-flow deposits are comparable

in magnitude to both the near-basal values and depthwise best-fit values estimated from laboratory experiments using the same debris (Table 3.5). The profound differences in magnitude of the diffusion coefficient among the experimental debris-flow deposits composed of sand and gravel (April and June 1994) are probably related to deposit disturbance during the June experiment. In the April experiment, flows traveled unconfined across the runout area and deposited their sediment. In the June experiments, however, flows slammed into a vertical wall located just down slope from the sensing plate. The leading waves of these flows recoiled away from the wall and fell back onto trailing flow emerging from the flume. The deposits left by these flows were greatly disturbed by this vigorous interaction during sediment deposition. As discussed earlier, part of the overburden load of these deposits probably was borne by the vertical wall. The larger magnitude values of the diffusion coefficients for the June deposits, compared to the April deposits, as well as the very rapid dissipation of nonequilibrium fluid pressures in the June deposits (see Figure 3.3), suggests that high-permeability flowpaths may have been established as a result of vigorous flow interaction during deposition. The large-magnitude diffusion coefficients of the June deposits are therefore not considered to be characteristic of the sand and gravel sediment mixtures used to create the experimental debris flows.

Effective Stress and Volume Strain

Predicted transient responses of effective stress and volume strain for the experimental deposits are similar to those for the quasistatic laboratory slurries (Figures 3.13a-c, 3.14a-c). Each set of profiles illustrates upward migration of the field fronts. Again, measurements from the experimental deposits extend the data to a later stage in the transient response of a debris-flow deposit overlying an impermeable base. Although elastic moduli for the sediments used in the flume experiments were estimated from triaxial tests (Table 3.7; Appendix A), I have shown from the laboratory experiments that the effective elastic moduli of sediment slurries are significantly lower than estimated moduli extracted from standard soil tests. Because no reliable measurements were made of surface displacements of the experimental deposits, the apparent effective bulk modulus estimated from laboratory experiments using a mixture of the sand, gravel, and loam flume sediment is used to compute the strain history. I have assumed here that the apparent effective bulk modulus of that loamy sediment is representative of the effective bulk modulus for the coarser-grained mixtures of sand and gravel.

DISCUSSION

Despite the fact that volume strains in the laboratory slurries, and probably also in the experimental deposits, are as large as several percent, the linear, constant-coefficient consolidation model presented here, valid strictly for infinitesimal strain, does a reasonable job of predicting gravity-driven, one-dimensional consolidation in granular sediment slurries. In the details, however, we see that there is divergence between theory and experiment. In many of the laboratory experiments measured nonequilibrium fluid pressures initially dissipated faster than predicted, then in the later stages of consolidation dissipated more slowly than predicted. In one case, divergence between theory and experiment can be explained, in part, by an unexpected partial disruption of grain contacts and rejuvenation of the nonequilibrium fluid pressure (C4 in Figure 3.7a). In that experiment, rejuvenation of fluid pressure caused measured pressures to appear to be to higher than expected during late stages of consolidation; thus, there is an apparent lag between predicted and measured values of fluid pressure. In other laboratory experiments the disparity between predicted and measured fluid pressures arises from applying a constant-coefficient model depthwise across the slurry. Measured fluid pressures indicate that the diffusion coefficient typically varied with depth in the slurry; values typically were larger in the upper parts and lower in the basal parts of slurries. In the single experiment in which the diffusion coefficient was determined to be the same at all measured levels (C5, Table 3.5, Figure 3.8a), the model fits the measured data exceptionally well. For many of the experimental debris-flow deposits, in which the diffusion model is fit to basal nonequilibrium fluid pressures, the model typically underpredicts the rate of pressure dissipation at early times and overpredicts the rate of pressure dissipation at later times (e.g., April 19, April 21, May 26, June 23, July 20, 1994, experiments in Figure 3.12). For the other deposits, the model overpredicts dissipation of fluid pressure at early times, and either matches or underpredicts fluid-pressure dissipation at later times (e.g., June 21, August 31, 1994, experiments in Figure 3.12). These results, and the results that show that the diffusion coefficient varies with depth in a slurry (Table 3.5), show clearly that gravity-driven consolidation is generally nonlinear even in shallow slurries, and that the diffusion coefficient, rather than being constant, is some function of the pressure field.

Insight into the cause of nonlinearity in the consolidation process can be gained from an analysis of the permeability and compressibility of the sediments used in the experiments. Constant-head permeameter tests, in which the head driving fluid flow was kept very low (Appendix B), show

that permeabilities of the wide variety of sediments used in the experiments vary over a relatively narrow range (10^{-9} to 10^{-14} m^2; 1 kilodarcy-10 millidarcy) (Figure 3.15). Test results further show that permeability varies exponentially with porosity for all debris-flow sediments tested (Figure 3.15; Table 3.8). As a result, small changes in porosity can yield large changes in permeability. Changes of as little as a few percent in porosity can result in changes in permeability of 2- to 5-fold or more. Changes in porosity as large 10 percent can cause 10- to 100-fold changes in permeability. Because the value of the diffusion coefficient is a function of both the permeability and the compressibility of the porous body (equation 3.18) variations in porosity within the sediment will affect diffusion and therefore the hydraulics of pore-fluid movement. When fluid pressure approaches lithostatic, effective stress achieves its minimum value (equation 3.7). Under these conditions pore spaces are held open by high fluid pressure and the medium cannot compress. As fluid pressure dissipates through fluid flow, effective stress increases, pore spaces compress, and porosity decreases. A reasonable postulate, then, is that porosity varies with effective stress. As pore spaces close, however, the body becomes elastically stiffer and harder to compress. Increased stiffness of the medium counteracts reduced permeability caused by pore closure, and works to maintain a constant value for the diffusion coefficient. The measured variation of diffusion coefficient with depth in the laboratory slurries indicates that reduced permeability resulting from pore closure outweighs increased stiffness of the slurry that results from pore closure, and therefore has a greater influence on the value of the diffusion coefficient. If porosity is postulated to vary with effective stress as (e.g., Been and Sills, 1981; R.M. Iverson, personal communication, 1995)

$$\phi = \phi_* - \kappa \ln \left| \frac{\sigma_e}{\sigma_*} \right| \tag{3.29}$$

where σ_* is a reference stress at which $\phi = \phi_*$, and if permeability assumes the form (Figure 3.15; Table 3.8)

$$k = k_0 e^{a\phi} \tag{3.31}$$

where k_0 is a reference value of permeability at a mythical state of zero porosity, it can be shown that the diffusivity coefficient assumes a form (R.M. Iverson, personal communication, 1995)

$$D = \frac{k_0 e^{a\phi_*}}{\mu\kappa} \sigma_e^{1-a\kappa} \sigma_*^{a\kappa} . \tag{3.31}$$

When $a\kappa > 1$, material is highly compressible and D decreases as effective stress increases. From the data presented in Table 3.8, $a \approx 20$. As long as $\kappa > 0.05$, $D \sim 1/\sigma_e$. Limited data for mud suspensions suggest $\kappa > 0.05$ (Been and Sills, 1981), and triaxial compression tests on a variety of moderately compacted debris-flow sediments at low effective stresses suggest $\kappa \approx 0.05$ (Appendix A). Qualitatively a nonlinear model of this form is consistent with observed behavior. Effective stresses were shown to diffuse from the base of the slurries upward as nonequilibrium fluid pressure dissipated, and diffusivity values were shown to vary with depth in a slurry (Table 3.5). In both the constant-coefficient and nonlinear models the highly compressible nature of dilated debris promotes the low diffusivity values common to consolidating, freshly deposited debris-flow sediments.

The laboratory experiments demonstrate that a permeable substrate influences the gravity-driven response of nonequilibrium fluid pressure. However, the experiments also demonstrate that, when the length-scale effect is removed from the analysis, a permeable substrate does not significantly alter the nondimensional time necessary for nonequilibrium fluid pressure to dissipate fully (for example, compare experiment C10 in Figure 3.8b and June 23, 1994, deposit in Figure 3.12b). The magnitude of the permeability of the substrate material has no effect on the transient response of nonequilibrium fluid pressure when the permeability of the substrate is an order of magnitude or more greater than the permeability of the overlying slurry (Figure 3.8b). A freely draining substrate permits a more rapid transient response of nonequilibrium fluid pressure than does an impermeable bed by providing an additional pathway for fluid to drain. Fluid at the base of the slurry is driven into the substrate by the large gravity-induced pressure gradient, but the rate at which fluid escapes is controlled by properties of the sediment slurry, not the substrate. As fluid is driven out of the lower part of the slurry, pore-fluid pressure drops and the weight of the overburden causes pore spaces to constrict, reducing the permeability of the slurry and hindering the escape of fluid downward through the slurry. Even though collapse of pore space makes the slurry more resistant to compression, this

increase in stiffness is apparently overwhelmed by a reduced permeability that produces a "self-sealing" at the base of the slurry, which diminishes the ability of fluid to escape through the base. As a result, nonequilibrium fluid pressures slightly above the base of the slurry do not dissipate as rapidly as predicted by the linear consolidation theory, even in the presence of a high pressure gradient. The measured depth-dependent variation of dissipation of nonequilibrium fluid pressure agrees qualitatively with anticipated behavior predicted by the postulated nonlinear model. Both the experimental debris-flow deposits (impermeable boundary) and the permeable-bed laboratory experiments required nondimensional times of order 2 for nonequilibrium fluid pressures to dissipate fully. Thus, when scaling effects are removed, the fundamental process of gravity-driven consolidation of granular slurries and the attendant diffusion of nonequilibrium fluid pressure are similar for both impermeable and freely draining substrates, a conclusion verified by the similarity in the depthwise best-fit values of diffusion coefficients between the impermeable- and permeable-bed experiments.

Strain accommodation in gravity-driven consolidating granular slurries is independent of basal boundary condition or sediment composition. Figures 3.10a-d and 3.14a-c show that volume strain during consolidation is accommodated initially, and primarily, at the base of the sediment column. These figures also show that the strain front migrates upward through the column as the nonequilibrium fluid pressure dissipates and the effective stress increases. Figures 3.16a and 3.16b show that evolving strain profiles across the sediment column are similar regardless of sediment composition or basal boundary condition. In deposits having different sediment compositions but an impermeable bed, strain profiles at similar nondimensional times are essentially identical (Figure 3.16a); profiles at similar nondimensional times overlap. Strain profiles in experimental slurries having the same sediment composition but different boundary conditions evolve in a similar fashion, but profiles in deposits overlying permeable beds evolve more rapidly (Figure 3.16b). Thus, in gravity-driven consolidation, most of the pore-space closure that accounts for the volume strain takes place near the base of the sediment column, where effective stresses are greatest, and the amount of pore-space closure gradually diminishes upwards. This pattern of pore-space closure is consistent with, and explains, the observation that the upper parts of both the laboratory slurries and the experimental debris-flow deposits remained soupy and easily liquefied late in the consolidation process whereas the lower parts of the sediment stratum generally were compact. These results indicate that the average porosity of a debris-flow deposit estimated by excavation methods of near-surface

sediment may not reflect the average porosity of the entire sediment column, but instead may reflect an initial porosity of the upper part of the deposit at the time of deposition.

Pore fluid that drained from the experimental deposits at the USGS flume consisted of both water and sediment, whereas fluid squeezed from pores in the quasistatic laboratory slurries appeared to be essentially clear water. The difference in pore-fluid composition between the experimental deposits and the laboratory slurries may be related to at least two factors: the rate of fluid escape and the direction in which fluid could flow. Fluid could flow laterally as well as vertically from the experimental deposits. Thus sediment transported by the pore fluid did not have to be lifted vertically but could be transported laterally. Transport direction probably was important for sediments transported by fluid that slowly seeped from the finer grained experimental deposits. In the laboratory experiments, fluid could flow in a vertical direction only, and the character of fluid that escaped through only the top of each slurry was noted. Sediment transported by upwardly migrating fluid may have had an opportunity to settle into pores before reaching the upper surface of the slurry as well as an opportunity to settle on the surface. Fluid from the experimental deposits composed of sand and gravel escaped rapidly as soon as the flow slowed and deposited sediment. The relatively high fluid velocity and the ability of the fluid to flow laterally may have affected its ability to transport sediment. Mixtures composed solely of sand and gravel were not studied in the laboratory, because particles settled too rapidly between the time slurries were mixed and then poured into the tank. Sediment concentrations in the pore fluid from the more granular debris-flow deposits were less than three percent by volume, and the sediment was composed dominantly of silt and clay. Ratios of silt to clay were 1.5:1 or less. Fluids that drained from finer grained deposits were more turbid, having sediment concentrations that were perhaps as large as 16 percent by volume. The sediment in these pore fluids consisted of fine sand in addition to silt and clay.

The generally dilute sediment concentrations do not greatly affect the viscosity of the pore fluid. For dilute suspensions that contain no more than 10 volume percent of dispersed chemically inert spherical particles, fluid viscosity is related to a simple function of particle concentration by (Einstein, 1906; see Barnes and others, 1989)

$$\eta = \eta_0(1 + 2.5C) \tag{3.32}$$

where η is the viscosity of the suspension, η_0 is the viscosity of the suspending medium, and C is the volume concentration of solid particles. For suspensions of spherical particles having diverse sediment concentrations an extension of Einstein's formulation (Thomas, 1965; Poletto and Joseph, 1995) appears to predict viscosity relatively well. This expression has the form

$$\eta = \eta_0 (1 + 2.5C + 10.05C^2 + 0.00273e^{16.6C}) . \tag{3.33}$$

If this relation holds for the relatively dilute pore fluids in debris-flow deposits, then viscosity of the pore fluid in the experimental debris flows was changed by less than 70 percent over that of clear water. This conclusion probably holds true for most natural debris flows. For those rare natural flows containing vast amounts of clay (tens of percent), or containing clay types that are highly reactive to water (such as montmorillonite), pore-fluid viscosity may increase by an order of magnitude or more beyond that of clear water.

The behavior of fluid pressure, effective stress, and volume strain predicted by the gravity-driven consolidation model has geomorphic significance regarding the nature of sediment deposition by debris flows and the character of the deposits following emplacement. Once particles begin to settle, consolidation proceeds upward from the bottom of the sediment column. As a result, effective stress increases, and strain is accommodated, initially at the base of the column, and these fields diffuse upward through the sediment. Because effective stress initially increases at the bottom of the sediment mass, this is the location where frictional forces resisting flow will first exceed forces driving flow. Thus, if consolidation of a debris flow occurs during flow deceleration, then a depositional front should migrate upward from the base of the flow. Vallance (1994) noted just such depositional mechanics in experiments using dry glass beads flowing down a chute. Such a style of deposition is contrary to that predicted by the popular Bingham model for debris flows. In that model, deposition occurs when stresses driving flow fall below the value of the intrinsic plastic yield strength of the debris, and a rigid block of debris having some critical thickness comes to a halt.

Analysis of one-dimensional, gravity-induced consolidation also yields insight into the lack of stratigraphic preservation of surges in vertical sections within debris-flow deposits. A simple comparison can be made between hypothetical surge periods and the characteristic time scale over which nonequilibrium fluid pressures should dissipate. The latter characteristic time scale is defined as L^2/D, where L is a characteristic length scale over which fluid must migrate and D is the depthwise best-fit value of the diffusion coefficient. For deposits overlying an impermeable bed, L is the thickness of the deposit, H. For deposits overlying a permeable bed, the longest path that fluid must migrate is one-half the deposit thickness, so that $L = H/2$. If the ratio of surge period to characteristic dissipation time, t_*, is large then nonequilibrium fluid pressures diffuse at time scales that are shorter than surge periods. If the ratio of these two time scales is small ($\ll 1$) then the period between surges is shorter than the time needed to dissipate nonequilibrium fluid pressures within deposits. Thus, when $t_* \gg 1$, deposits are relatively stable and not easily remobilized by successive surges, whereas when $t_* \ll 1$, deposits are unstable and potentially are easily remobilized by successive surges. Table 3.9 shows values of t_* for hypothetical surge periods of 0.01 hours (36 seconds) and 10 hours. In virtually all cases, the deposits are unstable with respect to the shorter surge period; and only a few are stable with respect to the longer surge period. Because surge periods of many natural debris flows are on the order of seconds to several minutes (e.g., Costa and Williams, 1984; Zhang, 1993), most natural debris-flow deposits probably are unstable during the lifetime of a single debris flow, and many are probably unstable during the emplacement of multiple debris flows that may occur within hours or days. As a result, it is very probable that at least part of the upper stratum of a debris-flow deposit is remobilized by succeeding surges, thus obliterating any stratigraphic distinction between surges within the interior texture of a deposit. Even if nonequilibrium fluid pressures have dissipated fully, the analysis shows that the upper part of the sediment stratum has undergone little compaction, and therefore might still be disturbed. Observations of debris-flow deposits and laboratory slurries show that the upper parts of debris-flow strata can remain saturated and soupy even after nonequilibrium fluid pressures have dissipated. Therefore, loading of saturated deposits by subsequent debris flows may regenerate nonequilibrium fluid pressures in the sediment through a conventional (surface loading) consolidation process. From the observations and analysis presented here, a likely speculation is that until pore fluid has drained fully from the upper section of a debris-flow deposit, subsequent flows may remobilize sediment even after original nonequilibrium fluid pressures have dissipated fully.

The results obtained above are valid strictly for one-dimensional consolidation. Debris flows and their deposits, however, have finite width and length as well as depth. An obvious concern, therefore, is the effect of multidimensional drainage on the evolution of nonequilibrium-fluid-pressure and effective-stress fields. The results presented in this chapter further show that addition of even a small amount of fine-grained debris greatly affects diffusion and increases the time scale over which nonequilibrium fluid pressure diffuses (e.g., compare April 1994 experiments with August 1994 experiment in Figure 3.3). Yet, the experimental debris flows composed of the finer grained mixtures did not travel any farther than those composed of the more granular mixtures. This observation suggests that simple one-dimensional diffusion of nonequilibrium fluid pressure in the sediment mass is not the only factor affecting sediment deposition by debris flows. These matters are the focus of Chapter 4.

CONCLUSIONS

Pore-fluid pressure and total normal stress measured at the base of large-scale experimental debris flows show that nonuniform, near-lithostatic to lithostatic fluid pressures exist during debris-flow deceleration and deposition. Hence, pore-fluid pressures are capable of balancing a substantial proportion of the weight of overlying debris at the time that sediment is deposited. These experimental data refute the hypothesis that uniform bodywide dissipation of nonequilibrium fluid pressure controls debris-flow mobility and deposition. The experimental data also show that the times needed to dissipate nonequilibrium fluid pressures in debris-flow deposits vary widely, resulting primarily from variations in sediment composition rather than from variations in deposit thickness. Addition of even a small amount (1 to 2 percent) of mud ($\leq 63\mu$m in diameter) can alter the pressure dissipation time by several orders of magnitude.

The pore fluid in the experimental debris flows, and presumably in natural granular debris flows as well, was composed of a dilute suspension of water, silt, and clay. Volume concentrations of sediment were as large as 16 percent, but typically were less than 10 percent. Because the pore-fluid suspension was relatively dilute, its viscosity exceeded that of clear water by no more than about 70 percent and probably by much less. Thus, observed variations in pore-fluid hydraulics were affected negligibly by fluid viscosity. If pore-fluid suspensions contain substantial amounts of clay,

or contain highly reactive clays, viscosity may greatly exceed that of clear water and may affect pore-fluid hydraulics.

This chapter presents an analysis of the consolidation of granular slurries subject to self-weight loading. The linear, one-dimensional model assumes that both the solid and fluid constituents of the slurry are incompressible, and that total stresses in the slurry are constant over time. Despite volume strains in laboratory experiments as large as several percent, and results that suggest that the process is inherently, and perhaps strongly, nonlinear, the simple, linear model closely approximates the consolidation process. The most fundamental difference between this model and a conventional consolidation model that neglects body forces is that submerged particle weight, rather than an external surface load, drives the generation of nonequilibrium fluid pressures that dissipate through Darcian flow. When slurry deposition is rapid, as is common with debris flows, gravity loading is assumed to be rapid relative to the time needed for pore fluid to begin diffusing. For this instantaneously undrained state, inclusion of the gravitational body force yields an initial nonequilibrium-fluid-pressure profile that is a linear function of depth rather than a uniform constant. The consequence of this initial condition is that changes in nonequilibrium fluid pressure, effective stress, and volume strain migrate upward from the base of the slurry rather than downward from the surface. This result is robust and holds regardless of the basal boundary condition. When the basal boundary is allowed to drain freely the magnitude of the permeability of the substrate has no effect on the consolidation process; dissipation of nonequilibrium fluid pressure is governed by the ability of fluid to escape the sediment slurry and not by its ability to flow into a more permeable substrate.

The experiments conducted in this study provide estimates of physical properties of a wide range of debris-flow sediments. Comparison of predicted and measured nonequilibrium fluid pressures in quasistatically consolidating laboratory slurries and in experimental debris-flow deposits indicates that diffusion coefficients for a wide range of debris are similar, about 10^{-6} to 10^{-7} m^2/s. Comparison of predicted surface displacements of consolidating slurries with measured surface displacements suggest that the effective bulk modulus of consolidating slurries is about 10^5 Pa, about one to two orders of magnitude lower than estimates extracted from standard tests in triaxial load cells. Hence, debris flows, and fresh debris-flow deposits, are highly compressible, which accounts for the extremely low values of the diffusion coefficient.

Stabilization of debris-flow deposits proceeds upward from the base. If later flows, or flow surges, invade deposited sediment before effective stresses of sufficient magnitude have migrated to the surface, the upper parts of debris-flow deposits will be remobilized, and stratigraphic distinction of those later surges may be muted or obliterated within deposits. If debris flows and their deposits are characterized as Bingham fluids, surge waves cannot remobilize only the upper parts of deposits. Instead, the full thickness of the deposit would have to be remobilized owing to the plastic yield strength of the debris.

Table 3.1. Grain-size characteristics of sediments used in large-scale debris-flow experiments at USGS flume

Sample	Median grain diameter (mm)	Mean grain diameter (mm)	Sorting coefficient (phi units)	Skewness coefficient (phi units)	Weight % gravel	Weight % sand	Weight % silt	Weight % clay	Ratio sand:silt:clay
4-7-93[1]	4.23	2.93	2.34	0.31	60.6	38.0	1.4[2]	-	96.4:3.6[3]
	7.36	3.68	2.39	0.53	63.3	35.6	1.1[2]	-	97:3[3]
4-8-93[1]	3.86	2.65	2.35	0.33	57.6	40.6	1.8[2]	-	95.8:4.2[3]
	5.28	3.23	2.31	0.41	64.6	33.8	1.6[2]	-	95.5:4.5[3]
	5.21	3.14	2.33	0.42	62.8	35.6	1.6[2]	-	95.7:4.3[3]
5-26-94	0.41	0.50	1.50	-0.34	13.5	84.4	1.9	0.2	97.6:2.2:0.2
	0.34	0.41	1.82	-0.30	12.8	83.3	3.6	0.3	95.5:4.1:0.3
	0.42	0.56	2.11	-0.31	19.6	76.1	3.9	0.4	94.7:4.9:0.5
	0.44	0.57	2.02	-0.28	19.2	76.7	3.7	0.4	94.9:4.6:0.5
7-20-94	1.10	1.20	1.91	-0.07	37.0	60.9	1.9	0.2	96.7:3:0.3
	1.20	1.29	1.96	-0.04	39.1	58.7	2.0	0.2	96.4:3.3:0.3
8-31-94	2.31	2.51	2.61	-0.01	51.8	46.6	1.5	0.1	96.7:3.1:0.2
	8.13	4.28	2.49	0.49	61.8	36.8	1.2	0.2	96.3:3.1:0.5
	3.12	2.72	2.69	0.14	54.2	43.8	1.8	0.2	95.6:3.9:0.5
	1.63	2.03	2.83	-0.06	48.0	49.9	1.9	0.2	96:3.6:0.4

Table 3.1 (continued)

[1] Pore-fluid pressures were not measured in these experiments. However, the sand and gravel mixtures used as source sediment in these experiments were similar to those used in the April and June, 1994, experiments in which pore-fluid pressures were measured.

[2] Weight percent of silt and clay combined.

[3] Ratio of sand:silt+clay.

Table 3.2. Characteristics of fluid that drained from experimental debris-flow deposits

Date	Concentration (mg/L)	Sediment weight (g)[1]	Sediment volume (cm^3)[1]	% solids by weight	% solids by volume	Coarsest size (mm)	% finer than 63μm	Mean size (mm)	Weight % sand	Weight % silt	Weight % clay
4-19-94	53,000	53	20.4	5.1	2	0.031	100	0.001	0	55.1	44.9
4-21-94	64,500	64.5	24.8	6.2	2.5	0.5	99.7	0.001	0.3	58.7	41.0
5-26-94[2]						2.0	3.0	1.18	71.3	2.7	0.3
6-21-94[3]	247,000	247	95	21.4	9.5	0.125	94.2	0.002	5.8	64.0	30.2
7-20-94	166,000	166	63.9	15.1	6.4	2.0	94.6	0.002	4.7	58.0	36.6
8-31-94[4]	428,000	428	164.6	33.9	16.5	1.0	68.2	0.006	31.8	49.2	19.0
4-26-95	104,000	104	40	9.8	4	0.063	99	--	0	--	--

[1] Per liter of fluid.
[2] Dried sample scraped from concrete surface.
[3] Sample container leaked a small, but unknown quantity of water prior to analysis.
[4] Sample collected using various suction devices to remove fluid from concrete surface.

Table 3.3. Grain-size characteristics of debris used in consolidation experiments

[5-26-94: May 26, 1994, flume debris; MSH NFT: Mount St. Helens debris flow sediment; Osceola: Osceloa Mudflow sediment]

Sample	Median grain diameter (mm)	Mean grain diameter (mm)	Sorting coefficient (phi units)	Skewness coefficient (phi units)	Weight % gravel	Weight % sand	Weight % silt	Weight % clay	Ratio sand:silt:clay
5-26-94 S1	0.41	0.50	1.50	-0.34	13.5	84.4	1.9	0.2	97.6:2.2:0.2
5-26-94 S2	0.34	0.41	1.82	-0.30	12.8	83.3	3.6	0.3	95.5:4.1:0.3
5-26-94 S3	0.42	0.56	2.11	-0.31	19.6	76.1	3.9	0.4	94.7:4.9:0.5
5-26-94 S4	0.44	0.57	2.02	-0.28	19.2	76.7	3.7	0.4	94.9:4.6:0.5
MSH NFT	0.52	0.51	3.76	0.06	29.6	50.3	18.3	1.8	71.4:26:2.6
Osceola	0.05	0.03	7.34	0.11	31.4	15.9	35.5	17.2	23.2:51.7:25.1

Median grain diameter (M_d) calculated from Inman (1952).
Mean grain diameter (M_z), sorting coefficient (σ_i), and skewness coefficient (Sk_i) calculated from Folk (1984).

Table 3.4. Initial fluid pressure and estimated initial porosity in experimental debris-flow deposits and laboratory debris-flow slurries

[ϕ, porosity; 1-ϕ, solids fraction; p, total fluid pressure; p_*, excess fluid pressure]

Experiment[§]	Domain level z (m)	p (Pa)	p_* (Pa)	Depth (m)	1-ϕ[†]	Initial porosity ϕ	p_*/p_h	Mean surface ϕ[‡]	Volume % solids
4-19-94	0	2350	1175	0.120	0.61	0.39	1.0	0.27-0.29	
4-21-94	0	2550	1325	0.125	0.65	0.35	1.08	0.29	
5-26-94	0	1760	950	0.083	0.71	0.29	1.17	0.33-0.38	67.3
6-21-94	0	4410	295	0.420	--	--	0.07	0.36	
6-23-94	0	7150	3920	0.330	0.74	0.26	1.21	0.28	
7-20-94	0	1570	880	0.070	0.78	0.22	1.29	0.36-0.38	
8-31-94	0	2550	1430	0.115	0.78	0.22	1.28	0.30	66.6
C4	.690	4700	2350	0.240	0.61	0.39	1.0		67.5
flume debris	.535	8040	4165	0.395	0.65	0.35	1.08		
	.365	11760	6225	0.565	0.68	0.32	1.12		
C5	.680	4310	2300	0.205	0.69	0.31	1.15		66.5
flume debris	.565	6615	3480	0.320	0.67	0.33	1.11		
	.390	10290	5440	0.495	0.68	0.32	1.12		
C6	.428	4115	2300	0.185	0.77	0.23	1.27		64.5
flume debris	.198	8625	4560	0.415	0.68	0.32	1.12		
	.028	11960	6225	0.585	0.66	0.34	1.09		
C7	.494	1960	1030	0.095	0.67	0.33	1.11		66.5
flume debris	.229	7640	4115	0.360	0.71	0.29	1.17		
	.009	11960	6270	0.580	0.67	0.33	1.10		
C8	.446	2840	1520	0.135	0.70	0.30	1.15		70.0
flume debris	.246	7050	3775	0.335	0.70	0.30	1.15		
	.001	11760	6075	0.580	0.65	0.35	1.07		
C9	.495	2350	1175	0.120	0.61	0.39	1.0		67.8
flume debris	.291	6740	3590	0.324	0.68	0.32	1.13		
	.007	12940	6980	0.608	0.71	0.29	1.17		
C10	.448	2250	1125	0.115	0.61	0.39	1.0		68.5
flume debris	.216	7350	3950	0.347	0.70	0.30	1.16		
	.003	11560	6075	0.560	0.67	0.33	1.11		

C11	.489	3040	1365	0.171	0.49	0.51	0.81	51.7
OSC	.251	7400	3390	0.409	0.51	0.49	0.85	
	.016	11560	5250	0.644	0.50	0.50	0.83	
C12	.896	470	295	0.018	--	--	1.67	57.8
OSC	.704	3800	1745	0.210	0.51	0.49	0.85	
	.401	4900	4870	0.513	0.59	0.41	0.97	
C13	.736	4200	2045	0.220	0.57	0.43	0.95	57.9
OSC	.596	7100	3575	0.360	0.61	0.39	1.01	
	.436	10125	5030	0.520	0.60	0.40	0.99	
	.056	17250	8430	0.900	0.58	0.42	0.96	
C14	.281	7645	3845	0.388	0.61	0.39	1.01	71.3
MSH	.192	10000	5325	0.477	0.69	0.31	1.14	
	.124	11470	6130	0.545	0.70	0.30	1.15	
	.001	12940	6395	0.668	0.59	0.41	0.98	
C15	.576	1695	588	0.113	0.32	0.26	0.53	61.1
OSC	.370	6225	3100	0.319	0.60	0.40	0.99	
	.193	9600	4740	0.496	0.59	0.41	0.98	
	.066	11960	5850	0.623	0.58	0.42	0.96	
C16	.877	3725	2030	0.173	0.73	0.27	1.20	68.1
MSH	.678	7250	3600	0.372	0.60	0.40	0.99	
	.403	13230	6890	0.647	0.66	0.34	1.09	
	.083	20290	10810	0.967	0.69	0.31	1.14	
C17	.803	3730	1930	0.183	0.65	0.35	1.08	61.5
MSH	.603	7550	3800	0.383	0.61	0.39	1.01	
	.428	11660	6190	0.558	0.69	0.31	1.13	
	.103	18720	10070	0.883	0.71	0.29	1.16	
C18	.564	2550	1250	0.128	0.63	0.37	1.03	68.7
MSH	.387	6470	2990	0.305	0.71	0.29	1.16	
	.176	10975	5920	0.516	0.71	0.29	1.17	
	.006	14600	7880	0.686	0.71	0.29	1.17	

§ Flume debris is mixture of sand, gravel, and loam; OSC is Osceola Mudflow; MSH is Mount St. Helens debris (see Table 3.3).

† Assumes that $\gamma_s - \gamma_f = 16170$ N/m^3.

‡ Unpublished data from R.M Iverson.

Table 3.5. Values of best-fit diffusion coefficient

Experiment*	Basal boundary	Slurry depth H (m)	Domain level z (m)	D (m^2/s)	Global best fit D (m^2/s)	C_v‡ (m^2/s)
C4	I†	0.930	0.690	3.0×10^{-6}	1.6×10^{-6}	
flume debris			0.535	1.6×10^{-6}		
			0.365	1.3×10^{-6}		
C5	I	0.885	0.680	1.3×10^{-6}	1.3×10^{-6}	
flume debris			0.565	1.3×10^{-6}		
			0.390	1.3×10^{-6}		
C6	F§	0.613	0.428	9.0×10^{-7}	1.3×10^{-6}	
flume debris			0.198	1.3×10^{-6}		
			0.028	9.0×10^{-7}		
C7	F	0.589	0.494	5.0×10^{-6}	1.4×10^{-6}	
flume debris			0.229	1.4×10^{-6}		
			0.009	3.1×10^{-7}		
C8	F	0.581	0.446	4.3×10^{-6}	1.2×10^{-6}	
flume debris			0.246	1.2×10^{-6}		
			0.001	9.5×10^{-9}		
C9	F	0.615	0.495	4.6×10^{-6}	2.3×10^{-6}	
flume debris			0.291	2.3×10^{-6}		
			0.007	1.6×10^{-6}		
C10	F	0.563	0.448	3.4×10^{-6}	2.8×10^{-6}	1.4×10^{-6}
flume debris			0.216	2.8×10^{-6}		
			0.003	4.6×10^{-8}		
C11	F	0.660	0.489	4.2×10^{-6}	1.5×10^{-6}	1.2×10^{-6}
OSC			0.251	1.5×10^{-6}		
			0.016	1.2×10^{-7}		
C12	I	0.914	0.896	1.5×10^{-5}	3.3×10^{-7}	8.6×10^{-7}
OSC			0.704	6.5×10^{-6}		
			0.401	3.3×10^{-7}		

Table 3.5 (continued)

C13	I	0.956	0.736	6.2×10^{-7}	4.9×10^{-7}	5.4×10^{-7}
OSC			0.596	5.8×10^{-7}		
			0.436	4.0×10^{-7}		
			0.056	4.1×10^{-7}		
C14	F	0.669	0.281	1.3×10^{-6}	4.8×10^{-7}	1.6×10^{-6}
MSH			0.192	5.3×10^{-7}		
			0.124	4.8×10^{-7}		
			0.001	1.3×10^{-7}		
C15	F	0.689	0.576	6.0×10^{-6}	4.0×10^{-7}	5.4×10^{-7}
OSC			0.370	3.8×10^{-7}		
			0.193	4.3×10^{-7}		
			0.066	1.4×10^{-7}		
C16	I	1.050	0.877	2.5×10^{-6}	1.0×10^{-6}	8.6×10^{-6}
MSH			0.678	2.5×10^{-6}		
			0.403	1.2×10^{-6}		
			0.083	9.0×10^{-7}		
C17	I	0.986	0.803	7.0×10^{-6}	1.9×10^{-6}	2.5×10^{-6}
MSH			0.603	2.3×10^{-6}		
			0.428	1.6×10^{-6}		
			0.103	1.2×10^{-6}		
C18	F	0.692	0.564	5.2×10^{-5}	5.5×10^{-6}	2.6×10^{-6}
MSH			0.387	1.0×10^{-5}		
			0.176	3.3×10^{-6}		
			0.006	1.5×10^{-7}		

* Flume debris is a mixture of sand, gravel and loam; OSC is Osceola Mudflow; MSH is Mount St. Helens debris (see Table 3.3).

† Impermeable basal boundary.

§ Freely draining basal boundary.

‡ Consolidation coefficient determined by $(t)^{1/2}$ method (ASTM, 1995).

Table 3.6 Bulk volume strain for one-dimensional consolidation experiments

Experiment	Initial thickness h_i (m)	Initial volume V (m^3)	Final thickness h_f (m)	Δh (m)	ΔV (m^3)	Volume strain $\Delta V/V$ [1]
C4	0.93	0.047	0.89	0.04	0.002	0.043
C5	0.885	0.045	0.84	0.045	0.002	0.051
C6	0.613	0.031	0.575	0.038	0.002	0.062
C7	0.589	0.030	0.559	0.03	0.002	0.051
C8	0.581	0.029	0.547	0.034	0.002	0.059
C9	0.615	0.031	0.585	0.03	0.002	0.049
C10	0.563	0.029	0.537	0.026	0.001	0.046
C11	0.66	0.033	0.594	0.066	0.003	0.10
C12	0.914	0.046	0.874	0.04	0.002	0.044
C13	0.956	0.048	0.888	0.068	0.003	0.072
C14	0.669	0.034	0.640	0.029	0.001	0.043
C15	0.689	0.035	0.637	0.052	0.003	0.075
C16	1.050	0.053	0.999	0.051	0.003	0.049
C17	0.986	0.050	0.948	0.038	0.002	0.039
C18	0.692	0.035	0.670	0.022	0.001	0.032

[1] Values represent minimum bulk volume strain.

Table 3.7. Physical properties of experimental material

[Data for flume debris are based on sediments ≤32mm in diameter tested in 6-inch and 15-inch diameter triaxial cells. Data for Mount St. Helens debris and Osceoloa Mudflow sediment are based on material ≤10mm in diameter that were tested in a 4-inch diameter triaxial cell. -- means no reliable data]

Property	Flume debris		MSH NFT	Osceola
	sand/gravel mix	loam mix [a]		
Grain properties [b]				
median diameter	3.86-7.36 mm	0.34-0.44 mm	0.52 mm	0.05 mm
mean diameter	2.65-3.68 mm	0.41-0.57 mm	0.51 mm	0.03 mm
Bulk material properties				
Folk sorting coefficient	2.31ϕ-2.39ϕ	1.50ϕ-2.11ϕ	3.76ϕ	7.34ϕ
porosity	0.26-0.39 [c] 0.27-0.29	0.29 [d] 0.33-0.38 0.33	0.33 [c]	0.44 [c]
permeability, k [f]	1.96×10^{-12} (0.26) 4.88×10^{-10} (0.37)	3.72×10^{-12} (0.34) 3.97×10^{-11} (0.41)	2.45×10^{-13} (0.35) 3.16×10^{-11} (0.50)	1.06×10^{-12} (0.48) 1.61×10^{-11} (0.60)
friction angle, ϕ_i [g]	39°, 35°	37°, 33°	33° c = 4 kPa	29° c = 9 kPa
Compression index [h]	0.053 0.050	0.087 --	0.10-0.11	0.10-0.70
Young's modulus, E [h,i] (secant modulus)	3×10^{8} Pa 4.6×10^{7} Pa	3.5×10^{8} Pa --	4×10^{6}-3×10^{7} Pa	2×10^{6}-2×10^{8} Pa
Constrained modulus, D_c [h,j]	5×10^{6} Pa 6×10^{6}-7×10^{6} Pa	3×10^{6} Pa --	1×10^{6}-3×10^{6} Pa	2×10^{5}-2×10^{6} Pa
Bulk modulus, K_b [l]	--	1×10^{5} Pa	1×10^{5} Pa 6×10^{6}-3×10^{7} Pa [m]	5×10^{4} Pa 3×10^{6}-2×10^{7} Pa [m]
Pore fluid properties				
viscosity, μ	10^{-3} Pa-s	10^{-3} Pa-s	10^{-3} Pa-s	10^{-3} Pa-s

Table 3.7 (continued)

[a] Material from May 26, 1994, flume experiment.

[b] See Tables 3.1 and 3.3.

[c] Top numbers refer to initial porosities computed from initial fluid pressures in flume deposits; bottom numbers refer to mean surface porosity of deposit (R.M. Iverson, unpublished data).

[d] Top number refers to initial porosity computed from initial fluid pressure in flume deposit; middle numbers refer to surface porosity of deposit (R.M. Iverson, unpublished data); bottom number refers to mean initial porosity computed from initial fluid pressures in laboratory experiments.

[e] Mean value of initial porosity computed from initial fluid pressures in laboratory experiments.

[f] Minimum and maximum values of permeability obtained from constant-head permeameter tests. Minimum value obtained for densely packed material; maximum value obtained for loosely packed material. Values in parentheses are porosities of material to which the permeability values correspond. See Appendix B and figure 3.15.

[g] For flume debris, first number refers to test in 6-inch-diameter triaxial cell; second number refers to test in 15-inch-diameter triaxial cell.

[h] For flume debris, top numbers refer to test in 6-inch-diameter triaxial cell; bottom numbers refer to test in 15-inch-diameter triaxial cell (see Appendix A).

[i] For sand/gravel and loam mixtures, values were determined from triaxial compression tests following K_o consolidation to a confining stress equal to 55 kPa. The secant modulus was determined from zero deviator stress to a value equal to one-half the peak deviator stress (see Appendix A).

[j] Values of constrained modulus were derived from estimates of compression index (see Appendix A).

[l] Value that provides best fit to measured surface displacement in laboratory experiments.

[m] Based on response of material during the first 10 seconds following a change in isotropic compressive stress.

Table 3.8. Relation between permeability and porosity

[Regresion expression has the form $k = k_0 e^{a\phi}$. Regression is based on values of permeability and porosity determined by compaction permeameter tests (Appendix B; see Figure 3.15)]

Material	k_0	a	no. points	r^2
Flume debris				
Sand and gravel	3.5×10^{-17}	42.3	6	0.81
Loam†	1.6×10^{-14}	18.2	9	0.34
	3.6×10^{-15}	21.7	8	0.83
Mount St. Helens†	7.2×10^{-16}	20.0	8	0.39
	1.4×10^{-17}	28.6	7	0.95
Osceola Mudflow	8.7×10^{-17}	19.8	7	0.69

† Top values include all data points. Bottom values exclude outlier data points.

Table 3.9. Comparison of hypothetical surge periods (36 seconds and 10 hours) to characteristic times of excess fluid pressure diffusion

[Experiments listed by date, e.g., 4-19-94, are large-scale debris-flow deposits; others are laboratory tests. See tables 3.1 and 3.3 for characteristics of sediment used in these experiments. H is deposit thickness; D is coefficient of diffusivity; t_* is dimensionless time ratio; see text for definition]

Experiment	Best fit D (m^2/s)	H (m)	H^2/D (s)	t_*		Deposit stability
				0.01 hours	10 hours	
4-19-94	2.5×10^{-4}	0.120	58	0.62	620	semi-stable
4-21-94	1.0×10^{-4}	0.125	156	0.23	230	semi-stable
5-26-94	8.0×10^{-7}	0.083	8611	4.2×10^{-3}	4.2	semi stable
6-21-94	4.0×10^{-2}	0.42	4	9	9000	stable
6-23-94	2.0×10^{-3}	0.33	54	0.67	667	semi-stable
7-20-94	8.5×10^{-7}	0.07	5765	6.2×10^{-3}	6.2	semi-stable
8-31-94	1.5×10^{-7}	0.115	86640	4.2×10^{-4}	0.40	unstable
C4 [1]	1.5×10^{-6}	0.93	576600	6.2×10^{-5}	0.06	unstable
C5 [1]	1.5×10^{-6}	0.885	522150	6.9×10^{-5}	0.07	unstable
C6 [1,2,3]	1.3×10^{-6}	0.613	72263	5.0×10^{-4}	0.50	unstable
C7 [1,2,3]	1.4×10^{-6}	0.589	61950	5.8×10^{-4}	0.58	unstable
C8 [1,2,4]	1.2×10^{-6}	0.581	70325	5.1×10^{-4}	0.51	unstable
C9 [1,2,5]	2.3×10^{-6}	0.615	41111	8.8×10^{-4}	0.88	unstable
C10 [1,2,5]	2.8×10^{-6}	0.563	28301	1.3×10^{-3}	1.27	unstable

Table 3.9 (continued)

C11 [2,5,6]	1.5×10^{-6}	0.660	72600	5.0×10^{-4}	0.50	unstable
C12 [6]	3.3×10^{-7}	0.914	2531503	1.4×10^{-5}	0.01	unstable
C13[6]	4.9×10^{-7}	0.956	1865175	1.9×10^{-5}	0.02	unstable
C14[2,3,7]	4.8×10^{-7}	0.669	932419	3.9×10^{-5}	0.04	unstable
C15[2,3,6]	4.0×10^{-7}	0.689	296700	1.2×10^{-4}	0.12	unstable
C16[7]	1.0×10^{-6}	1.050	1102500	3.3×10^{-5}	0.03	unstable
C17[7]	1.9×10^{-6}	0.986	511682	7.0×10^{-5}	0.07	unstable
C18[2,5,7]	5.5×10^{-6}	0.692	21766	1.7×10^{-3}	1.65	unstable

[1] Source debris from 5-26-94 experiment.
[2] Drained basal boundary; computation of characteristic diffusion time based on $(H/2)^2/D$.
[3] Gravel substrate.
[4] Uncompacted sand substrate.
[5] Compacted sand substrate.
[6] Osceola Mudflow debris.
[7] Mount St. Helens 1980 North Fork Toutle River debris-flow sediment.

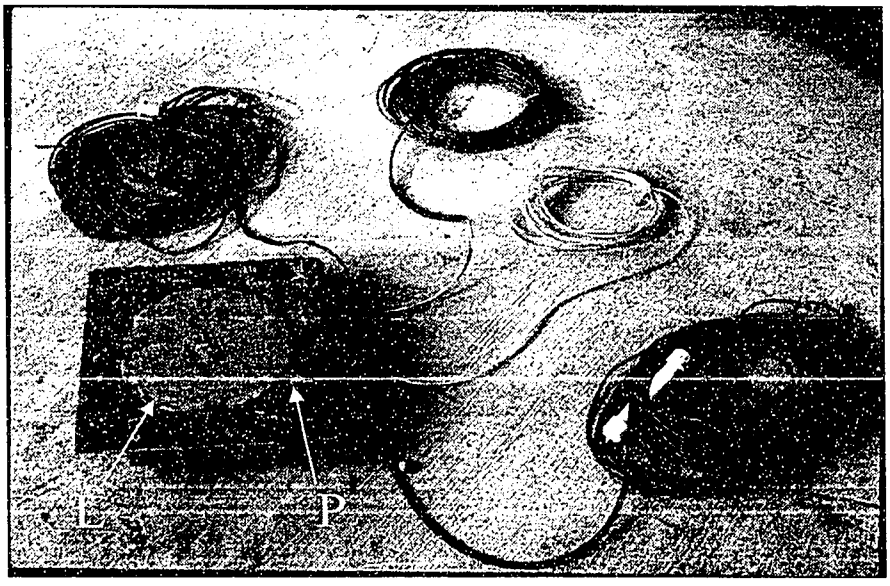

Figure 3.1. Instrumentation plate used to measure normal stress and fluid pressure at the base of experimental debris-flow deposits. A 200-lb (90-kg) capacity load cell is mounted beneath a 500-cm^2 round plate (L). A differential pressure sensor is mounted to a port hole in the plate (P) and vented to the atmosphere.

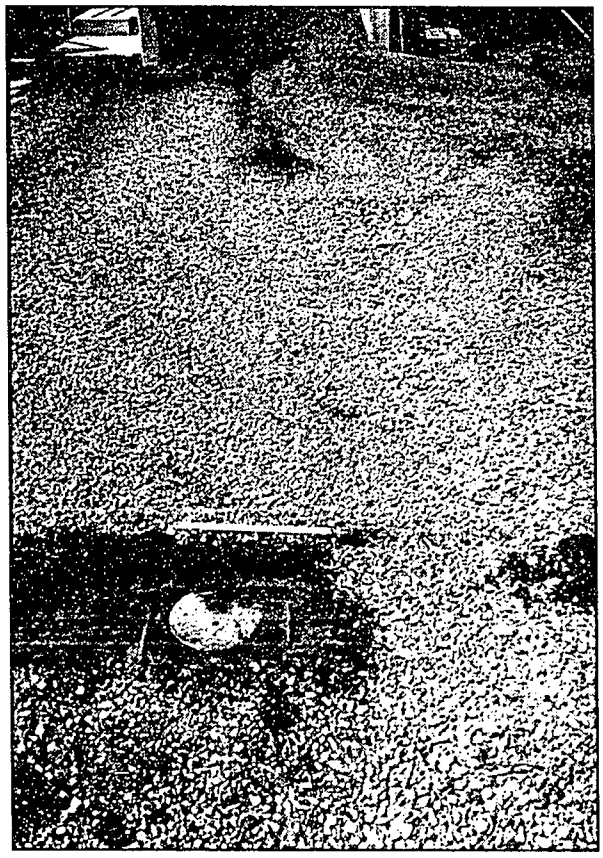

Figure 3.2. Instrumentation plate installed in runout surface at U.S. Geological Survey flume.

Figure 3.3. Measured response of total fluid pressure and total normal stress at the base of experimental debris-flow deposits. The date of the experiment and thickness of the deposit (H) are shown. Pulsatile increases in both fluid pressure and total bed stress at early time reflect loading of deposit by successive surges. Fluid pressure is shown in units of centimeters of water head to provide easy comparison with deposit thickness. Bed stress is given in Pa. Fluid pressure is converted to Pa units by multiplying by 98 (e.g., 10 cm of water head = 980 Pa). The plots show both the long term behavior of fluid pressure and bed stress, and an expanded view of the first several seconds during deceleration and deposition. A-D. Experiments using mixture of sand and gravel. E-G. Experiments using finer-grained mixtures of sand, gravel, and loam. See Table 3.1 for characterization of sediments.

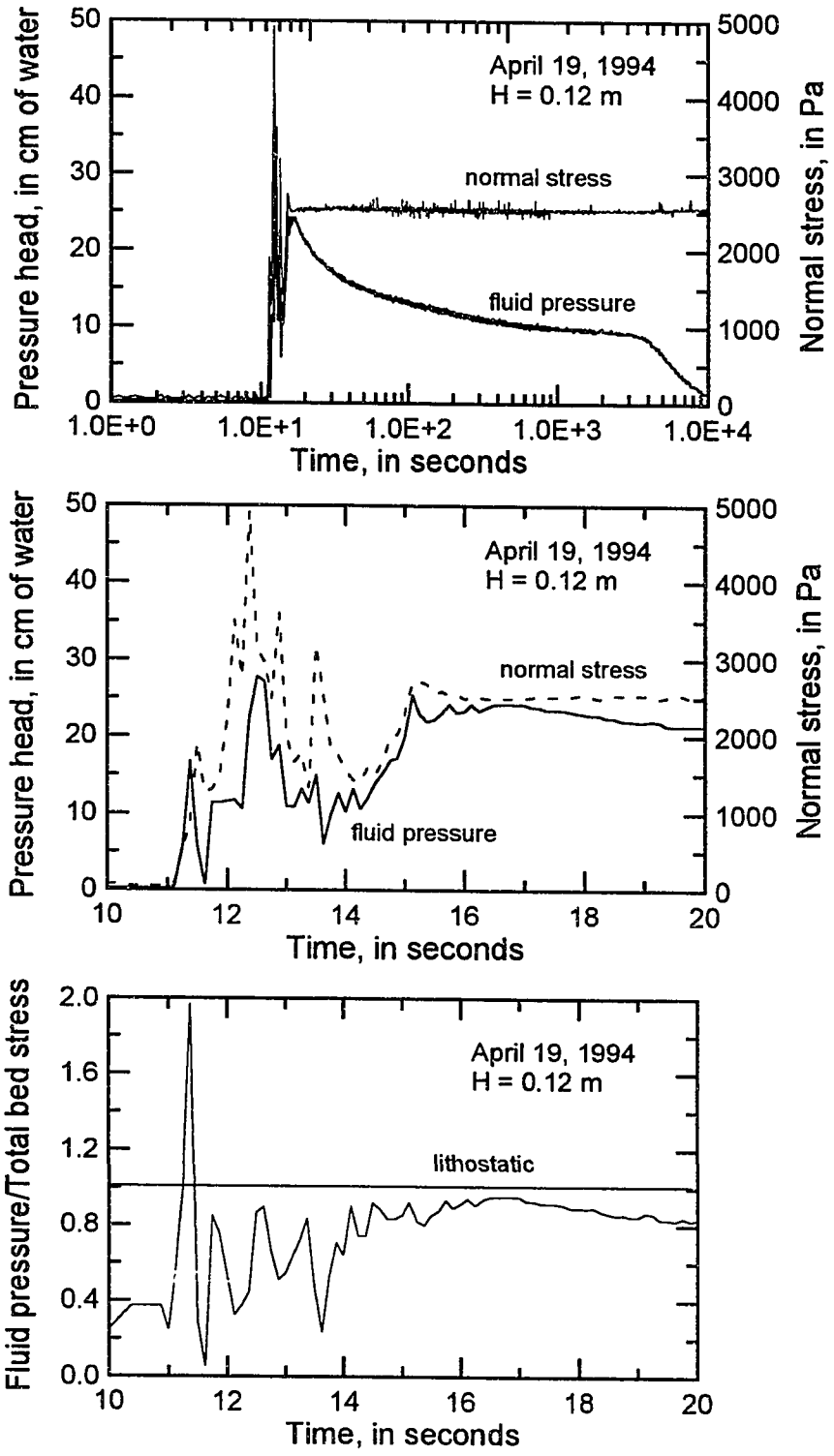
Pressure head, in cm of water
Normal stress, in Pa
April 19, 1994
H = 0.12 m
normal stress
fluid pressure
Time, in seconds
Pressure head, in cm of water
Normal stress, in Pa
April 19, 1994
H = 0.12 m
normal stress
fluid pressure
Time, in seconds
Fluid pressure/Total bed stress
April 19, 1994
H = 0.12 m
lithostatic
Time, in seconds

Figure 3.3a

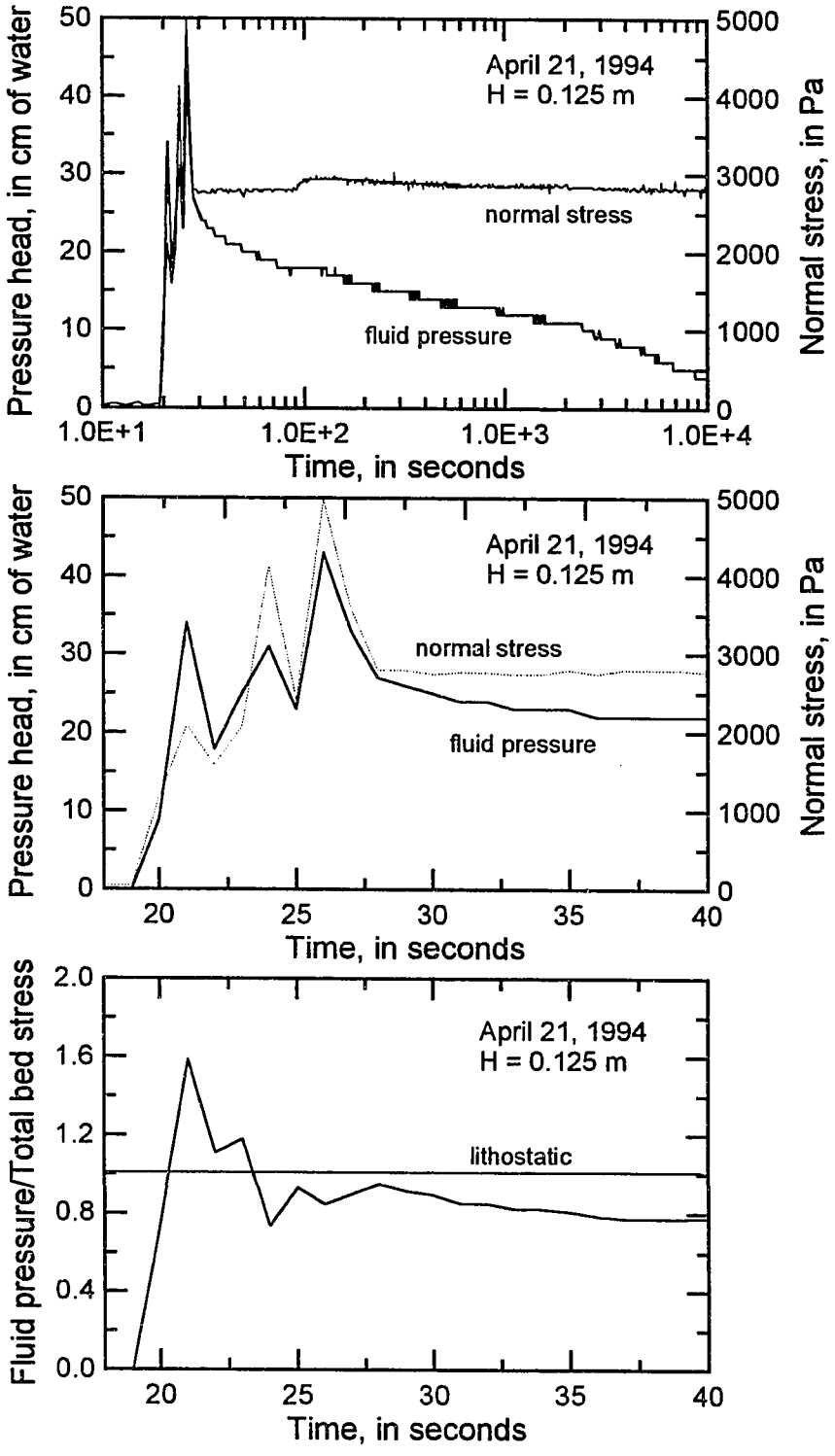
Pressure head, in cm of water
Normal stress, in Pa
April 21, 1994
H = 0.125 m
normal stress
fluid pressure
Time, in seconds
1.0E+1
1.0E+2
1.0E+3
1.0E+4
Fluid pressure/Total bed stress
lithostatic

Figure 3.3b

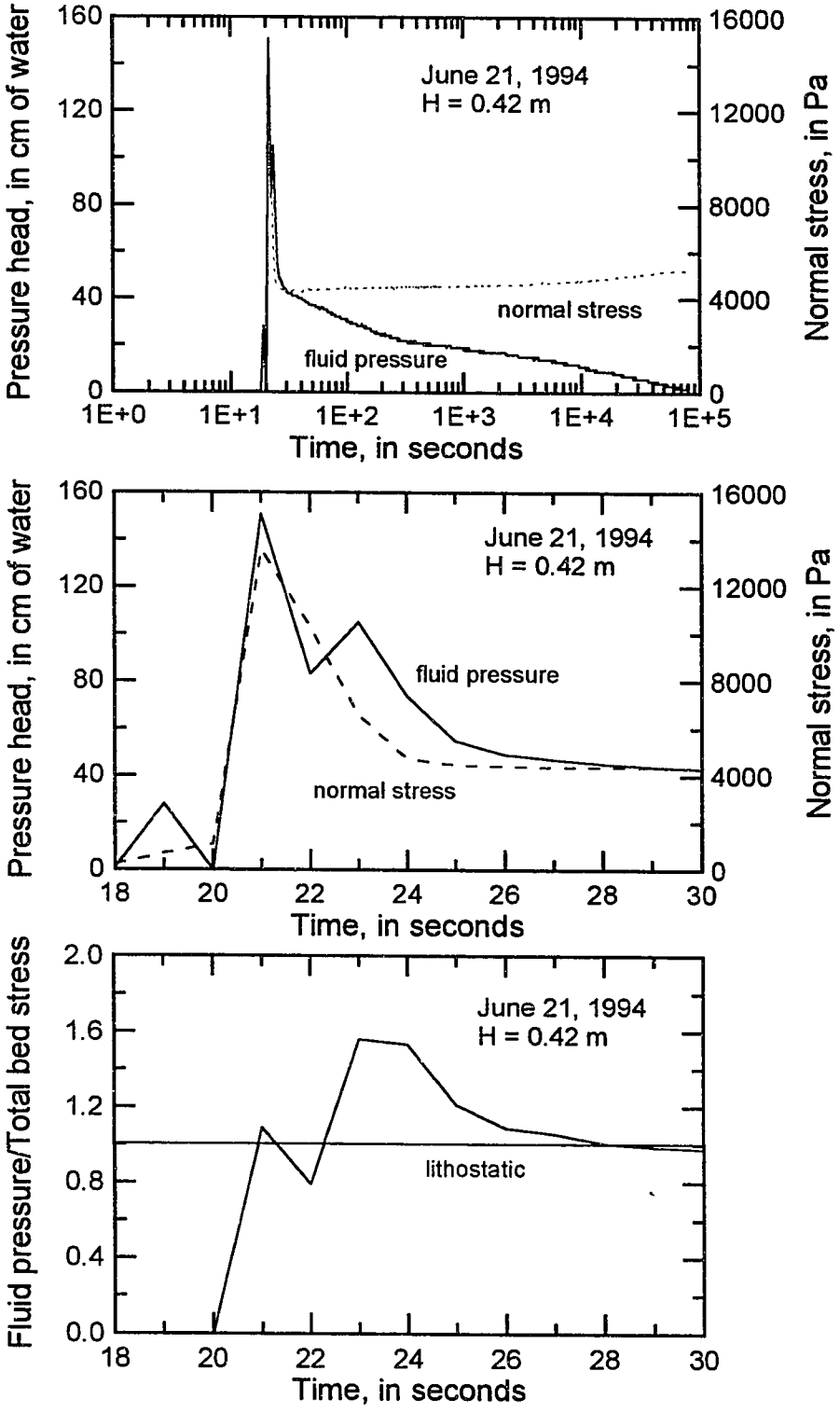
Pressure head, in cm of water
Normal stress, in Pa
June 21, 1994
H = 0.42 m
normal stress
fluid pressure
Time, in seconds
Fluid pressure/Total bed stress
lithostatic

Figure 3.3c

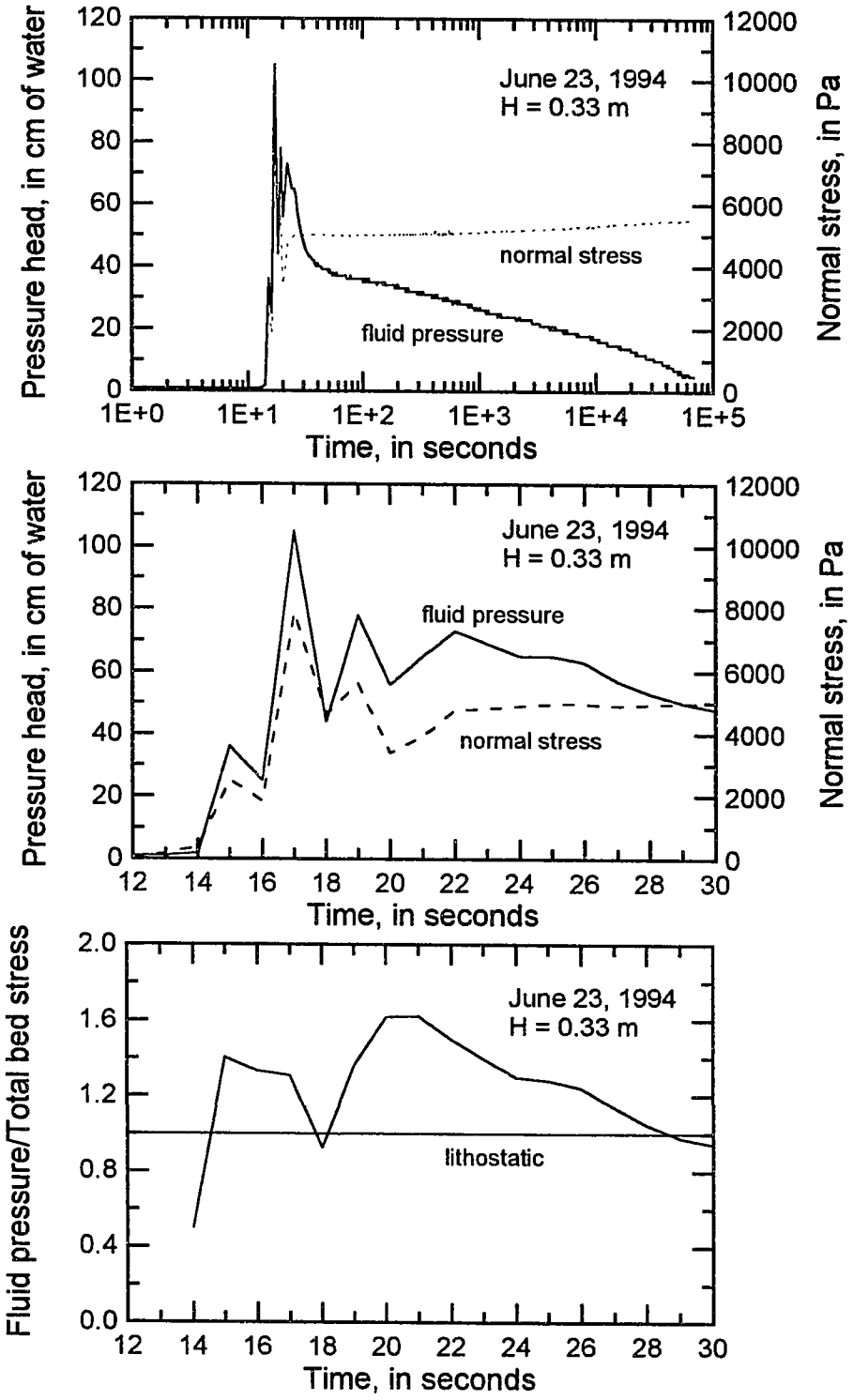
Pressure head, in cm of water
Normal stress, in Pa
June 23, 1994
H = 0.33 m
normal stress
fluid pressure
Time, in seconds
Pressure head, in cm of water
Normal stress, in Pa
June 23, 1994
H = 0.33 m
fluid pressure
normal stress
Time, in seconds
Fluid pressure/Total bed stress
June 23, 1994
H = 0.33 m
lithostatic
Time, in seconds

Figure 3.3d

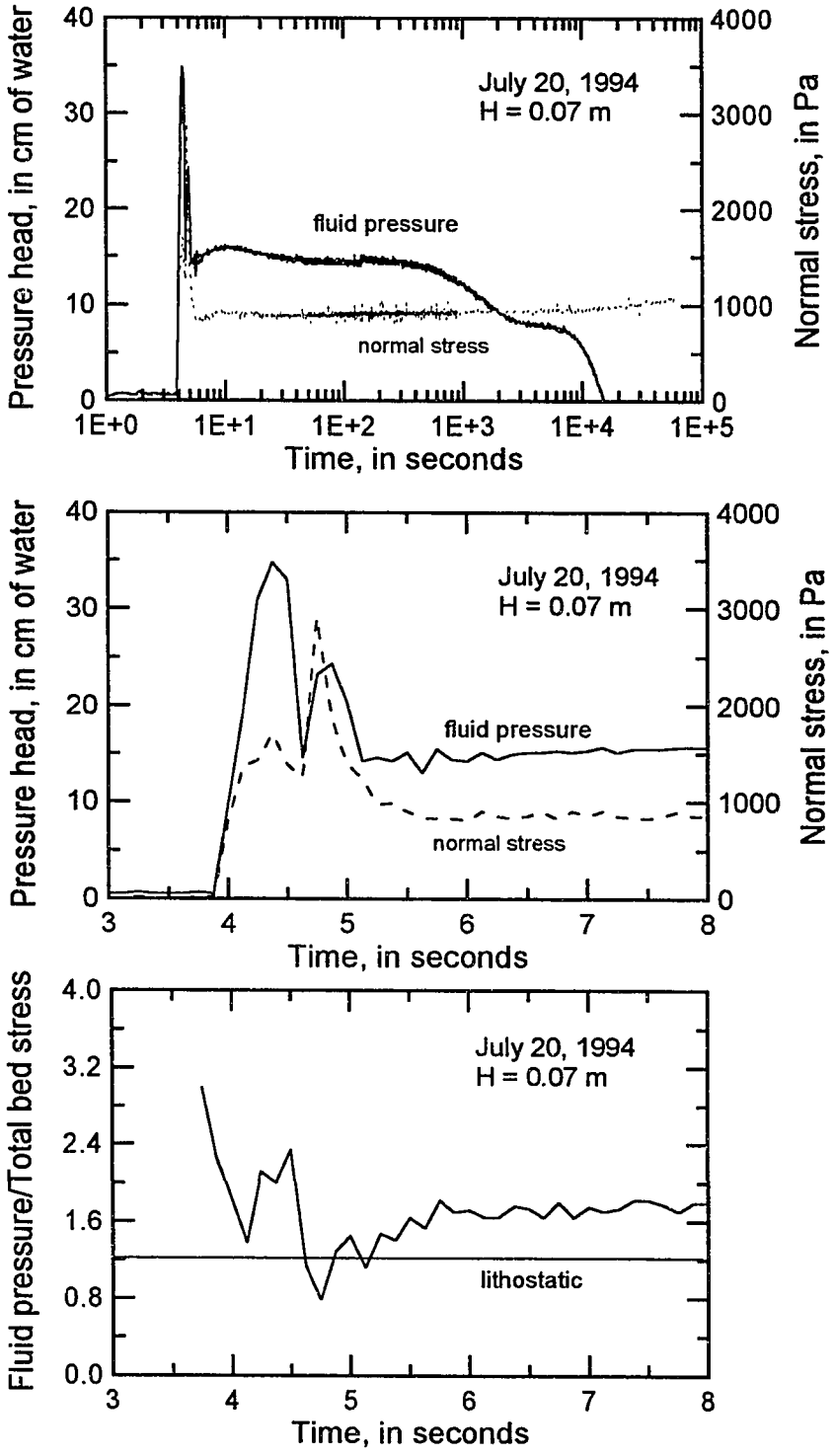
Pressure head, in cm of water
Normal stress, in Pa
July 20, 1994
H = 0.07 m
fluid pressure
normal stress
Time, in seconds
Fluid pressure/Total bed stress
lithostatic

Figure 3.3e

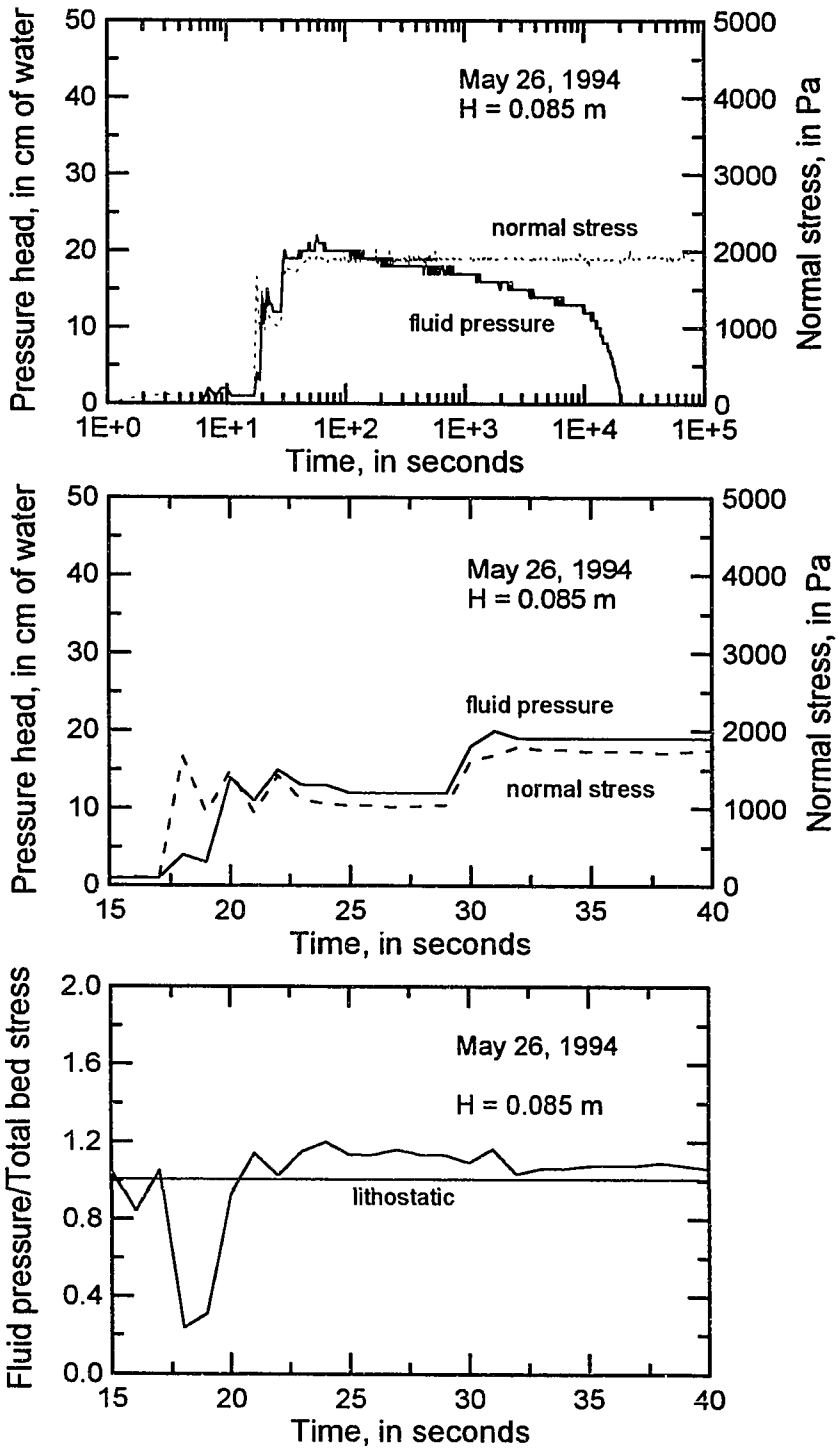
Pressure head, in cm of water
Normal stress, in Pa
May 26, 1994
H = 0.085 m
normal stress
fluid pressure
Time, in seconds
Pressure head, in cm of water
Normal stress, in Pa
May 26, 1994
H = 0.085 m
fluid pressure
normal stress
Time, in seconds
Fluid pressure/Total bed stress
May 26, 1994
H = 0.085 m
lithostatic
Time, in seconds

Figure 3.3f

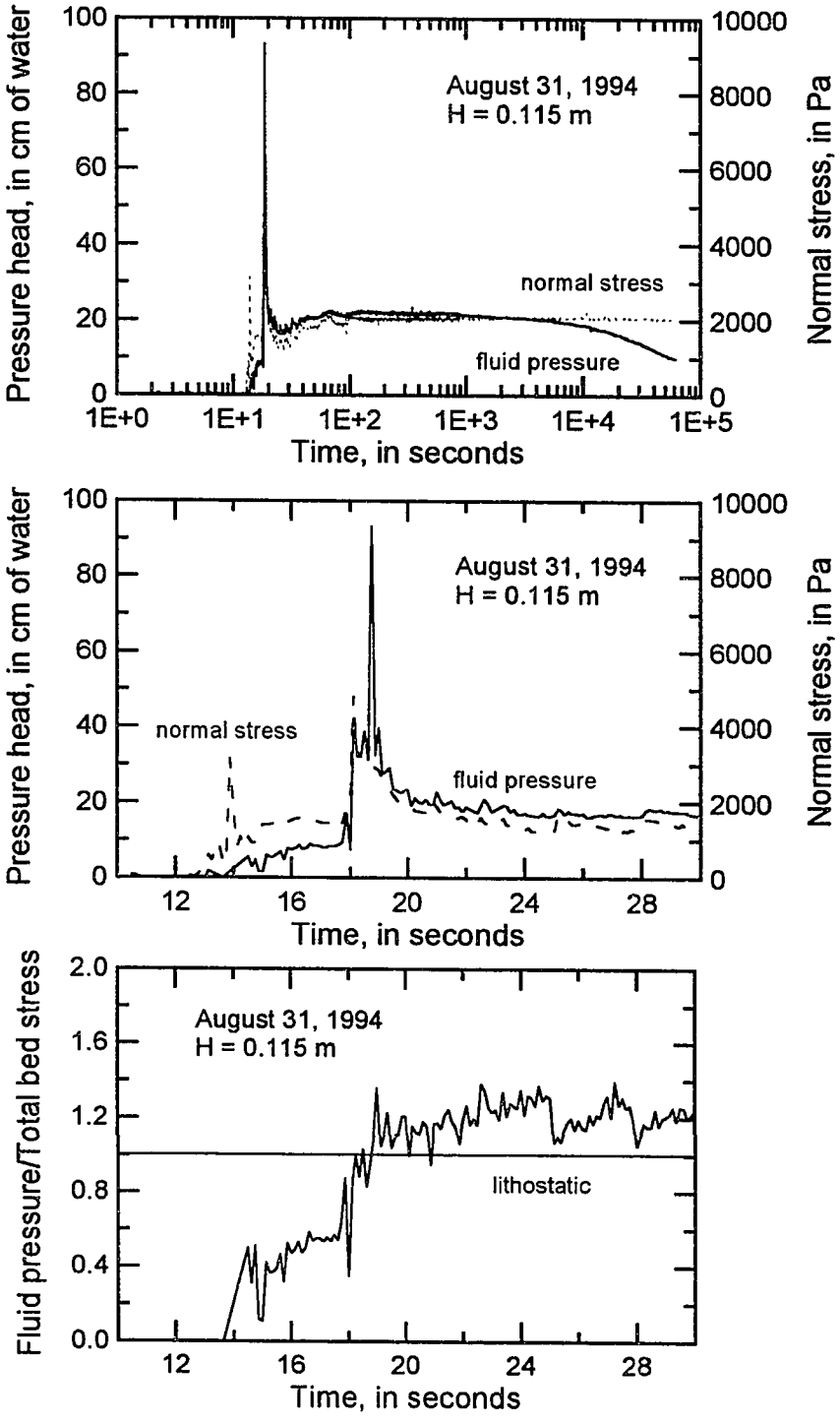
Pressure head, in cm of water
Normal stress, in Pa
August 31, 1994
H = 0.115 m
normal stress
fluid pressure
Time, in seconds
Fluid pressure/Total bed stress
lithostatic

Figure 3.3g

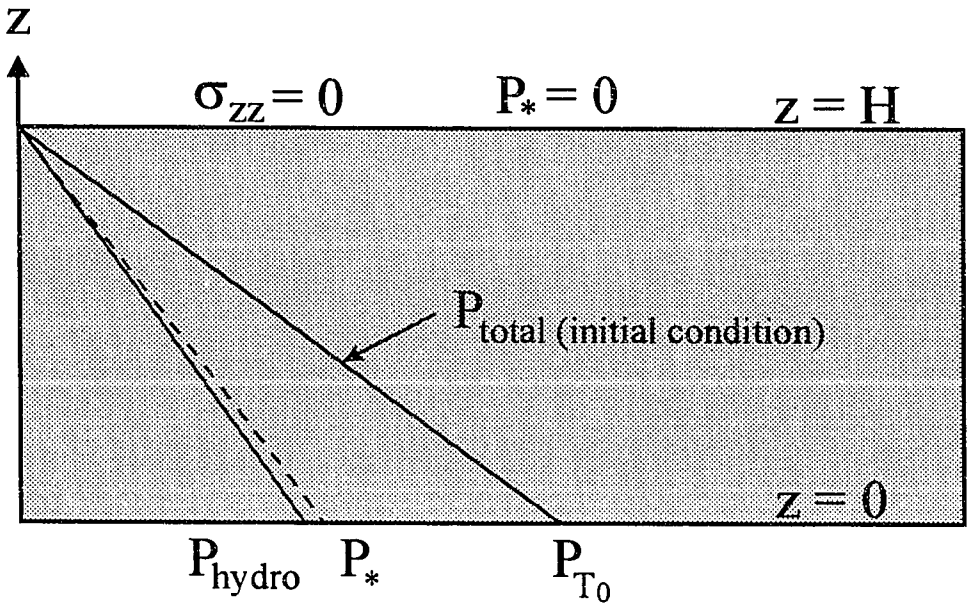

Figure 3.4. Definition sketch of element geometry, boundary conditions, and initial pressure profiles. P_{hydro} is hydrostatic fluid pressure; P_* is fluid pressure in excess of hydrostatic; and P_{T0} is the initial value of the total fluid pressure at the base of the sediment column.

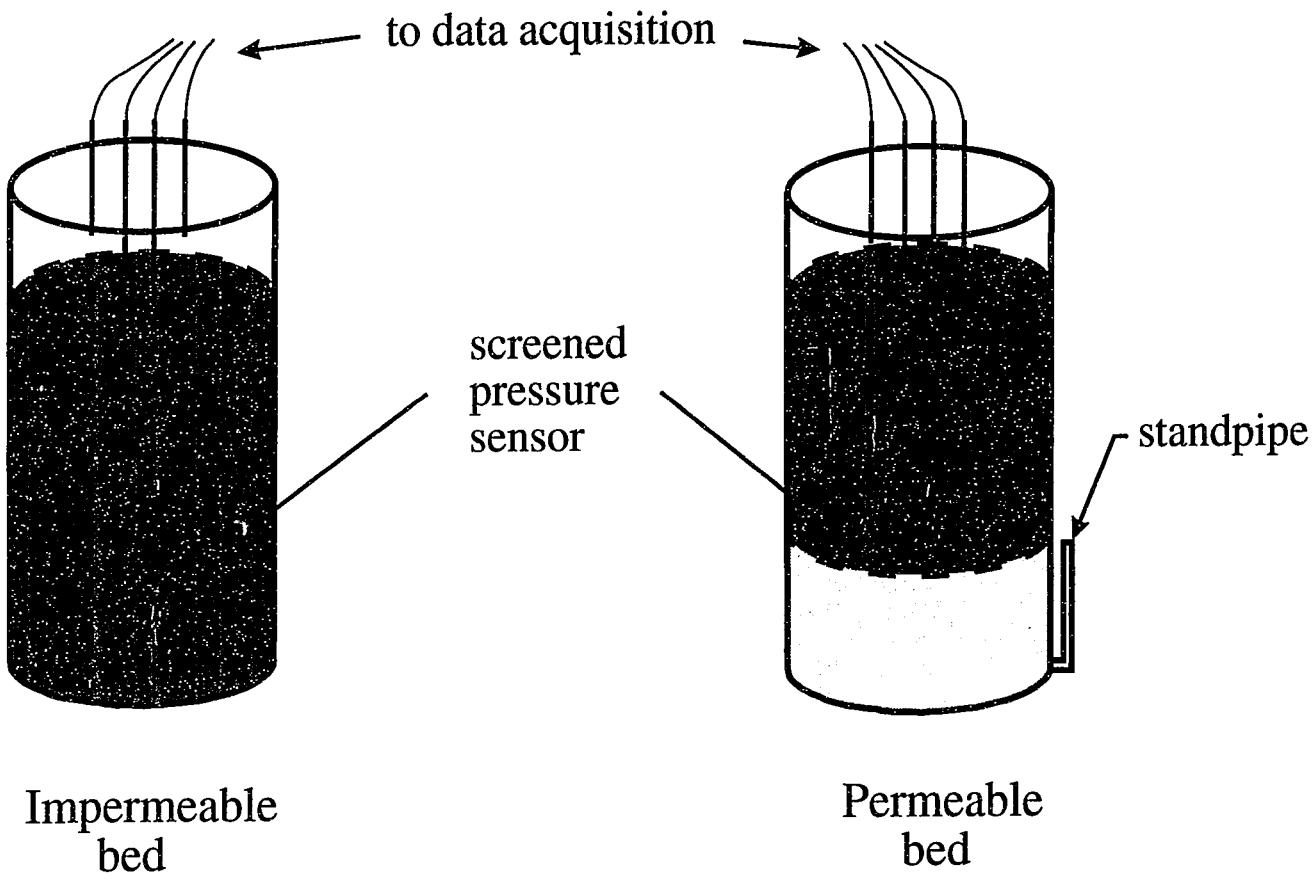

Figure 3.5. Schematic diagram of experimental apparatus. Screened pressure probes are suspended in the tank and slurry is introduced rapidly. Saturation of permeable bed is maintained by a fluid-filled standpipe.

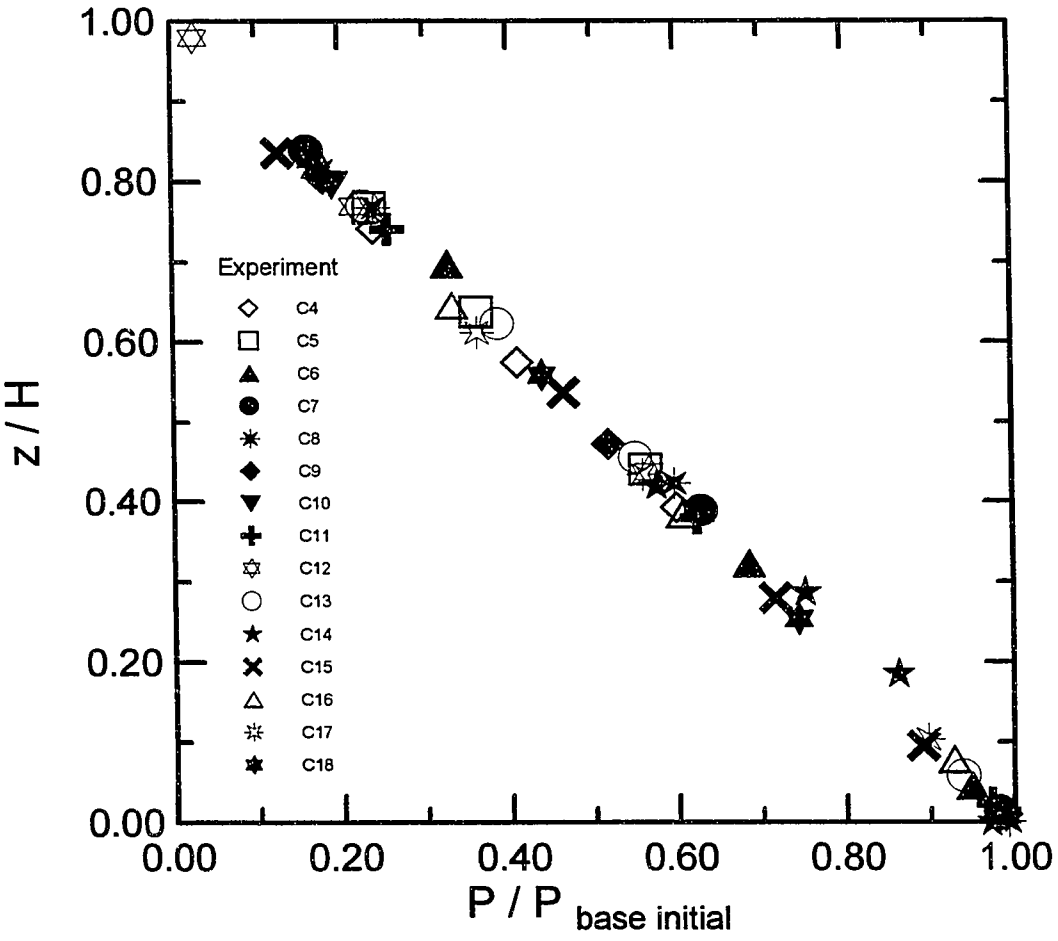

Figure 3.6. Initial total fluid pressure measured in laboratory experiments. Position within slurry is normalized by slurry depth; fluid pressure is normalized by initial value of fluid pressure at base of slurry. Open symbols are impermeable-bed experiments; solid symbols are permeable-bed experiments.

Figure 3.7. Measured response of total fluid pressure in one-dimensional laboratory experiments. Depth refers to the initial depth of pressure probe below slurry surface. Pulsatile increases in fluid pressure at early time reflect loading of slurry into tank. H is the initial thickness of the slurry; k is the permeability of substrate material. Paired impermeable- and permeable-bed experiments represent replicate tests. A. Impermeable-bed experiments using loam mix. B. Permeable-bed experiments using loam mix. C. Experiments using Osceola Mudflow sediment. D. Experiments using Mount St. Helens 1980 North Fork Toutle River debris-flow sediment (see Table 3.4).

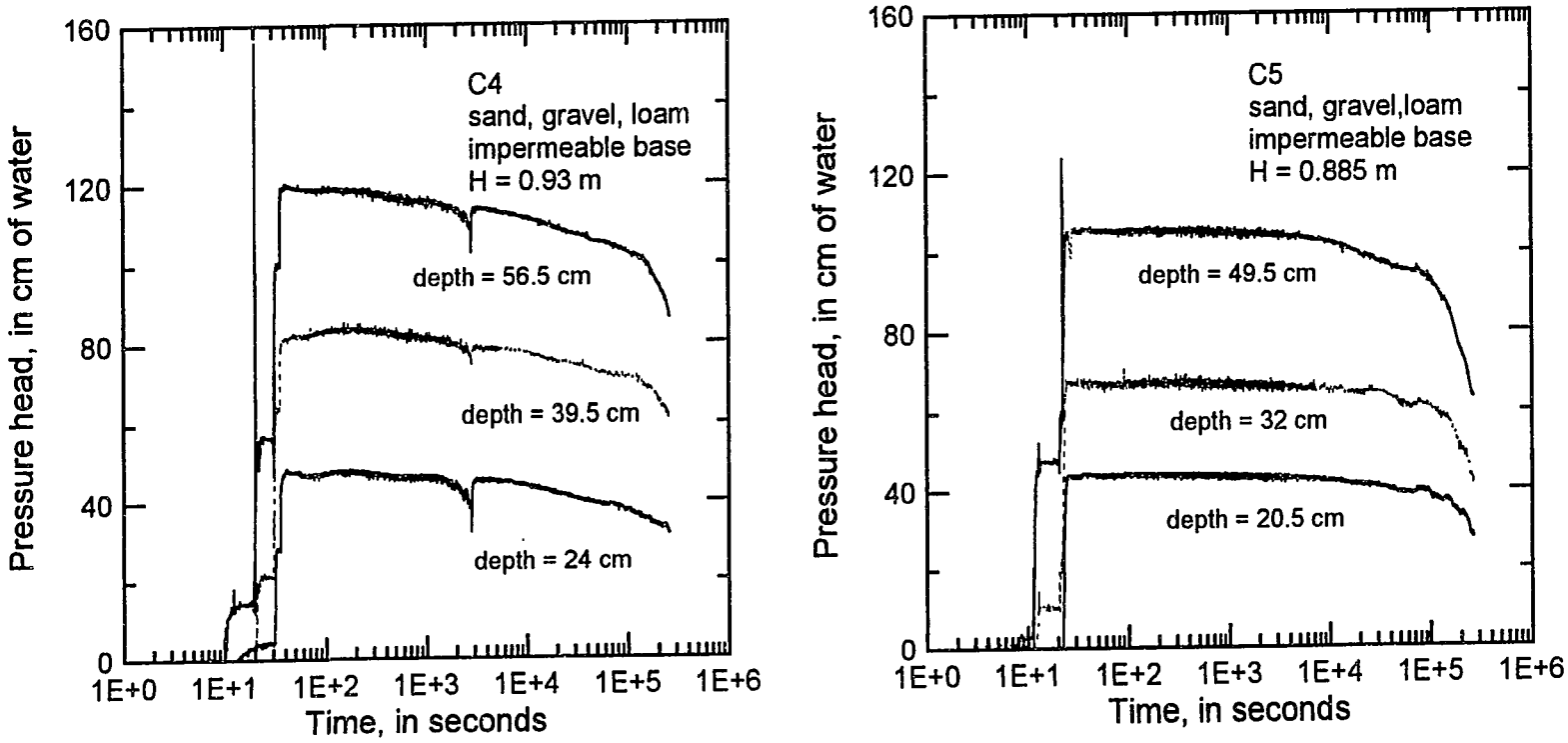
C4
sand, gravel, loam
impermeable base
H = 0.93 m
depth = 56.5 cm
depth = 39.5 cm
depth = 24 cm
Pressure head, in cm of water
Time, in seconds
160
120
80
40
0
1E+0
1E+1
1E+2
1E+3
1E+4
1E+5
1E+6
C5
sand, gravel,loam
impermeable base
H = 0.885 m
depth = 49.5 cm
depth = 32 cm
depth = 20.5 cm

Figure 3.7a

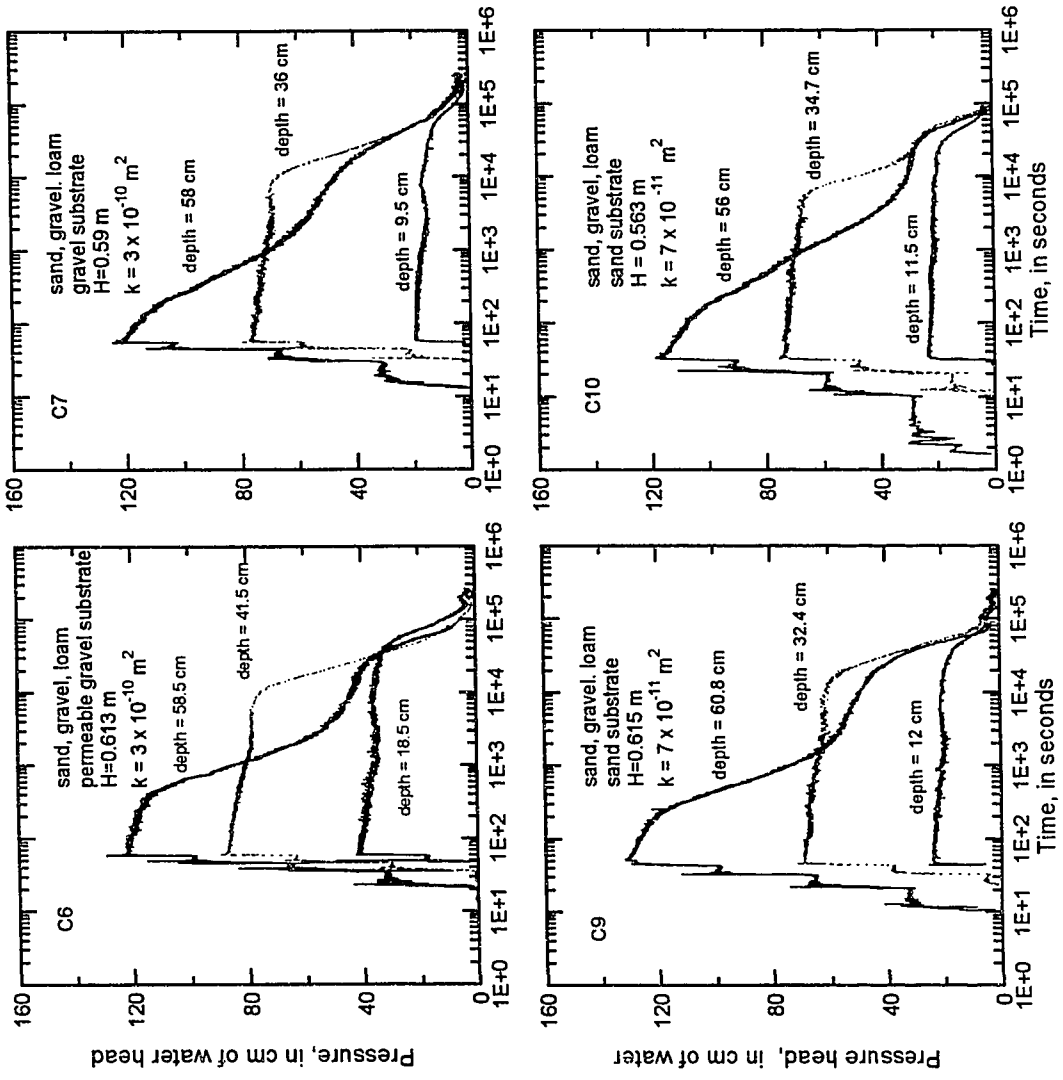
C6
sand, gravel, loam
permeable gravel substrate
H=0.613 m
k = 3 x 10^-10 m^2
depth = 58.5 cm
depth = 41.5 cm
depth = 18.5 cm
C7
sand, gravel, loam
gravel substrate
H=0.59 m
k = 3 x 10^-10 m^2
depth = 58 cm
depth = 36 cm
depth = 9.5 cm
C9
sand, gravel, loam
sand substrate
H=0.615 m
k = 7 x 10^-11 m^2
depth = 60.8 cm
depth = 32.4 cm
depth = 12 cm
C10
sand, gravel, loam
sand substrate
H = 0.563 m
k = 7 x 10^-11 m^2
depth = 56 cm
depth = 34.7 cm
depth = 11.5 cm
Pressure, in cm of water head
Pressure head, in cm of water
Time, in seconds
Time, in seconds

Figure 3.7b

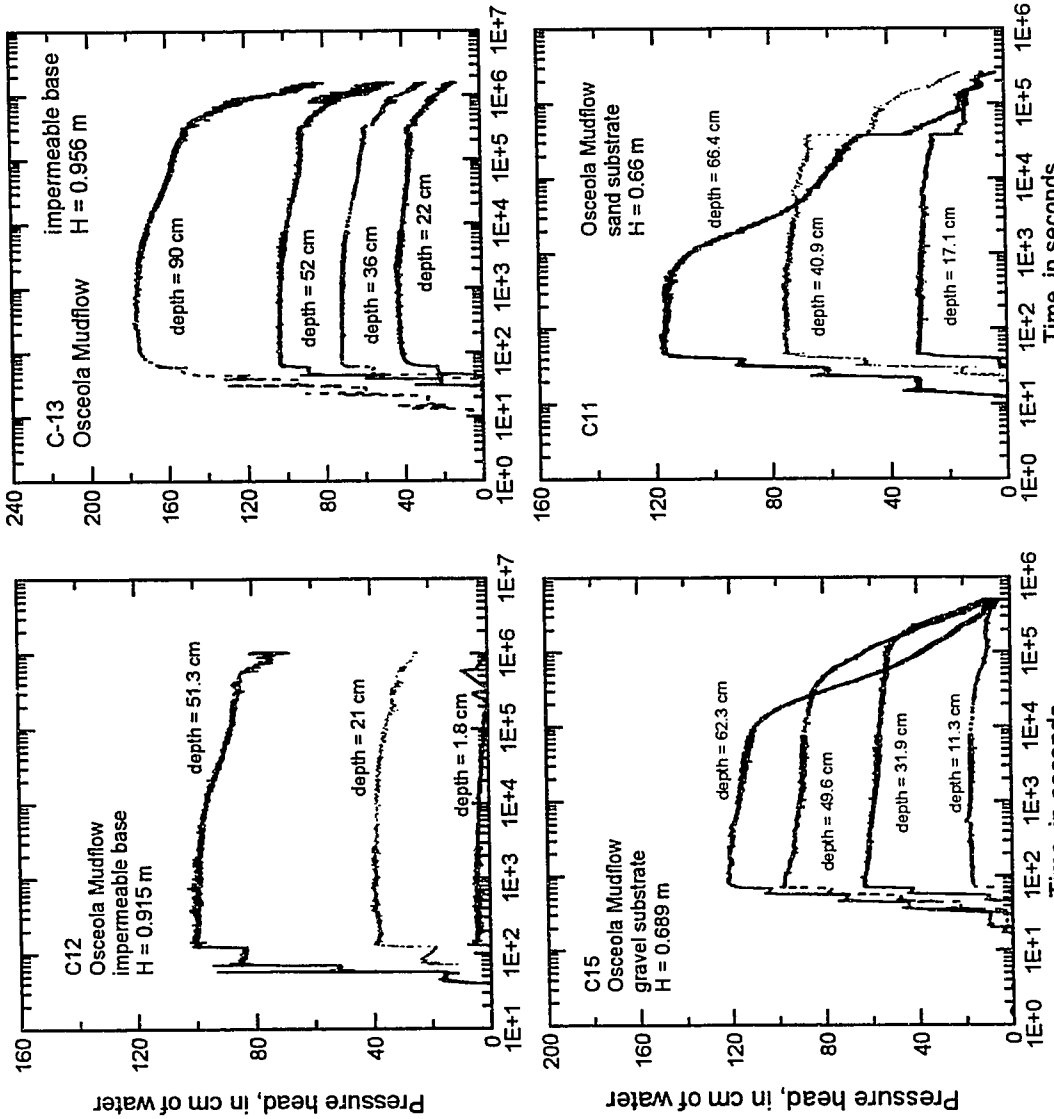
C-13
Osceola Mudflow
impermeable base
H = 0.956 m
depth = 90 cm
depth = 52 cm
depth = 36 cm
depth = 22 cm
C12
Osceola Mudflow
impermeable base
H = 0.915 m
depth = 51.3 cm
depth = 21 cm
depth = 1.8 cm
C11
Osceola Mudflow
sand substrate
H = 0.66 m
depth = 66.4 cm
depth = 40.9 cm
depth = 17.1 cm
C15
Osceola Mudflow
gravel substrate
H = 0.689 m
depth = 62.3 cm
depth = 49.6 cm
depth = 31.9 cm
depth = 11.3 cm
Pressure head, in cm of water
Time, in seconds

Figure 3.7c

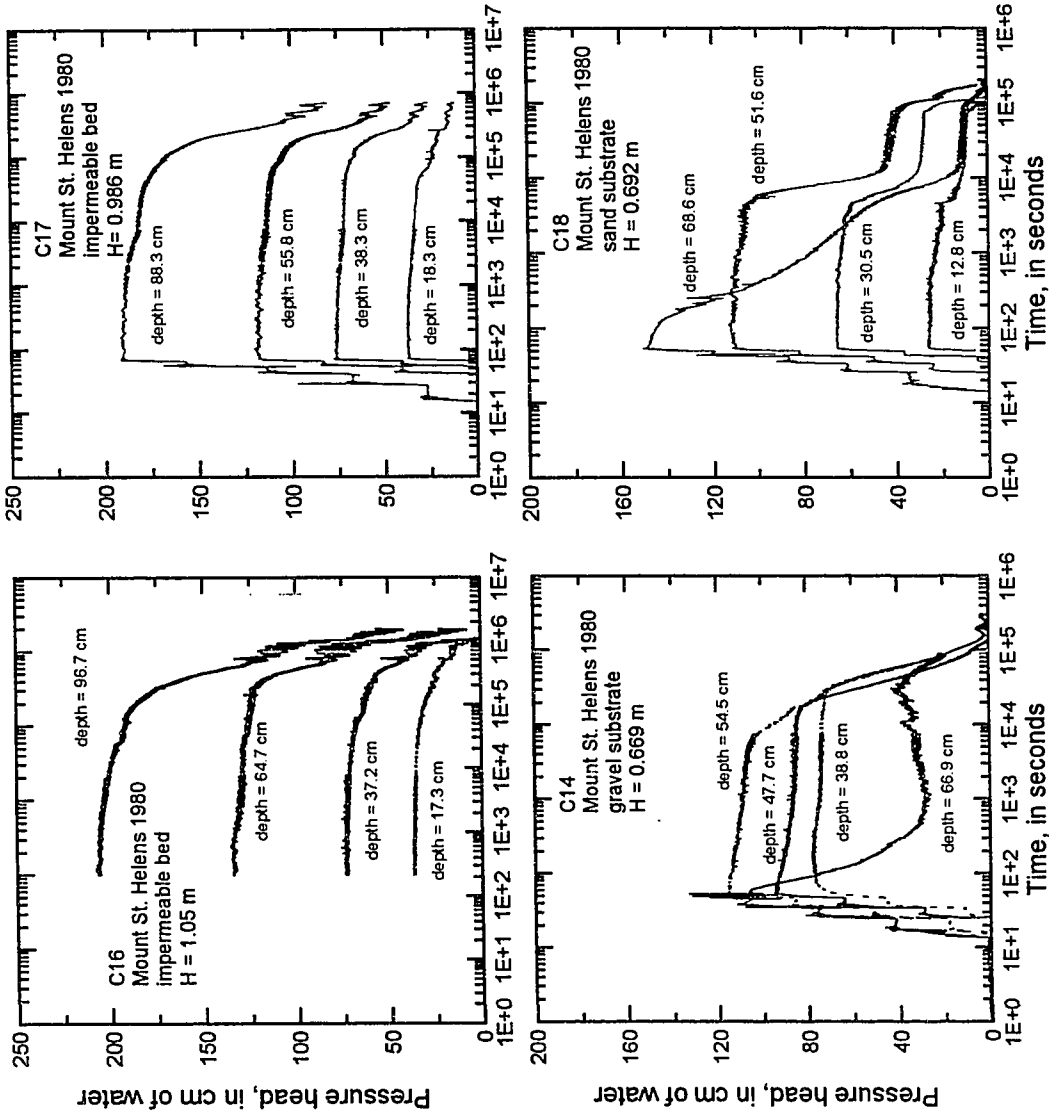
C16
Mount St. Helens 1980
impermeable bed
H = 1.05 m
depth = 96.7 cm
depth = 64.7 cm
depth = 37.2 cm
depth = 17.3 cm
C17
Mount St. Helens 1980
impermeable bed
H= 0.986 m
depth = 88.3 cm
depth = 55.8 cm
depth = 38.3 cm
depth = 18.3 cm
C14
Mount St. Helens 1980
gravel substrate
H = 0.669 m
depth = 54.5 cm
depth = 47.7 cm
depth = 38.8 cm
depth = 66.9 cm
C18
Mount St. Helens 1980
sand substrate
H = 0.692 m
depth = 68.6 cm
depth = 51.6 cm
depth = 30.5 cm
depth = 12.8 cm
Pressure head, in cm of water
Time, in seconds

Figure 3.7d

Figure 3.8. Comparison of predicted and measured transient behavior of nonequilibrium fluid pressure in one-dimensional laboratory experiments. Position within the slurry (z) represents the thickness of the slurry minus the depth of the probe below the surface (i.e., z=0 is slurry base; z=H is slurry surface). The position in the slurry is normalized by initial thickness of slurry. Nonequilibrium fluid pressure is normalized by initial value of nonequilibrium fluid pressure at the base of the slurry. D is the depthwise best-fit value of hydraulic diffusivity. Each curve represents an increment of time. Times have been nondimensionalized to remove effects of length scale (see text). A. Impermeable-bed experiments using loam mix. B. Permeable-bed experiments using loam mix. C. Experiments using Osceola Mudflow sediment. D. Experiments using Mount St. Helens 1980 North Fork Toutle River debris-flow sediment.

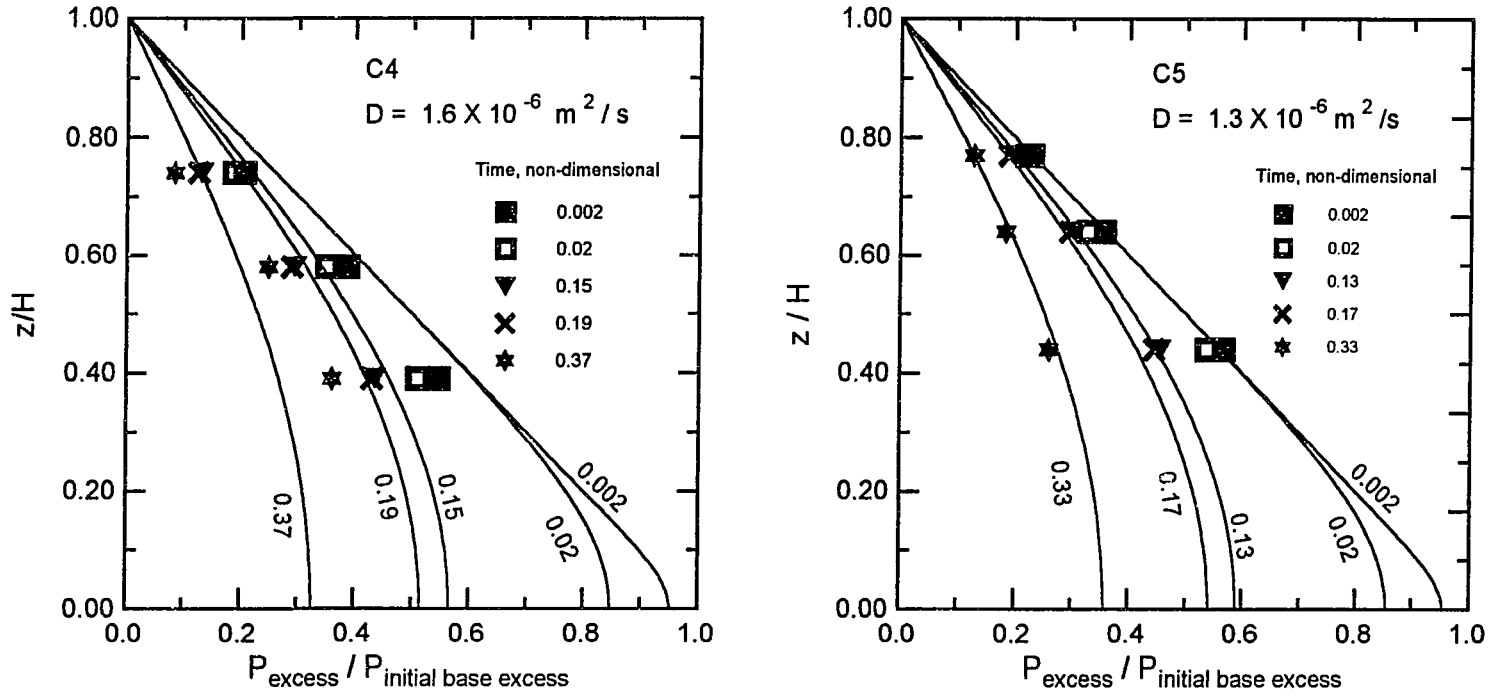
C4
D = 1.6 X 10 -6 m 2 / s
Time, non-dimensional
0.002
0.02
0.15
0.19
0.37
z/H
P excess / P initial base excess
C5
D = 1.3 X 10 -6 m 2 /s
Time, non-dimensional
0.002
0.02
0.13
0.17
0.33
z / H
P excess / P initial base excess

Figure 3.8a

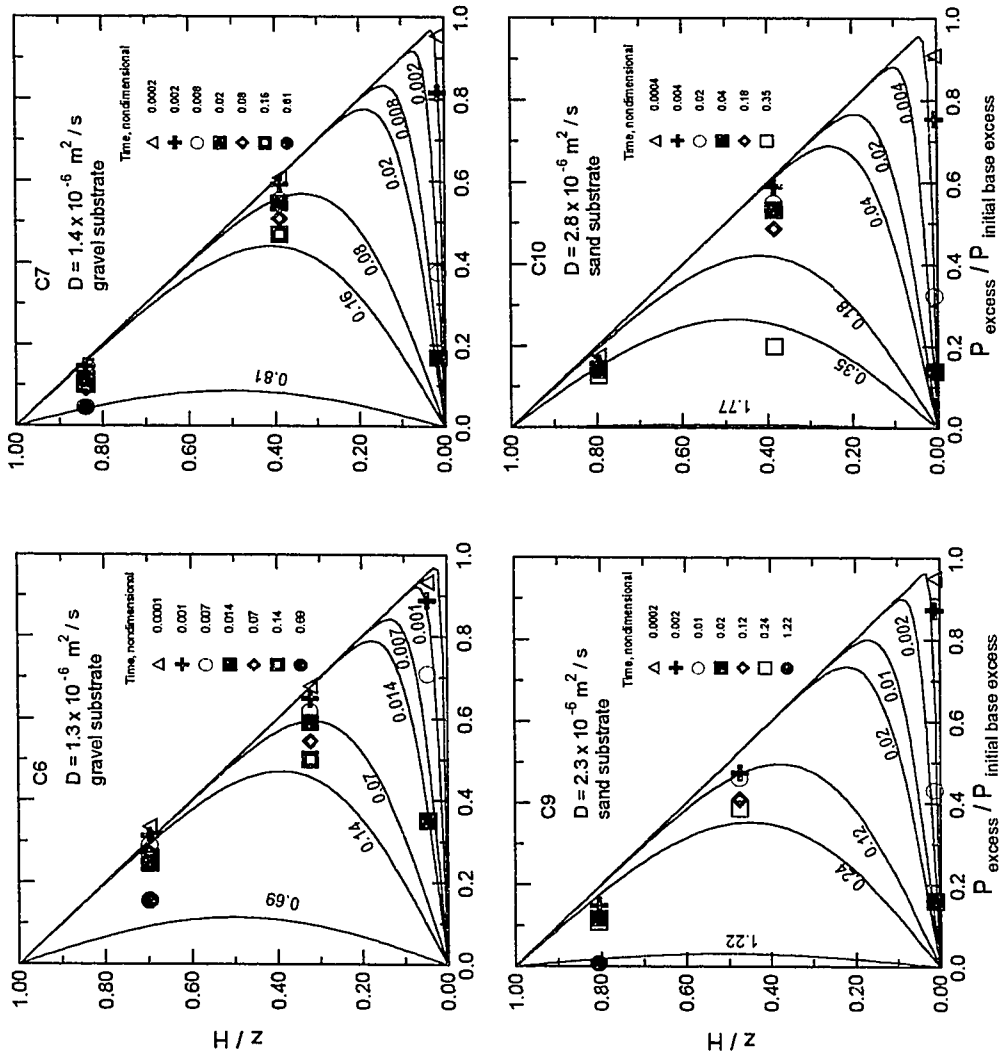
C6
D = 1.3 x 10^-6 m^2 / s
gravel substrate
C7
D = 1.4 x 10^-6 m^2 / s
gravel substrate
C9
D = 2.3 x 10^-6 m^2 / s
sand substrate
C10
D = 2.8 x 10^-6 m^2 / s
sand substrate
Time, nondimensional
z / H
P excess / P initial base excess

Figure 3.8b

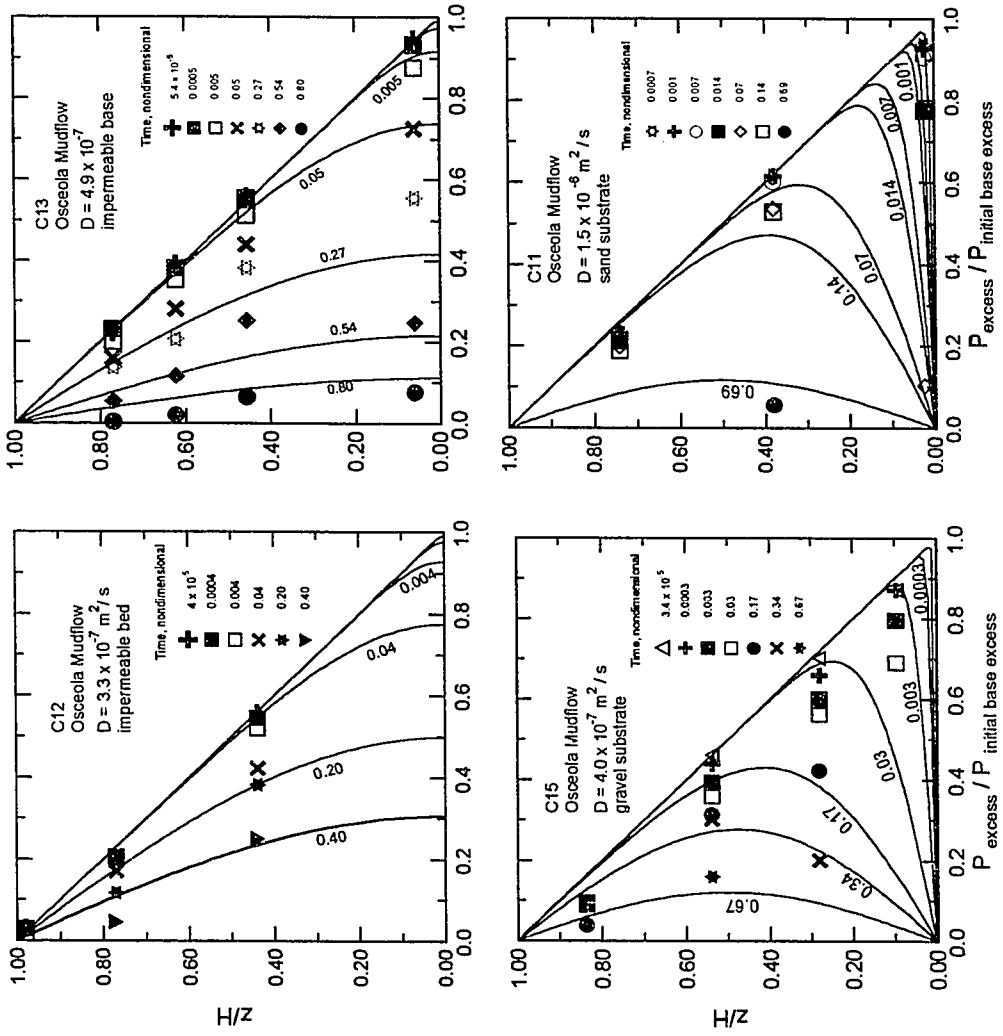
C13
Osceola Mudflow
D = 4.9 x 10^-7
impermeable base
Time, nondimensional
5.4 x 10^-5
0.0005
0.005
0.05
0.27
0.54
0.80
0.005
0.05
0.27
0.54
0.80
C12
Osceola Mudflow
D = 3.3 x 10^-7 m^2/s
impermeable bed
Time, nondimensional
4 x 10^-5
0.0004
0.004
0.04
0.20
0.40
0.004
0.04
0.20
0.40
C11
Osceola Mudflow
D = 1.5 x 10^-6 m^2/s
sand substrate
Time, nondimensional
0.0007
0.001
0.007
0.014
0.07
0.14
0.69
0.001
0.007
0.014
0.07
0.14
0.69
C15
Osceola Mudflow
D = 4.0 x 10^-7 m^2/s
gravel substrate
Time, nondimensional
3.4 x 10^-5
0.0003
0.003
0.03
0.17
0.34
0.67
0.0003
0.003
0.03
0.17
0.34
0.67
z/H
P excess / P initial base excess
P excess / P initial base excess

Figure 3.8c

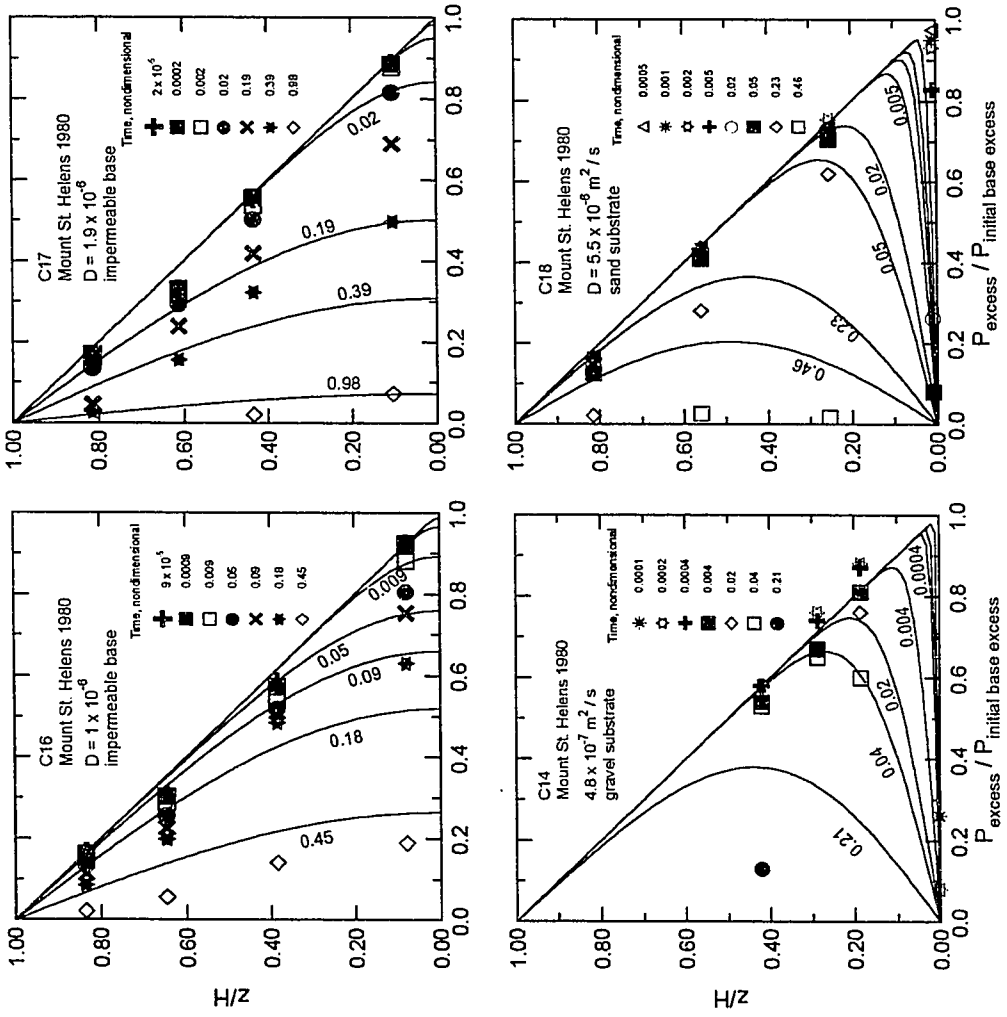
C16
Mount St. Helens 1980
D = 1 x 10^-6
impermeable base
Time, nondimensional
9 x 10^-5
0.0008
0.009
0.05
0.09
0.18
0.45
C17
Mount St. Helens 1980
D = 1.9 x 10^-6
impermeable base
Time, nondimensional
2 x 10^-5
0.0002
0.002
0.02
0.19
0.39
0.98
C14
Mount St. Helens 1980
4.8 x 10^-7 m^2 / s
gravel substrate
Time, nondimensional
0.0001
0.0002
0.0004
0.004
0.02
0.04
0.21
C18
Mount St. Helens 1980
D = 5.5 x 10^-6 m^2 / s
sand substrate
Time, nondimensional
0.0005
0.001
0.002
0.005
0.02
0.05
0.23
0.46
z/H
P_excess / P_initial base excess

Figure 3.8d

Figure 3.9. Comparison of predicted and measured transient behavior of effective normal stress in one-dimensional laboratory experiments. Position within slurry (z) is normalized by initial thickness of slurry. Effective normal stress is normalized by the value of hydrostatic pressure ($\rho_w gH$) at the base of the sediment column. The depthwise best-fit value of hydraulic diffusivity (D) and mean initial porosity (ϕ) are shown. Each curve represents an increment of time, nondimensionalized to remove effects of length scale. A. Impermeable-bed experiments using loam mix. B. Permeable-bed experiments using loam mix. C. Experiments using Osceola Mudflow sediment. D. Experiments using Mount St. Helens 1980 North Fork Toutle River debris-flow sediment.

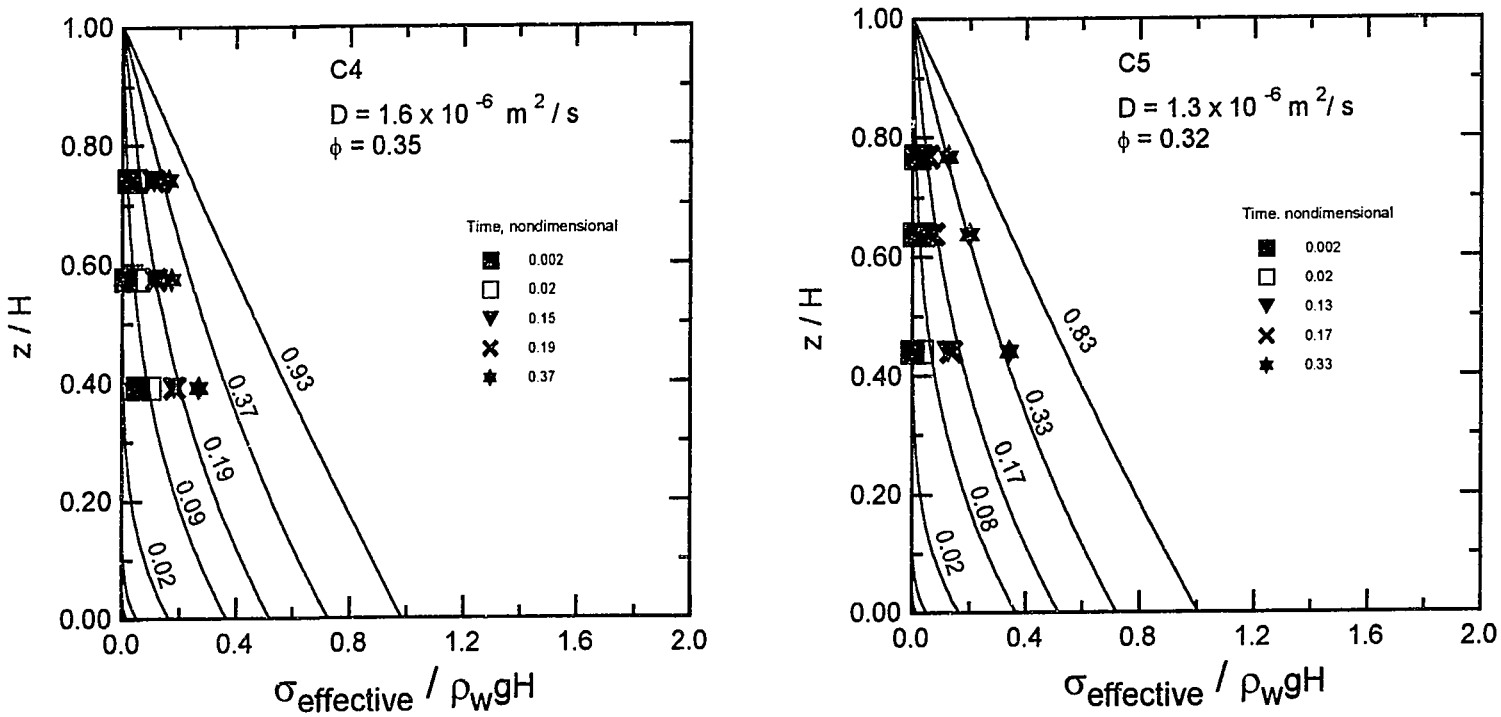
C4
D = 1.6 x 10 -6 m 2 / s
ϕ = 0.35
Time, nondimensional
0.002
0.02
0.15
0.19
0.37
0.93
0.37
0.19
0.09
0.02
z / H
σeffective / ρwgH
C5
D = 1.3 x 10 -6 m 2 / s
ϕ = 0.32
Time. nondimensional
0.002
0.02
0.13
0.17
0.33
0.83
0.33
0.17
0.08
0.02

Figure 3.9a

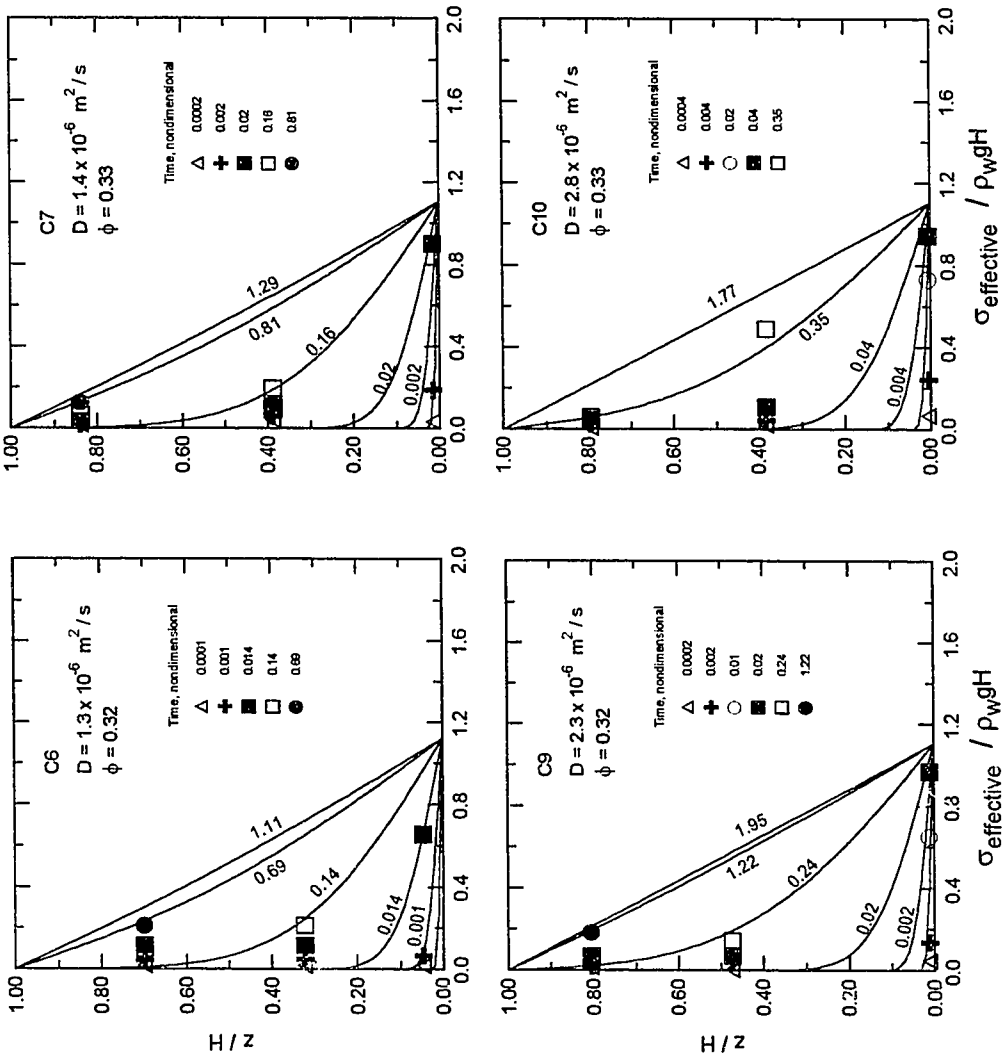
C6
D = 1.3 x 10^-6 m^2 / s
ϕ = 0.32
Time, nondimensional
0.0001
0.001
0.014
0.14
0.69
1.11
C7
D = 1.4 x 10^-6 m^2 / s
ϕ = 0.33
Time, nondimensional
0.0002
0.002
0.02
0.16
0.81
1.29
C9
D = 2.3 x 10^-6 m^2 / s
ϕ = 0.32
Time, nondimensional
0.0002
0.002
0.01
0.02
0.24
1.22
1.95
C10
D = 2.8 x 10^-6 m^2 / s
ϕ = 0.33
Time, nondimensional
0.0004
0.004
0.02
0.04
0.35
1.77
z / H
σeffective / ρwgH

Figure 3.9b

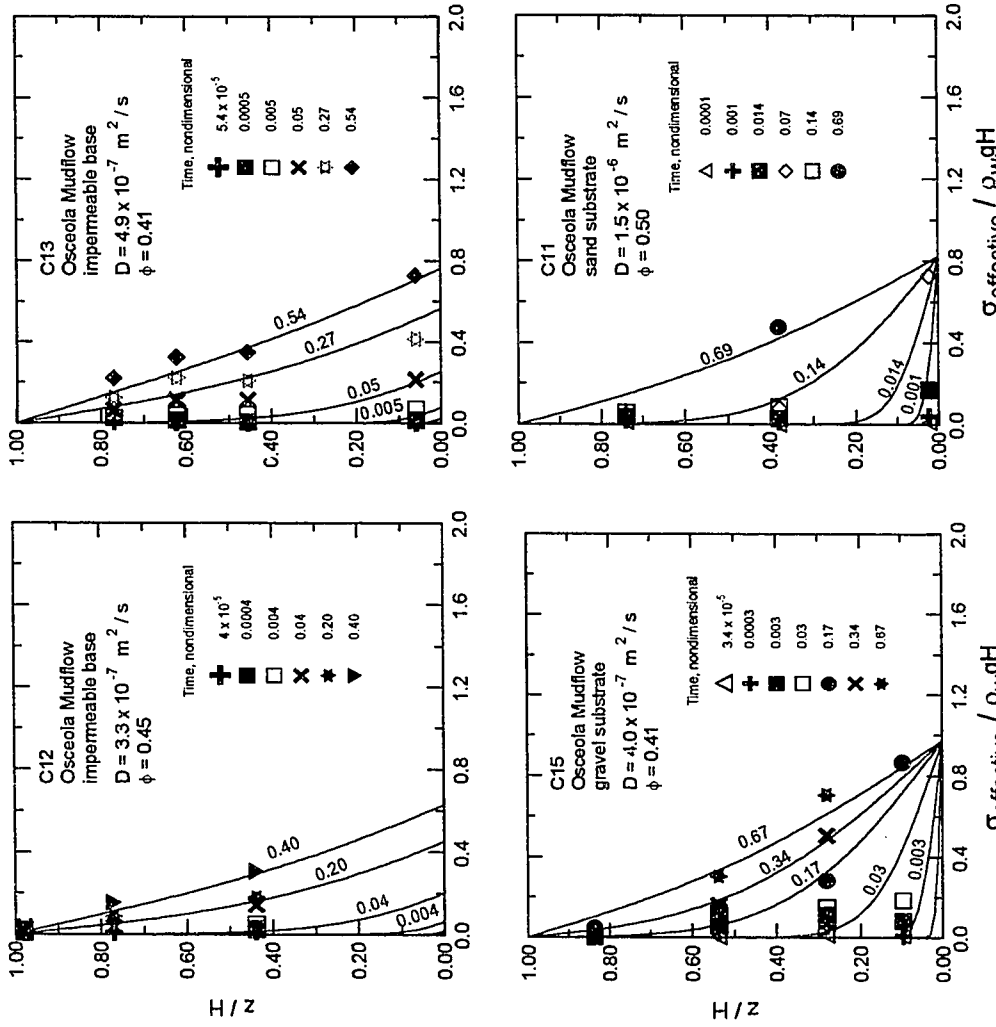
C13
Osceola Mudflow
impermeable base
D = 4.9 x 10^-7 m^2 / s
ϕ = 0.41
Time, nondimensional
5.4 x 10^-5
0.0005
0.005
0.05
0.27
0.54
C12
Osceola Mudflow
impermeable base
D = 3.3 x 10^-7 m^2 / s
ϕ = 0.45
Time, nondimensional
4 x 10^-5
0.0004
0.004
0.04
0.20
0.40
C11
Osceola Mudflow
sand substrate
D = 1.5 x 10^-6 m^2 / s
ϕ = 0.50
Time, nondimensional
0.0001
0.001
0.014
0.07
0.14
0.69
C15
Osceola Mudflow
gravel substrate
D = 4.0 x 10^-7 m^2 / s
ϕ = 0.41
Time, nondimensional
3.4 x 10^-5
0.0003
0.003
0.03
0.17
0.34
0.67
z / H
σeffective / ρwgH

Figure 3.9c

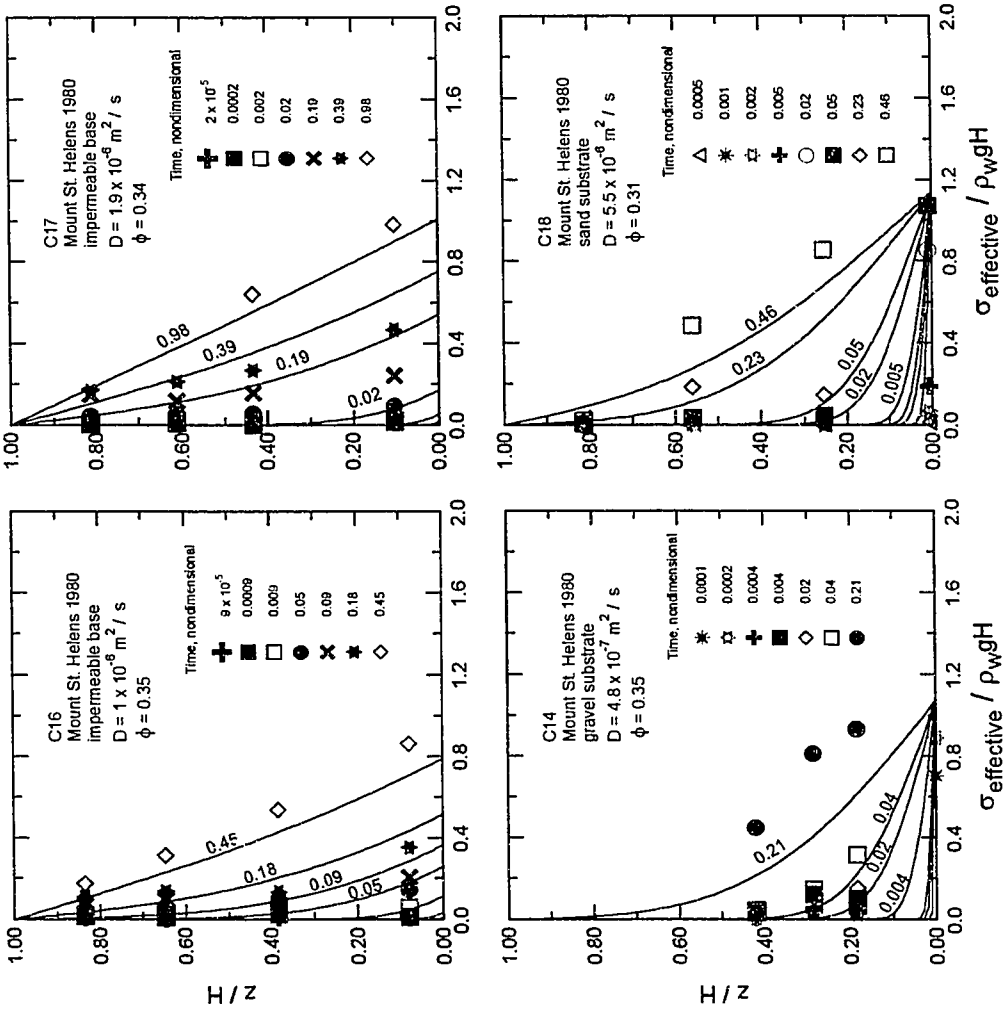
C16
Mount St. Helens 1980
impermeable base
D = 1 x 10^-6 m^2 / s
ϕ = 0.35
Time, nondimensional
9 x 10^-5
0.0009
0.009
0.05
0.09
0.18
0.45
C17
Mount St. Helens 1980
impermeable base
D = 1.9 x 10^-6 m^2 / s
ϕ = 0.34
Time, nondimensional
2 x 10^-5
0.0002
0.002
0.02
0.10
0.39
0.98
C14
Mount St Helens 1980
gravel substrate
D = 4.8 x 10^-7 m^2 / s
ϕ = 0.35
Time, nondimensional
0.0001
0.0002
0.0004
0.004
0.02
0.04
0.21
C18
Mount St Helens 1980
sand substrate
D = 5.5 x 10^-8 m^2 / s
ϕ = 0.31
Time, nondimensional
0.0005
0.001
0.002
0.005
0.02
0.05
0.23
0.46
z / H
σeffective / ρwgH

Figure 3.9d

Figure 3.10. Predicted transient behavior of volume strain in one-dimensional laboratory experiments. Position within slurry (z) is normalized by initial thickness of slurry. Volume strain at a given position is normalized by the volume strain at the base of the sediment column. Mean initial porosity (ϕ) is shown and the value of hydraulic diffusivity is the same as shown in previous figures. Each curve represents an increment of time, nondimensionalized to remove effects of length scale. A. Impermeable-bed experiments using loam mix. A bulk modulus of 10^5 Pa is assumed in the calculation. B. Permeable-bed experiments using loam mix. A bulk modulus of 10^5 Pa is assumed in the calculation (see text for discussion). C. Experiments using Osceola Mudflow sediment. A bulk modulus of 5×10^4 Pa is assumed in the calculation. D. Experiments using Mount St. Helens 1980 North Fork Toutle River debris-flow sediment. A bulk modulus of 10^5 Pa is assumed in the calculation (see text for discussion). See Figure 3.11 for determination of bulk modulus values.

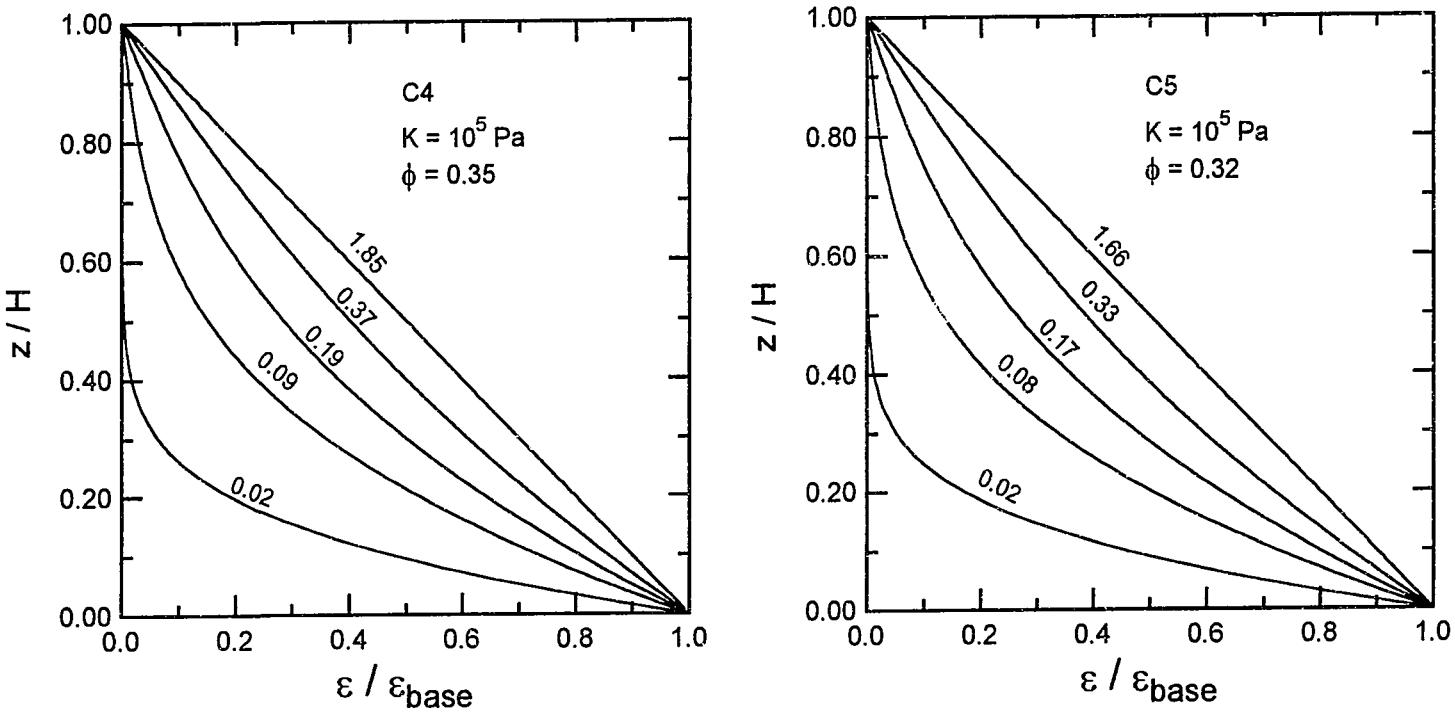
C4
K = 10^5 Pa
ϕ = 0.35
1.85
0.37
0.19
0.09
0.02
z / H
ε / ε_base
C5
K = 10^5 Pa
ϕ = 0.32
1.66
0.33
0.17
0.08
0.02
z / H
ε / ε_base

Figure 3.10a

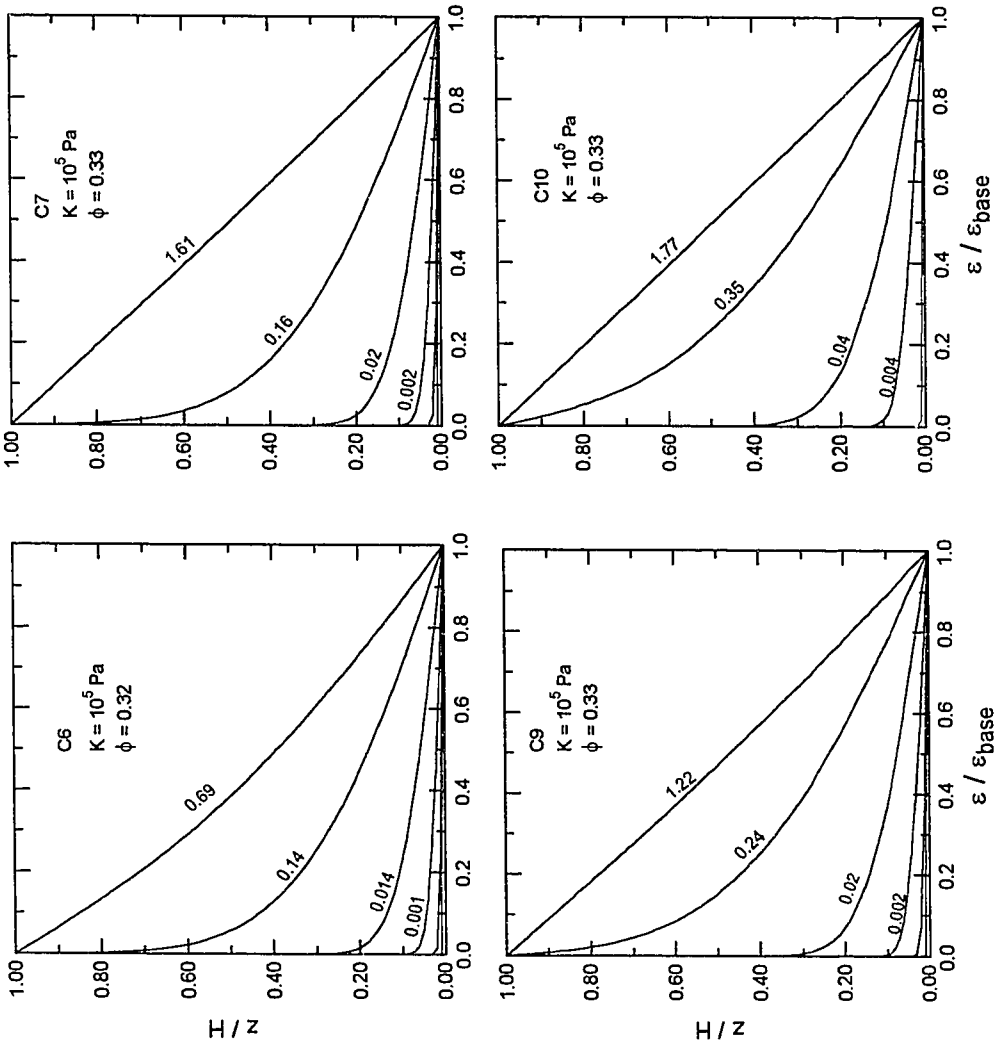
C7
K = 10^5 Pa
ϕ = 0.33
1.61
0.16
0.02
0.002
C10
K = 10^5 Pa
ϕ = 0.33
1.77
0.35
0.04
0.004
C6
K = 10^5 Pa
ϕ = 0.32
0.69
0.14
0.014
0.001
C9
K = 10^5 Pa
ϕ = 0.33
1.22
0.24
0.02
0.002
z / H
ε / ε_base

Figure 3.10b

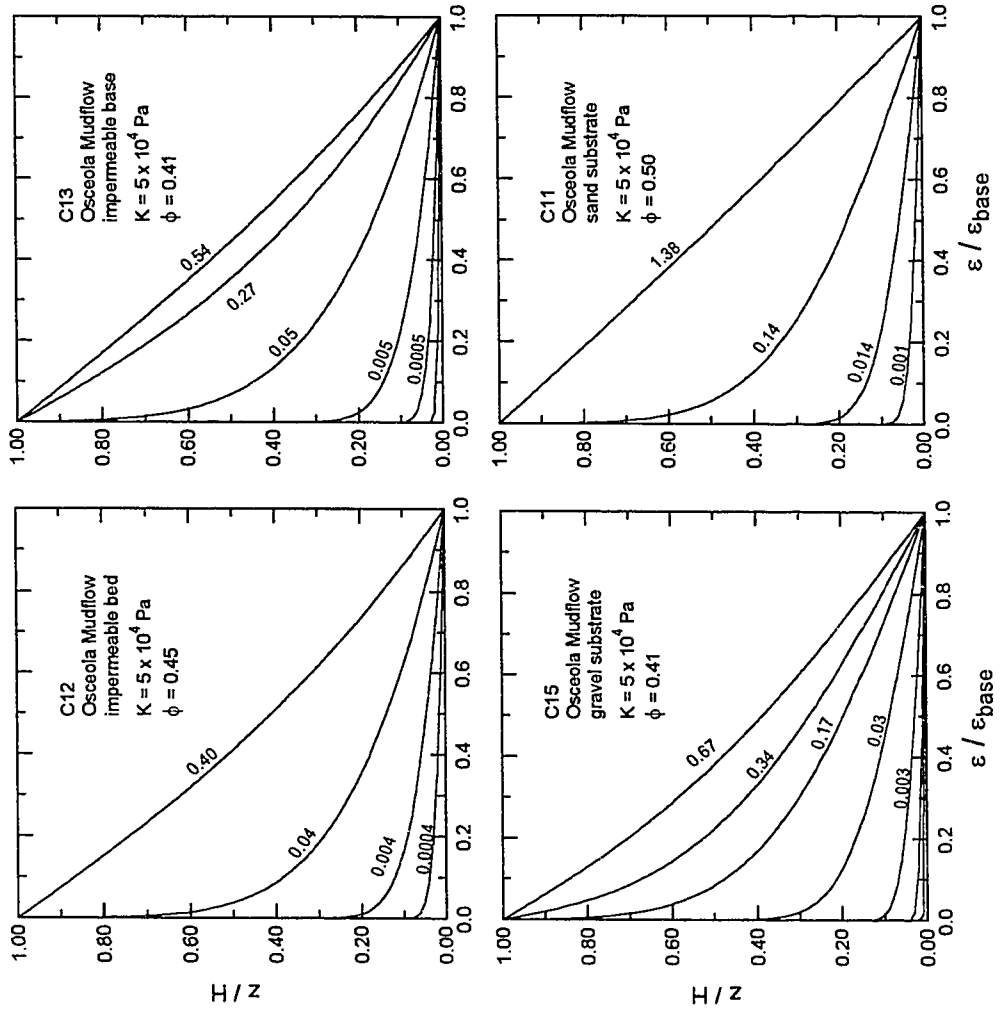
C13
Osceola Mudflow
impermeable base
K = 5 x 10^4 Pa
ϕ = 0.41
0.54
0.27
0.05
0.005
0.0005
C12
Osceola Mudflow
impermeable bed
K = 5 x 10^4 Pa
ϕ = 0.45
0.40
0.04
0.004
0.0004
C11
Osceola Mudflow
sand substrate
K = 5 x 10^4 Pa
ϕ = 0.50
1.38
0.14
0.014
0.001
C15
Osceola Mudflow
gravel substrate
K = 5 x 10^4 Pa
ϕ = 0.41
0.67
0.34
0.17
0.03
0.003
z / H
ε / εbase

Figure 3.10c

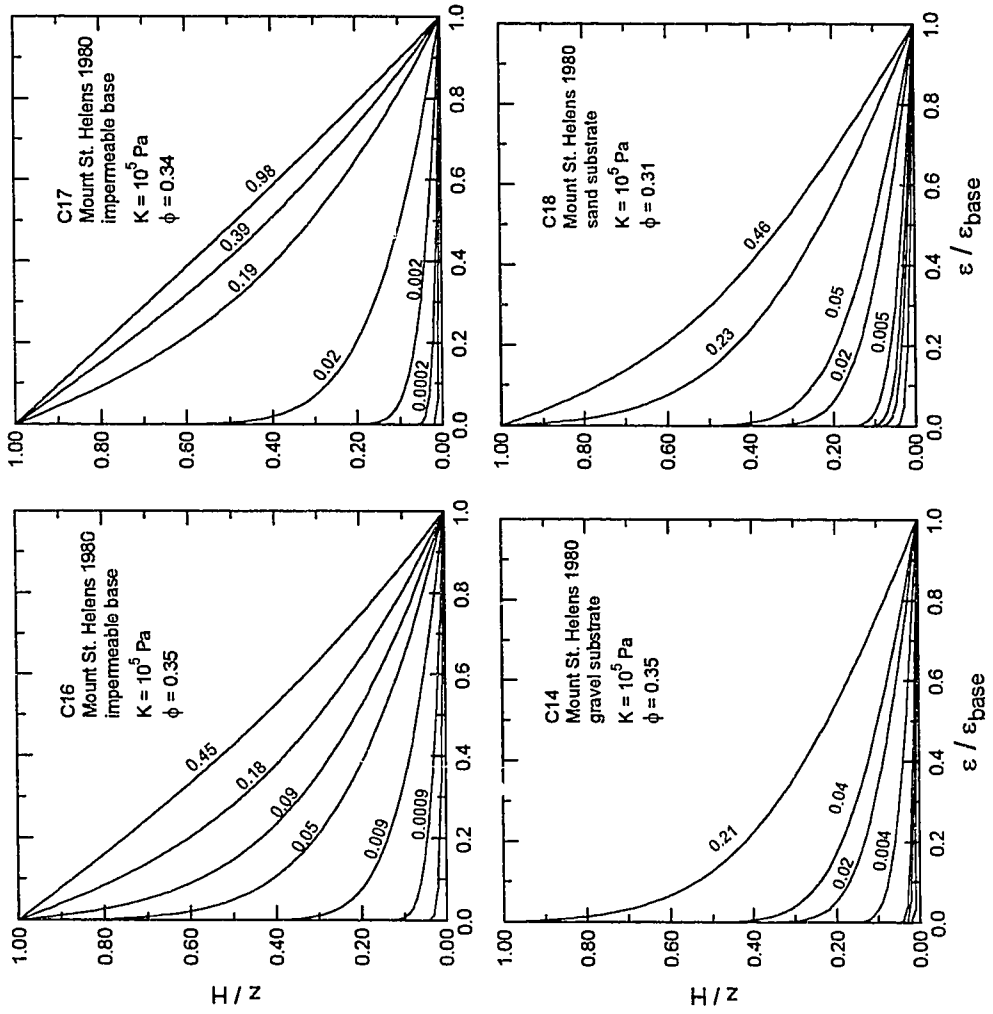
C16
Mount St. Helens 1980
impermeable base
K = 10^-6 Pa
ϕ = 0.35
0.45
0.18
0.09
0.05
0.009
0.0009
C17
Mount St. Helens 1980
impermeable base
K = 10^-5 Pa
ϕ = 0.34
0.98
0.39
0.19
0.02
0.002
0.0002
C14
Mount St. Helens 1980
gravel substrate
K = 10^-5 Pa
ϕ = 0.35
0.21
0.04
0.02
0.004
C18
Mount St. Helens 1980
sand substrate
K = 10^-5 Pa
ϕ = 0.31
0.46
0.23
0.05
0.02
0.005
z / H
ε / ε_base

Figure 3.10d

Figure 3.11. Comparison of predicted and measured transient behavior of surface displacement in one-dimensional laboratory experiments. Surface displacement (d) is normalized by initial thickness of slurry. Predicted displacement profiles for various values of bulk modulus are shown. A. Permeable-bed experiment using loam mix. B. Experiments using Osceola Mudflow sediment. C. Experiments using Mount St. Helens 1980 North Fork Toutle River debris-flow sediment.

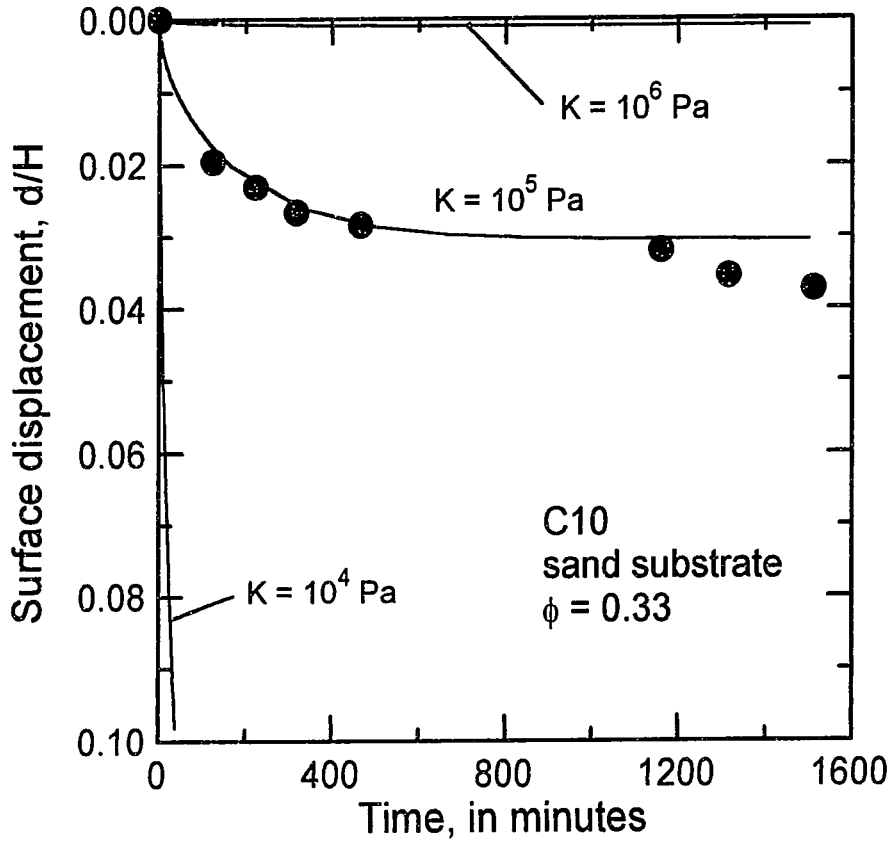
0.00
0.02
0.04
0.06
0.08
0.10
Surface displacement, d/H
K = 10^6 Pa
K = 10^5 Pa
K = 10^4 Pa
C10
sand substrate
ϕ = 0.33
0
400
800
1200
1600
Time, in minutes

Figure 3.11a

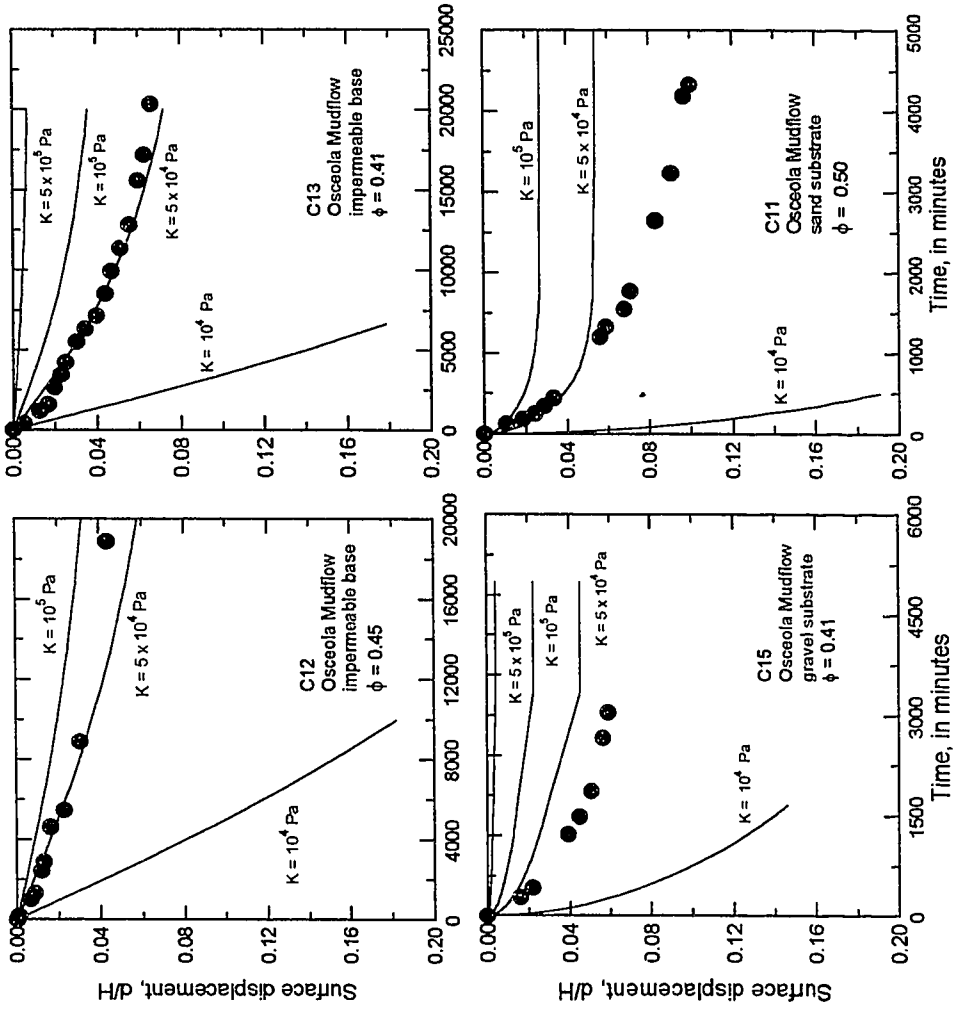
C13
Osceola Mudflow
impermeable base
ϕ = 0.41
K = 5 x 10^5 Pa
K = 10^5 Pa
K = 5 x 10^4 Pa
K = 10^4 Pa
C12
Osceola Mudflow
impermeable base
ϕ = 0.45
C11
Osceola Mudflow
sand substrate
ϕ = 0.50
C15
Osceola Mudflow
gravel substrate
ϕ = 0.41
Surface displacement, d/H
Time, in minutes

Figure 3.11b

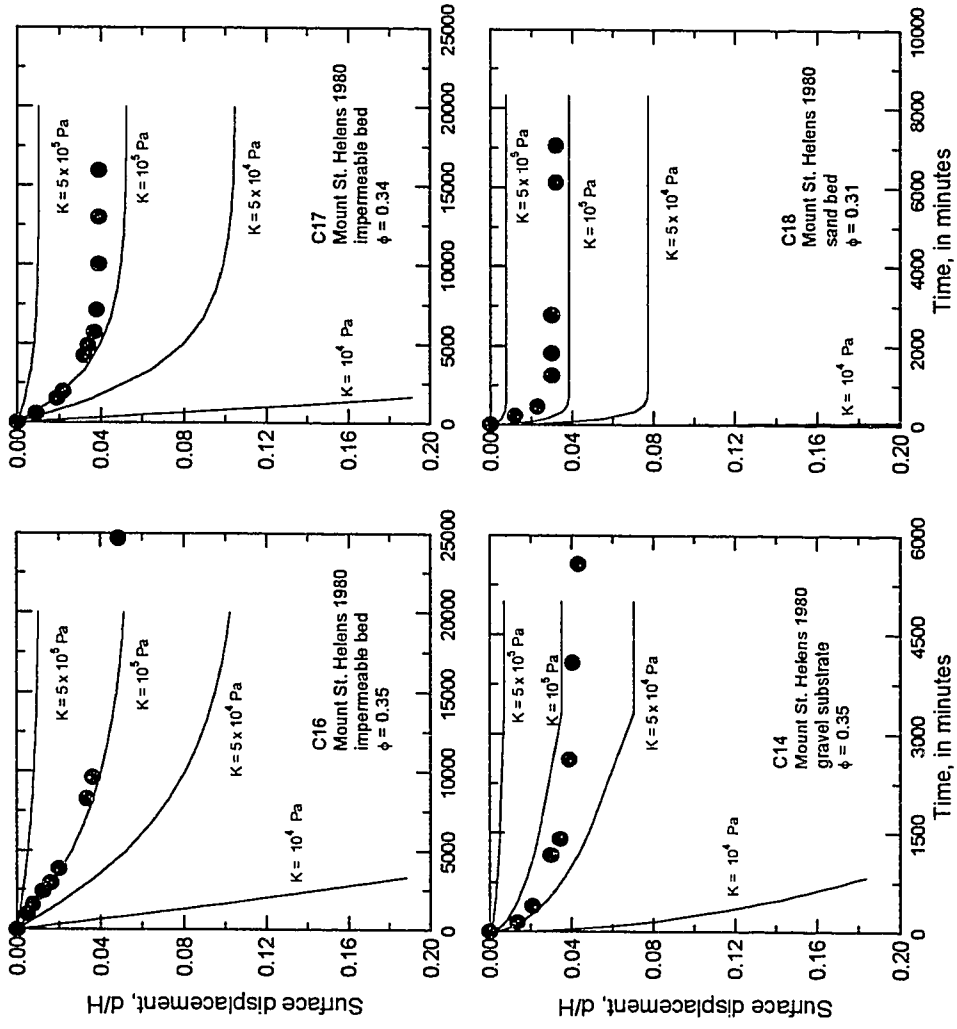
Surface displacement, d/H
Time, in minutes
C16
Mount St. Helens 1980
impermeable bed
ϕ = 0.35
C17
Mount St. Helens 1980
impermeable bed
ϕ = 0.34
C14
Mount St. Helens 1980
gravel substrate
ϕ = 0.35
C18
Mount St. Helens 1980
sand bed
ϕ = 0.31
K = 5 x 10⁵ Pa
K = 10⁵ Pa
K = 5 x 10⁴ Pa
K = 10⁴ Pa

Figure 3.11c

Figure 3.12. Comparison of predicted and measured transient behavior of nonequilibrium fluid pressure in experimental debris-flow deposits. Position within the deposit (z) is normalized by initial thickness of the deposit. Nonequlibrium fluid pressure is normalized by initial value of nonequilibrium fluid pressure at the base of the deposit. D is the best-fit value of hydraulic diffusivity.

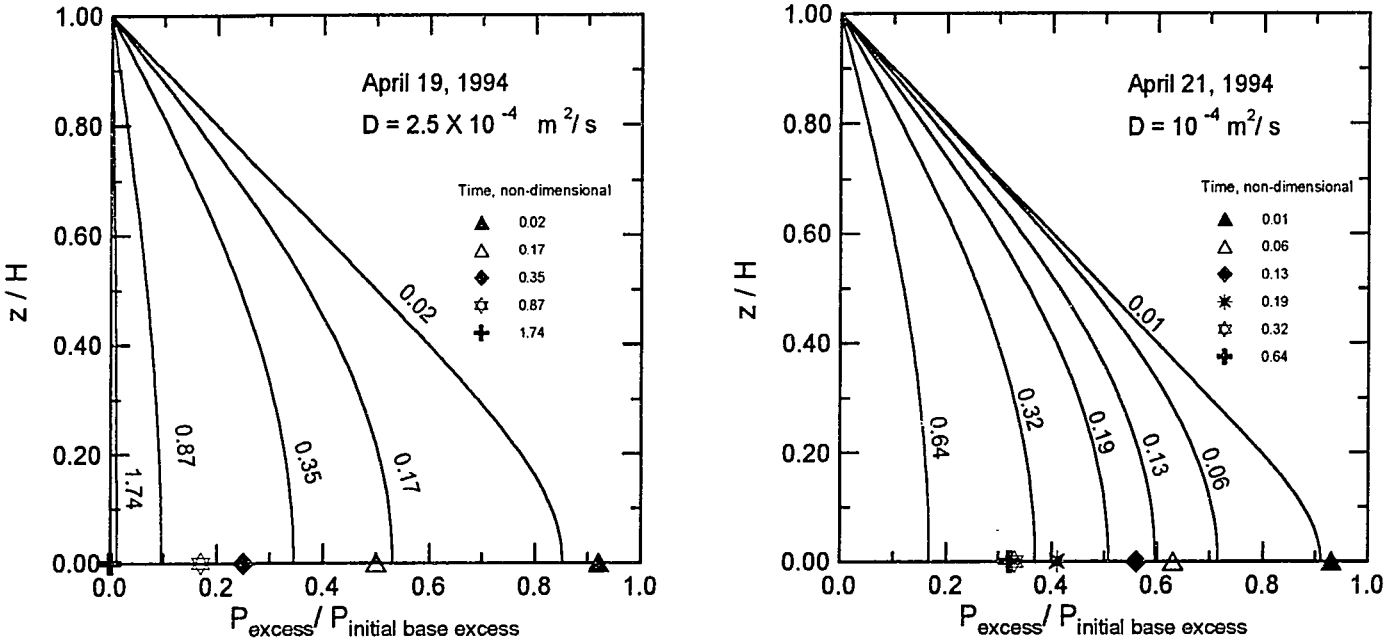
April 19, 1994
D = 2.5 X 10 -4 m 2/ s
Time, non-dimensional
0.02
0.17
0.35
0.87
1.74
z / H
P excess/ P initial base excess
April 21, 1994
D = 10 -4 m2/ s
Time, non-dimensional
0.01
0.06
0.13
0.19
0.32
0.64

Figure 3.12a

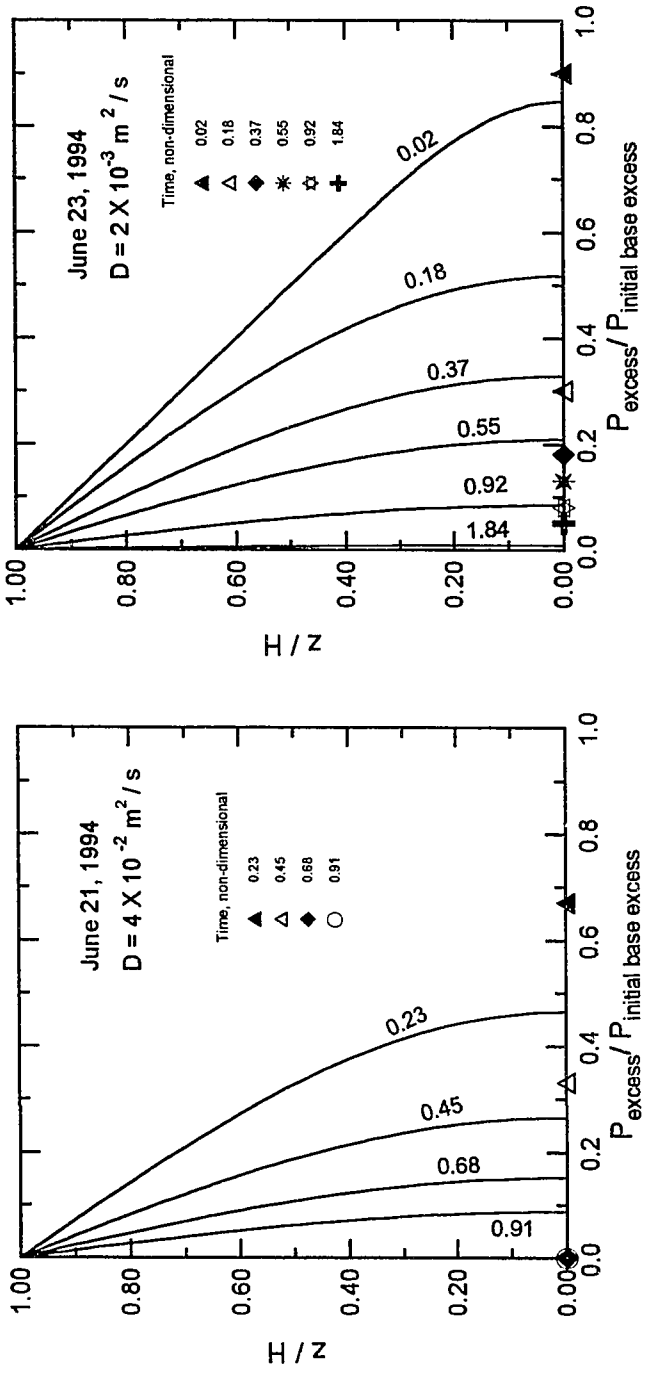
June 23, 1994
D = 2 X 10^-3 m^2 / s
Time, non-dimensional
0.02
0.18
0.37
0.55
0.92
1.84
0.02
0.18
0.37
0.55
0.92
1.84
H / z
P excess / P initial base excess
June 21, 1994
D = 4 X 10^-2 m^2 / s
Time, non-dimensional
0.23
0.45
0.68
0.91
0.23
0.45
0.68
0.91
H / z
P excess / P initial base excess

Figure 3.12b

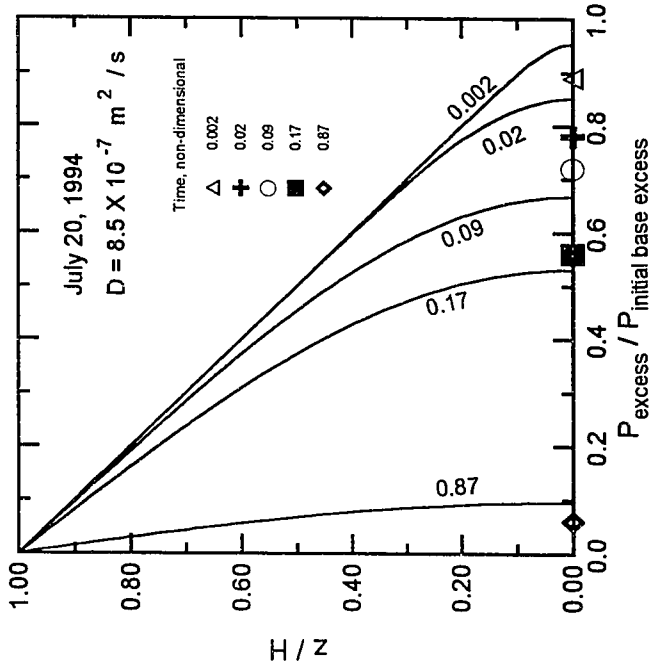
July 20, 1994
D = 8.5 X 10 -7 m 2 / s
Time, non-dimensional
0.002
0.02
0.09
0.17
0.87
0.002
0.02
0.09
0.17
0.87
H / z
1.00
0.80
0.60
0.40
0.20
0.00
0.0
0.2
0.4
0.6
0.8
1.0
P excess / P initial base excess

Figure 3.12c

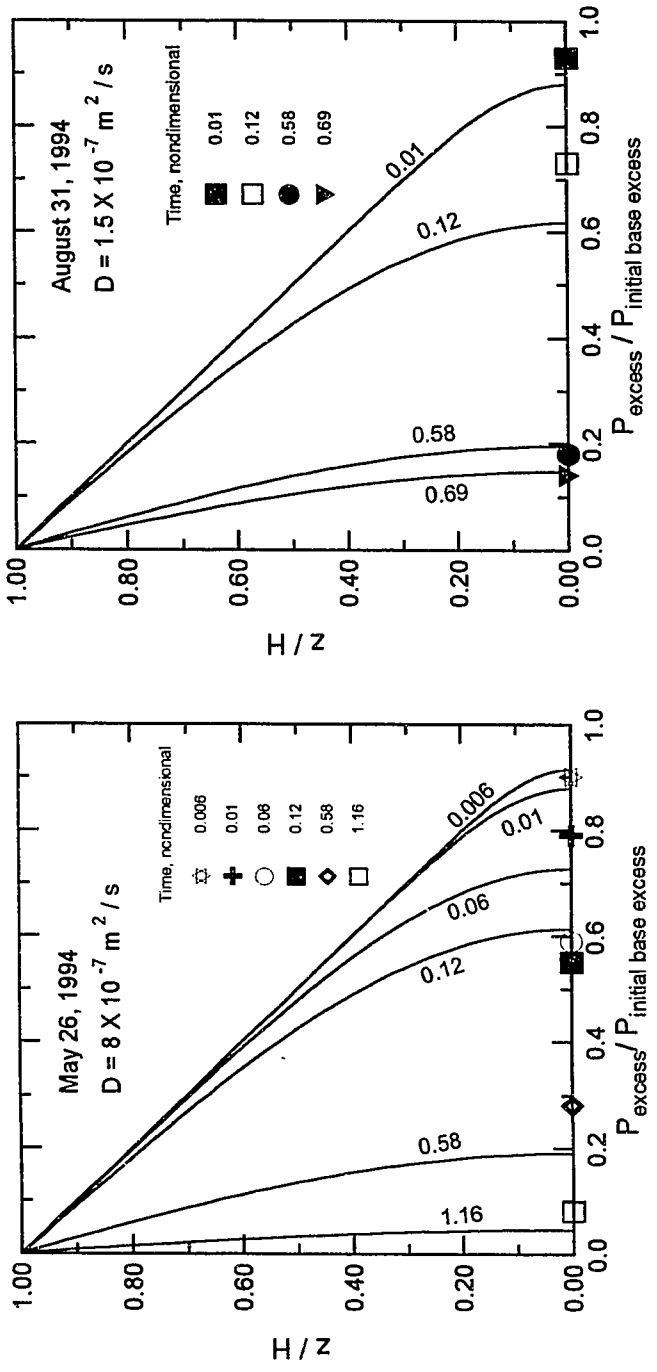
August 31, 1994
D = 1.5 X 10 -7 m 2 / s
Time, nondimensional
0.01
0.12
0.58
0.69
0.01
0.12
0.58
0.69
H / z
P excess / P initial base excess
May 26, 1994
D = 8 X 10 -7 m 2 / s
Time, nondimensional
0.006
0.01
0.06
0.12
0.58
1.16
0.006
0.01
0.06
0.12
0.58
1.16
H / z
P excess / P initial base excess

Figure 3.12d

Figure 3.13. Comparison of predicted and measured transient behavior of effective normal stress in experimental debris-flow deposits. Position within the deposit (z) is normalized by initial thickness of the deposit. Effective normal stress is normalized by the value of hydrostatic pressure ($\rho_w gH$) at the base of the deposit. The best-fit value of hydraulic diffusivity (D) and mean initial porosity (ϕ) are shown.

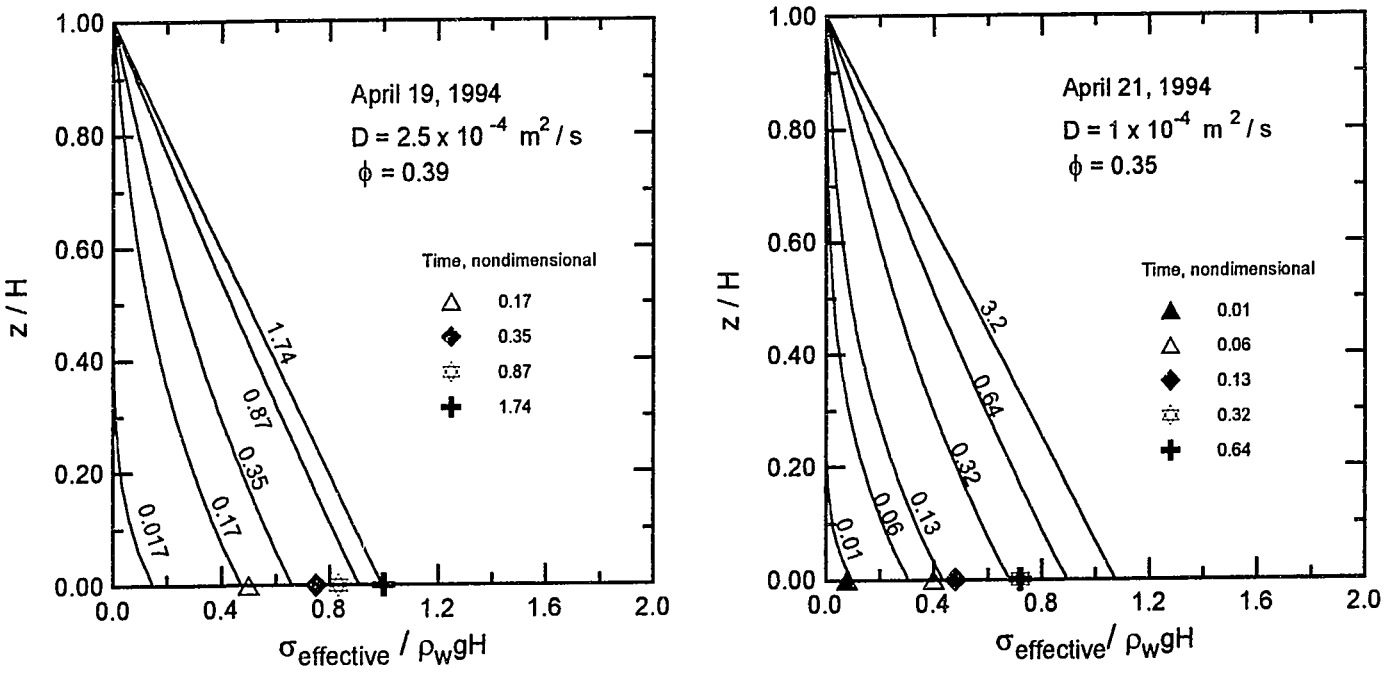
April 19, 1994
D = 2.5 x 10 -4 m2 / s
ϕ = 0.39
Time, nondimensional
0.17
0.35
0.87
1.74
1.74
0.87
0.35
0.17
0.017
z / H
σeffective / ρwgH
April 21, 1994
D = 1 x 10-4 m 2 / s
ϕ = 0.35
Time, nondimensional
0.01
0.06
0.13
0.32
0.64
3.2
0.64
0.32
0.13
0.06
0.01
z / H
σeffective/ ρwgH

Figure 3.13a

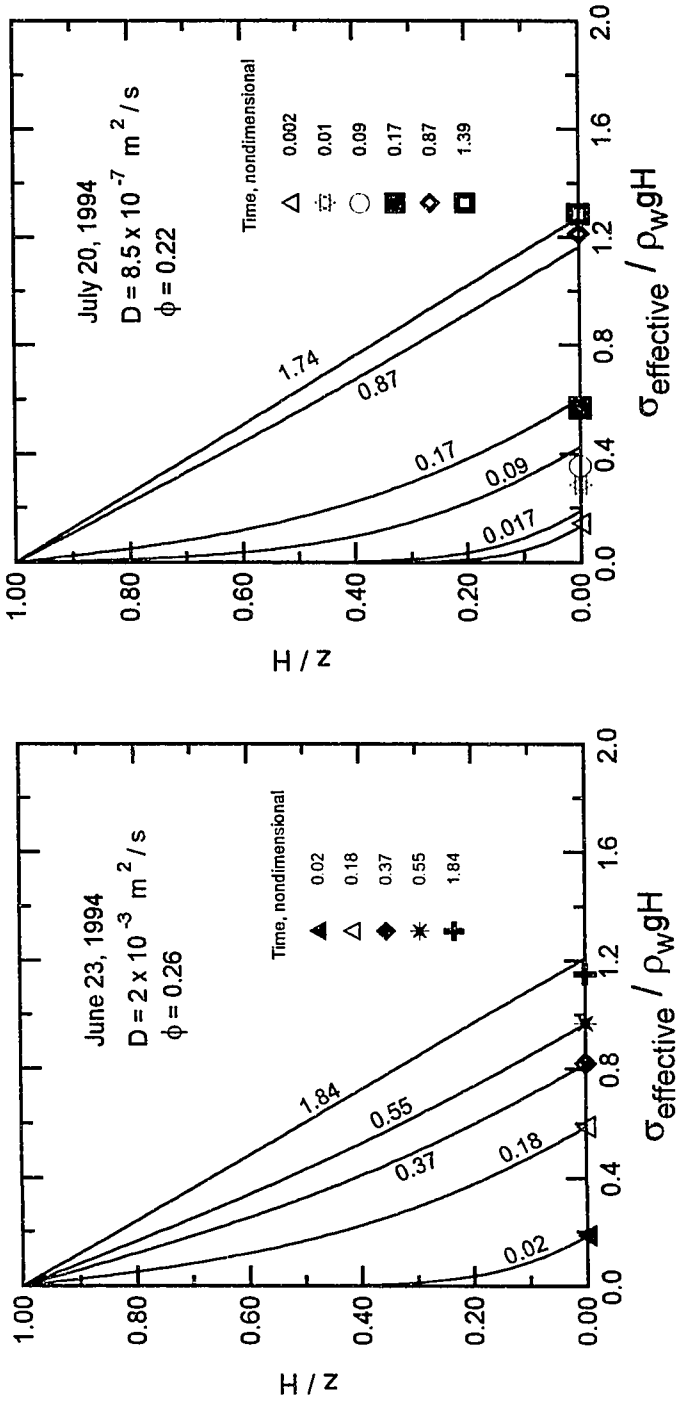
July 20, 1994
D = 8.5 x 10 -7 m 2 / s
ϕ = 0.22
Time, nondimensional
0.002
0.01
0.09
0.17
0.87
1.39
1.74
0.87
0.17
0.09
0.017
June 23, 1994
D = 2 x 10 -3 m 2 / s
ϕ = 0.26
Time, nondimensional
0.02
0.18
0.37
0.55
1.84
1.84
0.55
0.37
0.18
0.02
H / z
σeffective / ρwgH
1.00
0.80
0.60
0.40
0.20
0.00
0.0
0.4
0.8
1.2
1.6
2.0

Figure 3.13b

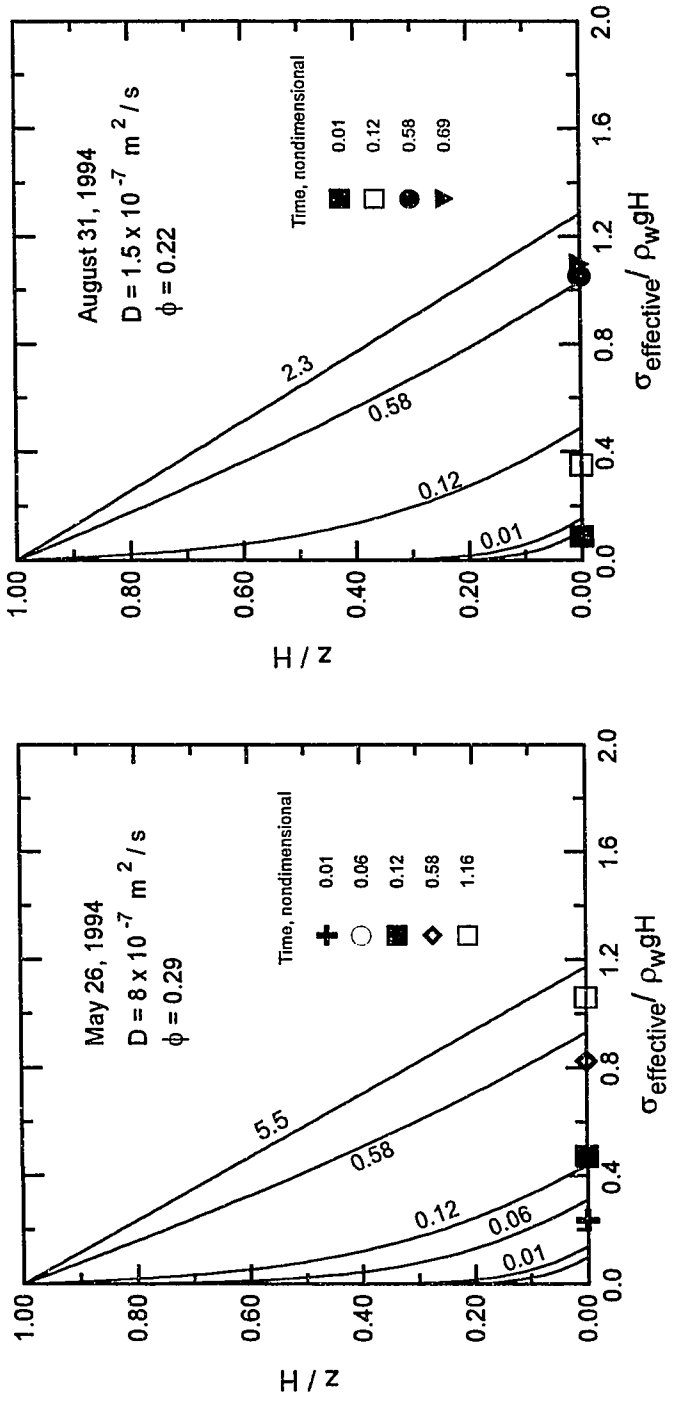
August 31, 1994
D = 1.5 x 10 -7 m 2 / s
ϕ = 0.22
Time, nondimensional
0.01
0.12
0.58
0.69
2.3
0.58
0.12
0.01
May 26, 1994
D = 8 x 10 -7 m 2 / s
ϕ = 0.29
Time, nondimensional
0.01
0.06
0.12
0.58
1.16
5.5
0.58
0.12
0.06
0.01
H / z
σeffective / ρwgH
1.00
0.80
0.60
0.40
0.20
0.00
0.0
0.4
0.8
1.2
1.6
2.0

Figure 3.13c

Figure 3.14. Predicted transient behavior of volume strain in experimental debris-flow deposits. Position within the deposit (z) is normalized by initial thickness of the deposit. Volume strain at a given position is normalized by the volume strain at the base of the deposit. Mean initial porosity (ϕ) is shown and the value of hydraulic diffusivity is the same as shown in previous figures. The effective bulk modulus used in the calculations is that determined from laboratory experiments using the May 26, 1994 sediment.

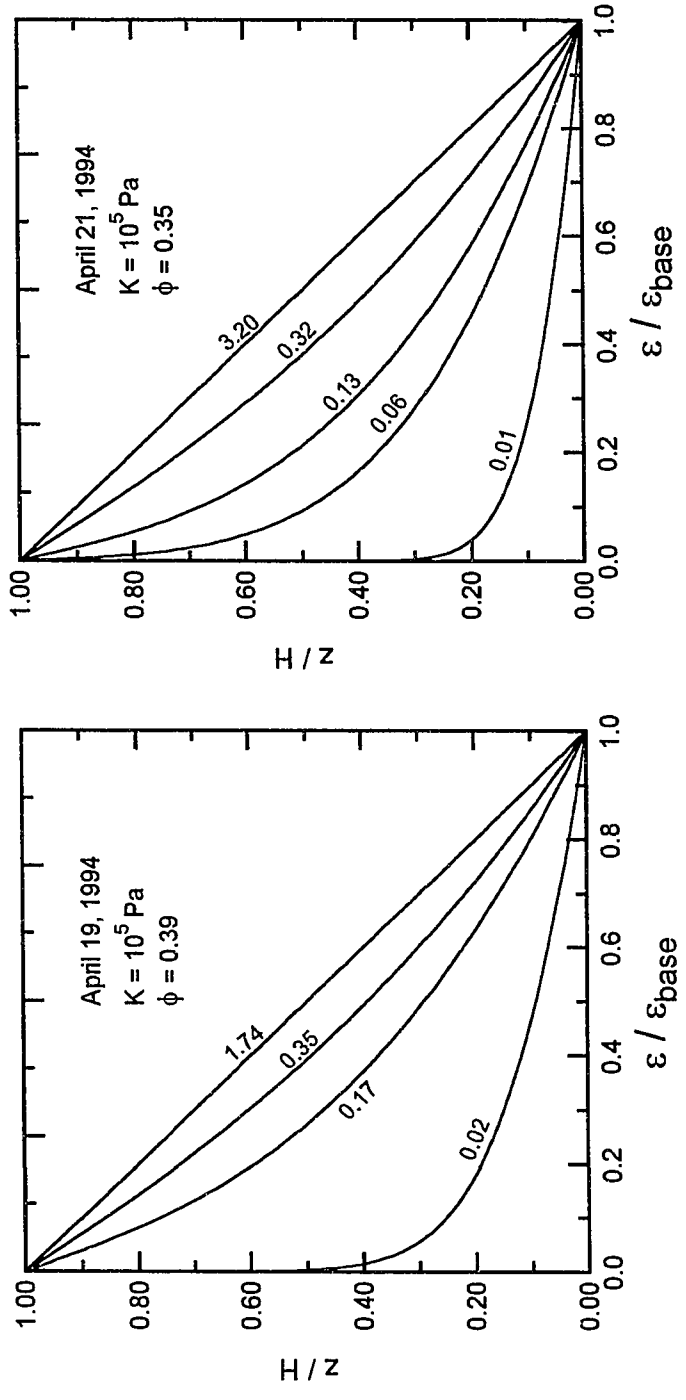
April 21, 1994
K = 10^5 Pa
ϕ = 0.35
3.20
0.32
0.13
0.06
0.01
April 19, 1994
K = 10^5 Pa
ϕ = 0.39
1.74
0.35
0.17
0.02
H / z
ε / εbase
1.00
0.80
0.60
0.40
0.20
0.00
0.0
0.2
0.4
0.6
0.8
1.0

Figure 3.14a

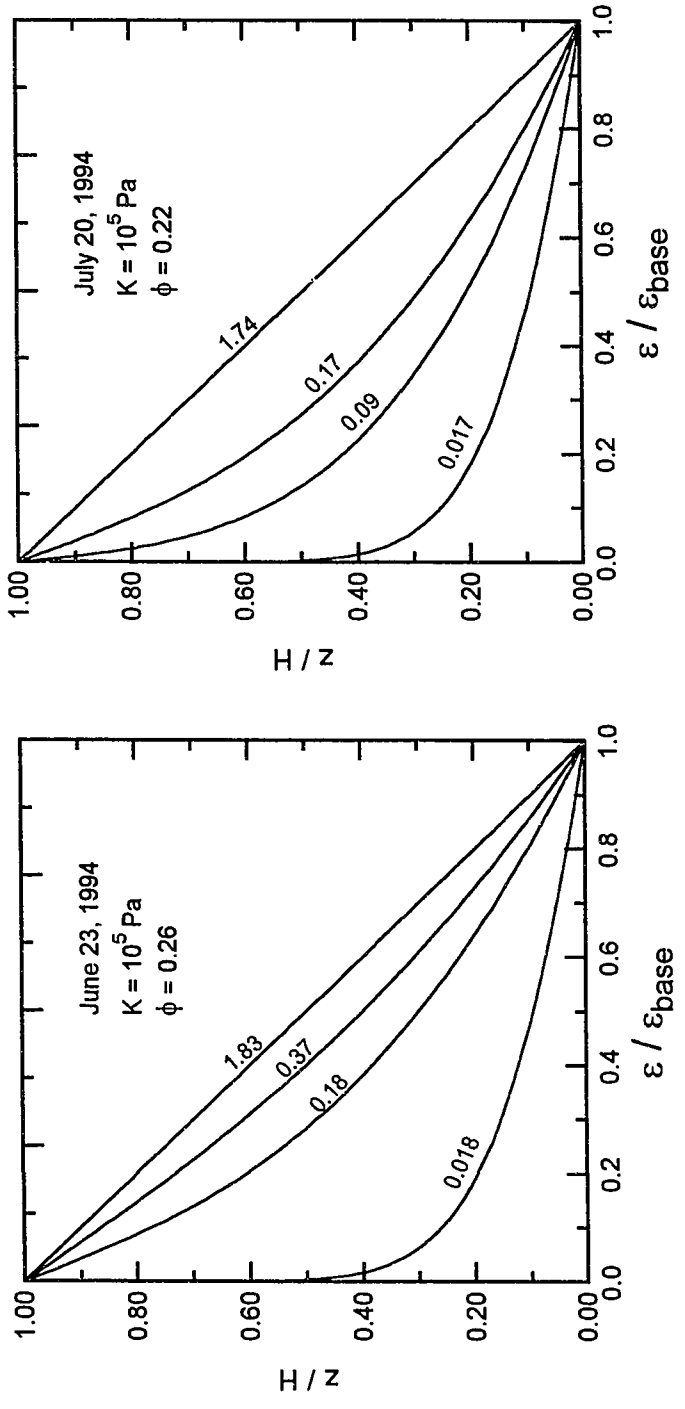
July 20, 1994
K = 10^5 Pa
ϕ = 0.22
1.74
0.17
0.09
0.017
H / z
ε / εbase
June 23, 1994
K = 10^5 Pa
ϕ = 0.26
1.83
0.37
0.18
0.018
H / z
ε / εbase

Figure 3.14b

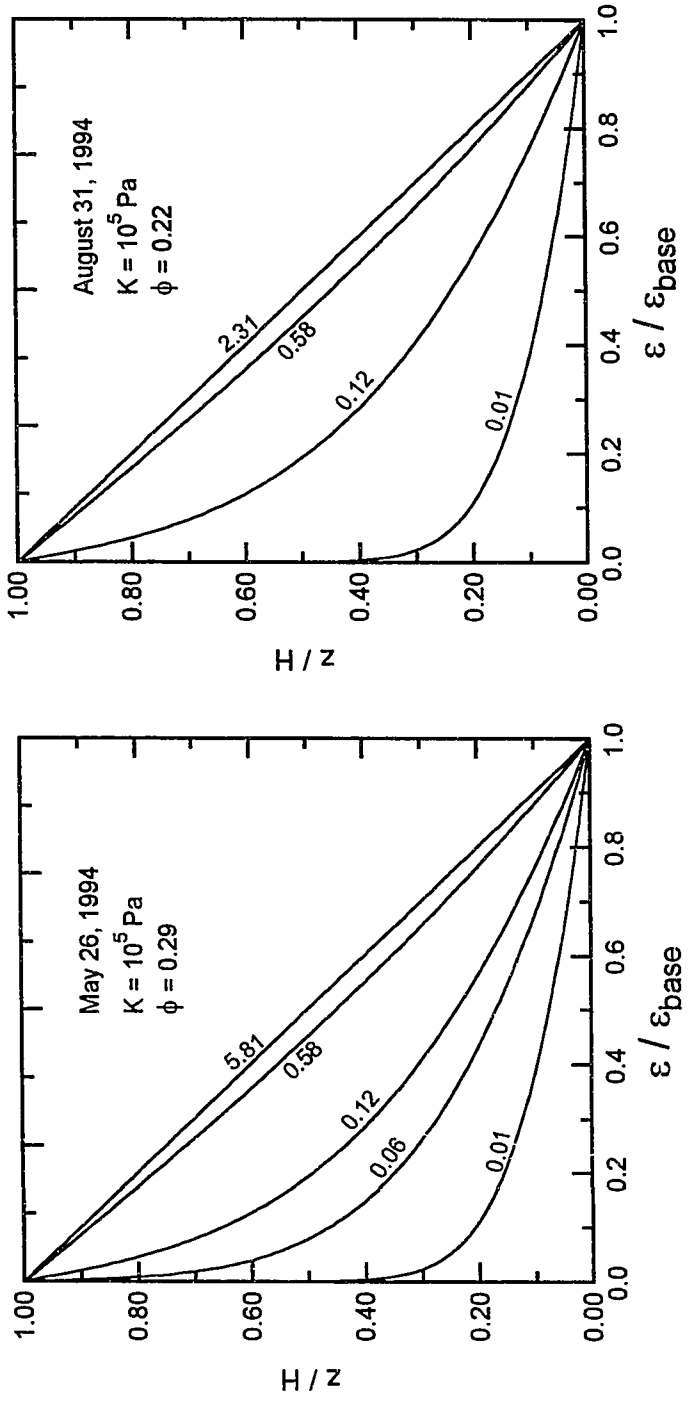
August 31, 1994
K = 10^5 Pa
ϕ = 0.22
2.31
0.58
0.12
0.01
May 26, 1994
K = 10^5 Pa
ϕ = 0.29
5.81
0.58
0.12
0.06
0.01
H / z
ε / ε_base
1.00
0.80
0.60
0.40
0.20
0.00
0.0
0.2
0.4
0.6
0.8
1.0

Figure 3.14c

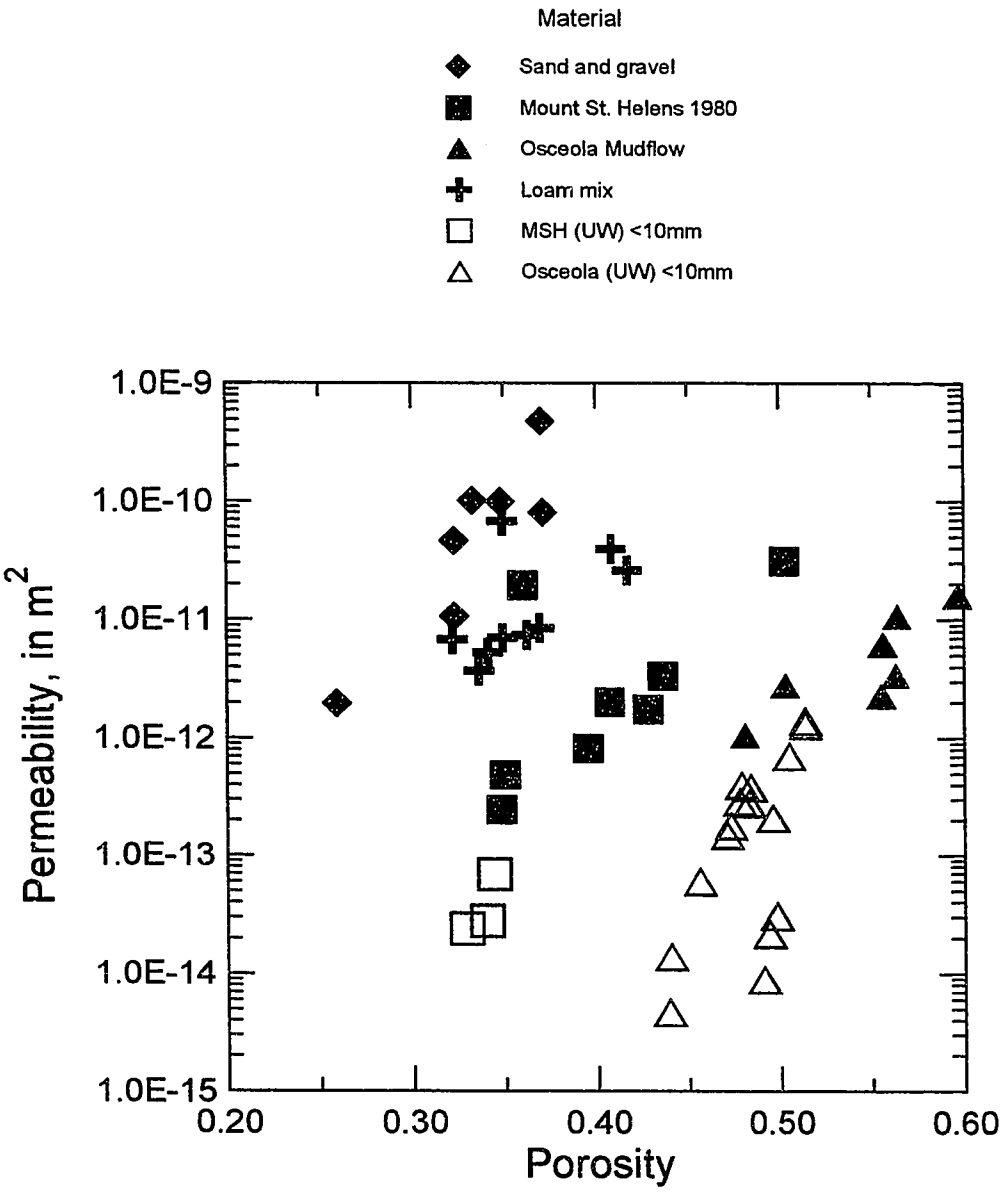

Figure 3.15. Relation between permeability and porosity based on constant-head permeameter tests. Solid symbols represent compaction-permeameter data; open symbols are triaxial load cell data (see Appendix B). Specimens included particles as large as 32 mm. Note that the permeability of debris having a broad range of physical characteristics varies by 5 orders of magnitude.

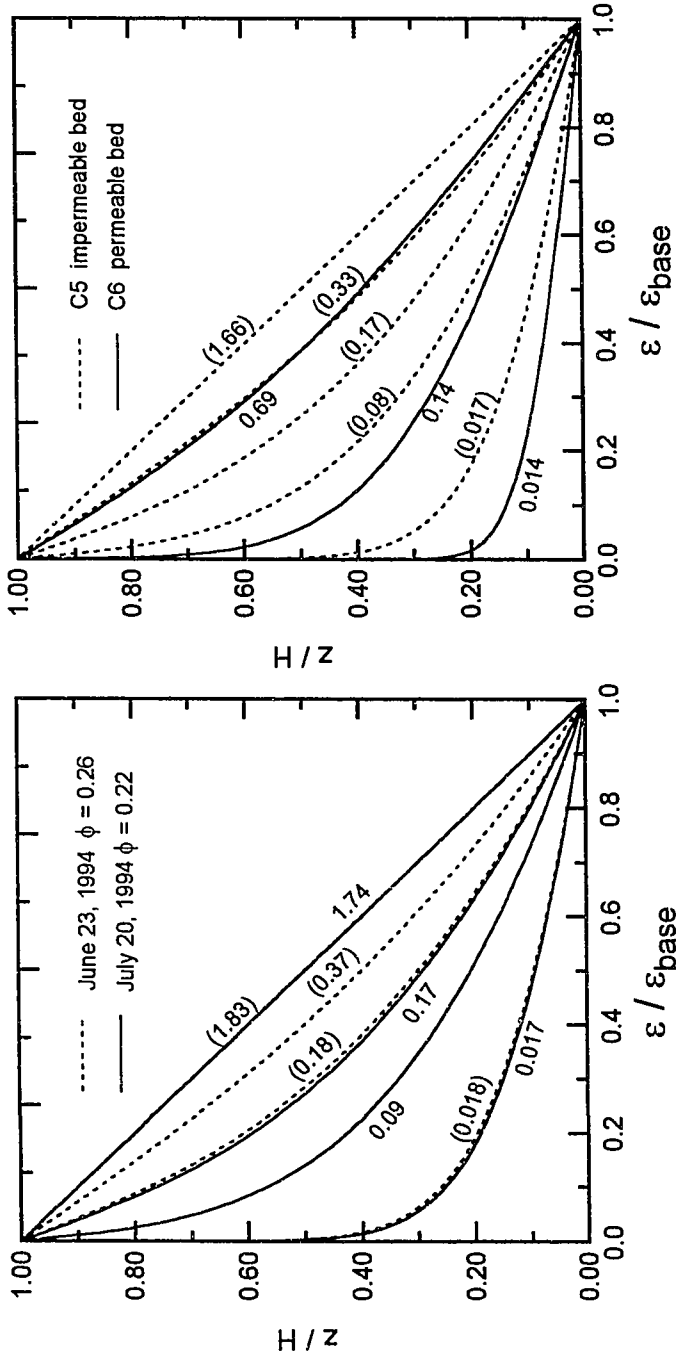

Figure 3.16. Comparisons of predicted transient volume strain. Times are nondimensional (see text). Times in ( ) refer to dashed lines. Left diagram shows predicted profiles for experimental debris-flow deposits having different sediment compositions but similar boundary conditions. Right diagram shows predicted profiles for one-dimensional laboratory experiments having same sediment composition but different basal boundary conditions.

CHAPTER 4

NUMERICAL ANALYSIS OF GRAVITY-DRIVEN, TWO-DIMENSIONAL CONSOLIDATION OF DEBRIS-FLOW SLURRIES

INTRODUCTION

Large-scale debris-flow experiments reveal that pore-fluid pressure is distributed nonuniformly behind the front of an advancing flow (Iverson, 1995a). Measurements also reveal that fluid pressure capable of balancing a substantial fraction of the weight of overlying debris persists during deceleration and deposition of debris (Chapter 3). Therefore, sediment deposition by debris flows occurs despite a broad distribution of nearly lithostatic pore-fluid pressure. Analysis of one-dimensional gravity-driven consolidation shows that small amounts of fine sediment greatly affect the migration of pore-fluid and the diffusion of pore-fluid pressure. Yet, experimental debris flows composed of sand, gravel, and loam did not travel farther than flows of comparable volume composed solely of sand and gravel (see Chapter 2). The measurements of high pore-fluid pressures *during* debris-flow deceleration and deposition and the nature of fluid-pressure diffusion in quasistatically consolidating debris indicate that uniform, bodywide dissipation of nonequilibrium fluid pressure does not control debris-flow deposition and that simple one-dimensional diffusion of fluid pressure is not the only factor affecting sediment deposition.

Debris flows and their deposits are three-dimensional bodies that have finite length and width as well as depth. Thus, when a debris flow deposits sediment, fluid can drain laterally as well as vertically from the deposit. In Chapter 3 I discussed the effect of a gravitational body force on simple, one-dimensional consolidation and showed that transient fluid-pressure and effective-stress fields evolve upward from the base of the body rather than downward from the top. Intuitively, then, if fluid is allowed to drain laterally as well as vertically, the transient responses of pore-fluid pressure and effective stress might evolve inward from the margins as well as upward from the base of deposit. But to what extent does lateral fluid flow modify one-dimensional gravity-driven fields? Does lateral fluid flow significantly change the time scale over which gravity-driven transient fields respond? If so, what are the pertinent conditions that produce significant modification of the response? These questions motivate a more general analysis of gravity-driven consolidation than the kinematically

restrictive one-dimensional analysis. In this chapter I examine two-dimensional consolidation numerically.

Biot (1941) introduced a general three-dimensional theory of consolidation in which changes in the stress field and the fluid-pressure field are coupled through changes in the strain field. That theory reduces to the more restrictive one-dimensional theory of consolidation proposed by Terzaghi (1923) when domain constituents are incompressible. A primary consequence of the one-dimensional theory is that the fluid-pressure field and the effective-stress field become uncoupled. As shown in Chapter 3, evolution of the fluid-pressure field in a one-dimensional problem is determined independently of the effective-stress field. The fluid-pressure and effective-stress fields do not uncouple for a multidimensional domain (e.g., Biot, 1941; Rice and Cleary, 1976; Roeloffs, 1988, 1996). In general, total stresses are not constant in space or time in the presence of two- or three-dimensional strain fields. The stress field and the fluid-pressure field in multidimensional domains uncouple only after these fields have achieved a steady state (Iverson and Reid, 1992). When debris-flow deposits that have finite length, width and depth consolidate, there is a feedback between the fluid-pressure and the effective-stress fields, especially near deposit margins where local fluid drainage certainly has multidimensional components and the strain field cannot be considered one dimensional.

MATHEMATICAL FORMULATION

The mathematical formulation for gravitationally induced stress and fluid-pressure changes in a two-dimensional, linearly elastic, porous body relies on expressions for the equilibrium of stresses, strains, mass balance, Darcy's law, compatibility, and constitutive equations that relate strains in a porous body and changes in the fluid mass content of the solid-fluid system to the state of stress and fluid pressure. The following development follows largely from works of Biot (1941), Rice and Cleary (1976), McTigue (1986, 1990), and Iverson and Reid (1992). Most treatments of poroelastic problems (e.g., Biot, 1941; Rice and Cleary, 1976; McTigue, 1986) omit gravitational potential of the pore fluid and also omit body forces acting on the system owing to the weight of the solid particles that make up the porous medium. In those studies, systems were assumed to be in geostatic equilibrium; only perturbations to this equilibrium state were considered. Body forces need to be included for the problem considered here, namely, that of gravity-driven, or self-weight,

deformation of a granular sediment slurry. The following treatment closely follows that of Iverson and Reid (1992), who incorporated a gravitational body force, but is cast in terms of fluid pressure rather than in terms of hydraulic head which is more suitable for analyses of groundwater flow and failure potential in hillslopes. In the following development, I assume that granular slurries are isothermal, that the pore fluid and the solid grains are incompressible, and that slurries are isotropic. Adopting the simplest possible approach, I assume that the porous skeleton of a slurry can be represented as a linearly elastic material subject only to infinitesimal strain, an assumption that requires that changes in porosity of the slurry are small. These assumptions would be relaxed in a more general treatment of the problem.

It may be argued that geological materials are inherently inelastic and that most geologic systems are inherently nonlinear. Indeed, in Chapter 3 I demonstrated that even simple one-dimensional consolidation of shallow slurries under low effective stresses is intrinsically nonlinear. In the face of these challenges, however, I adopt the simplifications stated above for reasons articulated by McTigue (1990): (1) a principal benefit of performing a simplified analysis is that it provides substantial insight into the physics of complex problems; (2) analyses of simplified systems permit one to distinguish clearly phenomena that are the result of boundary conditions imposed on the system from those that are the result of the material response; and (3) a simplified analysis lays the foundation upon which more complex analyses can be built.

In the following formulation indicial notation is used, and i, j, k refer to directions in a Cartesian coordinate system. The usual rule for summation over repeated indices applies. Following common practice in mechanics literature, stresses are defined positive in tension and fluid pressure positive in compression.

STRAIN, DISPLACEMENT, AND COMPATIBILITY

The most fundamental expressions that describe material deformation concern strains and their relations to material displacements. In the following formulation, displacements in the skeleton of a porous body are assumed to be small in comparison with the dimensions of the body; strains are assumed to be linear for short periods of stress application. Within these limitations, infinitesimal strains in the skeleton of a porous medium can be cast in terms of linear displacement gradients as

$$\varepsilon_{ij} = \frac{1}{2}\left(\frac{\partial u_j}{\partial x_i} + \frac{\partial u_i}{\partial x_j}\right). \tag{4.1}$$

For the two-dimensional problem considered here, these strains can be written explicitly as

$$\varepsilon_{xx} = \frac{\partial u_x}{\partial x} \tag{4.2a}$$

$$\varepsilon_{zz} = \frac{\partial u_z}{\partial z} \tag{4.2b}$$

$$\varepsilon_{zx} = \frac{1}{2}\left(\frac{\partial u_z}{\partial x} + \frac{\partial u_x}{\partial z}\right). \tag{4.2c}$$

In these expressions, u_x and u_z represent linear displacements of the solid material in the directions of the x and z coordinates, ε_{xx} and ε_{zz} represent the normal strains in the coordinate directions, and $\varepsilon_{zx}=\varepsilon_{xz}$ represent symmetric shear strains acting on planes perpendicular to the applied normal stress.

To ensure that no singularities exist between strains and displacements, and to prevent solutions that might satisfy equilibrium equations but not strain and displacement conditions, a kinematic compatibility constraint on the strain and displacement fields is introduced (e.g., Timoshenko and Goodier, 1970). This constraint is achieved by differentiating and combining equations (4.2a)-(4.2c), which yields

$$\frac{\partial^2 \varepsilon_{xx}}{\partial z^2} + \frac{\partial^2 \varepsilon_{zz}}{\partial x^2} = 2\frac{\partial^2 \varepsilon_{zx}}{\partial x \partial z}. \tag{4.3}$$

BALANCE OF LINEAR MOMENTUM -- THE STRESS-EQUILIBRIUM EQUATIONS

For a two-phase mixture of fluid and solid, balance laws can be written for each separate phase and then combined to yield a balance law for the mixture. The balance law of linear momentum to be satisfied states that the rate of change of linear momentum of the system is balanced by the momentum added to the system, the momentum lost from the system, and the sum of forces acting on the system. This balance leads to the well-known Cauchy equations of stress equilibrium.

The balance of linear momentum for the fluid within a quasistatically deforming mixture can be written (neglecting inertial terms) as

$$\frac{\partial \sigma^{f}_{ji}}{\partial x_j} + \rho_f \phi g_i - m_i = 0 \qquad (4.4)$$

where the first term on the left hand side represents the surface forces per unit volume of mixture, here total fluid pressure, acting on the fluid (σ^{f}_{ji}); the second term represents the gravitational body force acting on a unit volume of fluid, where ρ_f is the density of the pore fluid, ϕ is the volume fraction of fluid, or porosity of the body, and g_i is the gravitational acceleration in the coordinate direction; and the third term represents a rate of momentum exchange (loss) between the fluid and the solid matrix as a result of fluid drag, commonly assumed to be a simple viscous drag, which acts as a body force on the system.

The balance of linear momentum for the skeleton of solids in a quasistatically deforming mixture is given by

$$\frac{\partial \sigma^{s}_{ji}}{\partial x_j} + \rho_s (1-\phi) g_i + m_i = 0. \qquad (4.5)$$

Here, the first term on the left hand side represents surface forces per unit volume of mixture acting on the solids (σ^{s}_{ji}); the second term represents the gravitational body force acting on a unit volume of solids, where ρ_s is the grain density and $(1-\phi)$ is the volume fraction of solids; and the third term

represents momentum gained by the solid matrix as the result of fluid drag, which acts as a body force on the system. Combining (4.4) and (4.5) yields an expression for the balance of linear momentum for the solid-fluid mixture:

$$\frac{\partial \sigma_{ji}}{\partial x_j} + \rho_t g_i = 0 \tag{4.6}$$

where σ_{ji} are the quasistatic components of total stress ($\sigma^f_{ji}+\sigma^s_{ji}$), and ρ_t is the total bulk density of the solid-fluid system, defined as $\rho_f \phi+\rho_s (1-\phi)$.

The stress-equilibrium equations for the two-dimensional problem in which the z-component of the coordinate system is defined vertically upward above an arbitrary datum (Figure 4.1), and in which gravitational acceleration acts exclusively in the negative z direction, can be written explicitly from (4.6) as

$$\frac{\partial \sigma_{xx}}{\partial x} + \frac{\partial \sigma_{zx}}{\partial z} = 0 \tag{4.7a}$$

$$\frac{\partial \sigma_{zx}}{\partial x} + \frac{\partial \sigma_{zz}}{\partial z} - \rho_t g = 0. \tag{4.7b}$$

STRESS PARTITIONING -- THE EFFECTIVE STRESS CONCEPT

The stress-equilibrium equations (4.7a) and (4.7b) are cast in terms of total stresses. In a saturated porous medium, the total stresses acting on a system are partitioned between the stresses acting on the solid material and the pressures in the pore fluid. This partitioning of the total stress is conveniently expressed by introducing the concept of effective stress (Terzaghi, 1923; Skempton, 1960). The most general form of effective stress can be written as (e.g., Hubbert and Rubey, 1959)

$$\sigma'_{ij} = \sigma_{ij} + \alpha p \delta_{ij} \tag{4.8}$$

where σ'_{ij} is the effective stress, p is the pointwise total fluid pressure, and δ_{ij} is the Kronecker delta. Stress-equilibrium equations based on Biot-type constitutive relations (discussed below) are compatible with standard Hookean elastic equations only if $\alpha = (1\text{-}K_b/K_s)$ (Iverson and Reid, 1992), where K_b is the bulk modulus of the porous medium and K_s is the bulk modulus of individual solid grains. The effective stress rule most commonly used for partitioning the total stress acting in soils and in other granular Coulomb materials is given by (e.g., Terzaghi, 1923; Hubbert and Rubey, 1959; Jaeger and Cook, 1979)

$$\sigma'_{ij} = \sigma_{ij} + p \delta_{ij}. \tag{4.9}$$

Equations (4.8) and (4.9) are compatible only if the porous body is substantially more compressible than the individual solid grains that make up the body ($K_b \ll K_s$) (Iverson and Reid, 1992), a condition common for many granular geologic materials subject to low effective stresses. Note from these equations that only the normal stresses are partitioned into fluid-stress and solid-stress components; shear stresses are not partitioned into component stresses, and they can be thought of as either total or effective stresses. Substituting equation (4.9) into equations (4.7a) and (4.7b) yields explicit forms of the stress-equilibrium equations in terms of effective stresses:

$$\frac{\partial \sigma'_{xx}}{\partial x} + \frac{\partial \sigma'_{zx}}{\partial z} = \frac{\partial p}{\partial x} \tag{4.10a}$$

$$\frac{\partial \sigma'_{zx}}{\partial x} + \frac{\partial \sigma'_{zz}}{\partial z} = \rho_t g + \frac{\partial p}{\partial z}. \tag{4.10b}$$

Although these expressions provide a complete description of effective-stress equilibrium, the forces acting on the mixture in the present case become physically more transparent by recasting the total fluid pressure into its component parts. Noting that total fluid pressure can be partitioned as $p=p_h+p_*$, where p_h is the equilibrium hydrostatic fluid pressure and p_* is a nonequilibrium pressure in excess of hydrostatic, equations (4.10) can be recast, after some algebraic manipulation, as

$$\frac{\partial \sigma'_{xx}}{\partial x} + \frac{\partial \sigma'_{zx}}{\partial z} = \frac{\partial p_*}{\partial x} \tag{4.11a}$$

$$\frac{\partial \sigma'_{zx}}{\partial x} + \frac{\partial \sigma'_{zz}}{\partial z} = (\rho_s - \rho_f)(1 - \phi)g + \frac{\partial p_*}{\partial z} . \tag{4.11b}$$

Similar equations for effective-stress equilibrium, cast instead in terms of hydraulic head rather than nonequilibrium fluid pressure, are presented by Iverson and Reid (1992). In this form, it is transparent that gradients of nonequilibrium fluid pressure, which drive pore-fluid flow, act as body forces on the system, and that the term $(\rho_s-\rho_f)(1-\phi)g$ (which equals $(\rho_t-\rho_f)g$) represents the buoyant weight of the solids, which generates fluid pressure at those times when fluid bears particle weight.

Solution of the effective-stress field posed by the stress-equilibrium equations is indeterminate; there are more unknowns (σ'_{xx}, σ'_{zz}, σ'_{zx}, p_*) than there are equations. In order to solve for the stresses acting on the system, further expressions must be derived. Such expressions are formulated by introducing a rule that relates strains to the total stresses and fluid pressures acting on the system, by casting that rule in terms of strains and effective stresses, and then by combining the resulting expressions that relate strains and effective stresses with the expression that describes the kinematic compatibility constraint (4.3).

CONSTITUTIVE RELATIONS -- SOLID STRAIN, TOTAL STRESS, AND FLUID PRESSURE

The expressions for strain, displacement, and stress equilibrium discussed thus far are completely general for quasistatic states and are independent of the rheologic behavior of the solid and fluid components of the mixture. The only specific limitation placed on the system is the assumption that strains are small and are linearly related to the displacement gradients. To proceed, an assumption must be made regarding a rule that relates the strains that accumulate in the porous body during deformation to the stresses that are acting on the body. Here, a constitutive rule proposed by Biot (1941) for a porous, linearly elastic medium is used. This rule, which couples strains in the solids to total stresses and pore-fluid pressures, is presented in more traditional elasticity nomenclature by Rice and Cleary (1976). Their form of Biot's constitutive rule, in which all pore spaces are assumed connected and permit fluid flow (see, for example, Iverson and Reid, 1992, Appendix B), can be expressed as

$$\varepsilon_{ij} = \frac{1}{2G}[\sigma_{ij} + p\delta_{ij} - \frac{\nu}{1+\nu}(\sigma_{kk}+3p)\delta_{ij} - \frac{2G}{3K_s}p\delta_{ij}] \tag{4.12}$$

where G is the shear (rigidity) modulus and ν the drained Poisson's ratio of the porous body.

A more useful form of the constitutive rule can be obtained by adopting an identity that relates the shear modulus, bulk modulus, and Poisson's ratio of the porous body (e.g., Chou and Pagano, 1967):

$$\frac{2G}{3} = K_b(\frac{1-2\nu}{1+\nu}). \tag{4.13}$$

Substitution of (4.13) into (4.12) yields, after some algebraic manipulation,

$$\varepsilon_{ij} = \frac{1}{2G}[\sigma_{ij} - \frac{\nu}{1+\nu}\sigma_{kk}\delta_{ij}] + \frac{1}{3K_b}(1-\frac{K_b}{K_s})p\delta_{ij} \tag{4.14}$$

which, for the assumed condition that $K_b \ll K_s$, reduces to

$$\varepsilon_{ij} = \frac{1}{2G}[\sigma_{ij} - \frac{\nu}{1+\nu}\sigma_{kk}\delta_{ij}] + \frac{1}{3K_b}p\delta_{ij}. \tag{4.15}$$

Equation (4.15) shows the coupling that exists between the deformation of the skeleton of a porous body and the state of stress and the fluid pressure in the body. In the absence of pore fluid (that is, for zero fluid pressure), this equation reduces to that for a Hookean elastic material.

The constitutive rule can be cast, for present purposes, in terms of effective, rather than total, stresses. Substituting (4.9) into (4.15), and noting that for plane strain $\varepsilon_{yy}=0$, leads after considerable algebraic manipulation, explicitly to

$$\varepsilon_{xx} = \frac{1}{2G(1+\nu)}[(1-\nu^2)\sigma'_{xx} - \nu(1+\nu)\sigma'_{zz}] \tag{4.16a}$$

$$\varepsilon_{zz} = \frac{1}{2G(1+\nu)}[(1-\nu^2)\sigma'_{zz} - \nu(1+\nu)\sigma'_{xx}] \tag{4.16b}$$

$$\varepsilon_{zx} = \frac{\sigma'_{zx}}{2G}. \tag{4.16c}$$

Utilizing the identity $E=2G(1+\nu)$ (Fung, 1965), equations (4.16a)-(4.16c) can be recast in a slightly modified form as

$$\varepsilon_{xx} = \frac{1}{E}[(1-\nu^2)\sigma'_{xx} - \nu(1+\nu)\sigma'_{zz}] \tag{4.17a}$$

$$\varepsilon_{zz} = \frac{1}{E}[(1-\nu^2)\sigma'_{zz} - \nu(1+\nu)\sigma'_{xx}] \tag{4.17b}$$

$$\varepsilon_{zx} = \frac{(1+\nu)}{E}\sigma'_{zx}. \tag{4.17c}$$

Equations (4.17a)-(4.17c) can be combined with the imposed compatibility constraint (equation 4.3) to yield

$$(1-\nu)[\frac{\partial^2\sigma'_{xx}}{\partial z^2} + \frac{\partial^2\sigma'_{zz}}{\partial x^2}] - \nu[\frac{\partial^2\sigma'_{zz}}{\partial z^2} + \frac{\partial^2\sigma'_{xx}}{\partial x^2}] = 2\frac{\partial^2\sigma'_{zx}}{\partial x\partial z}. \tag{4.18}$$

Differentiating and combining the effective-stress equilibrium equations (4.11a) and (4.11b) yields

$$\frac{\partial^2\sigma'_{xx}}{\partial x^2} + \frac{\partial^2\sigma'_{zz}}{\partial z^2} - \frac{\partial}{\partial z}[(\rho_s - \rho_f)(1-\phi)g] - \frac{\partial^2 p_e}{\partial x^2} - \frac{\partial^2 p_e}{\partial z^2} = -2\frac{\partial^2\sigma'_{zx}}{\partial x\partial z}. \tag{4.19}$$

Combining (4.18) and (4.19) yields, after some manipulation,

$$[\frac{\partial^2}{\partial x^2} + \frac{\partial^2}{\partial z^2}][\sigma'_{xx} + \sigma'_{zz}] = \frac{1}{(1-\nu)}\left[(\frac{\partial^2}{\partial x^2} + \frac{\partial^2}{\partial z^2})p_e + \frac{\partial}{\partial z}[(\rho_s - \rho_f)(1-\phi)g]\right]. \tag{4.20}$$

Equation (4.20) expresses the compatibility constraint in terms of effective stresses and nonequilibrium fluid pressure. In the absence of nonequilibrium fluid pressure, such as when the pressure field is uniformly hydrostatic, and for a constant-porosity domain, standard expressions for a linear elastic material are recovered. Provided that a solution can be found, equations (4.11a), (4.11b), and (4.20) pose a mathematically complete description for the effective stresses and nonequilibrium pore-fluid pressure acting on a gravitationally loaded, saturated porous medium, subject to appropriate boundary conditions.

Thus far, expressions that describe the state of stress and fluid pressure in a porous body are developed based on the balance of linear momentum of the body and on a constitutive rule that relates strains in the skeleton of a porous body to the state of stress and fluid pressure. These expressions show that, except for steady state, the effective-stress field in the body is related to fluid flow driven by gradients of nonequilibrium fluid pressure and to buoyancy forces. Because the evolution of the effective-stress field in the skeleton is related to fluid pressure, and to fluid flow, mass balance laws and a constitutive rule that relates changes in the mass of the pore fluid to the state of stress must be considered.

BALANCE LAWS FOR MASS

Balance of Fluid Mass

Consider a representative volume of a mixture of solids and fluid in an Eulerian system for which the coordinates of the volume are fixed in space. The balance law to be observed states that the rate at which the fluid mass within the representative volume accumulates is balanced by the flux of fluid mass across the surface bounding that volume. The fluid mass per unit volume of mixture within the control volume is given by

$$\rho_f \phi \,. \tag{4.21}$$

The flux of fluid mass per unit area normal to the surface of the control volume is related to the fluid velocity (v^f_i), and is given by

$$\rho_f \phi v^f{}_i . \tag{4.22}$$

The balance law for fluid mass is obtained by integrating the accumulating fluid mass across the entire control volume, by integrating the fluid mass flux across the entire surface, and by applying Gauss' divergence theorem. The balance law for fluid mass is stated explicitly as

$$\frac{\partial \rho_f \phi}{\partial t} + \frac{\partial \rho_f \phi v^f{}_i}{\partial x_i} = 0. \tag{4.23}$$

Balance of Solid Mass

A similar balance can be constructed for the solid mass in the mixture. The solid mass per unit volume of mixture within the control volume is given by

$$\rho_s (1-\phi) . \tag{4.24}$$

Following arguments similar to those outlined for the balance of fluid mass, the balance law for the solid mass can be written as

$$\frac{\partial \rho_s (1-\phi)}{\partial t} + \frac{\partial \rho_s (1-\phi) v^s{}_i}{\partial x_i} = 0. \tag{4.25}$$

Here, $v^s{}_i$ represents solid-particle velocities normal to the surface of the control volume.

Balance of Mass of Solid-Fluid Mixture

A balance law for the mass of the mixture can be obtained by summing the individual mass balances for the fluid and the solid. If the constituents of the mixture are treated as incompressible, a condition common for many granular geological materials subject to low effective stresses, then equation (4.23) can be written in expanded form as

$$\frac{\partial \phi}{\partial t} + v^f{}_i \frac{\partial \phi}{\partial x_i} + \phi \frac{\partial v^f{}_i}{\partial x_i} = 0. \tag{4.26}$$

Adding and subtracting $v^s{}_i \, \partial\phi/\partial x_i$ to (4.26) yields

$$\frac{\partial \phi}{\partial t} + v^f{}_i \frac{\partial \phi}{\partial x_i} + \phi \frac{\partial v^f{}_i}{\partial x_i} + v^s{}_i \frac{\partial \phi}{\partial x_i} - v^s{}_i \frac{\partial \phi}{\partial x_i} = 0. \tag{4.27}$$

In a similar fashion, equation (4.25) can be expanded and regrouped as

$$-\frac{\partial \phi}{\partial t} - \phi \frac{\partial v^s{}_i}{\partial x_i} + \frac{\partial v^s{}_i}{\partial x_i} - v^s{}_i \frac{\partial \phi}{\partial x_i} = 0. \tag{4.28}$$

Summing together (4.27) and (4.28) leads to

$$\frac{\partial v^s{}_i}{\partial x_i} + v^f{}_i \frac{\partial \phi}{\partial x_i} + \phi \frac{\partial v^f{}_i}{\partial x_i} - v^s{}_i \frac{\partial \phi}{\partial x_i} - \phi \frac{\partial v^s{}_i}{\partial x_i} = 0. \tag{4.29}$$

This expression can be regrouped as

$$\frac{\partial v^s{}_i}{\partial x_i} + \frac{\partial \phi v^f{}_i}{\partial x_i} - \frac{\partial \phi v^s{}_i}{\partial x_i} = 0 \tag{4.30}$$

which leads to an exact expression of mass balance for a solid-fluid mixture having incompressible constituents:

$$\frac{\partial v^s{}_i}{\partial x_i} + \frac{\partial \phi (v^f{}_i - v^s{}_i)}{\partial x_i} = 0. \tag{4.31}$$

The first term in (4.31) reflects the volume change of the solid skeleton during deformation. The second term represents the divergence of the relative volume flux of fluid per unit area of the mixture, known as the Darcy flux. Note that Darcian flux of fluid in a deforming porous medium is proportional to the velocity of the fluid relative to the velocity of the solid, and not solely the velocity of the fluid. Defining q_i as the relative volume flux of fluid per unit area of porous body, the balance law for the mass of the solid-fluid mixture can be written as

$$\frac{\partial v^s{}_i}{\partial x_i} + \frac{\partial q_i}{\partial x_i} = 0. \tag{4.32}$$

Equation (4.32) for the mass balance of the mixture describes physically the coupling that exists between deformation of the skeleton of the porous body and fluid flow; dilation of the skeleton is accompanied by influx of fluid whereas compression of the skeleton is accompanied by outflow of fluid.

The expression for the mass balance of the mixture can be written explicitly in terms of volume strain of the porous body. For small deformations, the dilatation rate of the grains composing the skeleton of the porous body is related to the volumetric strain rate of the porous body by (McTigue, 1986)

$$\frac{\partial v^s{}_i}{\partial x_i} = \frac{1}{V}\frac{\partial V}{\partial t} \tag{4.33}$$

where V is the volume of the porous body. Utilizing a general definition of volume strain

$$\varepsilon = \frac{V - V_0}{V_0} \tag{4.34}$$

in which V_0 is the volume of the medium at some reference state, (4.33) can be written, after some manipulation, as

$$\frac{\partial v^s{}_i}{\partial x_i} = \frac{1}{1+\varepsilon}\frac{\partial \varepsilon}{\partial t}. \tag{4.35}$$

Upon linear expansion, (4.35) becomes (Beyer, 1987)

$$\frac{\partial v^s{}_i}{\partial x_i} = (1-\varepsilon+\varepsilon^2-\ldots)\frac{\partial \varepsilon}{\partial t} \tag{4.36}$$

which, for small ε, reduces to

$$\frac{\partial v^{s}_{i}}{\partial x_i} = \frac{\partial \varepsilon}{\partial t} . \tag{4.37}$$

Because strains in the porous body are assumed small, the mass balance for the mixture can be reduced to a mass balance for the pore fluid. The change of mass of pore fluid per unit volume of medium, m-m_0, is related to small volume strain of the medium and fluid density by m-m_0=$\rho_f \varepsilon$. Here m_0 is a constant value of m at some reference state. Using this relation, and combining (4.32) and (4.37), the mass balance of the mixture can be written in terms of the rate change of the mass of pore fluid per unit volume of medium and the mass flux of fluid per unit area of medium as

$$\frac{\partial m}{\partial t} + \frac{\partial \rho_f q_i}{\partial x_i} = 0 . \tag{4.38}$$

CONSTITUTIVE RELATIONS -- FLUID MASS, TOTAL STRESS, AND FLUID PRESSURE

Biot (1941) presents a second constitutive rule to account for the various types of compressibility in a poroelastic system. These include compressibility of the mixture, compressibility of the solids, and compressibility of the fluid. This constitutive rule, which relates the mass of pore fluid per unit volume of medium to the state of stress and fluid pressure, is expressed by Rice and Cleary (1976) as

$$m - m_0 = \frac{3\rho_o(\nu_u - \nu)}{2GB(1+\nu)(1+\nu_u)}\left[\sigma_{kk} + \frac{3}{B}p\right] . \tag{4.39}$$

Here ν_u is the undrained value of Poisson's ratio for the solid medium; B is Skempton's pore-pressure coefficient, which relates changes in pore-fluid pressure to changes in the mean compressive stress; and ρ_0 is the fluid density measured at some reference state. Because I have assumed that the fluid

and solids are incompressible, this constitutive rule adds no new information to the problem. I present this rule, however, for completeness and to show how the restrictive problem examined here fits into a broader poroelastic context. For incompressible pore fluid and incompressible solid grains, $\rho_0=\rho_f$ $B=1$, and $\nu_u=½$, thus

$$m-m_0=\frac{\rho_f(1-2\nu)}{2G(1+\nu)}[\sigma_{kk}+3p]\,. \tag{4.40}$$

Laminar flow of a linearly viscous fluid in a porous medium is described by Darcy's Law. The volume flux of fluid per unit area of porous medium is related to gradients in nonequilibrium pore-fluid pressure by

$$q_i=-\frac{k}{\mu}\frac{\partial p_*}{\partial x_i} \tag{4.41}$$

where k is the intrinsic permeability of the porous medium and μ is the dynamic viscosity of the pore fluid.

The mass balance of the pore fluid can be written in terms of total stress and gradients of nonequilibrium pore-fluid pressure by combining (4.38), (4.40), and (4.41) and recasting p as p_h+p_*. If, to a first approximation, the permeability of the medium is assumed constant, then

$$\frac{(1-2\nu)}{2G(1+\nu)}\frac{\partial}{\partial t}[\sigma_{kk}+3p_*]-\frac{k}{\mu}\frac{\partial^2 p_*}{\partial x_i\partial x_i}=0\,. \tag{4.42}$$

Note that this expression could be written in terms of the bulk modulus (K_b) by employing (4.13).

Similar to the equations for stress equilibrium, expression (4.42) for the mass balance of pore fluid can be partitioned into stresses acting on the solids and into fluid pressures. Combining (4.9) and (4.42), and utilizing an expression for the out-of-plane stress (σ_{yy}) that results from the condition of plane strain ($\varepsilon_{yy}=0$) (equation 4.15), the resulting expression can be manipulated to yield

$$\frac{(1-2\nu)}{2G}\frac{\partial}{\partial t}(\sigma'_{xx}+\sigma'_{zz})-\frac{k}{\mu}\frac{\partial^2 p_*}{\partial x_i \partial x_i}=0\,. \tag{4.43}$$

STRESS DIFFUSION

Equations (4.20) and (4.43) define the basic governing expressions describing the coupled, two-dimensional effective-stress and fluid-pressure fields in the presence of a gravitational body force. These expressions can be combined to yield, after some manipulation, an "effective-stress-diffusion" equation of the form:

$$\frac{\partial}{\partial t}[\sigma'_{xx}+\sigma'_{zz}]=D[\frac{\partial^2}{\partial x^2}+\frac{\partial^2}{\partial z^2}][\sigma'_{xx}+\sigma'_{zz}]-A\frac{\partial}{\partial z}[(\rho_s-\rho_f)(1-\phi)g] \tag{4.44}$$

where D is the "consolidation" or "stress diffusivity" coefficient and is given by

$$D=\frac{k}{\mu}\,[\frac{2G(1-\nu)}{(1-2\nu)}] \tag{4.45}$$

and

$$A=\frac{k}{\mu}\frac{2G}{1-2\nu}\,.$$

Thus, D takes the same form as the familiar hydraulic diffusivity coefficient defined for one-dimensional diffusion of nonequilibrium fluid pressure (equation 3.16).

Equation (4.44) represents an expression of fully coupled, two-dimensional, effective-stress diffusion in a porous, linearly elastic medium having incompressible constituents subject to small deformation under gravitational loading. Coupling of total stresses and nonequilibrium fluid pressures is implicit in the effective-stress formulation presented here. This expression is developed on the basis of balance laws for fluid and solid mass, stress equilibrium, compatibility of strain and displacement fields, Darcy's law, and a poroelastic constitutive expression. Derivation of this expression assumes that strains in the porous body are small and are related linearly to displacement gradients; that constituents are incompressible; that the fluid is linearly viscous; that Darcy's law is valid; and that, to a first approximation, the intrinsic permeability of the medium remains constant.

The first two terms of (4.44) have the form of a standard diffusion equation. The third term represents the influence of buoyancy forces, and reflects a forcing term. Under steady state conditions ($\partial/\partial t = 0$), the divergence of the effective-stress field is balanced by body forces acting on the buoyant solid particles (see Iverson and Reid, 1992).

DISPLACEMENT "DIFFUSION"

Although equation (4.44) poses a mathematically complete description of the effective-stress field when combined with appropriate boundary conditions, solution of this equation is difficult because boundary conditions in terms of stresses are not easily defined, and in most cases are not known. Instead, boundary conditions are more commonly, and more easily, defined in terms of displacements. Therefore, a more tractable set of expressions is obtained if the stress-equilibrium and mass balance equations are recast in terms of displacements.

Effective stresses can be written in terms of linear displacement gradients by combining equations (4.2a)-(4.2c) and (4.17a)-(4.17c). Manipulation of the resulting equations leads to

$$\sigma'_{xx} = \frac{E}{(1+\nu)}\left(\frac{\partial u_x}{\partial x}\right) + \frac{\nu E}{(1+\nu)(1-2\nu)}\left(\frac{\partial u_x}{\partial x} + \frac{\partial u_z}{\partial z}\right) \tag{4.46a}$$

$$\sigma'_{zz} = \frac{E}{(1+\nu)}\left(\frac{\partial u_z}{\partial z}\right) + \frac{\nu E}{(1+\nu)(1-2\nu)}\left(\frac{\partial u_x}{\partial x} + \frac{\partial u_z}{\partial z}\right) \tag{4.46b}$$

$$\sigma'_{zx} = \frac{E}{2(1+\nu)}\left(\frac{\partial u_z}{\partial x} + \frac{\partial u_x}{\partial z}\right). \tag{4.46c}$$

Substitution of equations (4.46a)-(4.46c) into (4.11a) and (4.11b), and considerable manipulation, leads to

$$\frac{E}{2(1+\nu)}\left(\frac{\partial^2 u_x}{\partial x^2} + \frac{\partial^2 u_x}{\partial z^2}\right) + \left[\frac{\nu E}{(1+\nu)(1-2\nu)} + \frac{E}{2(1+\nu)}\right]\left(\frac{\partial^2 u_x}{\partial x^2} + \frac{\partial^2 u_z}{\partial x \partial z}\right) = \frac{\partial p_*}{\partial x} \tag{4.47a}$$

$$\frac{E}{2(1+\nu)}\left(\frac{\partial^2 u_z}{\partial x^2} + \frac{\partial^2 u_z}{\partial z^2}\right) + \left[\frac{\nu E}{(1+\nu)(1-2\nu)} + \frac{E}{2(1+\nu)}\right]\left(\frac{\partial^2 u_z}{\partial z^2} + \frac{\partial^2 u_x}{\partial x \partial z}\right) = (\rho_s - \rho_f)(1-\phi)g + \frac{\partial p_*}{\partial z}. \tag{4.47b}$$

Differentiating (4.47a) and (4.47b) with respect to coordinate directions leads to

$$\frac{E}{2(1+\nu)}\left(\frac{\partial^3 u_x}{\partial x^3} + \frac{\partial^3 u_x}{\partial x \partial z^2}\right) + \left[\frac{\nu E}{(1+\nu)(1-2\nu)} + \frac{E}{2(1+\nu)}\right]\left(\frac{\partial^3 u_x}{\partial x^3} + \frac{\partial^3 u_z}{\partial x^2 \partial z}\right) = \frac{\partial^2 p_*}{\partial x^2} \tag{4.48a}$$

$$\frac{E}{2(1+\nu)}\left(\frac{\partial^3 u_z}{\partial x^2 \partial z}+\frac{\partial^3 u_z}{\partial z^3}\right) + \left[\frac{\nu E}{(1+\nu)(1-2\nu)}+\frac{E}{2(1+\nu)}\right]\left(\frac{\partial^3 u_z}{\partial z^3}+\frac{\partial^3 u_x}{\partial x \partial z^2}\right) = \frac{\partial}{\partial z}[(\rho_s-\rho_f)(1-\phi)g]+\frac{\partial^2 p_*}{\partial z^2}. \quad (4.48b)$$

Summing (4.48a) and (4.48b) yields

$$\left(\frac{\partial^2}{\partial x^2}+\frac{\partial^2}{\partial z^2}\right)\left(\frac{\partial u_x}{\partial x}+\frac{\partial u_z}{\partial z}\right) = \frac{(1+\nu)(1-2\nu)}{E(1-\nu)}\left[\left(\frac{\partial^2}{\partial x^2}+\frac{\partial^2}{\partial z^2}\right)p_* + \frac{\partial}{\partial z}[(\rho_s-\rho_f)(1-\phi)g]\right]. \quad (4.49)$$

Next, a mass balance expression must be cast in terms of displacement gradients. Substitution of (4.46a) and (4.46b) into (4.43) leads to

$$\frac{\partial}{\partial t}\left(\frac{\partial u_x}{\partial x}+\frac{\partial u_z}{\partial z}\right) - \frac{k}{\mu}\left(\frac{\partial^2}{\partial x^2}+\frac{\partial^2}{\partial z^2}\right)p_* = 0. \quad (4.50)$$

Combining (4.49) and (4.50) yields a "displacement diffusion" expression having the form

$$\frac{\partial}{\partial t}\left(\frac{\partial u_x}{\partial x}+\frac{\partial u_z}{\partial z}\right) = D\left(\frac{\partial^2}{\partial x^2}+\frac{\partial^2}{\partial z^2}\right)\left(\frac{\partial u_x}{\partial x}+\frac{\partial u_z}{\partial z}\right) - \frac{k}{\mu}\frac{\partial}{\partial z}[(\rho_s-\rho_f)(1-\phi)g] \quad (4.51)$$

in which D, the diffusivity coefficient, is defined by (4.45). Equation (4.51) has the same form as (4.44), but represents a more tractable problem because boundary conditions that constrain integration constants can be defined.

BOUNDARY CONDITIONS

Executing a numerical simulation was a two-step process. First, a gravitational load had to be applied to the domain "instantaneously" in order to generate a desired state of fluid pressure and effective stress. Then, using this state of stress and fluid pressure as an initial condition, the consolidation algorithm was executed and the stress and fluid pressure changes were calculated using approximations of the fully coupled equations described above. Each step required specification of appropriate boundary conditions. In the analyses described in this study the desired initial state was that measured in the experimental debris-flow deposits and in the laboratory slurries (Chapter 3), namely, a state of lithostatic fluid pressure and zero effective stress. To accomplish this, displacements and fluid fluxes along all boundaries of the domain were set to zero before gravitational loading was applied.

Following instantaneous gravity loading, and generation of the desired lithostatic initial fluid pressure, displacement, fluid-pressure, and fluid-flux boundary conditions were reset in order to execute the consolidation phase of the simulation. The boundary conditions for the consolidation phase of the analysis (Figure 4.2) specify that there are no stresses ($\sigma_{ij}n_j=0$) or nonequilibrium fluid pressures ($p_*=0$) acting on the free surfaces of the domain (planes ad, bc); that a no-flow boundary ($\partial p_*/\partial x_i=0$) is established at the base of the body (plane ab) and along the vertical centerline of the body (plane bc); and that there is no vertical displacement ($u_z=0$) along the base (plane ab) and no horizontal displacement ($u_x=0$) along the vertical centerline (plane bc) of the body. Mathematically, these boundary conditions are specified as (Figure 4.2):

$$u_x(L,z) = 0 \tag{4.52a}$$

$$u_z(x,0) = 0 \tag{4.52b}$$

$$p_*(0,z) = 0 \tag{4.52c}$$

$$p_e(x,H) = 0 \tag{4.52d}$$

$$\sigma'_{xx}(0,z) = 0$$
$$\sigma'_{zx}(0,z) = 0 \tag{4.52e}$$

$$\sigma'_{zz}(x,H) = 0$$
$$\sigma'_{zx}(x,H) = 0 \tag{4.52f}$$

$$\left.\frac{\partial p_e}{\partial z}\right|_{(x,0)} = 0 \tag{4.52g}$$

$$\left.\frac{\partial p_e}{\partial x}\right|_{(L,z)} = 0\,. \tag{4.52h}$$

NUMERICAL SOLUTION

Solution of the problem posed by equation (4.51), subject to the boundary conditions described by equations (4.52a)-(4.52h) and to a lithostatic initial fluid pressure (Figure 4.3), was accomplished using ABAQUS, a commercially available finite-element code (Hibbit, Karlsson, and Sorensen, Inc., 1993). This code computes approximate solutions for the displacements, strains, fluid pressures, and effective stresses for the coupled consolidation problem posed above. The code is extremely versatile, allowing for a great variety of element definitions, material properties, loading conditions, and kinematic constraints. The simulations in this study incorporated 8-node, biquadratic, isotropic, elastic

continuum elements; fluid pressure varied linearly across each element. Although the finite-element model is sufficiently versatile to allow both the fluid and solid constituents, as well as the bulk porous medium, to be compressible, I have analyzed only the simplest case in which the fluid and solid constituents are assumed to be incompressible. The low total stress exerted by gravitational loading on shallow slurries (order 10 kPa) and the generally large magnitudes of fluid (order 10^3 Mpa) and grain (order 10^4 Mpa) bulk moduli (e.g., Roeloffs, 1988) justify this assumption. Model input required definition of: an element mesh, element types, material properties of each element (Young's modulus, E; Poisson's ratio, ν; permeability, k; porosity, ϕ; fluid density; fluid viscosity; and a dry bulk density of the domain, ρ_t), a loading condition, and initial and boundary conditions.

For simplicity, a rectangular domain is used in these analyses (Figure 4.1). The domain represents an idealized cross-section through a porous body. Owing to the geometric symmetry of the problem, the domain represents one-half the total width of the body: the top and left hand sides of the domain represent free surfaces; the bottom and right hand sides of the domain represent no-flow boundaries. Most of the simulation results shown are for a domain having a height-to-width ratio of 1:5, which represents a deposit having a thickness-to-width ratio of 1:10. A few simulations show domains having height-to-width ratios of 1:0.5 (thickness-to-width ratio of 1:1); 1:1 (1:2); and 1:2.5 (1:5). In the figures depicting the various domains vertical exaggeration (labeled in the captions) must be kept in mind.

Each solution domain consists of 2000 quadrilateral elements: 20 elements in the vertical direction and 100 elements in the horizontal direction. Each element is of uniform size; near-surface elements were identical in size to those near no-flow boundaries. The location of the bottom boundary can greatly influence the near-surface stress predicted by elastic models (Iverson and Reid, 1992). Shallow bottom boundaries having zero vertical displacement may yield numerical computations that produce a zone of near-surface tension. The artificially sharp corners present in the simplified solution domains depicted in Figures 4.1 and 4.2 produce stress concentrations that can generate untenably large tensile and shear stresses that are not accommodated in a natural setting. Such stresses would modify the shape of the domain in those areas if a rule allowing material failure was included in the analysis. Material failure would subsequently feed back and modify the stress field (e.g., Miller, 1993). For present purposes I acknowledge but ignore these complications and instead focus attention on probable stress fields away from those problematic areas. In the analyses that follow, I

present contour diagrams of mean compressive principal effective stresses only. Tensile stresses are arbitrarily set to zero for contouring purposes. Therefore, zones of zero mean principal effective stress shown near the surface and the upper corners of the domains may in fact be zones of tensile stress.

Accuracy of solutions provided by the numerical model was estimated by comparing the numerical results of a one-dimensional domain against the analytical solution provided in Chapter 3 and by varying the number of elements used in a simulation. I did not systematically analyze the effect of grid element size on the accuracy of the numerical solution. Results of the numerical solution to the one-dimensional problem were identical to the analytical solution. Thus, at least for one-dimensional problems, the code provides very accurate solutions. A single numerical solution of a two-dimensional problem using a rectangular domain containing 500 elements (a 10x50 element mesh) was calculated, and the results were compared against those from a 20x100 element mesh. The numerical solution based on the 500-element mesh contained substantial numerical noise, particularly at early times when fluid pressures and effective stresses were evolving rapidly at the lateral free surface, whereas the 2000-element mesh generated relatively smooth solutions. Therefore, I adopted the 2000-element mesh as my solution standard. I do not have an analytical solution against which to compare results of the two-dimensional, gravity-driven numerical solution. However, the ABAQUS user's manual includes an example problem of two-dimensional consolidation of a strip of soil that has a surface load along part of its length. The numerical result describing the settlement history compares favorably with an exact solution provided by Gibson and others (1970). This comparison, in addition to the favorable comparison between the one-dimensional analytical and numerical solution, provides confidence that the model can simulate consolidation accurately. As an additional check I compared the results from an ABAQUS simulation against the results from a simple, uncoupled, two-dimensional finite-difference model. The fluid pressure field that develops using the ABAQUS code is similar to that developed by the uncoupled diffusion model (c.f. Figures 4.4 and 4.8).

NUMERICAL RESULTS

Results for the simple geometric domain used in this study illustrate the two-dimensional transient response of coupled nonequilibrium fluid pressures and effective normal (compressive) stresses in debris-flow deposits having a typical thickness-to-width ratio of 1:10 (see Table 2.1). The material physical properties used in these analyses (Table 4.1) were guided by physical properties of granular soils described in Chapter 3 (see Table 3.7). However, a range of properties, including some extreme values, was used to examine the influence of these properties on changes in fluid pressure and effective stress during consolidation.

Fluid pressures and effective stresses reported in this chapter have been nondimensionalized. Fluid pressure contours represent the pointwise total fluid pressure scaled by the value of the lithostatic fluid pressure at the base of the domain. A similar nondimensionalization was used in the reporting of results in Chapter 3; here, however, the hydrostatic fluid pressure remains embedded in the results. Nevertheless, the evolution of fluid pressure reflects the response of nonequilibrium fluid pressure. Effective stresses determined by the numerical solution have been converted to principal effective stresses, and the mean principal effective stress (σ'_m) has been scaled by $\rho_w g H$ (e.g., Iverson and Reid, 1992). This scaling provides an easy visualization of the magnitude of the mean principal effective stress with respect to the maximum value of hydrostatic stress. Local effective stresses (σ'_{ij}) are related to principal effective stresses, the maximum and minimum effective normal stresses that act on planes having zero shear stress, by (e.g., Jaeger and Cook, 1979, p. 14; Iverson and Reid, 1992):

$$\sigma'_1 = \frac{\sigma'_{xx} + \sigma'_{yy}}{2} + \sqrt{\left(\frac{\sigma'_{xx} - \sigma'_{yy}}{2}\right)^2 + \sigma'^{\,2}_{yx}} \tag{4.53a}$$

$$\sigma'_3 = \frac{\sigma'_{xx} + \sigma'_{yy}}{2} - \sqrt{\left(\frac{\sigma'_{xx} - \sigma'_{yy}}{2}\right)^2 + \sigma'^{\,2}_{yx}} \tag{4.53b}$$

Principal effective stresses act in a direction that is rotated from the local coordinate axes by an angle ψ:

$$\psi = \frac{1}{2}\arctan\left(\frac{2\sigma'_{yx}}{\sigma'_{xx} - \sigma'_{yy}}\right) \tag{4.54}$$

Because local effective stresses acting on any arbitrary plane can be deduced from the magnitude and orientation of the principal effective stresses, the principal effective stresses provide a complete picture of the nature of the stress field.

HOMOGENEOUS DOMAIN

Effect of Domain Shape

The numerical analyses show that, for typical height-to-width ratios of debris-flow deposits, the fluid-pressure and effective-stress fields evolve in an essentially one-dimensional manner (Figures 4.5-4.20). Figures 4.5-4.8 illustrate results of simulations for domains having height-to-width ratios of 1:0.5, 1:1, 1:2.5, and 1:5. These domains represent debris-flow deposits having thickness-to-width ratios of 1:1, 1:2, 1:5, and 1:10, respectively. Each domain is characterized by identical physical properties (Table 4.1); the only difference in these simulations is the aspect ratio of the domain. A progressively dominant one-dimensional character of fluid-pressure and effective-stress evolution emerges as body width increases relative to a constant body thickness. Within a few minutes, a broad effective-stress profile has developed along the margin of a deposit that is as wide as it is thick (Figure 4.5). Effective-stress contours are relatively evenly spaced indicating that lateral fluid flow has significantly influenced field development in the deposit interior. In contrast, effective-stress profiles of comparable magnitude take more than 30 minutes to a few hours to develop in deposits that are five to ten times as wide as they are thick (Figures 4.7 and 4.8). Even then the profiles in those deposits are compressed, creating large effective-stress gradients near the margin. Field development far from the margin of those deposits is affected little by lateral fluid flow. The response of fluid-pressure and effective-stress fields in wide, thin deposits is robust; variations in the physical properties of the soil

and variations in the homogeneity of the domain perturb the evolution of fluid pressures and effective stresses, but they only slightly alter the dominant one-dimensional nature of those fields (Figures 4.8-4.20). Global fluid-pressure and effective-stress fields that reflect the multidimensional nature of a domain evolve slowly in wide, thin, porous media having permeabilities and elastic properties that are commensurate with poorly sorted, granular debris (e.g., $k=10^{-14}$ to 10^{-10} m^2; $E\sim10^6$ Pa; $\nu\sim0.3$; see Table 3.7).

Fluid-pressure and effective-stress fields in homogeneous, wide, thin bodies characterized by $D\geq10^{-5}$ m^2/s evolve relatively rapidly (seconds to minutes) directly adjacent to the lateral free surface despite the dominantly one-dimensional nature and slow bodywide evolution of those fields (e.g., Figures 4.8, 4.10-4.13, 4.15, 4.16). In contrast, fluid-pressure and effective-stress fields evolve slowly (several hours) even adjacent to the lateral free surface in homogeneous bodies characterized by $D\leq10^{-7}$ m^2/s (e.g., Figures 4.9, 4.14, 4.17).

To determine the robustness and sensitivity of the numerical results, several solutions were obtained by varying different physical properties of soil. Young's modulus (E), Poisson's ratio (ν), permeability (k), and the porosity (ϕ) of the medium were all varied to determine their influence on the solution. Young's modulus, Poisson's ratio, and permeability affect the diffusivity of the domain (see equations 4.13, 4.44, 4.45, 4.51, and the identity $E=2G(1+\nu)$). Porosity affects the magnitude of the bulk density of the domain, ρ_f, and thus the magnitudes of lithostatic stress and buoyancy forces.

Effect of Young's Modulus

Young's modulus, serving here as a proxy for the bulk modulus, controls elastic deformation of a body under a given effective-stress field. The larger the magnitude of the modulus the more resistant the material is to compression. Based on the results of soil tests (Table 3.7; Appendix A), Young's modulus was chosen to vary from 10^4 to 10^8 Pa. Figures 4.8-4.10 illustrate the affect of Young's modulus on the transient response of fluid pressures and effective stresses. These solutions illustrate that nonequilibrium fluid pressures dissipate, and mean effective compressive stresses increase, faster in stiffer elastic material. The more compressible the material, or the less stiff it is elastically, the more an imposed load can be transferred from the skeleton of solids to the pore fluid.

At a given permeability, it takes longer for nonequilibrium fluid pressures to dissipate if the porous medium is easy to compress, which transfers load to the fluid.

Effect of Poisson's Ratio

Poisson's ratio (ν), the ratio of lateral to vertical strain, influences the relation between vertical and horizontal stresses (see equations 4.17a and 4.17b). As ν increases in value, the magnitude of the horizontal effective stress increases relative to the magnitude of the vertical effective stress. Poisson's ratio for granular soils has been reported in the range from 0.2 to 0.35 (Lambe and Whitman, 1969). However, the value of ν is not very well constrained. In the solutions provided here, three values of ν were used: 0.1, 0.25, and 0.3. Because ν is not well constrained for granular soils, these values were chosen to examine the effects of a broader range of values, but one that incorporated the range of values previously reported. Figures 4.8, 4.11, and 4.12 show that the value of this ratio has little significant influence on the evolution of the nonequilibrium fluid-pressure field. Although there are modest variations in the times of pressure-field snapshots, the differences between snapshots at similar time are subtle.

The value of ν has a more significant effect on the magnitude of the effective-stress field than on the fluid-pressure field. Although the evolution of the effective-stress field is very similar for each value of ν, there are subtle yet significant differences. The relative increase in horizontal stress that accompanies an increase in ν is manifest in the numerical solutions, which show that a greater magnitude of mean effective stress propagates farther inward from the lateral boundary at a given time than when ν has a smaller value (compare Figures 4.8 and 4.11). Thus, the larger the value of ν, the larger the value of the mean effective stress at any point in the system (because σ_{xx} is proportionately larger). Lower values of ν inhibit, albeit subtly, the development and transmission of effective stress away from the lateral surface by inhibiting lateral strain in the body. As a result, effective stresses remain depressed for somewhat longer periods of time in bodies characterized by lower values of ν than in bodies characterized by higher values of ν.

Effect of Permeability

The permeability of geological materials can range over an extraordinary 13 orders of magnitude (Freeze and Cherry, 1979). The permeability of poorly sorted sediments typical of debris-flow deposits varies over a more restricted, yet still large, range of about four or five orders of

magnitude (e.g., Figure 3.15; Appendix B). The sediments used in the static consolidation tests discussed in Chapter 3 had porosity-dependent permeabilities that varied from about 10^{-14} to 10^{-10} m^2 (10 millidarcy-100 darcy) (Appendix B). In the numerical solutions discussed here, I used three values of permeability: 10^{-11}, 10^{-14}, and 10^{-17} m^2. I chose these values to incorporate a range of permeabilities measured in typical debris-flow sediments and to examine the influence of a very low permeability on fluid-pressure- and stress-field development.

Permeability affects the ability of water to move through the voids in a porous medium. The influence of permeability is manifest in the diffusivity coefficient (equation 4.45). It is expected, therefore, that variations in material permeability will influence the evolution of fluid-pressure and effective-stress fields. The numerical solutions confirm this expectation (Figures 4.8, 4.13, 4.14). Similar distributions of pore-fluid pressure differ in time by slightly more than two orders of magnitude when the permeability of the domain changes by three orders of magnitude (for example, compare Figure 4.13, time=0.1, to Figure 4.8, time=30). When permeability approaches the upper bound typical of poorly sorted debris-flow sediment ($\sim 10^{-11}$ m^2; 10 darcy), a significant effective-stress field develops rapidly (within a few tens of seconds) throughout an extensive portion of the soil (Figure 4.13). On the contrary, when the soil domain is characterized by a substantially lower permeability (10^{-17} m^2; 0.01 millidarcy), the domain remains liquefied, except in a thin region along the margin (« domain thickness), for hundreds of hours (Figure 4.14).

Effect of Porosity

Porosity affects the evolution of the fluid-pressure and the effective-stress fields through the bulk density of the porous medium. The greater the porosity of the medium, the lower its bulk density. Variations in porosity therefore affect the magnitude of the gravitational body force that controls the generation of nonequilibrium fluid pressure and thence fluid flow. At higher porosities, the total bulk density of a saturated medium decreases because pore fluid comprises a greater proportion of the volume of the medium. As a result, the magnitude of the body force driving the generation of nonequilibrium fluid pressure is lower, and thus hydrostatic fluid pressure comprises a greater proportion of the total fluid pressure. Fluid-pressure profiles reflect the influence of hydrostatic fluid pressure (Figures 4.15a and 4.16a). The enhanced influence of hydrostatic fluid pressure on the profiles shows in the magnitudes of the normalized fluid-pressure contours. Because

hydrostatic pressure accounts for a larger proportion of the total fluid pressure, the ratio of total fluid pressure to initial basal fluid pressure is larger at any given point, at any given time, in the more porous debris. Thus, the total-fluid-pressure profile appears to evolve more slowly and to a lesser extent in the more porous debris. The enhanced influence of hydrostatic fluid pressure in more porous debris depresses the magnitude of the effective-stress field that develops in the medium (Figures 4.15b and 4.16b). Because hydrostatic fluid pressure accounts for a greater proportion of the total fluid pressure, a smaller proportion of that total fluid pressure can be transferred to the solid skeleton and thus the magnitude of the effective-stress field that develops in higher-porosity debris is lower than that developed in lower-porosity debris.

Effect of Diffusivity Coefficient

The combined effect of physical properties, manifest in the diffusivity coefficient, D, (equation 4.45) produces the most visible impact on the evolution of the fluid-pressure and effective-stress fields. In general, when D is large ($D \geq 10^{-3}$ m^2/s) fields can evolve rapidly and extensively within the soil domain. When D is small ($D \leq 10^{-5}$ m^2/s) field evolution is restricted to a thin zone near the lateral margin for several minutes to several tens of hours. To illustrate the point, Figures 4.9 and 4.17 represent two numerical solutions in which material physical properties were manipulated to produce a constant value of D (10^{-7} m^2/s); as the elastic modulus (E) increased, permeability was correspondingly decreased. Poisson's ratio was held constant. In one case, $E=10^4$ Pa and $k=10^{-14}$ m^2; in the other $E=10^6$ Pa and $k=10^{-16}$ m^2. Fluid viscosity was assumed to be 10^{-3} Pa-s. The two solutions, which represent domains having different elastic moduli and permeabilities, but the same value of diffusivity, produce identical results. A greater material compressibility, which was shown to maintain nonequilibrium fluid pressures in the soil domain, is offset by an increased permeability that allows a greater volume of fluid to flow and therefore dissipate nonequilibrium fluid pressures (see Darcy's law, equation 4.41). Conversely, an elastically stiffer material, in which nonequilibrium fluid pressures are not as easily maintained, is modified by a lower permeability, which hinders fluid flow and forces the fluid to bear all or part of the gravitational load for a longer period of time. Table 4.1 summarizes the values of D that characterize each numerical solution.

HETEROGENEOUS DOMAIN

Effects of heterogeneity were examined by constructing solution domains in which permeability varied spatially. Two problems were examined. In one analysis, a higher-permeability zone, two orders of magnitude greater than the permeability of the rest of the domain, composed the outermost ten percent of the domain (Figure 4.18; Table 4.1). In this case, the width of the higher-permeability zone was equal to one-half the thickness of the domain. This geometry was chosen to simulate a debris-flow deposit having coarser, more permeable material near its margin (e.g., Figures 2.15, 2.20D). A second domain, which contained variably sized, randomly scattered zones of higher-permeability debris (Figure 4.19), was developed to simulate distributed zones of coarse sediments that might be deposited by multiple flow surges (e.g., Figures 2.14, 2.15). The permeabilities of these two contrasting zones were arbitrarily chosen to vary by a factor of 100; for one zone $k=10^{-12}$ m^2, for the other, $k=10^{-14}$ m^2. The magnitude of permeability used for the higher-permeability zone is two or more orders of magnitude lower than is typical of well-sorted sediment commonly found near the margins of debris-flow deposits (e.g., Freeze and Cherry, 1979, p. 28; sand-and-gravel flume mixture, Figure 3.15, Appendix B). The magnitudes of permeability used in this simulation are, therefore, more representative of finer-grained debris-flow sediment, such as that from the 1980 North Fork Toutle debris flow from Mount St. Helens or that from the Osceola Mudflow from Mount Rainier (Figure 3.15), than they are of coarser grained sediment that perhaps is more characteristic of nonvolcanogenic debris flows. Nevertheless, these analyses provide insight, and perhaps limits, on fluid-pressure and effective-stress behavior that is possible in heterogeneous debris-flow deposits.

Effect of a Higher-Permeability Margin

In domains having higher-permeability zones near their lateral margins, changes in fluid pressure and effective stress can occur very rapidly. Within tens of seconds or less nonequilibrium fluid pressure can dissipate completely and a nearly lithostatic effective-stress profile can develop in a zone that is half as wide as the domain is thick when the permeability of that zone is $\geq 10^{-12}$ m^2 (1 darcy) (Figure 4.18; Table 4.1). Fluid pressures and effective stresses in a homogenous domain having a permeability of 10^{-11} m^2 ($D=10^{-2}$ m^2/s) also changed rapidly near the margin in a comparable timespan (Figure 4.13). However, a comparable magnitude of effective-stress

development in that homogeneous domain, extending inward to a distance equal to one-half the thickness of the domain, required a timespan approximately 30 times longer.

Complete dissipation of fluid pressure can occur within seconds in a higher-permeability marginal zone, yet fluid pressure changes little within the lower-permeability interior over the same timespan. Mechanically, a narrow zone having a nearly lithostatic effective-stress profile develops rapidly and bounds a broader zone of granular material that is essentially liquefied. The rate of dissipation of nonequilibrium fluid pressure and the development of effective stresses in the main body are limited by the permeability of that material. When the permeability of the main body is commensurate with that of very poorly sorted debris (10^{-14} m^2; 10 millidarcy), the higher-permeability zone near the margin acts as a free-surface boundary with respect to fluid flux once its fluid has drained. Evolution of the fluid-pressure and effective-stress fields then follows in a fashion similar to that documented for a homogeneous domain. Indeed, fluid-pressure and effective-stress profiles along the centerline of the domain (the right-hand margin as depicted in Figure 4.18) are identical to those that develop in a homogeneous domain of identical geometry having similar physical properties. The respective profiles developed in the vicinity of the higher-permeability zone are similar to, but slightly modified from, those profiles developed in a homogeneous domain, owing to the presence of the marginal zone (compare Figures 4.18 and 4.8).

The simulation of a domain characterized by a higher-permeability margin more clearly illustrates a conclusion based on simulations of homogeneous domains, namely, that fluid-pressure and effective-stress fields can evolve rapidly locally at domain margins. This is likely to be the case in natural debris-flow deposits, which in general are coarser near the margins than in more central sections of the deposit. This simulation shows clearly that nonequilibrium fluid pressure remains elevated, and effective stress depressed, everywhere except in the higher-permeability marginal zones for periods of several to several tens of minutes or longer when the central body is characterized by a permeability commensurate with that of poorly sorted debris.

Effect of Distributed Higher-Permeability Zones

Randomly dispersed higher-permeability zones within a debris-flow deposit, such as might develop as the result of deposition of coarse sediment by multiple surges, perturb the evolving fluid-pressure and effective-stress fields, but only slightly alter the overall one-dimensional character of the

consolidation process. Figure 4.19 illustrates the effect of variably sized, randomly distributed, higher-permeability zones on the development of the fluid-pressure and effective-stress fields. These results show that the higher-permeability zones perturb local development of the fluid-pressure and effective-stress fields, but that the dominant one-dimensional character of these fields persists in wide, thin bodies. The fluid-pressure and effective-stress fields in this analysis do not evolve as rapidly away from the lateral free surface as do fields influenced by higher-permeability margins. Although the fields begin to evolve rapidly directly adjacent to the lateral free surface within a matter of seconds, extensive field development to a significant distance beyond the free surface (>one-fourth the deposit thickness) requires several minutes to tens of minutes for material having a permeability of about 10^{-14} m^2 (10 millidarcy). This result is similar to the result from a homogeneous domain having similar physical properties. The lack of a direct connection between the higher-permeability zones and the free surfaces affects the development of the fluid-pressure and effective-stress fields in this simulation.

FINITE-STRAIN ANALYSIS

One of the limitations of the general theory of consolidation proposed by Biot (1941) is the assumption that displacements in the medium are everywhere small relative to the thickness of the medium; in other words, strains are small. For the assumed linearly elastic behavior of the medium, strains are considered to be infinitesimally small. In nature, strains are rarely infinitesimally small. Indeed, in the quasistatic laboratory tests presented in Chapter 3, it was shown that the mean volume strain, though small, was on the order of five percent. One of the strengths of numerical modeling is the ability to solve nonlinear problems. ABAQUS provides an approximation routine that permits nonlinearities caused by large changes in geometry as well as nonlinearities caused by changes in permeability resulting from changes in the porosity, or void ratio, of the body. I investigated the combined effect of large strain and nonconstant permeability (but maintained linear elasticity of the domain) in one numerical simulation. In this simulation I have allowed the permeability of a homogeneous domain to vary from 10^{-14} m^2 (10 millidarcy), in a medium having an initial porosity of 0.30, to 10^{-15} m^2 (1 millidarcy) in a medium having a final porosity of 0.22 (Table 4.1). Selection of these arbitrary values was guided by the permeabilities of debris-flow sediments summarized in Appendix B and by the relations between permeability and porosity illustrated in Figure 3.15 and

summarized in Table 3.8. The values chosen are consistent with relations obtained for the Mount St. Helens debris.

Despite allowing large geometric change and a nonconstant permeability, there is surprisingly little, if any, detectable difference between the finite-strain and infinitesimal-strain simulations (e.g., Figures 4.8, 4.20). Fluid-pressure and effective-stress fields evolve in the same manner, and at essentially the same rate, in each simulation. Perhaps this insignificant difference is not surprising. Unlike large sedimentary basins, or large engineering constructions, in which substantial compaction and porosity reduction occur in response to large-magnitude effective stresses (e.g., Audet and McConnell, 1992), debris-flow deposits are subject to very-low-magnitude effective stresses, typically <50 kPa. As a result, large-magnitude strains on the order of tens of percent, and significant reductions in porosity, which are conditions that typically drive nonlinear consolidation of sedimentary basins, do not occur in debris-flow deposits. Furthermore, although experimental results presented in Chapter 3 indicate that the process of one-dimensional, gravity-driven consolidation of granular slurries is generally a nonlinear process, it may be only weakly nonlinear; a linear one-dimensional consolidation model closely approximated the process. The results of this nonlinear simulation of two-dimensional, gravity-driven consolidation further bolster a conclusion reached in Chapter 3: that the consolidation of a debris-flow deposit, and its associated dissipation of nonequilibrium fluid pressure, is dominantly a one-dimensional process and that the essence of that one-dimensional process is closely approximated by a simple, linear, gravity-driven consolidation model.

DISCUSSION

Numerical analyses presented in this study show the effect of two-dimensional consolidation on the transient response of fluid-pressure and effective-stress fields that develop in gravitationally loaded, wide, thin porous bodies subject to a no-flux basal boundary and to a liquefied initial condition. The results are limited strictly to slurries that can be characterized (perhaps inappropriately) by a linearly elastic rheology, but insights from this analysis can probably be extrapolated to rapidly deposited granular slurries, such as deposits of debris flows, that sustain limited deformation under low effective stresses (see Chapter 3).

The results of this study are also limited to the simplified rectangular geometry used in the analysis. The rectangular nature of the solution domain almost certainly influences the development of shear and tensile stresses, and undoubtedly produces stress concentrations in the corners of the domain. However, unlike studies of effective-stress and groundwater-flow fields in two-dimensional hillslopes (Iverson and Reid, 1992), in which development of shear and tensile stresses is of paramount importance, the analysis presented here is focused on the evolution of the effective compressive-stress field. The mean effective compressive-stress fields that develop in these simulations are consistent with the evolving fluid-pressure field, and the fluid-pressure fields appear to be similar to those that develop using a simple two-dimensional diffusion model in which fluid-pressures are not coupled to the evolving effective-stress field (c.f. Figure 4.4). Thus, although the geometry of the solution domain is rectangular, the effective-stress-field results appear plausible. A more realistic geometry is one in which the margin of the domain assumes the shape of a wedge (e.g., Figure 2.10). A taper-shaped wedge is common in a two-dimensional domain everywhere on the verge of Coulomb failure (Dahlen, 1990). Several attempts were made to simulate a domain having a wedge-shaped margin, but each simulation ended in numerical instability. At present, I have numerical solutions only for rectangular domains. Although the simplified geometry and idealized mechanical behavior presented here limit the strict applicability of the results, the simulations provide substantial physical insight into the evolution of fluid-pressure and effective-stress fields in wide, thin slurries following rapid deposition.

The numerical analyses reveal that evolving fluid-pressure and effective-stress fields in debris-flow deposits bear a strong one-dimensional imprint, especially when the deposit is five or more times as wide as it is thick. Such a geometry is typical of natural debris-flow deposits. A lateral free surface affects field development only in a relatively thin zone (« body thickness) near that surface for several to several tens of minutes following gravity loading when the material is characterized by physical properties similar to those that characterize fine-grained debris. Only gradually, over periods of several tens of minutes to several hours, does the influence of lateral fluid flow propagate over a broad segment of the body. These time scales are probably shorter for coarser-grained debris (e.g., Figure 4.13).

Fluid drainage in a domain characterized by heterogeneous permeability can cause local changes in fluid pressure and effective stress to occur more rapidly (within tens of seconds or less)

than in a homogeneous domain. Spatial variation in permeability within a domain locally modifies the rate at which fluid pressures and effective stresses change only if a higher-permeability zone is hydraulically connected to a free surface. Only then can fluid in the higher-permeability zone drain more rapidly than it can from a lower permeability zone. When higher-permeability zones are randomly scattered throughout a deposit, and not hydraulically connected to a free surface, they have little influence on the rate of change of fluid pressures and effective stresses, because the fluid in those higher-permeability zones cannot escape any faster; the higher-permeability zones are surrounded by lower-permeability zones and the rate of fluid escape from the deposit is limited by its ability to escape from the lower-permeability material. When a domain is composed of higher-permeability sediment near its margin, it can evolve quickly into a body that can be characterized as a liquefied mixture of debris bounded by a porous dam. Fluid pressures and effective stresses then change in the lower-permeability, liquefied debris over periods of several tens of minutes to several hours. While debris-flow deposits may be characterized by randomly scattered zones of higher-permeability sediments deposited by surge waves, they commonly are characterized by accumulations of coarse sediment near their margins. Thus, physical insights from these analyses of heterogeneous domains have particular significance for debris-flow deposits.

The interplay of the physical properties of a soil, manifest in the combined parameter D, the diffusivity coefficient, has a more significant effect on changes in fluid-pressure and effective-stress fields during consolidation than does any single physical property. In fact, changes in some physical properties counteract changes in other physical properties. For example, as material compresses under load, pore spaces close. As a result, the material becomes increasingly more resistant to compression, and the elastic modulus of compression increases. As the material becomes more resistant to compression, a lesser amount of load is transferred to the pore fluid, and fluid flow dissipates the nonequilibrium fluid pressure more quickly. If this were the only physical property to change, the value of the diffusivity coefficient would increase (see equations 3.18 and 4.45) and effective-stress fields would evolve at a rate faster than if the compression modulus had remained unchanged. However, as pore spaces close, the permeability of the domain decreases. The decrease in permeability offsets the increase in domain stiffness by making it harder for fluid to escape the domain, thereby forcing the fluid to sustain part of the load for a longer period of time. The counteractive response of the system to changes in these two physical parameters makes it is possible for the value of the diffusivity coefficient to remain more nearly constant. This explains why a

constant diffusivity, one-dimensional model provided reasonable results even when it was demonstrated that the consolidation process is inherently nonlinear (Chapter 3). However, experimental data (Chapter 3) also suggest that changes in the magnitude of permeability outweigh changes in the magnitude of domain stiffness as pore spaces close. This leads to fluid-pressure (or effective-stress) dependence of the diffusivity coefficient, which in turn leads to the apparent nonlinearity observed in consolidation experiments (Chapter 3).

CONCLUSIONS

Subject to the assumptions regarding domain geometry and rheology, and to the limits of the physical parameters used in the model, numerical simulations of the evolution of fluid-pressure and effective-stress fields from an initially liquefied state in wide, thin, unbounded bodies show that:

1. The transient response of fluid-pressure and effective-stress fields is dominantly one-dimensional (vertical) when the width-to-thickness ratio of the domain is ≥ 5, a geometric ratio common in many natural debris flow deposits.

2. Horizontal drainage effects transient response of fluid-pressure and effective-stress fields only locally, along domain margins, over time scales that range from several minutes to several hours in domains characterized by material properties that are commensurate with those of fine-grained debris-flow deposits, such as the Mount St. Helens 1980 North Fork Toutle River debris flow or the Mount Rainier Osceola Mudflow. Time scales for local field changes are shorter for coarser grained debris.

3. Combined effects of physical properties of soils, manifest in the diffusivity coefficient, D, have more significant influences on field evolution than does any single physical property. Various combinations of values of elastic properties and permeability, manipulated to yield identical values of D, produce identical simulation results.

4. Fluid-pressure and effective-stress fields can change rapidly in a thin zone (« body thickness) near the lateral free surface in a homogeneous domain. Extensive bodywide changes in these fields require as much as several hours in materials having properties commensurate with poorly sorted debris.

5. In domains having higher-permeability zones near their lateral margins, changes in fluid pressure and effective stress can occur very rapidly. Within tens of seconds or less a nearly lithostatic effective-stress profile can develop in a zone that is half as wide as the domain is thick when the permeability of that zone is larger than about 10^{-12} m^2 (1 darcy). A comparable magnitude of effective-stress development in a homogeneous domain having similar permeability required a timespan approximately 30 times longer. Following rapid fluid drainage, the higher-permeability zone acts as a free-surface boundary with respect to fluid flow for the central part of the domain. In the lower-permeability part of the domain changes in fluid pressure and effective stress proceed significantly more slowly than along the margin. The higher-permeability margin provides a porous dam bounding a liquefied, poorly sorted sediment slurry for time scales that typically exceed the duration of many debris flows.

6. Higher-permeability zones that are randomly distributed in a lower-permeability body, and are not directly connected to a free surface, perturb, but do not significantly alter, the dominant one-dimensional character of fluid-pressure and effective-stress fields that evolve in homogeneous domains that have physical properties similar to the lower-permeability portion of the heterogeneous domain. Therefore, higher-permeability zones in debris-flow deposits have their greatest effect on evolving fluid-pressure and effective-stress fields only when those zones are hydraulically connected to a free surface.

7. The numerical results reveal that nonequilibrium pore-fluid pressures remain elevated, and effective (compressive) stresses depressed, everywhere except at deposit margins for time scales that range from several minutes to perhaps several days in debris-flow deposits that are on the order of 1 meter thick and which are characterized by sediments having physical properties commensurate with many fine-grained debris flows.

Table 4.1. Physical properties of soil material used in numerical analysis

Figure	Aspect ratio†	Elastic modulus, E (Pa)	Poisson's ratio, ν	Permeability, k (m^2)		Diffusivity D (m^2/s)	Porosity ϕ	Permeability constrast	Domain characteristics (see Figure 4.2)
				k_{high}	k_{low}			k_{high} / k_{low}	
Homogeneous domain									
4.5	1:0.5 (1:1)	10^6	0.30	10^{-14}	10^{-14}	10^{-5}	0.30	1	a
4.6	1:1 (1:2)	10^6	0.30	10^{-14}	10^{-14}	10^{-5}	0.30	1	a
4.7	1:2.5 (1:5)	10^6	0.30	10^{-14}	10^{-14}	10^{-5}	0.30	1	a
4.8	1:5 (1:10)	10^6	0.30	10^{-14}	10^{-14}	10^{-5}	0.30	1	a
4.9	1:5 (1:10)	10^4	0.30	10^{-14}	10^{-14}	10^{-7}	0.30	1	a
4.10	1:5 (1:10)	10^8	0.30	10^{-14}	10^{-14}	10^{-3}	0.30	1	a
4.11	1:5 (1:10)	10^6	0.10	10^{-14}	10^{-14}	10^{-5}	0.30	1	a
4.12	1:5 (1:10)	10^6	0.25	10^{-14}	10^{-14}	10^{-5}	0.30	1	a
4.13	1:5 (1:10)	10^6	0.30	10^{-11}	10^{-11}	10^{-2}	0.30	1	a
4.14	1:5 (1:10)	10^6	0.30	10^{-17}	10^{-17}	10^{-8}	0.30	1	a
4.15	1:5 (1:10)	10^6	0.30	10^{-14}	10^{-14}	10^{-5}	0.15	1	a
4.16	1:5 (1:10)	10^6	0.30	10^{-14}	10^{-14}	10^{-5}	0.50	1	a
4.17	1:5 (1:10)	10^6	0.30	10^{-16}	10^{-16}	10^{-7}	0.30	1	a
4.20	1:5 (1:10)	10^6	0.30	10^{-14} @ start 10^{-15} @ end			0.30 start 0.22 end		a
Heterogeneous domain									
4.18	1:5 (1:10)	10^6	0.30	10^{-12}	10^{-14}		0.30	100	b
4.19	1:5 (1:10)	10^6	0.30	10^{-12}	10^{-14}		0.30	100	c

Table 4.1 (continued)

† First ratio is height-to-width of solution domain; second ratio is thickness-to-width of simulated body. Owing to symmetry, solution domain represents one half the total body width.

For $\phi = 0.30$
ρ_t (dry) = 1855 kg/m^3
ρ_t (saturated) = 2155 kg/m^3
ρ_w = 1000 kg/m^3
$\mu = 10^{-3}$ Pa s

For $\phi = 0.15$
ρ_t (dry) = 2250 kg/m^3
ρ_t (saturated) = 2400 kg/m^3

For $\phi = 0.50$
ρ_t (dry) = 1325 kg/m^3
ρ_t (saturated) = 1825 kg/m^3

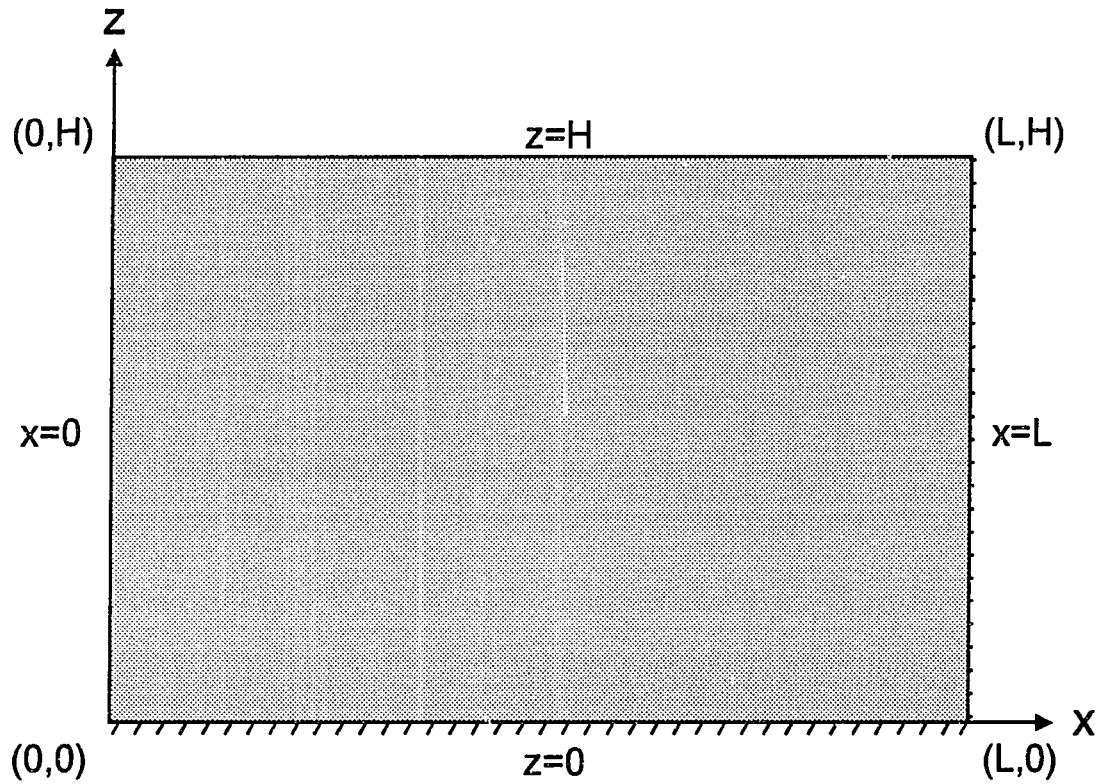

Figure 4.1. Definition sketch of numerically modeled domain. The domain represents one-half the width of a debris-flow deposit (width = 2L). The basal boundary is impermeable, and the right hand side of the domain represents a no-flow boundary along the centerline of the deposit. Cartesian coordinates of the corners of the domain are given.

Figure 4.2. Numerically modeled domains and boundary conditions imposed during consolidation. Domain A represents a homogeneous domain; domains B and C represent heterogeneous domains. In the heterogenous domains the permeability of the higher transmissivity zones (k_1) is two orders of magnitude larger than the permeability of the primary domain (k_2). In most analyses the domain width was several times greater than its thickness. Subsequent figures provide precise dimensions.

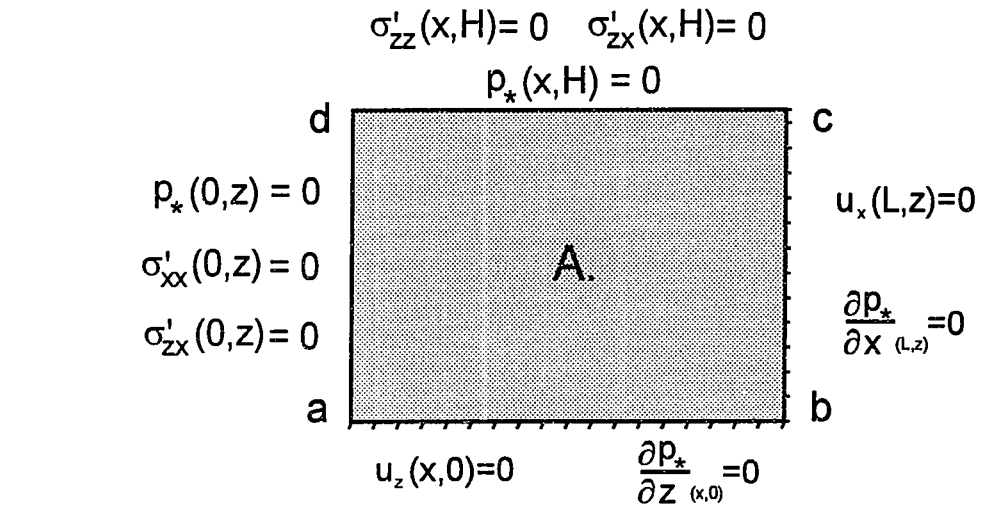
$\sigma'_{zz}(x,H)=0$ $\sigma'_{zx}(x,H)=0$
$p_*(x,H)=0$
d
c
$p_*(0,z)=0$
$\sigma'_{xx}(0,z)=0$
$\sigma'_{zx}(0,z)=0$
A.
$u_x(L,z)=0$
$\frac{\partial p_*}{\partial x}_{(L,z)}=0$
a
b
$u_z(x,0)=0$
$\frac{\partial p_*}{\partial z}_{(x,0)}=0$

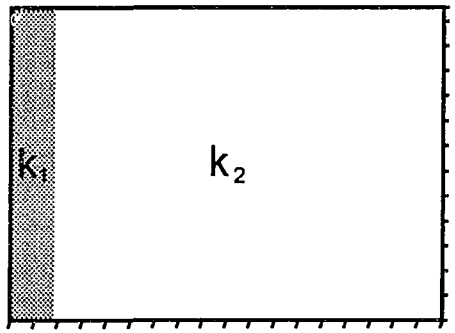
k_1
k_2

B.

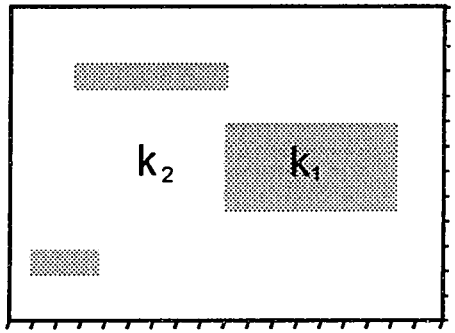
k_2
k_1

C.

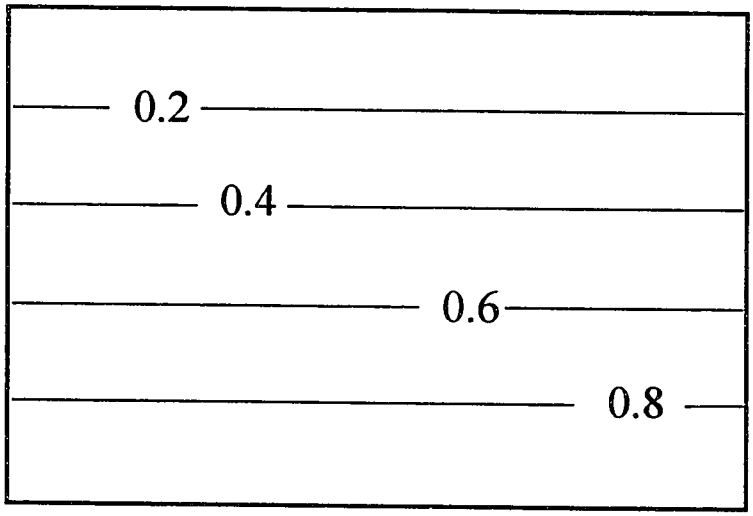

Figure 4.3. Fluid-pressure distribution following instantaneous application of gravity load. This fluid-pressure profile serves as the initial condition for the consolidation analysis. Fluid-pressure profile represents contours of total fluid pressure at a given level normalized by the total fluid pressure at the base of the domain (see text for discussion).

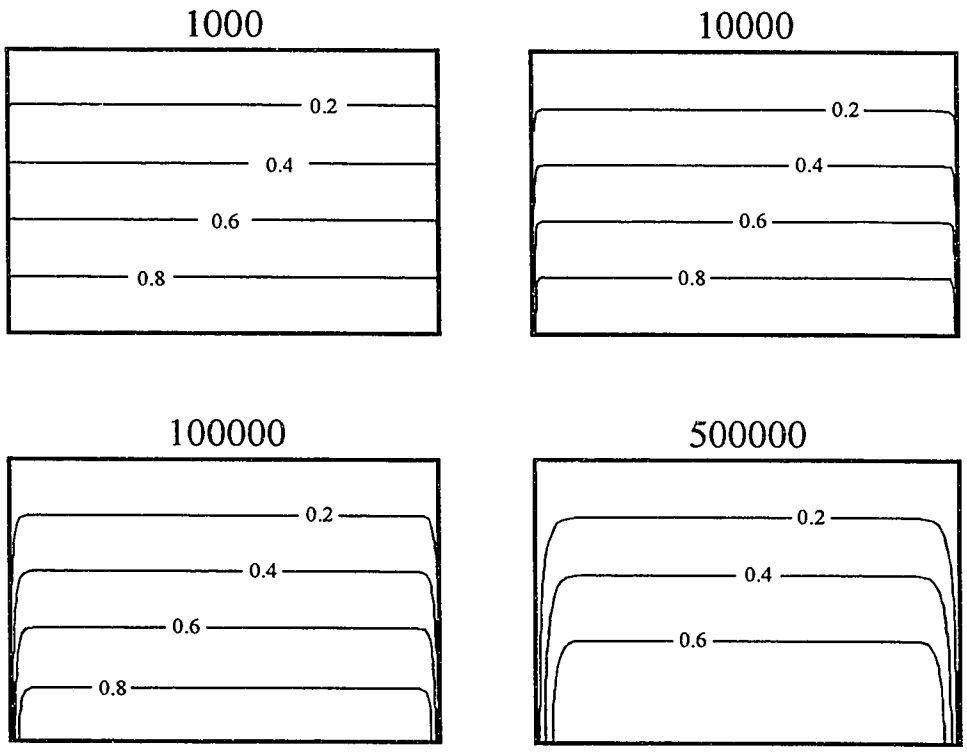

Figure 4.4. Numerical solution of nonequilibrium-fluid-pressure evolution. The solution is for a homogeneous domain and is based on a two-dimensional pressure-diffusion model that does not couple evolving fluid pressures and effective stresses. Each plot represents a time, in seconds, since an initially lithostatic pressure profile began to diffuse (see Figure 4.3). Contours represent nonequilibrium fluid pressure normalized by the initial lithostatic fluid pressure at the base of the domain. In this simulation $D = 10^{-7}$ m^2/s, identical to that shown in Figure 4.9a. Here, each plot shows the full domain width instead of the half-width. Domain ratio is 1:10. Note the similarity between the fluid-pressure profiles that develop in coupled (Figure 4.9a) and uncoupled models when domains are thin and wide and when effective stresses are low.

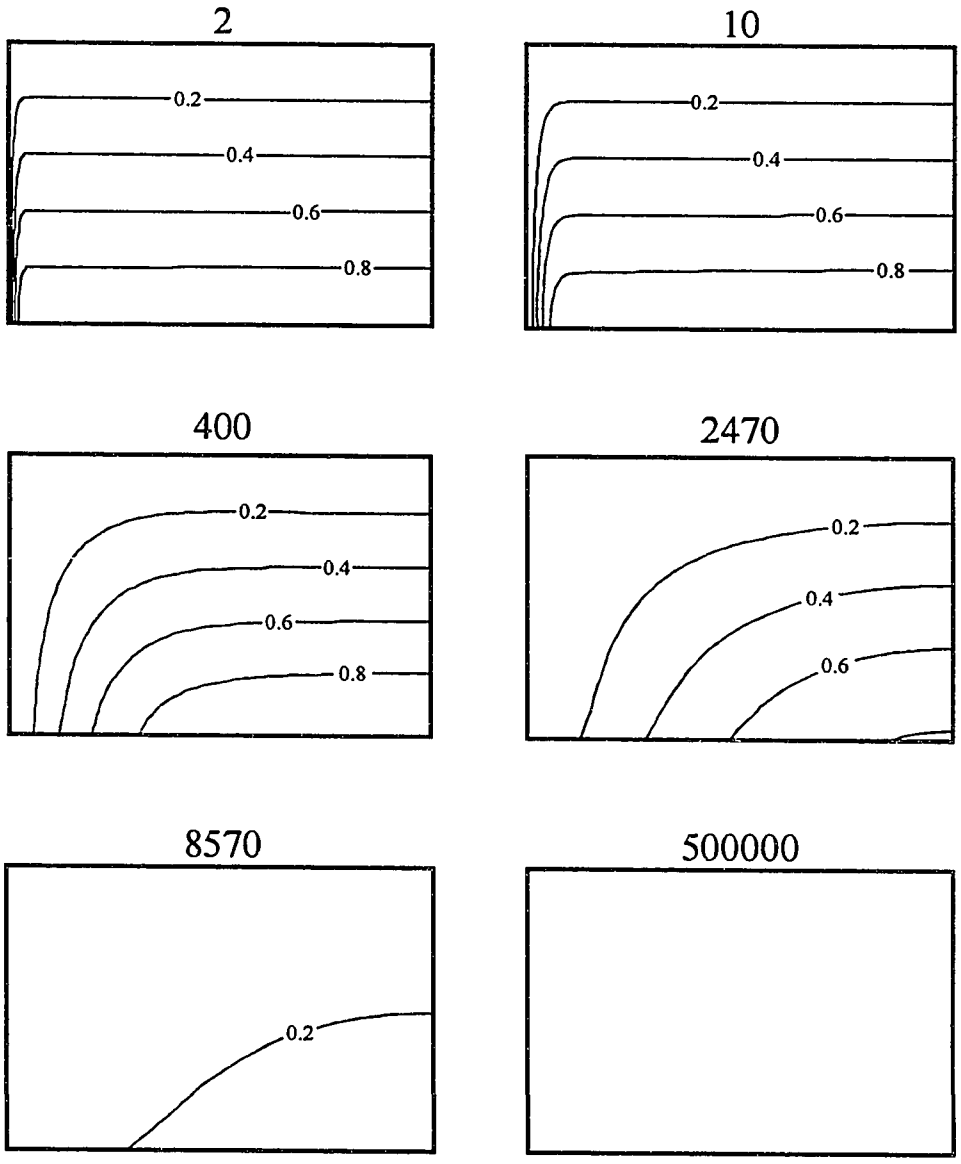

Figure 4.5a. Fluid-pressure contours at discrete times following initial gravity loading. Time given in seconds (e.g., 500000≈ 6 days). Contours represent fluid pressure at a given level normalized by the initial lithostatic fluid pressure at the base of the domain. Here, $E = 10^6$ Pa; $\nu = 0.30$; $k = 10^{-14}$ m^2; and $D = 10^{-5}$ m^2/s. See Table 4.1 for other physical properties. Domain ratio (H/L) is 1:0.5. Vertical exaggeration (v.e.) ≈ 0.3. Horizontal exaggeration ≈ 3.

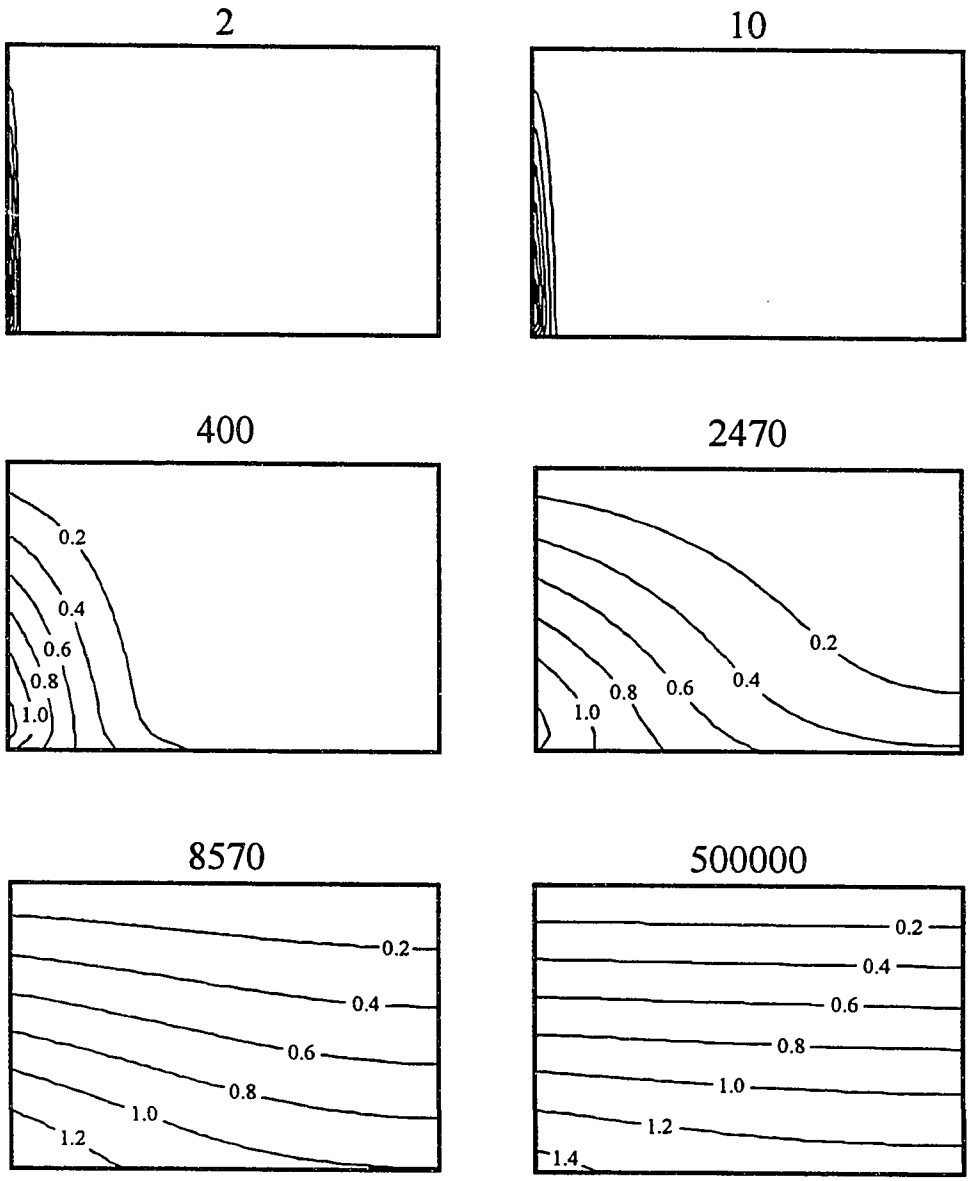

Figure 4.5b. Mean compressive principal effective stress contours at discrete times following initial gravity loading. Time given in seconds (e.g., 500000≈ 6 days). Contours represent mean compressive principal effective stress at a given level normalized by $\rho_w gH$. See Figure 4.5a for other definitions and physical properties of domain. Domain ratio (H/L) is 1:0.5. Vertical exaggeration (v.e.) ≈ 0.3. Horizontal exaggeration ≈ 3.

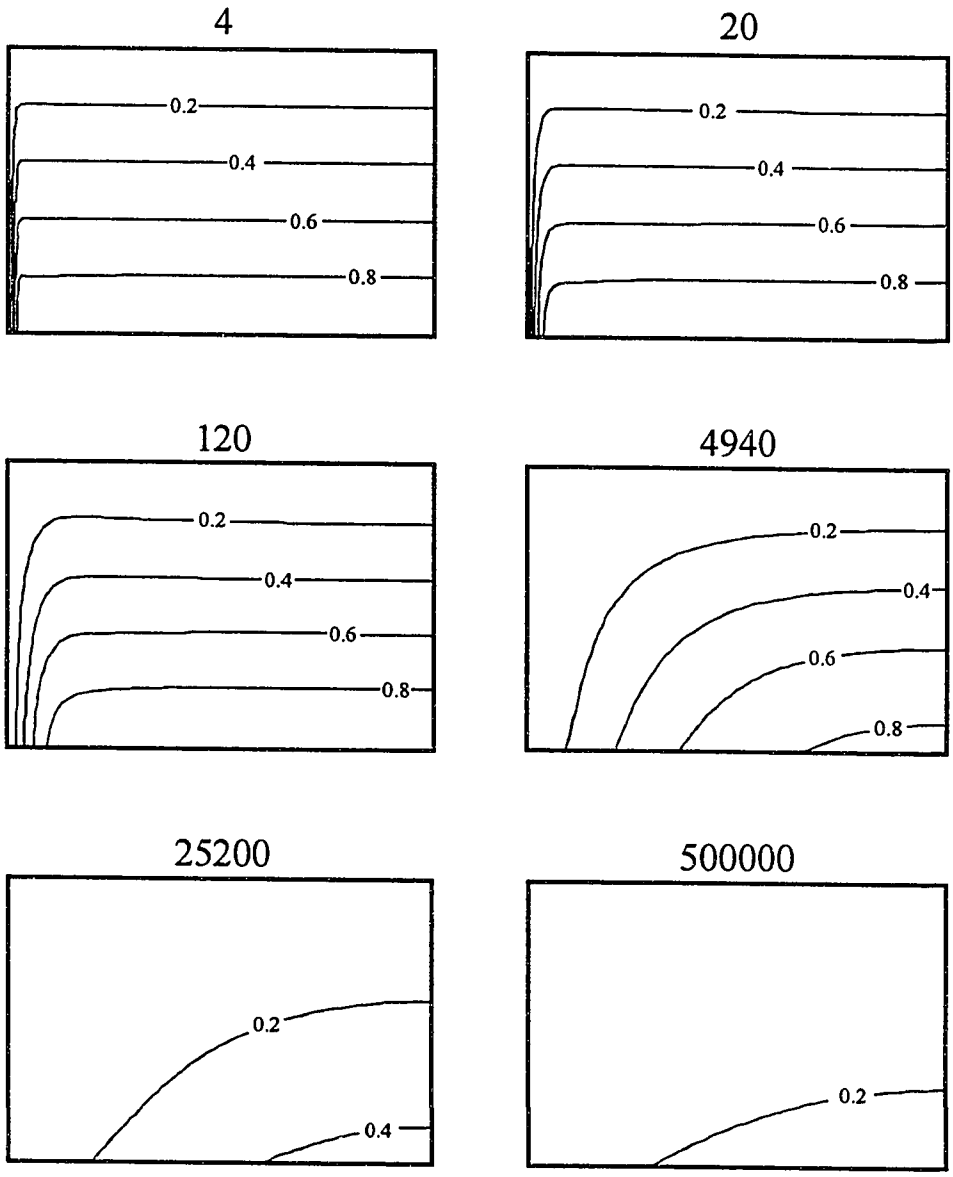

Figure 4.6a. Fluid-pressure contours at discrete times following initial gravity loading. Time given in seconds (e.g., 500000≈ 6 days). Contours represent fluid pressure at a given level normalized by the initial lithostatic fluid pressure at the base of the domain. Here, $E = 10^6$ Pa; $\nu = 0.30$; $k = 10^{-14}$ m^2; and $D = 10^{-5}$ m^2/s. See Table 4.1 for other physical properties. Domain ratio (H/L) is 1:1. Vertical exaggeration (v.e.) ≈ 0.7. Horizontal exaggeration ≈ 2.5.

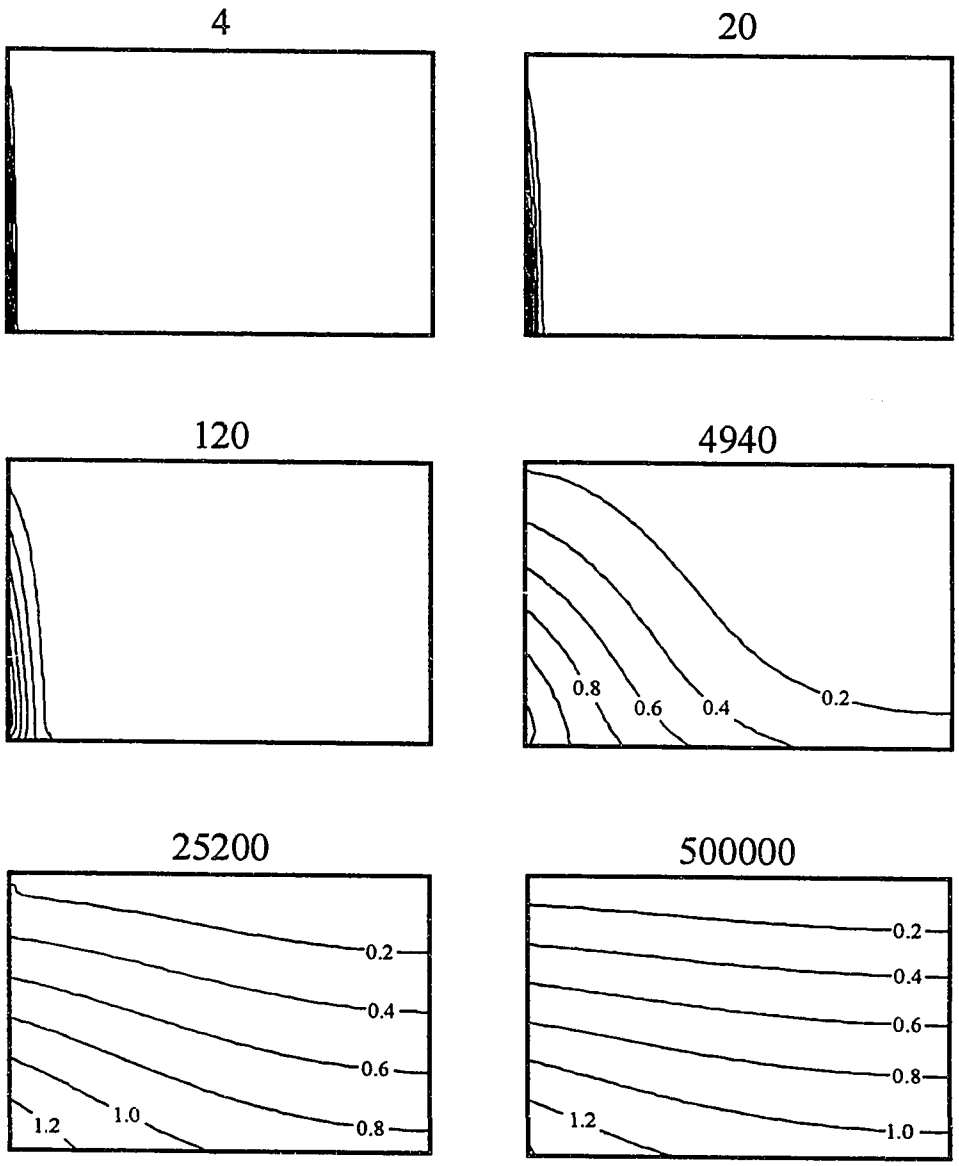

Figure 4.6b. Mean compressive principal effective stress contours at discrete times following initial gravity loading. Time given in seconds (e.g., 500000≈ 6 days). Contours represent mean compressive principal effective stress at a given level normalized by $\rho_w gH$. See Figure 4.6a for other definitions and physical properties of domain. Domain ratio (H/L) is 1:1. Vertical exaggeration (v.e.) ≈ 0.7. Horizontal exaggeration ≈ 2.5.

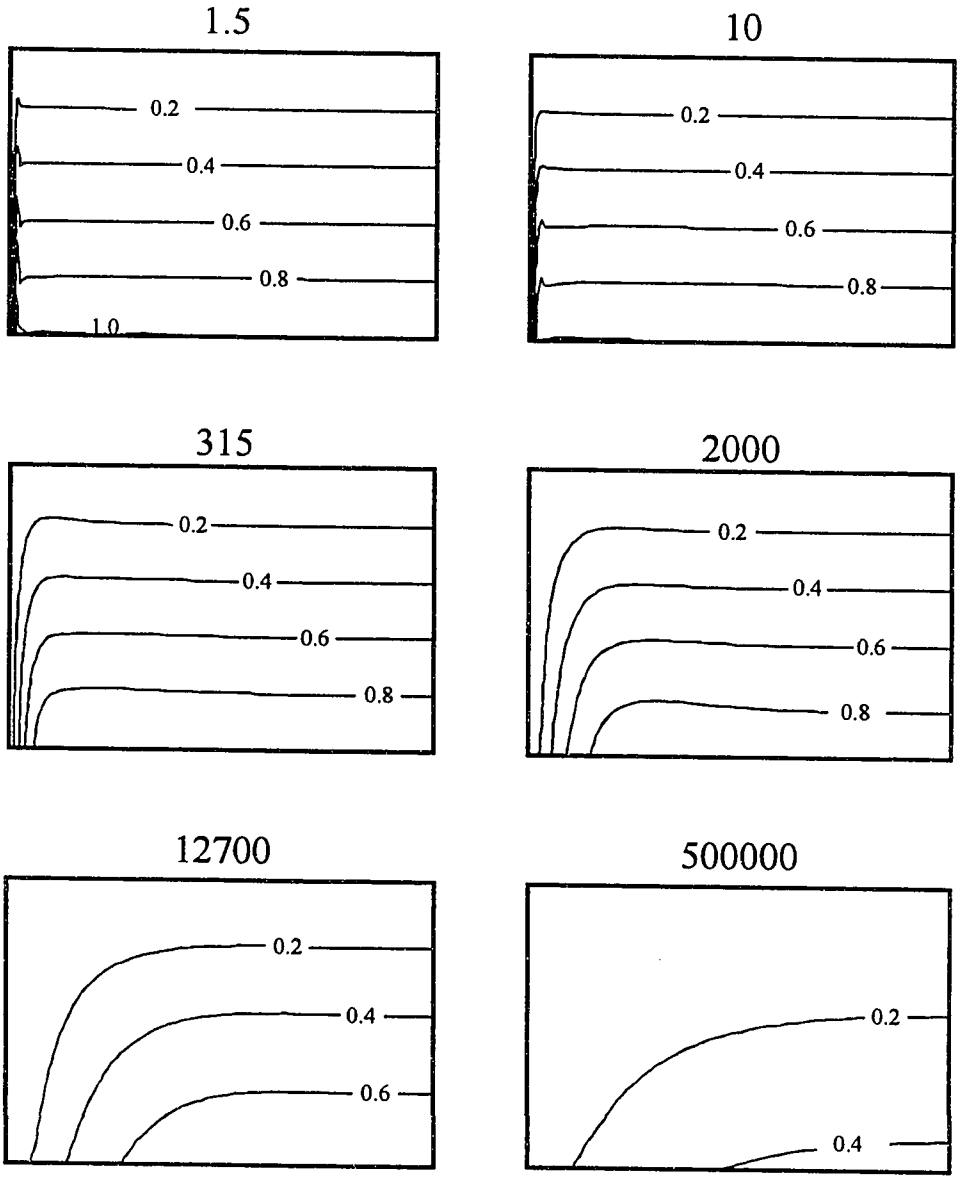

Figure 4.7a. Fluid-pressure contours at discrete times following initial gravity loading. Time given in seconds (e.g., 500000≈ 6 days). Contours represent fluid pressure at a given level normalized by the initial lithostatic fluid pressure at the base of the domain. Here, $E = 10^6$ Pa; $\nu = 0.30$; $k = 10^{-14}$ m^2; and $D = 10^{-5}$ m^2/s. See Table 4.1 for other physical properties. Domain ratio (H/L) is 1:2.5. Vertical exaggeration (v.e.) ≈ 1.7.

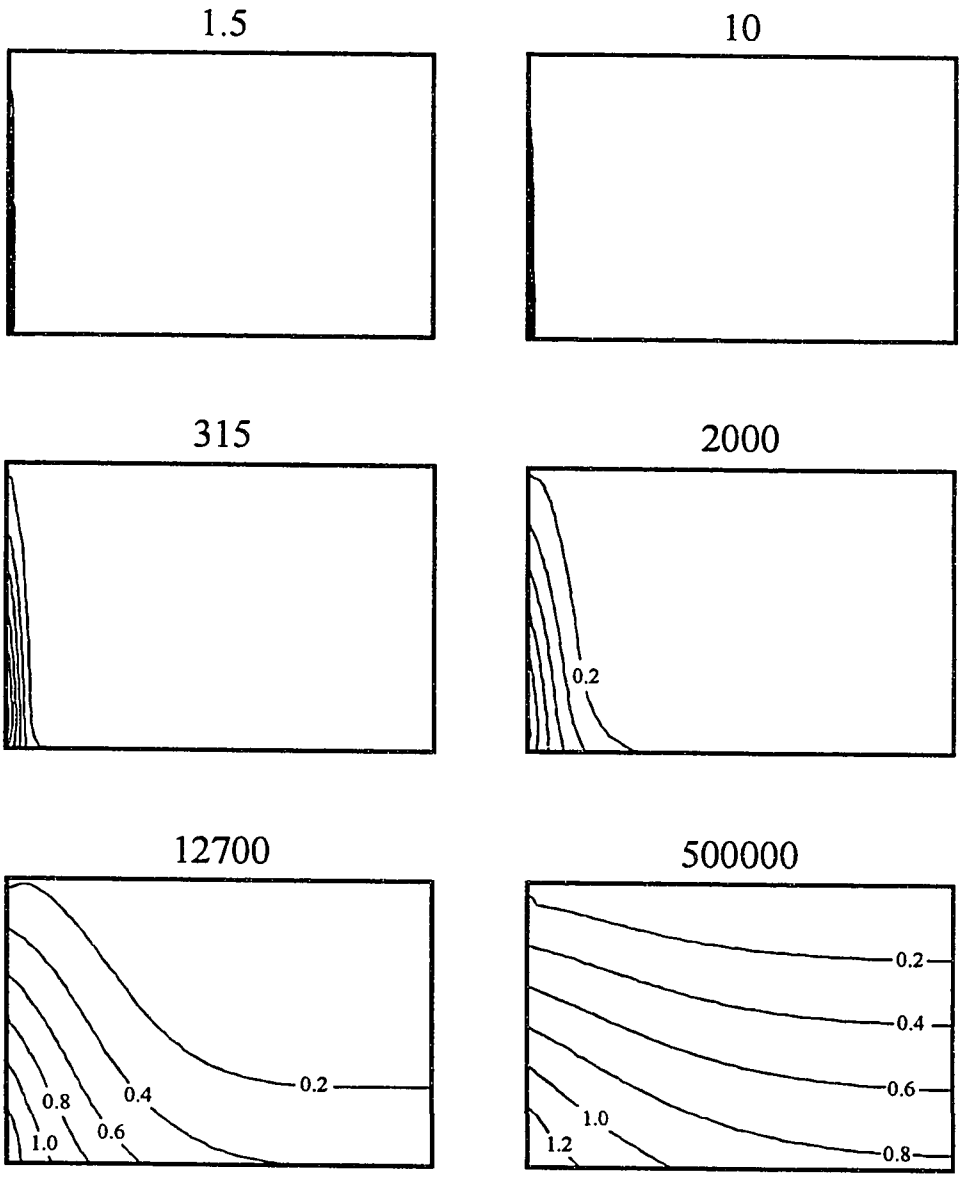

Figure 4.7b. Mean compressive principal effective stress contours at discrete times following initial gravity loading. Time given in seconds (e.g., 500000≈ 6 days). Contours represent mean compressive principal effective stress at a given level normalized by $\rho_w gH$. See Figure 4.7a for other definitions and physical properties of domain. Domain ratio (H/L) is 1:2.5. Vertical exaggeration (v.e.) ≈ 1.7.

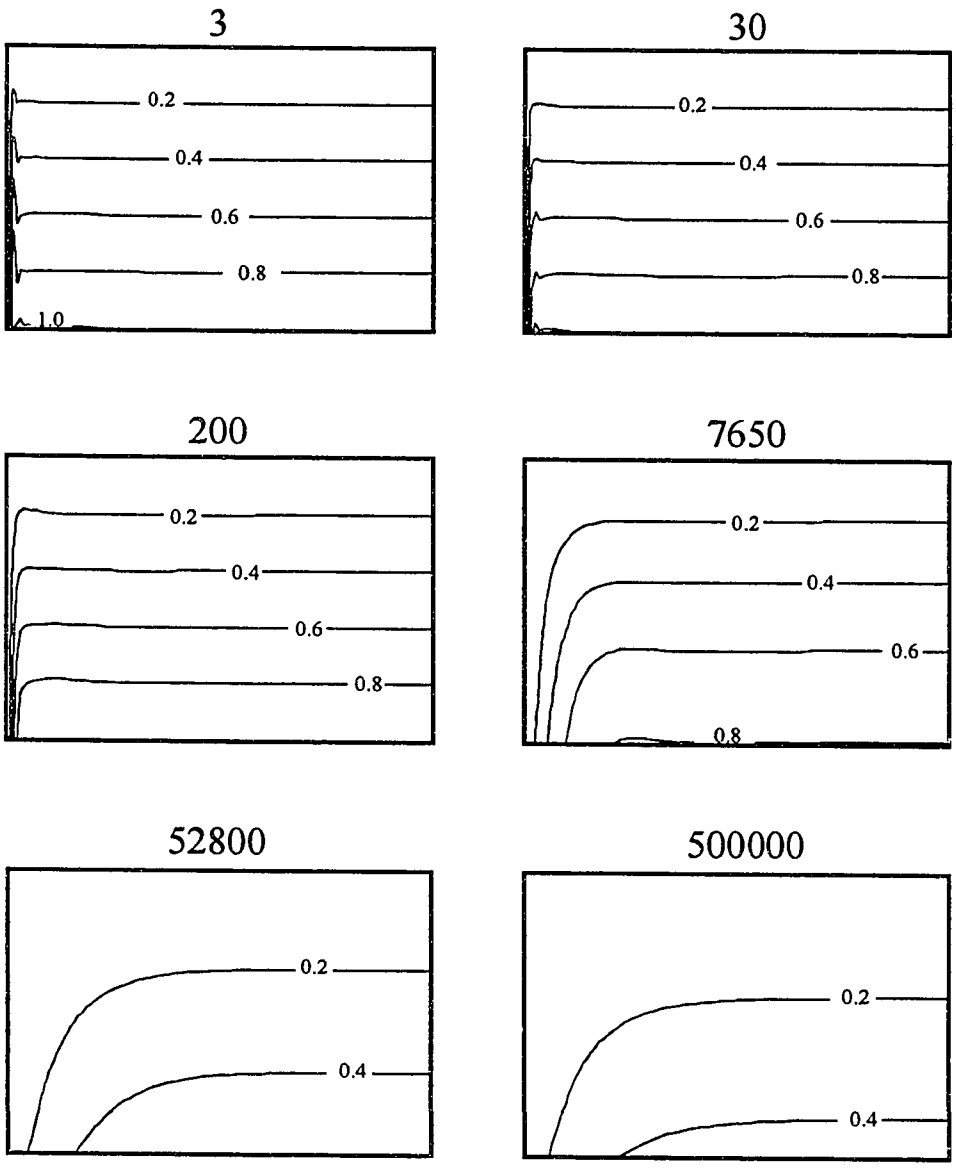

Figure 4.8a. Fluid-pressure contours at discrete times following initial gravity loading. Time given in seconds (e.g., 500000 ≈ 6 days). Contours represent fluid pressure at a given level normalized by the initial lithostatic fluid pressure at the base of the domain. Here, $E = 10^6$ Pa; $\nu = 0.30$; $k = 10^{-14}$ m^2; and $D = 10^{-5}$ m^2/s. See Table 4.1 for other physical properties. Domain ratio (H/L) is 1:5. Vertical exaggeration (v.e.) ≈ 3.5.

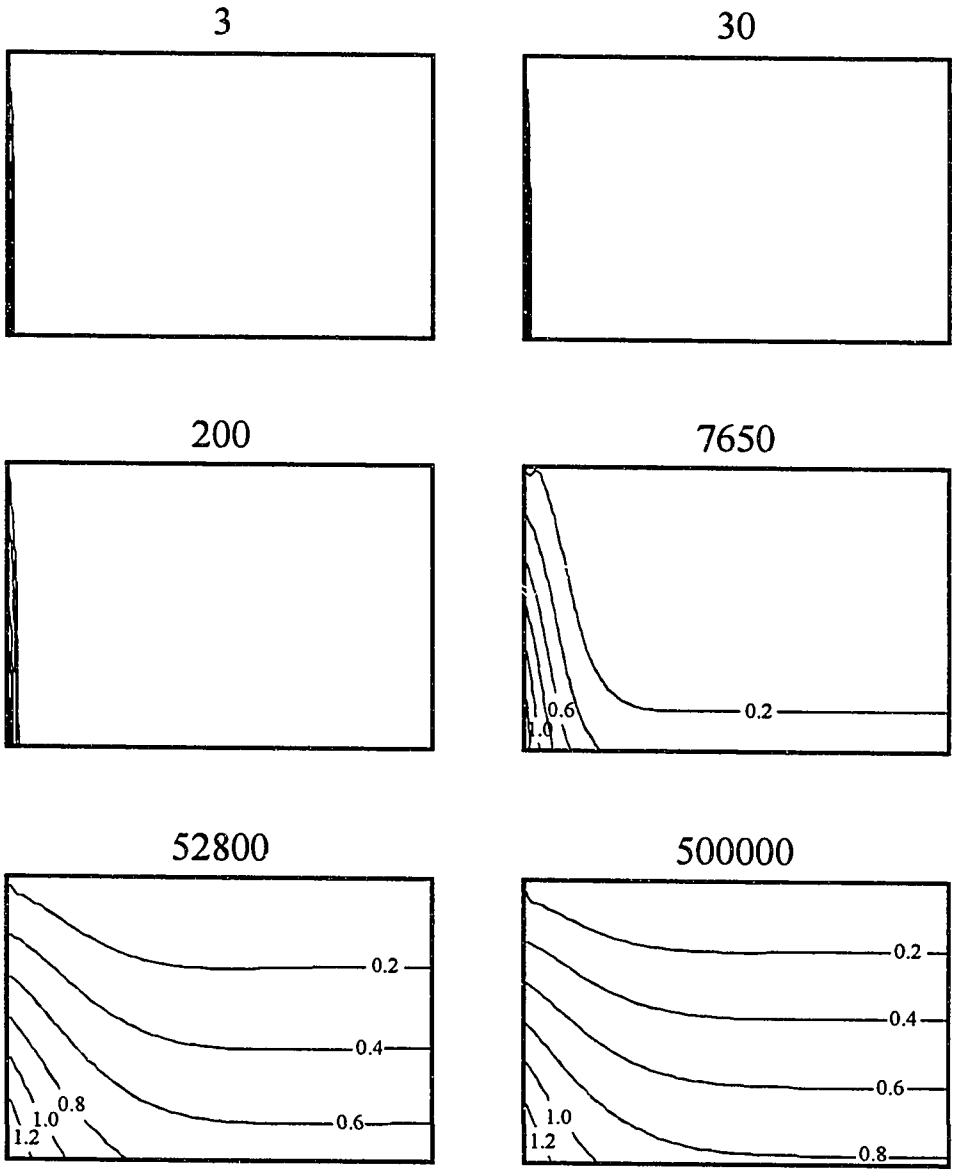

Figure 4.8b. Mean compressive principal effective stress contours at discrete times following initial gravity loading. Time given in seconds (e.g., 500000≈ 6 days). Contours represent mean compressive principal effective stress at a given level normalized by $\rho_w gH$. See Figure 4.8a for other definitions and physical properties of domain. Domain ratio (H/L) is 1:5; v.e. ≈ 3.5.

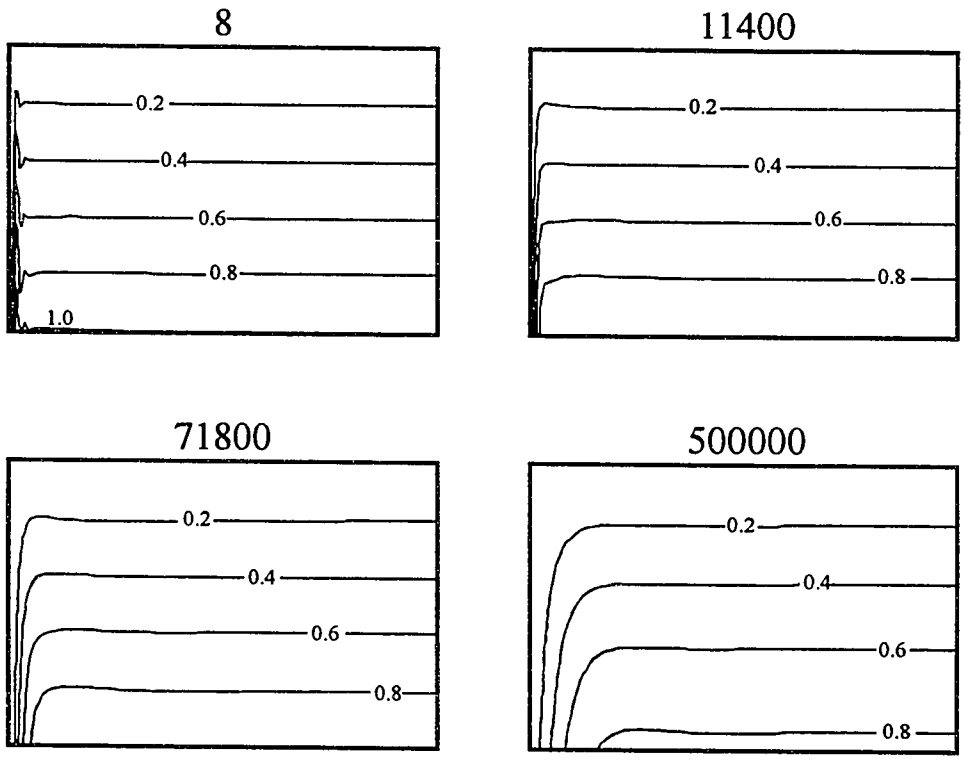

Figure 4.9a. Fluid-pressure contours. Time in seconds following gravity loading. Here, E=10^4 Pa; ν=0.30; k=10^{-14} m^2; and D=10^{-7} m^2/s. See Figure 4.8a for other definitions. Domain ratio (H/L) is 1:5; v.e. ≈ 3.5.

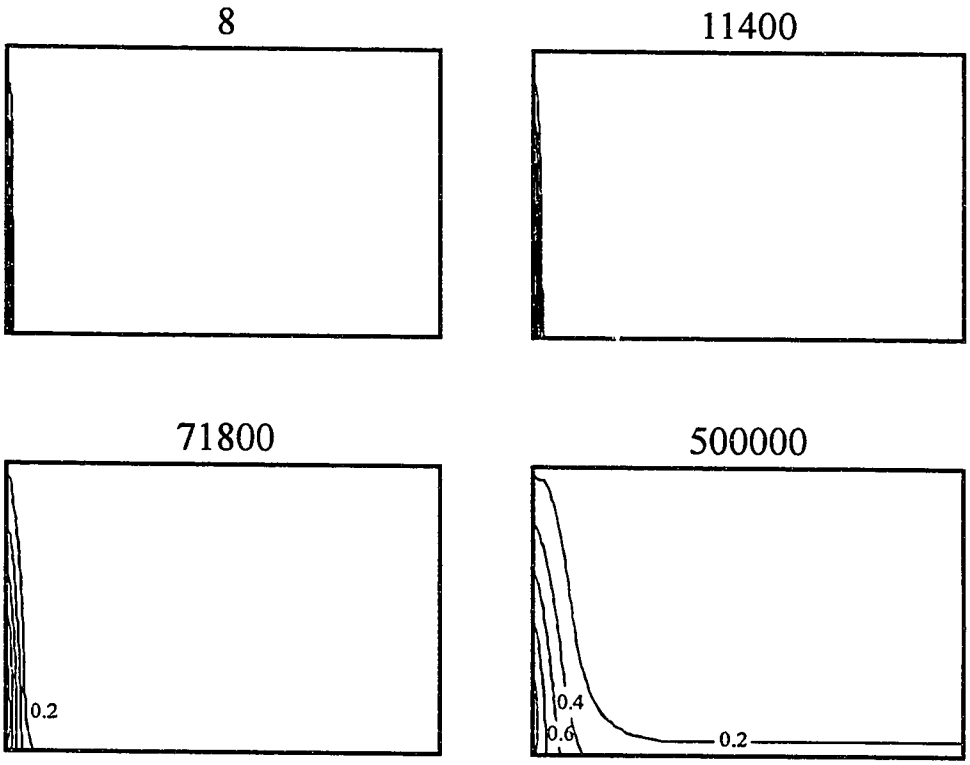

Figure 4.9b. Mean compressive principal effective stress contours. See Figures 4.8a and 4.9a for other definitions and physical properties of domain.

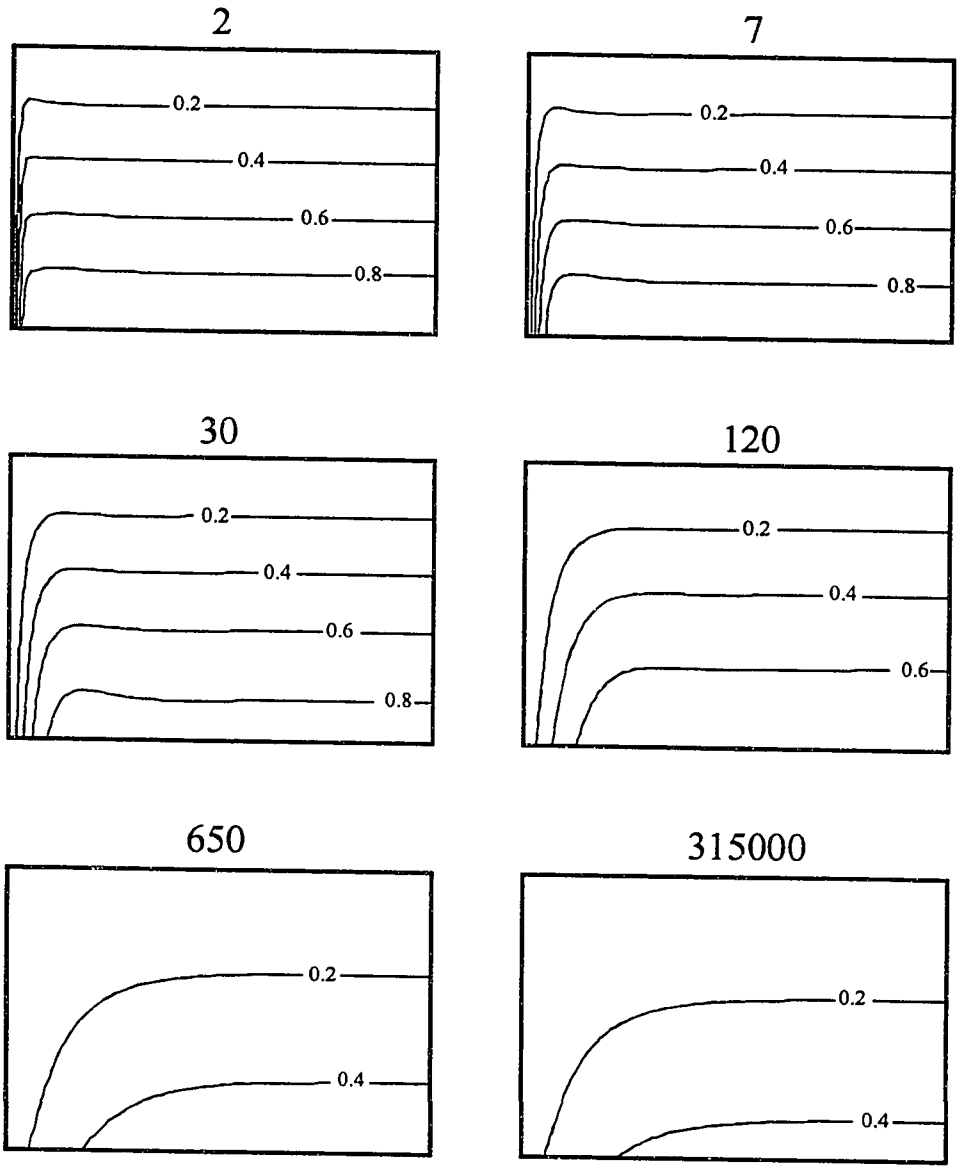

Figure 4.10a. Fluid-pressure contours. Time in seconds following gravity loading. Here, $E = 10^8$ Pa; $\nu = 0.30$; $k = 10^{-14}$ m^2; and $D = 10^{-3}$ m^2/s. See Fgure 4.8a for other definitions. Domain ratio (H/L) is 1:5; v.e. $\approx$ 3.5.

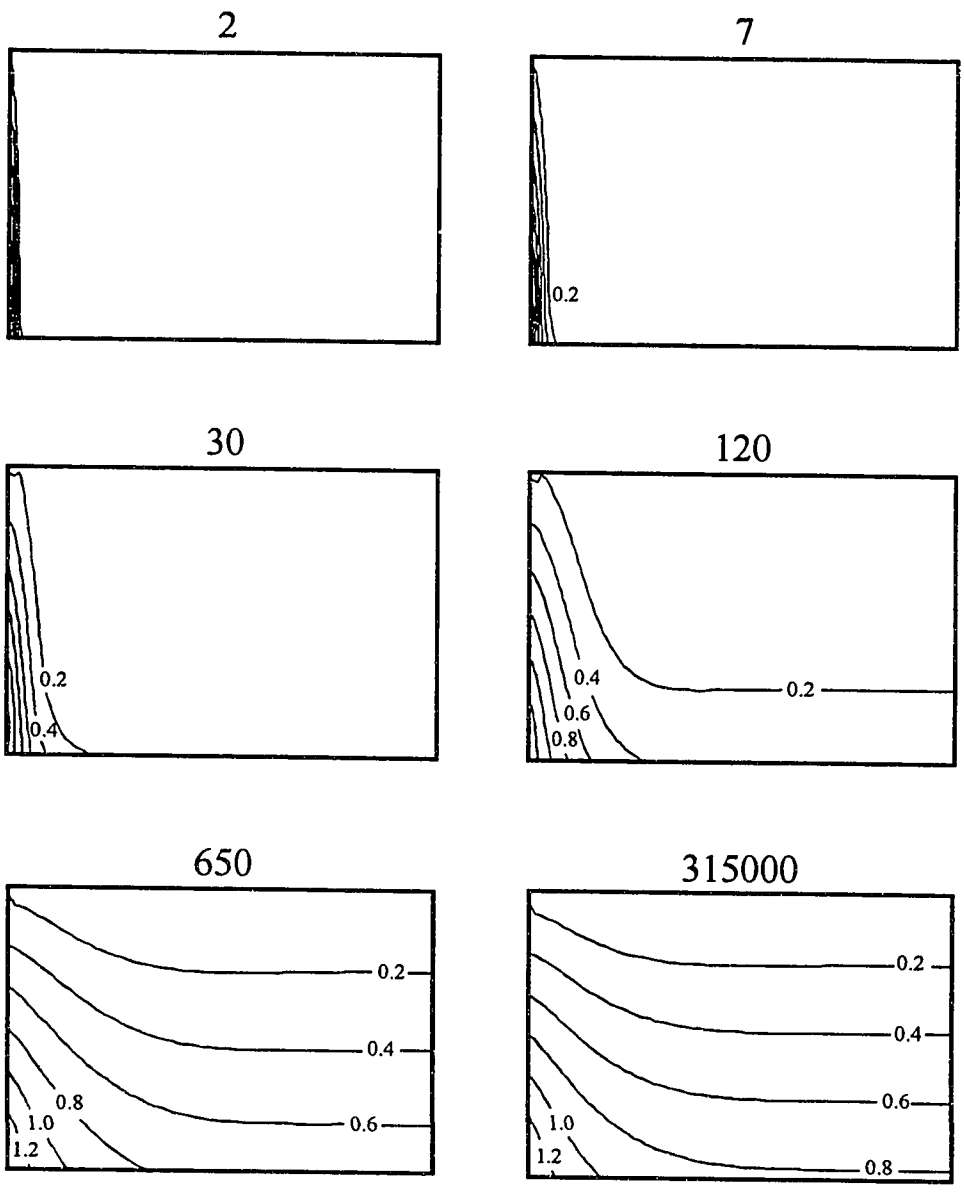

Figure 4.10b. Mean compressive principal effective stress contours. See Figures 4.8b and 4.9a for other definitions and physical properties of domain.

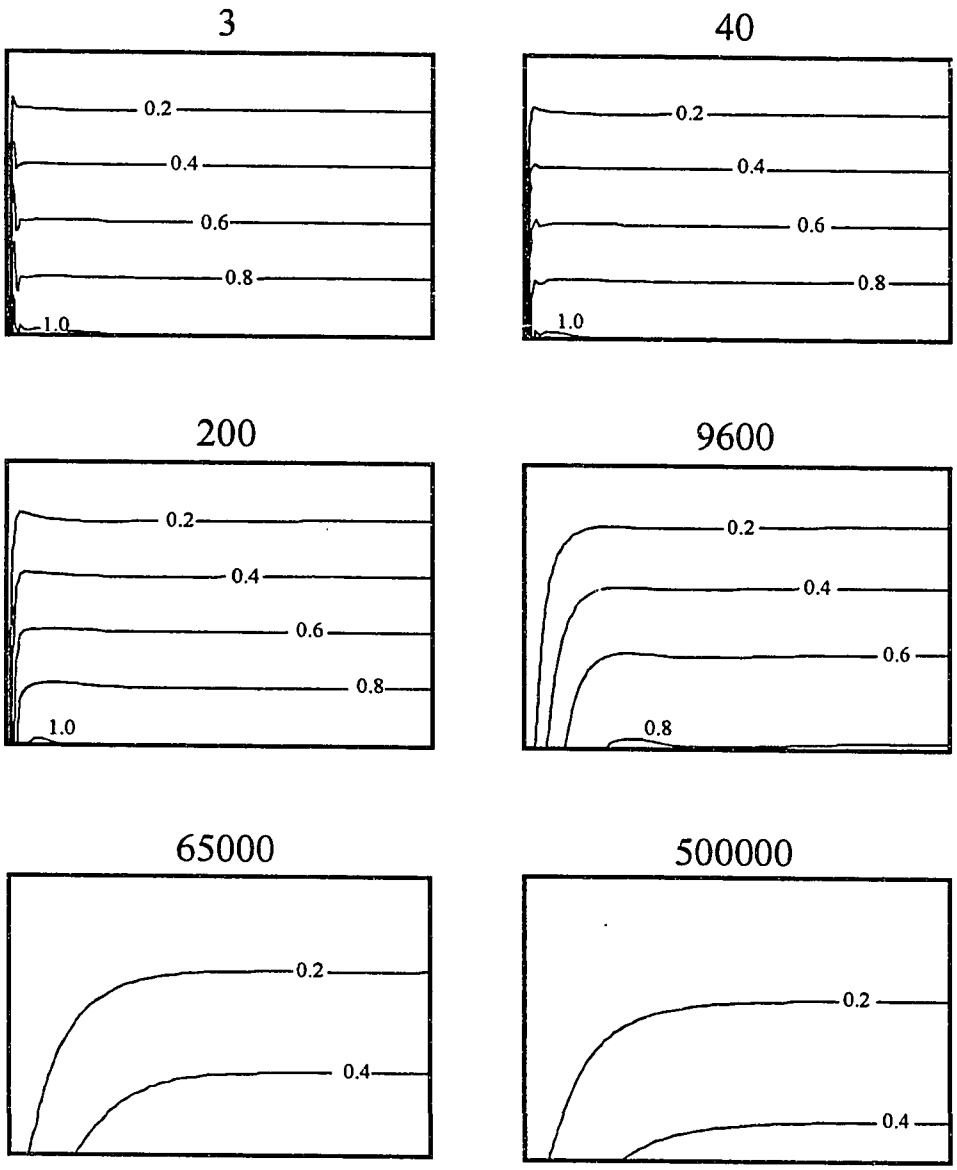

Figure 4.11a. Fluid-pressure contours. Time in seconds following gravity loading. Here, $E = 10^6$ Pa; $\nu = 0.10$; $k = 10^{-14}$ m^2; and $D = 10^{-5}$ m^2/s. See Figure 4.8a for other definitions. Domain ratio (H/L) is 1:5; v.e. ≈ 3.5.

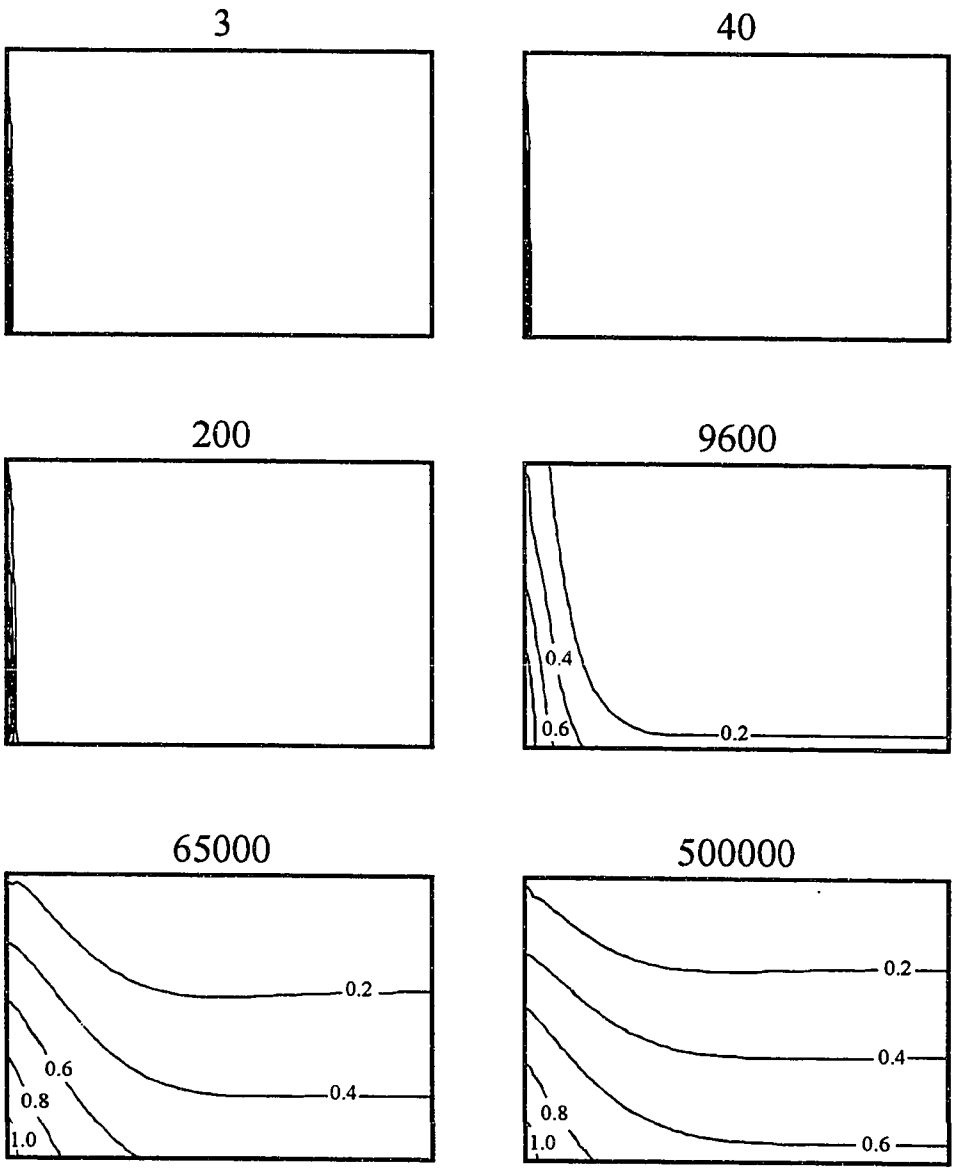

Figure 4.11b. Mean compressive principal effective stress contours. See Figures 4.8b and 4.11a for other definitions and physical properties of domain.

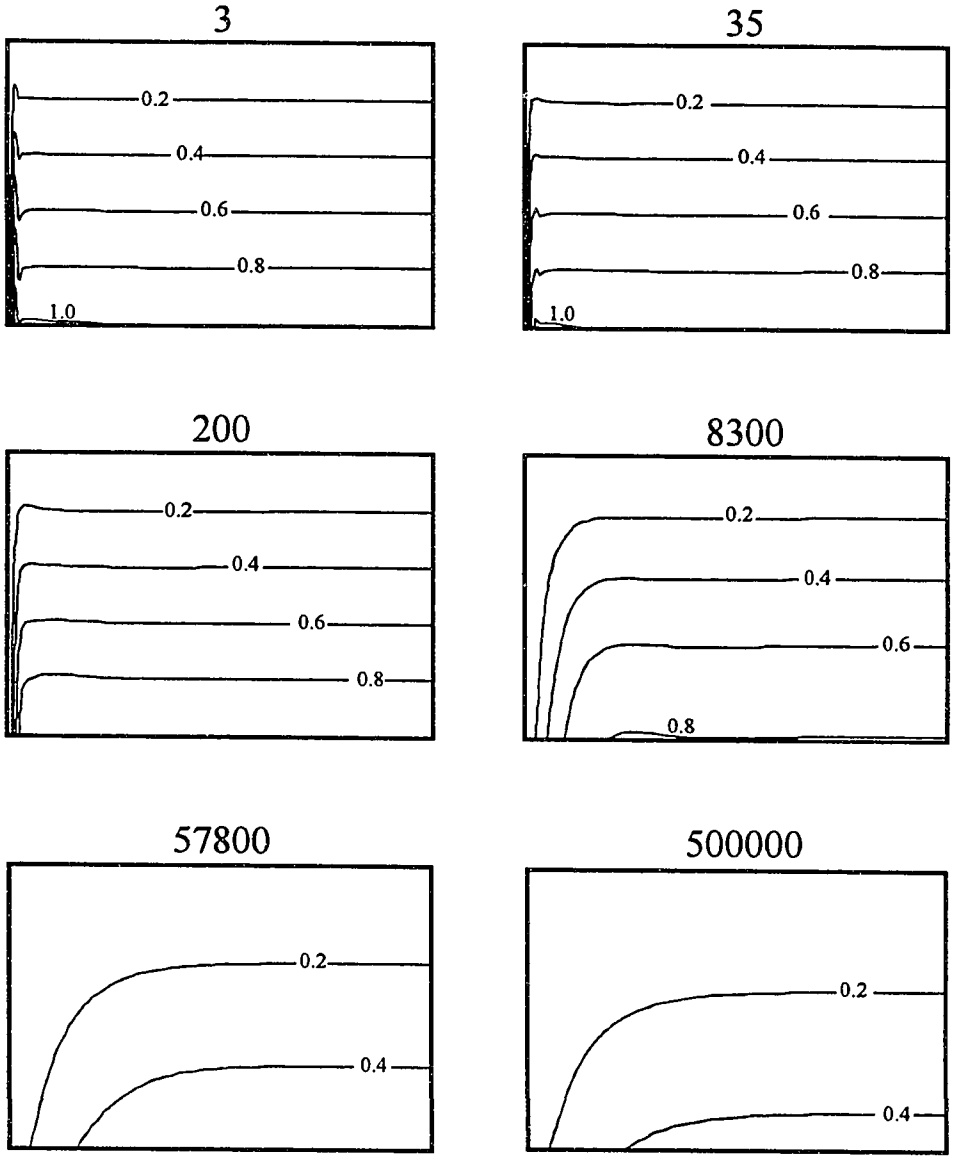

Figure 4.12a. Fluid-pressure contours. Time in seconds following gravity loading. Here, $E = 10^6$ Pa; $\nu = 0.25$; $k = 10^{-14}$ m^2; and $D = 10^{-5}$ m^2/s. See Figure 4.8a for other definitions. Domain ratio (H/L) is 1:5; v.e. ≈ 3.5.

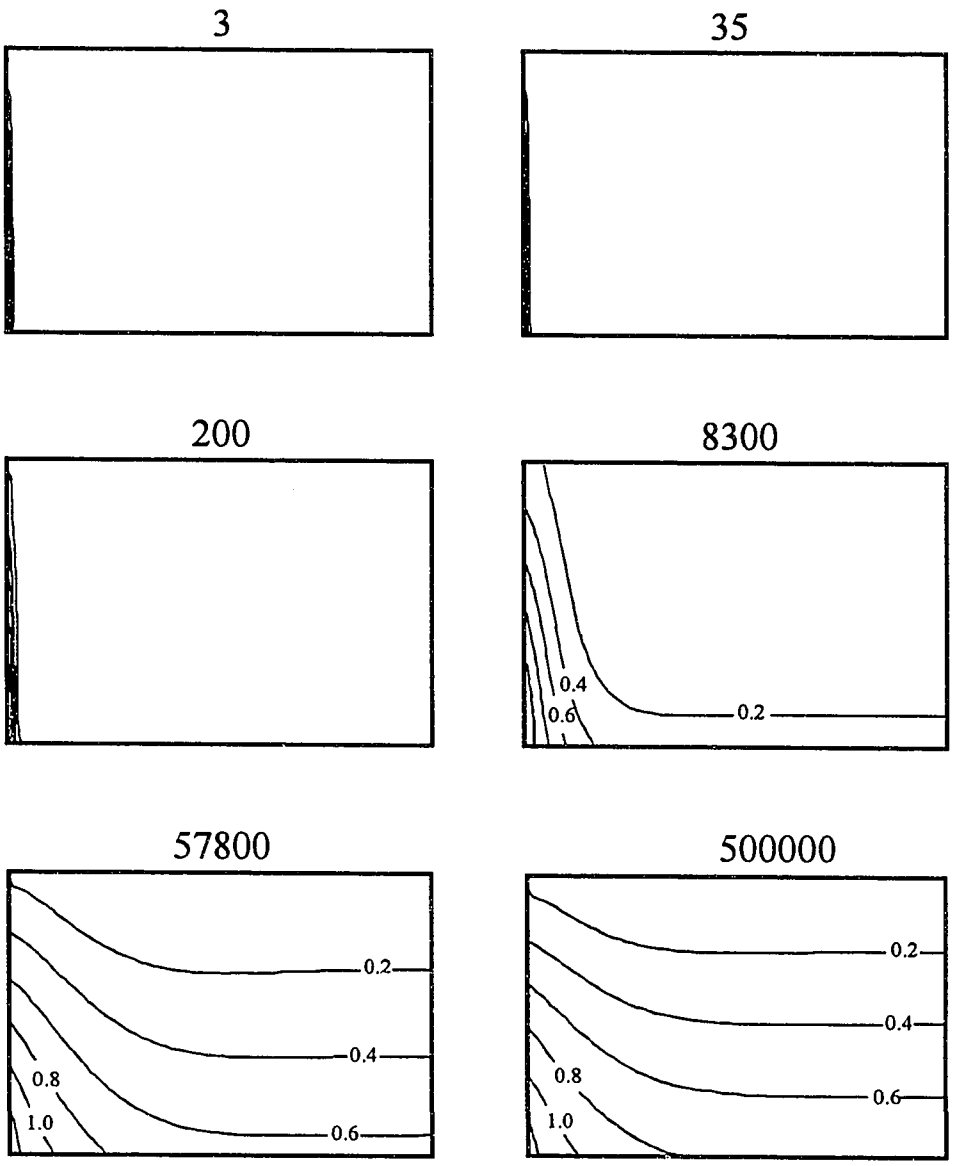

Figure 4.12b. Mean compressive principal effective stress contours. See Figures 4.8b and 4.12a for other definitions and physical properties of domain.

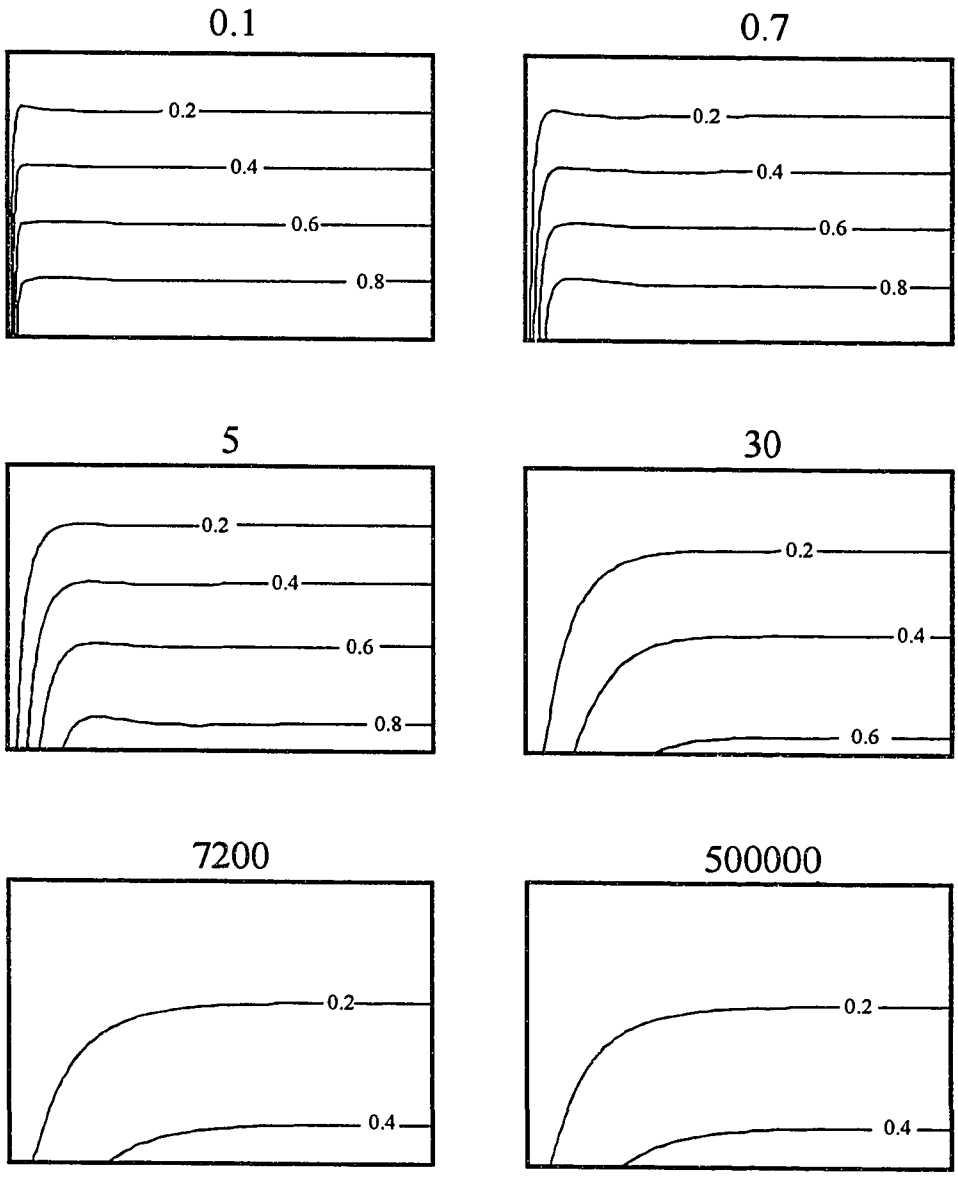

Figure 4.13a. Fluid-pressure contours. Time in seconds following gravity loading. Here, $E = 10^6$ Pa; $\nu = 0.30$; $k = 10^{-11}$ m^2; and $D = 10^{-2}$m^2/s. See Figure 4.8a for other definitions. Domain ratio (H/L) is 1:5; v.e. ≈ 3.5.

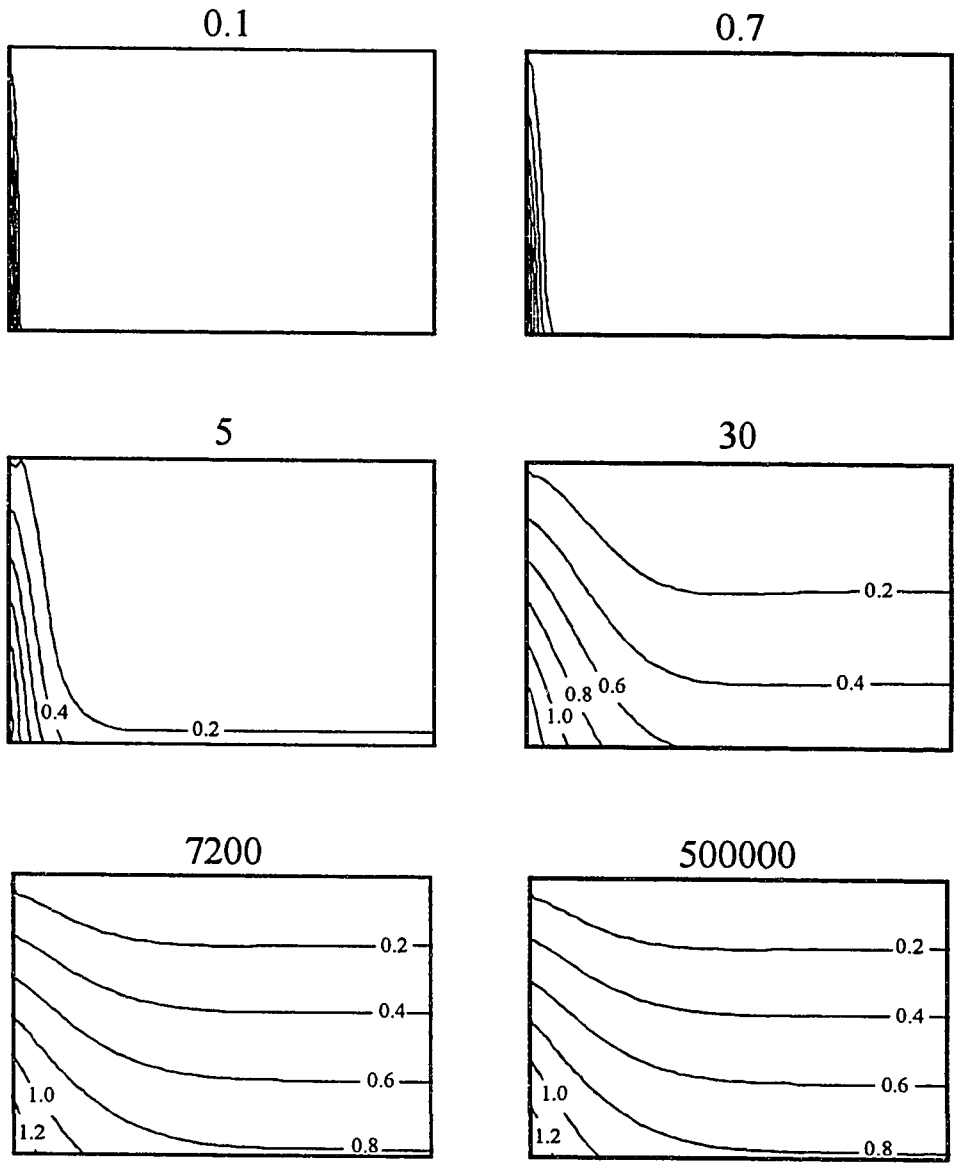

Figure 4.13b. Mean compressive principal effective stress contours. See Figures 4.8b and 4.13a for other definitions and physical properties of domain.

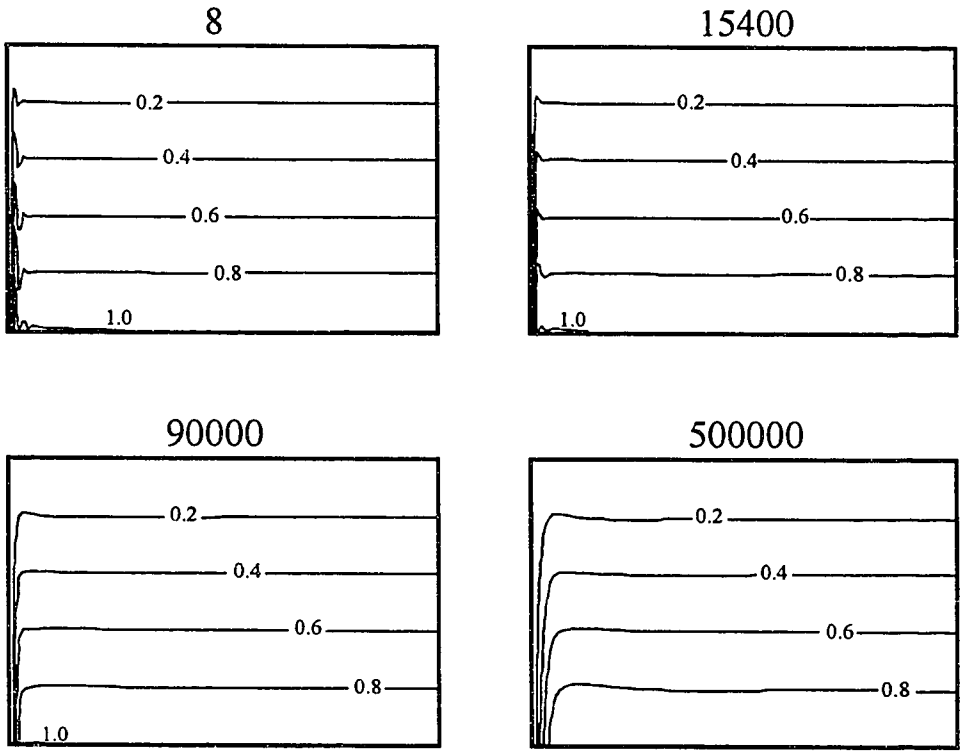

Figure 4.14a. Fluid-pressure contours. Time in seconds following gravity loading. Here, $E = 10^6$ Pa; $\nu = 0.30$; $k = 10^{-17}$ m^2; and $D = 10^{-8}$ m^2/s. See Figure 4.8a for other definitions. Domain ratio (H/L) is 1:5; v.e. ≈ 3.5.

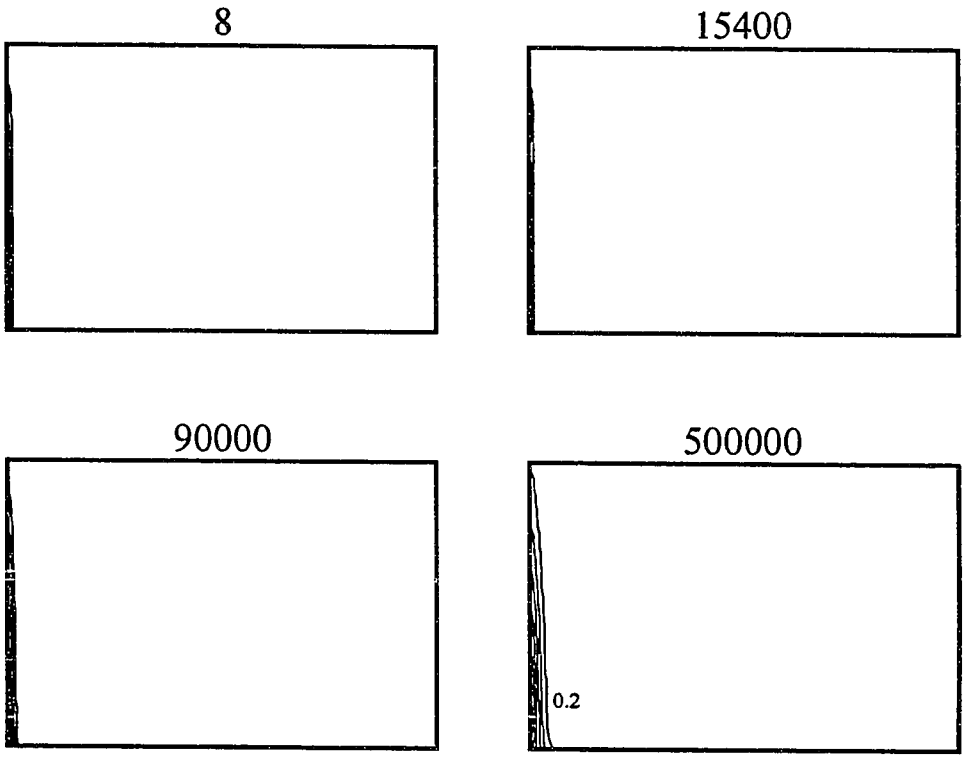

Figure 4.14b. Mean compressive principal effective stress contours. See Figures 4.8b and 4.14a for other definitions and physical properties of domain.

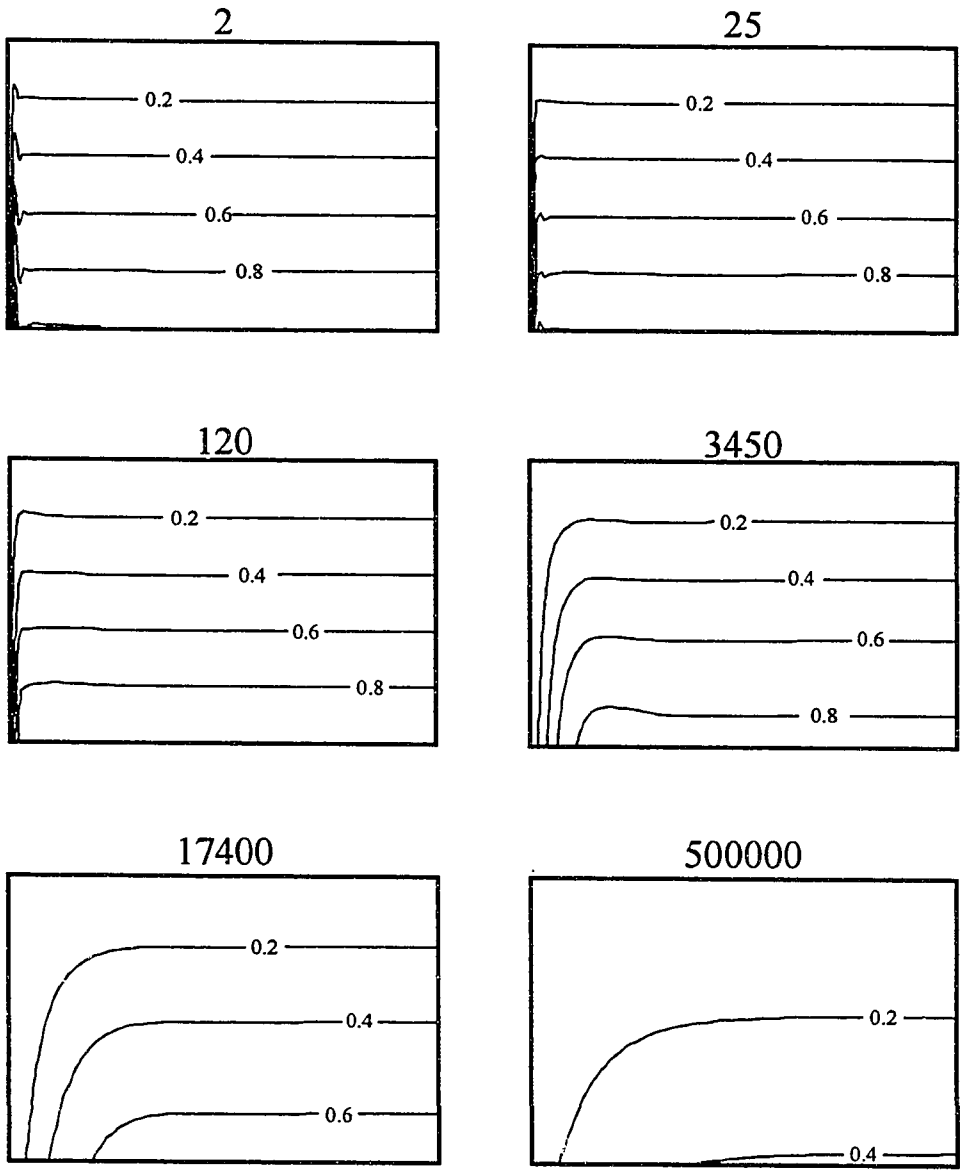

Figure 4.15a. Fluid-pressure contours. Time in seconds following gravity loading. Here, $E = 10^6$ Pa; $\nu = 0.30$; $k = 10^{-14}$ m^2; $\phi = 0.15$; and $D = 10^{-5}$ m^2/s. See Figure 4.8a for other definitions. Domain ratio (H/L) is 1:5; v.e. ≈ 3.5.

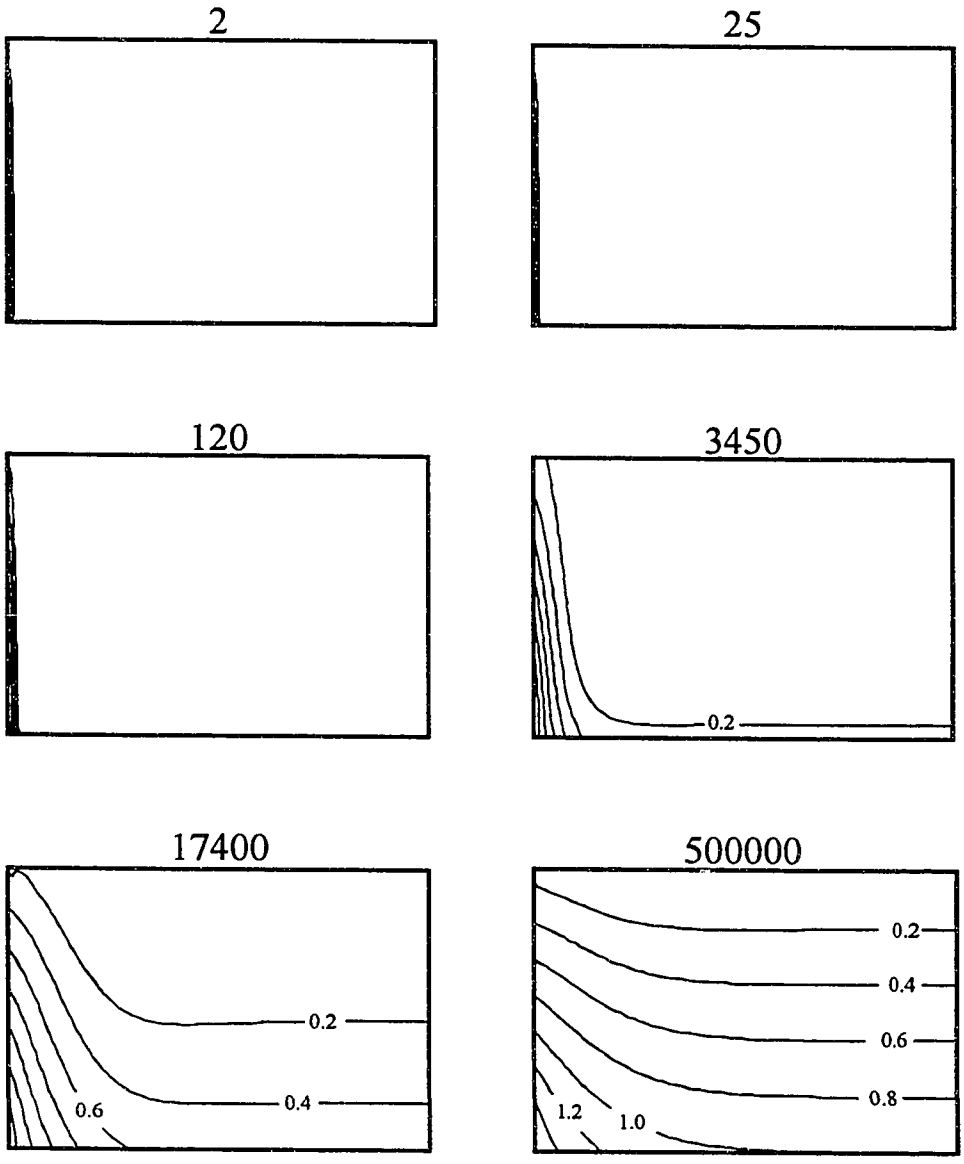

Figure 4.15b. Mean compressive principal effective stress contours. See Figure 4.8b and 4.15a for other definitions and physical properties of domain.

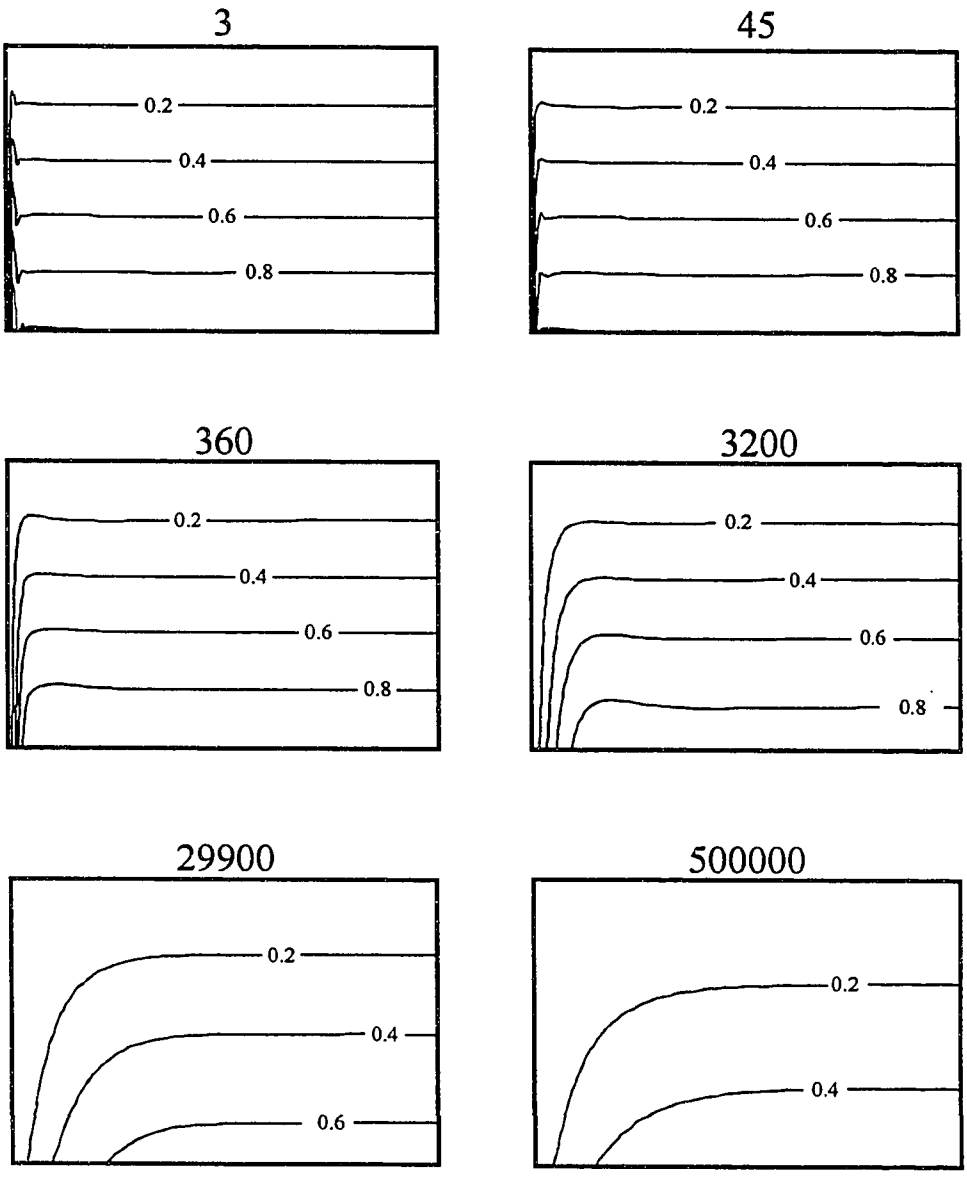

Figure 4.16a. Fluid-pressure contours. Time in seconds following gravity loading. Here, $E = 10^6$ Pa; $\nu = 0.30$; $k = 10^{-14}$ m^2; $\phi = 0.50$; and $D = 10^{-5}$ m^2/s. See Figure 4.8a for other definitions. Domain ratio (H/L) is 1:5; v.e. $\approx$ 3.5.

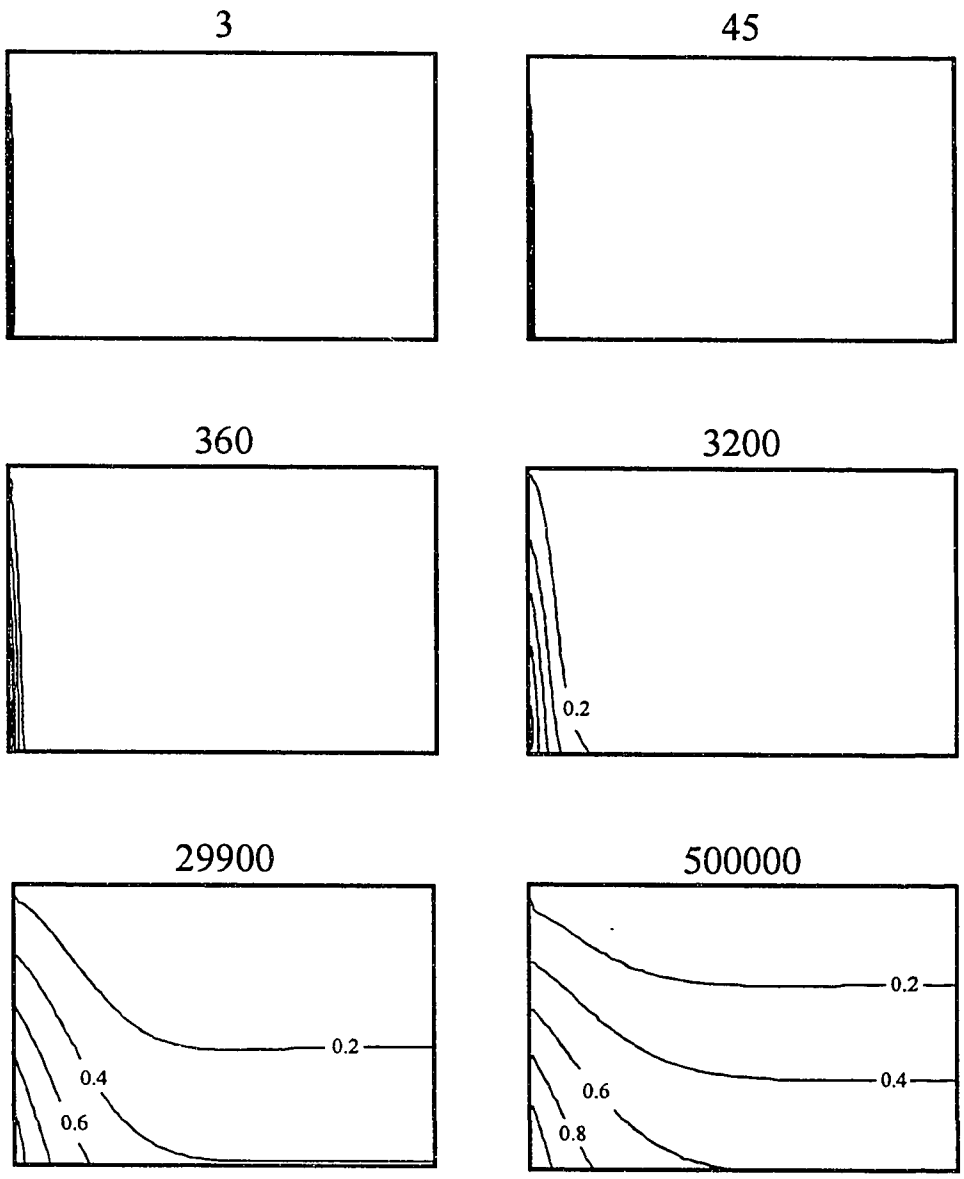

Figure 4.16b. Mean compressive principal effective stress contours. See Figure 4.8b and 4.16a for other definitions and physical properties of domain.

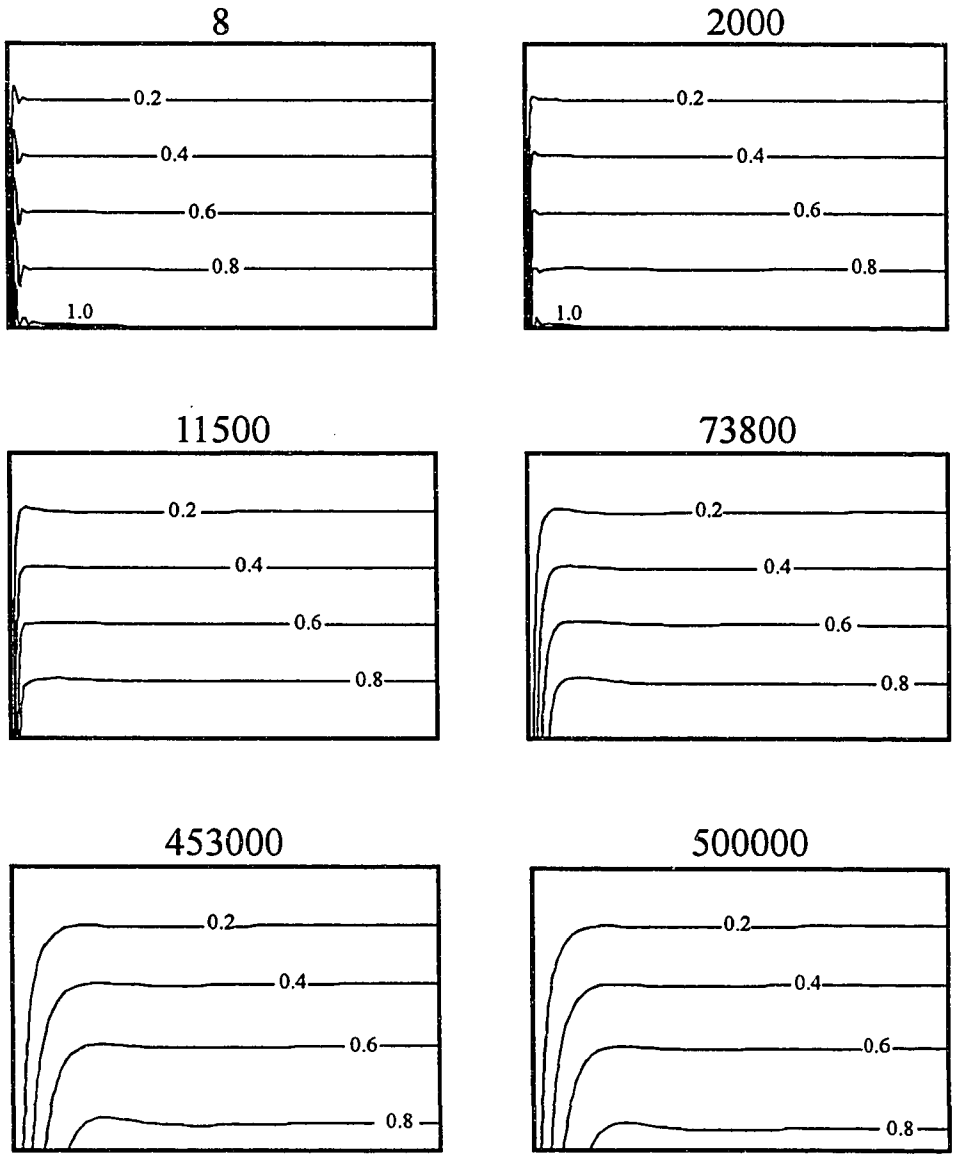

Figure 4.17a. Fluid-pressure contours. Time in seconds following gravity loading. Here, $E = 10^6$ Pa; $\nu = 0.30$; $k = 10^{-16}$ m^2; and $D = 10^{-7}$ m^2/s. See Figure 4.8a for other definitions. Domain ratio (H/L) is 1:5; v.e. ≈ 3.5.

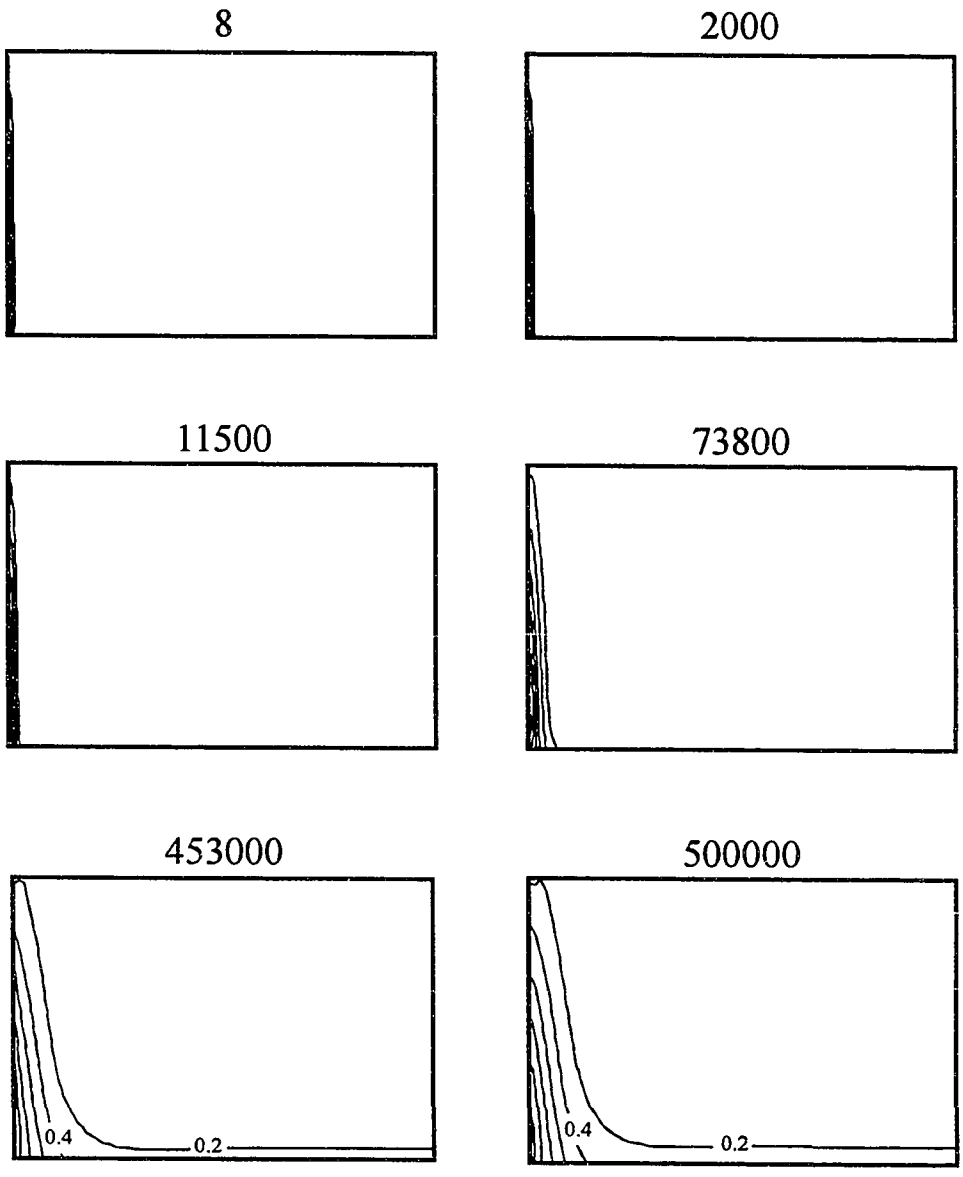

Figure 4.17b. Mean compressive principal effective stress contours. See Figures 4.8b and 4.17a for other definitions and physical properties of domain.

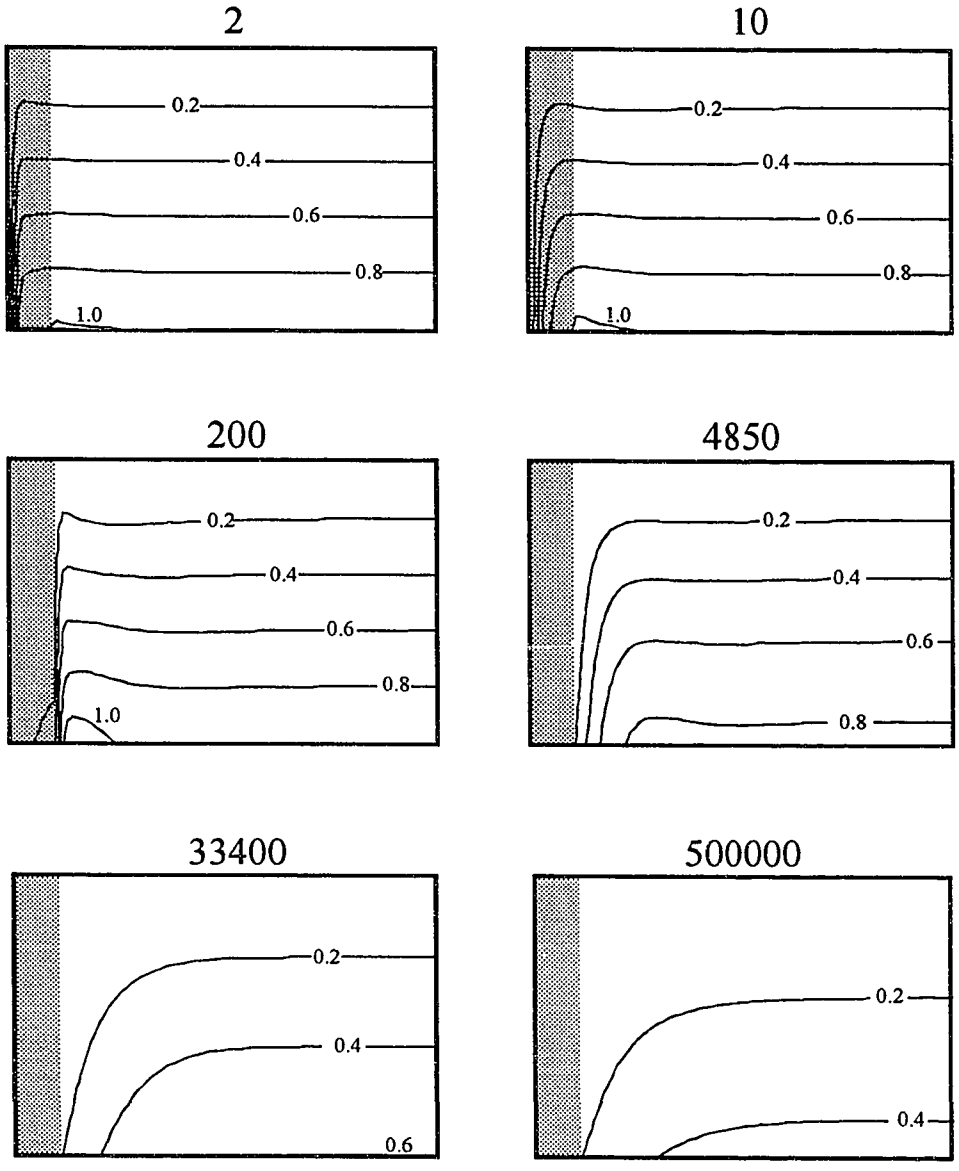

Figure 4.18a. Fluid-pressure contours in a heterogeneous medium. Time in seconds following gravity loading. Here, $E = 10^6$ Pa; $\nu = 0.30$; $k_1 = 10^{-12}$ m^2; and $k_2 = 10^{-14}$m^2. See Figures 4.2 and 4.8a for other definitions. Shading represents higher permeability zone (k_1). Domain ratio (H/L) is 1:5; v.e. $\approx$ 3.5.

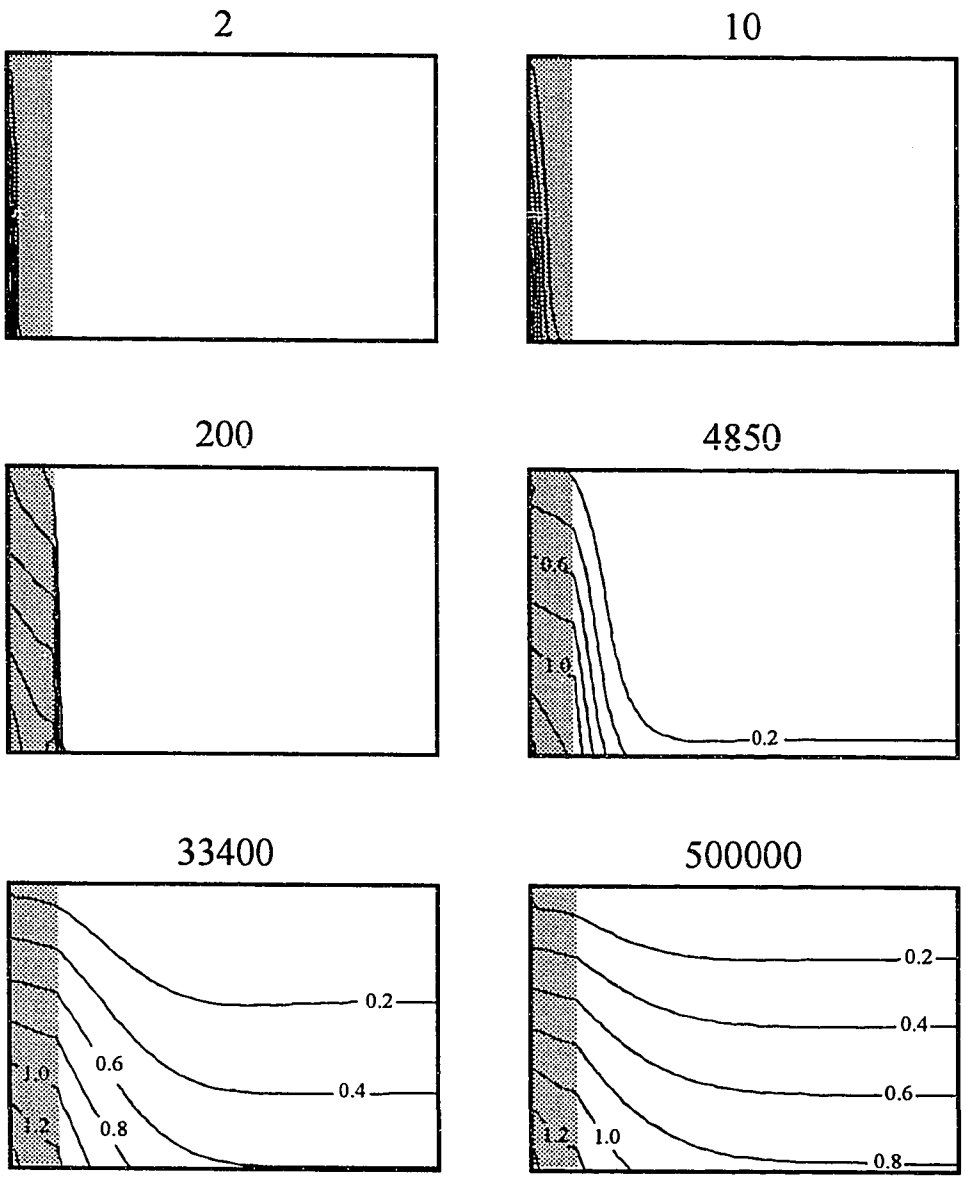

Figure 4.18b. Mean compressive principal effective stress contours in a heterogeneous medium. See Figure 4.8b and 4.18a for other definitions and physical properties of domain.

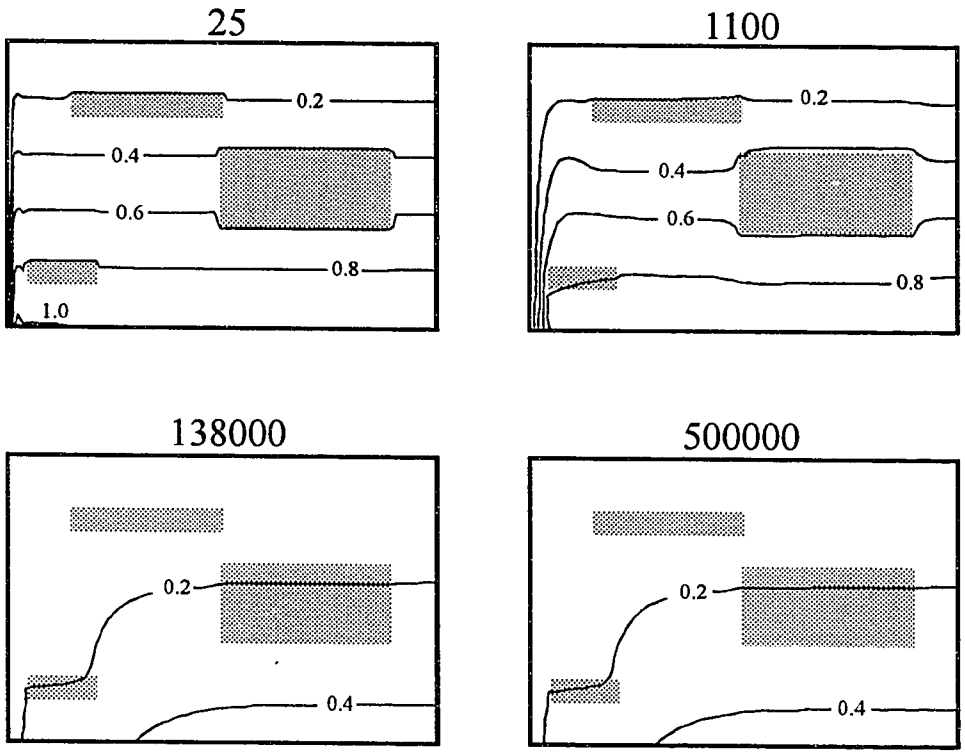

Figure 4.19a. Fluid-pressure contours in a heterogeneous medium. Time in seconds following gravity loading. Here, $E = 10^6$ Pa; $\nu = 0.30$; $k_1 = 10^{-12}$ m^2; and $k_2 = 10^{-14}$ m^2. See Figures 4.2 and 4.8a for other definitions. Shading represents higher permeability zone (k_1). Domain ratio (H/L) is 1:5; v.e. $\approx$ 3.5.

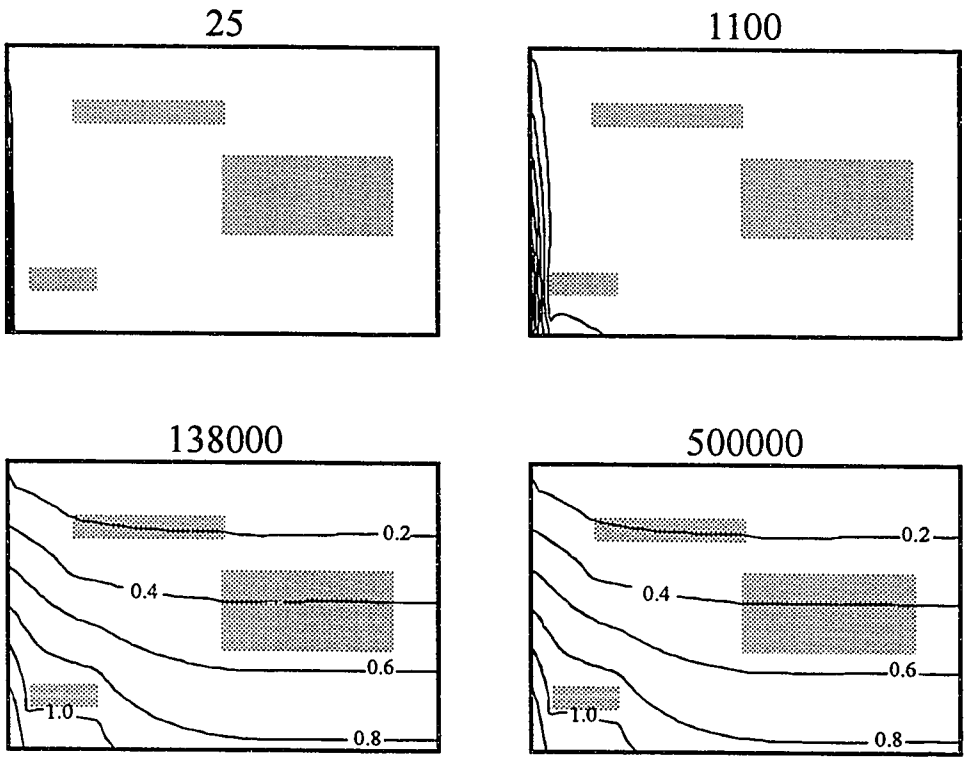

Figure 4.19b. Mean compressive principal effective stress contours in a heterogeneous medium. See Figures 4.8b and 4.19a for other definitions and physical properties of domain.

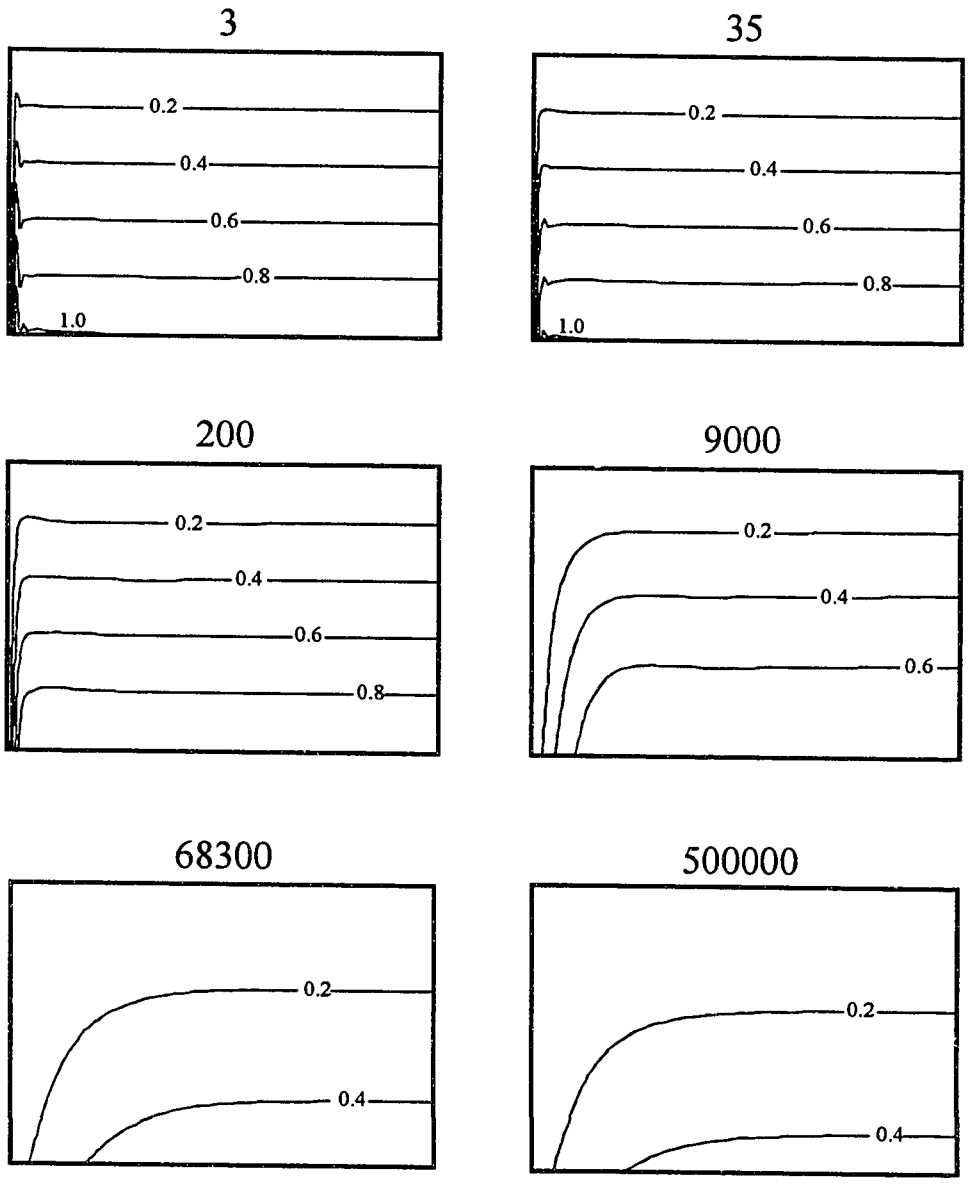

Figure 4.16a. Fluid-pressure contours in a homogeneous medium subject to large strain and nonconstant permeability. Time in seconds following gravity loading. Here, $E = 10^6$ Pa; $\nu = 0.30$; $k = 10^{-14}$ m^2 at start of simulation and $k = 10^{-15}$ m^2 at end of simulation. See Table 4.1 and Figure 4.8a for other definitions. Domain ratio (H/L) is 1:5; v.e.≈ 3.5.

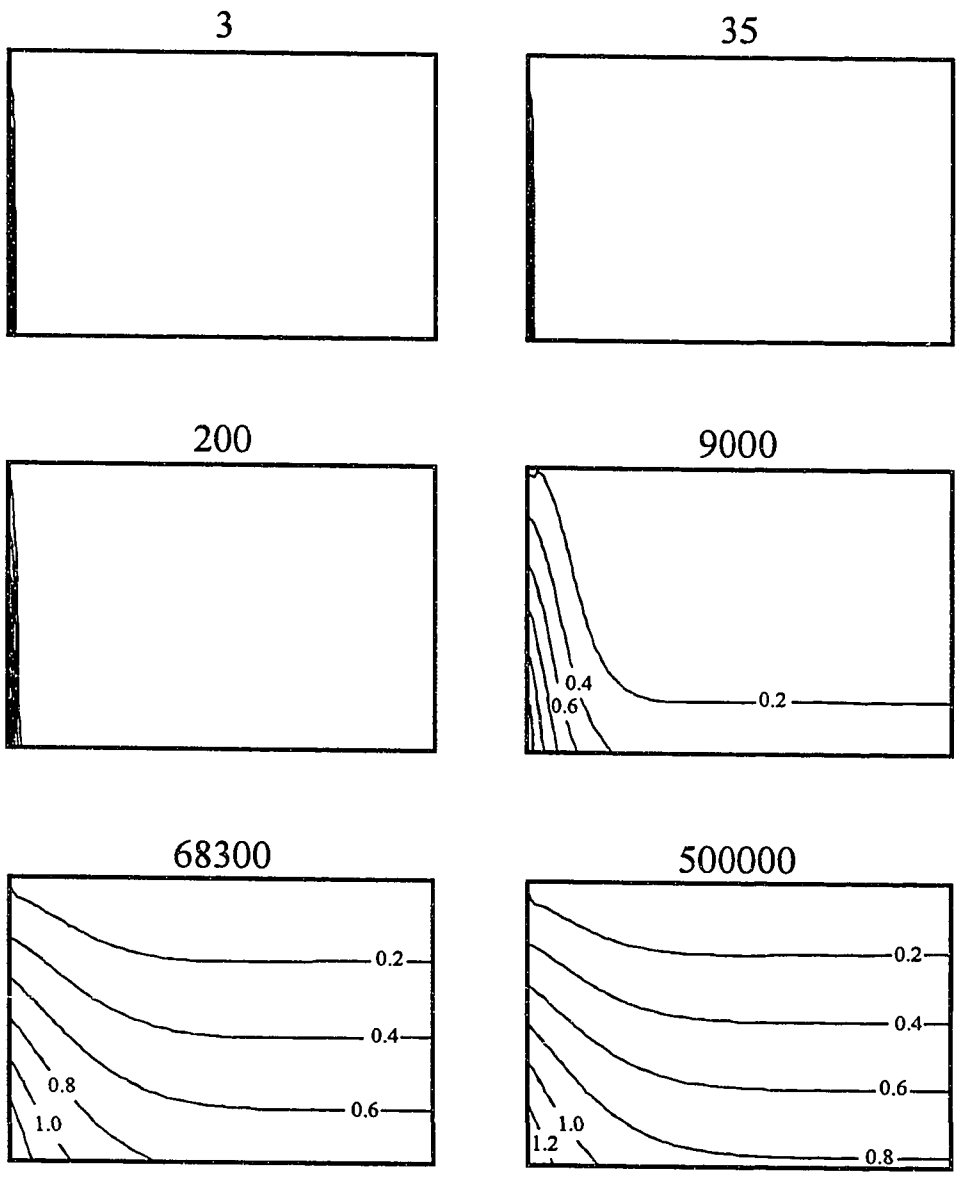

Figure 4.20b. Mean compressive principal effective stress contours in a homogeneous medium subject to large strain and nonconstant permeability. See Figures 4.8b and 4.20a for other definitions and physical properties of domain.

CHAPTER 5

FLUID PRESSURES IN DEBRIS-FLOW DEPOSITS: IMPLICATIONS FOR DEPOSITION

Pore-fluid pressure may modify the mechanics and mobility of landslides, debris flows, and other mass movements (e.g., Hubbert and Rubey, 1959; Shreve, 1968; Pierson, 1981; Hutchinson, 1986; Iverson and LaHusen, 1993a,b; Iverson, 1995a). In several models, fluid pressure in excess of hydrostatic commonly is generated during the initiation phase of a mass movement, and mobility is maintained as long as the total pore-fluid pressure balances much of the weight of the overlying mass. Mobility of a moving mass of rock and sediment diminishes as excess pore-fluid pressure within the mass gradually dissipates. When a significant proportion of the excess pore-fluid pressure has diminished, the mass stops. Although many models focus on excess pore-fluid pressures, even a simple hydrostatic pressure gradient can modify the flow behavior of granular debris (e.g., Iverson and LaHusen, 1993a).

Shreve (1968) proposed that a thin layer of compressed, highly pressurized air trapped at the base of the Blackhawk (CA) landslide supported the overlying weight of the debris and accounted for that landslide's extraordinary mobility. He also proposed that gradual leakage of this pressurized fluid along the margins and through the mass increased frictional resistance at the base of the mass, which brought the landslide to a halt. Because it is easier for the postulated compressed air to escape locally from the margins of the landslide than to permeate across the full thickness of the mass, Shreve (1968) suggested that marginal parts of the landslide came to a halt, and deposited sediment, prior to the cessation of motion of the central part of the landslide. In this view, landslide mobility is diminished, and sediment is deposited, in a piecemeal manner strongly affected by local changes in basal fluid pressure rather than by a uniform, bodywide change of basal fluid pressure.

Hutchinson (1986), too, proposed generation and dissipation of excess pore-fluid pressures as an explanation for the mobility and runout distance of cohesionless debris flows. In his model, a metastable network of grain contacts in loose, cohesionless debris collapses and generates excess pore-fluid pressure throughout the mass, uniformly along its length. Undrained loading leads to the temporary loss of the shear strength of the mass and to its correspondingly high mobility. The rigidly

translating body remains mobile until the basal excess pore-fluid pressure diminishes to the extent that the stress resisting sliding motion exceeds the driving shear stress. Hutchinson used a simple, one-dimensional consolidation model, which neglected gravity, to predict the time necessary for the excess pore-fluid pressure at the base of the otherwise rigid mass to diminish by the necessary amount. Dissipation time for the basal excess fluid pressure thus governs flow duration and the length of runout. We see in the hypotheses of Shreve and Hutchinson that the critical factors governing mobility and runout of mass movements are the existence of a basal fluid pressure of sufficient magnitude to balance the overlying weight of debris, an ability for pore fluid to move independently of the solid grains, and the time scale over which that basal fluid pressure dissipates.

Lithostatic to nearly lithostatic, nonuniform pore-fluid pressures have been measured during motion of large (10 m^3), experimental debris flows (Iverson and LaHusen, 1993b; Iverson, 1995a). Similar nonuniform, near-lithostatic fluid pressures persisted during flow deceleration and sediment deposition by several experimental debris flows (Chapter 3). These experimental data demonstrate unequivocally that pore-fluid pressures capable of balancing a substantial fraction of the weight of overlying debris exist, and can persist, within a debris flow from the initiation of an event through the deposition of sediment. If these results reflect the fluid-pressure fields that exist in natural debris flows, then what controls debris-flow deposition? Clearly, bodywide dissipation of excess pore-fluid pressure is not a necessary condition for debris-flow deposition, contrary to implications in previous studies (e.g., Pierson, 1981; Hutchinson, 1986).

One persistent model proposes that debris-flow deposition is controlled by the existence of a homogeneous yield strength. When the shear stress driving a debris flow diminishes to the value of the material yield strength, the flow stops moving and sediment is deposited *en masse*, effectively "freezing" in place (Johnson, 1965, 1970, 1984). This is the essence of the Bingham model, which treats a debris flow rheologically as a single-phase, viscoplastic material. This model is independent of fluid pressure, and debris-flow mobility and deposition are unaffected by the presence or absence of pore-fluid pressures. Iverson and Denlinger (1987) have argued that this simple model is, at best, an incomplete rheological representation of debris-flow behavior.

Experimental results presented in Chapter 2 show that sediment deposition by cohesionless debris flows is generally not compatible with the simple Bingham model. In that chapter I have shown

that source materials that contain the highest proportion of fine sediment (< 63 μm) produce the thinnest deposits. For example, experiments in October 1993, and in April, May, July, and August, 1994, all had initial source volumes of about 9-10 m^3 (Table 2.2), and the source debris for the May, July, and August experiments was the finest material used (Figure 2.3). Deposits of the May, July, and August experiments were thinner than deposits from coarser-grained flows emplaced under similar experimental conditions in October, 1993, and in April, 1994 (Figure 2.9). At equivalent solids concentrations, larger proportions of mud (< 63 μm) impart a larger yield strength to poorly sorted debris slurries (e.g., Trask, 1959; O'Brien and Julien, 1988; Major and Pierson, 1992). Therefore, one might expect that debris flows containing larger proportions of fine sediment would produce thicker deposits. On the contrary, results in Chapter 2 reveal precisely the opposite pattern.

If debris flows are considered to be multiphase mixtures of sediment and fluid, and if the strength of debris is considered to be that of a Coulomb material, then pore-fluid pressure can modify the strength of the debris. Results in Chapter 3 show that excess pore-fluid pressures are maintained for a longer period of time in mixtures that contain a larger proportion of fine sediment, owing to the substantial decrease of mixture permeability (see Table 3.8, Figure 3.15, and Appendix B). Thus, finer grained sediments maintain excess fluid pressures for a longer period of time than do coarser grained sediments, and they can spread out as thinner deposits despite having an apparently larger intrinsic yield strength. Unless the mixture is particularly cohesive, pore-fluid pressures that are nearly lithostatic produce negligible effective yield strength when averaged bodywide. Based on these considerations and on the data obtained from large-scale experiments, bodywide, homogeneous yield strength appears to be ineffective as the mechanism controlling debris-flow deposition.

An alternative view of transport and deposition by debris flows is founded on the assumption that momentum exchange and resistance to motion occur exclusively by collisions between solid particles (Takahashi, 1981; 1991; Takahashi and others, 1992) rather than by viscous processes. Under this assumption, the shear stress in the flow is proportional to stresses that arise as grains move past each other and collide, which in turn are proportional to the square of the velocity gradient, the square of the particle diameter, and the volume concentration of particles in the flow (Bagnold, 1954). Relying upon this constitutive assumption, Takahashi defines an equilibrium velocity at which steady-state motion occurs. When a debris flow moves onto a slope having some critical angle, and decelerates to a velocity that is less than the critical equilibrium velocity, deposition ensues. While

this model clearly attempts to account for the grain interactions observed in many debris flows (e.g., Costa and Williams, 1984; Johnson, 1984), it has some significant shortcomings (Iverson and Denlinger, 1987): (1) An assumption of uniformly dispersed solid grains of a single size leads to velocity profiles that are constrained to be concave upward, which cannot simulate the rigid zones that appear to exist in many natural debris flows. (2) The model constrains a critical slope angle below which motion of debris flows cannot occur. For typical values of internal friction angle, ϕ_i, fluid density, and particle density, Takahashi's critical slope angle is much steeper (~14°-18°) than the slopes across which many natural debris flows actually travel (commonly <1°-14°; Table 2.1). (3) Although the model incorporates effects of interstitial fluid, the effects contribute only to hydrostatic buoyancy of solid particles; interstitial fluid and fluid pressure do not affect the shear resistance of the flow. Clearly interactions between the solid particles in debris flows are important. However, recent work suggests that frictional interactions caused by prolonged particle contacts, and the modification of those interactions by interstitial fluid pressure, are perhaps more important in many debris flows than are collisions between particles (Major and Pierson, 1992; Iverson and LaHusen, 1993a; Iverson, 1995a).

In this thesis, I propose a mechanism controlling debris-flow deposition that harkens back to a general concept proposed by Shreve (1968) for the Blackhawk landslide; namely, that deposition by debris flows is controlled largely by a balance between driving stress and locally evolving effective stresses that resist flow. I further propose that local evolution of effective resisting stresses, owing to local fluid drainage and pressure dissipation at flow margins, is more important than uniform bodywide dissipation of pore-fluid pressure and consequent bodywide increase in effective resisting stresses. Support for this hypothesis is found on several fronts: (1) Observations of deposition by large-scale experimental debris flows document that sediment is deposited in a piecemeal fashion by numerous surges, that sediment in the central part of a deposit is the last part of the deposit to come to rest, and that sediment in the central part of the deposit is more easily remobilized than that along the margins (Chapter 2). (2) Measurements of pore-fluid pressures at the base of large-scale experimental debris flows document that pore-fluid pressures capable of balancing a substantial fraction of debris weight (typically $\geq$ 80 percent of lithostatic stress) persist during deceleration and deposition of debris flows and that sediment deposition occurs in the presence of this excess pore-fluid-pressure field (Chapter 3). (3) In an independent study, sediment from an experimental flow slide came to rest despite having pore-fluid pressures within the interior of the mass that were measured

to be in excess of a hydrostatic fluid pressure (Eckersely, 1990). (4) One-dimensional consolidation experiments reveal that the time scale required for the decay of excess pore-fluid pressures in quasistatic slurries having permeabilities typical of poorly sorted debris (100 millidarcy to 100 darcy) exceeds the typical duration of many debris flows (Chapter 3). Thus, simple bodywide dissipation of excess fluid pressure does not appear to govern flow mobility, runout distance, or sediment deposition. (5) Numerical simulations of the transient response of pore-fluid-pressure and effective-stress fields in quasistatic two-dimensional domains reveal that for fully saturated, wide, thin bodies, a geometry typical of many debris flows and debris-flow deposits, gravity-driven consolidation is primarily a one-dimensional process except within a narrow region (« deposit thickness) near the margin over time scales typically on the order of several to several tens of minutes or longer--time scales that exceed the common duration of many debris flows. Admittedly, the results of the physical and numerical experiments are for quasistatic debris. Diffusivity coefficients in moving debris may be larger, and pressure-dissipation times shorter. Values of these parameters presented in this thesis establish typical bounding values. However, the dominant one-dimensional nature of the consolidation process, and the more rapid evolution of fluid-pressure and effective-stress fields near domain boundaries, probably are characteristics of moving debris flows as well.

From the results summarized above it is clear that debris flows can stop and deposit sediment even when pore-fluid-pressures capable of supporting the weight of debris exist. Furthermore, dissipation of the excess fluid pressure at time scales that are shorter than the common duration of many debris flows occurs only in a narrow region near the domain margins. Together, the data and calculations presented in this thesis imply that the runout distance of, and sediment deposition by, debris flows is governed by a balance between a diminishing stress driving the motion of the flow and an increase, *locally at the flow margins*, of the stresses resisting flow.

Observations of several debris flows indicate that relatively dry, coarse sediment and organic debris accumulates at flow margins (e.g., Jahns, 1949; Sharp and Nobles, 1953; Costa and Williams, 1984). Similar acccumulations of coarse, dry sediment also have been observed and inferred in large experimental flows (Chapter 2; R.M. Iverson, unpublished data). Such observations have prompted others (e.g., Pierson, 1984; Coleman, 1993, and Whipple, 1994) to propose that a debris flow that has accumulated coarse sediment at its front might be envisioned as a fluid body trapped behind a moving sediment "dam". Coleman (1993) and Whipple (1994) examined a very simple static balance

of several forces acting on such a "dam" -- a gravitational body force, a hydrostatic fluid pressure pushing the dam downslope, and basal friction. These analyses concluded that a balance between the aspect ratio of the dam (ratio of dam height to length) and the friction coefficient at the base of the dam governed the ability of the dam to restrict flow movement. Balance of these forces (slightly modified from that given by Whipple) is given by (Dietrich, 1988; Iverson, 1995b; Appendix C)

$$\tan(\phi_b - \theta) = \frac{\rho_f}{\rho_{dam}}(\tan\alpha - \tan\theta) \tag{5.1}$$

in which θ is the bed slope, α is the surface slope of the dam, ϕ_b is the bed friction angle, ρ_f is the reservoir fluid density, and ρ_{dam} is the bulk density of the sediment dam. For the dam geometry shown in Appendix C, $\tan\alpha$-$\tan\theta$ can be replaced by H/L, where H is the vertical height, and L is the horizontal length of the wedge. Making this substitution yields

$$\tan(\phi_b - \theta) = \frac{\rho_f}{\rho_{dam}}\frac{H}{L} \tag{5.2}$$

a form similar to that given by Whipple (1994). Whipple (1994) treats ϕ_b as an apparent bed friction angle in order to account broadly for modification of the frictional resistance by fluid pressure. If the stresses involved are considered to be effective stresses, whereby fluid-pressure effects are explicitly taken into account, then physical properties need not be considered apparent properties. From this simple analysis, Whipple (1994) concluded that for sediment dams that are much longer than they are tall, $H \ll L$, the critical slope angle needed to maintain steady-state flow approaches the bed friction angle, and that under those conditions a sediment dam severely restricts flow mobility. Conversely, Whipple (1994) concluded that dams that are tall relative to their length exert little influence on flow mobility, because the critical slope angle for maintaining steady-state flow is much less than the bed friction angle.

The analysis by Whipple (1994) partly contradicts the hypothesis and findings of the present work. While his findings support the idea that resistance at the margins can greatly affect the mobility

of a debris flow, his analysis places restrictions on the geometry of the zone that resists stresses driving flow. The significance of these results based on a static balance of forces remains unclear, however. In the strictest sense, Whipple's analysis simply states that for an infinitely long body, the limiting equilibrium slope is equal to the angle of bed friction. For a plausible value of bed friction ($\phi_b \approx 30°$) (Iverson and LaHusen, 1993a), a wedge that has an approximate aspect ratio $H/L = 0.5$ achieves (for $\rho_{dam}=\rho_f$) limiting equilibrium when $\theta=3.5°$, and a wedge having $H/L > 0.5$ is unstable on any slope under these conditions. For constant θ, increases in H, which increase the driving force, must be accompanied by an increase in ϕ_b to resist sliding. Alternatively, for constant ϕ_b, increases in H produce instability on progressively shallower slopes. The restriction on wedge geometry for plausible values of ϕ_b requires that any wedge that might form at the margin of a debris flow have a taper angle of $\leq 27°$. While this ratio may not be uncommon for coarse margins of many debris flows, and while it greatly exceeds taper angles detected in accretionary sediment wedges modeled as deformable Coulomb materials (Dahlen, 1990), margin geometries of several experimental debris-flow deposits at the USGS flume had $H/L \approx 0.7$, and yet apparently influenced flow mobility.

These apparently contradictory results might be resolved if we consider that debris flow movement typically is not a steady-state phenomenon, and that forces driving flow are not constant as the flow moves downslope. As flows travel downslope, θ diminishes, which means that forces driving flow diminish. For a constant value of ϕ_b, this means that the term on the left hand side of (5.2) increases as flows progress downslope. Measurements at the USGS debris-flow flume demonstrate that experimental debris flows rapidly thin and elongate following release of source debris, but that in the lower confines of the flume and in the runout area mean flow depth is approximately constant (Iverson and LaHusen, 1993a). Thus, in the depositional area H can be considered more or less constant. From (5.2) we see that $\tan(\phi_b-\theta)$ is inversely proportional to the length of the sediment wedge, L. For constant H, if $\tan(\phi_b-\theta)$ increases as flow progresses downslope, then L must decrease. In other words, the aspect ratio of the sediment dam can increase as flows progress to flatter slopes, suggesting the possibility that wedges of drained sediment at the fronts of debris flows may have aspect ratios larger than those anticipated from a static, limit equilibrium force balance.

The results from modeling the elastic stress field in a quasistatic two-dimensional domain presented in Chapter 4 illustrate that effective stresses of sufficient magnitude to resist driving shear stress evolve only in a narrow region near the domain margin at relevant time scales. Although the geometry used in those analyses was highly simplified, the results nonetheless illustrate that extensive effective-stress fields do not develop far from the margin of a simple homogeneous domain over the time scales of interest. Admittedly these are results from analyses of quasistatic debris. Moving debris flows are more agitated, and probably have hydraulic diffusivity values that are larger than those measured in quasistatic debris. Thus, fluid pressures can diffuse, and effective stresses can evolve more rapidly in moving debris. However, the numerical results presented in Chapter 4 are robust; similar results were obtained using a wide range of values for the diffusivity coefficient (10^{-3} to 10^{-8} m^2/s; Table 4.1). Even for the largest value of hydraulic diffusivity, extensive bodywide effective stress fields in a homogeneous domain did not develop for several minutes or more. When a higher permeability zone characterized the margin of a heterogeneous domain, rapid evolution of effective stresses was restricted to that zone; rapid bodywide changes in effective stress did not occur. These numerical results, which bound the behavior of fluid pressures and effective stresses in a wide variety of quasistatic debris, combined with measured (nearly lithostatic) fluid pressures during deceleration of, and sediment deposition by, large-scale experimental debris flows suggest that even narrow zones of sediment resistant to deformation may modify flow mobility and induce debris-flow deposition, especially when driving stress is diminishing. Perhaps a numerical model of Coulomb material that allows domain shape to evolve in the presence of shear and tensile stresses would reveal that tapered-shaped wedges, having geometries similar to those predicted by the static force balance of a rigid wedge, develop along domain margins.

Results presented in Chapter 2 demonstrate that the nature of sediment deposition by large-scale experimental debris flows is generally incompatible with existing depositional models. Reasons for this incompatibility are that existing models do not account for the observed nonsteady nature of the debris flows, nor do they account for the effects of stress modification by fluid pressures. If we accept the premise that debris flows are multiphase mixtures of solids, liquid, and air, and that fluid pressures may significantly modify the dynamics of debris flows (e.g., Johnson, 1970, 1984; Hooke, 1967, 1987; Hutchinson, 1986; Iverson, 1995a), then we must also accept the premise that fluid pressures affect debris-flow deposition. One model that attempts to incorporate changes in fluid pressure as a mechanism controlling debris-flow runout and deposition (Hutchinson, 1986) assumes

that fluid pressures decay monotonically following debris-flow initiation. Results obtained by Iverson and LaHusen (1993b) and Iverson (1995a) as well as those presented in Chapter 3 illustrate, however, that fluid pressures in debris flows do not necessarily decay monotonically over the lifetime of a debris flow. Results presented in Chapters 3 and 4 illustrate that bodywide changes in fluid pressures within quasistatic masses of debris-flow sediment occur at time scales that generally are substantially longer than the duration of typical small-volume debris flows. Numerical simulations reveal that changes in fluid-pressure and effective-stress fields can evolve rapidly in two-dimensional domains, but only in narrow regions near the lateral free surface in poorly sorted debris typical of debris flows. Together, these data demonstrate that excess pore-fluid pressures can remain elevated, and effective stresses depressed, everywhere except along debris-flow margins for time scales of several to several tens of minutes or longer. Consideration of this cumulative body of data leads to the proposal that deposition by debris flows is controlled by a balance between driving stress and locally increasing resisting stress along flow margins.

CHAPTER 6

SUMMARY AND CONCLUDING REMARKS

Proper interpretation of Earth's geologic record requires an understanding of geologic processes. When geologists attempt to assess effects of some processes deemed to be natural hazards, an understanding of surface geologic processes is essential. Two chief surface-process hazards are floods and, in mountainous areas, debris flows. The hydraulics of open-channel water flow and the transport of sediment by water are well understood, primarily because numerous experimental studies have examined these processes and have related the character of water-laid deposits to the hydraulics of flow. Therefore, a geologist can make rather intricate inferences about flow behavior, such as flow regime, flow velocity, probable water depth, and current direction, from the sedimentary record of water-laid deposits. Debris flows, on the other hand, are more poorly understood, and their generally capricious nature makes observations and measurements both difficult and dangerous. Given the difficulties of making useful and relevant field observations of the natural process, there have been surprisingly few experimental studies of debris flows. Those that have been undertaken commonly have been, for logistical reasons, small-scale ventures. Scale-dependent effects, such as physico-chemical effects in cohesive materials and capillary forces, not necessarily important at the natural scale, cloud the applicability of the results of some of these studies. Despite the relatively poor understanding of the process, many geologists have drawn some fairly detailed and sweeping conclusions concerning depositional processes and properties of flow from sediments inferred to have been deposited by debris flows.

The primary goals of this study were to provide constraints regarding the process of sediment deposition by debris flows based, for the first time, on the study of large-scale experimental debris flows under controlled conditions and to assess the effect of pore-fluid pressure on debris-flow deposition. An ancillary goal was to provide constraints on interpretations that can be drawn from debris-flow sediments. This study presents data that have never before been measured, namely, the pore-fluid-pressure field and total normal bed stress in a debris flow at the time of sediment deposition, and the relation of the fluid-pressure field to the total normal stress field. These data are critical in the evaluation of any model that attempts to explain the mechanics of debris-flow transport and deposition.

In chapter 1, I posited the most optimistic hypothesis I could formulate concerning the relation between the flow behavior of a debris flow and the sedimentary characteristics of its deposit: the kinematic behavior and the nature of the depositional process of a debris flow are readily identified by the sedimentologic, stratigraphic, and morphologic features of its deposit. Analysis of several experimental debris-flow deposits, as well as analysis of recent debris-flow deposits in southwest China, refute this hypothesis (Chapter 2). Visual observations, as well as measurements of total bed normal stress during deposition, have shown that deposits of large-scale experimental debris flows can result from progressive incremental sedimentation when flow surges accrete sediment vertically. This style of sediment deposition, which produced otherwise massive deposits, is much different than the *en masse* style of deposition that is commonly inferred from debris-flow deposits. Clear evidence that deposits were the result of incremental deposition by multiple surges, rather than by simple *en masse* deposition from a single surge, was recorded in deposit morphology and surface sedimentology only. Despite the unequivocal incremental nature of sediment accumulation, the sedimentologic and morphologic characteristics of several experimental debris-flow deposits can easily be misinterpreted as having resulted from a single surge; incremental accretion may not be interpreted easily from the nature of debris-flow deposits, especially from interior sedimentary characteristics. Not only were individual surges typically indistinguishable in deposits, but in one experiment deposits from similar yet separate debris flows were not distinguishable without the aid of a marker horizon. In southwest China, river terraces typically were composed of monotonous sequences of massively textured sediment, reportedly deposited by multiple debris flows. In many terraces there were few, if any, detectable stratigraphic boundaries.

The inability to interpret the correct nature of debris-flow behavior from the sedimentary characteristics of deposits severely limits interpretations drawn from analyses of deposits. Previous studies have inferred that debris-flow deposits are characterized by lobate planforms, blunt margins, marginal levees, and generally massive, unsorted and unstratified sediment. The results from the experimental study presented here are consistent with that interpretation. However, this experimental study also demonstrates that inferences regarding the physical and rheological properties of debris flows based on the character of their deposits are probably invalid. In addition the results presented here demonstrate that evaluations of debris-flow hazards and geomorphic histories in river valleys and on alluvial fans based on inferences of event frequency and magnitude must be tempered with the realization that many debris flows need not be faithfully recorded in the sedimentary record.

Generation and dissipation of fluid pressure capable of balancing the weight of debris has been postulated as a mechanism controlling mobility and deposition of landslides and debris flows (e.g., Shreve, 1968; Hutchinson, 1986; Iverson, 1995a). Until recently, however, fluid pressures of sufficient magnitude remained speculative in rapidly deforming debris. Iverson and LaHusen (1993b) and Iverson (1995a) have now shown that pore-fluid pressures during motion of unsteady debris flows are distributed nonuniformly, and that near lithostatic to lithostatic fluid pressures exist in much of the mass.

In this study I show that a significant proportion of the weight of debris is balanced by pore-fluid pressure during deceleration and deposition of debris flows. Measurements from several experimental flows (Chapter 3) show that nonuniformly distributed basal pore-fluid pressure ranges from about 50 percent (hydrostatic) to approximately 100 percent (lithostatic) of measured total bed normal stress. Fluid pressure typically balanced about 80 percent or more of total bed normal stress behind the flow front. These high fluid pressures are maintained until sediment is completely deposited. Measurements also show that following deposition (0.1-0.4 m deep over the sensor), the time needed to dissipate excess pore-fluid pressure in the central parts of deposits ranged widely, over several orders of magnitude, depending upon sediment composition. In deposits composed of sand and gravel, excess pore-fluid pressure dissipated relatively rapidly, in tens of seconds to several minutes. However, in deposits composed of finer-grained sediment excess pore-fluid pressure remained elevated for tens of minutes to several hours. These measurements show that debris flows can come to rest and deposit sediment even though pore-fluid pressure balances a substantial fraction of the weight of debris. Thus, simple bodywide dissipation of excess pore-fluid pressure is not the mechanism controlling debris flow runout and deposition, as has been previously proposed (e.g., Pierson, 1981; Hutchinson, 1986).

Dissipation of fluid pressure is a diffusive process. I used a linear, one-dimensional, gravity-driven consolidation model to determine characteristic values of hydraulic diffusivity and dissipation times of excess fluid pressure in deposits of poorly sorted debris (Chapter 3). A series of simple laboratory experiments, which used sediments that bracket the physical characteristics of most debris flows in the western U.S. (and perhaps worldwide), revealed that the diffusive behavior of excess fluid pressure in debris-flow slurries is consistent with a simple, linear, gravity-driven model, despite volume strains as large as several percent. Results from the simple laboratory experiments indicate that a broad spectrum of quasistatically deforming, poorly sorted debris has characteristic values of

hydraulic diffusivity on the order of 10^{-6} to 10^{-7} m^2/s. The characteristic times for dissipation of excess pore-fluid pressure in such poorly sorted debris range from several minutes to several tens of hours or more for deposits that range in thickness from 0.1-1 meter. These time scales exceed typical periods of surging in debris flows or durations of debris flows, and reinforce the conclusion that simple bodywide dissipation of excess fluid pressure does not control debris-flow mobility and deposition.

The characteristic values of hydraulic diffusivity reported in this study are, admittedly, for quasistatic debris. In moving debris flows, values of hydraulic diffusivity may be larger, and characteristic fluid-pressure dissipation times shorter, but the results obtained in this study provide bounds on the characteristic values of these parameters. Estimates of diffusivity values for moving debris may be obtained from values of permeability and estimates of material compressibility. Numerous permeameter measurements (Chapter 3; Appendix B) indicate that permeabilities of most debris-flow sediments fall in the range of 100 darcy to 100 millidarcy (10^{-10} to 10^{-13} m^2/s). Estimates of the bulk modulus of debris-flow sediments obtained from the quasistatic consolidation tests (10^5 Pa) are 1 to 3 orders of magnitude smaller than values estimated from triaxial compression tests (Chapter 3; Appendix A). This difference reflects the highly compressible nature of liquefied debris-flow slurries. From the measured range of permeabilities and from the estimated bulk modulus, estimated values of hydraulic diffusivity in agitated debris range from perhaps 10^{-2} to 10^{-5} m^2/s.

The linear gravity-driven model of debris-flow-deposit consolidation provides a partial explanation for the lack of identifiable stratigraphic boundaries in such deposits. In that model, excess-fluid-pressure, effective-stress, and volume-strain fields evolve upward from the base the deposit. As a result, the upper parts of deposits remain unstable for a longer period of time than do the lower parts of deposits. Because debris-flow deposits can form by progressive vertical accretion of sediment transported by surges and because fluid-pressure dissipation times are long compared to typical surge periods, upper parts of deposit strata can be remobilized and any stratigraphic distinction of sediment emplacement by surges is probably muted or obliterated in the interior texture of the deposit.

Uniform bodywide dissipation of excess fluid pressure cannot explain debris-flow mobility and deposition. Measured fluid pressures during debris flow deceleration and deposition were capable of balancing much of the weight of the overlying debris. In addition, measurements from debris-flow deposits show that even modest amounts of fine debris greatly affect the hydraulic behavior of pore fluids in debris flows. Yet, finer-grained experimental debris flows at the debris-flow flume did not travel significantly farther than did those composed of coarser-grained sediment mixtures. Characteristic dissipation times for fluid pressure resulting from simple one-dimensional drainage are long compared to durations of debris flows. These observations and measurement indicate that simple one-dimensional drainage of pore fluid, and the resulting dissipation of excess pore-fluid pressure, were not the only factors affecting deposition by debris flows.

Debris flows and their deposits are multidimensional bodies having width and length as well as depth. In Chapter 4, the affect of an additional free-surface was examined numerically to determine how, and to what extent, the one-dimensional nature and time scales of response of gravity-driven fluid-pressure and stress fields were modified. A simple rectangular domain that simulates wide, thin bodies, a geometry typical of debris flows and debris-flow deposits, was used in the analyses.

Numerical simulations show that fluid-pressure and effective-stress fields bear a strong one-dimensional imprint in homogeneous wide, thin bodies characterized by permeabilities and elastic properties typical of poorly sorted debris. The one-dimensional imprint of these fields is especially strong when the body is five or more times as wide as it is thick. The two-dimensional nature of the body affects fluid-pressure- and effective-stress-field development only in a thin zone ($<$ body thickness) near the lateral free surface for several to several tens of minutes following gravitational loading. Only gradually, over periods of several tens of minutes to several hours, does the influence of the lateral free surface propagate over a broad segment of the body.

Wide, thin, heterogeneous domains characterized by spatially variable permeability show a similarly strong one-dimensional imprint on fluid-pressure and effective-stress fields. Spatially variable permeability in combination with the two-dimensional nature of the domain can strongly affect the evolution of fluid-pressure and effective-stress fields, but only locally. Fluid drainage in domains bounded by higher-permeability zones ($k \geq 10^{-12}$ m^2; 1 darcy) that are connected directly to

the lateral free surface causes *local* dissipation of fluid pressure and development of a nearly lithostatic effective-stress field within tens of seconds or less near the lateral margin. In the central part of the domain, characterized by lower-permeability material, excess-pore-fluid pressure dissipates, and effective stress increases, over periods of several tens of minutes to several hours.

The dominant conclusion from the experimental and numerical analyses presented in this study is that fluid-pressure and effective-stress fields can evolve rapidly only locally at domain margins; field evolution does not propagate inward rapidly in domains characterized by permeabilities typical of poorly sorted debris. Thus, in decelerating debris flows and in debris-flow deposits excess fluid pressures remain elevated, and effective stresses depressed, everywhere except at domain margins for several to several tens of minutes or longer.

The data and results presented in this study imply that sediment deposition by debris flows is controlled by a balance between a diminishing stress deriving flow and locally increasing stresses resisting flow. In this model, driving stress diminishes as flow moves onto flattening slopes and/or spreads laterally and reduces flow depth. Increased resistance along lateral boundaries, owing to fluid drainage and dissipation fluid pressure, brings flow margins to a stop prior to more central parts of flow. This behavior is well documented in the large-scale experimental debris flows at the USGS debris-flow flume, and has been inferred for other large scale mass movements (e.g., Shreve, 1968). I have demonstrated in this thesis that a homogeneous material yield strength, posited in the Bingham model as the mechanism that causes deposition by debris flows, is ineffective as the mechanism causing deposition of a typical debris flow. Another model based on particle collisions (Takahashi, 1981; 1991) clearly attempts to account for grain interactions observed in many debris flows, but this model constrains deposition to slopes that typically are steeper than those across which actual debris flows can travel. Recent work demonstrates that debris flows may be modeled as Coulomb materials, in which persistent frictional contacts govern momentum exchange and energy dissipation (Iverson and LaHusen, 1993a). In this model, pore-fluid pressures can greatly modify the dynamics and deposition of debris flows.

The work presented in this thesis provides a model of debris-flow deposition that is alternative to existing models that describe the nature of debris flows, yet is based loosely on concepts that have been present in the literature for nearly 30 years (e.g., Shreve, 1968; Hooke, 1967; 1987). I have

shown that debris flows can deposit sediment in an incremental fashion, and yet have demonstrated that such a style of deposition is only poorly, if at all, recorded in the stratigraphy and interior sedimentology of the deposits. I have discussed possible explanations for the inability of deposits to record accurately the style of sediment deposition by debris flows, and I have discussed the implications of this inexact sedimentary record on interpretations that can be drawn from debris-flow deposits. While this study has perhaps raised more questions than it has answered regarding the nature of sediment deposition by debris flows, I believe that it shows the direction of, and provides a starting point for, future studies aimed at refining the mechanics of deposition by debris flows.

REFERENCES

American Society for Testing and Materials (ASTM), 1995, Annual book of standards: Soil and rock standards D420-D4914, v. 4, no. 8, p. 197-206, 885-895.

Anderson, S.A., and Sitar, N., 1995, Analysis of rainfall-induced debris flows: Journal of Geotechnical Engineering, v. 121, p. 544-552.

Arguden, A.T., and Rodolfo, K.S., 1990, Sedimentologic and dynamic differences between hot and cold laharic debris flows of Mayon Volcano, Philippines: Geological Society of America Bulletin, v. 102, p. 865-876.

Audet, D.M., and McConnell, J.D.C., 1992, Forward modeling of porosity and pressure evolution in sedimentary basins: Basin Research, v. 4, p. 147-162.

Bagnold, R.A., 1954, Experiments on a gravity-free dispersion of large solid spheres in a Newtonian fluid under shear: Proceedings of the Royal Society of London, v. 225-A, p. 49-63.

Barnes, H.A., Hutton, J.F., and Walters, K., 1989, An introduction to rheology. Elsevier, Amsterdam,199 p.

Battaglia, M., 1993, On pyroclastic flow emplacement: Journal of Geophysical Research, v. 98, p. 22,269-22,272.

Been, K., and Sills, G.C., 1981, Self-weight consolidation of soft soils: An experiment and theoretical study: Geotechnique, v. 31, p. 519-535.

Biot, M.A., 1941, General theory of three-dimensional consolidation: Journal of Applied Physics, v. 12, p. 155-164.

Beyer, W.H., ed., 1987, CRC Standard Mathematical Tables. CRC Press, Boca Raton, 674 p.

Blackwelder, E., 1928, Mudflow as a geologic agent in semi-arid mountains: Geolological Society of America Bulletin, v. 39, p. 465-484.

Blair, T.C., and McPherson, J.G., 1994, Alluvial fans and their natural distinction from rivers based on morphology, hydraulic processes, sedimentary processes, and facies assemblages: Journal of Sedimentary Research, v. A64, p. 450-489.

Bowles, J.E., 1978, Engineering properties of soils and their measurement. McGraw-Hill, New York, 213 p.

Bowles, D.S., 1985, Delineation of landslide, flash flood, and debris flow hazards in Utah. Utah Water Research Laboratory General Series Report UWRL/G-85/03, Utah State University, 592 p.

Branney, M.J., and Kokelaar, P., 1992, A reappraisal of ignimbrite emplacement: progressive aggradation and changes from particulate to non-particulate flow during emplacement of high-grade ignimbrite: Bulletin of Volcanology, v. 54, p. 504-520.

Carey, S.N., 1991, Transport and deposition of tephra by pyroclastic flows and surges, in Fisher, R.V. and Smith, G.A., eds., Sedimentation in Volcanic Settings. SEPM Special Publication no. 45, p. 39-57.

Carslaw, H.S., and Jaeger, C.J., 1959, Conduction of Heat in Solids. Oxford University Press, Oxford, 510 p.

Carter, J.P., Booker, J.R., and Small, J.C., 1979, The analysis of finite elasto-plastic consolidation: International Journal of Numerical and Analytical Methods in Geomechanics, v. 3, p. 107-129.

Cas, R.A.F., and Landis, C.A., 1987, A debris-flow deposit with multiple plug-flow channels and associated side accretion deposits: Sedimentology, v. 34, p. 901-910.

Chou, P.C., and Pagano, N.J., 1967, Elasticity: tensor, dyadic, and engineering approaches. Van Nostrand Co., Princeton, NJ, 290 p.

Coleman, P.F., 1993, A new explanation of the debris flow phenomenon: EOS, Transactions of the American Geophysical Union, v. 74, no. 16, p. 154.

Collinson, J.D., and Thompson, D.B., 1989, Sedimentary Structures. Unwin Hyman, London, 207 p.

Cooley, M.E., Aldridge, B.N., and Euler, R.C., 1977, Effects of the catastrophic flood of December 1966, north rim area, eastern Grand Canyon, Arizona: U. S. Geological Survey Professional Paper 980, 43 p.

Costa, J.E., 1984, Physical geomorphology of debris flows, *in* Costa, J.E. and Fleischer, P.J., eds., Developments and Applications of Geomorphology. Springer-Verlag, New York, p. 269-317.

Costa, J.E., 1992, Characteristics of a debris fan formed at the U.S. Geological Survey debris-flow flume, H.J. Andrews Experimental Forest, Blue River, OR: EOS, Transaction of the American Geophysical Union, v. 73, no. 43, p. 227.

Costa, J.E., and Jarrett, R.D., 1981, Debris flows in small mountain stream channels of Colorado and their hydrologic implications: Bulletin of the Association of Engineering Geologists, v. 18, p. 302-322.

Costa, J.E., and Wieczorek, G.F., 1987, eds., Debris Flows/Avalanches: Processes, Recognition, and Mitigation. Geological Society of America Reviews in Engineering Geology, v. 7, 239 p.

Costa, J.E., and Williams, G., 1984, Debris flow dynamics: U.S. Geological Survey Open-file Report 84-606.

Coussot, P., Leonov, A.I., and Piau, J.M., 1993, Rheology of concentrated dispersed systems in a low molecular weight matrix: Journal of Non-Newtonian Fluid Mechanics, v. 46, p. 179-217.

Coussot, P., and Piau, J.M., 1995, A large-scale field coaxial cylinder rheometer for the study of the rheology of natural coarse suspensions: Journal of Rheology, v. 39, p. 105-124.

Cruden, D.M., and Lu, Z.Y., 1992, The rockslide and debris flow from Mount Cayley, B.C., in June 1984: Canadian Geotechnical Journal, v. 29, p. 614-626.

Curry, R.R., 1966, Observations of alpine mudflows in the Tenmile Range, central Colorado: Geological Society of America Bulletin, v. 77, p. 771-776.

Dade, W.B., 1992, Studies on boundary conditions for fine-sediment transport. Ph.D. thesis, University of Washington, Seattle, WA, 269 p.

Dahlen, F.A., 1990, Critical taper model of fold-and-thrust belts and accretionary wedges: Annual Review of Earth and Planetary Sciences, v. 18, p. 55-99.

Davies, T.R.H., 1986, Large debris flows: a macroviscous phenomenon: Acta Mechanica, v. 63, p. 161-178.

Davies, T.R.H., 1988, Debris flow surges -- A laboratory investigation: Mitt. No. 96 der Versuchsanstalt für Wasserbau, Hydrologie and Glaziologie, ETH Zürich, Switzerland, 122 p.

Davies, T.R.H., 1990, Debris-flow surges -- experimental simulation: New Zealand Journal of Hydrology, v. 29, p. 18-46.

Davies, T.R.H., 1993, Research needs for debris flow disaster prevention: Hydraulic Engineering '93, Proceedings of ASCE 1993 conference, San Francisco, CA, July 25-30, p. 1284-1287.

Davies, T.R.H., Phillips, C.J., Pearce, A.J., and Bao, Z.X., 1991. New aspects of debris flow behavior: Proceedings of the U.S.-Japan Symposium on Snow Avalanche, Landslide, Debris Flow Prediction and Control, 443-451.

Davis, E.H., and Raymond, G.P., 1965, A nonlinear theory of consolidation: Geotechnique, v. 15, p. 161-173.

DeGraff, J.V., 1994, The geomorphology of some debris flows in the southern Sierra Nevada, California: Geomorphology, v. 10, p. 231-252.

Dietrich, J.H., 1988, Growth and persistence of Hawaiian volcanic rift zones: Journal of Geophysical Research, v. 93, p. 4258-4270.

Dorava, J.M., May, B.A., Meyer, D.F., and Myers, L.V., 1993, Channel geometry data of streams in the lower Drift River basin affected by the 1989-90 eruptions of Redoubt volcano, Alaska: U.S. Geological Survey Open-file Report 93-94, 66 p.

Dorava, J.M., and Meyer, D.F., 1994, Hydrologic hazards in the lower Drift River basin associated with the 1989-90 eruptions of Redoubt Volcano, Alaska: Journal of Volcanology and Geothermal Research, v. 62, p. 387-407.

Drake, L.D., 1974, Till fabric control by clast shape: Geological Society of America Bulletin, v. 85, p. 247-250.

Eckersely, J.D., 1990, Instrumented laboratory flowslides: Geotechnique, v. 40, p. 489-502.

Einstein, A., 1906, Eine neue Bestimmung der Molekuldimensions: Ann. Physik, v. 19, p. 289-306.

Ellen, S.D., and Fleming, R.W., 1987, Mobilization of debris flows from soil slips, San Francisco Bay region, CA, *in* Costa, J.E., and Wieczorek, G.F., eds., Debris Flows/Avalanches: Processes, Recognition, and Mitigation. Geological Society of America Reviews in Engineering Geology, v. 7, p. 31-40.

Enos, P., 1977, Flow regimes in debris flow: Sedimentology. v. 24, p. 133-142.

Fairchild, L.H., 1985, Lahars at Mount St. Helens, Washington. Ph.D. thesis, University of Washington, Seattle, WA, 374 p.

Fairchild, L.H., and Wigmosta, M., 1983, Dynamic and volumetric characteristics of the 18 May 1980 lahars on the Toutle River, Washington: Proceedings of Symposium on Erosion Control in Volcanic Areas, Ministry of Construction, Government of Japan, Public Works Research Institute Technical Memorandum no. 1903, p. 131-153.

Fannin, R.J., and Rollerson, T.P., 1993, Debris flows: Some physical characteristics and behaviour: Canadian Geotechnical Journal, v. 30, p. 71-81.

Fink, J., Malin, M., D'Alli, R.E., and Greeley, R., 1981, Rheological properties of mudflows associated with the spring 1980 eruption of Mount St. Helens volcano, Washington: Geophysical Research Letters, v. 8, p. 43-46.

Fisher, R.V., 1966, Mechanism of deposition from pyroclastic flows: American Journal of Science, v. 264, p. 350-363.

Fisher, R.V., 1971, Features of coarse-grained, high-concentration fluids and their deposits: Journal of Sedimentary Petrology, v. 41, p. 916-927.

Folk, R.L., 1984, Petrology of sedimentary rocks. Hemphill, Austin, TX, 185 p.

Franz, W.J., and Voight, B., 1995, Shear strength of granular debris from the Osceola Mudflow, Mount Rainier volcano, Washington: EOS, Transactions of the American Geophysical Union, v. 76, no. 46, p. F651.

Freeze, R.A., and Cherry, J.A., 1979, Groundwater. Prentice-Hall, Englewood Cliffs, NJ., 604 p.

Fritz, W.J., and Ogren, D.E., 1984, Clast orientations in the Mount St. Helens sediment flows: Geological Society of America Abstracts with Programs, Annual Meeting, v. 16, p. 513.

Fung, Y.C., 1965, Foundations of Solid Mechanics. Prentice-Hall, Englewood Cliffs, NJ., 525 p.

Gallino, G.L., and Pierson, T.C., 1985, Polallie Creek debris flow and subsequent dam-break flood of 1980, East Fork Hood River Basin, Oregon: U.S. Geological Survey Water-Supply Paper 2273, 22 p.

Ghibaudo, G., 1992, Subaqueous sediment gravity flow deposits: practical criteria for their field description and classification: Sedimentology, v. 39, p. 423-454.

Gibson, R.E., England, G.L., and Hussey, M.J.L., 1967, The theory of one-dimensional consolidation of saturated clays -- Finite nonlinear consolidation of thin homogeneous layers: Geotechnique, v. 17, p. 261-273.

Gibson, R.E., Schiffman, R.L., and Pu, S.L., 1970, Plane-strain and axially symmetric consolidation of a clay layer on a smooth impervious base: Quarterly Journal of Mechanics and Applied Mathematics, v. 23, p. 505-520.

Hampton, M.A., 1975, Competence of fine-grained debris flows: Journal of Sedimentary Petrology, v. 49, p. 834-844.

Harris, S.A., and Gustafson, C.A., 1993, Debris flow characteristics in an area of continuous permafrost, St. Elias Range, Yukon Territory: Zeitschrift für Geomorphologie, v. 37, p. 41-56.

Hibbit, H.D., Karlsson, B.I., and Sorenson, Inc., 1993, ABAQUS User's Manual.

Hiscott, R.N., and Middleton, G.V., 1979, Fabric of coarse, deep-water sandstones, Tourelle Formation, Quebec, Canada: Journal of Sedimentary Petrology, v. 50, p. 703-722.

Hooke, R.L., 1967, Processes on arid-region alluvial fans: Journal of Geology, v. 75, p. 438-460.

Hooke, R.L., 1987, Mass movement in semi-arid environments and the morphology of alluvial fans, *in* Anderson, M.G., and Richards, K.S., eds., Slope Stability. Wiley and Sons, New York, p. 505-529.

Hooke, R.L., and Rohrer, W.L., 1979, Geometry of alluvial fans: Effect of discharge and sediment size: Earth Surface Processes and Landforms, v. 4, p. 147-166.

Howard, A.D., 1995, Rate laws for bedrock erosion by debris flows: EOS, Transactions of the American Geophysical Union, v. 76 , no. 46, p. F263.

Hubbert, M.K., and Rubey, W.W., 1959, Role of fluid pressure in mechanics of overthrust faulting, I: Geological Society of America Bulletin, v. 70, p. 115-166.

Hungr, O., Morgan, G.C., and Kellerhals, R., 1984, Quantitative analysis of debris torrent hazards for design of remedial measures: Canadian Geotechnical Journal, v. 21, p. 663-677.

Hutchinson, J.N., 1986, A sliding-consolidation model for flow slides: Canadian Geotechnical Journal, v. 23, p. 115-126.

Iman, R.L., and Conover, W.J., 1983, A modern approach to statistics. John Wiley, New York, 497 p.

Inman, D.L., 1952, Measures for describing the size distribution of sediments: Journal of Sedimentary Petrology, v. 22, p. 125-145.

Innes, J.L., 1983, Debris flows: Progress in Physical Geography, v. 7, p. 469-501.

Iverson, R.M., 1994, Lahar dynamics: Geological Society of America Abstracts with Programs, Annual Meeting, v. 26, no. 7, p. A336-A337.

Iverson, R.M., 1995a, How do fluid pressures affect landslide/debris-flow dynamics?: EOS, Transactions of the American Geophysical Union, v. 76 , no. 46, p. F264.

Iverson, R.M., 1995b, Can magma-injection and groundwater forces cause massive landslides on Hawaiian volcanoes?: Journal of Volcanology and Geothermal Research, v. 66, p. 295-308.

Iverson, R.M., Costa, J.E., and LaHusen, R.G., 1992, Debris-flow flume at H.J. Andrews Experimental Forest, Oregon: USGS Open-file report 92-483.

Iverson, R.M., and Denlinger, R.P., 1987, The physics of debris flows -- a conceptual assessment, *in* Beschta, R.L., Blinn, T., Grant, G.E., Ice, G.G., and Swanson, F.J., eds., Erosion and Sedimentation in the Pacific Rim. International Association of Hydrological Sciences Publication no. 165, p. 155-165.

Iverson, R.M., and LaHusen, R.G., 1989, Dynamic pore-pressure fluctuations in rapidly shearing granular materials: Science, v. 246, p. 796-799.

Iverson, R.M., and LaHusen, R.G., 1993a, Friction in debris flows--Inferences from large-scale flume experiments: Hydraulic Engineering '93, Proceedings of ASCE 1993 conference, San Francisco, CA, July 25-30, p. 1604-1609.

Iverson, R.M., and LaHusen, R.G., 1993b, Pore-pressure dynamics in debris-flow experiments: EOS, Transactions of the American Geophysical Union, v. 74, no. 43, p. 310.

Iverson, R.M., LaHusen, R.G., and Major, J.J., and Zimmerman, C.L., 1994, Debris flow against obstacles and bends: dynamics and deposits: EOS, Transactions of the American Geophysical Union, v. 75, no. 44, p. 274.

Iverson, R.M., and Major, J.J., 1986, Groundwater seepage vectors and the potential for hillslope failure and debris flow mobilization: Water Resources Research, v. 22, p. 1543-1548.

Iverson, R.M., and Reid, M.A., 1992, Gravity-driven groundwater flow and slope failure potential 1. Elastic effective-stress model: Water Resources Research, v. 28, p. 925-938.

Jaeger, J.C., and Cook, N.G.W., 1979, Fundamentals of rock mechanics. Chapman and Hall, London, 593 p.

Jahns, R.H., 1949, Desert floods: Engineering and Science Journal, v. 23, p. 10-14.

Janda, R.J., Scott, K.M., Nolan, K.M., and Martinson, H.A., 1981, Lahar movement, effects, and deposits, *in* Lipman, P.W., and Mullineaux, D.R., eds., The 1980 Eruptions of Mount St. Helens, Washington. U.S. Geological Survey Professional Paper 1250, p. 461-478.

Johnson, A.M., 1965, A model for debris flow. Ph.D. thesis, The Pennsylvania State University, State College, Pennsylvania, 232 p.

Johnson, A.M., 1970, Physical Processes in Geology. Freeman, Cooper, and Co., San Francisco, 577 p.

Johnson, A.M., 1984, Debris flow, *in* Brunsden, D. and Prior, D.B., eds., Slope Instability. Wiley and Sons, New York, p. 257-361.

Kamb, W.B., 1959, Ice petrofabric observations from Blue Glacier, Washington, in relation to theory and experiment: Journal of Geophysical Research, v. 64, p. 1891-1904.

Kim, S.B., Chough, S.K., and Chun, S.S., 1995, Bouldery deposits in the lowermost part of the Cretaceous Kyokpori Formation, SW Korea: cohesionless debris flows and debris falls on a steep-gradient delta slope: Sedimentary Geology, v. 98, p. 97-119.

Kohlbeck, F., Mojica, J., and Scheidegger, A.E., 1994, Clast orientation of the 1985 lahars of the Nevado del Ruiz, Colombia and implications for depositional processes: Sedimentary Geology, v. 88, p. 175-183.

Koster, E.H., and Steel, R.J., eds., 1984, Sedimentology of Gravels and Conglomerates. Canadian Society of Petroleum Geologists Memoir 10, 441 p.

Lambe, T.W., and Whitman, R.V., 1969, Soil mechanics. Wiley and Sons, New York, 553 p.

Lawson, D.E., 1979, A comparison of pebble orientations in ice and deposits of the Matanuska Glacier, Alaska: Journal of Geology, v. 87, p. 629-645.

Lawson, D.E., 1982, Mobilization, movement, and deposition of active subaerial sediment flows, Matanuska Glacier, Alaska: Journal of Geology, v. 90, p. 279-300.

Lee, K. and Sills, G.C., 1981, The consolidation of a soil stratum, including self-weight effects and large strains: International Journal of Numerical and Analytical Methods in Geomechanics, v. 5, p. 405-428.

Li, J., and Luo, D., 1981, The formation and characteristics of mudflow and flood in the mountain area of the Dachao River and its prevention: Zeitschrift für Geomorphologie, v. 25, p. 470-484.

Li, J., Yuan, J., Bi, C., and Luo, D., 1983, The main features of the mudflow in Jiangjia Ravine: Zeitschrift für Geomorphologie, v. 27, p. 325-341.

Liu, X., 1995, Model experiments on risk range of debris flow fan, *in* Sassa, K., ed., Proceedings of the XX IUFRO World Congress Technical Session on Natural Disasters in Mountainous Areas. Tampere, Finland, August 7-10, 1995, p. 27-37.

Lindsay, J.F., 1968, The development of clast fabric in mudflows: Journal of Sedimentary Petrology, v. 38, p. 1242-1253.

Lowe, D.R., 1982, Sediment gravity flows: II. Depositional models with special reference to the deposits of high-density turbidity currents: Journal of Sedimentary Petrology, v. 52, p. 279-297.

Major, J.J., 1993, Rheometry of natural sediment slurries: Hydraulic Engineering '93, Proceedings of ASCE 1993 Conference on Hydraulic Engineering, San Francisco, CA, July 25-30, p. 1415-1421.

Major, J.J., Janda, R.J., and Daag, A.S., 1996, Watershed disturbance and lahars on the east side of Mount Pinatubo during the mid-June 1991 eruptions, *in* Newhall, C.G., and Punongbayan, R.S., eds., Fire and Mud: Eruptions and Lahars of Mount Pinatubo,

Philippines. Quezon City, Philippine Institute of Volcanology and Seismology, and Seattle, University of Washington Press, p. 895-919.

Major, J.J., and Newhall, C.G., 1989, Snow and ice perturbation during historical volcanic eruptions and the formation of lahars and floods: Bulletin of Volcanology, v. 52, p. 1-27.

Major, J.J., and Pierson, T.C., 1992, Debris flow rheology: Experimental analysis of fine-grained slurries: Water Resources Research, v. 28, p. 841-857.

Major, J.J., and Voight, B., 1986, Sedimentology and clast orientations of the 18 May 1980 southwest-flank lahars, Mount St. Helens, Washington: Journal of Sedimentary Petrology, v. 56, p. 691-705.

Mark, D.M., 1973, Analysis of axial orientation data, including till fabrics: Geological Society of America Bulletin, v. 84, p. 1369-1374.

Masson, D.G., Huggett, Q.J., and Brunsden, D., 1993, The surface of the Sahara Debris Flow deposit and some speculations on submarine debris flow processes: Sedimentology, v. 40, p. 583-598.

McTigue, D.F., 1986, Thermoelastic response of fluid-saturated porous rock: Journal of Geophysical Research, v. 91, p. 9533-9542.

McTigue, D.F., 1990, Flow to a heated borehole in porous, thermoelastic rock: Analysis: Water Resources Research, v. 26, p. 1763-1774.

Middleton, G.V., 1990, Sediment gravity flows revisited: 13th International Sedimentological Congress, Nottingham, England, 26-31 August, p. 357.

Middleton, G.V., and Southard, J.B., 1977, Mechanics of sediment movement. SEPM Short Course 3, 401 p.

Miller, D.J., 1993, Topographically induced stress fields and patterns of bedrock fracturing. Ph.D. thesis, University of Washington, Seattle, 286 p.

Mills, H.H., 1984, Clast orientation in Mount St. Helens debris-flow deposits, North Fork Toutle River, Washington: Journal of Sedimentary Petrology, v. 54, p. 626-634.

Mills, H.H., 1991, Three-dimensional clast orientation in glacial and mass-movement sediments: Compilation and preliminary analysis: U.S. Geological Survey Open-file report 90-128, 71 p.

Mironova, E.M., and Yablonskiy, V.V., 1992, A mathematical model of shear debris flow, *in* Walling, D.E., Davies, T.R.H., Hasholt, B., eds., Erosion, Debris Flows, and Environment in Mountain Regions. International Association of Hydrological Sciences publication no. 209, p. 273-281.

Mizuyama, T., and Uehara, S., 1983, Experimental study of the depositional process of debris flows: Transactions Japanese Geomorphological Union, v. 4, p. 49-64.

Morton, D.M., and Campbell, R.H., 1974, Spring mudflows at Wrightwood, Southern California: Quarterly Journal of Engineering Geology, v. 7, p. 377-383.

Murray, T., 1990, Deformable glacier beds: measurement and modeling. Ph.D thesis, University of Wales, U.K., 321 p.

Nemec, W., and Steel, R.J., 1984, Alluvial and coastal conglomerates: Their significant features and some comments on gravelly mass-flow deposits, *in* Koster, E.H. and Steel, R.J., eds., Sedimentology of Gravels and Conglomerates. Canadian Society of Petroleum Geologists Memoir 10, p. 1-31.

Niyazov, B.S., and Degovets, A.S., 1975, Estimation of the parameters of catastrophic mudflows in the basins of the Lesser and Greater Almatinka Rivers: Soviet Hydrology, v. 2, p. 75-80.

O'Brien, J.S., and Julien, P.Y., 1988, Laboratory analysis of mudflow properties: Journal of Hydraulic Engineering, v. 114, p. 877-887.

O'Brien, J.S., Julien, P.Y., and Fullerton, W.T., 1993, Two-dimensional water flood and mudflow simulation: Journal of Hydraulic Engineering, v. 119, p. 244-261.

Okuda, S., Suwa, H., Okunishi, K., Yokoyama, K., and Nakano, M., 1980, Observations on the motion of a debris flow and its geomorphological effects: Zeitschrift für Geomorphologie, v. 35, p. 142-163.

Owens, I.F., 1973, Alpine mudflows in the Nigel Pass area, Canadian Rocky Mountains. Ph.D. thesis, University of Toronto, Toronto, Canada, 167 p.

Phillips, C.J., and Davies, T.R.H., 1991, Determining rheological parameters of debris flow material: Geomorphology, v. 4, p. 101-110.

Pierson, T.C., 1980, Erosion and deposition by debris flows at Mt. Thomas, North Canterbury, New Zealand: Earth Surface Processes, v. 5, p. 227-247.

Pierson, T.C., 1981, Dominant particle support mechanisms in debris flows at Mt. Thomas, New Zealand, and implications for flow mobility: Sedimentology, v. 28, p. 49-60.

Pierson, T.C., 1984, Why debris flows stop: Geological Society of America Abstracts with Programs, v. 16, no. 6, p. 623.

Pierson, T.C., 1985a, Initiation and flow behavior of the 1980 Pine Creek and Muddy River lahars, Mount St. Helens, Washington: Geological Society of America Bulletin, v. 96, p. 1056-1069.

Pierson, T.C., 1985b, Effects of slurry composition on debris flow dynamics, Rudd Canyon, Utah, *in* Bowles, D.S., ed., Delineation of landslide, flash flood, and debris flow hazards in Utah. Utah Water Research Laboratory General Series Report UWRL/G-85/03, Utah State University, p. 132-152.

Pierson, T.C., 1986, Flow behavior in channelized debris flows, Mount St. Helens, Washington, *in* Abrahams, A.D., ed., Hillslope Processes. Allen and Unwin, Boston, Mass., p. 269-226.

Pierson, T.C., 1995, Flow characteristics of large eruption-triggered debris flows at snow-clad volcanoes: constraints for debris-flow models: Journal of Volcanology and Geothermal Research, v. 66, p. 283-294.

Pierson, T.C., Daag, A.S., Delos Reyes, P.J., Regelado, M.T.M., Solidum, R.U., and Tubianosa, B.S., 1996, Flow and deposition of post-eruption hot lahars on the east side of Mount Pinatubo, July-October, 1991, *in* Newhall, C.G., and Punongbayan, R.S., eds., Fire and Mud: Eruptions and Lahars of Mount Pinatubo, Philippines. Quezon City, Philippine Institute of Volcanology and Seismology, and Seattle, University of Washington Press, p. 921-950.

Pierson, T.C., Janda, R.J., Thouret, J.-C., and Borrero, C.A., 1990, Perturbation and melting of snow and ice by the 13 November 1985 eruption of Nevado del Ruiz, Colombia, and consequent mobilization, flow, and deposition of lahars: Journal of Volcanology and Geothermal Research, v. 41, p. 17-66.

Pierson, T.C., and Scott, K.M., 1985, Downstream dilution of a lahar: Transition from debris flow to hyperconcentrated streamflow: Water Resources Research, v. 21, p. 1511-1524.

Poletto, M., and Joseph, D.D., 1995, Effective density and viscosity of a suspension: Journal of Rheology, v. 39, p. 323-343.

Postma, G., 1986, Classification for sediment gravity-flow deposits based on flow conditions during sedimentation: Geology, v. 14, p. 291-294.

Rappol, M., 1985, Clast-fabric strength in tills and debris flows compared for different environments: Geologie en Mijnbouw, v. 64, p. 327-332.

Reid, M.E., 1994, A pore-pressure diffusion model for estimating landslide-inducing rainfall: Journal of Geology, v. 102, p. 707-717.

Rice, J.R., and Cleary, M.P., 1976, Some basic stress diffusion solutions for fluid-saturated elastic porous media with compressible constituents: Reviews of Geophysics and Space Physics, v. 14, p. 227-241.

Rodolfo, K.S.,Arguden, A.T., Solidum, R.U., and Umbal, J.V., 1989, Anatomy and behavior of a post-eruptive rain lahar triggered by a typhoon on Mayon Volcano, Philippines: Bulletin International Association of Engineering Geology, v. 40, p. 55-66.

Rodolfo, K.S., Umbal, J.V., Alonso, R.A., Remotigue, C.T., Paladio-Melosantos, M.L., Salvador, J.H.G., Evangelista, D., and Miller, Y., 1996, Two years of lahars on the western flank of Mount Pinatubo: Initiation, flow processes, deposits, and attendant geomorphic and hydraulic changes, *in* Newhall, C.G., and Punongbayan, R.S., eds., Fire and Mud: Eruptions and Lahars of Mount Pinatubo, Philippines. Quezon City, Philippine Institute of Volcanology and Seismology, and Seattle, University of Washington Press, p. 989-1013.

Roeloffs, E.A., 1988, Fault stability changes induced beneath a reservoir with cyclic variations in water level: Journal of Geophysical Research, v. 93, p. 2107-2124.

Roeloffs, E.A., 1996, Poroelastic techniques in the study of earthquake-related hydrologic phenomena, *in* Dmowska, R., and Saltzman, B., eds., Advances in Geophysics, v. 37. Academic Press, San Diego, p. 135-195.

Rosenbloom, N.A., and Anderson, R.S., 1994, Hillslope and channel evolution in marine terraced landscape, Santa Cruz, California: Journal of Geophysical Research, v. 99, p. 14,013-14,029.

Scott, K.M., 1988a, Origins, behavior, and sedimentology of lahars and lahar-runout flows in the Toutle-Cowlitz River system: U.S. Geological Survey Professional Paper 1447-A, 76 p.

Scott, K.M., 1988b, Origin, behavior, and sedimentology of prehistoric catastrophic lahars at Mount St. Helens, Washington, *in* Clifton, H.E., ed., Sedimentologic Consequences of Convulsive Geologic Events. Geological Society of America Special Paper 229, p. 23-36.

Scott, W.E., Hoblitt, R.P., Torres, R.C., Self, S., Martinez, M.L., and Nillos, T., 1996, Pyroclastic flows of the June 15, 1991, climactic eruption, Mount Pinatubo, *in* Newhall, C.G., and Punongbayan, R.S., eds., Fire and Mud: Eruptions and Lahars of Mount Pinatubo, Philippines. Quezon City, Philippine Institute of Volcanology and Seismology, and Seattle, University of Washington Press, p. 545-570.

Selby, M.J., 1982, Hillslope Materials and Processes. Oxford University Press, Oxford, 260 p.

Shaller, P.J., 1991, Analysis of a large moist landslide, Lost River Range, Idaho, U.S.A.: Canadian Geotechnical Journal, v. 28, p. 584-600.

Sharp, R.P., and Nobles, L.H., 1953, Mudflow of 1941 at Wrightwood, southern California: Geological Society of America Bulletin, v. 66, p. 1489-1498.

Shreve, R.L., 1968, The Blackhawk Landslide: Geological Society of America Special Paper 108, 47 p.

Shultz, A.W., 1984, Subaerial debris-flow deposition in the Upper Paleozoic Cutter Formation, western Colorado: Journal of Sedimentary Petrology, v. 54, p. 759-772.

Skempton, A.W., 1960, Significance of Terzaghi's concept of effective stress, *in* From Theory to Practice in Soil Mechanics. Wiley and Sons, New York, p. 42-53.

Smith, G.A., and Lowe, D.R., 1991, Lahars: volcano-hydrologic events and deposition in the debris flow-hyperconcentrated flow continuum, *in* Fisher, R.V., and Smith, G.A., eds., Sedimentation in volcanic settings. SEPM Special Publ. 45, p. 59-70.

Sparks, R.S.J., 1976, Grain-size variations in ignimbrites and implications for the transport of pyroclastic flows: Sedimentology, v. 23, p. 147-188.

Takahashi, T., 1981, Debris flows: Annual Review of Fluid Mechanics, v. 13, p. 57-77.

Takahashi, T., 1991, Debris Flow. A.A. Balkema, Rotterdam, 165 p.

Takahashi, T., Nakagawa, H., Harada. T., and Yamashiki, Y., 1992, Routing debris flows with particle segregation: Journal of Hydraulic Engineering, v. 118, p. 1490-1507.

Terzaghi, K., 1923, Die Berechnung der Durchlassigkeitsziffer des Tones aus dem Verlaug der Hydrodynamischen Spannungsercheinungen: Akademie der Wissenchaften in Wein, Sitzungsberichte: Mathematish Naturwissenschaftliche Klasse, Part IIa, v. 132, n. 3/4, p. 125-138.

Timoshenko, S.P., and Goodier, J.N., 1970, Theory of elasticity. McGraw-Hill, New York, 567 p.

Thomas, D.G., 1965, Transport characteristics of suspensions, VIII. A note on the viscosity of Newtonian suspensions of uniform spherical particles: Journal of Colloidal Science, v. 20, p. 267-277.

Trask, P.D., 1959, Effect of grain size on strength of mixtures of clay, sand, and water: Geological Society of America Bulletin, v. 70, p. 569-580.

Vallance, J.W., 1994, Experimental and field studies related to the behavior of granular mass flows and the characteristics of their deposits. Ph.D. thesis, Michigan Technological University, Houghton, Michigan, 197 p.

Van Steijn, H., de Ruig, J., and Hoozemans, F., 1988, Morphologic and mechanical aspects of debris flows in parts of the French Alps: Zeitschrift für Geomorphologie, v. 32, p. 143-161.

Van Steijn, H., and Coutard, J.P., 1989, Laboratory experiments with small debris flows: Physical properties related to sedimentary characteristics: Earth Surface Processes and Landforms, v. 14, p. 587-596.

Voight, B., Janda, R.J., Glicken, H., and Douglass, P.M., 1983, Nature and mechanics of the Mount St. Helens rockslide-avalanche of 18 May 1980: Geotechnique, v. 33, p. 243-273.

Waitt, R.B., 1989, Swift snowmelt and floods (lahars) caused by great pyroclastic surge at Mount St. Helens volcano, Washington, 18 May 1980: Bulletin of Volcanology, v. 52, p. 138-157.

Waldron, H.H., 1967, Debris flow and erosion control problems caused by the ash eruptions of Irazu volcano, Costa Rica: U.S. Geological Survey Bulletin 1241-I, p. 1-37.

Walton, A.W., and Palmer, B.A., 1988, Lahar facies of the Mount Dutton Formation (Oligocene-Miocene) in the Marysvale volcanic field, southwestern Utah: Geological Society of America Bulletin, v. 100, p. 1078-1091.

Wasson, R.J., 1978, A debris flow at Reshun, Pakistan Hindu Kush: Geografiska Annaler, v. 60, p. 151-159.

Watanabe, M., and Ikeya, H., 1981, Investigation and analysis of volcanic mudflows on Mount Sakurajima, Japan, *in* Walling, D.E., and Tacconi, P., eds., Measurement of Erosion and Transport of Sediments. International Association of Hydrological Sciences publication no. 133, p. 245-256.

Watters, R.J., 1983, A landslide induced waterflood-debris flow: Bulletin International Association of Engineering Geology, v. 28, p. 177-182.

Webb, R.H., Pringle, P.T., and Rink, G.R., 1989, Debris flows from tributaries of the Colorado River, Grand Canyon National Park, Arizona: U.S. Geological Survey Professional Paper 1492, 39 p.

Webb, R.H., Pringle, P.T., Reneau, S.L., and Rink, G.R., 1988, Monument Creek debris flow, 1984: Implications for formation of rapids on the Colorado River in Grand Canyon National Park: Geology, v. 16, p. 50-54.

Weirich, F.H., 1989, The generation of turbidity currents by subaerial debris flows, California: Geological Society of America Bulletin, v. 101, p. 278-291.

Whipple, K.X, 1992, Predicting debris-flow runout and deposition on fans: the importance of the flow hydrograph, *in* Walling, D.E., Davies, T.R.H., Hasholt, B., eds., Erosion, Debris Flows, and Environment in Mountain Regions. International Association of Hydrological Sciences publication no. 209, p. 337-345.

Whipple, K.X, 1994, Debris-flow fans: Process and form. Ph.D. thesis, University of Washington, Seattle, WA, 205 p.

Whipple, K.X, and Dunne, T., 1992, The influence of debris flow rheology on fan morphology, Owens Valley, California: Geological Society of America Bulletin, v. 104, p. 887-900.

Wigmosta, M.S., 1983, Rheology and flow dynamics of the Toutle debris flows from Mount St. Helens: M.S. thesis, University of Washington, Seattle, WA, 184 p.

Woodcock, N.H., 1977, Specification of fabric shapes using an eigenvalue method: Geological Society of America Bulletin, v. 88, p. 1231-1236.

Zhang, S., 1993, A comprehensive approach to the observation and prevention of debris flows in China: Natural Hazards, v. 7, p. 1-23.

Zimmerman, M., 1991, Formation of debris flow cones: Results from model tests: Proceedings of the U.S.-Japan Symposium on Snow Avalanche, Landslide, Debris Flow Prediction and Control, p. 463-470.

APPENDIX A. SOIL-TEST DATA

Physical characteristics of soils used in this study were measured in 4-inch, 6-inch, and 15-inch diameter triaxial load cells. Tests were conducted to obtain information on properties that describe the resistance of the material to shearing and that describe the stiffness and compressibility of the soil skeleton under low stresses. Large-diameter triaxial cells were used so that representative soil specimens, including the gravel component, could be tested. Analyses of the flume debris were conducted by Bob Donaghe, U.S. Army Corps of Engineers, using the 6-inch and 15-inch diameter cells. These analyses incorporated the full distribution of particle sizes (up to 32 mm) in the test material. Analyses of the Mount St. Helens North Fork Toutle River and Osceola Mudflow debris were conducted under the supervision of Dave McTigue, University of Washington, using a 4-inch diameter cell. In these analyses particles larger than 10mm were removed from the material to prevent large particles from unduly influencing test results. Standards established by the American Society for Testing and Materials (ASTM, 1995) call for the largest particle to be smaller than 1/6 the specimen diameter. Samples tested in the 4-inch-diameter triaxial cell were consolidated under varying effective confining stresses prior to application of a vertical load whereas samples tested in the larger triaxial cells were consolidated under an effective confining stress of 55 kPa prior to application of a vertical load. All specimens were saturated prior to testing.

Test specimens were prepared by tamping several layers of material into the respective molds. Specimens were tamped in an effort to achieve dry bulk densities in the range from 1500-2000 kg/m^3. Following hand compaction, the specimen cap was placed on top of filter paper and a porous capstone and the rubber membrane was pulled around that cap and sealed against it with o-rings. After assembly, a small vacuum (about 16 kPa) was applied to the specimen and the mold removed. Specimens were saturated by percolating deaired water through the specimen from bottom to top. When water appeared in a tube at the top of specimens in the 6-inch and 15-inch cells, the specimens were assumed saturated. For specimens in the 4-inch cell, the pore-fluid pressure within the sample and the stress confining the sample were set to achieve the desired effective confining stress, then both pressures were increased simultaneously until imposed changes in confining stress were matched identically by changes in pore-fluid pressure (i.e. until $B=\Delta p/\Delta\sigma=1$ (Lambe and Whitman, 1969)). When $B=1$, the specimen is considered saturated.

Isotropic compression tests as well as conventional triaxial compression tests were conducted in the 4-inch cell. During each test fluid drainage was permitted only from the top of the sample, and pore-fluid pressure was maintained at the level needed to ensure saturation. Specimen permeability was measured prior to testing and following each phase of isotropic and triaxial compression (see Appendix B). During triaxial compression, specimens were loaded using a constant displacement rate of 0.51mm/min.

Specimens tested in the larger triaxial cells were first consolidated under K_0 conditions (Lambe and Whitman, 1969) to an effective confining stress of 55 kPa. K_0 consolidation requires continual adjustment of confining stress as axial stress is increased in order to maintain a constant specimen cross section. The goal of this procedure is to consolidate the specimen under conditions of zero lateral strain. During these tests, fluid was allowed to drain from both ends of the specimen; pore-fluid pressures within the specimen were assumed to be zero. During triaxial compression, specimens were loaded at a constant rate of strain. The rates of strain used varied from 0.01%/min to 0.13%/min.

The ability of a granular soil to resist shearing stresses is described, in part, by the angle of internal friction. Angles of internal friction for the materials used in this study were determined from envelopes bounding Mohr circles that define the stress state of specimens at failure (Figures A1, A2). The states of stress at failure represent the peak points of the stress-strain curves (Lambe and Whitman, 1969). Friction angles for the materials used in this study ranged from 29°-39° (see Figures A1, A2, and Table 3.7).

Properties that describe the stiffness and compressibility of elastic materials include Young's modulus, the constrained modulus, and the bulk modulus. Another measure of compressibility commonly used in analyses of soils is the compression index. Young's modulus describes the relation between axial stress and axial strain in an elastic specimen that is loaded uniaxially. Standard triaxial compression tests (constant confining stress and increasing axial stress) provide a measure of Young's modulus. However, because soils are not truly elastic materials, it is common practice to define Young's modulus as the secant modulus determined from zero deviator stress to a deviator stress having a value equal to one-half of the peak deviator stress (Lambe and Whitman, 1969). Figures A3-

A5 illustrate the stress-strain relations for the materials used in this study. Table 3.7 summarizes the values of secant Young's modulus computed from these data.

The bulk modulus and compression index provide some measure of the compressibility of soils. The bulk modulus relates isotropic stress to volumetric strain in an elastic specimen. This quantity is inversely related to the compressibility of material: the larger the modulus, the less compressible is the material. The compression index relates changes in void ratio (e) to changes in applied vertical effective stress (σ'_v) on a logarithmic scale by

$$C_c = -\frac{\Delta e}{\Delta(\log \sigma'_v)}. \tag{A1}$$

Another type of modulus that describes the stiffness of elastic material is the constrained modulus, D_c, which relates axial stress to axial strain in a confined specimen having no lateral strain. It is analogous to Young's modulus, but is defined for confined compression. The constrained modulus, defined as

$$D_c = \frac{\Delta \sigma'_v}{\Delta \varepsilon_v} \tag{A2}$$

where ε_v is the volume strain in the sample, can be estimated for a soil if one has some knowledge of the compression index. In confined compression, the volume strain is related to changes in void ratio by (Lambe and Whitman, 1969)

$$\varepsilon_v = \frac{\Delta e}{1 + e_0} \tag{A3}$$

where e_0 is the initial void ratio of the specimen. Combining (A1)-(A3) yields

$$D_c = \frac{\Delta\sigma_v'(1+e_0)}{C_c\Delta(\log\sigma_v')}. \qquad \text{(A4)}$$

SAND AND GRAVEL DEBRIS, 6-INCH DIAMETER TRIAXIAL CELL

Total volume after saturation	5263 cm^3
Volume solids	3520 cm^3
Volume voids	1743 cm^3
Initial void ratio	0.495

Deviatoric stress (kPa)	Confining stress (kPa)	Vertical stress (kPa)	Cumulative volume change (cm^3)	New total volume (cm^3)	New void volume (cm^3)	Void ratio	Δe
34.1	20.7	54.8	-3.5	5260	1740	0.494	0.001
41.8	27.6	69.4	-37.2	5226	1706	0.485	0.010
48.7	34.5	83.2	-39.2	5224	1704	0.484	0.011
58.3	41.4	99.7	-50.9	5213	1692	0.481	0.014
67.9	48.3	116.2	-67.1	5196	1676	0.476	0.019
76.7	55.2	131.9	-81.3	5182	1662	0.472	0.023

From a plot of these data (Figure A6), we find $C_c \approx 0.053$ and $D_c \approx 5\text{x}10^6$ Pa.

LOAM DEBRIS, 6-INCH DIAMETER TRIAXIAL CELL

Total volume after saturation	5347 cm^3
Volume solids	3519 cm^3
Volume voids	1828 cm^3
Initial void ratio	0.519

Deviatoric stress (kPa)	Confining stress (kPa)	Vertical stress (kPa)	Cumulative volume change (cm^3)	New total volume (cm^3)	New void volume (cm^3)	Void ratio	Δe
37.3	20.7	58.0	-9.4	5338	1818	0.517	0.002
40.6	27.6	68.2	-18.0	5329	1810	0.514	0.005
46.0	34.5	80.4	-35.2	5312	1793	0.509	0.010
55.7	41.4	97.1	-64.5	5282	1763	0.501	0.018
61.1	48.3	109.4	-79.0	5268	1749	0.497	0.022
71.8	55.2	126.9	-110.9	5236	1717	0.488	0.031

From a plot of these data (Figure A6), we find $C_c \approx 0.087$ and $D_c \approx 3 \times 10^6$ Pa.

SAND AND GRAVEL DEBRIS, 15-INCH DIAMETER TRIAXIAL CELL

Total volume after saturation	104710 cm^3
Volume solids	72770 cm^3
Volume voids	31940 cm^3
Initial void ratio	0.439

Deviatoric stress (kPa)	Confining stress (kPa)	Vertical stress (kPa)	Cumulative volume change (cm^3)	New total volume (cm^3)	New void volume (cm^3)	Void ratio	Δe
45.2	40.7	85.8	-715	103996	31226	0.429	0.010
43.8	48.3	92.1	-717	103994	31224	0.429	0.010
59.9	54.5	114.4	-1128	103583	30813	0.423	0.016

From a plot of these data (Figure A6), we find $C_c \approx 0.050$ and $D_c \approx 6.5 \times 10^6$ Pa.

MOUNT ST. HELENS 1980 NORTH FORK TOUTLE RIVER DEBRIS

4-INCH DIAMETER TRIAXIAL CELL

ISOTROPIC COMPRESSION

Sample	Effective confining stress (kPa)	Pore-fluid pressure (kPa)	Initial volume V (cm^3)	ΔV (cm^3)	Time for volume change	$\Delta\sigma_0$ (kPa)	$\Delta V/V$	Bulk modulus K_b (Pa)
MSH-1	17.2	149	1732.3	9.0	5 min	13.8	0.005	$2.6x10^6$
	31.0		1718.8	26.3	22 min	13.8	0.015	$9x10^5$
	51.7		1692.3	20.0	20 min	20.7	0.012	$1.8x10^6$
	72.4		1672.3	19.6	30 min	20.7	0.012	$1.8x10^6$
	17.2		1732.3	3.6	10 secs	13.8	0.002	$6.6x10^6$
MSH-3	17.2	272.4	1773.2	6.2	3 min	13.8	0.003	$3.9x10^6$
	17.2		1773.2	3.8	1 min	13.8	0.002	$6.4x10^6$
MSH-4	34.5	220.7	1798.7	16.1	20 min	27.6	0.009	$3.1x10^6$
	34.5		1798.7	1.5	10 secs	27.6	0.0008	$3.3x10^7$

TRIAXIAL COMPRESSION

Sample MSH-4

Total volume after saturation:	1810.3 cm^3
Volume solids:	1187.9 cm^3
Volume voids:	622.4 cm^3
Initial void ratio:	0.524

Deviatoric stress (kPa)	Effective confining stress (kPa)	Effective vertical stress (kPa)	Cumulative volume change (cm^3)	New total volume (cm^3)	New void volume (cm^3)	Void ratio	Δe
15.8	6.9	22.7	-0.45	1809.9	622.0	0.524	0
16.8		23.7	-1.6	1808.7	620.8	0.523	0.001
21.1		28.0	-3.8	1806.5	618.6	0.521	0.003
25.2		32.1	-8.3	1802.0	614.1	0.517	0.007
27.8		34.7	-14.0	1796.3	608.4	0.512	0.012
30.3		37.2	-17.1	1793.2	605.3	0.510	0.014

From a plot of these data (Figure A6) we find $C_c \approx 0.098$ and $D_c \approx 1.0 \times 10^6$ Pa.

Sample MSH-4 (after isotropic consolidation)

Total volume after saturation: 1782.6 cm^3

Volume solids: 1187.9 cm^3

Volume voids: 594.7 cm^3

Initial void ratio: 0.501

Deviatoric stress (kPa)	Effective confining stress (kPa)	Effective vertical stress (kPa)	Cumulative volume change (cm^3)	New total volume (cm^3)	New void volume (cm^3)	Void ratio	Δe
49.6	34.5	84.1	-0.5	1782.1	594.2	0.500	0.001
64.4		98.9	-1.7	1780.9	593.0	0.499	0.002
70.3		104.8	-2.6	1780.0	592.1	0.498	0.003
79.9		114.4	-4.2	1778.4	590.5	0.497	0.004
94.7		129.2	-7.1	1775.5	587.6	0.495	0.006
103.0		137.5	-10.7	1771.9	584.0	0.492	0.009
1.403		138.8	-12.3	1770.3	582.4	0.490	0.011

From a plot of these data (Figure A6) we find $C_c \approx 0.112$ and $D_c \approx 3.0\text{x}10^6$ Pa.

MOUNT RAINIER OSCEOLA MUDFLOW, 4-INCH DIAMETER TRIAXIAL CELL

ISOTROPIC COMPRESSION

Sample	Effective confining stress (kPa)	Pore-fluid pressure (kPa)	Initial volume V (cm^3)	ΔV (cm^3)	Time for volume change	$\Delta\sigma_0$ (kPa)	$\Delta V/V$	Bulk modulus K_b (Pa)
MR-1	17.2	237.9	1628.7	15.7	16 min	13.8	0.010	$1.4\text{x}10^6$
	31.0		1613.0	39.2	12 min	13.8	0.024	$5.7\text{x}10^5$
	51.7		1573.8	48.3	12 min	20.7	0.031	$6.7\text{x}10^5$
	72.5		1525.0	20.5	22 min	20.7	0.013	$1.5\text{x}10^6$
	17.2		1628.7	7.7	10 secs	13.8	0.0047	$2.9\text{x}10^6$
MR-3	24.1	234.5	1599.8	4.3	3 min	13.8	0.003	$5.1\text{x}10^6$
	44.8		1595.5	5.7	2 min	20.7	0.004	$5.8\text{x}10^6$
	65.5		1579.8	13.1	25 min	20.7	0.008	$2.5\text{x}10^6$
	79.3		1566.7	7.4	20 min	13.8	0.005	$2.9\text{x}10^6$
	24.1		1599.8	0.95	10 secs	13.8	0.0006	$2.3\text{x}10^7$
MR-4	34.5	206.9	1722.6	74.4	10 min	31.0	0.043	$7.2\text{x}10^5$
	34.5		1772.6	18.9	10 secs	31.0	0.011	$2.8\text{x}10^6$

TRIAXIAL COMPRESSION

Sample MR-1

Total volume after saturation: 1505.0 cm^3

Volume solids: 783.8 cm^3

Volume voids: 721.3 cm^3

Initial void ratio: 0.920

Deviatoric stress (kPa)	Effective confining stress (kPa)	Effective vertical stress (kPa)	Cumulative volume change (cm^3)	New total volume (cm^3)	New void volume (cm^3)	Void ratio	Δe
35.8	72.5	108.3	-1.9	1503.1	719.4	0.918	0.002
39.2		111.7	-5.2	1499.8	716.1	0.914	0.006
42.7		115.2	-7.2	1497.8	714.1	0.911	0.009
46.0		118.5	-10.5	1494.5	710.8	0.907	0.013
48.3		120.8	-14.3	1490.7	707.0	0.902	0.018
51.7		124.2	-17.2	1487.8	704.1	0.898	0.022
55.0		127.5	-20.0	1485.0	701.3	0.895	0.025
58.4		130.9	-23.4	1481.6	697.9	0.890	0.030
61.7		134.2	-26.2	1478.8	695.1	0.887	0.033
63.9		136.4	-28.1	1476.9	693.2	0.884	0.036
82.3		154.8	-45.3	1459.7	676.0	0.862	0.058
93.9		166.4	-55.3	1449.7	666.0	0.850	0.070
106.1		178.6	-65.3	1439.7	656.0	0.837	0.083

From a plot of these data (Figure A6) we find $C_c \approx 0.377$ and $D_c \approx 1.0 \times 10^6$ Pa.

Sample MR-4

Total volume after saturation: 1754.6 cm^3

Volume solids: 853.5 cm^3

Volume voids: 901.1 cm^3

Initial void ratio: 1.056

Deviatoric stress (kPa)	Effective confining stress (kPa)	Effective vertical stress (kPa)	Cumulative volume change (cm^3)	New total volume (cm^3)	New void volume (cm^3)	Void ratio	Δe
14.9	3.5	18.4	-0.9	1753.7	900.2	1.055	0.001
17.1		20.6	-2.3	1752.3	898.8	1.053	0.003
18.1		21.6	-3.6	1751.0	897.5	1.052	0.004
20.0		23.5	-14.4	1740.2	886.7	1.039	0.017
20.9		24.4	-19.9	1734.7	881.2	1.032	0.024
21.5		25.0	-28.9	1725.7	872.2	1.022	0.034

From a plot of these data (Figure A6) we find $C_c \approx 0.366$ and $D_c \approx 2.5 \times 10^5$ Pa.

Sample MR-4 (after isotropic consolidation)

Total volume after saturation: 1667.1 cm^3

Volume solids: 853.5 cm^3

Volume voids: 813.6 cm^3

Initial void ratio: 0.953

Deviatoric stress (kPa)	Effective confining stress (kPa)	Effective vertical stress (kPa)	Cumulative volume change (cm^3)	New total volume (cm^3)	New void volume (cm^3)	Void ratio	Δe
22.1	34.5	56.6	-4.1	1663.0	809.5	0.948	0.005
27.7		62.2	-9.0	1658.1	804.6	0.943	0.010
35.4		69.9	-16.7	1650.4	769.9	0.934	0.019
42.0		76.5	-23.0	1644.1	790.6	0.926	0.027
51.7		86.2	-32.9	1635.0	780.7	0.915	0.038
56.9		90.5	-40.6	1626.5	773.0	0.906	0.047
62.1		96.6	-45.6	1621.5	768.0	0.900	0.053

64.0	98.5	-49.6	1617.5	764.0	0.895	0.058
68.1	102.6	-53.7	1613.4	759.9	0.890	0.063
74.9	109.4	-62.7	1604.4	750.9	0.880	0.073
78.3	112.8	-69.9	1597.2	743.7	0.871	0.082
80.0	114.5	-72.6	1594.5	741.0	0.868	0.085

From a plot of these data (Figure A6) we find $C_c \approx 0.355$ and $D_c \approx 1.2\text{x}10^6$ Pa.

Sample MR-3 (during isotropic compression)

Total volume after saturation: 1599.8 cm^3

Volume solids: 825.3 cm^3

Volume voids: 774.5 cm^3

Initial void ratio: 0.938

Deviatoric stress (kPa)	Effective confining stress (kPa)	Effective vertical stress (kPa)	Cumulative volume change (cm^3)	New total volume (cm^3)	New void volume (cm^3)	Void ratio	Δe
0.0	24.1	24.1	-4.3	1595.5	770.2	0.933	0.005
0.0	44.8	44.8	-20.0	1579.8	754.5	0.914	0.024
0.0	65.5	65.5	-33.1	1566.8	741.4	0.898	0.040
0.0	79.3	79.3	-40.7	1559.1	733.8	0.889	0.049

From a plot of these data (Figure A6) we find $C_c \approx 0.103$ and $D_c \approx 1.6\text{x}10^6$ Pa.

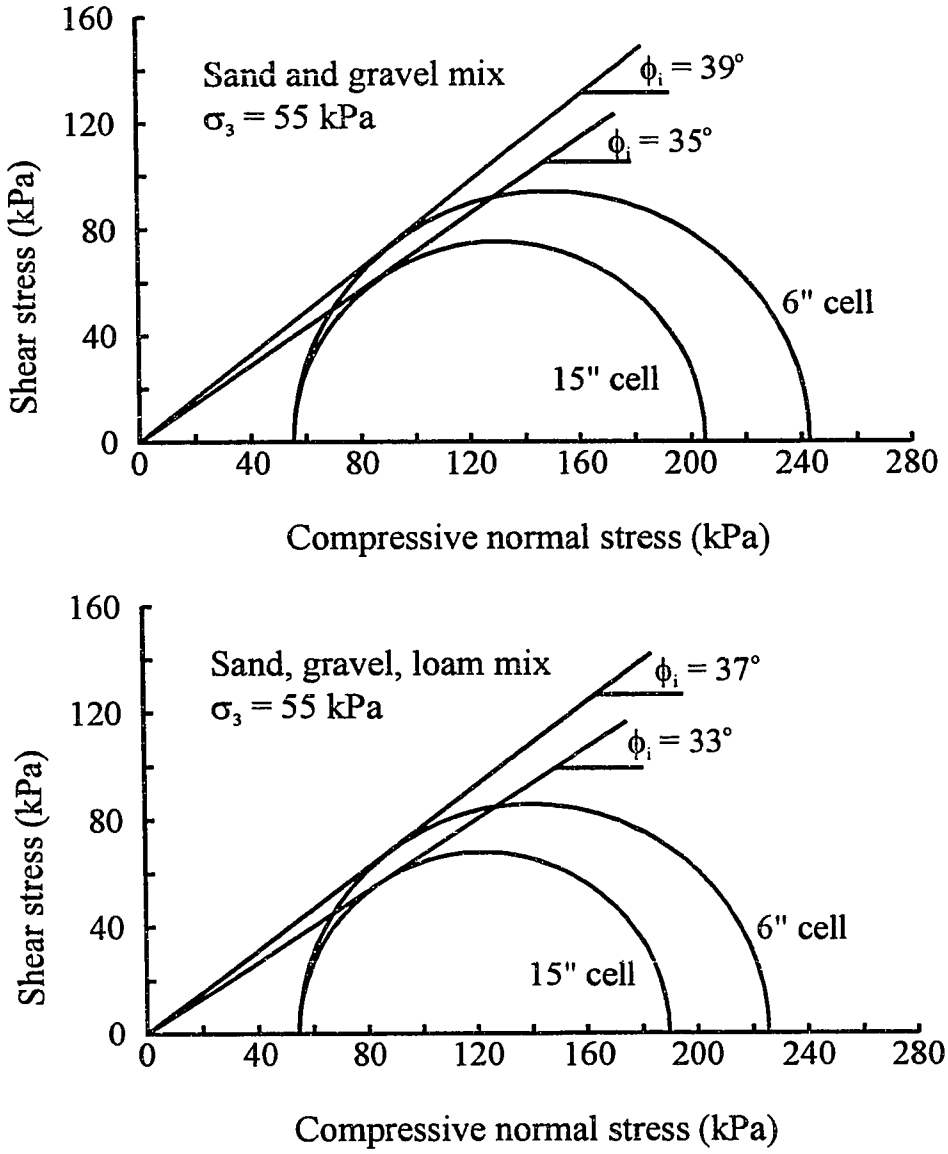

Figure A1. Mohr-circle diagrams illustrating failure envelopes of flume debris.

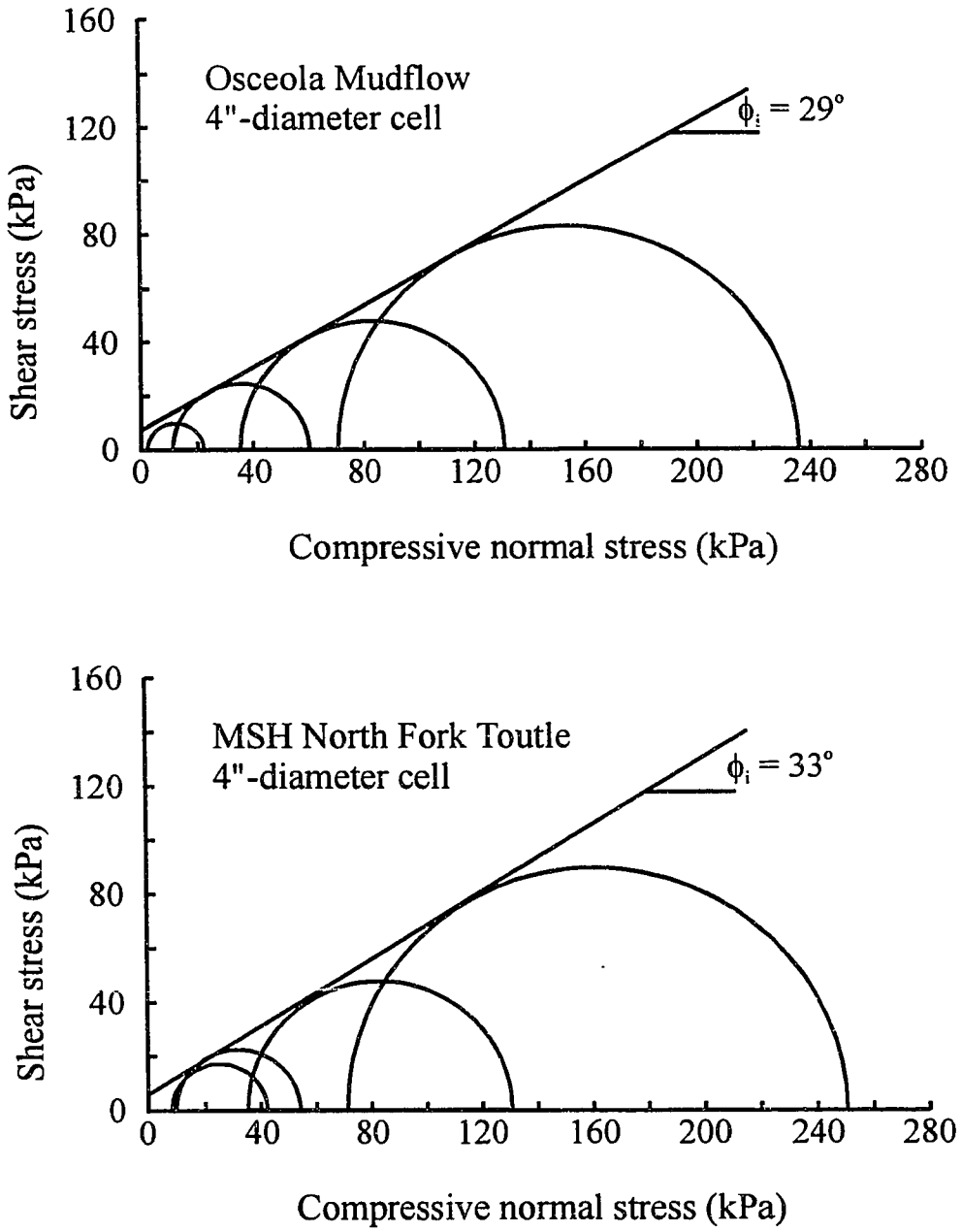

Figure A2. Mohr-circle diagrams illustrating failure envelopes of Osceola Mudflow and Mount St. Helens North Fork Toutle debris.

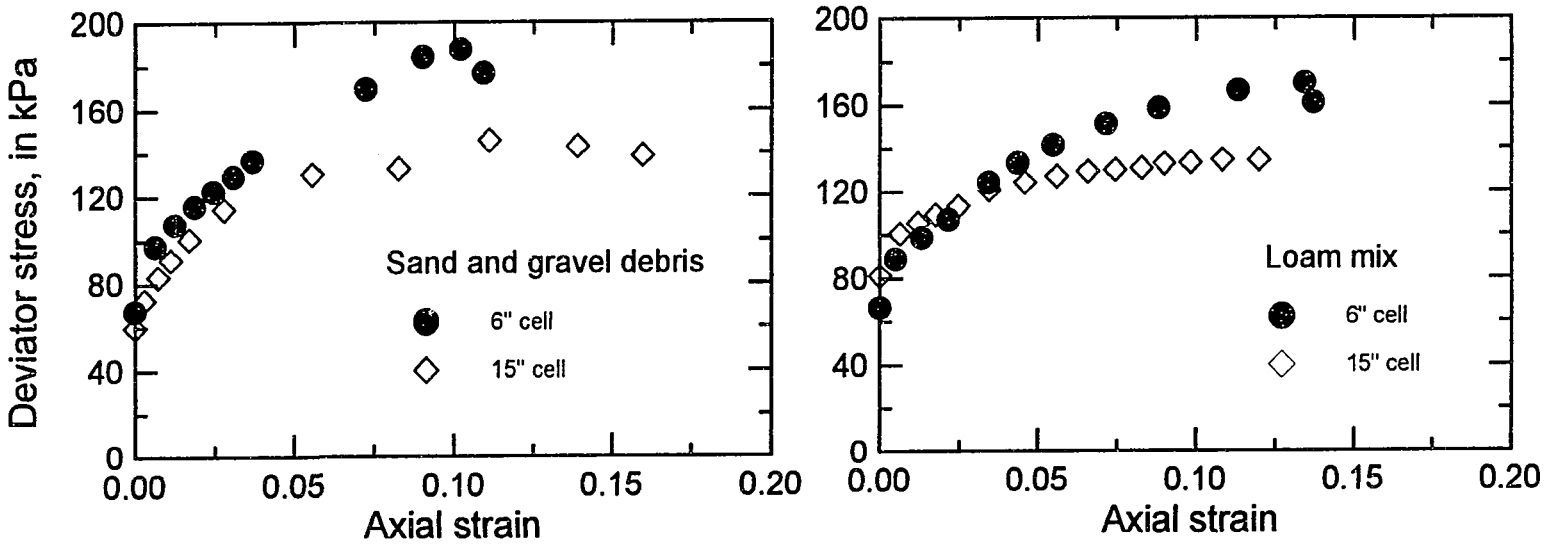

Figure A3. Stress-strain relations for samples of flume debris. Data from triaxial shear tests conducted at a confining stress of 55 kPa.

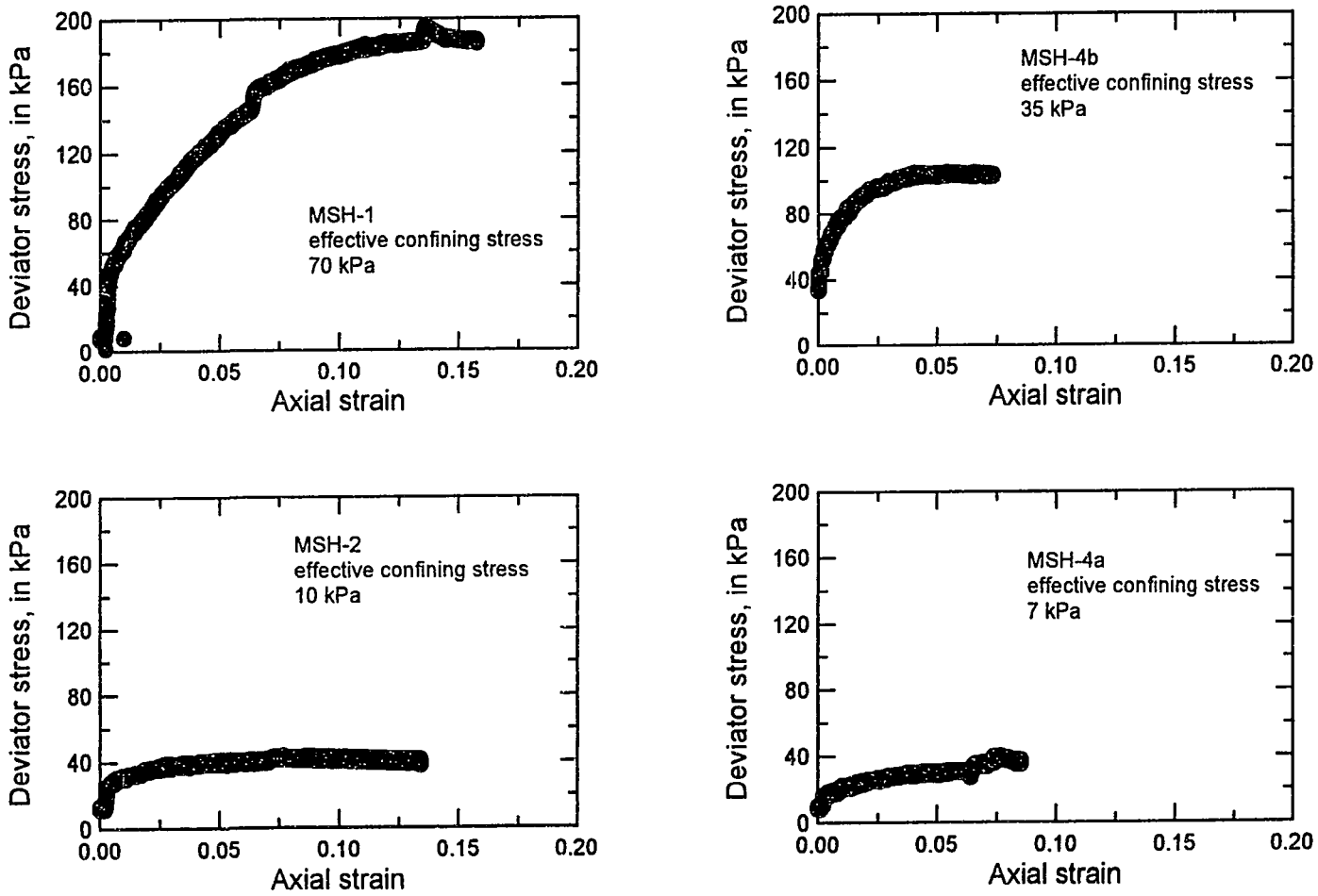

Figure A4. Stress-strain relations for samples of Mount St. Helens 1980 North Fork Toutle River debris.

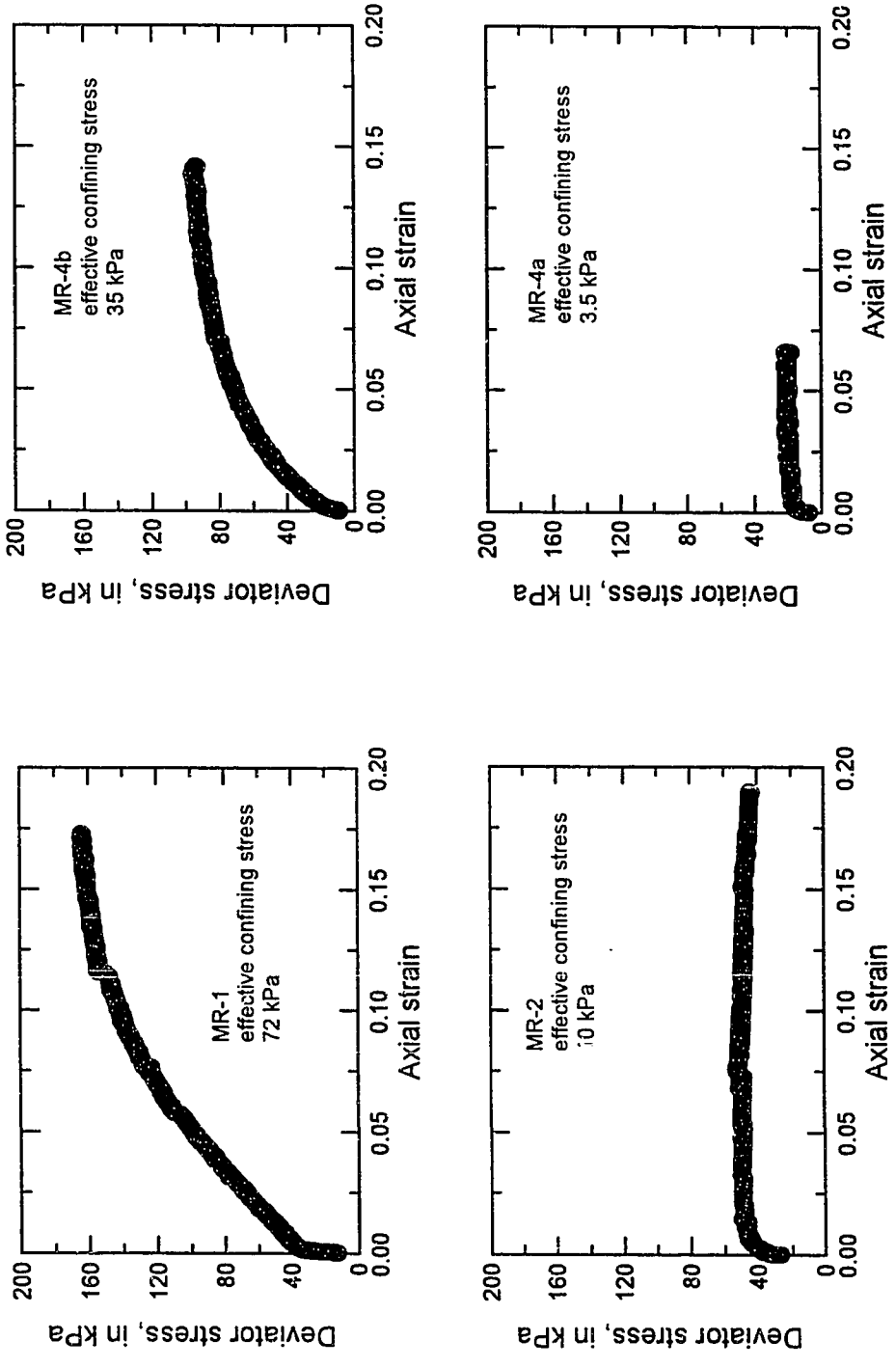

Figure A5. Stress-strain relations for samples of Osceola Mudflow debris.

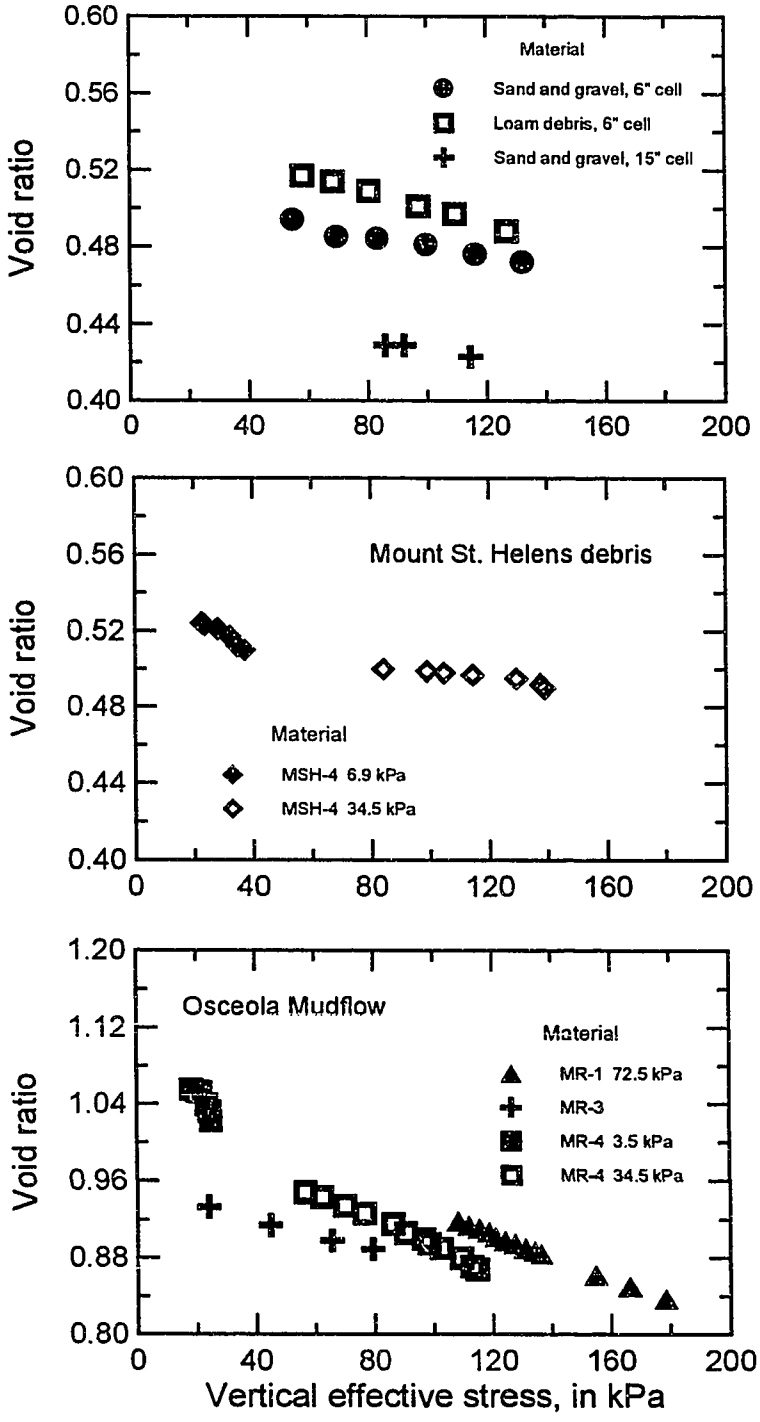

Figure A6. Relations between void ratio and vertical effective stress.

APPENDIX B. CONSTANT-HEAD PERMEAMETER ANALYSES

Constant-head permeameter tests were conducted to characterize the permeability of materials used in this study under a range of porosities. Forty-eight analyses were conducted using a modified compaction permeameter. An additional 20 analyses were conducted during compression tests using a 4-inch-diameter triaxial load cell.

Specimens on the order of 3500 cm^3 volume were tested in a standard 15.25-cm-diameter compaction permeameter that was modified to permit upward, rather than downward, flow through the sediment. Filter cloth was used in place of porous stones in order to maximize the permeability of the permeameter. Particles larger than about 16 mm were removed from specimens of the Mount St. Helens and Mount Rainier (Osceola) debris; for a few analyses particles larger than 4 mm removed. Specimens of flume debris were unsieved (maximum size was 32 mm). Test specimens were prepared in three ways to vary initial porosity. To achieve maximum initial porosity, material was loosely poured into the permeameter. Moderately dense specimens were prepared by tamping thin layers of material into the permeameter mold. Specimens having minimum initial porosities were prepared by heavily tamping thin layers of material into the mold. In addition to these preparation methods, two specimens of Mount St. Helens debris (K45, K46) and one specimen of Mount Rainier (Osceola Mudflow) debris (K44) were first mixed with water to create slurries and then poured into the mold. After the specimens were packed into the mold, the permeameter was weighed, and a subsample of the specimen was oven dried to determine initial bulk density and porosity of the specimen.

Following sample preparation, material was saturated by slowly percolating water through the specimen from bottom to top. Heads used to saturate the material were kept low; at no time were specimens allowed to liquefy. After specimens were saturated, a low value of constant differential hydraulic head (< 15 cm) was used to drive water through the sediment. Hydraulic gradients were determined using the length of the sediment column after saturation. Some specimens, especially those poured loosely into the mold, underwent significant collapse and shortening upon saturation. Those specimens can be identified by noting differences between initial porosity (before saturation) and final porosity (after saturation) in the following table. With few exceptions (K18, K45, K46, and K50), hydraulic gradients during tests were ≤ 0.380.

Volume flux of water through a specimen was measured by gathering outflow from the permeameter in a graduated cylinder for periods up to several minutes. Fluid collection was timed until a minimum of 75 to 100 ml of water was gathered. In most cases, far more water was gathered. This procedure was repeated a minimum of 5 times for each specimen. An average flux rate was determined from these data. Temperature of the outflow was measured for all tests.

Specimen permeability was determined from Darcy's law. Darcy's law states that fluid flux per unit area of specimen is proportional to hydraulic conductivity and hydraulic gradient (e.g., Freeze and Cherry, 1979). Computed values of hydraulic conductivity were converted to values of intrinsic permeability of the specimen, and all values were standardized to a water temperature of 20° C (Bowles, 1978).

Permeabilities of specimens prepared for triaxial compression tests were measured before and after each phase of isotropic and triaxial compression. A differential pressure of 6.9 to 13.8 kPa was applied to each specimen in the triaxial cell to drive water through the sediment from the bottom to the top. In these tests, hydraulic gradients were much larger (3.2 to 9.6) than were those in the compaction permeameter. Confining stresses applied to the specimens prevented liquefaction of the sediment under these very high gradients. Volume flux of water through a specimen was measured by gathering outflow in a graduated burrette for periods up to several minutes. Fluid was collected until the volume flux achieved a reasonably steady state. An average flux rate was determined from these data, and the intrinsic permeability was determined for an assumed fluid density of 1000 kg/m^3 and fluid viscosity of 10^{-3} Pa-s.

CONSTANT-HEAD PERMEAMETER TEST DATA

Test[§]	Material[†]	Size mm	Initial density[*] g/cm^3	Final density g/cm^3	Q cm^3/s	Hydraulic gradient I	Permeability k m^2	Initial porosity	Final porosity
K2	MSH	< 4	1.36	1.37	0.160	0.205	4.62×10^{-12}	0.48	0.48
K3	MSH	< 4	1.58	1.56	0.058	0.373	9.21×10^{-13}	0.40	0.41
K4	OSC	< 4	1.34	1.32	0.163	0.312	3.01×10^{-12}	0.50	0.50
K5	OSC	< 4	1.13	1.15	0.520	0.361	8.10×10^{-12}	0.57	0.57
K6	MSH	< 4	1.49	1.49	0.140	0.351	2.14×10^{-12}	0.44	0.44
K7	S&G	< 4	1.71	1.69	0.108	0.362	1.60×10^{-12}	0.36	0.36
K8	S&G	unsieved	1.97	1.96	0.133	0.365	1.96×10^{-12}	0.26	0.26
K9	S&G	unsieved	1.58	1.67	9.550	0.100	4.88×10^{-10}	0.43	0.37
K11	MSH	< 16	1.13	1.68	0.971	0.274	1.95×10^{-11}	0.58	0.36
K12	MSH	< 16	1.58	1.60	0.057	0.386	8.17×10^{-13}	0.40	0.40
K13	MSH	< 16	1.45	1.52	0.139	0.396	1.76×10^{-12}	0.45	0.43
K14	MSH	< 4	1.13	1.38	1.160	0.462	1.38×10^{-11}	0.57	0.48
K15	MSH	< 4	1.92	1.93	0.525	0.309	8.70×10^{-12}	0.28	0.27
K16	MSH	< 4	1.40	1.57	0.166	0.428	2.03×10^{-12}	0.47	0.41
K17	MSH	< 4	1.01	1.51	0.349	0.532	3.29×10^{-12}	0.62	0.43

Appendix B (continued)

K18	MSH	< 4	1.80	1.91	0.283	0.559	$2.61x10^{-12}$	0.32	0.28
K20	S&G	unsieved	1.70	1.73	0.612	0.034	$1.0x10^{-10}$	0.36	0.35
K21	S&G	unsieved	1.82	1.79	0.748	0.374	$1.07x10^{-11}$	0.31	0.32
K22	S&G	unsieved	1.78	1.79	2.337	0.245	$4.67x10^{-11}$	0.33	0.32
K23	S,G,&L	unsieved	1.80	1.80	0.413	0.368	$6.81x10^{-12}$	0.32	0.32
K25	MSH	< 4	0.99	1.44	0.914	0.516	$9.30x10^{-12}$	0.63	0.46
K26	S&G	unsieved	1.48	1.67	1.270	0.086	$8.14x10^{-11}$	0.44	0.37
K27	S&G	< 4	1.50	1.50	1.237	0.327	$2.19x10^{-11}$	0.44	0.44
K28	S&G	< 4	1.25	1.42	1.660	0.223	$4.19x10^{-11}$	0.53	0.47
K29	S,G,&L	unsieved	1.67	1.67	0.568	0.365	$8.57x10^{-12}$	0.37	0.37
K30	S,G,&L	unsieved	1.47	1.57	2.110	0.299	$3.97x10^{-11}$	0.44	0.41
K31	S,G,&L	unsieved	1.43	1.54	1.001	0.219	$2.63x10^{-11}$	0.46	0.42
K32	S&G	unsieved	1.5	1.77	1.737	0.097	$1.03x10^{-10}$	0.43	0.33
K33	S,G,&L	unsieved	1.76	1.76	0.236	0.366	$3.72x10^{-12}$	0.34	0.34
K34	S,G,&L	unsieved	1.69	1.69	0.396	0.309	$7.40x10^{-12}$	0.36	0.36
K35	MSH	< 16	1.25	1.32	1.910	0.357	$3.16x10^{-11}$	0.53	0.50
K36	MSH	< 16	1.5	1.49	0.207	0.346	$3.37x10^{-12}$	0.43	0.44
K37	MSH	< 16	1.57	1.57	0.120	0.351	$2.02x10^{-12}$	0.41	0.41

Appendix B (continued)

K38	OSC	< 16	1.21	1.18	0.127	0.333	$2.26x10^{-12}$	0.54	0.55
K39	OSC	< 16	1.18	1.18	0.343	0.328	$6.19x10^{-12}$	0.55	0.56
K40	OSC	< 16	0.98	1.07	0.684	0.239	$1.61x10^{-11}$	0.63	0.60
K41	OSC	< 16	1.21	1.16	0.194	0.330	$3.39x10^{-12}$	0.54	0.56
K42	OSC	< 16	1.33	1.32	0.162	0.335	$2.79x10^{-12}$	0.50	0.50
K43	OSC	< 16	1.01	1.15	0.471	0.252	$1.08x10^{-11}$	0.62	0.56
K44	OSC	< 16	1.34	1.37	0.075	0.399	$1.06x10^{-12}$	0.50	0.48
K45	MSH	< 16	1.73	1.73	0.048	1.101	$2.46x10^{-13}$	0.35	0.35
K46	MSH	< 16	1.73	1.72	0.062	0.751	$4.88x10^{-13}$	0.35	0.35
K47	S&G	< 4	1.48	1.48	0.777	0.379	$1.18x10^{-11}$	0.44	0.44
K48	S&G	< 4	1.61	1.60	0.250	0.190	$7.593x10^{-12}$	0.39	0.40
K49	S&G	< 4	1.29	1.40	1.400	0.117	$7.11x10^{-11}$	0.51	.47
K50	S,G,&L	unsieved	1.75	1.75	0.746	0.754	$5.31x10^{-12}$	0.34	0.34
K51	S,G,&L	unsieved	1.72	1.73	0.506	0.376	$7.06x10^{-12}$	0.35	0.35
K52	S,G,&L	unsieved	1.53	1.72	1.350	0.414	$6.81x10^{-11}$	0.42	0.35
K53	PERM	nylon	1.00	1.00	7.580	0.019	$2.56x10^{-9}$		
K54	PERM	no filter	1.00	1.00	39.20	0.174	$1.33x10^{-9}$		
MR-1a	OSC	< 10			0.651	6.87	$1.2x10^{-12}$		0.514

Appendix B (continued)

MR-1b	OSC	<10	0.103	3.53	4.0×10^{-13}	0.479
MR-1c	OSC	<10	0.017	3.76	6.1×10^{-14}	0.456
MR-1d	OSC	<10	0.009	8.08	1.4×10^{-14}	0.443
MR-1e	OSC	<10	0.003	8.71	4.7×10^{-15}	0.439
MR-2a	OSC	<10	0.115	7.18	2.1×10^{-13}	0.496
MR-2a	OSC	<10	0.022	7.84	3.1×10^{-14}	0.496
MR-2c	OSC	<10	0.017	8.63	2.2×10^{-14}	0.494
MR-2d	OSC	<10	0.009	9.61	9.0×10^{-15}	0.491
MR-3a	OSC	<10	0.212	7.00	3.8×10^{-13}	0.484
MR-3b	OSC	<10	0.150	7.00	2.8×10^{-13}	0.483
MR-3c	OSC	<10	0.156	7.04	2.9×10^{-13}	0.478
MR-3d	OSC	<10	0.094	7.04	1.8×10^{-13}	0.473
MR-3e	OSC	<10	0.083	7.07	1.5×10^{-13}	0.471
MR-4a	OSC	<10	0.334	3.21	1.3×10^{-12}	0.514
MR-4b	OSC	<10	0.189	3.32	7.0×10^{-13}	0.505
MSH-4a	MSH	<10	0.035	6.31	6.9×10^{-14}	0.344
MSH-4b	MSH	<10	0.017	6.98	2.8×10^{-14}	0.340
MSH-4c	MSH	<10	0.015	7.61	2.0×10^{-14}	0.329

Appendix B (continued)

[§] Samples beginning with K represent specimens tested in a modified compaction permeameter; samples beginning with M represent specimens tested in a 4-inch-diameter triaxial load cell.

[†] S&G = Sand and gravel mix; S,G,&L = loam mix; MSH = Mount St. Helens 1980 debris; OSC = Osceola Mudflow debris; PERM = permeameter without sediment. See chapter 3 for descriptions of sediment characteristics.

[*] Initial density and porosity values characterize the material prior to saturation; final values characterize material after saturation.

APPENDIX C. BALANCE OF FORCES ON A RIGID WEDGE

Consider a rigid wedge that dams a fluid reservoir. Stability of the wedge against failure by sliding relies on a balance between a hydrostatic fluid pressure and a gravitational body force driving the wedge along the slip surface, and a basal friction force resisting sliding. The following analysis treats only rigid-wedge translation; it ignores the rotational moment about the centroid of mass. The analysis assumes that seepage forces arising from fluid moving through the wedge are negligible. A rigid-translation analysis which incorporates seepage forces in the context of landslide stability can be found in Iverson (1995b). Figure C1 illustrates the forces acting on the hypothetical wedge. The wedge has a height, H, a horizontal extent, L, and a surface slope, α. The slip surface dips at an angle, θ. The density of the fluid in the reservoir is ρ_f, and the bulk density of the wedge is ρ_{dam}.

HYDROSTATIC FLUID FORCE

The force arising from the pressure of a hydrostatic fluid driving the wedge down the slip surface is determined as follows. The horizontal force acting at a point on the rear surface of the wedge is given by

$$dF_{px} = \rho_f g z dA$$

where F_{px} is the hydrostatic fluid force in the x direction, g is gravitational acceleration, z is the vertical coordinate direction, and A is the area of the rear of the wedge. For a wedge of unit width, $dA = dz$. Hence,

$$dF_{px} = \rho_f g z dz .$$

Integrating over the rear surface of the wedge yields

$$F_{px} = \int_0^H \rho_f g z dz$$

$$F_{px} = \frac{1}{2}\rho_f g H^2.$$

Resolving this horizontal force into the component forces acting parallel and normal to the slip surface yields

$$F_{p\tau} = \frac{\rho_f g H^2}{2}\cos\theta \qquad \text{(C1a)}$$

$$F_{pn} = -\frac{\rho_f g H^2}{2}\sin\theta\,. \qquad \text{(C1b)}$$

GRAVITATIONAL BODY FORCE

The body force acting on the wedge is given by

$$F_g = m \cdot g$$

where $m = \rho_{dam} \cdot$ volume of wedge. The volume of the wedge is given by (figure C1B)

$$volume = \frac{1}{2}(W+R)\cdot Q\,.$$

For the geometry shown,

$$Q = H\cos\alpha$$

$$R = H\sin\alpha$$

$$P = \frac{L}{\cos\theta}$$

$$W = P\cos(\alpha - \theta)\,.$$

Thus

$$volume = \frac{1}{2}\left[\frac{LH\cos\alpha\cos(\alpha-\theta)}{\cos\theta} + H^2\sin\alpha\cos\alpha\right].$$

The gravitational body force acting on the wedge is therefore

$$F_g = \frac{\rho_{dam}}{2}g\left[\frac{HL\cos\alpha\cos(\alpha-\theta)}{\cos\theta} + H^2\sin\alpha\cos\alpha\right].$$

Resolving this force into component forces acting parallel and normal to the slip surface yields

$$F_{g\tau} = \frac{\rho_{dam}}{2} g \sin\theta \left[\frac{HL\cos\alpha\cos(\alpha-\theta)}{\cos\theta} + H^2 \sin\alpha\cos\alpha \right] \qquad \text{(C2a)}$$

$$F_{gn} = \frac{\rho_{dam}}{2} g \cos\theta \left[\frac{HL\cos\alpha\cos(\alpha-\theta)}{\cos\theta} + H^2 \sin\alpha\cos\alpha \right]. \qquad \text{(C2b)}$$

BASAL FRICTION FORCE

The basal friction force acting along the base of the wedge is assumed to be well described by Coulomb's rule, which states

$$F_{f\tau} = (\sum F_n) \tan\phi_b$$

where $\sum F_n$ is the sum of forces acting normal to the slip surface and ϕ_b is the angle of bed friction. The net force acting normal to the slip surface is given by

$$\sum F_n = F_{gn} + F_{pn}.$$

From equations (C1b) and (C2b), this yields

$$\sum F_n = \frac{\rho_{dam}}{2} \left[\frac{HL\cos\alpha\cos(\alpha-\theta)}{\cos\theta} + H^2 \sin\alpha\cos\alpha \right] g\cos\theta - \frac{\rho_f}{2} g H^2 \sin\theta .$$

Thus, the frictional force resisting sliding along the slip surface is given by

$$F_{F\tau} = \left[\frac{\rho_{dam}}{2}\left[\frac{HL\cos\alpha\cos(\alpha-\theta)}{\cos\theta} + H^2\sin\alpha\cos\alpha\right]g\cos\theta - \frac{\rho_f}{2}gH^2\sin\theta\right]\tan\phi_b . \quad \text{(C3)}$$

BALANCE OF FORCES

Balancing the forces given by (C1a), (C2a), and (C3) leads to

$$\frac{\rho_f}{\rho_{dam}}\frac{H}{L}\left[1+\tan\phi_b\tan\theta\right] = \left[\frac{\cos\alpha\cos(\alpha-\theta)}{\cos\theta} + \frac{H}{L}\sin\alpha\cos\alpha\right]\left[\tan\phi_b - \tan\theta\right].$$

Manipulating this expression, and utilizing the trigonometric identity

$$\tan\left[\phi_b - \theta\right] = \frac{\tan\phi_b - \tan\theta}{1+\tan\phi_b\tan\theta}$$

yields

$$\frac{\rho_f}{\rho_{dam}}\frac{H}{L} = \left[\frac{\cos\alpha\cos(\alpha-\theta)}{\cos\theta} + \frac{H}{L}\sin\alpha\cos\alpha\right]\left[\tan(\phi_b - \theta)\right]. \quad \text{(C4)}$$

Noting from the geometry shown in figure C1 that $H/L = \tan\alpha - \tan\theta$, and utilizing the identity

$$\cos(\alpha-\theta) = \cos\alpha\cos\theta + \sin\alpha\sin\theta$$

we find that (C4) reduces to

$$\tan(\phi_b - \theta) = \frac{\rho_f}{\rho_{dam}}(\tan\alpha - \tan\theta)$$

which is equation (5.1) given in the text, and is comparable to expressions for rigid-wedge analyses given by Dietrich (1988) and Iverson (1995b).

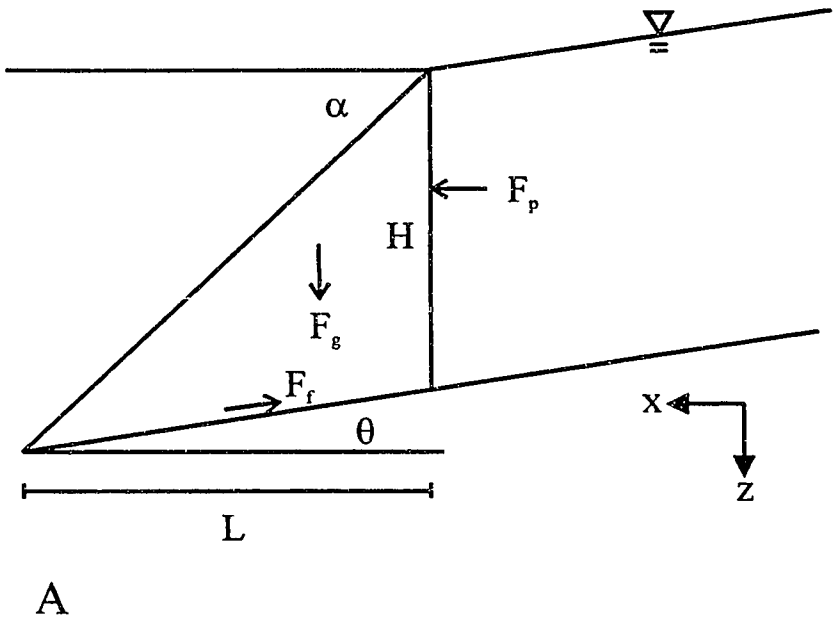

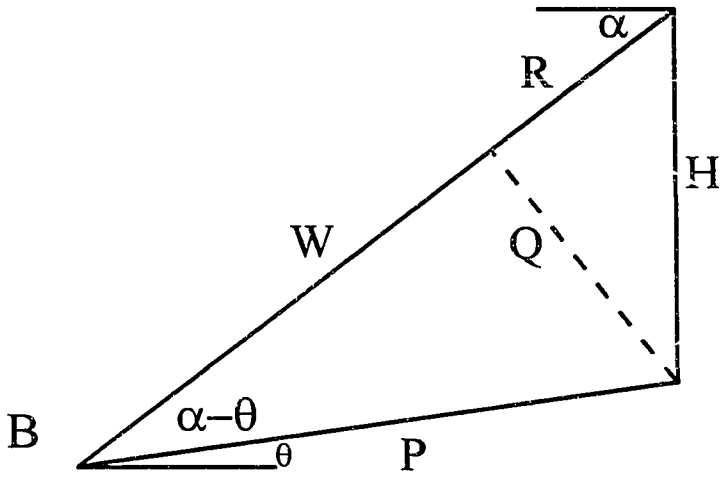

Figure C1. Schematic representation of wedge. A. Wedge geometry illustrating forces acting on wedge. See text for definitions. B. Angles and lengths used to compute wedge volume.

APPENDIX D. SOLUTIONS FOR ONE-DIMENSIONAL PERMEABLE BED ANALYSIS

Solution of equation (3.15) subject to a freely draining surface, a freely draining base, and an initial lithostatic fluid pressure defined in (3.21) (see Figure 3.4) is accomplished using the standard method of separation of variables for solving partial differential equations. At both the surface and the base of the domain the nonequilibrium fluid pressure, p_*, is zero for all time. Solution of the diffusion equation (3.15) subject to these initial and boundary conditions yields

$$p_* = 2p_{*0}\sum_{n=1}^{\infty}\frac{1}{n\pi}\sin(\lambda_n z)e^{-\lambda_n^2 D t} \tag{D1}$$

in which

$$\lambda_n = \frac{n\pi}{H}.$$

Combining (3.4), (3.7), (3.21) and (D1) yields an expression for the transient behavior of effective stress

$$\sigma'_{zz} = -(\rho_s - \rho_f)(1-\phi)g\left[(H-z) - 2H\sum_{n=1}^{\infty}\frac{1}{n\pi}\sin(\lambda_n z)e^{-\lambda_n^2 D t}\right]. \tag{D2}$$

The transient behavior of volume strain can be found by substituting (D2) into (3.10) to yield

$$\varepsilon_{zz} = -\frac{(1-2\nu)}{2G(1-\nu)}(\rho_s - \rho_f)(1-\phi)g\left[(H-z) + 2H\sum_{n=1}^{\infty}\frac{1}{n\pi}\sin(\lambda_n z)e^{-\lambda_n^2 D t}\right]. \tag{D3}$$

Integrating (D3), imposing the boundary condition that $u(0,t) = 0$, and setting $z = H$ yields an expression for transient behavior of surface displacement

$$u_H = \frac{(1-2\nu)}{2G(1-\nu)}(\rho_s - \rho_f)(1-\phi)g \cdot \left[2H\sum_{n=1}^{\infty}\frac{1}{n\pi\lambda_n}e^{-\lambda_n^2 Dt} - \frac{H^2}{2} - 2H\sum_{n=1}^{\infty}\frac{1}{n\pi\lambda_n}\cos(\lambda_n z)e^{-\lambda_n^2 Dt}\right]. \quad \text{(D4)}$$

VITA

JON J. MAJOR

BORN: November 25, 1958

EDUCATION

BS: University of Dayton, 1980

MS: The Pennsylvania State University, 1984

PhD: University of Washington, 1996

HONORS

Geological Society of America E.B.Burwell Award, 1991

SELECTED PUBLICATIONS

Major, J.J., and Voight, B., 1986, Sedimentology and clast orientations of the 18 May 1980 southwest flank lahars, Mount St. Helens, Washington: *Journal of Sedimentary Petrology*, v. 56, p. 691-705.

Iverson, R.M., and Major, J.J., 1986, Groundwater seepage vectors and the potential for hillslope failure and debris flow mobilization: *Water Resources Research*, v. 22, p. 1543-1548.

Iverson, R.M., and Major, J.J., 1987, Rainfall, groundwater flow, and seasonal movement at Minor Creek landslide, northwestern California: Physical interpretation of empirical relations: *Geological Society of America Bulletin*, v. 99, p. 579-594.

Major, J.J., and Scott, K.M., 1988, Volcaniclastic sedimentation in the Lewis River valley, Mount St. Helens, Washington--processes, extent, and hazards: *U.S. Geological Survey Bulletin 1383-D*, 38 p.

Major, J.J., and Newhall, C.G., 1989, Snow and ice perturbation during historical volcanic eruptions and the formation of lahars and floods: *Bulletin of Volcanology*, v. 52, p. 1-27.

Major, J.J., and Pierson, T.C., 1992, Debris flow rheology: Experimental analysis of fine-grained slurries: *Water Resources Research*, v. 28, p. 841-857.

Major, J.J., 1993, Rheometry of natural sediment slurries: Hydraulic Engineering '93, *Proceedings of ASCE 1993 Conference on Hydraulic Engineering*, San Francisco, CA, July 25-30, p. 1415-1421.

Trabant, D.C., Waitt, R.B., and Major, J.J., 1994, Disruption of Drift Glacier and origin of floods during the 1989-1990 eruptions of Redoubt Volcano, Alaska: *Journal of Volcanology and Geothermal Research*, v. 62, p. 369-385.

Waitt, R.B., Gardner, C.A., Pierson, T.C., Major, J.J., and Neal, C.A., 1994, Unusual diamicts emplaced during the December 15, 1989 eruption of Redoubt Volcano, Alaska: *Journal of Volcanology and Geotherma! Research*, v. 62, p. 409-428.

Major, J.J., Janda, R.J., and Daag, A.S., 1996, Watershed disturbance and lahars on the east side of Mount Pinatubo during the mid-June 1991 eruptions, *in* Newhall, C.G., and Punongbayan, R.S., eds., *Fire and Mud: Eruptions and Lahars of Mount Pinatubo, Philippines*. Quezon City, Philippine Institute of Volcanology and Seismology, and Seattle, University of Washington Press, p. 895-919.